

**BEARING BEHAVIOUR AND DESIGN OF
ALUMINIUM SUB-HEADS IN WINDOW WALL
FRAMES**



MASOUMEH AKBARI

**School of Engineering and Built Environment
Griffith University**

**Submitted in fulfilment of the requirements of the degree of
Doctor of Philosophy**

November 2020

ABSTRACT

A unique combination of properties makes aluminium one of the most desirable materials in many construction sectors including façade industry. Aluminium window walls as a façade system provide resistance against wind load and are decisive elements in the performance of the building envelope. In considering their complex functions, they are subjected to numerous criteria and continuing research and improvement. Window walls are commonly made of glass supported by aluminium framing members, and occupy a considerable share of the building cost. The aluminium frames of window walls (comprised of heads, sills, and mullions) transfer the wind loads from glass panels to the aluminium sub-frames (comprised of sub-heads and sub-sills). The sub-frames then transfer the loads to the slab through the bolt connections. Under this loading condition, the aluminium sub-heads (at the top of the system) are the dominante wind load bearing elements, and are prone to bearing failure due to their long flange length. This phenomenon of bearing failure has never been researched in the past. To address this gap, the structural performance of aluminium sub-heads subjected to concentrated load was investigated in this study using comprehensive experimental and numerical studies. Furthermore, accurate design rules were developed to predict the bearing capacities of aluminium sub-heads.

Two types of typical sub-head sections, known as C-shaped sub-heads and sub-heads with removable beads, were used in the experimental study. The main difference between these two sections is that the later included two parts (the base and the bead) which can facilitate effective installation and assembly of façade panels. Two series of experimental tests were conducted to investigate and evaluate the bearing behaviour of the aluminium C-shaped sub-heads and the sub-heads with removable beads. Four C-shaped sub-head sections and six sub-head with removable bead sections were tested subjected to bearing loads considering different loading and boundary conditions as well as different bearing widths. The governing modes of failure were found to be yielding and fracture at the web-to-flange junction, as a result of the bending of the cantilever flange. Following experimental tests, finite element models were developed to further investigate the bearing behaviour of the aluminium sub-heads. The general-purpose software ABAQUS, with implicit solver, was used to simulate the bearing behaviour of aluminium sub-heads. The models were validated using the

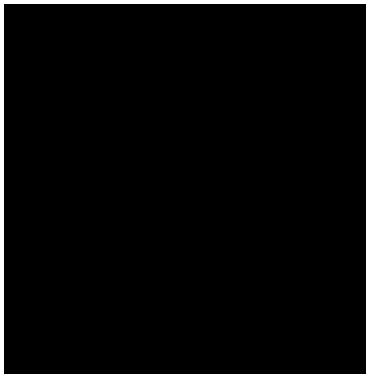
experimental results and a good agreement was achieved in terms of the ultimate strengths, the load-deflection responses and the failure modes. Subsequently, parametric studies were performed using validated models to investigate a wide range of aluminium sub-head sections with varying thicknesses, flange widths, loading conditions, and bearing widths.

Failure of aluminium sub-heads in the window walls under wind loading bear strong resemblance to the most prevalent failure mode in the cold-formed steel stud-to-track connection of a Light Gauge Steel (LSF) wall, which is the failure of the track under concentrated load. Since current aluminium standards do not have design criteria to predict the bearing strength of aluminium sub-head sections subjected to out-of-plane forces in window walls, the results acquired from this research were compared with the nominal bearing strengths predicted by the currently available cold-formed steel design rules (the North American Standard for Cold-Formed Steel Structural Framing (AISI S240, 2015), U.S. Army Corps of Engineers (TI 809-07, 1998), and Steel Stud Manufacturers Association (SSMA, 2000)) for the tracks in the stud walls. As a result of the comparisons, weaknesses in the current design standards were identified. Hence, based on the experimental and numerical results, new design rules were proposed which accurately predict the bearing capacities of aluminium sub-head sections. The findings of this research demonstrated that the proposed equations for estimating the ultimate bearing capacities of aluminium sub-head sections are reliable and in precise agreement with the experimental and numerical results.

DECLARATION

This work has not been previously submitted for a degree or diploma in any university. To the best of my knowledge and belief, this thesis contains no material previously published or written by another person except where due reference is made in the thesis itself.

Signed: _



Date: 14/11/2020

ACKNOWLEDGEMENT OF PAPERS IN THIS THESIS

Section 9.1 of the Griffith University Code for the Responsible Conduct of Research (“Criteria for Authorship”), in accordance with Section 5 of the Australian Code for the Responsible Conduct of Research, states:

To be named as an author, a researcher must have made a substantial scholarly contribution to the creative or scholarly work that constitutes the research output, and be able to take public responsibility for at least that part of the work they contributed. Attribution of authorship depends to some extent on the discipline and publisher policies, but in all cases, authorship must be based on substantial contributions in a combination of one or more of:

- Conception and design of the research project
- Analysis and interpretation of research data
- Drafting or making significant parts of the creative or scholarly work or critically revising it so as to contribute significantly to the final output.

Section 9.3 of the Griffith University Code (“Responsibilities of Researchers”), in accordance with Section 5 of the Australian Code, states:

Researchers are expected to:

- Offer authorship to all people, including research trainees, who meet the criteria for authorship listed above, but only those people.
- Accept or decline offers of authorship promptly in writing.
- Include in the list of authors only those who have accepted authorship.
- Appoint one author to be the executive author to record authorship and manage correspondence about the work with the publisher and other interested parties.
- Acknowledge all those who have contributed to the research, facilities or materials but who do not qualify as authors, such as research assistants, technical staff, and advisors on cultural or community knowledge.
- Obtain written consent to name individuals.


Listed below are co-authored papers resulted from this study and are presented in this thesis as Chapters 3, 4, 5 and 6. My contribution to each co-authored publication is outlined in the beginning of the relevant chapter. The bibliographic details of the papers are given below:

Akbari, M., Gunalan, S., Gilbert, B.P., Guan, H., Baleshan, B. Experimental Investigation on the Bearing Behaviour of Aluminium Sub-heads in Façade Systems. Thin-Walled Structures, 156 (2020). (Published)

Akbari, M., Gunalan, S., Gilbert, B.P., Talebian, N., Guan, H., Numerical Study on Bearing Behaviour and Design of Aluminium Sub-heads in Façade Systems. Thin-Walled Structures, Under review, 2020.

Akbari, M., Gunalan, S., Gilbert, B.P., Guan, H., Baleshan, B. Bearing Behaviour of Aluminium Sub-heads with Removable Beads in Façade Systems. Structures, Under review, 2020.

Akbari, M., Gunalan, S., Gilbert, B.P., Guan, H., Numerical Study on Bearing Behaviour and Design of Aluminium Sub-heads with Removable Beads in Façade Systems. Thin-Walled Structures, (In preparation in submitting).

(Signed)  (Date) 14.11.2020

Masoumeh Akbari

(Countersigned) _____ (Date) 14.11.2020

Dr Shanmuganathan Gunalan (Principal supervisor and co-author)

(Countersigned) _____ (Date) 14.11.2020

Professor Hong Guan (Associate supervisor and co-author)

(Countersigned) _____ (Date) 14.11.2020

Dr Hassan Karampour (Associate supervisor)

ACKNOWLEDGEMENTS

First and foremost, I would like to express my deepest gratitude to my principal supervisor, Dr Shanmuganathan Gunalan for his continuous support of my PhD study. His encouragement, trust, kindness and patience were always my motivation to continue and finish this challenging and novel research. His guidance helped me in all the time of research and writing of this thesis. I am very grateful to have had such an excellent supervisor.

I would like to thank my associate supervisors, Associate professor Benoit P. Gilbert for his encouragement, guidance, insightful academic advice, and ideas in this research, especially in the experimental test design and FE modelling, and Professor Hong Guan and Dr Hassan Karampour for their great guidance, encouragement and support from the initial to final stages of this PhD project. Professor Guan your supports were outstanding!! Especially during the write-up stage of my journal papers. My sincere thanks also go to Dr Nima Talebian for his technical guidance and advice in the FE modelling.

I would also like to thank my external partner for his experimental materials and professional support, Dr Balachandren Baleshan from G.James Glass & Aluminium, Pty Ltd.

I am greatly thankful to the technical staff, Chuen Yio Lo, Geoffrey Turner, David Bellchambers, Ian Underhill, and James Webster for helping me to conduct laboratory experiments.

I would like to express my appreciation to my parents for their continuous encouragement. I am grateful to them for supporting me spiritually throughout my study. Their support was my greatest motivation to move forward.

This research was made possible through the necessary laboratory facilities and accessible numerical facilities provided by Griffith University, and the financial support from Griffith

University International Postgraduate Research Scholarship and Griffith University
Postgraduate Research Scholarship.

TABLE OF CONTENTS

ABSTRACT.....	I
DECLARATION	III
ACKNOWLEDGEMENT OF PAPERS IN THIS THESIS.....	IV
ACKNOWLEDGEMENTS	VI
TABLE OF CONTENTS.....	VIII
LIST OF FIGURES	XIV
LIST OF TABLES	XXI
List of Symbols	XXIII
1. INTRODUCTION	1
1.1. General	1
1.2. General aluminium properties	1
1.3. Extrusion	3
1.4. Aluminium window wall frame	4
1.5. Definition and types of window walls	6
1.6. Bearing failure of sub-head in window-wall frame	6
1.7. Research question.....	9
1.8. Research aims and objectives.....	11
1.9. Proposed research/methodology	11
1.10. Thesis outlines.....	12
2. LITERATURE REVIEW	15
2.1. History of façade	15
2.2. Literature review on structural behaviour of aluminium façade system	15
2.3. Literature review on cold formed steel stud-to-track connection in LSF walls	18
2.3.1. Wind.....	18
2.3.2. Blast	32

2.3.3. Earthquake	36
2.4. Current design rules	39
2.4.1. North American Standard for Cold-Formed Steel Structural Framing (AISI S240, 2015)	40
2.4.2. U.S. Army Corps of Engineers (TI 809-07, 1998)	41
2.4.3. Bolte and LaBoube's method (2004)	42
2.5. Literature review findings	43
3. EXPERIMENTAL INVESTIGATION ON THE BEARING BEHAVIOUR OF ALUMINIUM SUB-HEADS IN FAÇADE SYSTEMS	44
3.1. Introduction	46
3.2. Experimental study	49
3.2.1. Test specimens	49
3.2.2. Material properties	52
3.2.3. Test Set-up and procedure	53
3.2.4. Preliminary tests	56
3.3. Test results and discussion	58
3.3.1. Load-displacement curves	58
3.3.2. Ultimate deformation limit	65
3.3.3. Ultimate loads	67
3.3.4. Failure modes	71
3.4. Design rules	73
3.4.1. Current design rules	73
3.4.2. Comparison of current design rules with test results	76
3.4.3. Proposed design rules	77
3.4.4. Comparison of test results with proposed design equations	83
3.4.5. Capacity reduction factor (ϕ_w)	88
3.4.6. Limitation of proposed design rules	89
3.5. Conclusion	90
4. Numerical Study on Bearing Behaviour and Design of Aluminium Sub-heads in Façade Systems	91
4.1. Introduction	93

4.2. Brief overview of experimental investigation	96
4.3. Finite element modelling.....	98
4.3.1. Geometry, element types and mesh	99
4.3.2. Material properties	101
4.3.3. Boundary conditions	103
4.3.4. Contacts.....	104
4.4. Analysis results and validation.....	105
4.4.1. Ultimate loads	105
4.4.2. Load-displacement curves	108
4.4.3. Failure modes.....	109
4.5. Parametric study.....	112
4.5.1. Effects of selected parameters	116
4.6. Design rules.....	125
4.6.1. Current design rules	125
4.6.2. Comparison of the FEA results with current design rules ($P_{FEA}/P_{Predicted}$).....	128
4.6.3. Proposed design rules	132
4.6.4. Capacity reduction factor	134
4.7. Conclusions	135
5. BEARING BEHAVIOUR OF ALUMINIUM SUB-HEADS WITH REMOVABLE BEADS IN FAÇADE SYSTEMS	136
5.1. Introduction	137
5.2. Experimental study.....	142
5.2.1. Test specimens	142
5.2.2. Material properties	145
5.2.3. Test set-up and procedure	146
5.3. Test results and discussion	149
5.3.1. Load-displacement curves	149
5.3.2 Ultimate loads (based on maximum load and ultimate deformation limit)	156
5.3.3. Failure modes.....	161
5.4. Design rule proposal.....	167
5.4.1. Current design rules	167

5.4.2. Comparison with current design rules	171
5.4.3. Derivation of proposed equation for sub-heads with removable beads	175
5.4.4. Comparison of test results with the proposed design equations	178
5.5. Capacity reduction factor (ϕw)	181
5.6. Conclusion.....	182
6. NUMERICAL STUDY ON BEARING BEHAVIOUR AND DESIGN OF ALUMINIUM SUB-HEAD WITH REMOVABLE BEAD SECTIONS IN FAÇADE SYSTEMS.....	184
6.1. Introduction	186
6.2. Brief overview of experimental investigation	189
6.3. Finite Element modelling	190
6.3.1. Geometry, element types and mesh	191
6.3.2. Material properties	192
6.3.3. Load and boundary conditions	194
6.3.4. Contact definition.....	195
6.4. Analysis results and validation.....	196
6.5. Parametric study	203
6.5.1. Effects of different parameters on the bearing capacities	207
6.5.2. Comparison between the ACSH sections and the ASHWRB sections.....	216
6.6. Design rules.....	218
6.6.1. Current design rules	218
TI 809-07 (1998) and SSMA (2000) recommend Equation (5) for estimating the bearing capacities P_n of cold-formed steel stud-to-track connections,	219
AISI S240 (2015) suggests Equation (6) for calculating P_n ,	220
6.6.2. Comparison of the FEA results with current design rules ($P_{FEA}/P_{Predicted}$)	222
6.6.3. Proposed design rules	227
6.6.4. Capacity reduction factor	229
6.7. Conclusions	230
7. Conclusions and Recommendations	232
7.1. Thesis findings	232
7.2. Significant outcomes of this research.....	234

7.3. Recommendations for future research.....	235
REFERENCE LIST	236
APPENDIX A. ALUMINIUM TENSILE COUPON TEST RESULTS	244
A.1. Section 675-027.....	244
A.2. Section 475-077.....	246
A.3. Section 475-057.....	248
A.4. Section 475-071.....	250
A.5. Section 165863	252
A.6. Section 475059	253
A.7. Section 475066.....	254
A.8. Section 475072	255
A.9. Section 475073	256
A.10. Section 520902.....	259
A.11. Section 675019	261
A.12. Section 675028	262
A.13 Section 875103	262
APPENDIX B. EXPERIMENTAL LOAD-DEFLECTION CURVES AND FAILURE MODES 263	
B.1 C-shaped sub-heads	263
B.1.1. 675-027.....	263
B.1.2. 475-077.....	268
B.1.3. 475-057.....	274
B.1.4. 475-071.....	286
B.2. Sub-heads with removable beads	297
B.2.1. 675028-475073.....	297
B.2.2. 475066-165863.....	301
B.2.3. 475059-520902.....	305
B.2.4. 875103-475073.....	309
B.2.5. 675019-520902.....	313

B.2.6. 475072-475073.....	316
---------------------------	-----

LIST OF FIGURES

Figure 1.1 Comparison between typical stress–strain curves for aluminium alloy and steel (Mazzolani, 2004).	2
Figure 1.2 Extrusion technique.	4
Figure 1.3 Details of window wall frame.	5
Figure 1.4 Bearing failure of the sub-head.	8
Figure 1.5 C-shaped sub-head sections (https://gjames.com/).	9
Figure 1.6 Sub-head with removable bead sections (https://gjames.com/).	9
Figure 2.1 Bearing failure of the sub-head under concentrated load.	17
Figure 2.2 Test apparatus (Lewis and Fox, 1999).	20
Figure 2.3 Stud-to-track connection (Lewis and Fox, 1999).	21
Figure 2.4 Failure mode: (a) stud web crippling, (b) track punch-through (Fox and Schuste, 2000).	22
Figure 2.5 Test set up (Bolte and LaBoube, 2004).	22
Figure 2.6 Failure in the screw-attached connection (Bolte and LaBoube, 2004).	23
Figure 2.7 Track failure: (a) failure pattern; (b) deflection (Bolte and LaBoube, 2004).	24
Figure 2.8 Test setup (Gerloff et al., 2004).	25
Figure 2.9 Typical load versus displacement curve (Gerloff et al., 2004).	26
Figure 2.10 Deformation model for the track (Rahman, 2005).	27
Figure 2.11 Jamb studs at interior location (Lewis, 2008).	27
Figure 2.12 Test setup (Lewis, 2008).	28
Figure 2.13 Typical web crippling: (a) failure mode, (b) load-displacement curve (Lewis, 2008).	29
Figure 2.14 Track punch-through: (a) failure mode, (b) test load-displacement curve (Lewis, 2008).	29
Figure 2.15 Screw pull-out: (a) failure mode, (b) load-displacement curve (Lewis, 2008).	30
Figure 2.16 Flange deformation under stud loading, (a) test setup, (b) track flange deformation (Espinoza et al., 2018).	31
Figure 2.17 Slotted track peak strength model (Espinoza et al., 2018).	31
Figure 2.18 Test setup (Bondok et al., 2015).	33
Figure 2.19 End-connection failure modes: (a) screw shear failure; (b) screw tilting and bearing failure; (c) bolt pullover failure (Bondok et al., 2015).	33

Figure 2.20 Bending and prying action test results: (a) Experiment; (b) FE model (Bewicket al., 2014).	34
Figure 2.21 FE model developed for conventional stud-to-track connection model (Bondok and Salim (2014)).	35
Figure 2.22 Developed finite-element model (Bondok et al. (2015))......	35
Figure 2.23 Test setup (Rahmanishamsi et al., 2016).....	37
Figure 2.24 Damage mechanisms of stud-to-track connections in the out-of-plan direction: (a) initial condition, (b) track-flange deformation, (c) permanent displacement of the stud, (d) stud-web crippling, (e) screw pull-out (Rahmanishamsi et al., 2016).	38
Figure 2.25 Sample numerical experimental hysteresis comparisons of specimen series.....	39
Figure 2.26 Failure pattern for the sub-head's flange.....	41
Figure 3.1 Details of window wall frame, sub-head and sub-sill.	47
Figure 3.2 Cantilever flange bending under concentrated load from mullion.	48
Figure 3.3 Sub-head sections.	51
Figure 3.4 Bolt connection details.	51
Figure 3.5 Tensile coupon test set-up.	52
Figure 3.6 Loading frame and position.....	54
Figure 3.7 Bearing test set-up.	55
Figure 3.8 Displacement monitoring positions for different bearing widths (Top view).....	56
Figure 3.9 Different bearing plate arrangements.	57
Figure 3.10 Load-displacement curves for different bearing plate arrangements.	58
Figure 3.11 Typical load-displacement curves.	59
Figure 3.12 Stages of the bearing tests for different engagement lengths.	61
Figure 3.13 Load-displacement curves for different bolt connection details for Section 475-057.....	62
Figure 3.14 Load-displacement curves for different engagement lengths and bolt connection details for Section 475-057.	64
Figure 3.15 Load-displacement curves for different section geometries with 50 mm bearing width and 25 mm engagement length.	65
Figure 3.16 Ultimate bearing capacity based on ultimate deformation limit (UDL).....	67
Figure 3.17 Ultimate load versus bearing widths for different section geometries.	71
Figure 3.18 Bearing failure modes of Section 475-057 under different bearing widths.	72
Figure 3.19 Bearing failure modes of Section 475-057.....	73
Figure 3.20 Stress distribution in sub-head flange element.	74

Figure 3.21 Comparison of effective sub-head length (w_{dt}) against bearing width (N).....	79
Figure 3.22 Comparison of effective sub-head length (w_{dt}) against flange width (b_f).....	79
Figure 3.23 Comparison of effective sub-head length (w_{dt}) against slip gap (e).	80
Figure 3.24 Relationship between θ and slip gap-flange thickness, based on maximum load.	81
Figure 3.25 Relationship between θ and slip gap-flange thickness, based on ultimate deformation limit (UDL).....	82
Figure 3.26 Comparison of experimental ultimate strengths ($P_{Exp-Max.}$) with those of current and proposed design rules ($P_{Predicted}$), based on maximum load.	84
Figure 3.27 Comparison of experimental ultimate strengths ($P_{Exp-UDL.}$) with those of current and proposed design rules ($P_{Predicted}$), based on ultimate deformation limit (UDL).	84
Figure 3.28 Comparison of experimental ultimate strengths ($P_{Exp-Max.}$) with those of proposed design rules ($P_{Predicted}$) for different structural parameters, based on maximum load.....	86
Figure 3.29 Comparison of experimental ultimate strengths ($P_{Exp-UDL.}$) with those of proposed design rules ($P_{Predicted}$) for different structural parameters, based on ultimate deformation limit (UDL).....	88
Figure 4.1 Details of window wall system.....	94
Figure 4.2 Bearing test setup and ASH section profile (Akbari et al., 2020a).	97
Figure 4.3 Bolt connection details (Akbari et al., 2020a).....	97
Figure 4.4 Finite element model.	98
Figure 4.5 a) Different segments on the sub-head cross-section, b) Centerline of the simplified cross-section for the sub-head modelled with shell elements.....	100
Figure 4.6 Simplified geometry of the sub-head cross-section.....	100
Figure 4.7 Ultimate load versus mesh size for 675-027/25/50/2B specimen.	101
Figure 4.8 Stress-strain curves of Section 475-057.	102
Figure 4.9 Boundary conditions and bolted connection.	104
Figure 4.10 Interactions between elements (master surface shown in red and slave surface shown in purple).	105
Figure 4.11 Representative experimental load-displacement curve showing maximum load (Max) and ultimate deformation limit (UDL).....	106
Figure 4.12 Comparison of experimental and numerical load-displacement curves.....	109
Figure 4.13 Comparison of experimental and numerical failure modes under 15 mm engagement length.	111

Figure 4.14 Comparison of experimental and numerical failure modes under 25 mm engagement length.	112
Figure 4.15 Different shapes of the web-flange junction of the ASH: (a) combination of curved and straight surfaces, (b) curved shape, (c) sharpened edge.	113
Figure 4.16 Cross-sections of the FE model used for validation and parametric study.	114
Figure 4.17 Bi-linear CSM model for 6063-T6 aluminium alloy.	116
Figure 4.18 Ultimate bearing capacity (P_{FEA}) versus bearing width (N) for different sectional geometries (UFT with different flange widths and thicknesses).	117
Figure 4.19 Ultimate bearing capacity (P_{FEA}) of ASH sections (with UFT and NUFT) versus flange width (b_f) for different thicknesses (t) (models with $N = 50$ mm).	119
Figure 4.20 Ultimate bearing capacity (P_{FEA}) versus thickness (t) for different bearing widths (N) (models with $b_f = 40$ mm).	120
Figure 4.21 Load-displacement curves for different engagement lengths (D) for Section 1 (with $b_f = 40$ mm, $t = 2$ mm, and $N = 50$ mm).	121
Figure 4.22 Ultimate bearing capacity (P_{FEA}) versus engagement length (D) for different bearing widths (N) and thicknesses (t) (models with $b_f = 40$ mm).	122
Figure 4.23 Ultimate bearing capacity (P_{FEA}) versus (e/t) for different bearing widths (N) and thicknesses (t) (models with $b_f = 65$ mm).	123
Figure 4.24 Ultimate bearing capacity (P_{FEA}) versus (e/t) ² for different bearing widths (N) and thicknesses (t) (models with $b_f = 65$ mm).	124
Figure 4.25 Failure pattern for the sub-head flange.	127
Figure 4.26 Comparison between experimental and numerical bearing capacities, and predictions of the DRSs.	129
Figure 4.27 Comparison between experimental and numerical capacities and predictions of the DRA_I (Akbari et al., 2020a).	131
Figure 4.28 Ultimate load obtained from FE parametric models, based on maximum load criterion (Max).	131
Figure 4.29 Comparison between experimental and numerical capacities and predictions of the DRA_P	134
Figure 5.1 Window wall system (Herston quarter- Brisbane).	138
Figure 5.2 Details of window wall frame and sub-head to mullion connection.	139
Figure 5.3 Geometric details of sub-head sections.	141
Figure 5.4 Sub-heads with removable beads.	145
Figure 5.5 Engineering tensile stress-strain plot of Section 675028.	146

Figure 5.6 Test set up.....	148
Figure 5.7 Typical load-displacement curves.	150
Figure 5.8 Comparison of load-displacement curves for different section geometries with 50 mm bearing width and 25 mm engagement length.....	151
Figure 5.9 Load-displacement curves and stages of the bearing tests corresponding to 25 mm engagement lengths for 675019-520902/25/50.	152
Figure 5.10 Comparison of load-displacement curves for different section geometries with 50 mm bearing width and 15 mm engagement length.	153
Figure 5.11 Load-displacement curves and stages of the bearing tests corresponding to 15 mm engagement lengths for 875103-475073/15/50.	154
Figure 5.12 Load-displacement curves with different engagement length for Specimen 675028-475073.	156
Figure 5.13 Ultimate bearing capacity based on ultimate deformation limit (UDL).....	158
Figure 5.14 Comparison of ultimate load versus bearing width for different section geometries.	161
Figure 5.15 Flange deformation and failure modes under concentrated loading.	163
Figure 5.16 Bearing failure modes under 25 mm engagement length.	164
Figure 5.17 Bearing failure modes under 15 mm engagement length.	165
Figure 5.18 Comparison of experimental failure modes for C-shaped sub-head and sub-head with removable bead.	166
Figure 5.19 Stress distribution in the bead flange.....	168
Figure 5.20 Variation of the effective sub-head length (w_{dt}) against bearing width (N).	176
Figure 5.21 Variation of the effective sub-head length (w_{dt}) against flange width (b_f).	176
Figure 5.22 Variation of the effective sub-head length (w_{dt}) against slip gap (e).....	177
Figure 5.23 Relationship between θ and slip gap-flange thickness.	178
Figure 5.24 Comparison of experimental ultimate strengths ($P_{Exp-Max2.}$) with those of current and proposed design rules ($P_{Predicted}$), based on maximum load.	180
Figure 5.25 Comparison of experimental ultimate strengths ($P_{Exp-UDL.}$) with those of current and proposed design rules ($P_{Predicted}$), based on ultimate deformation limit (UDL).	181
Figure 6.1 Window wall system.	187
Figure 6.2 Bearing test set-up and ASHWRB section profile Akbari et al., 2020b).	190
Figure 6.3 Simplified FE models (Test set-up).....	191
Figure 6.4 Stress-strain curve (675028 section).	193
Figure 6.5 FE boundary conditions and bolted connection.	195

Figure 6.6 Interactions between elements (master surface shown in red and slave surface shown in purple).	196
Figure 6.7 Typical experimental load-displacement curve showing the maximum load (Max) and ultimate deformation limit (UDL) Akbari et al. (2020b).	197
Figure 6.8 Comparison of experimental and numerical load versus vertical displacement curves.	199
Figure 6.9 Comparison of experimental and numerical failure modes under 15 mm engagement length.	201
Figure 6.10 Comparison of experimental and numerical failure modes under 25 mm engagement length.	202
Figure 6.11 Cross sections of the FE model used for parametric study and validation.....	205
Figure 6.12 Load-displacement curves for different web height (d) of the bead ($b_f = 65$ mm and $t = 3$ mm, $N = 50$ mm).	205
Figure 6.13 Bi-linear CSM model for 6063-T6 aluminium alloy.....	207
Figure 6.14 Load-displacement curves for different bearing widths (N) with 15 mm engagement length (D) for Section 6 ($b_f = 65$ mm and $t = 4$ mm).	208
Figure 6.15 Ultimate bearing capacity (P_{FEA}) versus bearing width (N) for different sectional geometries (with different flange widths (b_f) and thicknesses (t)).	209
Figure 6.16 Ultimate bearing capacity (P_{FEA}) of the ASHWRB sections versus flange width (b_f) for different thicknesses (t) (models with $N = 50$ mm).	210
Figure 6.17 Load-displacement curves for different flange widths (b_f) (models with $D = 20$ mm, $N = 50$ mm, and $t = 4$ mm).	211
Figure 6.18 Load-displacement curves for different thicknesses (t) (models with $D = 30$ mm, $N = 150$ mm, and $b_f = 65$ mm).	212
Figure 6.19 Ultimate bearing capacity (P_{FEA}) versus thickness (t) for different bearing width (N) (models with $b_f = 50$ mm).	213
Figure 6.20 Load-displacement curves for different engagement lengths (D) for Section 6 (with $b_f = 65$ mm and $t = 4$ mm, $N = 150$ mm).	214
Figure 6.21 Ultimate bearing capacity (P_{FEA}) versus engagement length (D) for different bearing widths (N) and thicknesses (t) (models with $b_f = 50$ mm).	214
Figure 6.22 Ultimate bearing capacity (P_{FEA}) versus (e/t) for different bearing width (N) and thicknesses (t) (models with $b_f = 65$ mm).	215
Figure 6.23 Ultimate bearing capacity (P_{FEA}) versus $(e/t)^2$ for different bearing widths (N) and thicknesses (t) (models with $b_f = 65$ mm).	216

Figure 6.24 Comparison of load-displacement curves for the ACSH sections (C) and ASHWRB (RB) for 25 mm engagement length (models with $b_f = 100$ mm and $t = 3$ mm)...	218
Figure 6.25 Simplified stress distribution on the bead flange.	219
Figure 6.26 Comparison between numerical bearing capacities, and predictions based on DRSs (AISI S240, 2015; TI 809-07, 1998; SSMA, 2000; Bolte and LaBoube, 2004).	223
Figure 6.27 Comparison between numerical capacities and predictions based on DRA (Akbari et al., 2020b).	225
Figure 6.28 Ultimate load obtained from the FE parametric models.	226
Figure 6.29 Comparison between numerical capacities and predictions based on DRA (Akbari et al., 2020b).	227
Figure 6.30 Comparison between numerical capacities and predictions based on DRA_p	229

LIST OF TABLES

Table 3.1 Test specimen details.	50
Table 3.2 Geometric details of the aluminium sub-head sections.	51
Table 3.3 Mechanical properties of sub-head sections.	53
Table 3.4 Comparison of experimental ultimate strengths with current and proposed design rules, based on maximum load.....	68
Table 3.5 Comparison of experimental ultimate strengths with current and proposed design rules, based on ultimate deformation limit (UDL).....	69
Table 4.1 Geometric details of the ASH sections.	98
Table 4.2 Mechanical properties of the ASH sections.....	103
Table 4.3 Comparison of experimental and FEA bearing capacities based on maximum load (Max) and ultimate deformation limit (UDL).....	107
Table 4.4 Parametric study model details of the ASH sections.	115
Table 4.5 Proposed coefficients for effective sub-head length (w_{dt}).	128
Table 4.6 Comparison of mean and COV values of bearing capacity ratios ($P_{FEA}/P_{Predicted}$).	132
Table 5.1 Number of tests for all test specimens.	144
Table 5.2 Geometric details of the aluminium sub-head sections with removable beads.	144
Table 5.3 Mechanical properties of test specimens.	146
Table 5.4 Laser positions from the mid length in mm.	149
Table 5.5 Experimental ultimate loads for aluminium sub-head with removable bead, based on maximum load and ultimate deformation limit (UDL).....	159
Table 5.6 Proposed coefficients for the effective sub-head length (w_{dt}).	171
Table 5.7 Experimental ultimate loads and comparisons with current design rules.....	172
Table 5.8 Experimental ultimate loads and comparisons with proposed design rules.	174
Table 6.1 Geometric details of the ASHWRB sections (Akbari et al., 2020b).	190
Table 6.2 Mechanical properties of the ASHWRB sections (Akbari et al., 2020b).	193
Table 6.3 Comparison of test and ABAQUS FEA results for maximum load and ultimate deformation limit.	198
Table 6.4 Parametric study model details of the ASHWRB sections.....	203
Table 6.5 Comparison of the average values of the ACSH to the ASHWRB bearing capacity ratios considering different parameters.....	217

Table 6.6 Comparison of average bearing capacity ratios between different parameters for the ACSH sections and the ASHWRB sections.	217
Table 6.7 Proposed coefficients for the effective sub-head length (w_{dt}).	222
Table 6.8 Comparison of mean and COV values of bearing capacity ratios ($P_{FEA}/P_{Predicted}$).	223

List of Symbols

NOTATION

The following symbols are used in this thesis:

f_y	yield stress
$f_{0.2}$	0.2% proof stress
$f_{0.1}$	stress at a residual strain of 0.1%
b_{eff}	effective track length
L_U	effective flange length in the upper flange
L_L	effective flange length in the lower flange
S	stud spacing
w_{stud}	stud flange width
Δ	partial track length
d	section depth
t_w	web thickness
$t_{f,max}$	maximum flange thickness
$t_{f,min}$	minimum flange thickness
$t_{w,max}$	maximum web thickness
$t_{w,min}$	minimum web thickness
t_f	flange thickness
r_i	internal radius
L	specimen length
N	bearing length
D	engagement length
1B	one-bolt connection
2B	two-bolt connection
E	elastic modulus
f_u	ultimate strength
ϵ_f	elongation at fracture
RHS	rigid support
D_0	initial displacement observed in Stage 1

UDL	Ultimate deformation limit
D_E	yield displacement
M	bending moment
Z_x	section modulus
e	slip gap
e/t	slip gap to thickness ratio
P_n	nominal strength
w_{dt}	effective sub-head length
θ	derive angle
b_f	sub-head's flange width
ϕ_w	capacity reduction factor
M_m	mean of the material factor = 1.1
V_M	COV of the material factor = 0.06
F_m	mean of the fabrication factor = 1.0
V_F	COV of the fabrication factor = 0.05
V_Q	COV of the load effect = 0.21
β_0	target reliability index = 2.5
C_n	correction factor depending on the number of tests (n)
P_m	mean value of the test-to-predicted load ratio
V_P	COV of the test-to-predicted load ratio
E_{sh}	strain hardening slope
ε_u	ultimate strain
f_u	ultimate stress
ε_y	yield strain
σ_t	true stress
ε_t	true strain
σ_e	engineering stress
ε_e	engineering strain
UDL	ultimate deformation limit criterion
M	Maximum load criterion
UFT	uniform flange thickness
NUFT	non-uniform flange thickness
DRA _I	initially proposed design rules for ASH sections

<i>DRS_s</i>	current cold-formed steel design rules
<i>DRA_p</i>	proposed design rules
<i>ASH</i>	aluminium sub-head
<i>ACSH</i>	aluminium C-shaped sub-head
<i>ASHRB</i>	aluminium sub-head with removable bead

1. INTRODUCTION

1.1. General

In the building sector, the application of aluminium alloys in load carrying structures as well as building envelopes has received attention over the past decades. The aluminium industry has evolved constantly over the last century. In 1930, aluminium began to be utilized in the construction market. Most famously, the Empire State Building was one of the first modern structures to rely mostly on aluminium. With the arrival of extrusions and curtain wall technology after World War II, aluminium was first used to clad buildings (Kissell and Ferry, 2002). The 1960s experienced the fastest development of the market for aluminium. However, no codifications and recommendations were found at that time regarding aluminium structures. The first international recommendation for aluminium alloy structures was published in 1978 (Mazzolani, 1978) with the purpose of unifying computational methods for the design of aluminium constructions in civil engineering and in other structural applications.

1.2. General aluminium properties

Aluminium represents a wide variety of alloys whose mechanical properties vary widely from one group to another (Mazzolani, 1978). Aluminium is attractive in many applications in comparison with steel, not only in terms of the favourable life-cycle price of aluminium, but also with respect to its physical properties, the production process, and technological features (Mazzolani, 2004). Aluminium is one of the lightest and strongest available materials with a density equal to one third that of steel. Aluminium also provides great resistance to corrosion due to the natural oxide coating that forms on the aluminium surface when it is exposed to air. Furthermore, the extrusion fabrication process allows aluminium to be easily formed to any shape. Aluminium also has a unique combination of properties such as durability, recyclability, ductility, and good thermal and electrical conductivities. Some of these advantages are surpassed by the fact that the elastic modulus of aluminium alloys is only one third that of steel. Hence, a structural component consisting of an aluminium alloy will have larger deformations and be more susceptible to instability than a geometrically similar structural component made of steel.

From the comparison of the two typical stress–strain curves in Figure 1.1, it can be inferred that both materials behave linearly in the elastic region with a different slope (elastic modulus E) up to the yield stress f_y (elastic limit $f_{0.2}$). After the elastic range, aluminium alloys have a strain-hardening behaviour without yield plateau in stress-strain curves (Mazzolani, 2004), whereas steel has a perfectly plastic branch after the yielding.

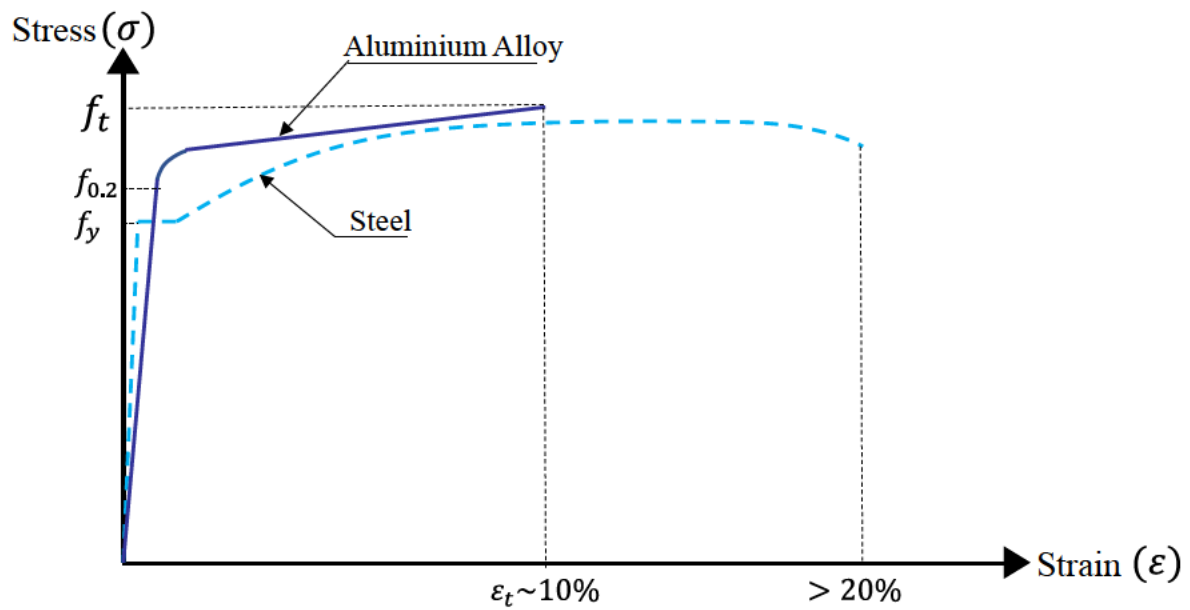


Figure 1.1 Comparison between typical stress–strain curves for aluminium alloy and steel (Mazzolani, 2004).

The Ramberg-Osgood model is the most typical equation illustrating the generalized relationship between stress and strain of aluminium alloy (Ramberg and Osgood, 1943):

$$\epsilon = (\sigma/E) + 0.002(\sigma/f_{0.2})^n \quad (1.1)$$

where E is the initial elastic modulus, $f_{0.2}$ is the 0.2% proof stress, namely the nominal yield strength, and n is the exponent of Ramberg-Osgood expression. The three coefficients are specified based on tensile coupon tests.

The exponent n of the Ramberg–Osgood law is expressed by Eq. (1.2):

$$n = \frac{\ln 2}{\ln \left(\frac{f_{0.2}}{f_{0.1}} \right)} \quad (1.2)$$

where $f_{0.1}$ is the stress at a residual strain of 0.1%.

1.3. Extrusion

Aluminium framing is used in facade systems due to the extrusion ability of aluminium, which provides elegant and complex building enclosures. Extrusion is the process of shaping aluminium into objects with a specific cross-sectional profile by forcing it to flow through a die opening, as shown in Figure 1.2. Aluminium is first heated to become soft, but does not melt. A die made of cast steel (which resists high temperatures and pressures) is then used to form the profile. Typical extrusion products ranging from rod, bar or tube to complex cross-sectional designs are used in transportation, building and construction.

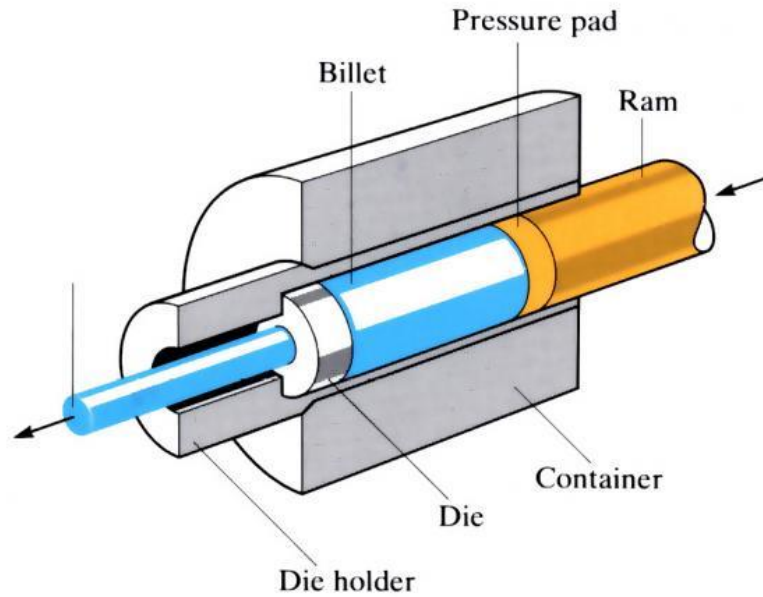


Figure 1.2 Extrusion technique.

(From <https://www.open.edu/openlearn/science-maths-technology/engineering-technology/manupedia/hot-extrusion>)

1.4. Aluminium window wall frame

In the exterior surface of a building structure a transparent façade system is formed which plays complex function roles. An aluminium window wall is a type of building façade which represents a considerable proportion of the total cost of the construction industry. The window wall has arisen as a substitute for the common curtain wall to accommodate the requirements of flexibility, time and cost. Curtain walls are installed at the front of the slab, while window walls are positioned between the slabs and provide a distinct separation between the floor levels. Since window walls are installed from the inside of a building and between floors, the risk of sound transmittance is greatly reduced as noise cannot reverberate across the entire system. Furthermore, window walls offer high performance design requirements such as air infiltration and water resistance, and afford design building displacements. A window wall system typically consists of extruded aluminium frame walls with infill glazing. The glazing units provide natural light, wind resistance and a wide view from inside a building. Although window wall framing supports its own internal elements and stabilises the glazing units, it does not provide any stiffness to the building structure. Aluminium window walls include a number of individual components responsible for

fulfilling all the functions of a façade. These elements are known as mullions, heads, sills, sub-heads, and sub-sills, which most frequently are tubular and open complex sections.

A mullion is a vertical divider that separates the window walls into different panels. Vertical members (mullions) and horizontal members (head and sill transoms) are screwed together to make a frame. This frame is enclosed in areas between the sub-head and sub-sill (connected to the structure), as schematically illustrated in Figure 1.3. However, no screw connection exists between the heads and sub-heads, due to the requirements of space for structural movement and thermal expansion, as well as fabrication and installation tolerances of the aluminium frame. Hence, under the wind load, the sub-head (with long flange length) moves with the slab to ensure that the windows of the building are not crushed or do not disengage.

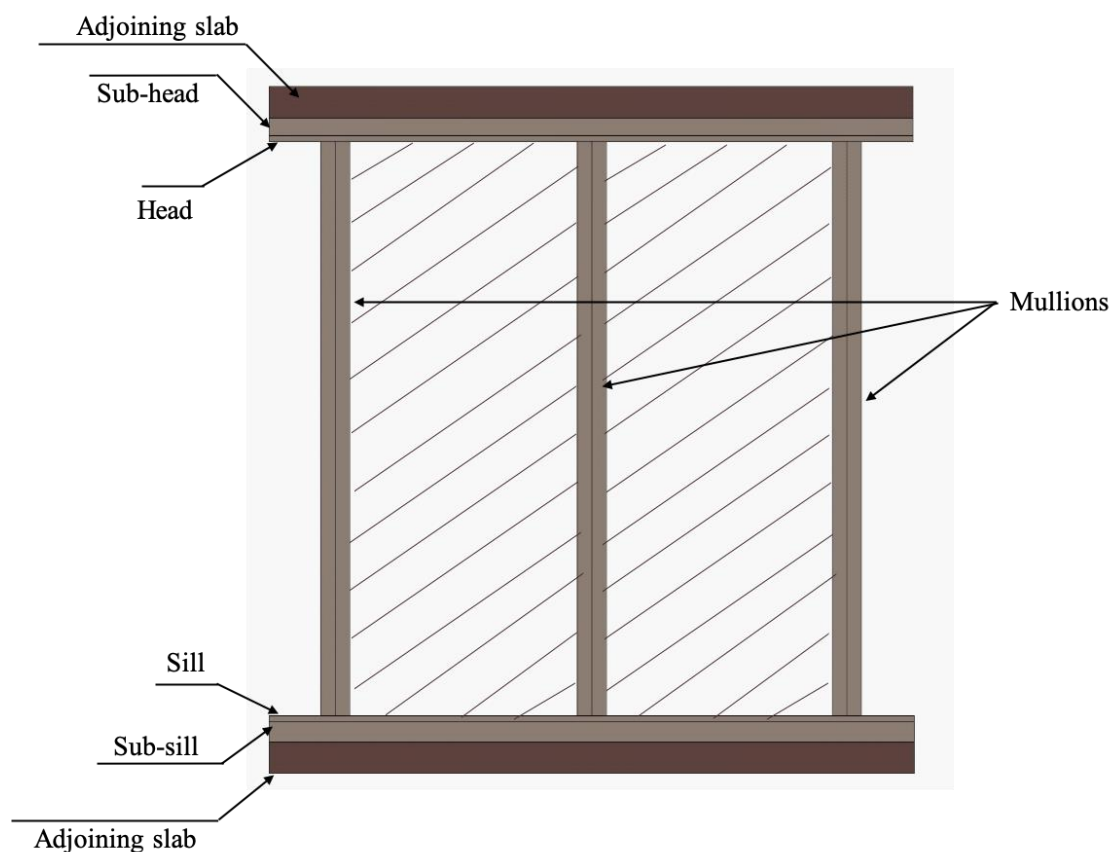


Figure 1.3 Details of window wall frame.

1.5. Definition and types of window walls

To improve understanding of the processes involved in the production of a window wall system, several definitions must be clarified, such as of fabrication, assembly, glazing, and installation. Fabrication includes all machining operations which can be performed on the aluminium extrusion members such as drilling, cutting, and punching. Assembly includes the fastening of aluminium framing members together to create a frame which supports the glass panel. Glass plates are widely used as glazing panels attached to the aluminium frame due to the unique quality of transparency and their acceptable strength. To make the frame air and watertight, sealant must be applied on the joints in the frame.

Facades are generally produced in three ways, namely stick-built, semi-unitized, and unitized systems. Stick-built wall is manufactured piece by piece, assembled and glazed at the site. In stick-built, vertical members (mullions) are assembled first, then horizontals are connected to the verticals. Finally, glazing panels are installed after the framing is made ready. Stick-built walls have higher labour costs and a longer schedule. Additionally, stick-built systems are often installed outdoors with exposure to the weather; hence, it is difficult to obtain proper sealant and adhesion in variable weather conditions outdoors. In the semi-unitized system, the mullion members are installed first, then pre-assembled frames are positioned between them. Window wall systems are produced in a unitized way. This system is composed entirely of large frame units, assembled and glazed at the factory under controlled conditions, and shipped to the site and installed in a sequential manner. The mullion member is connected to the sill and head members, and with a glass panel, in the factory. Then, this frame is positioned between sub-head and sub-sill members at the site. Unitized window wall systems minimize time and dependence on field labour and allow for rapid closure of the building. Quality is also significantly improved, in comparison with site-built facade walls, due to fabrication in an automated manufacturing process.

1.6. Bearing failure of sub-head in window-wall frame

The window wall system absorbs, transmits and sustains the loads acting on it through carefully designed vertical and horizontal bearing elements. Hence, these complex structures are subject to various criteria and accordingly to ongoing research. Apart from the self-

weight, the main loads applied on the window wall are wind, rain, temperature and earthquake. Pressure in building envelopes loaded with wind is much higher than those on the central parts of the buildings. Hence, wind is the governing load of façade systems. Poor design and damage to the window wall under wind load would jeopardize the façade stability and lead to destruction of the building. The effects of the strong suction force of wind are specifically dominant on the junctions and connections of the structures and on the top parts of the façade near the roof. Thus, the exposure to high wind pressures must be taken into consideration in the design of the aluminium window wall frames in high-rise buildings. When a window wall frame is subjected to wind pressure through the glass panel, this load is transferred towards the frame consisting of mullions, heads and sills. The aluminium frame then transfers this load to the sub-frame (the sub-heads and sub-sills). Finally, the load is transferred to the building structure through the connections of the sub-frames to the building.

Under this loading condition, the window frame (mullion and head) will bend and then make contact with the sub-frame comprised of sub-head and sub-sill. Sub-heads at the top of the window wall are more vulnerable to bearing failure than sub-sills owing to their longer flange length (see Figure 1.4).

In this study, bearing width was conservatively assumed to be concentrated at the mullion reactions, while the head transom distributes the load from the mullion and contacts the flange. The contact length depends on several parameters, such as the mullion width, the stiffness of the head, and the spacing between mullions. However, the estimation of contact lengths with regard to this study is uncertain and challenging. Hence, different bearing widths are adopted in this research. Figure 1.4 shows the sub-head being subjected to a transverse concentrated load from the mullions. Once the load is high, these sub-heads are at risk of localised bearing failures. Bending of the cantilever flange and yielding at the web-flange junctions (Figure 1.4)) are common bearing failure modes, and these failures should be addressed in the aluminium window wall design. Furthermore, in this study bearing width was conservatively assumed to be concentrated at the mullion reactions, while the head transom distributes the load from the mullion and contacts the flange.

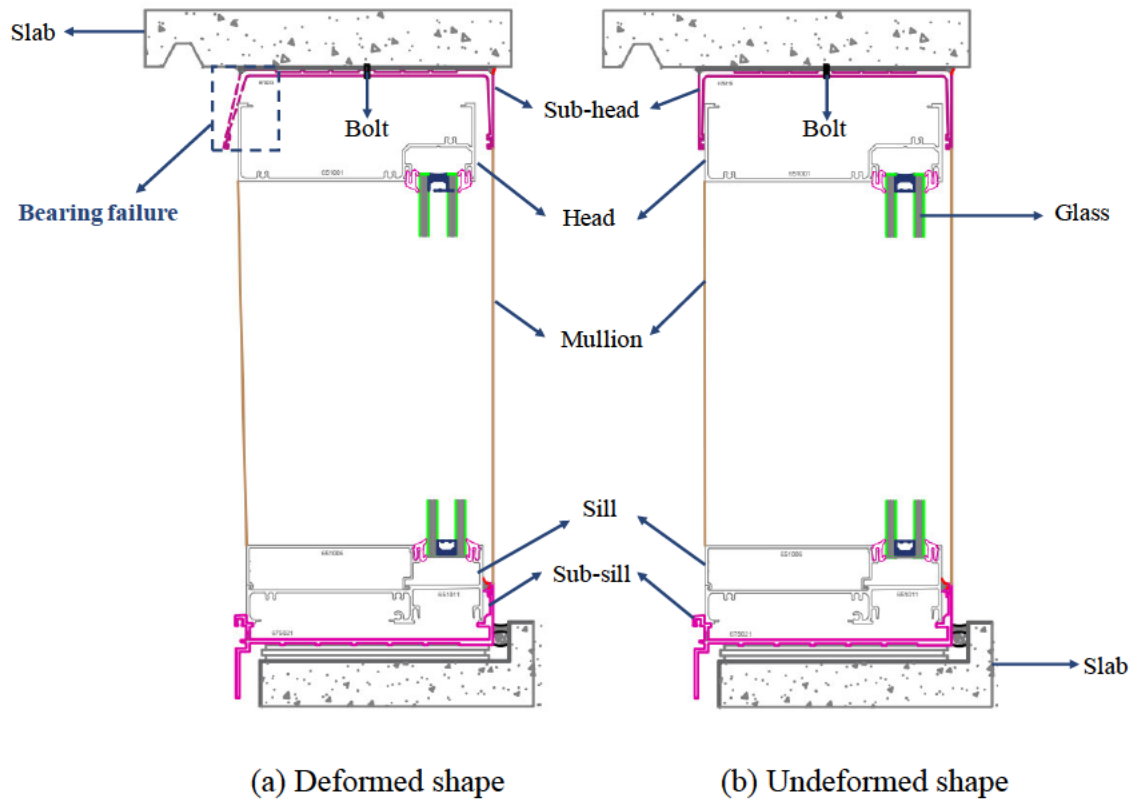


Figure 1.4 Bearing failure of the sub-head.

Details of two types of typical sub-heads, C-shaped sub-heads and sub-heads with removable beads, are demonstrated in Figure 1.5 and Figure 1.6, respectively. The main difference between these two sections is that the sub-head with a removable bead included two parts (a base and a bead), which are connected together without any screw fastener. This facilitates installation, easy removal of the bead from the system in the event of construction faults, and achieves desired performance in window walls. This difference has a strong impact on bearing behaviours, failure modes and bearing capacities of aluminum C-shaped sub-heads and sub-heads with removable beads under concentrated load applied by mullion, which needs comprehensive investigation.

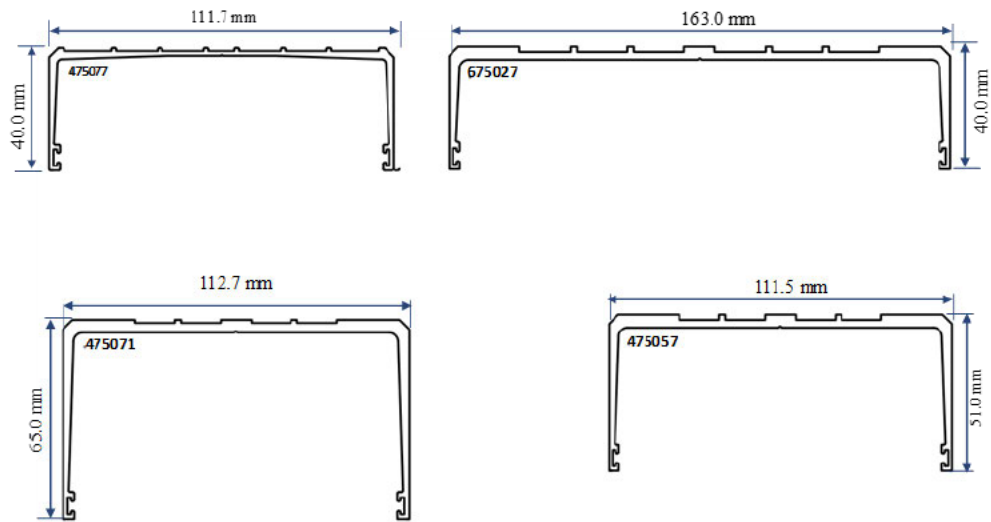


Figure 1.5 C-shaped sub-head sections (<https://gjames.com/>).

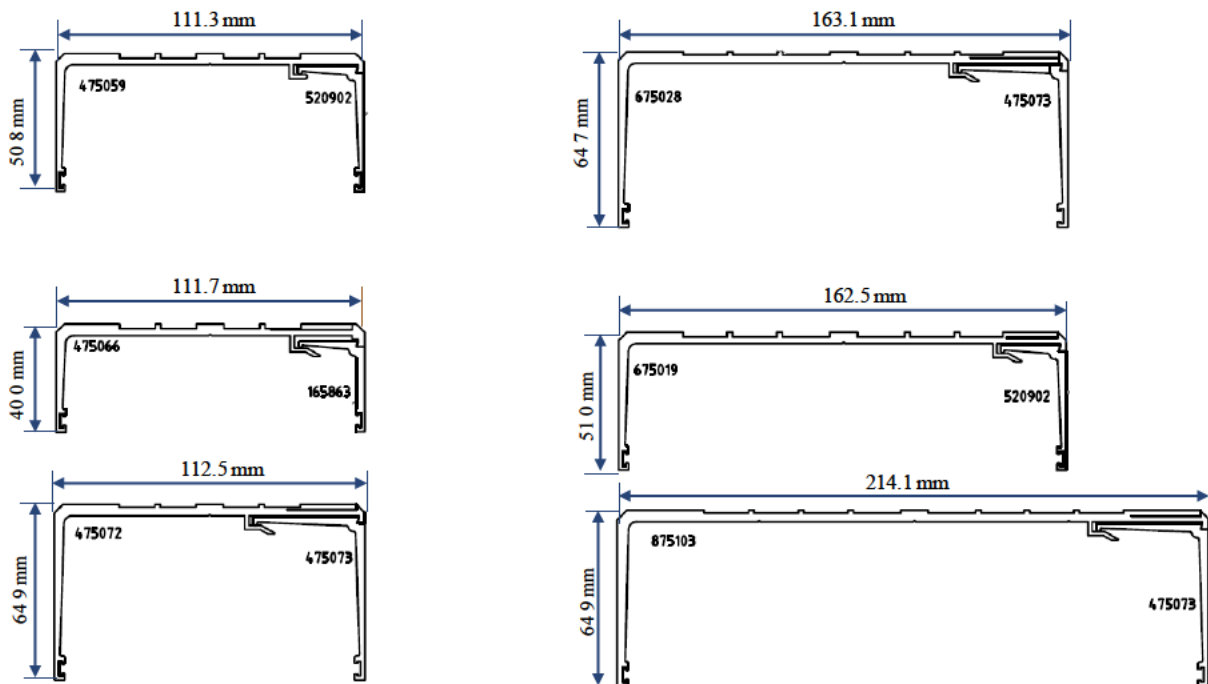


Figure 1.6 Sub-head with removable bead sections (<https://gjames.com/>).

1.7. Research question

Façade engineering is an area of immense growth, which is attracting significant interest from industry in Australia. An assessment of façade system performance has been encouraged in Australia to avoid large expense and ensure safety during the service life of the structures. In aluminium window wall design, substantial focus has been placed on protecting

the window wall from wind loads. As mentioned in Section 1.6., under wind load, the horizontal members at the top of the frame, known as sub-heads, are susceptible to bearing failure and yielding at the web-flange junctions. However, the main challenge in the façade manufacture industry is related to the lack of standardization criteria to predict the bearing strength of aluminium sub-head sections subjected to out-of-plane forces. Due to this lack of design provisions, several manufacturers are presently producing aluminium sub-heads with different cross-sectional shapes, which are not economical. Thus, manufacturers and the aluminium industry are moving towards development of a standard for the evaluation and economical design of the sub-heads to minimize waste and increase productivity and efficiency.

In this regard, understanding the bearing behaviour of aluminium sub-head under lateral wind load is of great importance. Since aluminium alloys share many similarities with cold-formed steel, investigating the bearing behaviour of cold-formed steel structures may give insight into the design of similar structural aluminium elements. The lateral load bearing cold-formed steel stud wall consists of studs laterally connected at the bottom and top of the wall to a track section, with the stud-to-track connection typically being made with self-drilling screws or welds. The most prevalent failure mode in the stud-to-track connection of a stud wall is the failure of track under concentrated load; this failure closely resembles that of the aluminium sub-head in the window wall under wind loading. Even though, studies into the bearing behaviour of cold-formed steel stud-to-track connections have been extensively carried out by various researchers, no research has been undertaken to study the bearing mechanism of aluminium sub-head sections under wind loads. Hence, detailed experimental and numerical studies need to be undertaken to investigate the bearing behaviour and strength of aluminium sub-head sections in window wall frames.

The North American Standard (AISI S240-15, 2015), U.S. Army Corps of Engineers (TI 809-07, 1998), and Steel Stud Manufacturers Association (SSMA, 2000) provide design rules to predict nominal stud-to-track connection strength in stud walls. However, with reference to the previous argument, a review of currently available aluminium provisions has indicated the shortcomings of design equations for predicting the bearing capacity of aluminium sub-heads subjected to out-of-plane forces imposed by mullions in a window wall. Hence, the

suitability of current cold-formed standards must be assessed and then enhanced to provide designers and industry with more accurate means of designing aluminium sub-head sections.

1.8. Research aims and objectives

This doctoral research is pioneering research aimed at meeting manufacturing concerns through investigating the structural behaviour of aluminium sub-heads, and developing reliable design rules for the economic design of aluminium sub-heads. The aim is to

1. Investigate the bearing behaviour of aluminium sub-heads in window wall frames, considering the influence of parameters such as bearing widths, loading and boundary conditions, and various geometric sections;
2. Assess the accuracy and reliability of the current design rules provided by the North American Standard (AISI S240-15, 2015), the U.S. Army Corps of Engineers (TI 809-07, 1998), and the Steel Stud Manufacturers Association (SSMA, 2000);
3. Establish the most economical and practical equations that would accurately predict the bearing capacity of aluminium sub-head sections under wind load, and guarantee the accountability and safety of aluminium sub-heads under designed loading conditions.

1.9. Proposed research/methodology

Experimental testing and FE-modelling are incorporated as main research approaches for this study. To achieve the above research objectives, the following tasks are conducted.

1. Review previous experimental and numerical investigations into the bearing behaviour of cold-formed steel stud-to-track connections under different loading conditions.
2. Conduct a series of 42 experiments to investigate the bearing behaviour and strength of aluminium C-shaped sub-heads in window wall frames including four section geometries (Figure 1.5), two loading conditions, two boundary conditions, and four bearing widths.

3. Conduct a total of 36 experiments to investigate the bearing behaviour and strength of aluminium sub-heads with removable beads including six section geometries (Figure 1.6), two loading conditions, one boundary condition, and three bearing widths.
4. Conduct numerical studies to investigate the bearing behaviour and strength of aluminium C-shaped sub-heads and sub-heads with removable beads in the window wall systems using FE analyses to verify the experimental study. This numerical study accurately models the material properties and boundary and loading conditions of the test setup.
5. Conduct comprehensive parametric studies using the verified FE models to further gain the understanding of the bearing behaviour of aluminium sub-heads covering a wide range of parameters.
6. Assess the accuracy of the bearing capacity predictions of the available cold-formed steel design guidelines (AISI S240-15, 2015; TI 809-07, 1998; SSMA, 2000) against the acquired experimental and numerical results.
7. Develop a unique design approach for predicting the bearing capacities of aluminium C-shaped sub-heads and sub-heads with removable beads in window wall frames based on the experimental and parametric results.

1.10. Thesis outlines

This thesis is organized based partially on a series of peer-reviewed papers and is structured as follows.

Chapter 1 presents an introduction of aluminium sub-head sections and describes their applications in the façade system. Brief explanations of the bearing failure mechanism, and relevant cold-formed steel standards are also presented in this chapter. Finally, research objectives and the methodologies used to achieve the aims of this research project are described in detail.

Chapter 2 presents the literature review findings of experimental and numerical studies conducted in the past to investigate the bearing behaviour of cold-formed steel stud-to-track sections under different loadings. The relevant design standards provided in North American

Standard (AISI S240, 2015), U.S. Army Corps of Engineers (TI 809-07, 1998), and Steel Stud Manufacturers Association (SSMA, 2000) are also presented.

Chapter 3 is based on the published journal paper, which presents the details of an experimental study conducted on the bearing behaviour of aluminium **C-shaped sub-head** sections in window wall systems under wind load. Details of the test set-up, test procedure, and test results (failure modes, ultimate loading capacities, and load-deformation responses) are presented. Furthermore, a comparison of test results with current design rules is conducted. Suitable modifications are implemented in the current design equations, and consequently the modified equations are proposed for the sub-head sections considered in the experimental study.

Chapter 4 is based on the submitted journal paper, which presents the details of the development and validation of FE models of aluminium **C-shaped sub-head** sections (based on Chapter 3) subjected to bearing load. Based on the validated FE models, a comprehensive parametric study using a generalized sub-head cross-section is presented. Accordingly, modifications are implemented in the proposed design rules in Chapter 3 for wide range of sub-head sections.

Chapter 5 is based on the submitted journal paper, which presents the details of an experimental study conducted on bearing behaviour of aluminium **sub-heads with removable beads** in window wall systems under concentrated load. Details of the test set-up, test procedure and test results (failure modes, ultimate loading capacities, and load-deformation responses) are presented. Furthermore, a comparison of test results with current design rules is conducted. Suitable modifications are implemented in the current design equations and consequently the modified equations are proposed for the sub-head sections considered in the experimental study.

Chapter 6 is based on the submitted journal paper, which presents the details of the development and validation of FE models of aluminium **sub-head sections with removable**

beads (based on Chapter 5) subjected to bearing load. Based on the validated FE models, a comprehensive parametric study using a generalized sub-head cross-section is presented. Accordingly, the modifications are implemented in the proposed design rules in Chapter 5 to cover wide range of sub-head sections.

Chapter 7 provides the thesis findings and recommendations for future research.

2. LITERATURE REVIEW

2.1. History of façade

The modern window is a complex structure, consisting of glass and frame, that protects buildings against environmental actions and provides architectural decoration to buildings. In early 19th Century, a gradual changing from the usual load bearing masonry to a framed structural system made of steel and concrete led to the development of façade systems, and became more common from the 1930's when aluminium was made available as a construction material for the first time (Mijović et al., 2018). The technological improvements and extrusion process that followed the Second World War resulted in the spread of high-rise commercial construction and industrialized buildings. This trend has increased the usage of aluminium for external envelope of buildings, which provides elegant face, better economy and reduces maintenance as well. Hence, aluminum windows with large areas occupy a distinguished place in the construction industry. Continuous strips or partly fixed window walls became more prevalent instead of the traditional isolated window. An early installation of aluminum window-frames was at the University Library at Cambridge in 1936 (Dwight, 1998).

In the mid-19th century, the exterior walls no longer had a bearing role and thus were much lighter than the masonry load bearing walls of the past. Later in the 20th century, it began to appear as industrialized production. Double or triple thicknesses of glass separated by air space for insulation were also frequently used in modern windows known as double or triple-glazed windows. This led to increased use of glass as an exterior façade. In recent decades, the façade engineering industry developed unitized façade systems for efficient on-site installation. The aluminium frames and glazing units are firstly fabricated and pre-assembled as unitized panels in factories. Then these panels are shipped to construction sites and erected to high storeys.

2.2. Literature review on structural behaviour of aluminium façade system

A façade system is the first aesthetical feature of a building, which evacuated considerable amount of the cost of the entire structure. An assessment of façade system performance has been encouraged to avoid large expenses and ensure safety during the service life of the

structures. Advanced movement in technology led to using extruded aluminium in window wall systems. An aluminium window wall is a kind of façade, which does not carry any vertical loading and is installed between floors. In a window wall system, an aluminium frame usually comprises mullions, a head and a sill. This frame is positioned between the sub-frame comprises of a sub-head (at the top) and a sub-sill (at the bottom) without any screw connections. As mentioned in Chapter 1, substantial focus must be placed on protecting aluminium window walls from wind loads. Wind loads are initially imposed on the glazing panels of window walls, then transferred to aluminium frames. Against wind actions, the mullions are mainly subjected to bending. A pair of mullion sections is usually used in aluminium frames in façade systems. There is no connection between these mullions to facilitate the movement of panels during temperature variation and building deflections. This provides easier alteration during the fabrication process. The structural behaviour of mullion sections has been investigated in prior research (Hui et al., 2015; Skejic et al., 2016; Naqash, 2016; Yang et al., 2017; Kesawan et al., 2018; Kesawan and Mahendran, 2018; Kesawan and Mahendran, 2019).

Mullions transfer the wind load to the horizontal elements of sub-frames (sub-sills and sub-heads). Consequently, wind loads imposed on window walls are transferred to the main building structure through connections with slabs. As shown in Figure 2.1 displacement imposed by wind load is accommodated using the head-of-wall where the mullion is connected to the sub-head. Hence, the importance of this connection is highlighted. Under this loading condition, one sub-head flange is directly loaded by the mullion and endures bearing failure. Although, as mentioned above, a large body of literature exists on investigating the behaviour of mullions, detailed investigation by these authors revealed that no research was found to investigate the bearing behaviour of the aluminium sub-heads in the window wall systems subjected to wind loads. Furthermore, no design rule exists in current Australian standards relevant to wind load and façade system (AS 4055-2012, AS 2047 2014, AS 1288-2006, AS/NZS 1170.2:2011) to estimate the resistance of aluminium sub-heads in window wall system subjected to wind load.

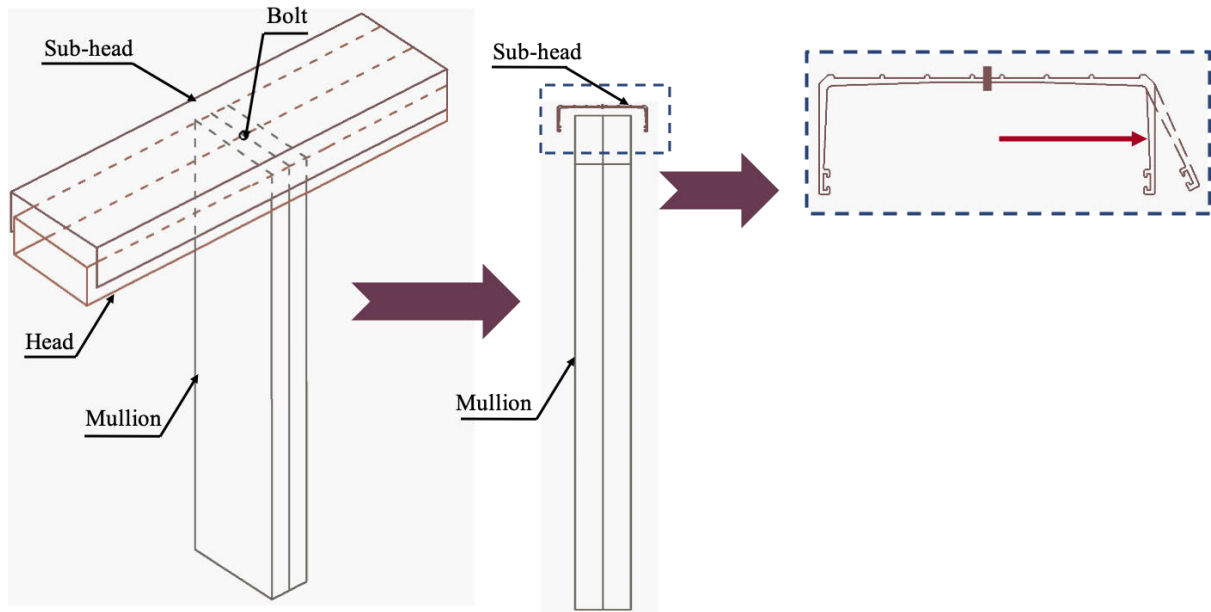


Figure 2.1 Bearing failure of the sub-head under concentrated load.

Since aluminium alloys share many similarities with cold-formed steel, the application of the design methods developed for cold-formed steel structures may give insight into the design of similar structural aluminium elements. One common function of cold-formed steel members is related to lateral load bearing walls such as light gauge steel frame walls (LSF walls). These walls are commonly used in the support of the building envelope, and transferring lateral loads, such as wind load, to the main structural members of the building. The load bearing cold-formed steel stud wall consists of studs laterally connected at the bottom and top of the wall to a track section, with the stud-to-track connection typically being made with self-drilling screws or welds. The most prevalent failure mode in the stud-to-track connection of a stud wall is the failure of the tracks under concentrated load, which closely resembles that of the aluminium sub-head failure in the window wall under wind loading. It needs to be mentioned that design rule to predict nominal stud-to-track connection strength in stud walls was not provided in cold-formed steel Australian standard (AS/NZS 4600: 2018). The North American Standard (AISI S240-15, 2015), U.S. Army Corps of Engineers (TI 809-07, 1998) and Steel Stud Manufacturers Association (SSMA, 2000) provide design rules to predict nominal stud-to-track connection strength in stud walls. However, the main challenge in the façade manufacturing industry is related to the lack of standardization criteria to predict the bearing strength of aluminium sub-head sections subjected to out-of-plane forces. Due to these lack of design provisions, several manufacturers are presently producing aluminium

sub-heads with different cross-sectional shape, which are not economical. Thus, manufacturers and the aluminium industry are moving towards development of a standard for the evaluation and economical design of the sub-heads to minimize waste and increase productivity and efficiency.

Several researchers have conducted experimental and numerical studies to gain understanding of the structural behaviour of stud-to-track connections in LSF walls under wind, earthquake, and blast, and have developed appropriate design rules. Since, no research exists on aluminium sub-heads in window wall systems, besides the research on LSF walls under wind, relevant literature on cold-formed steel stud-to-track connection in stud walls subjected to blast and earthquake is also presented in the following Sections of this chapter with similar test setup and failure modes for aluminium sub-heads subjected to wind. This literature review also summarizes available cold-formed steel design rules provided by aforementioned standards (AISI S240-15, 2015; TI 809-07, 1998; SSMA, 2000).

2.3. Literature review on cold formed steel stud-to-track connection in LSF walls

2.3.1. Wind

As mentioned earlier, cold-formed steel has become a favourite building material for wall framing in buildings, with common application being non-structural systems such as curtain walls and stud walls. The stud walls are positioned between track members at the top and bottom of wall assemblies. The main purpose of these walls is to transfer lateral loads to the main structure, while not supporting any gravity loads. The research also showed that the out-of-plane stiffness and strength of non-structural walls depend on the behaviour of stud-to-track connections and must be considered in the design of the stud walls. Two connections exist between the stud and the track, namely screw attached stud-to-track connections and deflection track connections. In the screw attached stud-to-track connections, the stud is connected to the track flange through self-drilling screws. However, in deflection track connections there are no screw connections between the studs and the tracks in order to facilitate vertical movement between floors. In the second connection, the wall stud transfers

lateral load to one flange of the top track. Both of these connections have been investigated through experimental study. However, they are seldom considered in current wind design methodology. Limited research studies were carried out in recent years in order to evaluate the performance of steel stud walls under wind load. These studies investigated the capacities and failure modes of stud walls subjected to wind loads. The main failure modes considered in the design of wind load bearing stud walls includes web crippling of studs, excessive flange bending of tracks, pulled-out of screws, and punching of track flanges. It was concluded that the main parameters affecting the stud-to-track connection strengths are the thickness of track and stud, the slip gap between the stud and the web of track, as well as the number, the size and the location of fasteners in the stud-to-track connections.

Through a review of relevant literature, Pekoz (1990) compiled results of 3500 tests from the United States, Canada, Sweden and the Netherlands to provide design rules for stud-to-track screw connections. Modifications were implemented in the European Recommendations provisions. Consequently, the recommended design equations for shear, pull-out and pull-over strength were proposed.

Drysdale and Breton (1991) carried out 109 stud-to-track connection tests at McMaster University. 70 of these 109 tests were screwed stud-to-track connections. The parameters such as the stud and the track web depth and thickness, the end gap, and the location of the connection were varied to investigate the behaviour of the stud-to-track connections. In many cases, the screw pull-out of the stud flange at the failure point was observed. The authors also concluded that the connection between the stud and the track is the most prominent factor affecting the strength of the assembly. Furthermore, it was shown that the capacities of assemblies with two screws in the flange was 114% greater than the capacity of those assemblies without a screw.

Marinovic (1994) conducted an experimental study at Cornell University on screw connected stud-to-track connections. No web crippling occurred in the tests. However, track punch-through failure and track tearing through of the fasteners in a number of tests were observed.

Schumacher et al. (1998) investigated the behaviour of built-up members typical of jamb studs with six different types of test specimen configurations. These configurations consisted of pairs of single studs and built-up 'I' sections. The connections between the tracks and the studs as well as built-up stud members were created using screws. The location of fasteners connecting the track to the substrate was changed either between the studs or in close vicinity of the studs. Two failure modes were noticed in the tested specimens, namely web crippling and screw pull-out of the upper compression flange. The authors concluded that in the lighter thickness single stud assemblies, a single screw between each stud connecting the track to the supporting frame was sufficient. However, it was found that a fastener at each side of the built-up members was needed to appropriately transfer the load from the track to the supporting structure.

A series of end-one-flange tests on pairs of single stud-to-track connections was conducted by Lewis et al. (1999) to investigate the bearing behaviour of the stud-to-track connections, as shown in Figure 2.2.

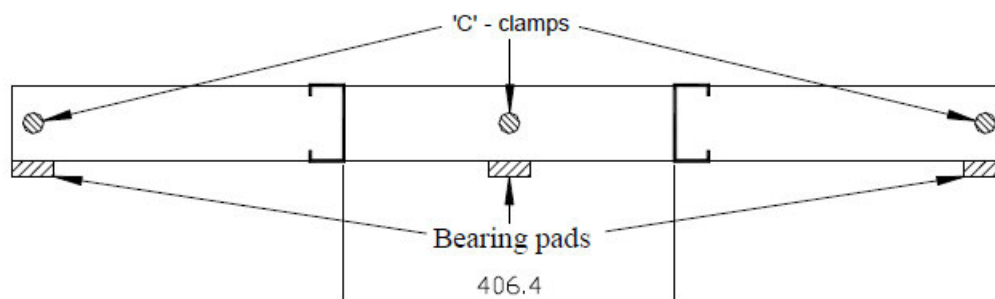


Figure 2.2 Test apparatus (Lewis and Fox, 1999).

As remarked by the authors, the web of the track is connected to the substrate with a single fastener, at distances of 900 mm (see Figure 2.3).

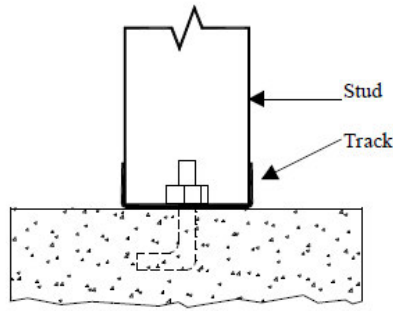
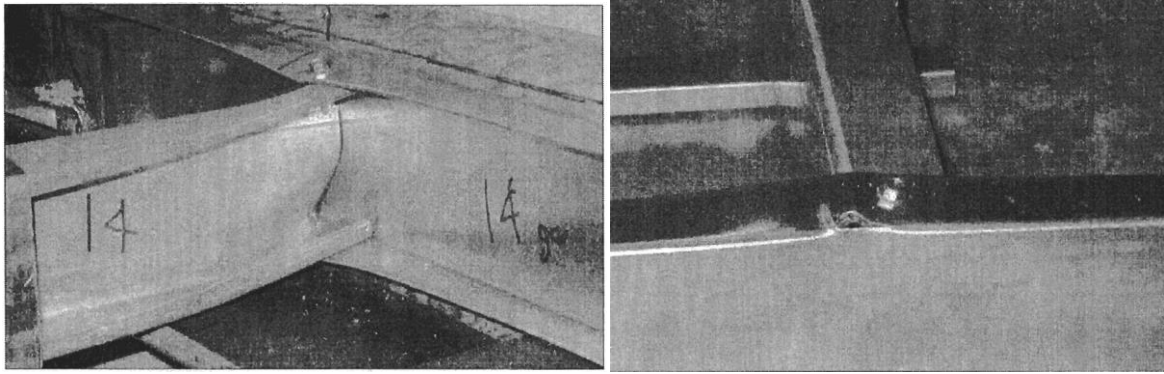


Figure 2.3 Stud-to-track connection (Lewis and Fox, 1999).

The effect of various track and stud thicknesses and end gaps on the stud-to-track connection behaviour were investigated. Two modes of failure (web crippling and track punch-through) were observed. Track punch-through occurred, when the track thickness was thinner than the stud thickness. As a result, the track thickness must be greater or equal to the thickness of the stud to prevent a premature track punch-through failure.

Fox and Schuster (2000) explored the lateral load capacities of stud-to-track connections. The results and analysis of end-one-flange web crippling tests of common stud-to-track connections were discussed thoroughly. The effects of the gap between the end of the stud and the web of the track, as well as the effects of missing screws in the stud-to-track connection were investigated. The results indicated that two failure modes in the stud-to-track connections occurred, namely web crippling of the stud and punch-through of the track flange, as shown in Figure 2.4 (a) and (b). Based on these two modes of failure, design equations were developed to predict ultimate capacities of the connections.



(a)

(b)

Figure 2.4 Failure mode: (a) stud web crippling, (b) track punch-through (Fox and Schuste, 2000).

The lateral load capacity of the industry standard curtain wall stud-to-track connections used in cold formed steel stud walls under wind load was investigated experimentally by Bolte and LaBoube (2004). Both the screw-attached stud-to-track connection at the bottom of wall stud and deflection track connection at the top of wall assembly were evaluated in this research. Bolte and LaBoube (2004) mentioned that at the top track, the lateral load was transferred from the wall stud to the track flange. A detailed test setup can be seen in Figure 2.5 .



Figure 2.5 Test set up (Bolte and LaBoube, 2004).

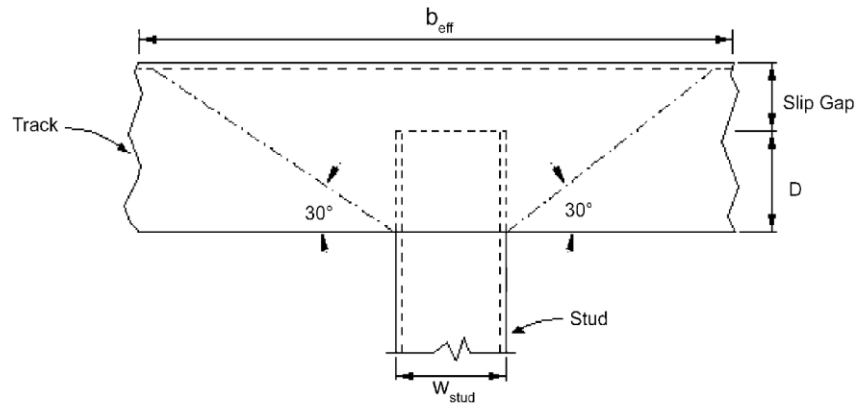
The track was bolted to the centre of a vertical support. To ensure that the ultimate failure occurred in the connection, bearing stiffeners were placed under the loading point and at the simply supported end to prevent web crippling in these regions of the C-sections. The concentrated load was applied at a 305 mm distance from the stud-to-track connection. In the screw-attached stud-to-track connections, a web crippling failure was first noticed in the stud, as illustrated in Figure 2.6 .

By increasing the load, the ultimate failure was attained when the screw in the top flange of the stud experienced a pull-out (see Figure 2.6).

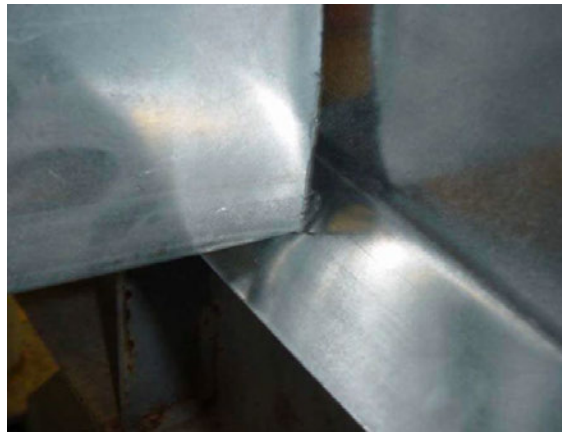


Figure 2.6 Failure in the screw-attached connection (Bolte and LaBoube, 2004).

In the deflection track, the failure load depended on the distributed load on the track flange (b_{ff}), as depicted in Figure 2.7 (a). The track web to flange junction experienced failure when the track flange was yielded (Figure 2.7 (b)).



(a)



(b)

Figure 2.7 Track failure: (a) failure pattern; (b) deflection (Bolte and LaBoube, 2004).

Comparison of test results with the available design guidelines indicated that those equations were conservative. Then modifications to the existing design equations were implemented to determine the stud-to-track connection capacity. For this purpose, an equation for web crippling of screw-attached stud-to-track connections was proposed. Bolte and LaBoube (2004) also proposed equations for the calculation of deflection track strength in cold formed steel stud-to-track connections, based on estimation of the effective track length (b_{eff}).

Gerloff et al. (2004) investigated nominal strength of the slip-track connections, as well as the effective distribution width of the track. Tests were conducted on track connections at the stud locations. Fasteners were placed in the centre of the track web at the stud locations similar to Bolte and LaBoube's (2004) test setup. The test setup consisted of two cold-formed

steel studs (See Figure 2.8). stud was connected to a track at the bottom of the stud Each without any mechanical means. To avoid rotational restraint of the studs, blocking was placed at the end of the studs (close to the slip-track).

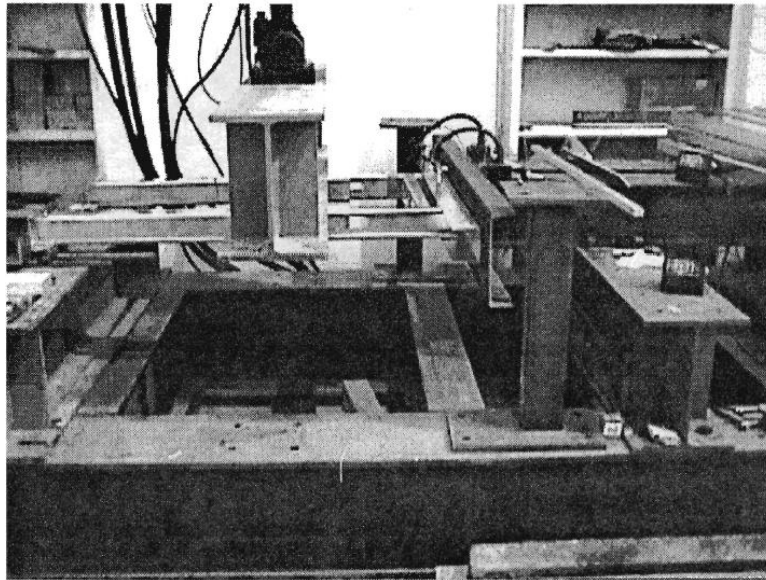


Figure 2.8 Test setup (Gerloff et al., 2004).

The impact of parameters such as the track and the stud thickness, the track leg length, the track nominal depth, the slip gap, the stud flange width, the stud spacing, the stud nominal depth, and stud thickness on slip-track connections strengths were investigated. The design gap and the thickness of the track were found to be the main parameters affecting the effective width. On the other hand, the stud spacing, and the flange width had a shadowing impact on the effective width. Figure 2.9 shows the typical load-displacement curve of a test.

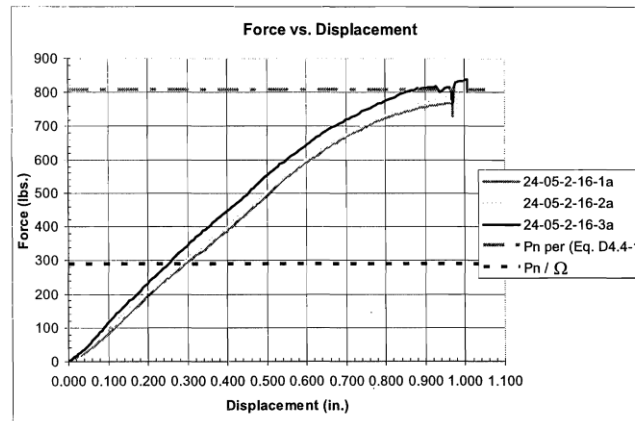


Figure 2.9 Typical load versus displacement curve (Gerloff et al., 2004).

Each specimen was tested to the ultimate load, when increase in the displacement did not result in any increase in the load. Large deflections and rotation of the track and the stud as well as local yielding of the track at the web-flange junction were the main failure modes noticed at the ultimate loads. Consequently, based on the experimental results, design rules were proposed. A relationship between the design gap and the track thickness ($e^{0.5}/t^{1.5}$) with the effective width of the track were developed through curve fitting and regression analysis. The proposed design equations were used as an addition to the North American Specification (AISI S240-15, 2015).

Rahman (2005) investigated the behaviour of single deep leg tracks based on strength and deformation criteria. He discussed the design checks required for the deep leg tracks. In this note, the design rules for predicting the strength of the deflection track based on allowable stress and ultimate strength provided in the North American Standard (AISI S240-15, 2015) and U.S. Army Corps of Engineers (TI 809-07, 1998), respectively were presented and discussed in detail. The author proposed a rational mechanics-based model to estimate the track flange deflection. His model assumed uniform track flange curvature over the entire track flange's effective width. In this model, the total deformation of the track leg consisted of 3 parts: deformation of the track between fasteners to the structure (Δ_1), deformation of the track leg due to rotation of track web (Δ_2), and deformation of the track leg due to bending (Δ_3) (see Figure 2.10).

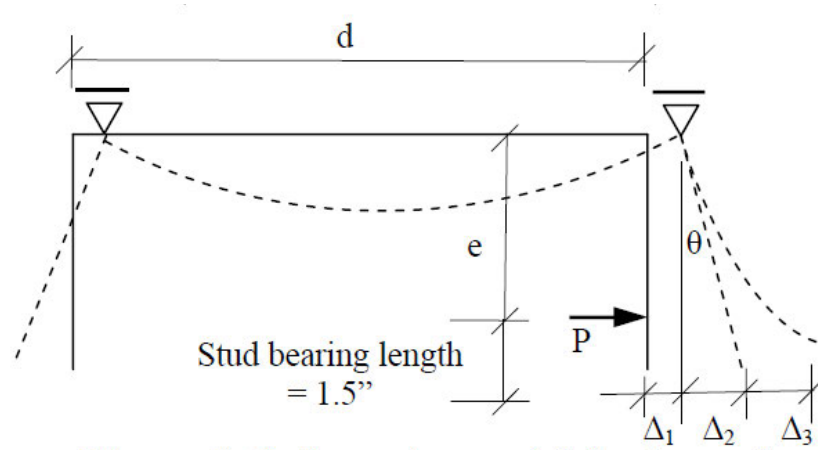


Figure 2.10 Deformation model for the track (Rahman, 2005).

A total of 94 jamb stud assembly tests subjected to end-one-flange loading were carried out by Lewis (2008). The stud-to-track connections consisted of single C-section studs and a built-up jamb made up of two studs located at the end of a track simulating a door or window opening. In the scope of the experimental investigation, the effect of different stud and track depths and thickness, different configurations of jamb studs (back-to-back, toe-to-toe and single), different location of jamb studs in the track (interior and end), various screw sizes (#8, #10 and #12), and screw location were investigated. The aim of this research was to investigate the failure modes, and to develop design rules to predict the capacity of these connections for two limit states: web crippling of the jamb stud and punch-through of the track. The web crippling design expression was taken from the North American Specification for the Design of Cold-Formed Steel Structural Members (AISI, 2007), and new coefficients were developed based on the experimental study. Figure 2.11 illustrates two jamb configurations at a window opening.

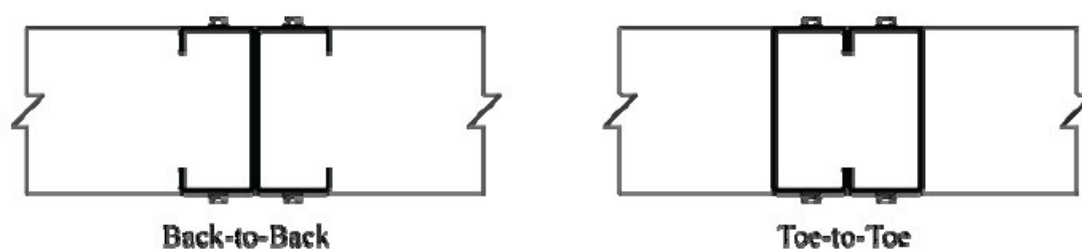


Figure 2.11 Jamb studs at interior location (Lewis, 2008).

The test setup included a series of concentrated loading tests on simply supported built-up jamb assemblies focusing on the connection between built-up stud members and the bottom track. The lengths of jamb studs were 1220 mm, connected in toe-to-toe or back-to-back configurations. Figure 2.12 shows the detailed test setup. For the single stud tests, the single end of the reinforcing stud was kept 152 mm stud was reinforced with a second stud, but away from the track. Other pieces of track were added to the assemblies to avoid a flexural failure or a web crippling failure of the jamb stud. The concentrated load was applied one foot away from the stud-to-track connection. The unconnected end of the test specimen was placed on a load cell, to make the specimen statically determinate. The load at the stud-to-track connection was monitored through the readings from the load cell. The displacement data was recorded by placing a low-voltage displacement transducer (LVDT) above the junction of the stud-to-track connection (shown in Figure 2.12).

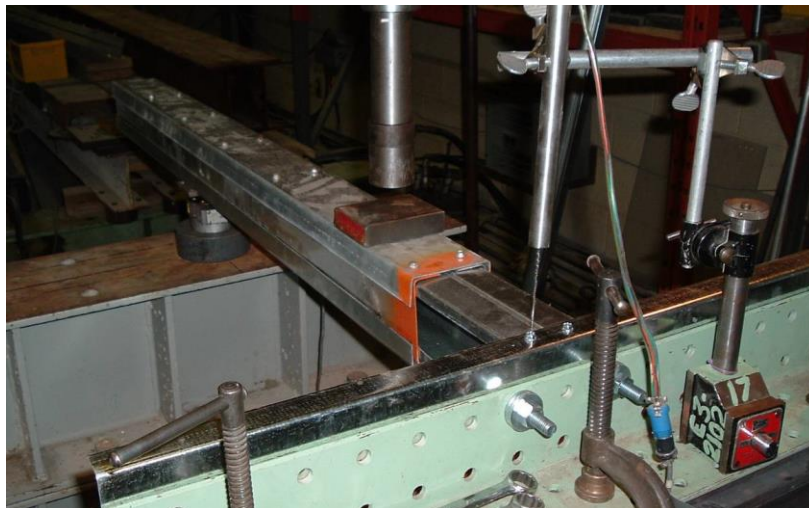


Figure 2.12 Test setup (Lewis, 2008).

In addition to recording the ultimate failure load, failure modes were monitored. As some specimens began to fail in web crippling, track punch-through started, and then screw failure took place. Web crippling of the stud was the most prominent failure mode observed in this test program and occurred in all tests under paired toe-to-toe, or single stud configurations. Figure 2.13 shows a typical web crippling mode and the corresponding load-displacement curve. In this figure, the amount of deformation and load associated with a web crippling failure is illustrated. After this point, any increased load led to high degrees of

deformation, which was not usable. A serviceability limit of 3 mm of deflection at the stud-to-track connection was used in this study.

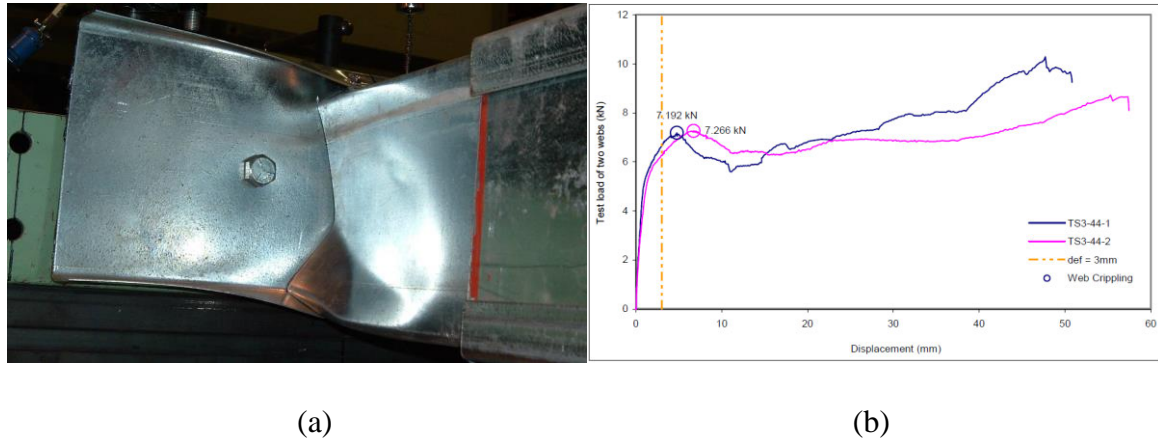


Figure 2.13 Typical web crippling: (a) failure mode, (b) load-displacement curve (Lewis, 2008).

Figure 2.14 illustrates a punch-through failure mode and a typical load-displacement curve. Track punch-through occurred when the jamb stud sheared through the track flange. This mode happened due to the studs being thicker than track or when the web crippling of the stud did not occur.

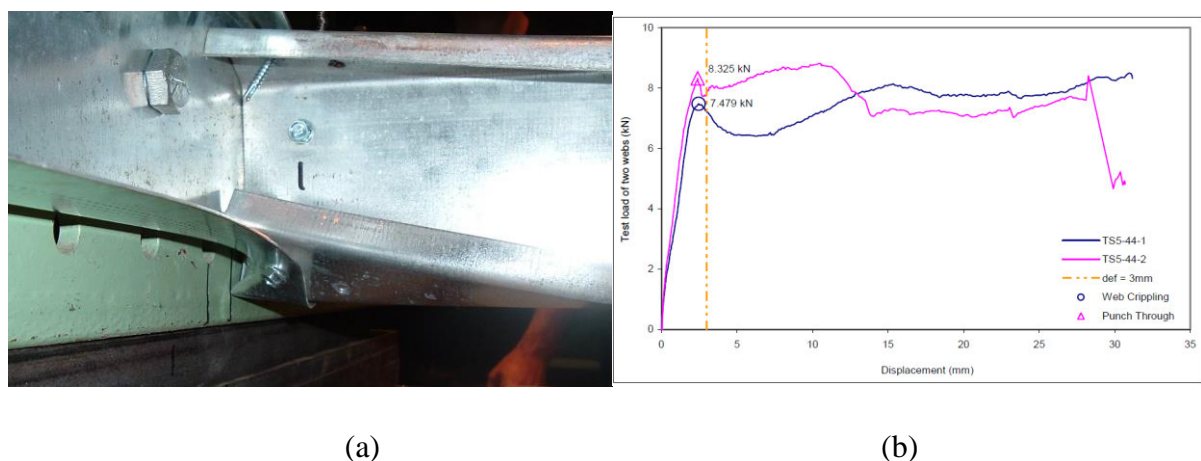


Figure 2.14 Track punch-through: (a) failure mode, (b) test load-displacement curve (Lewis, 2008).

The other failure modes observed in the tests were pull out of the screw in the stud-to-track connections (see Figure 2.15).

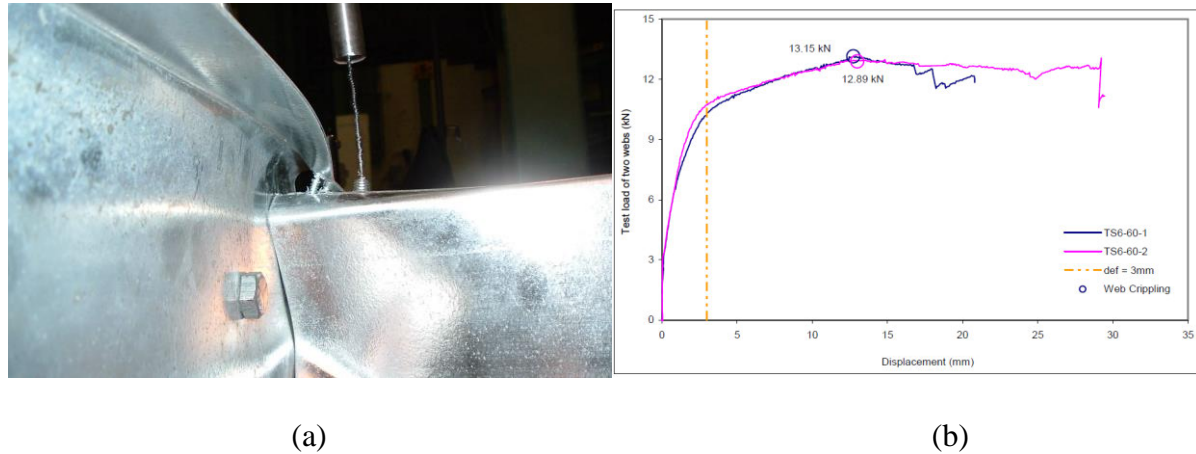
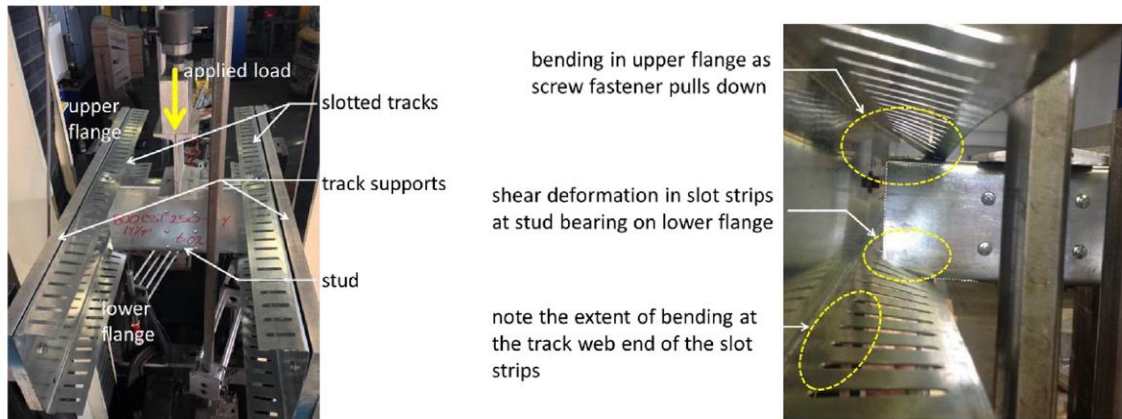


Figure 2.15 Screw pull-out: (a) failure mode, (b) load-displacement curve (Lewis, 2008).

The author mentioned that it is necessary to specify the screw size based on the thickness of the connected material. Lewis (2008) also stated that it is desirable to have the failure occur in the member with a ductile connector, rather than a connector with a more brittle manner. He noted that a single screw in the top flange would inhibit a web crippling or track punch-through failure and lead to excessive deformation of the track flange. However, web crippling or track punch-through occurred in the stud-to-track connection with larger screw size.

Espinoza et al. (2018) investigated the strength of cold-formed steel slotted track connections subjected to out-of-plane loads through experimental study. In this paper, current design rules for estimating the resistance of head-of-wall tracks subjected out-of-plane forces provided by the North American Standard (AISI S240-15, 2015) and U.S. Army Corps of Engineers (TI 809-07, 1998) were discussed. However, the authors stated that none of these provisions provided design rules for deflection of track. The test setup and deformation of track flange under stud loading are shown in Figure 2.16.



(b)

Figure 2.16 Flange deformation under stud loading, (a) test setup, (b) track flange deformation (Espinoza et al., 2018).

Espinoza et al. (2018) proposed mechanics-based equations to estimate the design strength and serviceability load of cold-formed steel slotted track connections for out-of-plane loads. They assume vertical displacements over an effective flange length in the upper flange (L_U) and in the lower flange (L_L) as shown in the slotted track structural model (see Figure 2.17).

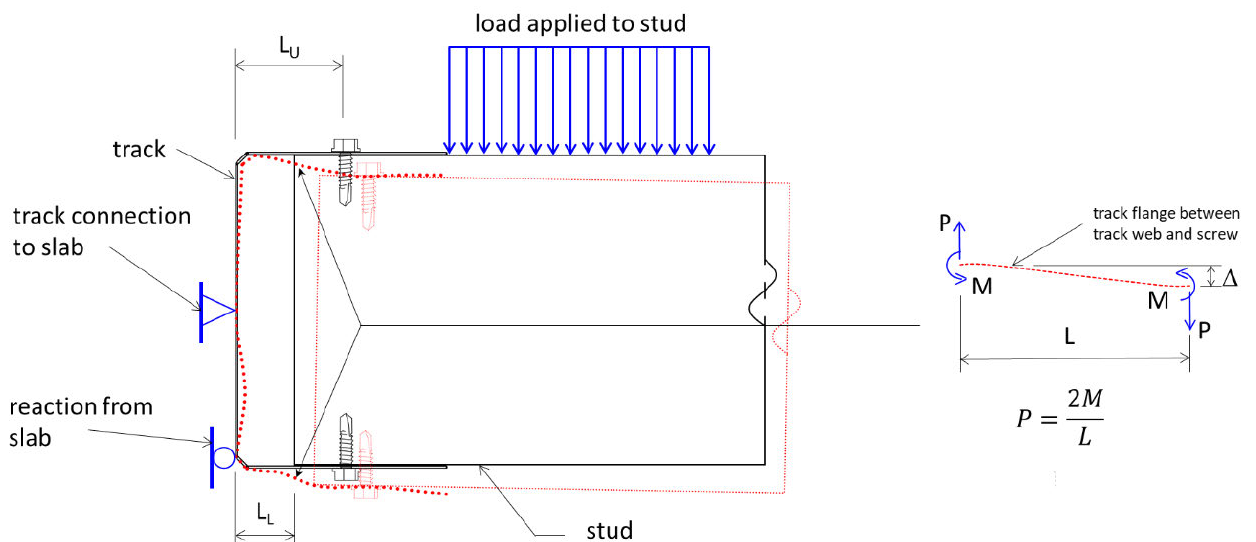


Figure 2.17 Slotted track peak strength model (Espinoza et al., 2018).

It was found that in the lower flange, capacity was controlled by the punching shear strength of a strip. However, in the upper flange, the capacity was controlled by the moment capacity at the corner strip. The equations based on the strength and serviceability were calibrated with test results. Strong agreement between estimated strengths and values determined from tests for different combinations of track thicknesses and web depths was found.

2.3.2. Blast

In the structural design under wind loads, attempts have been made to make the structure perform in elastic range. However, in the blast design, substantial bending and permanent deformation happen in the structure with the goal of absorbing more energy and resisting higher loads. Thus, the response limit is beyond the yield point under blast. In this regard, toughness, the ability of the structure to deform plastically and to absorb energy before fracturing, play a key role in the blast design. End connections (stud-to-track connection) were also found to be decisive elements affecting the failure under blast loads.

Since 2000, several researchers have investigated the blast-resistant behaviour of cold-formed steel studs experimentally (Salim et al., 2004; Bewick et al., 2010; Bewick et al., 2013; Bondok et al., 2015; Whelan et al., 2015).

Bondok et al. (2015) assessed and improved the capacities and static resistance of conventional cold-formed steel stud walls for blast-resistant design, by conducting quasi-static experiments. The effects of the stud and the track gauges, the screw sizes, and the screw layout on the resistance of the stud wall were also investigated. The experimental tests were conducted using 16-point loading (as displayed in Figure 2.18).



Figure 2.18 Test setup (Bondok et al., 2015).

Figure 2.19 illustrates various failure modes occurred in the test

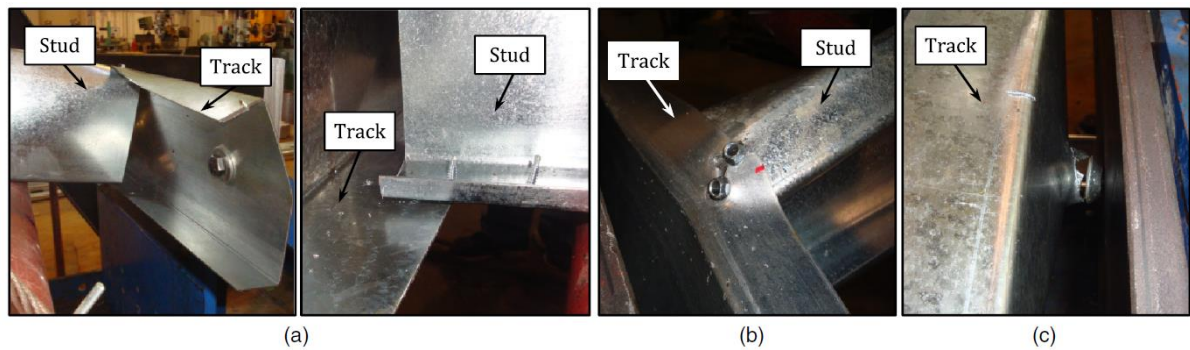


Figure 2.19 End-connection failure modes: (a) screw shear failure; (b) screw tilting and bearing failure; (c) bolt pullover failure (Bondok et al., 2015).

Experimental study showed that increasing the number of screws in the lighter gauge samples improved the resistance and the shear capacity of connections.

Large-scale blast tests are time consuming, expensive and difficult. Hence computational models are required to evaluate different design options before conducting full-scale experiments. Blast-resistant design using cold-formed steel studs has also been the focus of several numerical investigations (Bewick et al., 2014; Bondok et al., 2015).

Bewick et al. (2014) developed finite-element models of steel stud wall systems subjected to blast load to simulate the tensile membrane action (TMA) and bending and prying action (BPA) tests. These models were in good agreement with previous testing in terms of the peak load, the deformation behaviour and the failure modes of steel stud wall systems. Figure 2.20 shows failure modes obtained from a typical BPA FE model and corresponding test results.

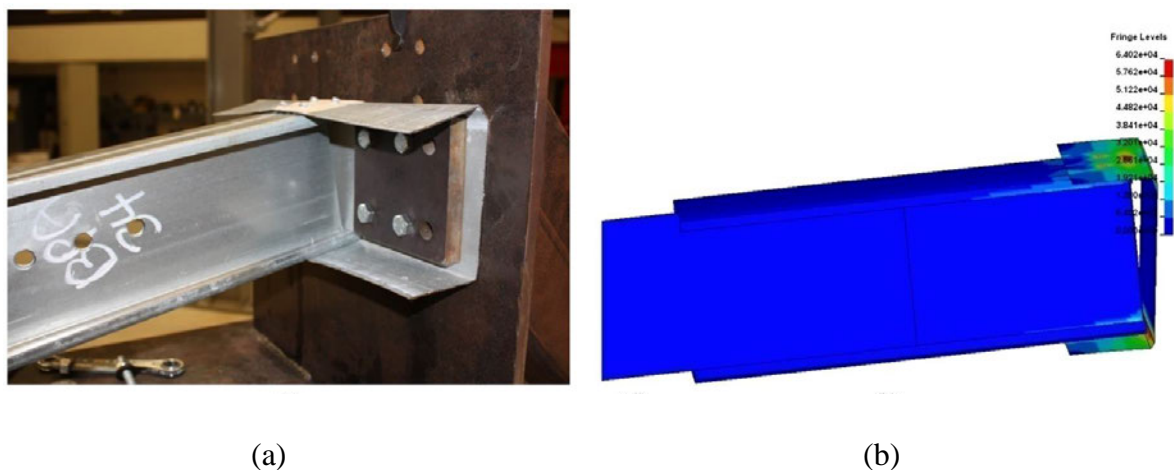


Figure 2.20 Bending and prying action test results: (a) Experiment; (b) FE model (Bewicket al., 2014).

Results from the finite-element models demonstrated that the approach adopted in this research is suitable for predicting the response of steel stud wall systems subjected to large deformations and for conducting parametric studies.

Bondok and Salim (2014) developed a nonlinear numerical model validated by experimental results (see Figure 2.21), which accurately predicted the resistance of conventional walls subjected to blast load. The arc-length technique (static Riks method) in ABAQUS was used to predict the load-displacement response. S4R, S3R shell elements were used for modelling studs and tracks. The bolts connecting the tracks to the floors were modelled by pinned points. An elastic-plastic material model with isotropic strain hardening was used to define steel. Two types of boundary conditions (the steel-hinge end condition and the track end condition) were simulated. The effects of the end condition type, the utility holes, stud

thickness, screw sizes and layouts of the resistance and toughness of the walls were investigated. It was found that the developed model could predict the toughness accurately. The steel stud resistance function (bending, softening, and tension-membrane) was also predicted accurately.

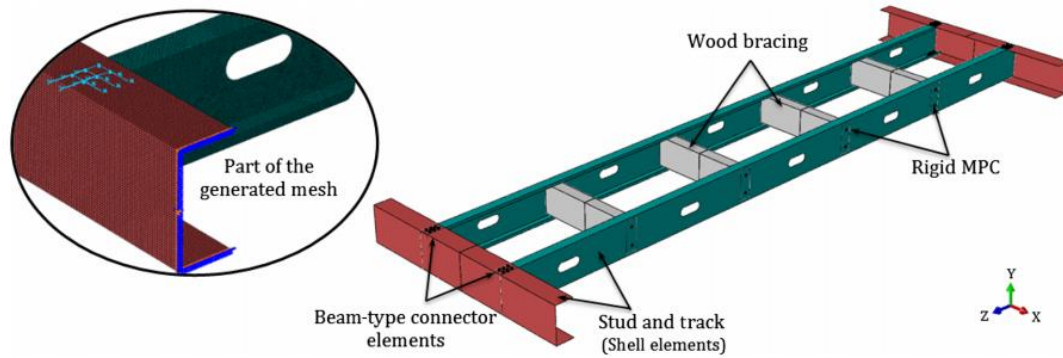


Figure 2.21 FE model developed for conventional stud-to-track connection model (Bondok and Salim (2014)).

Bondok et al. (2015) assessed and improved the capacities and static resistance of conventionally connected cold-formed steel stud-track walls for blast-resistant design. A numerical study validated the experimental results and provided an economical tool to explore the resistance of conventional cold-formed steel stud-track walls. The arc-length in the modified Riks algorithm was adopted as the analysis technique in this study. S4R, S3R shell elements were chosen for modeling the studs and tracks. Furthermore, the lateral wood bracings were simulated using C3D8R element. Figure 2.22 demonstrates details of developed finite-element model.

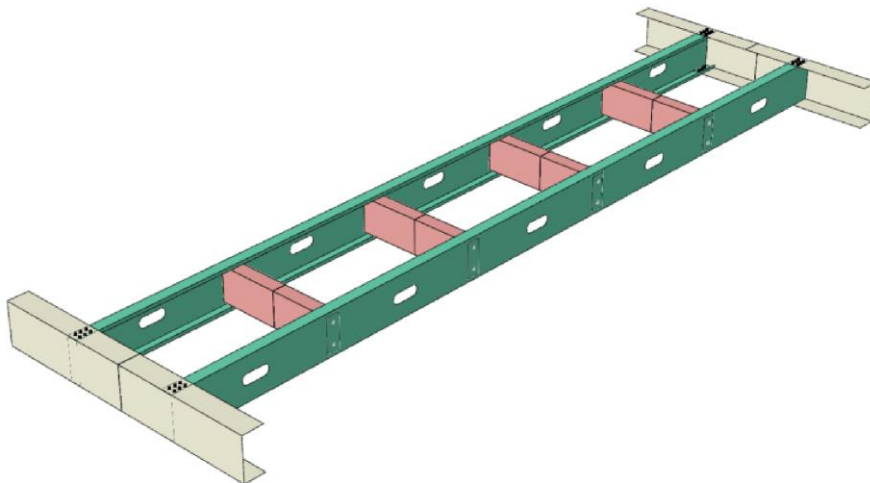


Figure 2.22 Developed finite-element model (Bondok et al. (2015)).

The effects of stud and track gauges, screw sizes, and screws layout on the resistance of the wall were also investigated. The FE model predicted the toughness with high level of accuracy. Based on finite-element model, a failure criterion was developed, which provided a reliable prediction of the quasi-static resistance behaviour of experimental tests.

2.3.3. Earthquake

At the time of earthquakes, non-structural systems are subjected to dynamic behaviour. As a result, significant damage and economic loss were observed in non-structural systems in recent earthquakes. Consequently, it can lead to property and functionality loss of critical facilities. In this respect, experimental studies were conducted to evaluate the seismic performance of steel-framed partition and stud walls (Iuorio et al., 2014; Rahmanishamsi et al., 2016; Jenkins et., 2016). The main failures observed from these experiments were collapse of partition walls, out-of-plane damage of partition walls, bending of studs, track-to-slab connection failures, and popping out of studs from top tracks.

Rahmanishamsi et al. (2016) conducted a total of 26 tests, classified in six series, to evaluate the out-of-plane behaviour of stud-to-track connections in non-structural steel-framed partition walls. The effects of various stud-to-track gap dimensions, stud and track thicknesses, and screw-attachment configurations on the load-displacement responses and failure modes of stud-to-track connections were investigated. The accuracy of current design rules in terms of ultimate connection capacity was also evaluated. Based on experimental tests, capacity fragility curves were presented. A detail of test setup and tested specimen is shown in Figure 2.23 .

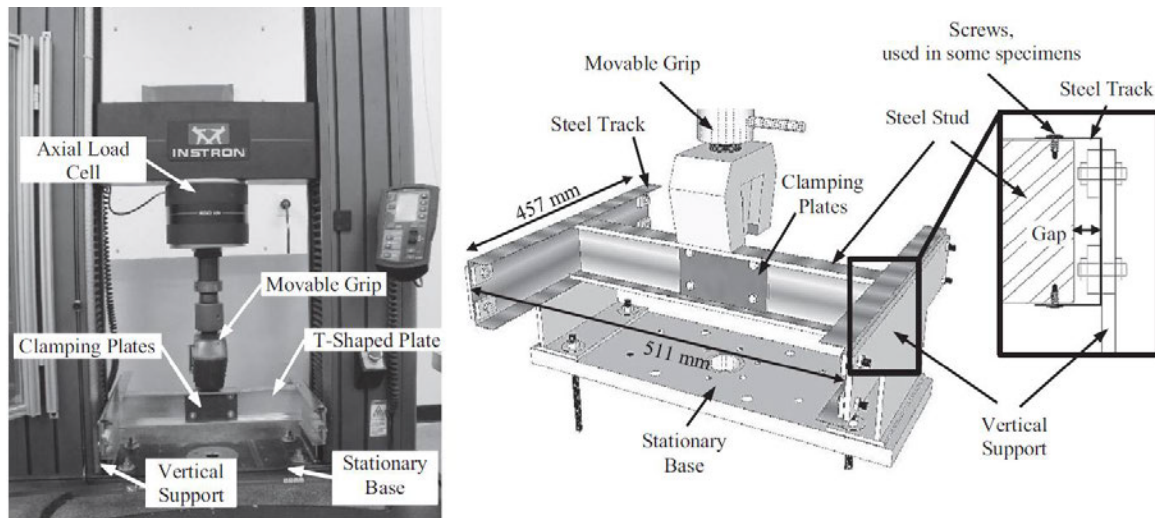


Figure 2.23 Test setup (Rahmanishamsi et al., 2016).

The test setup consisted of one steel stud and two steel tracks. The tracks were bolted to vertical supports and the stud was nested into the tracks. The gap between the end of the stud and the web of the tracks ranged from 3 mm to 22 mm. Two screws were used to connect the stud to the tracks in some specimens. However, no screw connections existed in others to depict a deflection track configuration. Two steel plates attached in the middle of the stud were used to avoid the bending of the stud and limit the deformation of stud-to-track connections.

Figure 2.24 shows the failure modes of a stud undergoing increasing track connection-to-stud displacement. At the beginning of the test a small track flange displacement was noticed as the stud moved downward (Figure 2.24 (b)), followed by an excessive track-flange deformation (Figure 2.24 (c)) for deflection-track configurations with large stud-to-track gaps. For other specimens, increasing the downward displacement led to crippling of the stud web, where screws were used to attach the stud to tracks (Figure 2.24 (d)). Consequently, the screws were pulled out from the studs (Figure 2.24 (e)).

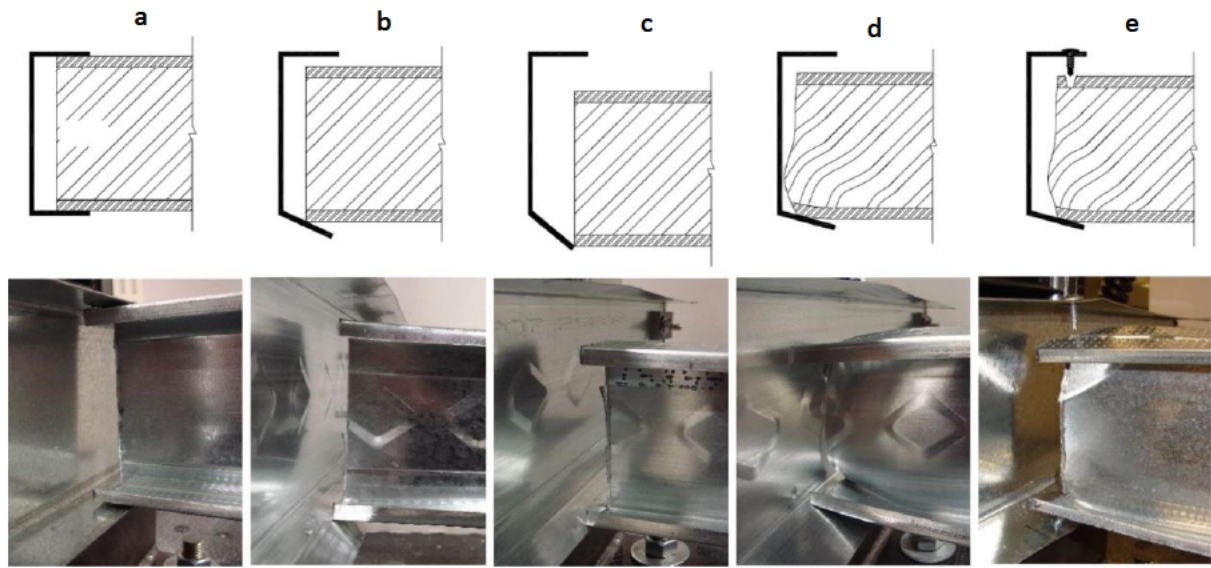


Figure 2.24 Damage mechanisms of stud-to-track connections in the out-of-plan direction: (a) initial condition, (b) track-flange deformation, (c) permanent displacement of the stud, (d) stud-web crippling, (e) screw pull-out (Rahmanishamsi et al., 2016).

The authors concluded that the proposed equations by Bolte and LaBoube (2004) and the North American Specification (AISI S240-15, 2015) could accurately predict the ultimate capacity of the connection. The stud-to-track gap was shown to be a dominant factor affecting the failure mechanism. Lower initial stiffness as well as smaller capacity and failure displacement were outcomes of increasing the gap. The fragility analysis displayed that a small stud-to-track gap enhances the connection performance in the first and third damage states, but may degrade the connection performance in the second damage states. Moreover, Rahmanishamsi et al. (2016) concluded that connections with thicker studs/tracks are more vulnerable in all damage states, and extra screws delayed the failure of the connection.

Rahmanishamsi et al. (2016) developed a series of nonlinear numerical hinge models and calibrated with the out-of-plane hysteresis behavior of stud-to-track connections. A one-dimensional hysteresis load-displacement relationship was defined using the “Pinching4” uniaxial material as well as a “zeroLength” element in Open Sees.

To find the best correlation between numerical results and experimental results, all parameters of “Pinching4” material were calibrated for each specimen. The comparison of numerical and experimental results is displayed in Figure 2.25.

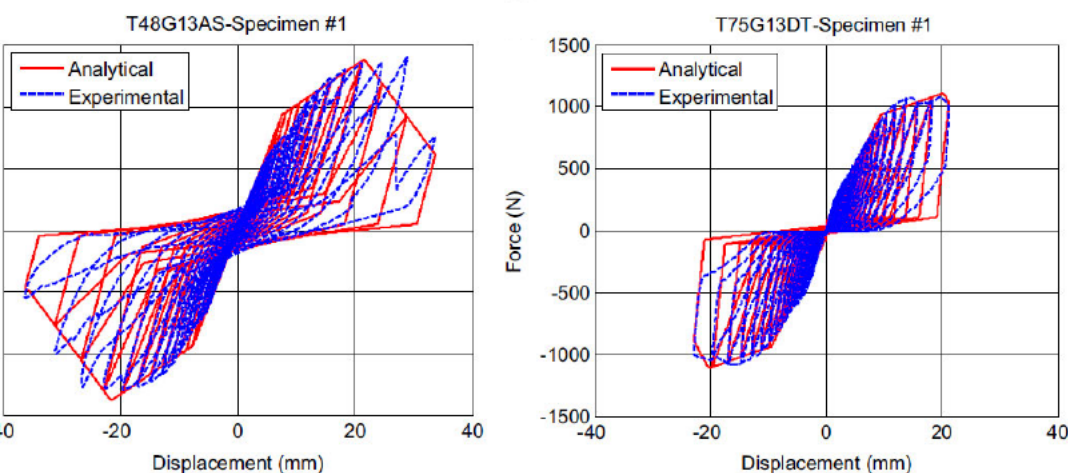


Figure 2.25 Sample numerical experimental hysteresis comparisons of specimen series

2.4. Current design rules

One of the largest challenges in the façade fabrication industry is the lack of standardization, that can guarantee safety and economical design of aluminium sub-heads under wind load. Hence, the manufacturer intends to use a unique design approach for aluminium sub-heads, which is practical and can be implemented to increase productivity and efficiency. Under wind load, the concentrated load is applied at the internal surface of the flange element (away from the web element) in aluminium sub-heads, similar to the track flange which is directly loaded by the framing stud. The North American Standard for Cold-Formed Steel Structural Framing (AISI S240, 2015), U.S. Army Corps of Engineers (TI 809-07, 1998), and Steel Stud Manufacturers Association (SSMA, 2000) provide design rules to predict nominal cold-formed steel stud-to-track connection strength in stud walls. The design rules for cold-formed steel structures in U.S. Army Corps of Engineers (TI 809-07, 1998) are identical to those in the Steel Stud Manufacturers Association (SSMA, 2000), and hence only TI 809-07, 1998 design rules are discussed in this chapter. Bolte and LaBoube (2004) also proposed design equations for the design of cold-formed steel tracks. Thus, to provide a better understanding of the bearing behaviour of an aluminium sub-head under wind load, a review of current cold-formed steel standards (AISI S240, 2015 and TI 809-07, 1998) as well as the proposed equations by Bolte and LaBoube (2004) is presented in the following Sections.

2.4.1. North American Standard for Cold-Formed Steel Structural Framing (AISI S240, 2015)

The following design rules for the nominal strength of a single deflection track subjected to transverse loads is specified in Section B3.2.5.2.2 of AISI S240 (2015) standard:

$$P_n = \frac{w_{dt} t^2 F_y}{4e} \quad (2.1)$$

$$w_{dt} = 0.11\alpha^2(e^{0.5}/t^{1.5}) + 5.5\alpha \leq S \quad (2.2)$$

where P_n is stud end reaction, w_{dt} is effective track length, S is stud spacing, t is track design thickness, F_y is design yield strength of track material, e is slip gap (distance between stud web at the end of stud and track web), and α (Coefficient for conversion of units) = 25.4 where e , t and S are in mm (see Figure 2.26).

Notably, fastener spacing shall not be greater than the stud spacing (S). Furthermore, the horizontal distance from the web side of the stud to the end of the track shall not be less than half the effective track length (w_{dt}).

Eq. (2.2) is limited to track section depths up to 152.4 mm, track thicknesses between 1.14 mm and 1.81 mm, yield strength up to 345 MPa, and flange widths between 50.8 mm and 76.3 mm.

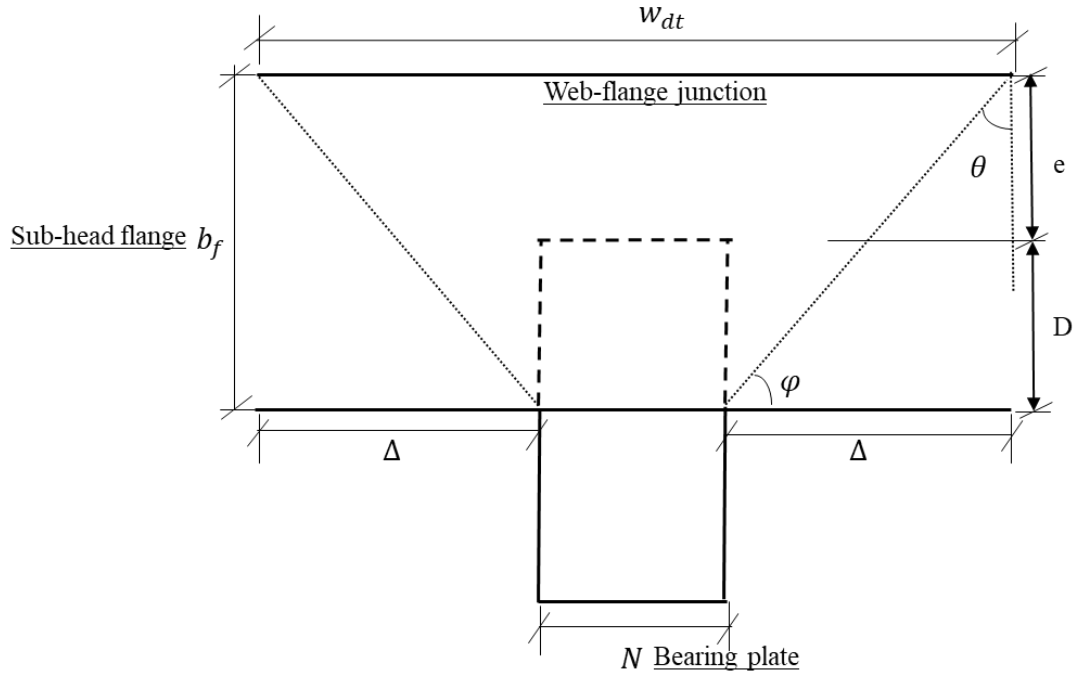


Figure 2.26 Failure pattern for the sub-head's flange.

2.4.2. U.S. Army Corps of Engineers (TI 809-07, 1998)

The following design rules for the nominal strength of the deflection track is provided by the U.S. Army Corps of Engineers technical instructions (TI 809-07, 1998):

$$P_n = \frac{w_{dt} t^2 F_y}{6e} \quad (2.3)$$

$$w_{dt} = 2 \left[\frac{e + D}{\tan(30)} \right] + w_{stud} \leq S \quad (2.4)$$

where D is the depth of track bearing contact length between stud and track flange, and w_{stud} is stud flange width (see Figure 2.26). w_{dt} , t , F_y , and e are outlined as above.

It is worth mentioning that the Steel Stud Manufacturers Association (SSMA, 2000) procedure is based on the U.S. Army Corps of Engineers (TI 809-07, 1998) procedure with small modifications.

The main differences between design equations provided by U.S. Army Corps of Engineers (TI 809-07, 1998) and the North American Standard for Cold-Formed Steel Structural Framing (AISI S240, 2015) is related to the assumed strength limit moment, and the effective track width (w_{dt}) expressions. Eq. (2.1) is based on plastic limit moment and ultimate strength, whereas Eq. (2.3) is based on elastic limit moment and allowable stress design

2.4.3. Bolte and LaBoube's method (2004)

Bolte and LaBoube (2004) also proposed equations for calculation of deflection track strength (P_n) using Eq. (2.1) based on the effective track length (w_{dt}), and the plastic section modulus (Z_x) (Eq. (2.5)).

$$Z_x = \frac{w_{dt} t^2}{4} \quad (2.5)$$

The effective track length (w_{dt}) was expressed by Eq. (2.6).

$$w_{dt} = \Delta + w_{stud} \quad (2.6)$$

where Δ is the partial track length (Figure 2.26), and was defined by Eq. (2.7a) and Eq. (2.7b).

$$\text{For } (e/t)^2 < 100; \Delta = \frac{300(e/t)^2}{100} \quad (2.7a)$$

$$\text{For } (e/t)^2 \geq 100; \Delta = 300 \quad (2.7b)$$

2.5. Literature review findings

This chapter presents a detailed literature review of experimental and numerical studies conducted on the bearing behaviour of cold-formed steel stud-to-track connections in LSF walls under wind, earthquake, and blast. The currently available design rules were also presented in this chapter. The key literature review findings relevant to this thesis are,

1. Under wind load, aluminium sub-heads in window wall systems are loaded by the mullion and undergo bearing failure. Although, several studies have been conducted to investigate the structural behaviour of mullions, no literature exists to investigate the bearing behaviour of the aluminium sub-heads when subjected to wind loads.
2. The failure of the cold-formed steel stud-to-track connections in light gauge steel frame (LSF) walls under lateral load is closely similar to the aluminium sub-head failure in the window wall under wind loading. Thus, to improve our understanding in regard to the bearing behaviour of aluminium sub-heads, a review of the research on the bearing behaviour of cold-formed steel tracks in LSF walls under wind, earthquake, and blast was addressed in this literature review.
3. It was found that the main parameters affecting the stud-to-track connection strengths are the thicknesses of track and stud, the slip gap between the stud and the web of track, as well as the number, size and location of fasteners in the stud-to-track connections.
4. The main bearing failure modes considered in the design of wind load bearing stud walls include web crippling of studs, excessive flange bending of tracks, pulled-out of screws, and punching of track flanges.
5. The current cold-formed steel design standards (including the North American Standard for Cold-Formed Steel Structural Framing (AISI S240, 2015), the U.S. Army Corps of Engineers (TI 809-07, 1998), and the Steel Stud Manufacturers Association (SSMA, 2000)), as well as Bolte and LaBoube (2004) provide design provisions and technical information for the bearing design of cold-formed steel stud-to-track connections in LSF walls.
6. The current aluminium standards do not include any design rules to predict the bearing behavior of aluminium sub-heads in window wall systems.

3. EXPERIMENTAL INVESTIGATION ON THE BEARING BEHAVIOUR OF ALUMINIUM SUB-HEADS IN FAÇADE SYSTEMS

(Published)

This chapter includes a co-authored paper. The bibliographic details of the co-authored paper, including all authors, are:

Akbari, M., Gunalan, S., Gilbert, B.P., Guan, H., Baleshan, B.

Experimental Investigation on the Bearing Behaviour of Aluminium Sub-heads in Façade Systems

Thin-walled structures

My contribution to the paper involved:

Literature review, experimental works, result analysis, discussion of the results, writing, editing and response to reviewers.

(Signed) _____ (Date) 14.11.2020

Name of Student: Masoumeh Akbari

(Countersigned) _____ (Date) 14.11.2020

Corresponding author of paper: Dr Shanmuganathan Gunalan

(Countersigned) _____ (Date) 14.11.2020

Supervisor: Dr Shanmuganathan Gunalan

Experimental Investigation on the Bearing Behaviour of Aluminium Sub-heads in Façade Systems

Abstract

In the building sector, the application of aluminium alloys in load carrying structures as well as building envelopes has received attention over the past decades. Under wind loading, the vertical members of window walls known as mullions, carry the horizontal load transferred from the glass panels. This load is then transferred to the sub-heads at the top and the sub-sills at the bottom which are connected to the structure. The aluminium sub-head flange due to its long length is susceptible to bending (bearing failure) under this loading condition, a phenomenon that has hitherto not been adequately researched. Hence the performance of aluminium sub-head sections subjected to bearing failure was investigated through a series of 42 tests. This study mainly explores the impacts of parameters such as the bearing width, the loading and boundary conditions, as well as various geometric sections, on the bearing failure of aluminium sub-heads. The significant failure modes observed in the tests were yielding at web-flange junction and slipping of the bearing plate. Currently, no design rules are available to predict the bearing capacity of aluminium sub-heads. Hence a comparison of the ultimate bearing capacities of the test results and the design capacities obtained using the available cold-formed steel design specifications was performed. The code-predicted design strengths were found to be overly conservative for aluminium sub-head sections in window walls. Therefore, new design equations were developed to ensure safe, economic and reliable design of aluminium sub-heads using a wide range of bearing capacity data obtained from the experimental studies. The proposed design rules were found to be in precise agreement with the experimental values.

Keywords

Aluminium structures, Window frame, Sub-heads, Bearing failure, Concentrated load

3.1. Introduction

Aluminium has become the most favoured material for façade systems due to its desirable characteristics such as strength, lightness, extrudability, and corrosion resistance. The aluminium window wall systems are popular in the façade industry due to many advantages, including high quality and lower cost through savings in material and labour, attributable to the automated fabrication process. In a window wall frame, vertical members (mullions) and horizontal members (head and sill transoms) are screwed together and placed in between the sub frame (sub-head and sub-sill), as schematically illustrated in Figure 3.1. The sub-head and sub-sill are open sections (typically channel section), having various thicknesses in the web and non-uniform thicknesses in the flange. The window wall frame is not screwed to the sub-heads due to the necessity of space between them for building movements, thermal expansion and fabrication and installation tolerances of the aluminium frame. The main function of the window wall is to transfer out-of-plane loads to the structure while not supporting any superimposed gravity loads from the building. Hence a gap exists between the top of the mullion and the sub-head such that when the building deflects vertically, the sub-head moves with the slab to ensure that the windows of the building do not crush or disengage.

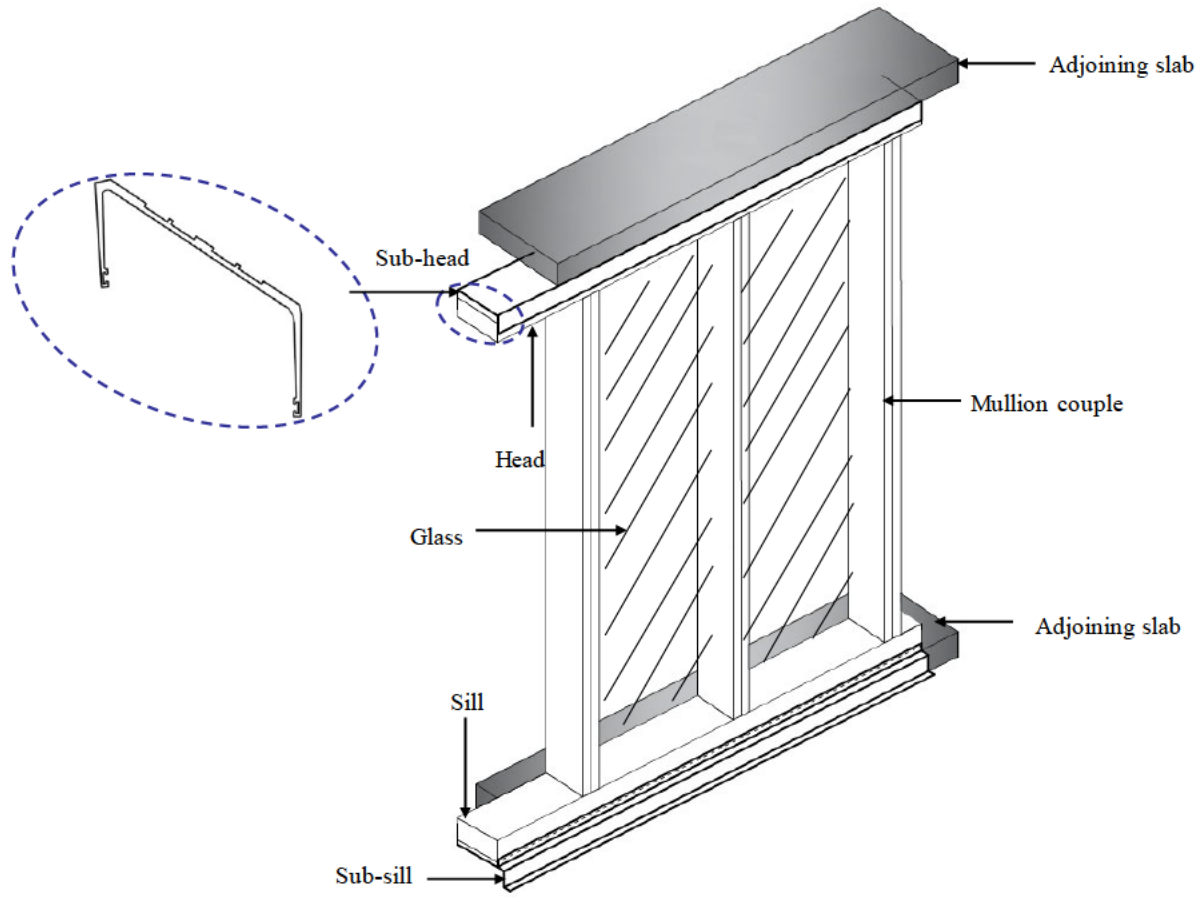


Figure 3.1 Details of window wall frame, sub-head and sub-sill.

Window wall is one of the most expressive and vital features of a building envelope, which creates a separation between the indoor and outdoor atmosphere of a building and provides protection against environmental actions such as wind. Thus, in its design, exposure to wind loads must be considered. The lateral wind pressure imposed on the glass panel (the infill material in a typical window wall system) is transferred to the aluminium frame (mullions, heads and sills) first. The aluminium frame then transfers this load to the main building structure through the sub frame. Under this loading condition, aluminium mullions are subjected to bending and twisting behaviours, which have been investigated in the past (Wang, 2006; Huang, 2014; Hui et al., 2015; Skejic et al., 2016). On the other hand, sub-heads, due to their longer flange length (to allow the gap mentioned before), are more susceptible to bearing failure than sub-sills. Figure 3.2 displays a sub-head subjected to an internal transverse concentrated load, being exposed to this type of failure. Consequently, this loading could potentially lead to a localized bearing failure (yielding failure at web-flange

junctions due to the bending of the flange). It should be highlighted that this is the governing failure mechanism in a sub-head which must be considered in the aluminium façade design.

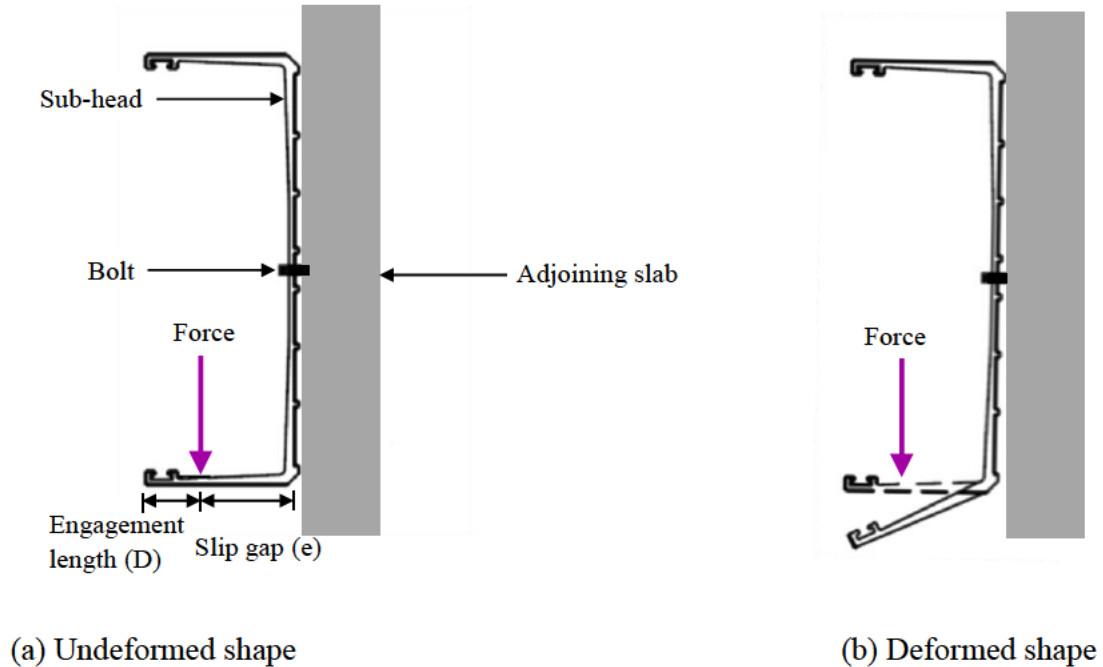


Figure 3.2 Cantilever flange bending under concentrated load from mullion.

A similar failure mode has been observed in cold-formed steel tracks subjected to wind load on light gauge steel frame (LSF) walls. The LSF wall consists of axial load bearing studs laterally attached at the bottom and top of the wall to a track section. Studies into the bearing behaviour of cold-formed steel stud-to-track connections have been extensively carried out by various researchers (Fox and Schuster, 2000; Bolte, 2003; Bolte and LaBoub, 2004; Gerloff, 2004; Rahman, 2005; LaBoube and Findlay, 2007; Lewis, 2008; Espinoza et al, 2018; Drysdale and Breton, 1991). The lateral load capacity of the industry standard stud-to-track connections used in cold-formed steel stud walls under wind loading pressure was experimentally investigated in (Bolte and LaBoub, 2004; LaBoube and Findlay, 2007). Although experimental studies have been conducted on cold-formed steel members in the past, no research work has considered the bearing behaviour of aluminium sub-heads.

The North American Standard for Cold-Formed Steel Structural Framing (AISI S240, 2015), the U.S. Army Corps of Engineers (TI 809-07, 1998), and the Steel Stud Manufacturers

Association (SSMA, 2000) provide design rules to predict nominal strength of head-of-wall tracks in cold-formed LSF walls under one flange bearing load conditions. However, a review of currently available aluminium provisions has indicated the shortcomings in regard to the design equations for predicting the bearing capacity of aluminium sub-head to out-of-plane forces imposed by mullions in a window wall.

In addressing the research gap identified in the literature and current standards, an experimental study was conducted in the structural laboratory of Griffith University, Australia, as the first step in understanding the bearing strength of aluminium sub-heads. The results and analysis of the bearing capacity tests are comprehensively described in this paper. Additionally, a detailed assessment of the accuracy and reliability of the aforementioned cold-formed steel specifications (AISI S240, 2015; TI 809-07, 1998; SSMA, 2000) was carried out to verify the applicability of these design rules to the extruded aluminium sections. As these provisions were found to underestimate the bearing capacities of aluminium sub-heads, new design equations for predicting the ultimate strengths of aluminium sub-heads were developed, and are presented herein.

3.2. Experimental study

3.2.1. Test specimens

The test procedure involved conducting 42 concentrated loading tests on aluminium sub-head sections with various structural parameters as shown in Table 3.1. About half of the 42 tests were repeated (See Table 3.1). The results of the repeated tests were very close to each other with an insignificant difference of less than 5%, confirming the consistency of the test results. Details of the test results are presented in Section 3.3. The sub-head sections are commercial products provided by G.James Glass and Aluminium Pty Ltd, and were fabricated by extrusion. 6063-T6 heat-treated aluminium alloy was selected because of its higher strength and good finishing property. All the profiles were from the same batch, and every section of any particular type had the same material properties. Four different sub-head section sizes were tested, as schematically shown in Figure 3.3, in which the symbols represent the section depth (d), flange width (b_f), web thickness (t_w), flange thickness (t_f), internal radius (r_i). Table 3.2 summarises these geometric details and the specimen length (L) based on the

average values of three measured dimensions. A specimen length of 1300 mm was considered in this study to simulate a typical mullion spacing of 1200 mm in a window wall frame allowing for an overhang of 50 mm on each side. The load reaction was conservatively assumed to be concentrated at the mullion bearing on the sub-head, with some small amount of load redistribution across a short distance of the window head either side of the mullion. The length of load redistribution was affected by various factors, such as the mullion width, the stiffness of heads, and the spacing between mullions. Note that an accurate estimation of the contact lengths with regard to this study was uncertain and challenging. Hence, different bearing plates of widths $N = 50, 100, 150$ and 200 mm were considered in the experimental study (see Table 3.1). Moreover, two different engagement lengths (D) of 25 mm and 15 mm were studied to assess the impact of loading positions on the bearing capacity (Figure 3.2). Two different bolt connection details (i.e., boundary conditions) between the sub-head and the adjoining slab were also considered, as demonstrated in Figure 3.4. In brief, three loading and boundary conditions were defined (1 bolt with 25 mm engagement length, 2 bolts with 25 mm engagement length and 1 bolt with 15 mm engagement length), as shown in Table 3.1.

Table 3.1 Test specimen details.

Engagement length	D = 25 mm								D = 15 mm			
Boundary condition	1 Bolt				2 Bolts				1 Bolt			
Bearing width	50 mm	100 mm	150 mm	200 mm	50 mm	100 mm	150 mm	200 mm	50 mm	100 mm	150 mm	200 mm
Section 675-027	√	√	√	-	√	√	√	-	√	√	√	-
Section 475-077	√	√√	√	-	√	√√	√	-	√	√√	√	-
Section 475-057	√√	√	√√	√√	√√	√√	√√	√√	√√	√√	√√	√√
Section 475-071	√√	√√	√√	√√	√√	√√	√√	√√	√√	√√	√√	√

√√ 2 tests were performed to check the repeatability.

√ 1 test was performed.

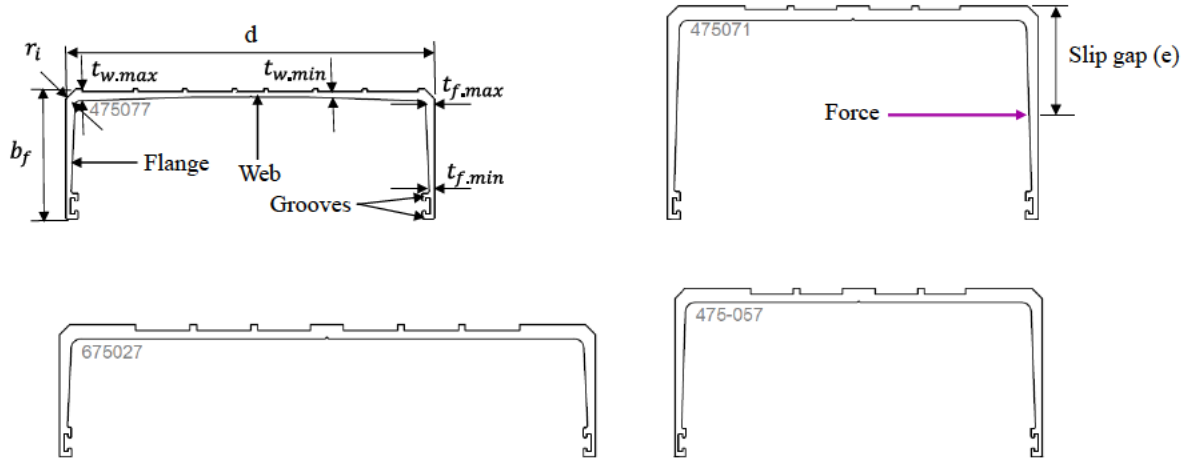
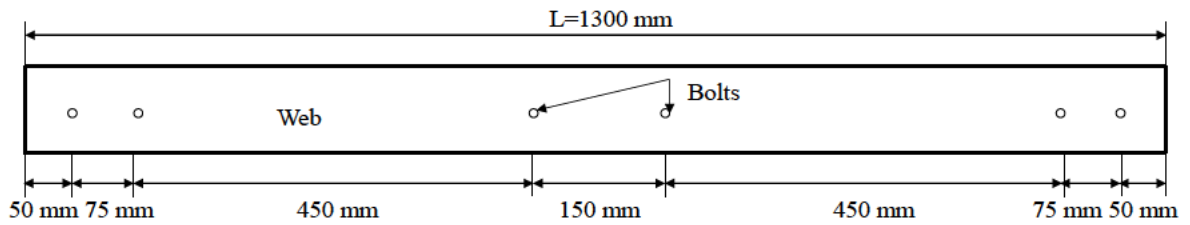
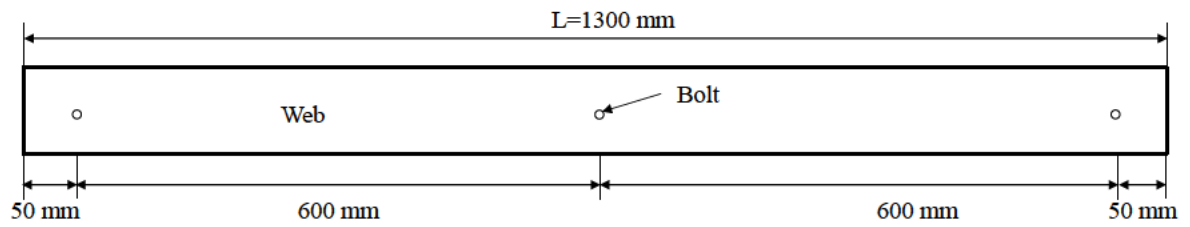


Figure 3.3 Sub-head sections.



(a) Two-bolt connection



(b) One-bolt connection

Figure 3.4 Bolt connection details.

Table 3.2 Geometric details of the aluminium sub-head sections.

Section	d (mm)	b _f (mm)	t _{w,max} (mm)	t _{w,min} (mm)	t _{f,max} (mm)	t _{f,min} (mm)	r _i (mm)	L (mm)
675-027	163	40	4.1	2.46	3.48	2.3	4.5	1300
475-077	111.7	40	3.65	1.5	2.64	1.5	3	1300
475-057	111.5	51	3.95	2.21	3.24	1.95	4.3	1300
475-071	112.7	65	4.2	3.13	3.65	2	4.5	1300

The specimens were labelled in the order of section, bolt connection details, engagement length and bearing width. For example, in the 475-057/1B/25/50 label, the first tag denotes Section 475-057, “1B” represents 1 bolt connection, “25” denotes 25 mm engagement length and “50” identifies 50 mm bearing width.

3.2.2. Material properties

Four tensile coupon tests per sub-head section type were conducted in accordance with the Australian Standard AS 1391 (SA, 1997) to measure the mechanical properties of the aluminium sub-heads, using 12 mm wide and 80 mm gauge length coupons, fitted with a 25 mm gauge length extensometer. The tensile coupons were taken from the centre of the web plate in the longitudinal direction of the sub-head. The thickness and width of each specimen were measured at three points, and the average measurements were calculated to obtain the cross-sectional area of the coupons. A 30 kN Instron displacement-controlled testing machine was used for the coupon tests at a constant strain rate of 0.01 mm/mm/min until failure, as demonstrated in Figure 3.5. In-built data acquisition system was used to record the load and strain at regular intervals during the tests. The material properties as the average of four tests per section are summarised in Table 3.3, which includes the measured elastic modulus (E), the static 0.2% tensile proof stress (f_y), the ultimate strength (f_u), and the elongation at fracture (ϵ_f).

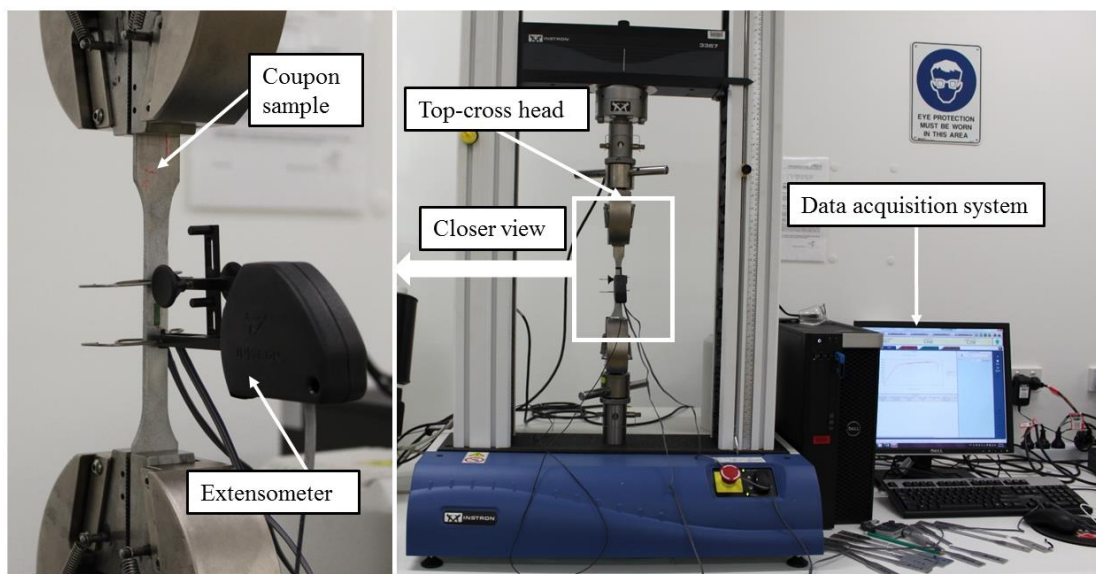


Figure 3.5 Tensile coupon test set-up.

Table 3.3 Mechanical properties of sub-head sections.

Section	E (MPa)	f_y (MPa)	f_u (MPa)	ϵ_f (mm)
675-027	62854	193	214	4.9
475-077	63768	217	233	5.7
475-057	65319	206	224	4.6
475-071	64147	188	210	4.9

3.2.3. Test Set-up and procedure

A 500 kN capacity MTS universal testing machine was used to apply a concentrated compressive force to the test specimens to investigate the bearing behaviour of various aluminium sub-head sections. A uniquely designed loading frame was used to induce a concentrated load at the bottom flange at mid span of the specimen by means of a bearing plate which acts at the internal surface of the flange element (Figure 3.6). The high-grade steel bearing plates were bolted to the bottom of the loading frame. Grease was smeared on the bearing plates and the bottom flanges to minimise friction, and the bearing plate was rounded to avoid localized tearing of the flange. Details of the test set up are shown in Figure 3.7. The sub-head was connected to a rigid support (RHS) replicating a concrete slab. A displacement-controlled loading scheme was used to drive the hydraulic actuator at a constant rate of 2 mm/min for all test specimens until failure. Three laser displacement transducers (Lasers 1, 2 and 3) were used to measure the vertical displacement of the bottom flange, whereas one laser (Laser 4) was used to monitor the vertical displacement of the bearing plate, as shown in Figure 3.8.

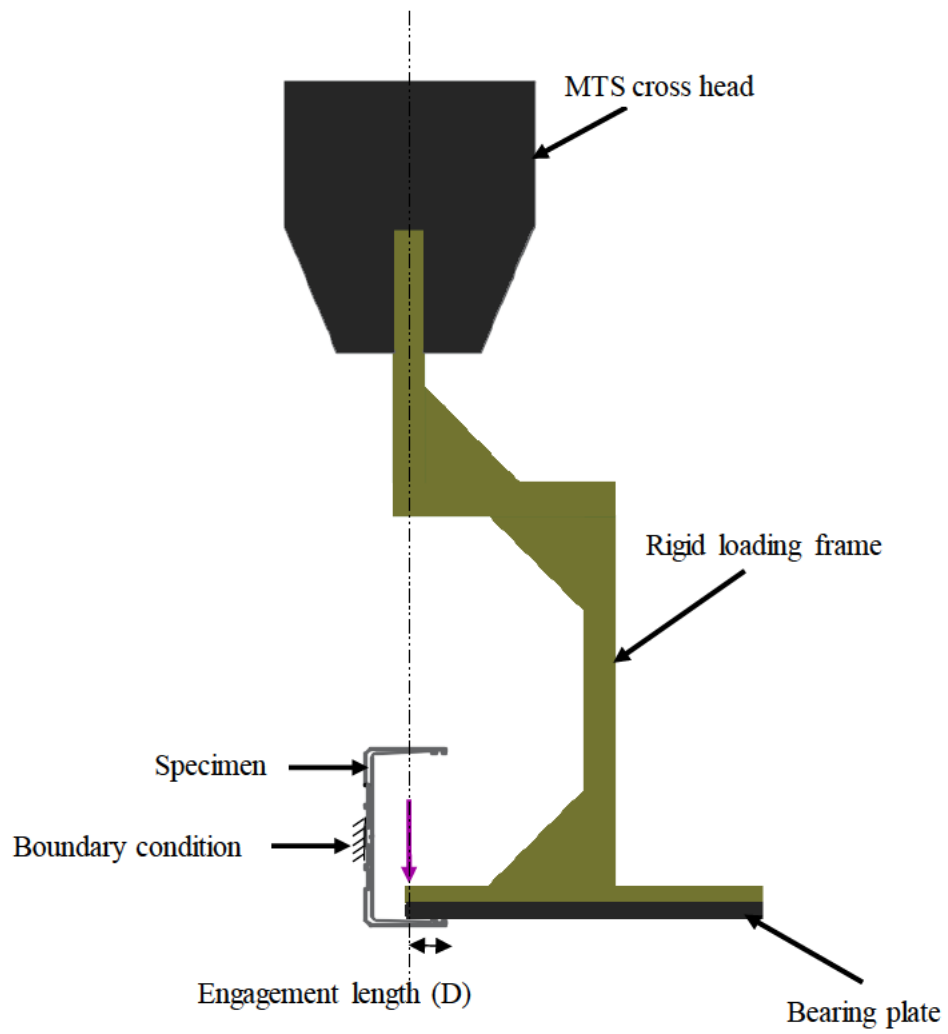


Figure 3.6 Loading frame and position.

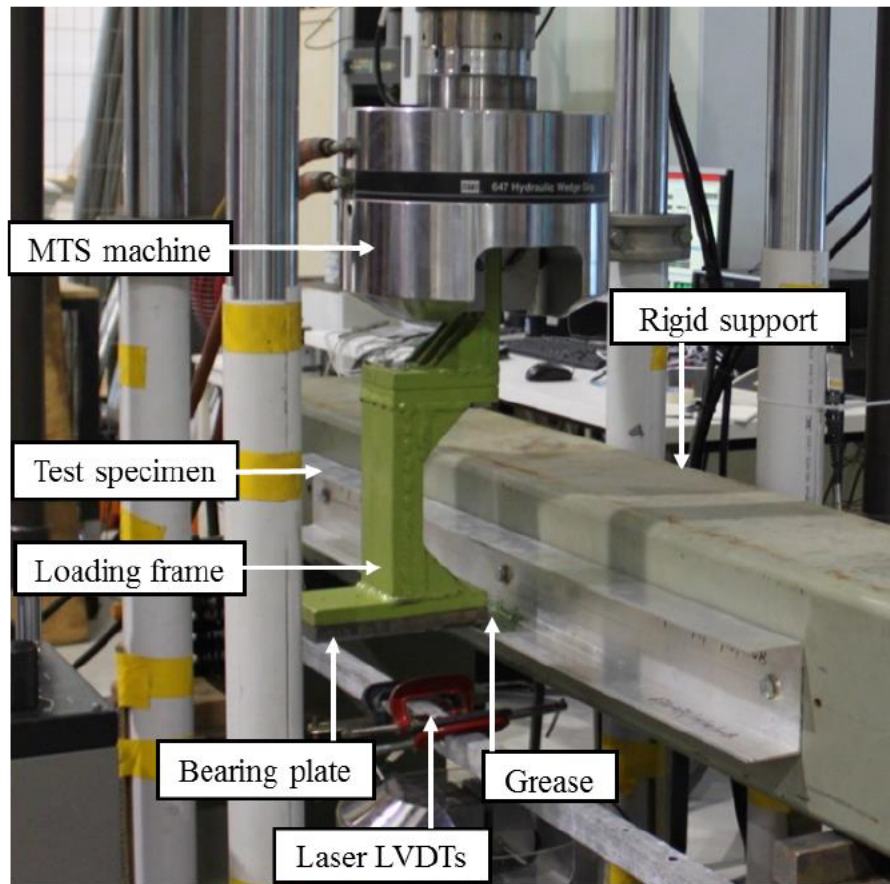
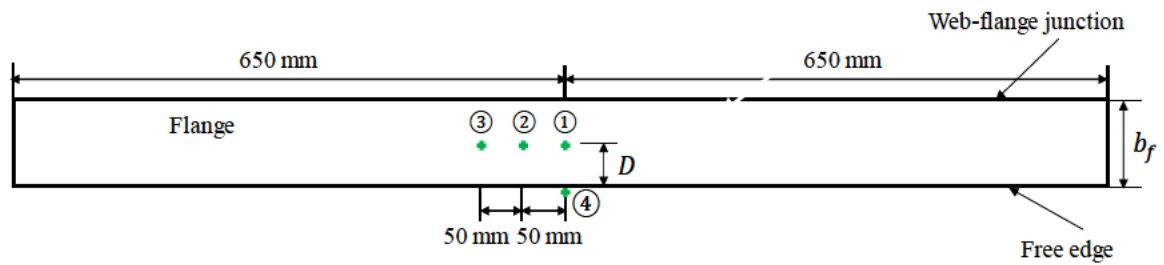
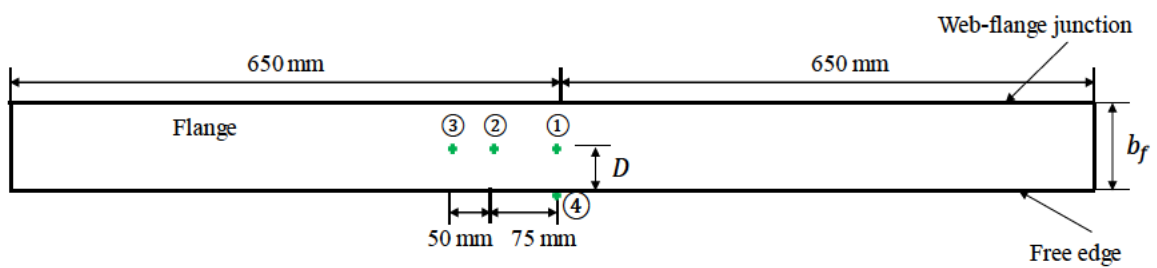


Figure 3.7 Bearing test set-up.



(a) 50 mm and 100 mm



(b) 150 mm

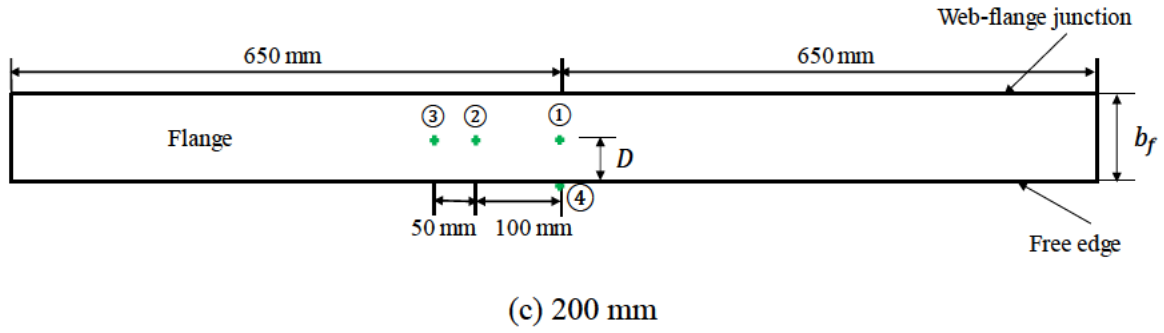
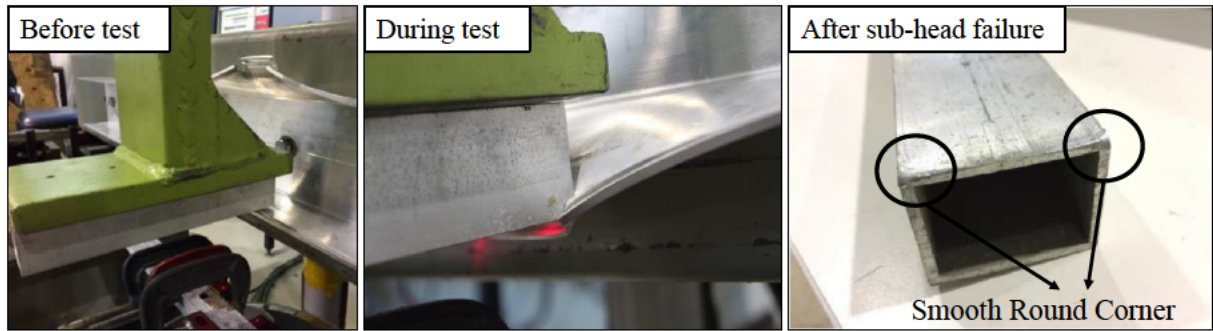


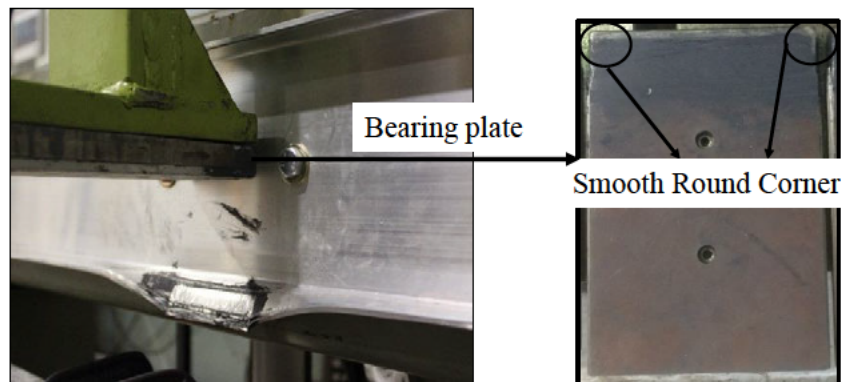
Figure 3.8 Displacement monitoring positions for different bearing widths (Top view).

3.2.4. Preliminary tests

Before conducting the comprehensive experimental study, three types of bearing plates (aluminium RHS, a sharp steel plate and a rounded steel plate with smeared grease) were considered in the test set-up (see Figure 3.9), to validate the appropriateness of using a rounded steel bearing plate with smeared grease instead of aluminium mullions. Tests were performed on Section 475-071 under 50 mm bearing width and 25 mm engagement length. Note that the aluminium RHS simulates the actual interaction between the aluminium mullion couple and sub-heads. However, as shown in Figure 3.9 (a), the sharp corners of the aluminium RHS deformed during the tests to form a smooth round corner. Figure 3.10 presents a comparison of the load-displacement curves of the different types of bearing plates. The ultimate bearing capacities obtained from the tests using the aluminium RHS and the rounded steel plate were similar, while the ultimate bearing capacity obtained from the sharp steel plate was significantly higher. Apart from the higher capacity provided by the sharp corner steel plate, tearing of the sub-head flange was also observed during the bearing test, as shown in Figure 3.9 (b). However, this tearing did not happen in the test with rounded steel plate (see Figure 3.9 (c)). Hence to minimise the material waste and time required to set up the tests, it was decided to use the rounded steel bearing plate with smeared grease as a reliable replacement for the aluminium RHS.



(a) Aluminium RHS



(b) Sharp steel plate

(c) Rounded steel plate

Figure 3.9 Different bearing plate arrangements.

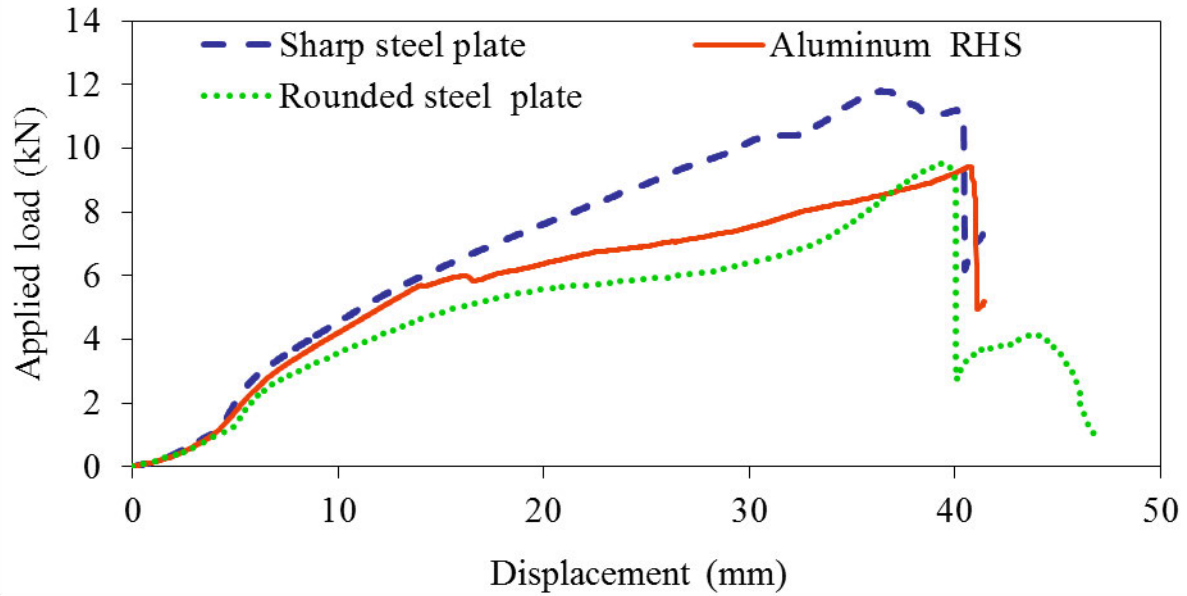
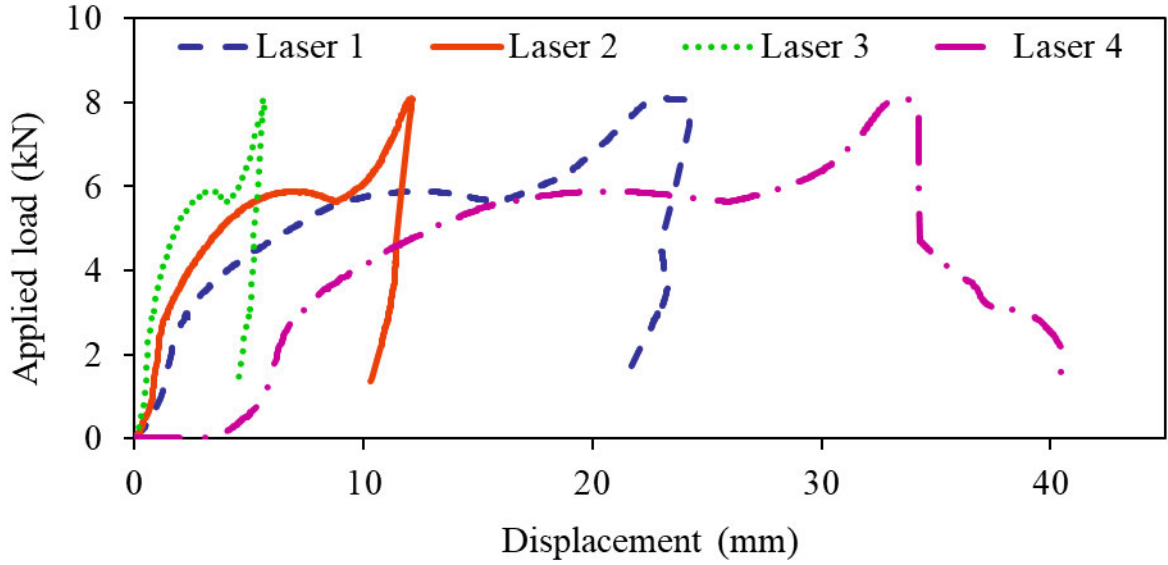


Figure 3.10 Load-displacement curves for different bearing plate arrangements.

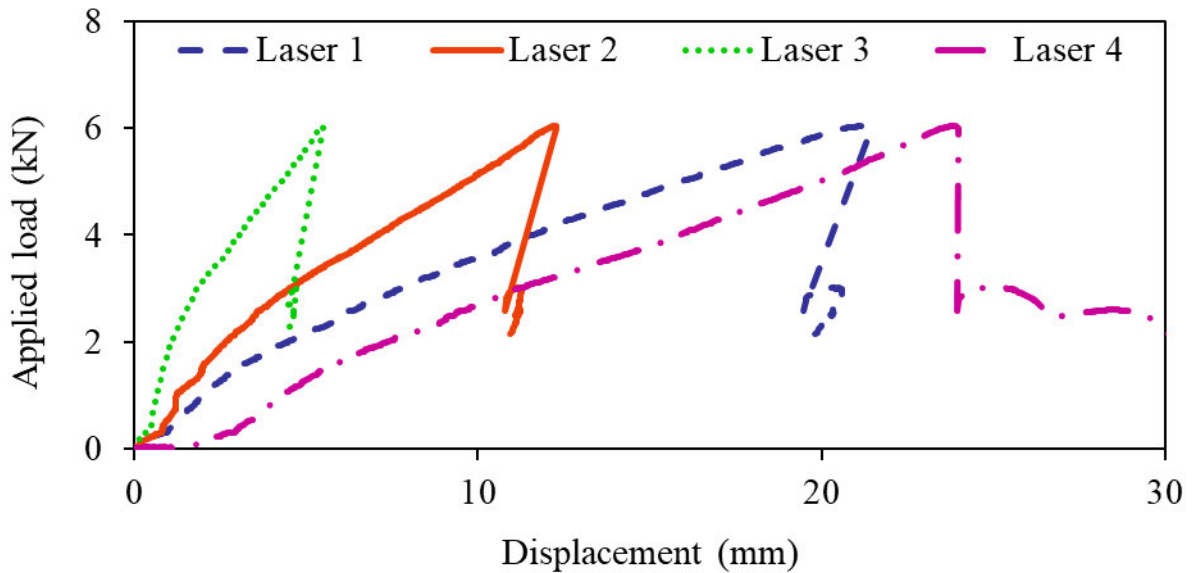
3.3. Test results and discussion

3.3.1. Load-displacement curves

Figure 3.11 (a) and (b) demonstrate the typical load-displacement curves (obtained from 4 Lasers) for Specimens 475-057/1B/25/50 and 475-057/1B/15/50, respectively. It was found that the load-displacement responses were influenced by the engagement lengths, bolt connection details, bearing widths and the section geometries. All the load-displacement curves of different sections under the same boundary conditions follow a similar pattern, therefore only the behaviours of Section 475-057 with different engagement lengths and bearing widths, and bolt connection details are discussed in Sections 3.3.1.1. to 3.3.1.3..



(a) Specimen 475-057/1B/25/50



(b) Specimen 475-057/1B/15/50

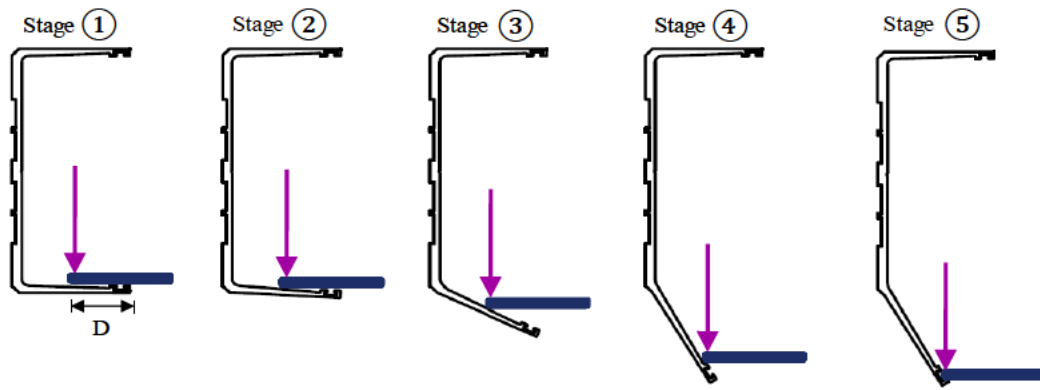
Figure 3.11 Typical load-displacement curves.

3.3.1.1. Engagement lengths

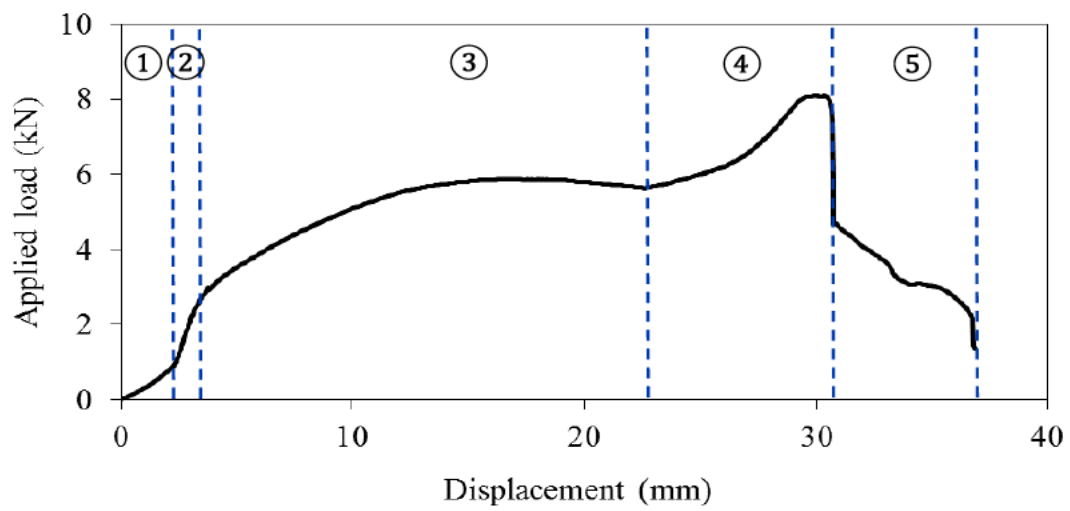
The engagement length plays a pivotal role in the behaviour and pattern of the load-displacement response. Figure 3.12 demonstrates the typical load-displacement curves of Section 475-057 with 15 mm and 25 mm engagement lengths (for 50 mm bearing width) along with the deformed shapes of the sub-heads at various stages. Five stages were

identified from the load-displacement curve of the specimen with 25 mm engagement length (Figure 3.12 (a) and (b)). In Stage ①, the bearing plate was in contact with the groove of the flange and in this case, the section endured approximately 1 kN before changing the slope in Stage ②. It should be emphasised that the groove is at the end of the flange tip to accommodate the rubber joint and to ensure the façade being weatherproofed. After Stage ①, the bearing plate was disconnected from the groove but in contact with the flange, resulting in an increased stiffness due to the reduction in eccentric loading (measured from the web-flange junction) applied on the cantilever flange. In Stages ② (elastic behaviour) and ③ (nonlinear behaviour – plastic deformation in the web-flange junction), the bearing plate slipped along the internal surface of the bottom flange smoothly. After this, the plate was mechanically locked at the first element of the groove (at the end of the flange) in Stage ④. This led to a sharp rise in the load-displacement curve. The ultimate load was obtained in this stage, before the bearing plate crushed the first element of the groove. The applied load dropped suddenly after reaching the ultimate load, whereas the displacement continued to increase in Stage ⑤ until the bearing plate crushed the second element of the groove and detached completely from the flange.

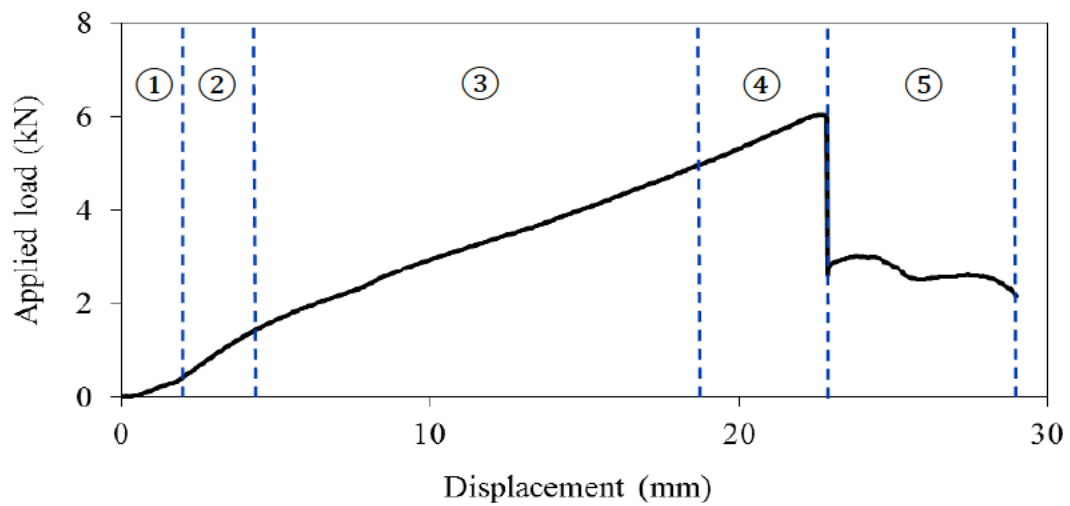
Stages ① to ⑤ of a typical load-displacement curve corresponding to the specimen with 15 mm engagement length were similar to those with 25 mm engagement length (Figure 3.12 (c)). However, it should be noted that in the test under 15 mm engagement length, the bearing plate had less distance to slip along the flange compared to those with 25 mm engagement length. Hence the variations of the load-displacement curve at different stages were less significant (i.e., gradual increase in Stages ② and ④). Also, when the bearing plate slipped along the flange (Stage ③), it reached the first element of the groove without noticeable plastic deformation at the web-flange junction. As a result, the stiffness in stage ②, the ultimate load and the ductility of the specimens with 15 mm engagement length were noticeably less than those with 25 mm length.



(a) Stages



(b) 25 mm engagement length



(c) 15 mm engagement length

Figure 3.12 Stages of the bearing tests for different engagement lengths.

3.3.1.2. Bolt connection details

Figure 3.13 displays the load versus displacement curves for Section 475-057 with 50 mm bearing width and with different connection details on the web. A similar trend was observed for the load-displacement behaviour of the 25 mm engagement length with one-bolt and two-bolt connection details. However, the specimen with two-bolt connection produced a marginally higher capacity, in comparison with the one-bolt connection counterpart, due to a higher restraint provided by the extra bolt connection on the web. Notably, this trend was almost consistently observed for all the four sections with different bearing widths.

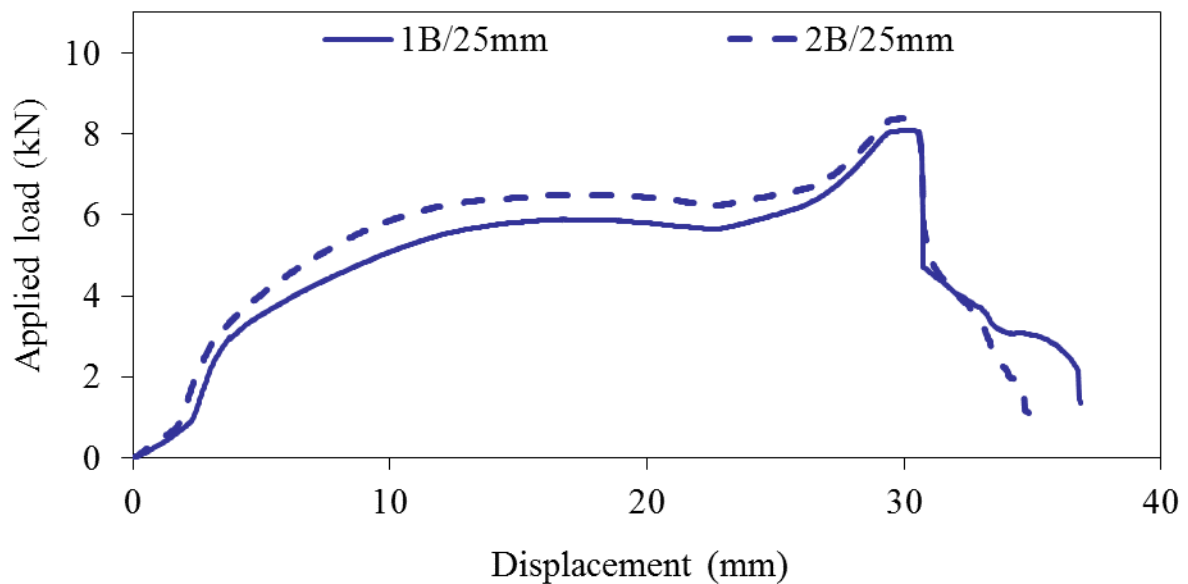
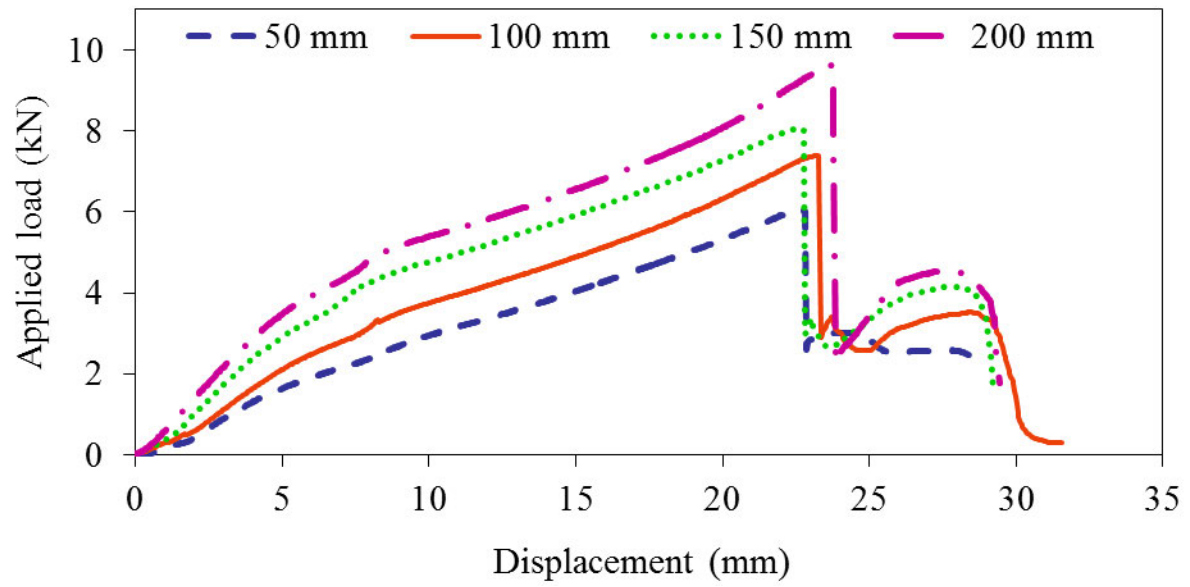


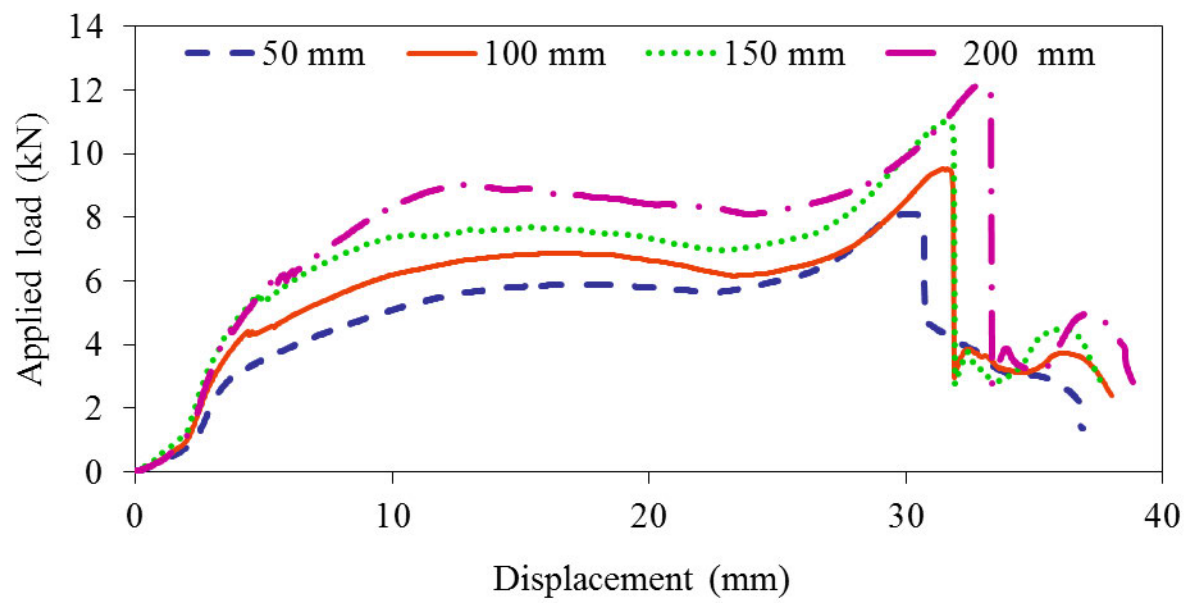
Figure 3.13 Load-displacement curves for different bolt connection details for Section 475-057.

3.3.1.3. Bearing widths

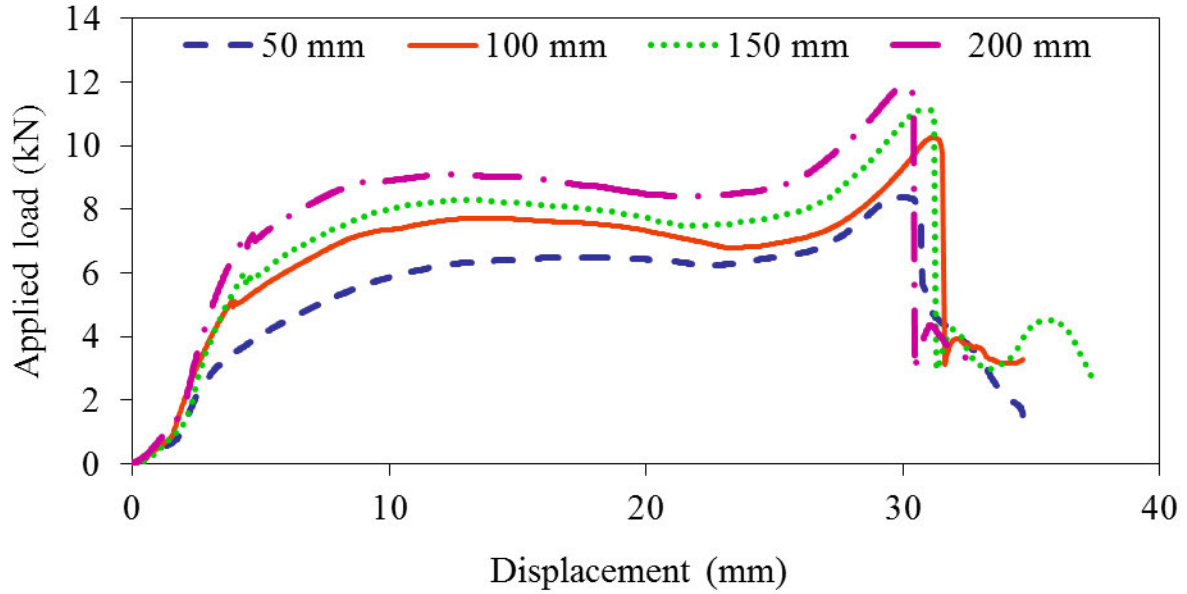
Figure 3.14 (a) to (c) show the comparisons of the load-displacement curves between four bearing widths for different engagement lengths and bolt connection details for Specimen 475-057. The graphs reveal some similarities in the clearly exhibited upward trend. For all three cases shown in Figures 14 (a) to (c), increasing bearing width can considerably enhance the bearing capacity of the aluminium sub-heads.



(a) 15 mm/1B



(b) 25 mm/1B



(c) 25 mm/2B

Figure 3.14 Load-displacement curves for different engagement lengths and bolt connection details for Section 475-057.

3.3.1.4. Section geometries

Figure 3.15 presents the load-displacement curves of aluminium sub-heads of different section geometries with 25 mm engagement length, one-bolt connection and 50 mm bearing width. Among four different sections, the highest bearing capacity is attributed to Section 675-027, as contrasted with Section 475-077 with the lowest strength. This can be explained as Section 675-027 has larger flange thickness (t_f), despite the fact that their flange widths (b_f) are equal (see Table 3.2). In addition, as Section 475-071 has the longest flange width (Table 3.2), the displacement at the ultimate load for this section is higher than that of the other sections. From the above comparison, both the flange width and thickness are found to be the most crucial geometric factors affecting the behaviour and ultimate capacity of various sub-head sections.

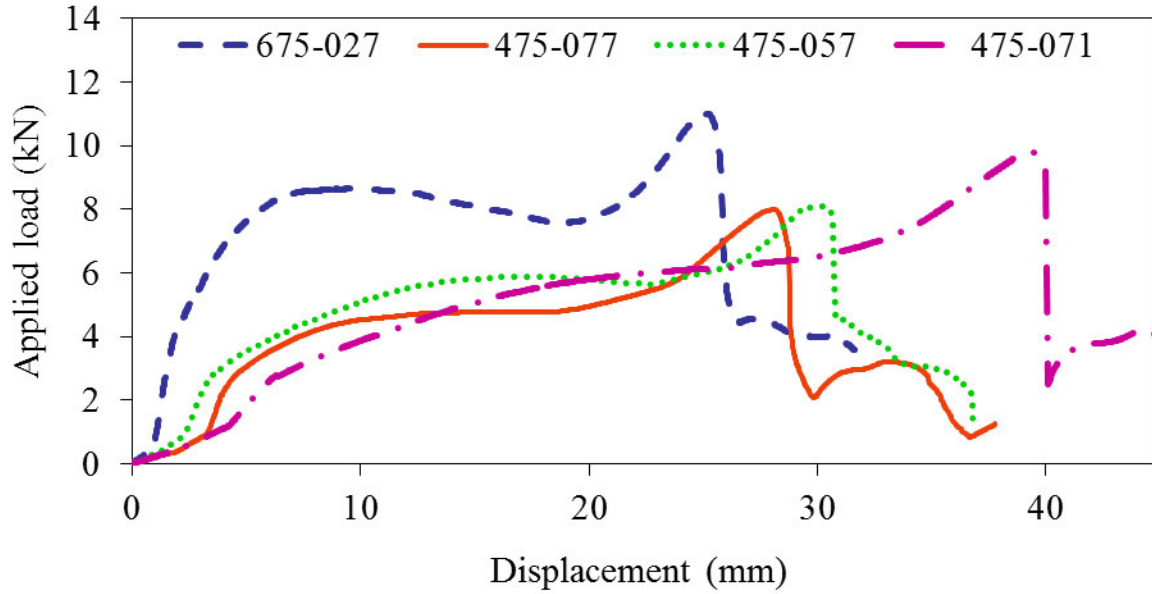


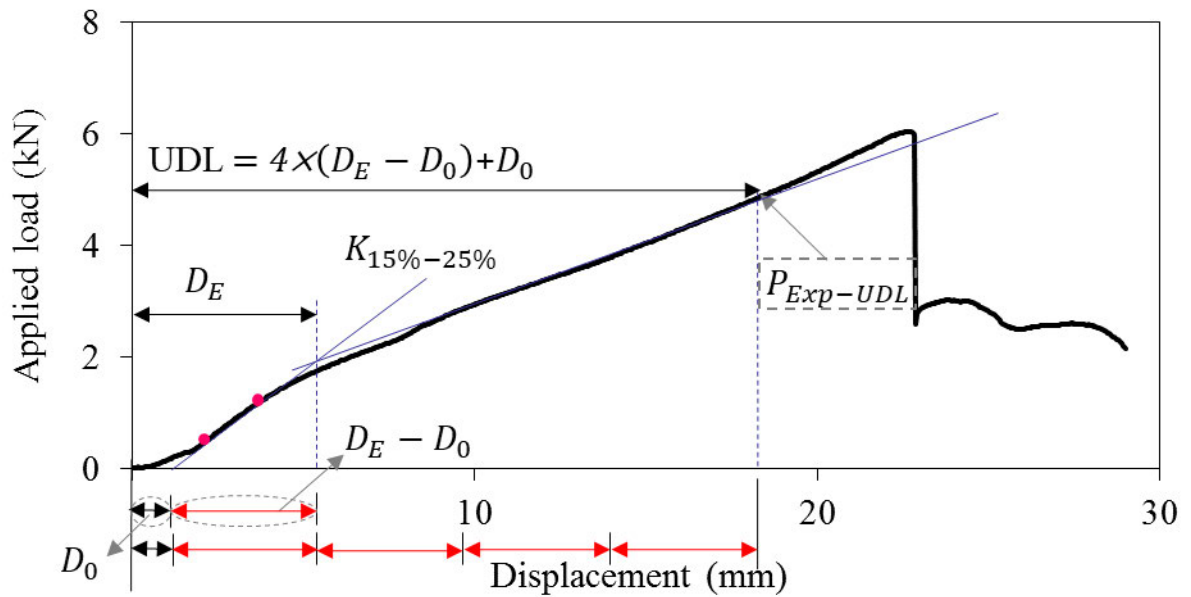
Figure 3.15 Load-displacement curves for different section geometries with 50 mm bearing width and 25 mm engagement length.

3.3.2. Ultimate deformation limit

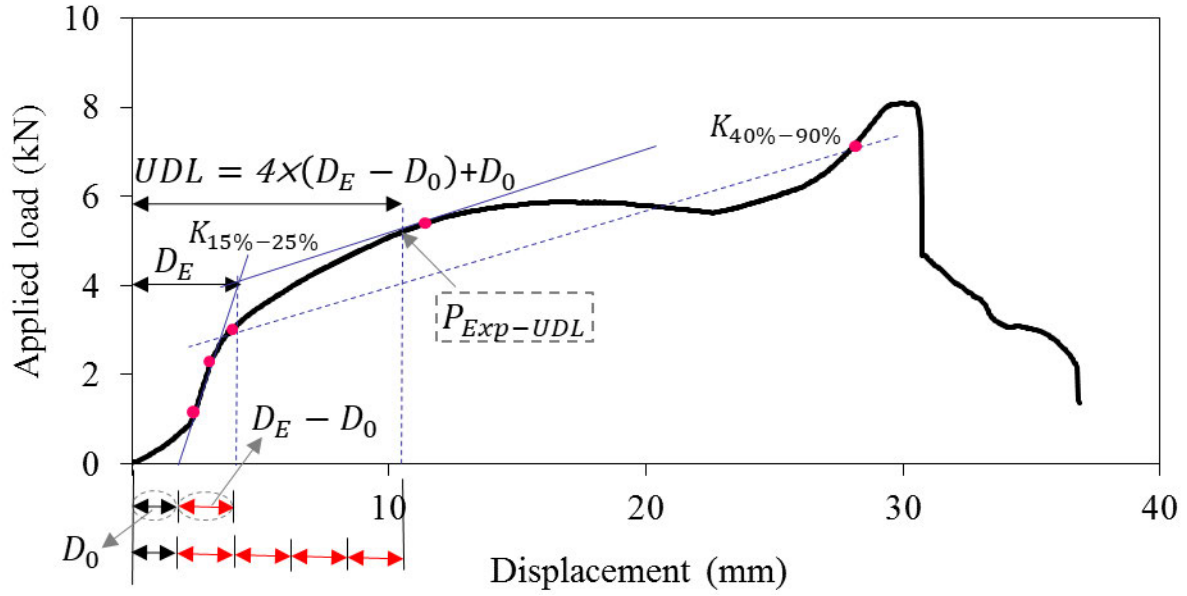
In this study, a maximum load was reached after a very large deformation occurred in the sub-head. This load may depend on the shape of the groove in which the mullion mechanically locks in Stage ④ (see Section 3.3.1.1). Therefore, while the overall behaviour described herein is generic for sub-head products, the maximum load may be manufacturer specific rather than product specific. A different shape and size of groove may lead to different maximum loads. Hence an appropriate criterion must be set to define the ultimate load. In this study, an ultimate deformation limit (UDL) of four times the first yield displacement is considered as suggested by (Gilbert and Rasmussen, 2011; Yura, 1981; AS 4084, 2012). The initial displacement observed in Stage ① (D_0) was due to the adjustment of the MTS machine and the shift of loading point from groove to the flange. Hence this displacement (D_0) must be disregarded in the calculation of first yield displacement. Therefore, the load corresponding to the UDL (obtained from Eq. (3.1) below) is defined as $P_{Exp-UDL}$ as illustrated in Figure 3.16 (a) and Figure 3.16 (b).

$$UDL = 4 \times (D_E - D_0) + D_0 \quad (3.1)$$

where the total first yield displacement D_E is calculated as explained below for 15 mm and 25 mm engagement lengths. Two obvious linear regions were observed in tests with 15 mm engagement length. For this condition, based on AS 4084, 2012, D_E is calculated as the deformation at the intersection between the line representing the elastic and inelastic stiffness deformations as illustrated in Figure 3.16 (a). However, no obvious linear region after elastic region was observed in load-displacement curves under 25 mm engagement length. For this kind of load displacement curve, aluminium and cold-formed steel design standards do not provide any criterion for the calculation of D_E . Hence the criterion proposed by (Brühl et al., 2011; Yasumura and Kawai, 1998) has been chosen in this paper to estimate the point of yielding and D_E . In this criterion, the initial stiffness corresponding to 10% and 40% of the peak load of the elastic slop is set. Then, a straight line measured between 40% and 90% of the peak load is drawn, and a straight-line tangent to the load-displacement curve and parallel to the 40% and 90% secant line is also determined. The displacement corresponding to the intersection point of the initial stiffness and a tangent with a slope of a secant passing through 40% and 90% of the peak load is established as D_E as shown in Figure 3.16 (b). However, in this study, the 10% to 40% of the peak load for some specimens is out of range of the elastic deflection, so the stiffness corresponding to 15% to 25% was considered for initial stiffness.



(a) 15 mm engagement length



(b) 25 mm engagement length

Figure 3.16 Ultimate bearing capacity based on ultimate deformation limit (UDL).

3.3.3. Ultimate loads

Table 3.4 and Table 3.5 present the bearing capacities of the aluminium sub-head sections as obtained from the experimental tests of 42 specimens based on the maximum load ($P_{Exp-Max.}$) and ultimate deformation limit ($P_{Exp-UDL.}$), respectively. Figure 3.17 displays the relationships between the maximum load and bearing width with different engagement lengths and bolt connection details for the four different sections. In most cases a linear increase in the ultimate bearing capacity was recognised as the bearing width was increased for various engagement lengths and bolt connection details. Referring to Figure 3.17, and as discussed in Section 3.3.1.2, the ultimate maximum load showed very little sensitivity to the extra bolt connection. Additionally, even though there are some minor discrepancies in the slopes of all the trend lines, the overall slope (the variation of the ultimate maximum load with respect to the bearing width) was almost equal for all cases (15mm/1B, 25mm/1B and 25mm/2B).

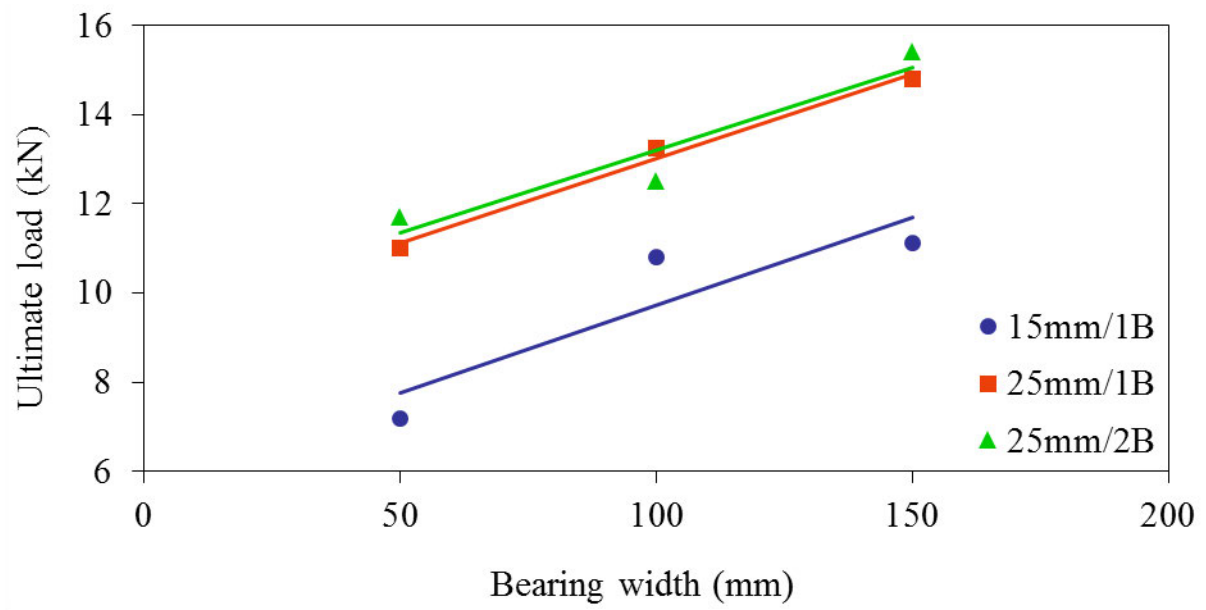
Table 3.4 Comparison of experimental ultimate strengths with current and proposed design rules, based on maximum load.

Specimen details			$P_{Exp-Max.}$ (kN)	P_{AISI} (kN)	P_{TI} (kN)	$P_{Prop-Max.}$ (kN)	$\frac{P_{Exp-Max.}}{P_{AISI}}$	$\frac{P_{Exp-Max.}}{P_{TI}}$	$\frac{P_{Exp-Max.}}{P_{Prop-Max.}}$
Loading and boundary conditions	Section	N (mm)							
1B/15mm	675-027	50	8.4	4.9	3.1	9.0	1.71	2.71	0.93
		100	10.8	4.9	3.9	10.3	2.21	2.75	1.05
		150	11.1	4.9	4.8	11.5	2.27	2.32	0.96
	475-077	50	5.7	3.6	2.0	5.8	1.58	2.86	0.98
		100*	6.8	3.6	2.5	6.6	1.89	2.68	1.02
		150	7.6	3.6	3.1	7.4	2.13	2.48	1.03
	475-057	50*	6.2	3.3	2.3	7.0	1.85	2.66	0.88
		100	7.4	3.3	2.9	7.8	2.20	2.58	0.94
		150*	8.2	3.3	3.4	8.6	2.46	2.43	0.96
		200*	9.6	3.3	3.9	9.4	2.87	2.45	1.02
	475-071	50*	7.1	2.7	2.3	7.2	2.59	3.04	0.98
		100*	7.6	2.7	2.8	7.9	2.78	2.76	0.97
		150*	8.8	2.7	3.2	8.5	3.19	2.73	1.03
		200*	9.0	2.7	3.6	9.2	3.27	2.46	0.98
1B/25mm	675-027	50	11.0	8.1	5.5	10.9	1.36	2.01	1.01
		100	13.2	8.1	7.0	13.1	1.64	1.9	1.01
		150	14.8	8.1	8.5	15.4	1.83	1.74	0.96
	475-077	50	8.0	5.7	3.5	7.3	1.4	2.30	1.10
		100*	9.5	5.7	4.4	8.7	1.65	2.13	1.09
		150	10.2	5.7	5.4	10.2	1.78	1.89	1.01
	475-057	50*	8.2	4.5	3.3	8.1	1.83	2.48	1.01
		100*	9.6	4.5	4.0	9.2	2.14	2.37	1.04
		150*	11.2	4.5	4.8	10.4	2.49	2.33	1.08
		200*	12.0	4.5	5.5	11.5	2.69	2.17	1.05
	475-071	50*	9.9	3.3	3.0	10.4	2.95	3.34	0.95
		100*	10.7	3.3	3.5	11.2	3.21	3.06	0.96
		150*	11.6	3.3	4.1	12.0	3.47	2.86	0.96
		200*	13.0	3.3	4.6	12.9	3.88	2.82	1.01
2B/25mm	675-027	50	11.7	8.1	5.5	10.9	1.45	2.14	1.07
		100	12.5	8.1	7.0	13.1	1.55	1.80	0.95
		150	15.4	8.1	8.5	15.4	1.91	1.82	1.00
	475-077	50	8.2	5.7	3.5	7.3	1.43	2.36	1.13
		100*	9.8	5.7	4.4	8.7	1.71	2.20	1.12
		150	11.0	5.7	5.4	10.2	1.91	2.03	1.08
	475-057	50*	8.3	4.5	3.3	8.1	1.86	2.52	1.03
		100*	10.3	4.5	4.0	9.2	2.3	2.55	1.12
		150*	11.1	4.5	4.8	10.4	2.48	2.32	1.08
		200*	11.6	4.5	5.5	11.5	2.59	2.10	1.01
	475-071	50*	10.3	3.3	3.0	10.4	3.08	3.49	0.99
		100*	10.6	3.3	3.5	11.2	3.18	3.03	0.95
		150*	11.8	3.3	4.1	12.0	3.54	2.92	0.98
		200	12.2	3.3	4.6	12.9	3.66	2.66	0.95
Mean							2.33	2.48	1.01
COV							0.30	0.17	0.06
ϕ_w							1.49	2.00	0.94

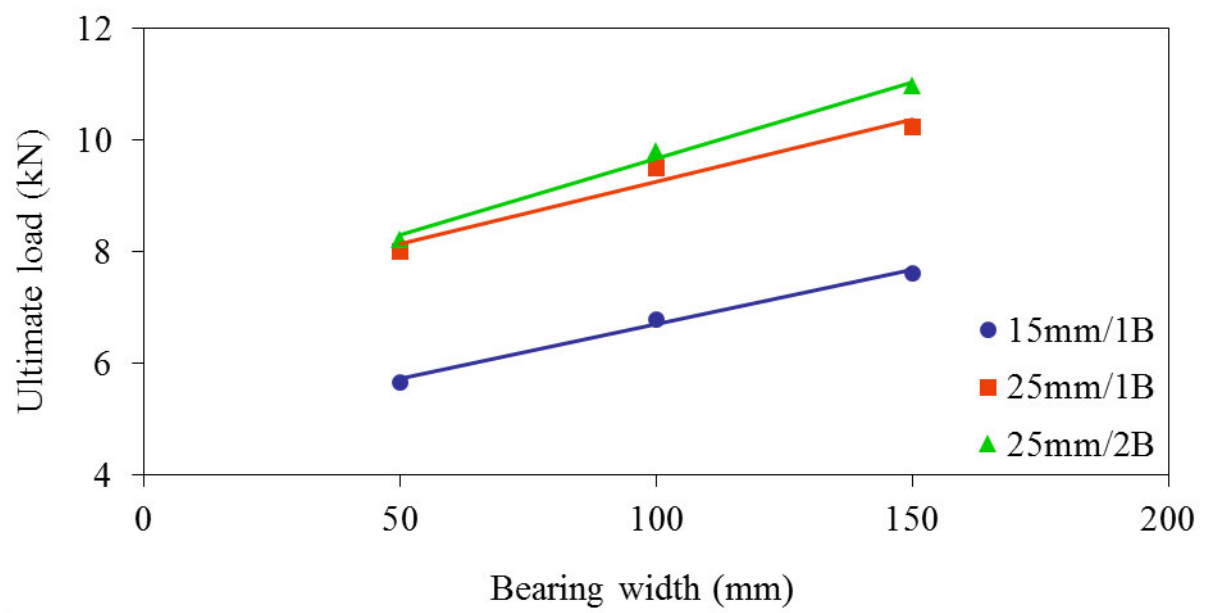
Table 3.5 Comparison of experimental ultimate strengths with current and proposed design rules, based on ultimate deformation limit (UDL).

Specimen details			$P_{Exp-UDL}$ (kN)	P_{AISI} (kN)	P_{TI} (kN)	$P_{Prop-UDL}$ (kN)	$\frac{P_{Exp-UDL}}{P_{AISI}}$	$\frac{P_{Exp-UDL}}{P_{TI}}$	$\frac{P_{Exp-UDL}}{P_{Prop-UDL}}$
Loading and boundary conditions	Section	N (mm)							
1B/15mm	675-027	50	7.9	4.9	3.1	8.6	1.62	2.57	0.92
		100	10.4	4.9	3.9	9.9	2.13	2.65	1.05
		150	11.1	4.9	4.8	11.2	2.27	2.33	0.99
	475-077	50	5.0	3.6	2.0	5.4	1.40	2.52	0.92
		100*	6.8	3.6	2.5	6.2	1.90	2.69	1.09
		150	6.6	3.6	3.1	7.0	1.83	2.14	0.93
	475-057	50*	6.2	3.3	2.3	6.3	1.85	2.66	0.98
		100	7.7	3.3	2.9	7.1	2.30	2.70	1.08
		150*	8.2	3.3	3.4	7.9	2.46	2.43	1.04
		200*	9.5	3.3	3.9	8.7	2.84	2.43	1.09
	475-071	50*	5.8	2.7	2.3	6.1	2.11	2.48	0.95
		100*	6.4	2.7	2.8	6.8	2.33	2.31	0.94
		150*	7.3	2.7	3.2	7.4	2.67	2.28	0.98
		200*	8.3	2.7	3.6	8.1	3.04	2.29	1.03
1B/25mm	675-027	50	8.5	8.1	5.5	7.9	1.05	1.56	1.07
		100	11.9	8.1	7.0	10.2	1.47	1.71	1.17
		150	12.2	8.1	8.5	12.4	1.51	1.44	0.98
	475-077	50	4.5	5.7	3.5	5.2	0.78	1.29	0.86
		100*	5.6	5.7	4.4	6.7	0.98	1.26	0.84
		150	6.4	5.7	5.4	8.1	1.12	1.18	0.79
	475-057	50*	5.4	4.5	3.3	5.4	1.21	1.64	0.99
		100*	6.3	4.5	4.0	6.6	1.41	1.56	0.96
		150*	7.7	4.5	4.8	7.7	1.72	1.61	1.00
		200*	8.6	4.5	5.5	8.8	1.92	1.55	0.98
	475-071	50*	6.1	3.3	3.0	6.0	1.82	2.06	1.01
		100*	6.3	3.3	3.5	6.9	1.89	1.80	0.92
		150*	7.2	3.3	4.1	7.7	2.17	1.79	0.94
		200*	8.2	3.3	4.6	8.5	2.44	1.77	0.96
2B/25mm	675-027	50	9.8	8.1	5.5	7.9	1.21	1.79	1.24
		100	10.3	8.1	7.0	10.2	1.27	1.47	1.01
		150	13.3	8.1	8.5	12.4	1.64	1.57	1.07
	475-077	50	5.1	5.7	3.5	5.2	0.88	1.45	0.97
		100*	5.9	5.7	4.4	6.7	1.03	1.32	0.88
		150	7.4	5.7	5.4	8.1	1.29	1.37	0.91
	475-057	50*	6.2	4.5	3.3	5.4	1.38	1.88	1.14
		100*	7.6	4.5	4.0	6.6	1.69	1.88	1.16
		150*	8.1	4.5	4.8	7.7	1.80	1.68	1.05
		200*	8.8	4.5	5.5	8.8	1.96	1.58	0.99
	475-071	50*	6.6	3.3	3.0	6.0	1.99	2.25	1.10
		100*	6.5	3.3	3.5	6.9	1.94	1.85	0.94
		150*	7.6	3.3	4.1	7.7	2.27	1.87	0.99
		200	8.2	3.3	4.6	8.5	2.44	1.77	0.96
Mean							1.79	1.92	1.00
COV							0.31	0.24	0.09
ϕ_{wz}							1.12	1.38	0.91

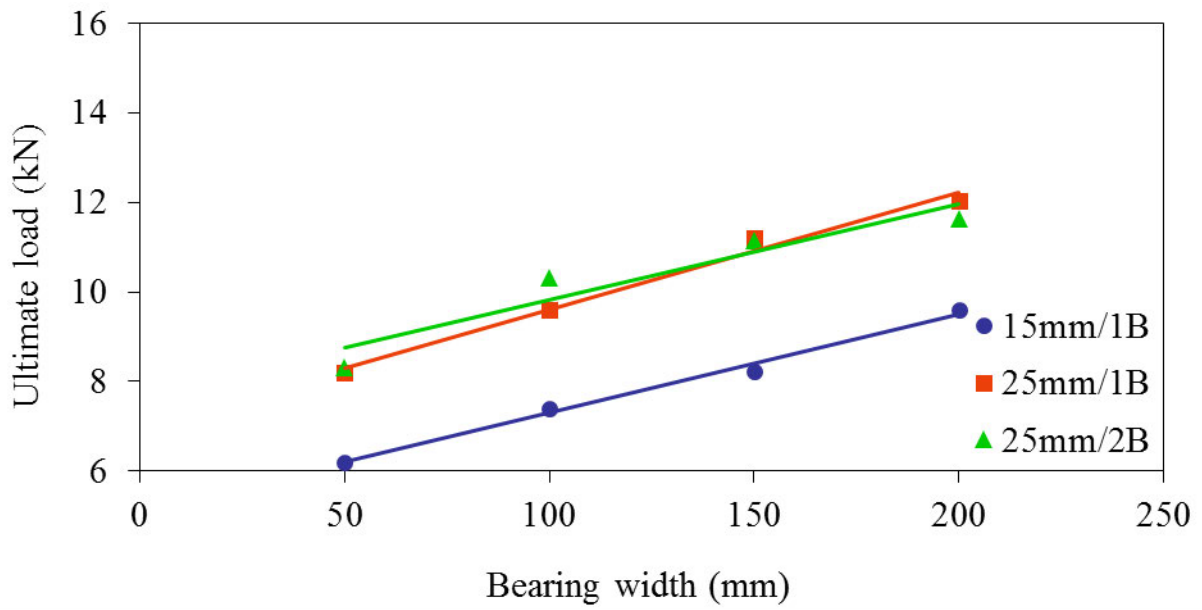
*Tests were repeated and the average values of two tests are reported.



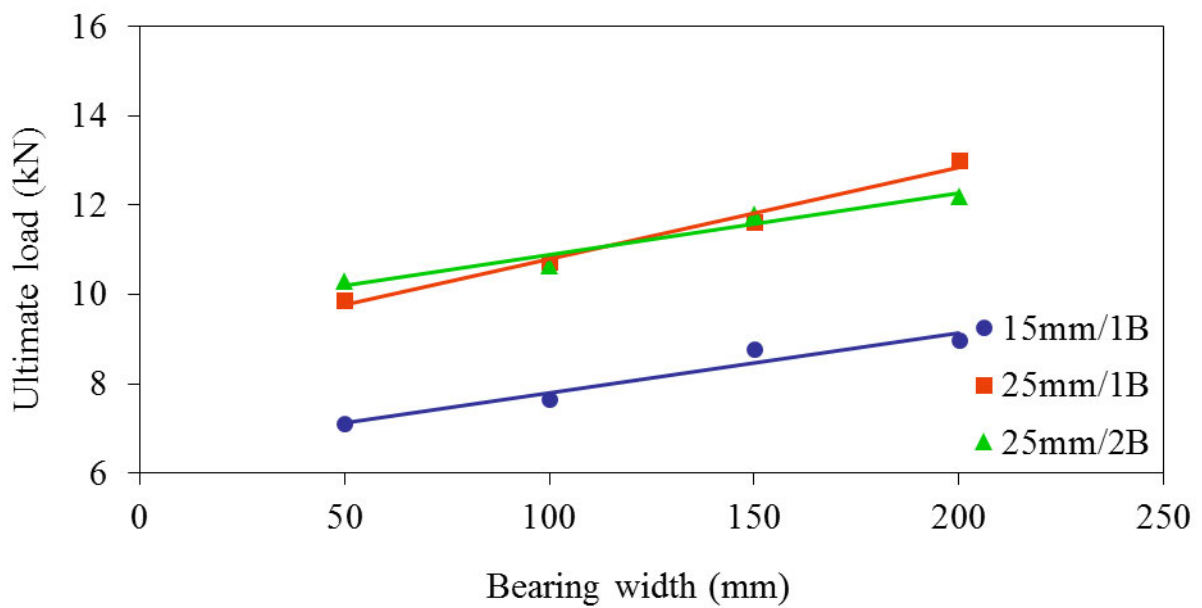
(a) Section 675-027



(b) Section 475-077



(c) Section 475-057



(d) Section 475-071

Figure 3.17 Ultimate load versus bearing widths for different section geometries.

3.3.4. Failure modes

It should be noted that, the maximum bending stress occurred at the web-flange junction, where the bending moment of the cantilever flange peaks. Two kinds of failure mechanisms governed the bearing behaviour of the aluminium sub-head sections which are, i) yielding at

the web-flange junction due to the bending of the cantilever flange, ii) slipping of the bearing plate after the flange groove was crushed (Figure 3.18). As demonstrated in Figure 3.19, the length of the influenced zone was expanded with the increment of the bearing width. Flange bending and the corresponding length of the influenced zone are more distinguished in samples with longer flanges and extended engagement length (25 mm).

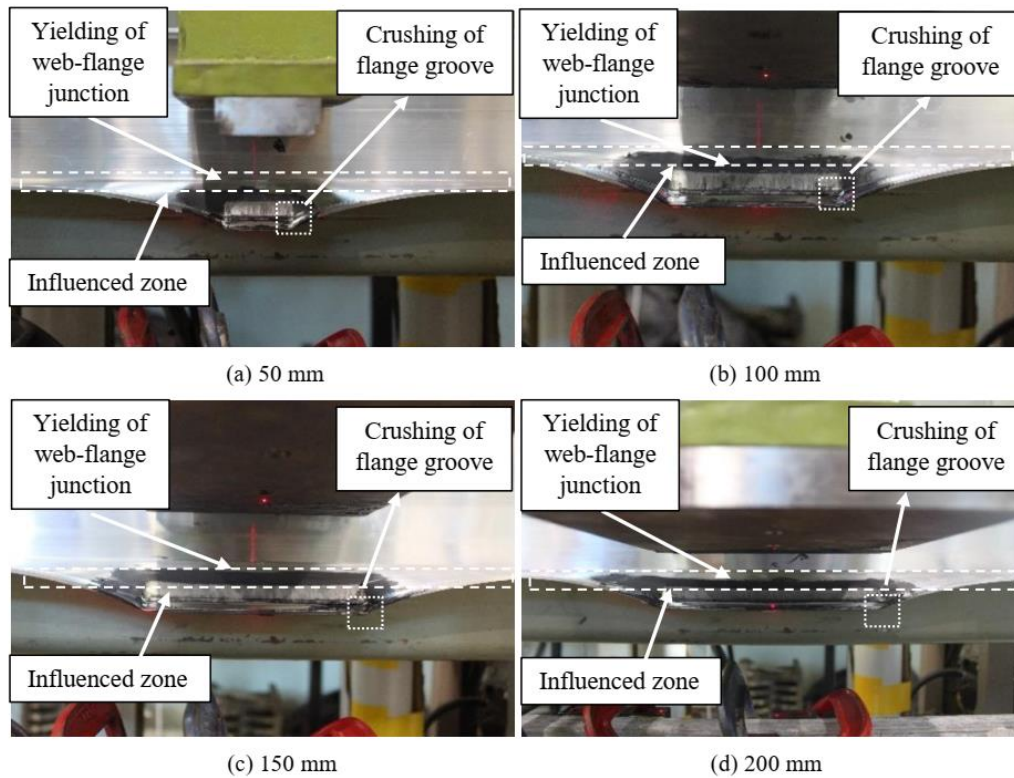
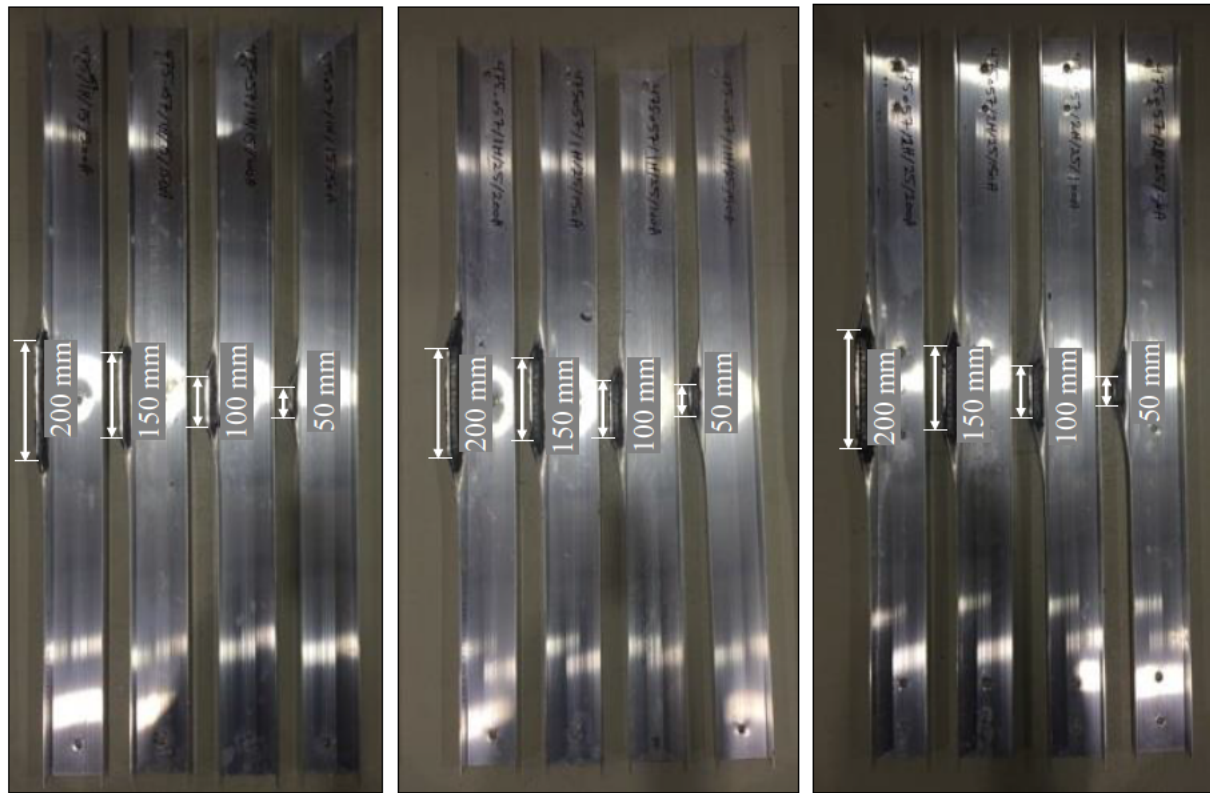


Figure 3.18 Bearing failure modes of Section 475-057 under different bearing widths.



(a) 15 mm/1B

(b) 25 mm/1B

(c) 25 mm/2B

Figure 3.19 Bearing failure modes of Section 475-057.

3.4. Design rules

3.4.1. Current design rules

Bending of the flange is one of the common failure modes observed in the aluminium sub-head subjected to the bearing load acting on the internal surface of the flange, which closely resembles the failure of a track flange in LSF walls when one track flange is directly loaded. In this regard, design rules that can predict the nominal strength of the track in an LSF wall subjected to a transverse load are provided by the North American Standard for cold-formed steel structural framing (AISI S240, 2015), the U.S. Army Corps of Engineers (TI 809-07, 1998) and the Steel Stud Manufacturers Association (SSMA, 2000). The main difference of the design rules provided by AISI S240 (2015) and TI 809-07 (1998) is that the first one (AISI S240, 2015) is based on the ultimate strength design, however the second one (TI 809-07, 1998) is based on the allowable stress design. Noteworthy is that SSMA (2000) procedure to calculate the nominal capacity of the track is established based on TI 809-07 (1998). A

detailed assessment to the suitability of design guidelines recommended in the AISI S240 (2015) and TI 809-07 (1998) were conducted in this study by comparing them with experimental results.

The flange of the sub-head could be considered as a cantilever beam subjected to a concentrated load. The bending moment acting on the web-flange junction can be calculated as the product of the applied load (P) and the slip gap (e) (distance from the loading point to the web-flange junction (see Figure 3.20)). Thus, the ultimate strength of the sub-head under bearing load can be precisely estimated by means of the theoretical bending equation and the section modulus (Eq. (3.2a)). It should be noted that AISI S240 (2015) is based on the plastic limit moment, whereas TI 809-07 (1998) considers the first yield moment.

$$M = Z_x f_y \quad (3.2a)$$

$$\text{with } M = Pe \quad (3.2b)$$

where M is the bending moment (N·mm); Z_x is the section modulus (mm³); f_y is the yield strength (MPa); and e is the slip gap (mm) (see Figure 3.20).

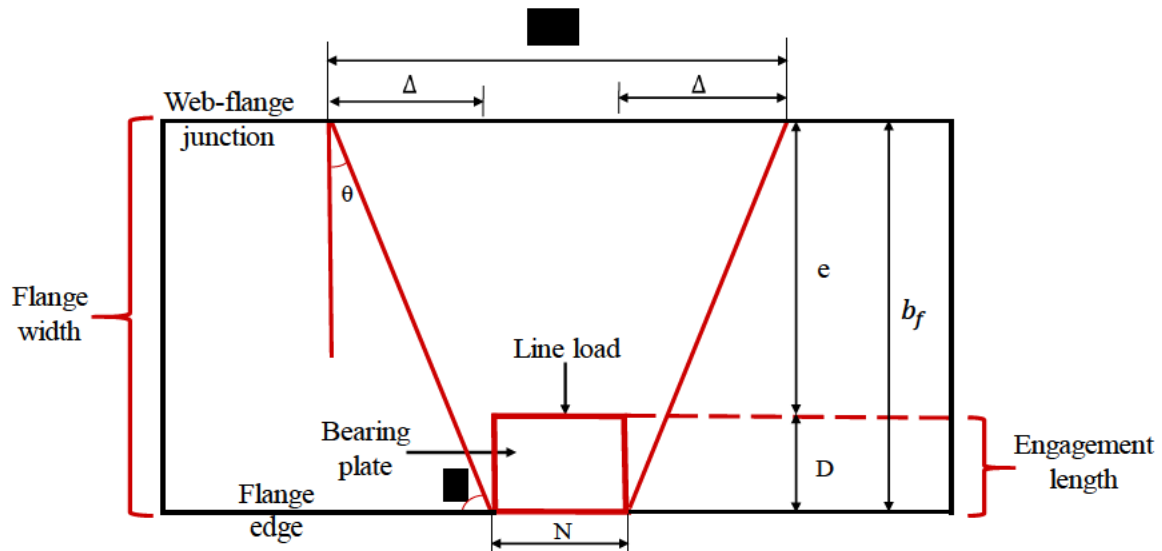


Figure 3.20 Stress distribution in sub-head flange element.

3.4.1.1. AISI S240 (2015)

The design rule for predicting the nominal strength (P_n) of a single deflection track subjected to concentrated loads and connected to its support can be found from Section B3.2.5.2 of the AISI S240 (2015) standard.

The plastic section modulus (Eq. (3.3a)) is used in the derivation of the equation for predicting the nominal strength. By substitution Eq. (3.2b) and Eq.(3.3a) into Eq. (3.2a), the nominal capacity is obtained from Eq. (3.3b).

$$Z_x = \frac{w_{dt} t^2}{4} \quad (3.3a)$$

$$P_n = \frac{w_{dt} t^2 f_y}{4e} \quad (3.3b)$$

$$\text{with } w_{dt} = 0.11\alpha^2(e^{0.5}/t^{1.5}) + 5.5\alpha \leq S \quad (3.3c)$$

$$\text{and } e = b_f - D \quad (3.3d)$$

where w_{dt} is the effective track length (mm) (see Figure 3.20); t is the thickness of the track (mm); b_f is the track flange width (mm); D is the engagement length (mm); α is a coefficient for conversion of units = 25.4; and S is the stud spacing (mm). All other parameters are defined in Section 4.1.

Notably, fastener spacing shall not be greater than the stud spacing (S). Furthermore, the horizontal distance from the web side of the stud to the end of the track shall not be less than half the effective track length (w_{dt}). Additionally, in Eq. (3.3b), the limitation of section depths up to 152.4 mm, track thicknesses between 1.14 mm and 1.81mm, yield strength up to 345 MPa, and flange widths between 50.8 mm and 76.3 mm must be satisfied.

3.4.1.2. TI 809-07 (1998)

TI 809-07 (1998) also provides the design rule to estimate the nominal strength of the deflection track using the elastic section modulus (Eq. (3.4a)). Substituting Eq. (3.4a) and Eq. (3.2b) into Eq. (3.2a) gives Eq. (3.4b) for the track nominal strength.

$$Z_x = \frac{w_{dt} t^2}{6} \quad (3.4a)$$

$$P_n = \frac{w_{dt} t^2 f_y}{6e} \quad (3.4b)$$

$$\text{with } w_{dt} = 2 \left[\frac{e + D}{\tan \varphi} \right] + N \leq S; \varphi = 30^\circ \quad (3.4c)$$

where N is the stud flange width (mm) (see Figure 3.20); All other parameters are defined above.

3.4.2. Comparison of current design rules with test results

The ultimate strengths, in terms of the maximum load ($P_{Exp-Max.}$) and that based on the ultimate deformation limit ($P_{Exp-UDL}$), obtained from the bearing tests were compared with the predictions of the above-mentioned standards (AISI S240, 2015; TI 809-07, 1998)) for cold-formed structures, as given in Table 3.4 and Table 3.5. In terms of the maximum load, the mean values of the test-to-predicted load ratios based on AISI S240 (2015) and TI 809-07 (1998) are 2.33 (with a Coefficient of Variation (COV) of 0.30) and 2.48 (with a COV of 0.17), respectively. However, according to the ultimate deformation limit, these values are 1.79 (with a COV of 0.31) and 1.92 (with a COV of 0.24), respectively. This implies that the current cold-formed steel design rules are overly conservative and unreliable, and are unable to estimate the bearing capacity of aluminium sub-heads accurately. Hence, a set of new design rules are proposed next, to provide an appropriate method for safe and economic design of aluminium sub-head sections in window wall frames.

3.4.3. Proposed design rules

Based on the definitions presented above (Eq. (3.2a), Eq. (3.2b) and Eq. (3.3a)), the nominal bearing capacity (P_n) of an aluminium sub-head under concentrated load can be accurately estimated by Eq. (3.3b). In this equation, t is the flange thickness. The thickness of the aluminium sub-head flange varies along the flange element and typically the thickest portion of the flange is located at the web-flange junction ($t_{f,max}$). Hence Eq. (3.3b) can be re-written as follows to predict the bearing capacity of aluminium sub-heads.

$$P_{prop.} = \frac{w_{dt} t_{f,max}^2 f_y}{4e} \quad (3.5)$$

In the above equation, w_{dt} is the effective sub-head length (see Figure 3.20), which is the width of the flange that can effectively resist bending at the web-flange corner. In the experimental study, it was observed that the deflection along the free edge of the bottom flange extended beyond the bearing plate width. Hence, determination of the effective sub-head length (w_{dt}) is critical to compute the resistance provided by the sub-head flange. This length could be empirically derived through correlation with the test results obtained for aluminium sub-heads under concentrated loads. Section 3.4.3.1 details the proposed equation to predict effective sub-head length (w_{dt}) using the measured ultimate loads obtained from the experimental study.

As explained in Section 3.3.2, the ultimate loads shown in Table 3.4 and Table 3.5 are obtained from testing the sub-heads of one manufacturer. Note that further evaluation of the design rules developed herein for a wide range of manufacturers is beyond the scope of this study. Nevertheless, the proposed rules still represent a first-hand approach in the design of aluminium sub-head profiles.

3.4.3.1. Derivation of effective sub-head length (w_{dt})

The effective track length (w_{dt}) given in Eq. (3.3c) (AISI S240, 2015) is specified as a function of the track thickness (t) and the slip gap (e), whereas in Eq. (3.4c) (TI 809-07,

1998), it is expressed as a function of the stud flange width (N), which is equivalent to the bearing width in this study, the slip gap (e), and the engagement length (D). It should be noted that $(e+D)$ in Eq. (3.4c) is equivalent to the flange width (b_f) (see Figure 3.20). Hence the four main parameters influencing the effective sub-head length (w_{dt}) are assumed to be the (1) bearing width (N), (2) flange width (b_f), (3) slip gap (e) and (4) flange thickness ($t_{f,max}$). Thus, this paper proposes Eq. (3.6) to calculate w_{dt} , as shown in Figure 3.20. Note that Eq. (3.6) is similar to Eq. (3.4c), where θ was proposed as 60° (equivalent to $\varphi = 30^\circ$). However, to consider all the four relevant parameters affecting the effective sub-head length (w_{dt}), θ should be defined as a function of the slip gap (e) and the flange thickness (t) which will be further explained in Section 3.4.3.2.

$$w_{dt} = N + 2 * b_f * \tan(\theta) \quad (3.6)$$

Figure 3.21 and Figure 3.22 were used to derive Eq. (3.6) in relation to the bearing width (N) and the flange width (b_f), respectively. These figures demonstrate the variations of the effective sub-head length (w_{dt}) (calculated from Eq. (3.5) and the experimental ultimate loads) with respect to different structural parameters considered in the experimental study (Table 3.1).

Figure 3.21 shows the relationship between the effective sub-head length (w_{dt}) and the bearing width (N) for different sections. For each sub-head section, the values of w_{dt} for three loading and boundary conditions (1B/15 mm, 1B/25 mm and 2B/25 mm) were used to observe the trend in Figure 3.21. From which, it is reasonable to assume that w_{dt} increases linearly with increased bearing width (N) (as proposed in Eq. (3.6)) when the flange width (b_f) and the engagement length (D) (and hence the slip gap (e)) are kept unchanged.

The relationship between the effective sub-head length (w_{dt}) and the flange width (b_f) for different bearing widths is presented in Figure 3.22. The variations of w_{dt} with respect to the three loading and boundary conditions (1B/15 mm, 1B/25 mm and 2B/25 mm) for each bearing width were examined. The trend lines shown in Figure 3.22 indicate that w_{dt} also increases linearly with increased flange width (b_f) (as proposed in Eq. (3.6)).

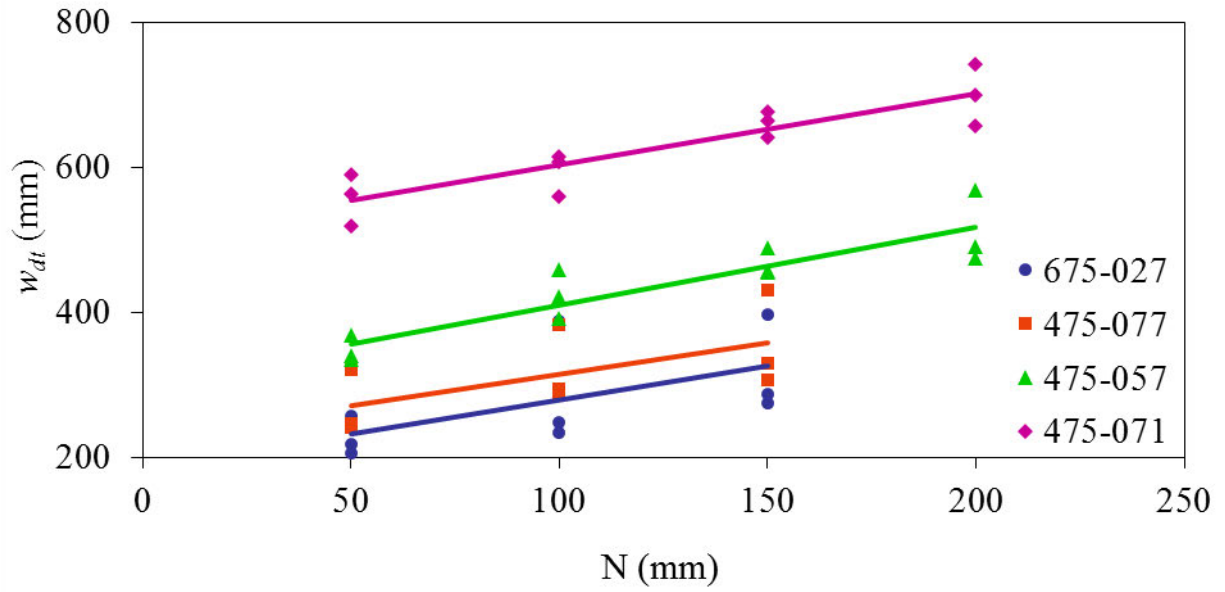


Figure 3.21 Comparison of effective sub-head length (w_{dt}) against bearing width (N).

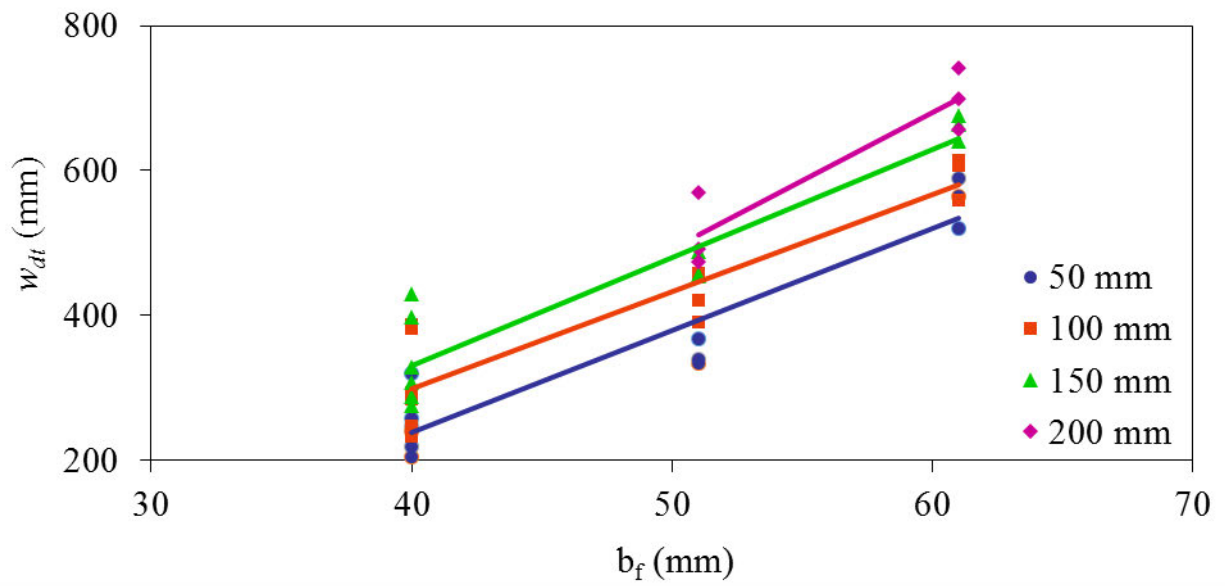


Figure 3.22 Comparison of effective sub-head length (w_{dt}) against flange width (b_f).

3.4.3.2. Derivation of angle (θ)

The variations of the effective sub-head length (w_{dt}) with respect to the slip gap (e) for different sub-head sections is displayed in Figure 3.23. It should be noted that the slip gap (e)

is a function of the engagement length (D) and the flange width (b_f) (i.e., $e = b_f - D$). The trend lines in Figure 3.23 were obtained using the w_{dt} values for all the four bearing widths (50 mm, 100 mm, 150 mm, and 200 mm) for each sub-head section. Overall, it was found that w_{dt} has a non-linear relationship (large increase, moderate increase and then decrease) with respect to the slip gap (e). This phenomenon helps to derive angle (θ) with respect to the slip gap (e) and the flange thickness (t), as explained next.

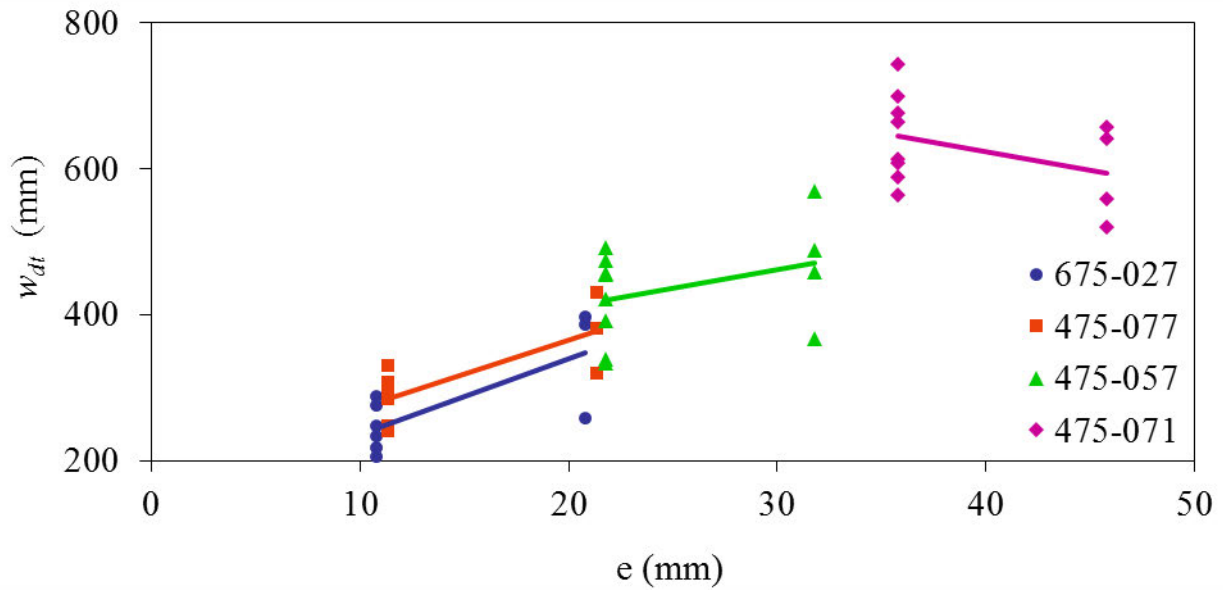
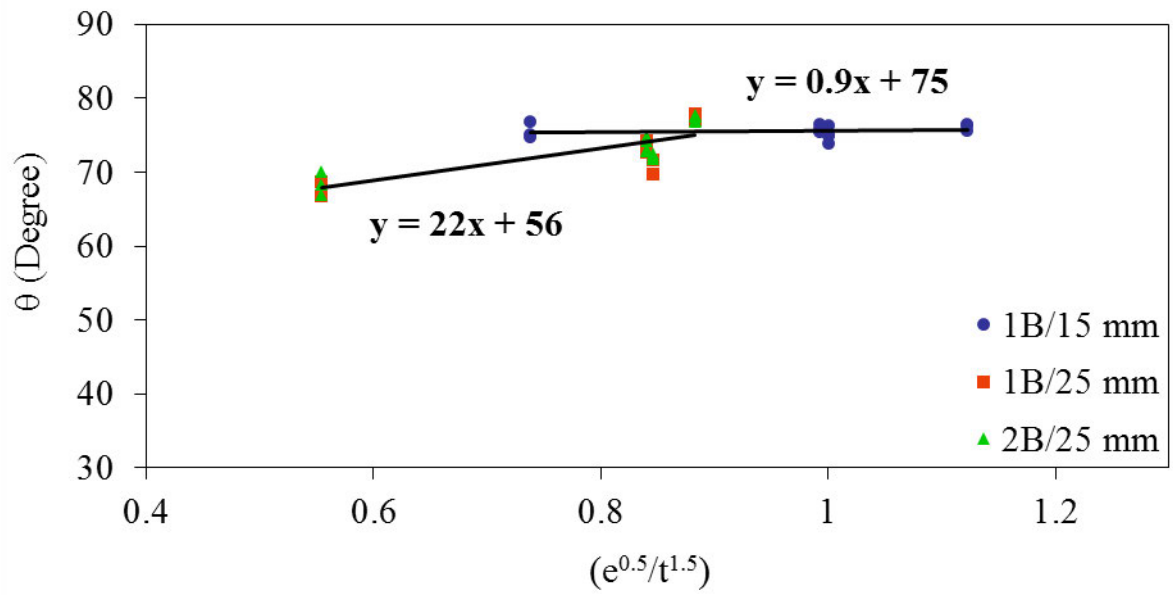


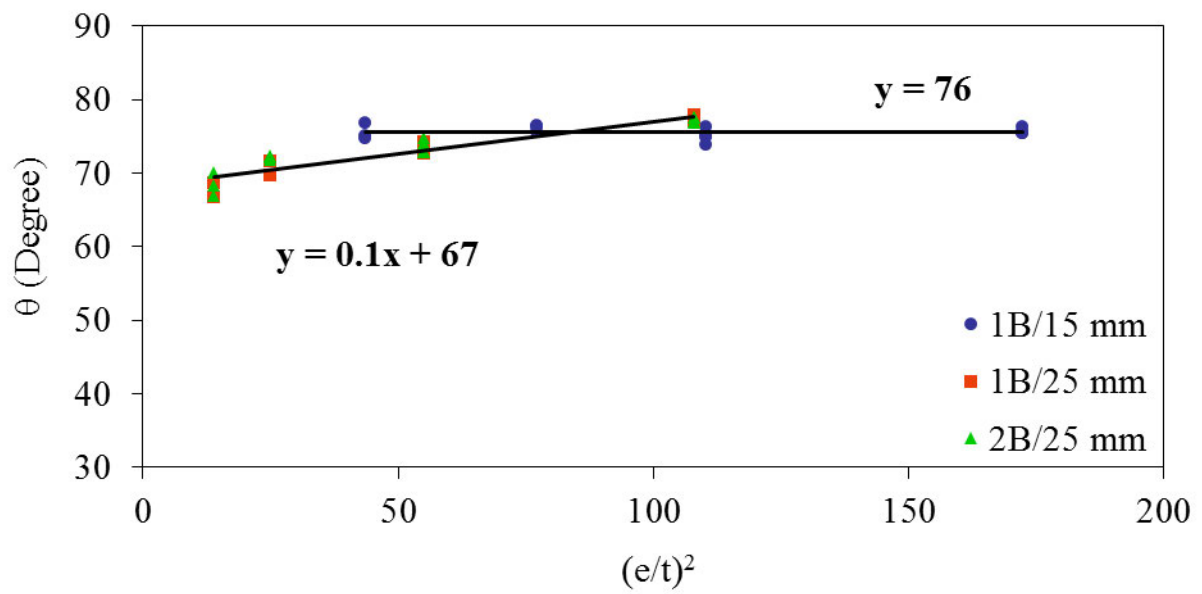
Figure 3.23 Comparison of effective sub-head length (w_{dt}) against slip gap (e).

Note that AISI S240 (2015) and Bolte and Laboube (2004) used the terms $(e^{0.5}/t^{1.5})$ and $(e/t)^2$ to empirically determine the effective track length (w_{dt}), respectively. Both of these terms were considered in the current study to demonstrate the relationship between them and θ (and hence the effective sub-head length (w_{dt})) resulted from the maximum load as shown in Figure 3.24 (a) and Figure 3.24 (b) and the ultimate deformation limit shown in Figure 3.25 (a) and Figure 3.25 (b). It is evident that both terms showed a clear linear trend in relation to θ ; however, data points in Figure 3.24 (b) and Figure 3.25 (b) seem to be less scattered. Accordingly, the term $(e/t)^2$ was incorporated in the proposed design rules, and θ could be calculated using Eq. (3.7). Eq. (3.5) can now be used in conjunction with Eq. (3.6) and Eq. (3.7) to predict the bearing capacities of aluminium sub-heads.

$$\theta = a * (e/t)^2 + b \quad (3.7)$$

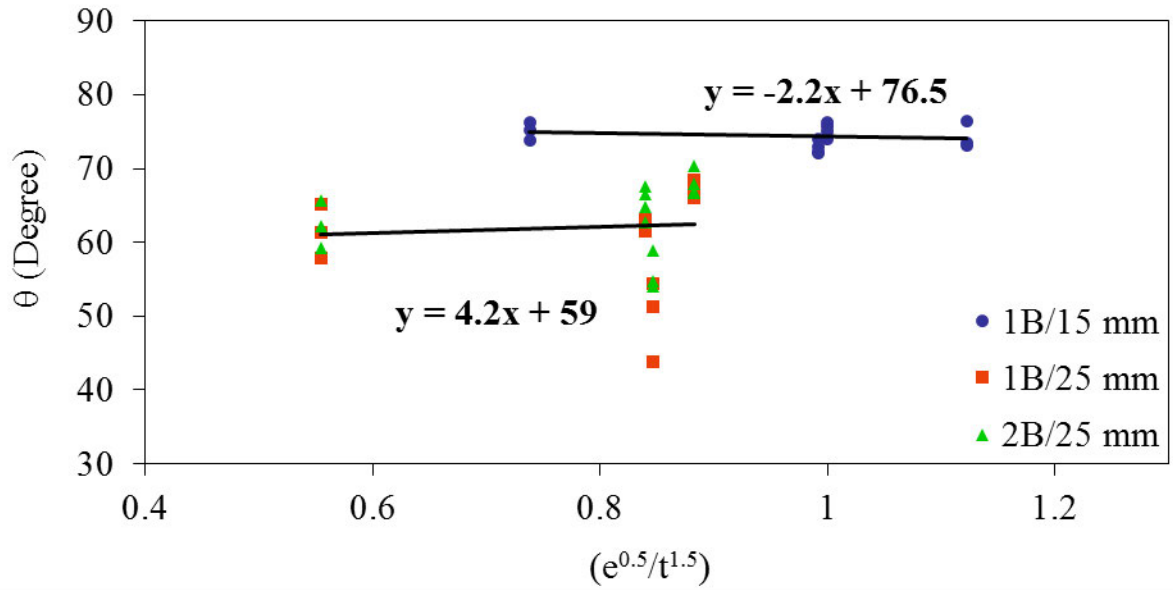


(a) Based on AISI S240 (2015)

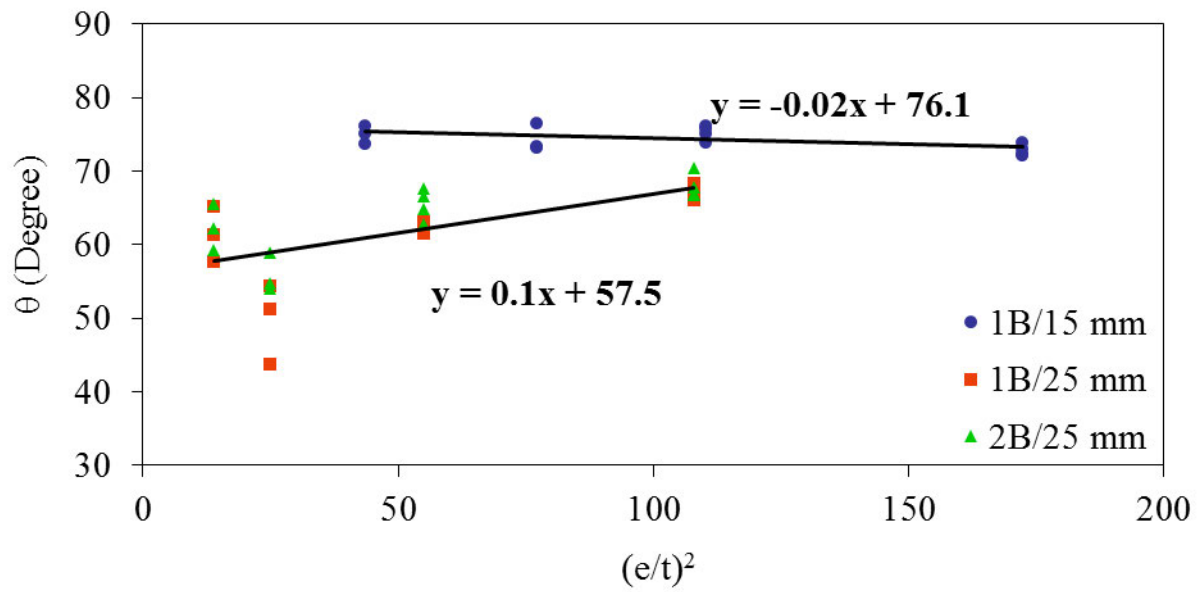


(b) Based on Bolte and Laboube (2004)

Figure 3.24 Relationship between θ and slip gap-flange thickness, based on maximum load.



(a) Based on AISI S240 (2015)



(b) Based on Bolte and Laboube (2004)

Figure 3.25 Relationship between θ and slip gap-flange thickness, based on ultimate deformation limit (UDL).

where based on maximum load, $a=0$ and $b=76$ for 15 mm engagement length, and $a=0.1$ and $b=67$ for 25 mm engagement length. However, based on ultimate deformation limit, $a=-0.02$ and $b=76.1$ for 15 mm engagement length, and $a=0.1$ and $b=57.5$ for 25 mm engagement length.

3.4.4. Comparison of test results with proposed design equations

Table 3.4 and Table 3.5 show the comparisons between the experimental ultimate loads ($P_{Exp-Max}$ and $P_{Exp-UDL}$) and those with the proposed design rules ($P_{Prop-Max}$ and $P_{Prop-UDL}$), based on the measured cross-sectional dimensions and material properties of each specimen presented in Table 3.2 and Table 3.3. The prediction accuracy of the above-mentioned equations can be evaluated by the ratios $P_{Exp-Max}/P_{Prop-Max}$ and $P_{Exp-UDL}/P_{Prop-UDL}$, as given in Table 3.4 and Table 3.5, showing the mean values of 1.01 and 1.00 with reasonably good COV values of 0.06 and 0.09, respectively. Figure 3.26 and Figure 3.27 display the comparisons of the experimental ultimate capacity values ($P_{Exp-Max}$ and $P_{Exp-UDL}$) with the nominal design strengths ($P_{Predicted}$) predicted by the current cold-formed steel provisions (AISI S240, 2015, TI 809-07, 1998), and the proposed design rules, by utilising the values presented in Table 3.4 and Table 3.5. A strong correlation is found between the test and predicted capacities using the proposed design rules, as most of the data points lie within the limits of 10%. Similar plots of $P_{Predicted}$ (using the proposed equations) versus $P_{Exp-Max}$ and $P_{Exp-UDL}$ are presented in Figure 3.28 and Figure 3.29, respectively, to verify the applicability of the proposed design rules for aluminium sub-heads with different structural parameters including engagement lengths and bolt connection details, bearing widths and section geometries. Therefore, it can be concluded that the proposed equations are reliable and can be used to accurately predict the bearing capacities of tested aluminium sub-heads. Hence, further study should be conducted for aluminium sub-heads with general sections.

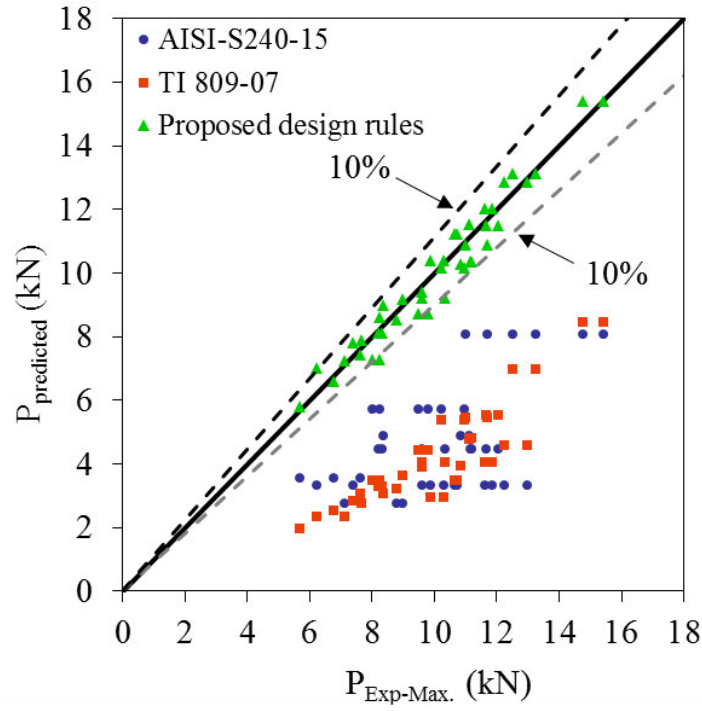


Figure 3.26 Comparison of experimental ultimate strengths ($P_{Exp-Max}$) with those of current and proposed design rules ($P_{Predicted}$), based on maximum load.

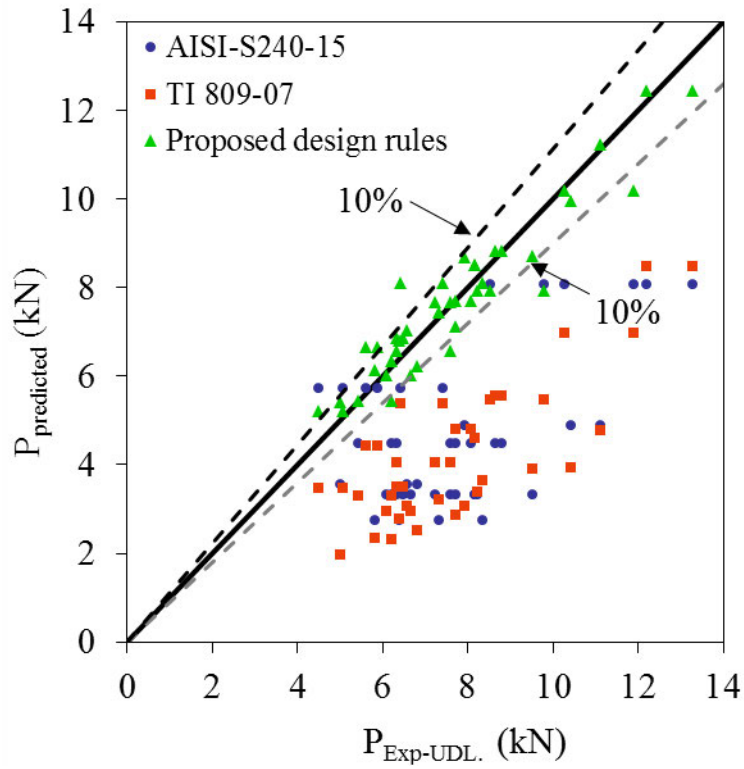
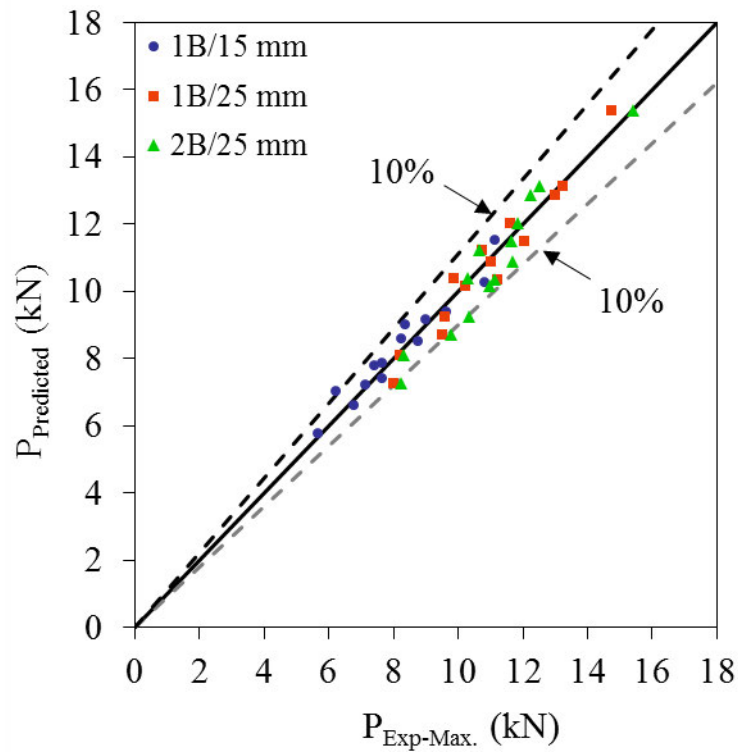
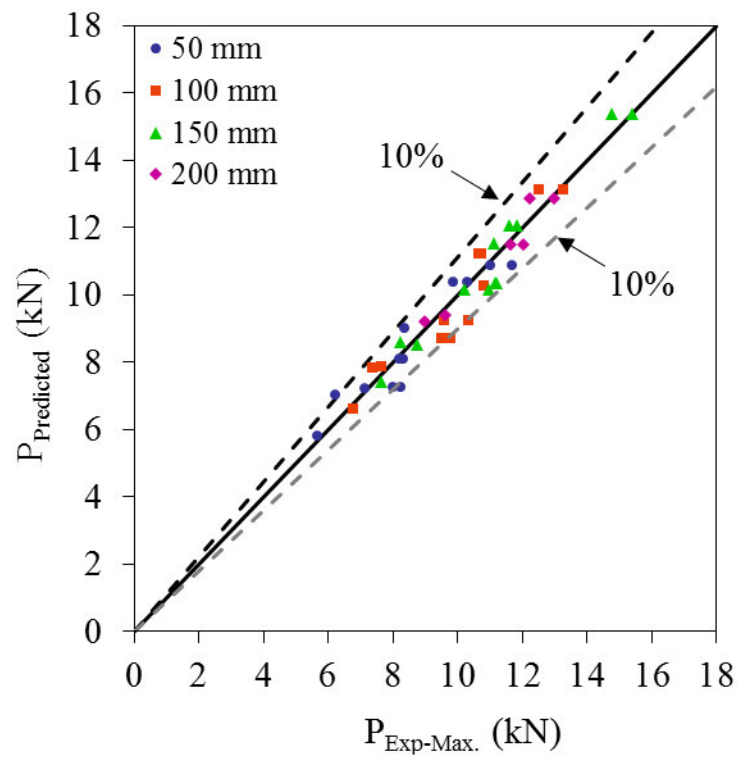


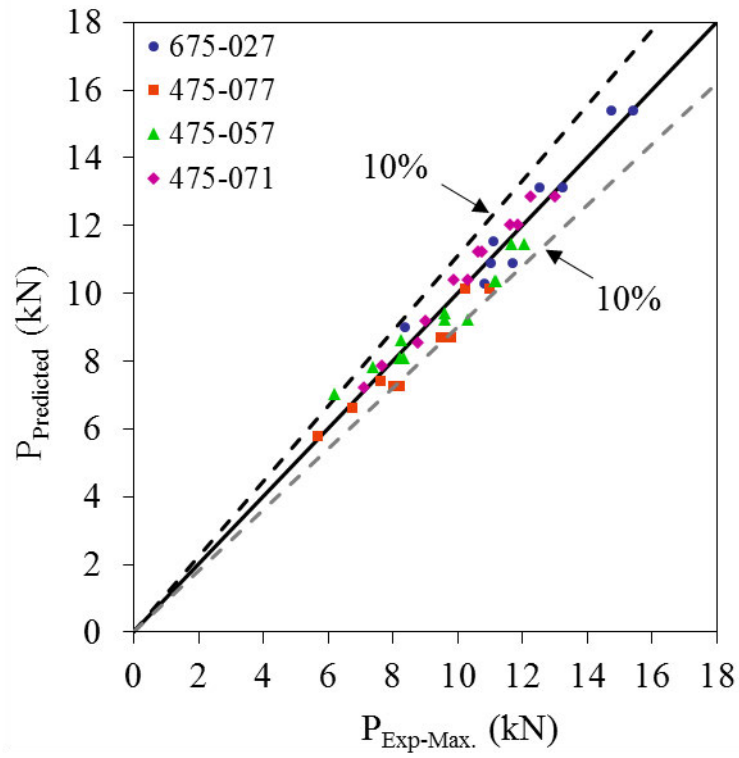
Figure 3.27 Comparison of experimental ultimate strengths ($P_{Exp-UDL}$) with those of current and proposed design rules ($P_{Predicted}$), based on ultimate deformation limit (UDL).



(a) Engagement lengths and bolt connection details

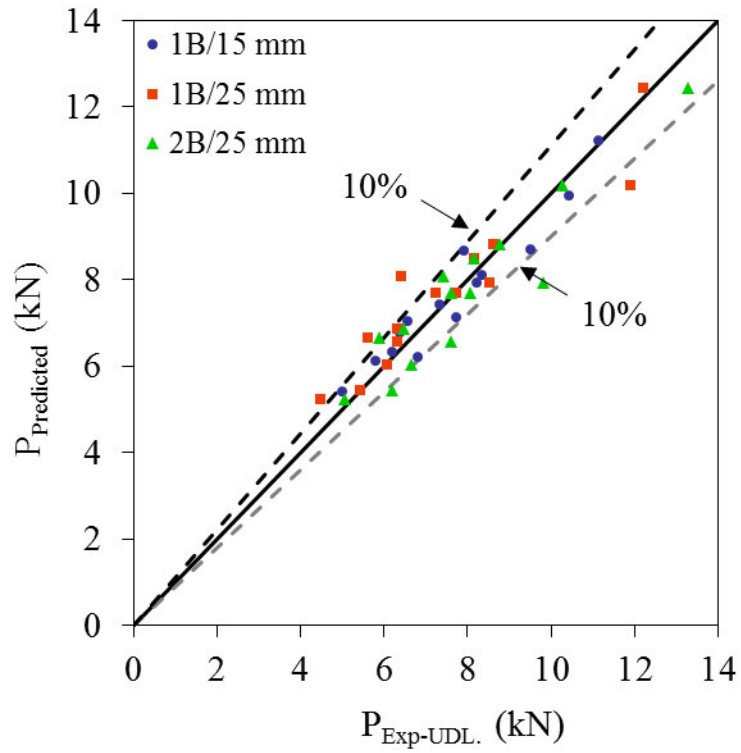


(b) Bearing widths

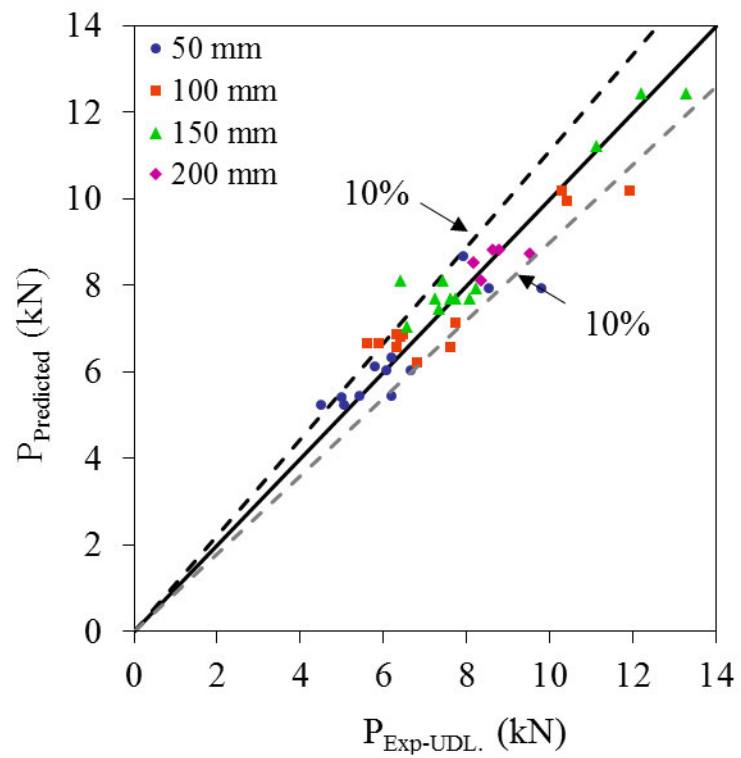


(c) Section geometries

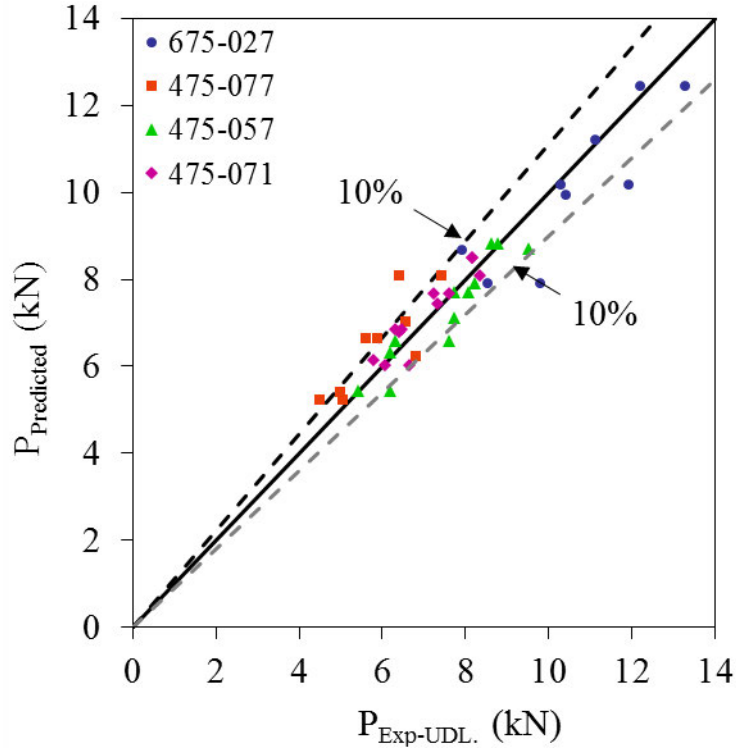
Figure 3.28 Comparison of experimental ultimate strengths ($P_{Exp-Max.}$) with those of proposed design rules ($P_{Predicted}$) for different structural parameters, based on maximum load.



(a) Engagement lengths and bolt connection details



(b) Bearing widths



(c) Section geometries

Figure 3.29 Comparison of experimental ultimate strengths ($P_{Exp-UDL}$) with those of proposed design rules ($P_{Predicted}$) for different structural parameters, based on ultimate deformation limit (UDL).

3.4.5. Capacity reduction factor (ϕ_w)

The North American Specification (AISI, 2016) recommends a statistical model to determine the capacity reduction factor which can be used in conjunction with the proposed capacity equations. This model accounts for the variations in material, fabrication, and loading effects. The capacity reduction factor can be expressed by Eq. (3.8a).

$$\phi_w = 1.52M_mF_mP_me^{-\beta_0\sqrt{V_M^2+V_F^2+C_nV_P^2+V_Q^2}} \quad (3.8a)$$

where ϕ_w is resistance factor; based on the AA Specification (2015), M_m , $V_M = 1.1$, 0.06 are, respectively, the mean and the COV of the material factor; F_m and $V_F = 1.0$, 0.05 are, respectively, the mean and COV of the fabrication factor; $V_Q = 0.21$ is the COV of the load

effect; $\beta_0 = 2.5$ is the target reliability index for aluminium structural members which is recommended as a lower limit in the AA Specification (2015); $C_n = \frac{n^2-1}{n^2-3n}$ is the correction factor depending on the number of tests (n); P_m is the mean value of the test-to-predicted load ratio; V_P is the COV of the test-to-predicted load ratio.

Eq. (3.8b) can be computed by substituting all the above-mentioned values into Eq. (3.8a) as follows:

$$\phi_w = 1.672P_m e^{-2.5\sqrt{0.0502+C_nV_P^2}} \quad (3.8b)$$

Eq. (3.8b) was used to determine the capacity reduction factors for the ultimate capacity values obtained from the proposed design rules as well as those from the current design standards. As shown in Table 3.4 and Table 3.5, the capacity reduction factors (ϕ_w) according to the proposed equation (Eq. (3.5), Eq. (3.6) and Eq. (3.7)) are 0.94 and 0.91, respectively, based on the maximum load and the ultimate deformation limit. Therefore, it is recommended to incorporate a ϕ_w factor of 0.90 in the proposed design equations to estimate the bearing capacity of aluminium sub-head sections. The accuracy of the design rules was further confirmed by β_0 (target reliability index). Based on $\phi_w = 0.90$, β_0 can be estimated from Eq. (3.8b), and is equal to 2.71 and 2.55 for maximum load and ultimate deformation limit (UDL), respectively. This finding endorses the reliability of the proposed design rules.

3.4.6. Limitation of proposed design rules

Even though the bearing behaviour and capacity of the aluminium sub-heads were investigated in detail, the proposed design rules still represent a first-hand approach in the design of aluminium sub-head profiles.

1. The proposed design rules developed herein would benefit from further verification using experimental and numerical studies with a wide range of sub-heads.

2. There is a need to accurately predict the contact length between the aluminium sub-heads and window wall frame (mullion and head) under wind loads. This contested issue could be investigated through experimental and numerical studies using full scale façade systems.

3.5. Conclusion

This paper details an extensive experimental study conducted with the aim of evaluating the performance of aluminium sub-head sections in window wall façade systems subjected to bearing failure, through a series of 42 tests. The effect of various bearing widths, bolt connection details, loading and boundary conditions and section geometries was investigated. A concentrated load was applied on the internal surface of the sub-head flange through a uniquely designed loading frame. Experimental testing demonstrated that the sub-head sections failed as a result of the yielding of the web-flange junction due to the flange bending and slipping due to groove crushing. This study concluded that the ultimate bearing capacity increased linearly with the increment of the bearing width, and the larger engagement length led to a considerable increase of the ultimate capacity. Furthermore, the flange width (b_f), bearing width (N), slip gap (e), and flange thickness (t) were found to have a profound impact on the effective sub-head length (w_{dt}) and hence the ultimate bearing capacity. The bearing capacities of aluminium sub-head sections obtained from the experiments were then compared with the nominal strengths calculated using the AISI S240 (2015) and TI 809-07 (1998) design codes for cold-formed steel structures. Generally, the nominal strengths predicted by the codified design provisions are shown to be overly conservative. As no design equations are available in the aluminium provisions for predicting the bearing capacity of aluminium sub-head sections under a concentrated load, new design equations for aluminium sub-head sections were hence developed in this study. The calculation results demonstrated that the proposed equations for estimating the ultimate bearing capacities of tested aluminium sub-head sections compares well with the experimental values and hence the reliability of the proposed design rules was confirmed.

4. Numerical Study on Bearing Behaviour and Design of Aluminium Sub-heads in Façade Systems

(Under Review)

This chapter includes a co-authored paper. The bibliographic details of the co-authored paper, including all authors, are:

Akbari, M., Gunalan, S., Talebian, N., Gilbert, B.P., Guan, H.

Numerical Study on Bearing Behaviour and Design of Aluminium Sub-heads in Façade Systems

Submitted in *Thin-walled structures*

My contribution to the paper involved:

Literature review, experimental works, result analysis, discussion of the results, writing, editing and response to reviewers.

(Signed) _____ (Date) 14.11.2020

Name of Student: Masoumeh Akbari

(Countersigned) _____ (Date) 14.11.2020

Corresponding author of paper: Dr Shanmuganathan Gunalan

(Countersigned) _____ (Date) 14.11.2020

Supervisor: Dr Shanmuganathan Gunalan

Numerical Study on Bearing Behaviour and Design of Aluminium Sub-heads in Façade Systems

Abstract

A sub-head refers to the horizontal member at the top of an aluminium window wall system. Under wind load, bearing failure of the aluminium sub-head (ASH) flange due to its long length is a common failure mode, being subjected to high concentrated load transferred from the vertical members (mullions). The bearing behaviour of ASH sections was initially investigated experimentally by the authors through 42 tests, and suitable equations for predicting the bearing capacities were proposed. These initially proposed design rules for ASH sections (DRA_I) were manufacturer and product specific and only applicable for sections considered in the test plan. To address these limitations, the present study further investigates the behaviour and design of ASH sections through non-linear static analyses using ABAQUS, based on implicit integration schemes. Characterisation of the analysis techniques of ASH sections under different loading and boundary conditions was addressed. The finite element models were validated against the test results in terms of ultimate loads, load-displacement curves and failure modes, and the validated model was then used to perform an extensive parametric study. A broad range of ASH sections covering flange widths ranging from 40 to 100 mm, thicknesses varying between 2 and 4 mm, bearing widths ranging from 50 to 150 mm, and six engagement lengths (5 to 30 mm) was considered in the parametric study. It should be noted that the ultimate loads obtained from the parametric study are not product nor manufacturer specific. Since no aluminium design rules exist to predict the bearing capacities of ASH sections, the accuracy of the current cold-formed steel design rules (DRSs) and that of DRA_I were assessed. Both DRSs and DRA_I were found not to be suitable for ASH sections in window walls, hence appropriate modifications were made in this study and the proposed design rules (DRA_P) predicted accurate bearing capacities which agreed well with the numerical results.

Keywords

Numerical analysis, Façades, Aluminium, Sub-heads, Bearing failure, Design rules

4.1. Introduction

A unique combination of features such as high strength, durability, corrosion resistance and ductility, as well as good economic benefits make aluminium a favourable material which has been utilised widely in construction all over the world. From the 1940s, aluminium applications began to expand into various industries, including the façade industry. Leading façade manufacturers in Australia aim to utilise advanced technological tools and design methodology to ensure the best quality products with low costs. The problematic issue, in this case, is the substandard design rules for façades. Façade systems such as window walls, curtain walls, and cladding panels not only provide an envelope but also maintain a level of architectural appearance for the building. A window wall is usually comprised of an aluminium-framed wall, containing in-fills of glass which protect the interior environment of the building from external wind, heat, and rain. It is installed between the floor levels in the building structure, and does not carry any other structural weight other than its own. Lateral wind loads imposed on a window wall are first applied to the glass panels, then transferred to the aluminium frame (mullions, heads and sills) and sub-frames (sub-heads and sub-sills), and finally from sub-frames to the building structure (See Figure 4.1) (Akbari et al., 2020a). Under this loading condition, the flange of the ASH is subjected to high concentrated loads and is highly prone to bearing failure due to bending of its long flange. Since failure of the ASH could result in the loss of strength and stiffness of window walls and in turn lead to subsequent structural damage, such potential damage must be taken into consideration in aluminium façade design. ASH failure is also rather complex, due to various factors, including the manufacturer or product specific grooves (at the end of the flanges to contain sealing), the level of restraints provided by the web-flange junction, the non-uniform stress distributions in the ASH flange, and the loading conditions. Therefore, besides the experimental investigations conducted to explore the bearing failure of these complex aluminium sections under lateral loads, a computational approach is considered a viable and effective alternative to further understand the bearing failure mechanisms.

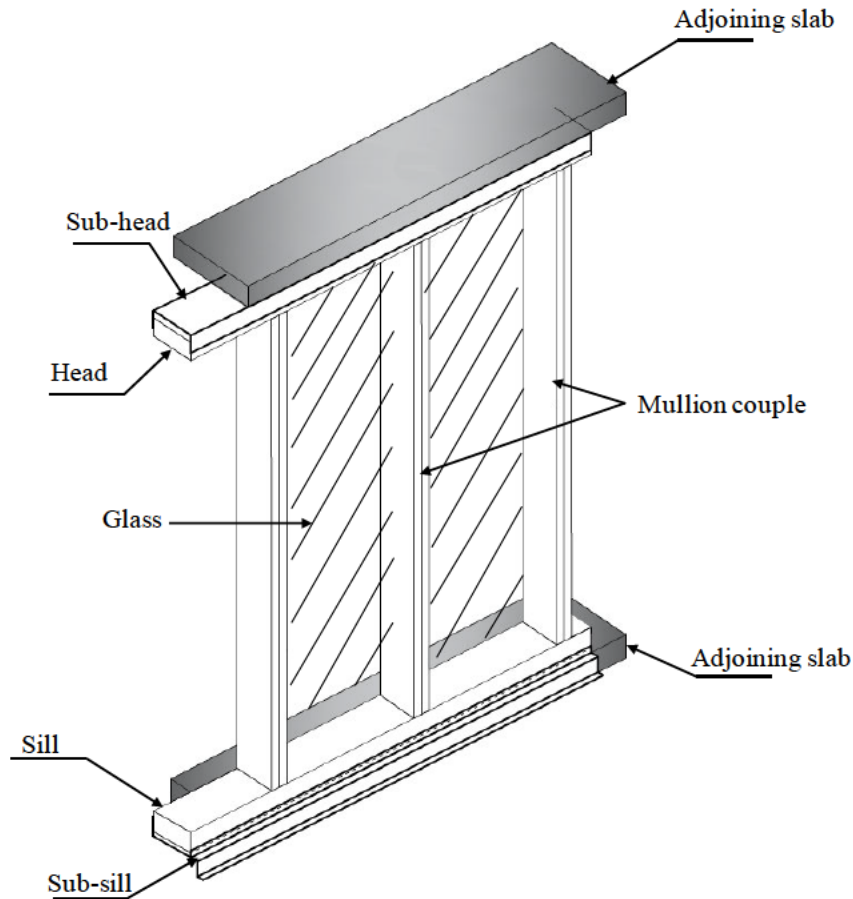


Figure 4.1 Details of window wall system.

Failure of ASH in the window wall under wind loading bears strong resemblance to the most prevalent failure mode in the cold-formed steel stud-to-track connection of a LSF (Light Gauge Steel) wall, which is the failure of the track under concentrated load. Although extensive experimental and numerical investigations have been conducted to explore the response and damage mechanisms of cold-formed steel tracks in LSF walls (Fox and Schuster, 2020; Bolte, 2003; Bolte and LaBoube, 2004; Rahman, 2005; LaBoube and Findlay, 2007; Espinoza et al., 2018; Bewick and Williamson, 2014; Bondok et al., 2015; Bondok and Salim, 2014; Iuorio et al., 2014; Jenkins et al., 2016; Moghimi and Ronagh, 2009), no finite element analysis has been performed to simulate the bearing behaviour of the tracks subjected to lateral wind load. Furthermore, in the literature, no research was available regarding numerical analysis of ASH sections. Notwithstanding, the bearing capacities of the ASH sections was recently investigated experimentally at Griffith University by Akbari et al. (2020a) using the ASH sections supplied by a particular Australian's manufacturer. Based on

the results of our experimental study, a series of initial design rules (equations) (DRA_I) suitable for the tested sections was proposed (Akbari et al., 2020a). Since these design equations were developed using a limited number of tests, the accuracy, reliability and applicability of the equations require further improvement by conducting numerical investigations covering a wider range of sections and parameters which motivates this study.

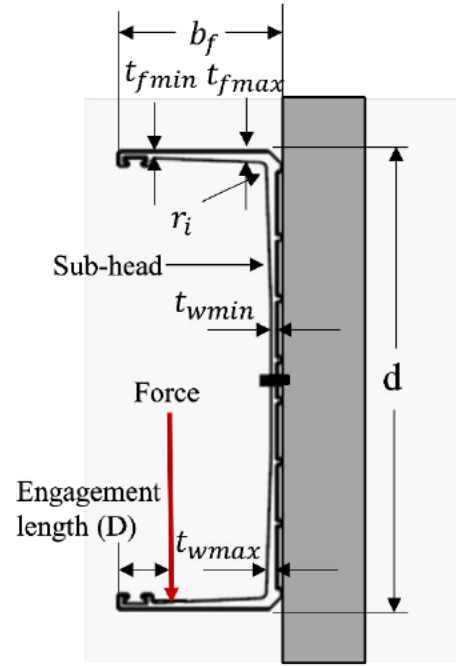
In this paper, simulations of the ASH sections subjected to bearing failure were performed using ABAQUS software (ABAQUS, 2014). Geometric and material non-linearities were considered in the finite element models. Particular attention was devoted to the comparison of the numerical and experimental results in terms of ultimate loads, load-displacement curves, and failure modes. The developed FE model was verified against test results reported in Akbari et al. (2020a) with good agreement. Thereafter, the validated numerical model was utilised to conduct a comprehensive parametric study covering a wide range of ASH dimensions (flange widths and thicknesses), engagement lengths, and bearing widths. For comparison, an assessment of the accuracy and reliability of the DRSs and the DRA_I was carried out. It should be mentioned that the DRSs refer to the design rules to predict the nominal strength of cold-formed steel stud-to-track connections, based on the cold-formed steel standards (the North American Standard for Cold-Formed Steel Structural Framing (AISI S240, 2015), the U.S. Army Corps of Engineers (TI 809-07, 1998), and the Steel Stud Manufacturers Association (SSMA, 2000)) and the equations proposed by Bolte and LaBoube (2004). The DRSs (Bolte and LaBoube, 2004; AISI S240, 2015; TI 809-07, 1998; SSMA, 2000) and the DRA_I (Akbari et al., 2020a) were found to be unreliable in predicting the bearing capacities of a large variety of the ASH sections in the parametric study. Consequently, appropriate modifications were made to improve the accuracy and applicability of the DRA_I (Akbari et al., 2020a). This leads to the proposed design rules in this paper (DRA_P) and their predictions correlated well with the numerical results. This paper gives a detailed presentation of the finite element simulations, numerical and parametric study results as well as DRA_P .

4.2. Brief overview of experimental investigation

Akbari et al. (2020a) conducted a series of 42 bearing tests (63 tests including 21 repeated tests) on beams made up of the ASH sections under different loading and boundary conditions. The specimens were fabricated by extrusion, using 6063-T6 heat-treated aluminum alloy. Detailed test setup and the corresponding cross-sectional profile are shown in Figure 4.2 (a) and (b). Four different ASH sections were used in the experimental study, and their cross-sectional dimensions are given in Table 4.1 in reference to Figure 4.2 (b) and Figure 4.3. In this study, the bearing tests were conducted using a 500 kN Material Testing System (MTS) universal testing machine. A displacement control was used to drive the cross-head of the MTS machine at a constant speed of 2 mm/min for all test specimens until the test beam failed. High-grade steel plates of precise lengths (50 mm, 100 mm, 150 mm and 200 mm) with rounded edges were bolted to the bottom of a specially designed loading frame to apply force to the bottom flange at mid span. The ASH was attached to a stiff rectangular hollow section (rigid support) using M12 bolts in the middle of the ASH's web. In total, two bolt connection details between the ASH and the rigid support (boundary conditions) (see Figure 4.3) and two engagement lengths of 15 mm and 25 mm (loading conditions) were considered in the experimental study. It should be mentioned that the engagement length refers to as the distance from the loading position to the flange grooves, as shown in Figure 4.2 (b). Concisely, three loading and boundary conditions were considered in the experimental study: one-bolt with a 15 mm engagement length, one-bolt with a 25 mm engagement length, and two-bolt with a 25 mm engagement length. The designations of the specimens intended to describe the ASH sections with the bolt connection detail, the engagement length, and the bearing width. For example, in the label “475-071/2B/25/100” “475-071” denotes the section name, “2B” depicts a two-bolt connection, “25” (mm) is the engagement length, and “100” (mm) is the bearing width.

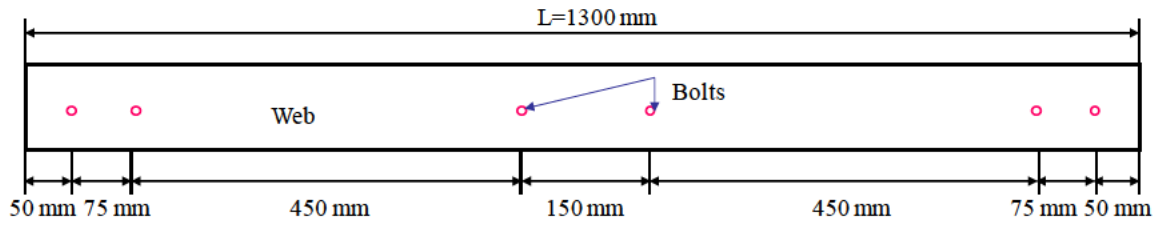


(a) Test setup

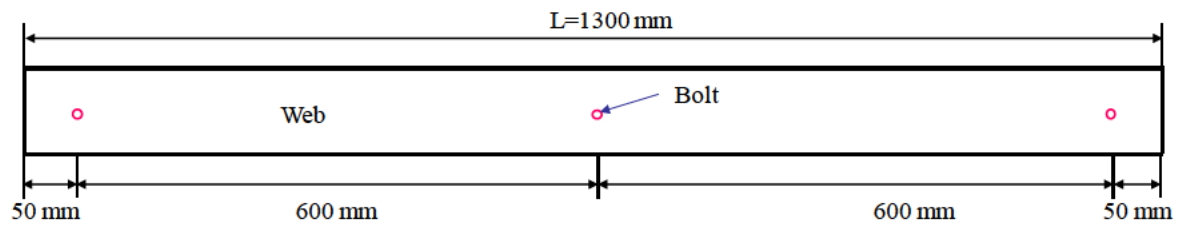


(b) Cross-section profile

Figure 4.2 Bearing test setup and ASH section profile (Akbari et al., 2020a).



(a) Two-bolt connection



(b) One-bolt connection

Figure 4.3 Bolt connection details (Akbari et al., 2020a).

Table 4.1 Geometric details of the ASH sections.

Section	d (mm)	b _f (mm)	t _{w,max} (mm)	t _{w,min} (mm)	t _{f,max} (mm)	t _{f,min} (mm)	r _i (mm)	L (mm)
675-027	163	40	4.1	2.46	3.48	2.3	4.5	1300
475-077	111.7	40	3.65	1.5	2.64	1.5	3	1300
475-057	111.5	51	3.95	2.21	3.24	1.95	4.3	1300
475-071	112.7	65	4.2	3.13	3.65	2	4.5	1300

4.3. Finite element modelling

The finite element modelling of the ASH sections subjected to various bearing loads is detailed hereafter using FE software ABAQUS version 6.14. The quasi-static method was selected to perform geometric and material non-linear analyses in ABAQUS. The FE model consists of three main components, namely the ASH section, the rigid bearing plate, and the rigid support, as shown in Figure 4.4. Notably, as the impact of initial geometrical imperfections on the bearing capacities of the ASH sections was shown to be negligible, imperfections were hence not considered in this study.

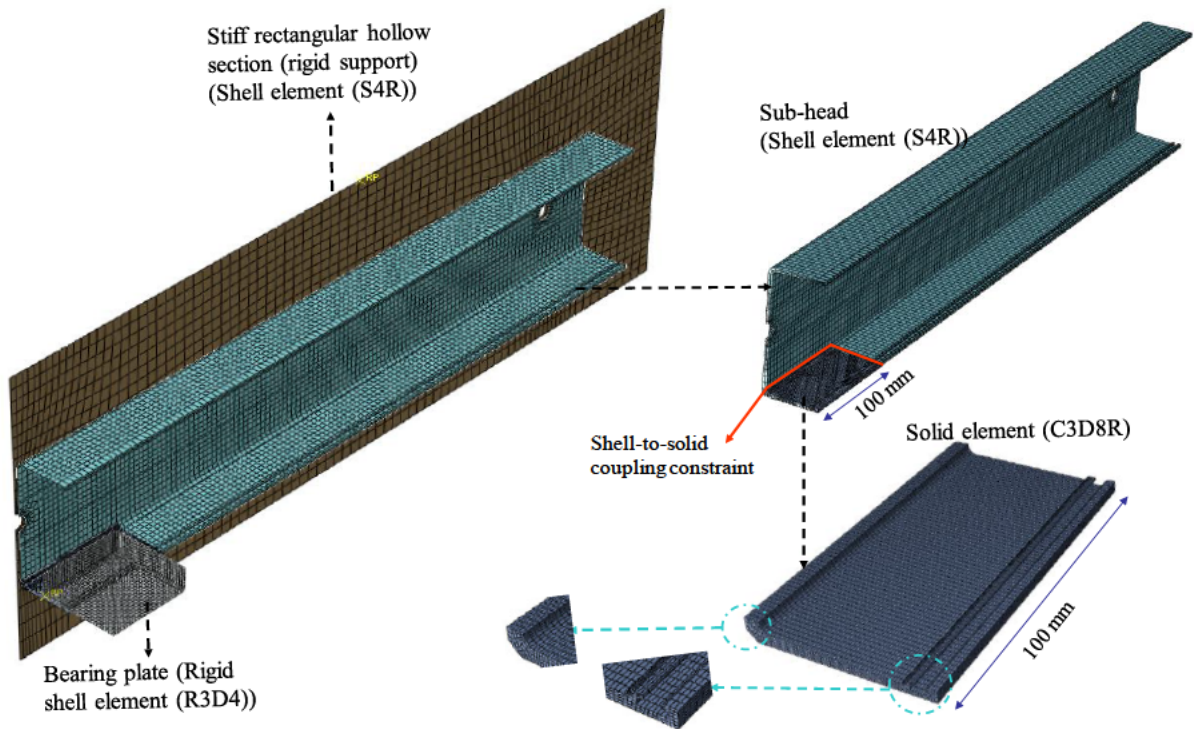


Figure 4.4 Finite element model.

4.3.1. Geometry, element types and mesh

In the present work, four-node reduced integration shell elements (S4R) were used to model the rigid support and the ASH sections (Natario et al., 2014), due to their simple geometry and wide applications in thin-walled structural analyses (Natario et al., 2014). As shown in Figure 4.4, the flange and the web thicknesses of the ASH are not entirely uniform. In order to well capture the bearing failure and deformation of the ASH, only part of the bottom flange (with a 100 mm length) under the bearing plate was modelled using 8-node linear brick solid elements (C3D8R) to account for the exact geometry of the ASH cross-section. A shell-to-solid coupling constraint was used to connect these solid elements to the rest of the ASH with shell elements (see red lines in Figure 4.4). The ASH cross-section with S4R elements was simplified by dividing it into different segments, and an average measured thickness was assigned to each segment, as shown in Figure 4.5. Figure 4.5 (a) illustrates the different segments of the ASH (475-071) cross-section and Figure 4.5 (b) depicts the centerline of the simplified cross-section. Slight curves within the flange grooves were ignored. For the corners that have a flat outer surface and a curved inner surface, uniform thickness was considered. The flange width was broken down into four equal segments. Figure 4.6 shows the simplified geometry of the ASH cross-section. 4-node rigid shell elements (R3D4) were assigned to the bearing plate.

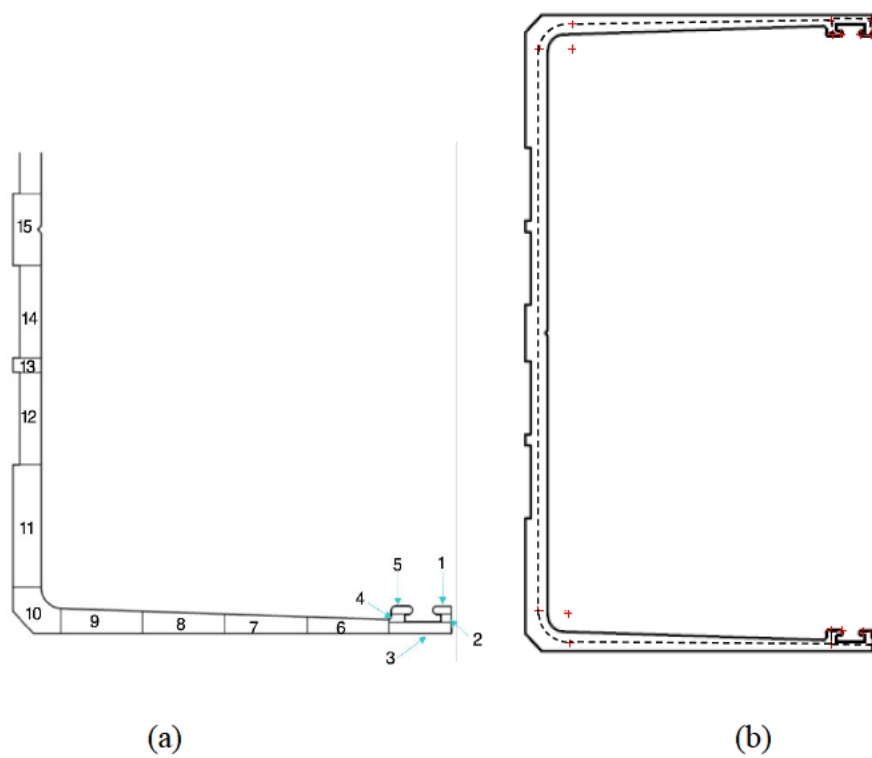


Figure 4.5 a) Different segments on the sub-head cross-section, b) Centerline of the simplified cross-section for the sub-head modelled with shell elements.

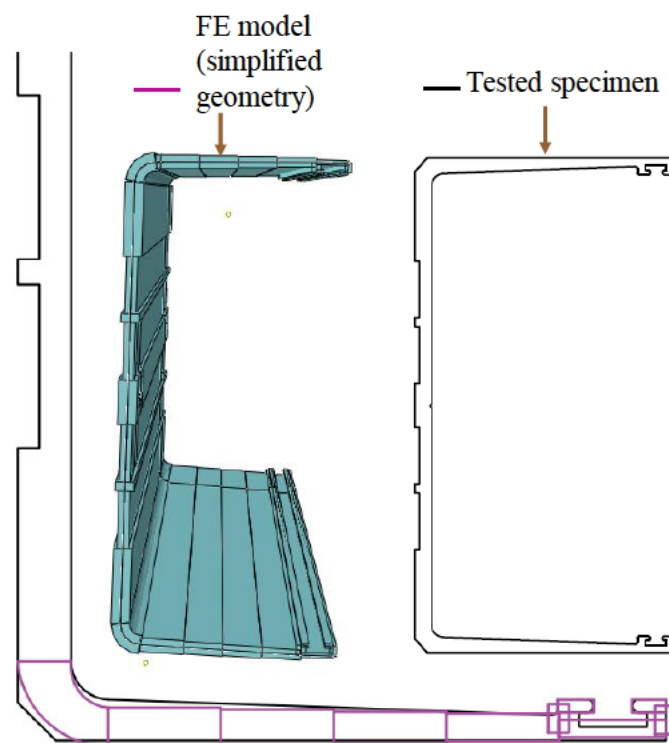


Figure 4.6 Simplified geometry of the sub-head cross-section.

The reliability and accuracy of the finite element modelling depends considerably on the degree of mesh refinement. Based on the convergence studies performed on a single ASH, the mesh size of the ASH with the S4R elements was found to be $5 \text{ mm} \times 5 \text{ mm}$ (See Figure 4.7). To accurately capture the deformation and bearing failure, finer mesh sizes between 0.5 mm to 1 mm were considered for the corner, the grooves, and the part of the bottom flange under the bearing plate, as shown in Figure 4.4. The mesh size was also refined locally around the bolt holes to account for the stress concentrations (Talebian et al., 2019). $3 \text{ mm} \times 3 \text{ mm}$ and $15 \text{ mm} \times 15 \text{ mm}$ mesh sizes were assigned to the bearing plate and the rigid support, respectively.

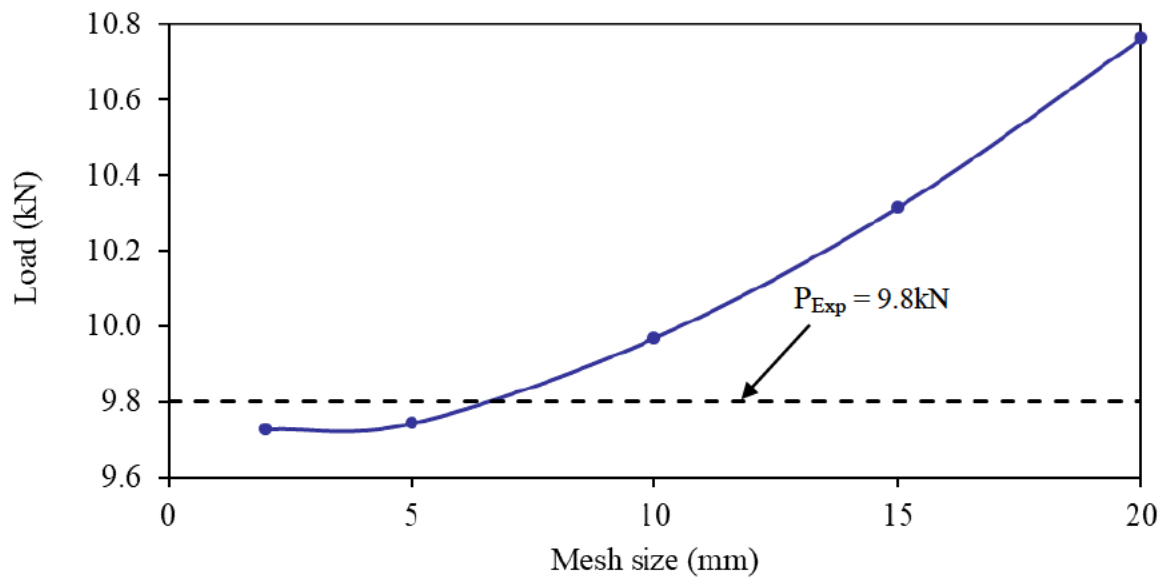


Figure 4.7 Ultimate load versus mesh size for 675-027/25/50/2B specimen.

4.3.2. Material properties

The material non-linearity of the ASH sections was modelled using the von Mises yield criterion and isotropic hardening approach. Tensile tests on coupons cut from the web of the ASH sections with uniform thicknesses were carried out in (Akbari et al., 2020a) based on AS 1391(SA, 1998). Table 4.2 summarises the average measured material properties of the ASH sections. True stress and true plastic strain were employed in the numerical model. Therefore, the engineering stress–strain data from tensile coupon tests were converted to the true stress and true plastic strain using the following equations (Talebian et al., 2020):

$$\sigma_t = \sigma_{eng}(1 + \varepsilon_e) \quad (4.1)$$

$$\varepsilon_t = \ln(1 + \varepsilon_e) \quad (4.2a)$$

$$\varepsilon_{t(pl)} = \varepsilon_t - \frac{\sigma_t}{E} \quad (4.2b)$$

where σ_t is the true stress (MPa), ε_t is the true strain, $\varepsilon_{t(pl)}$ is the true plastic strain, σ_e is the engineering stress (MPa) and ε_e is the engineering strain. Figure 4.8 plots the true and engineering stress-strain curve of the 6063-T6 aluminium alloy for the 475-057 specimen.

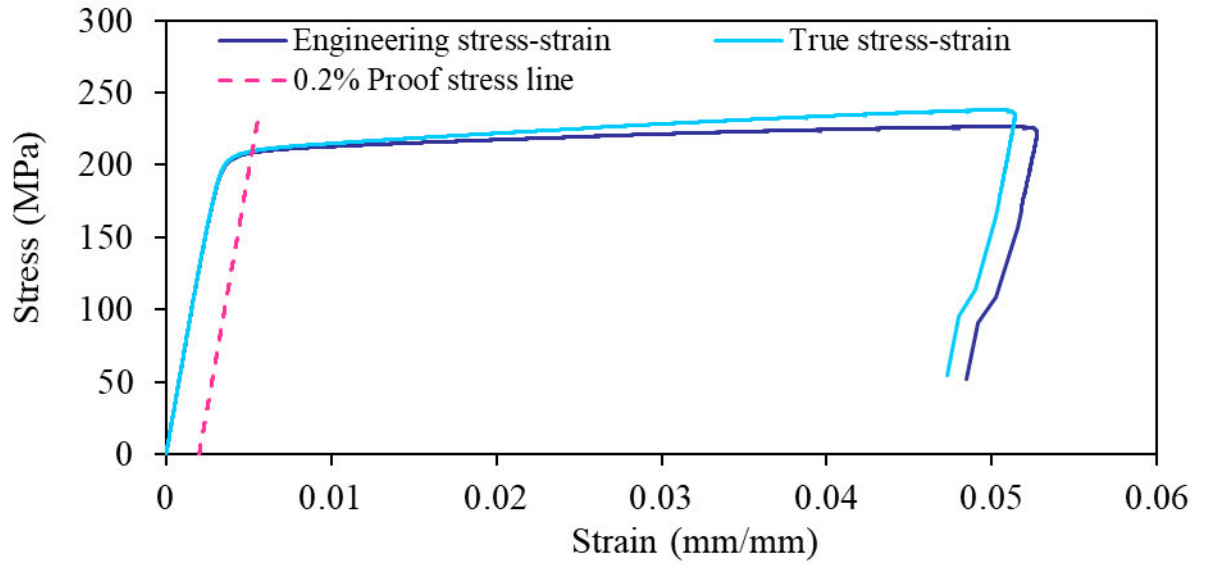


Figure 4.8 Stress-strain curves of Section 475-057.

Table 4.2 Mechanical properties of the ASH sections.

Section	E (MPa)	f_y (MPa)	f_u (MPa)
675-027	62854	193	214
475-077	63768	217	233
475-057	65319	206	224
475-071	64147	188	210

Note: E is elastic modulus, f_y is the static 0.2% tensile proof stress, and f_u is the ultimate strength.

4.3.3. Boundary conditions

Due to symmetry in geometry and loading, half of the test setup was simulated, as shown in Figure 4.9, which details the boundary conditions of the ASH at the symmetric plane, the bearing plate, and the rigid support. The boundary condition of the bearing plate was assigned to the reference node defined at the point of load application and only the translational DOF in the direction of the vertical y-axis was released. As can be seen in Figure 4.3, the ASH is bolted to the rigid support. The bolted connections were not physically modelled, but the bolt holes on the ASH were constrained to the centre of the holes on the rigid support using MPC tie constraints (ABAQUS, 2014), as shown in Figure 4.9. Furthermore, the six degrees of freedom at the rigid support were all fixed (see Figure 4.9).

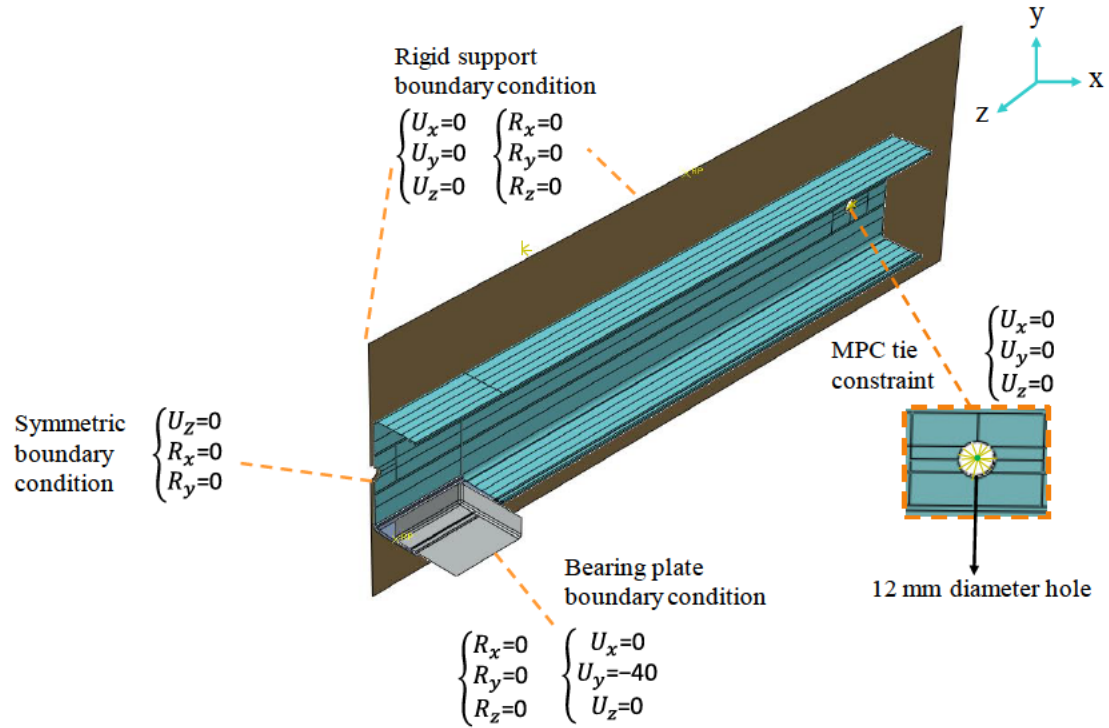
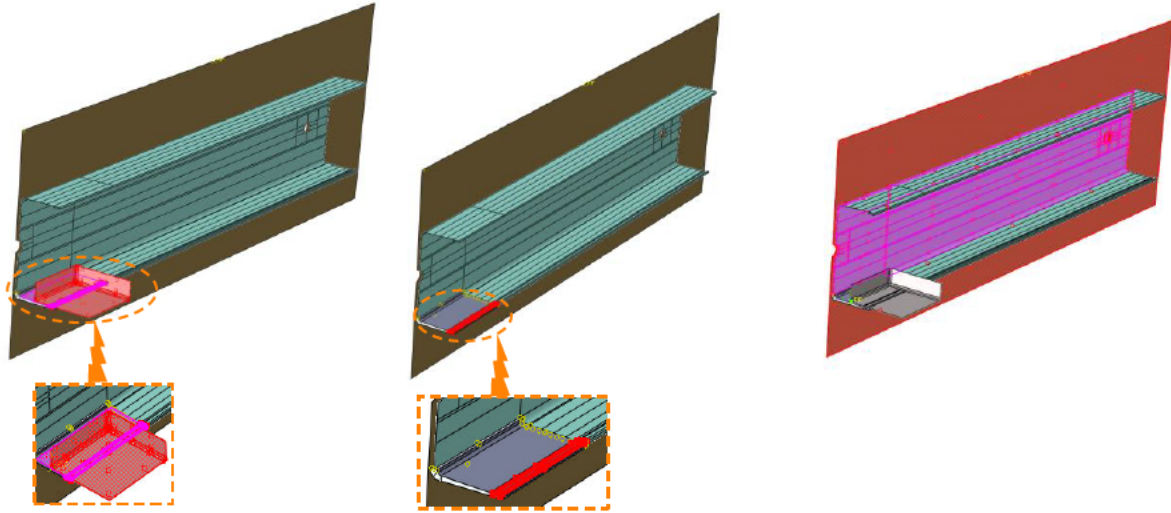


Figure 4.9 Boundary conditions and bolted connection.

4.3.4. Contacts

Interactions between elements were modelled using contact pairs in ABAQUS, as shown in Figure 4.10. Contacts between (i) the bearing plate and the bottom flange of the ASH, and (ii) the ASH and the rigid support were simulated using the surface-to-surface discretization method with finite sliding. In these contacts, the deformable body (ASH) was defined as a slave surface, whereas the bearing plate and the rigid support were considered as master surfaces. Normal contact was defined between the rigid support and the ASH's web. Due to the application of sufficient amount of grease between the flange and the bearing plate in the test, hard contact with friction coefficient equal to 0 was found to accurately replicate the bearing failure. Self-contact was also defined in the flange grooves with friction coefficient of 0.



(a) Sub-head and bearing plate (b) Self-contact in the flange groove (c) Sub-head and rigid support

Figure 4.10 Interactions between elements (master surface shown in red and slave surface shown in purple).

4.4. Analysis results and validation

This section discusses the results of the numerical analyses of the ASH sections under different bearing loads. A total of 42 ASH sections were numerically analysed using non-linear static analysis method. The experimental results were compared with the finite element results in terms of the ultimate loads, the load-displacement curves and the failure modes.

4.4.1. Ultimate loads

Two failure criteria were defined by Akbari et al. (2020a), known as the maximum load (Max) and the ultimate deformation limit (UDL). In the test, a maximum load ($P_{Exp-Max}$) occurred at a very large displacement when the bearing plate was wedged in the flange groove. Hence, a deformation limit (UDL) of four times the elastic displacement was set to define the ultimate load ($P_{Exp-UDL}$) (Akbari et al., 2020a; Gilbert and Rasmussen, 2011; Yura et al., 1981; SA, 2012; Brühl, 2011; Yasumura and Kawai, 1998). This is illustrated in Figure 4.11. The comparisons of the ultimate capacities of all specimens obtained from the test results (P_{EXP}) and finite element analysis results (P_{FEA}) based on the maximum load (Max) and ultimate deformation limit (UDL) (Akbari et al., 2020a) are given in Table 4.3. The

mean values of the ratios of the ultimate capacities obtained from the tests and the finite element analyses were 0.98 and 1; respectively, following the maximum load (Max) and the ultimate deformation limit (UDL) criteria. The corresponding coefficients of variation (COV) were 0.05 for both criteria. These results show that the non-linear static analyses of the FE models produced accurate ultimate capacities.

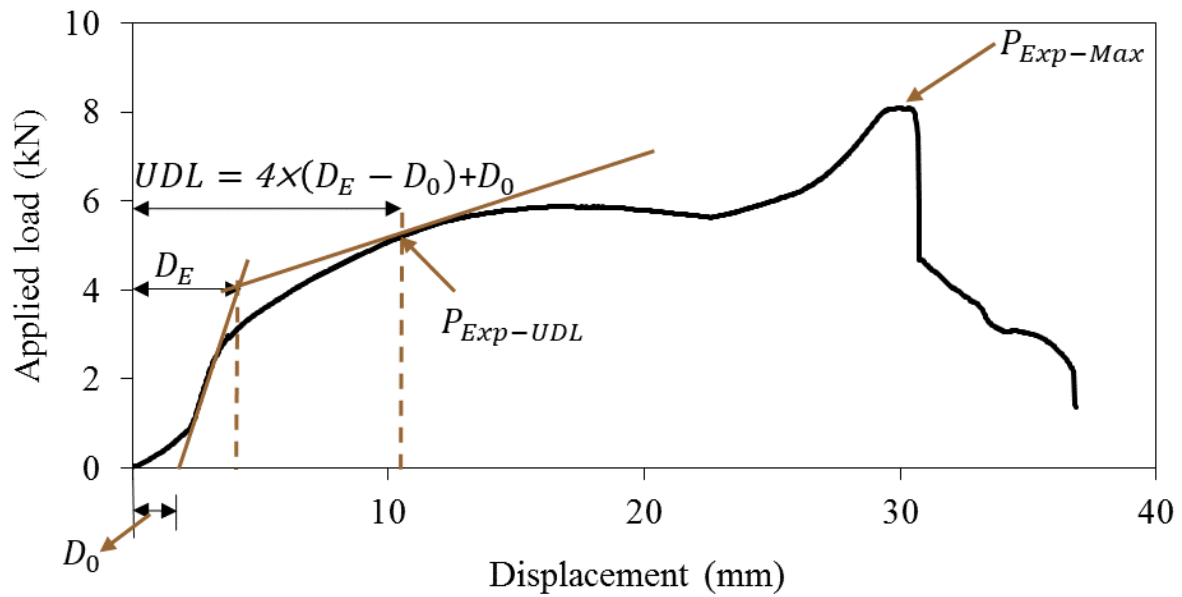


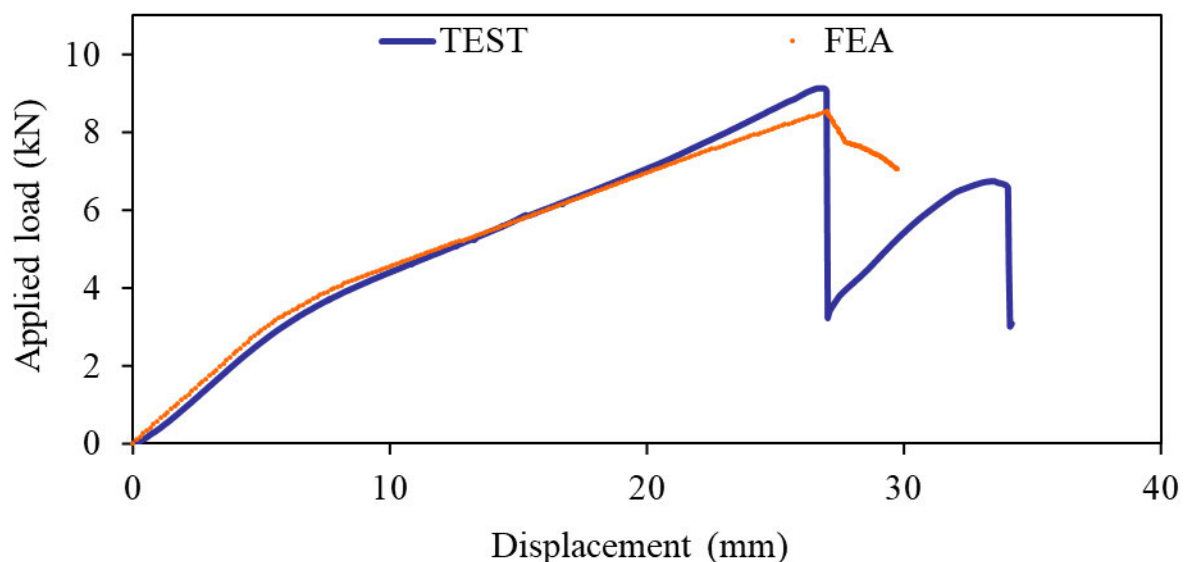
Figure 4.11 Representative experimental load-displacement curve showing maximum load (Max) and ultimate deformation limit (UDL).

Table 4.3 Comparison of experimental and FEA bearing capacities based on maximum load (Max) and ultimate deformation limit (UDL).

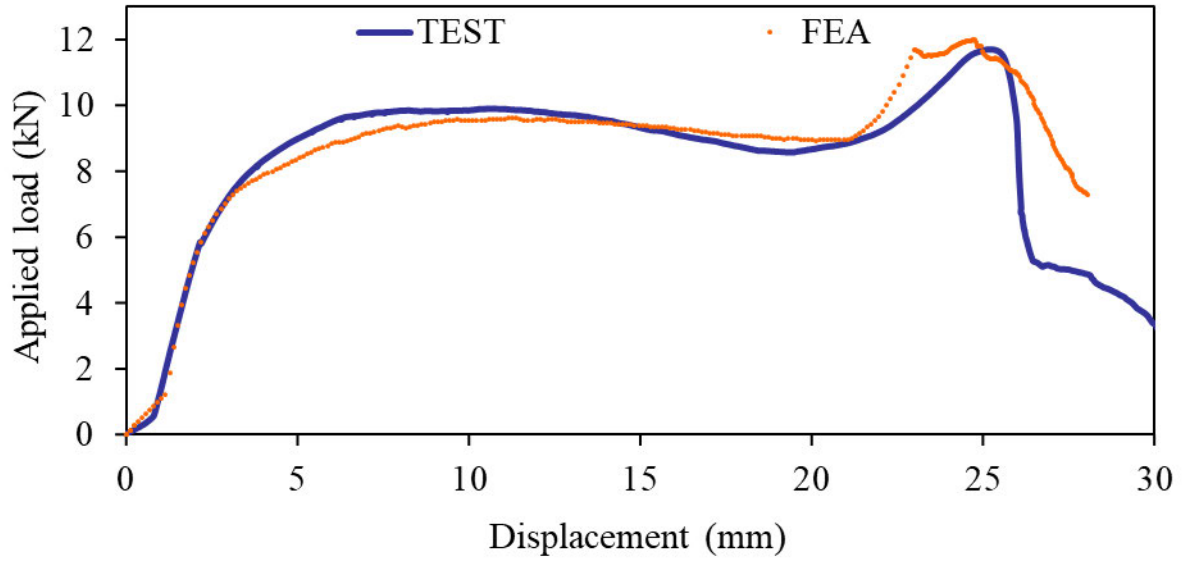
Specimen details			$P_{Exp-UDL}$ (kN)	P_{FEM-UD} (kN)	$P_{Exp-Max}$ (kN)	$P_{FEM-Max.}$ (kN)	$\frac{P_{Exp-UDL.}}{P_{FEA-UDL}}$	$\frac{P_{Exp-Max.}}{P_{FEA-Max}}$
Loading and boundary	Section	N (mm)						
1B/15mm	675-027	50	5.4	6.0	8.3	8.8	0.90	0.94
		100	10.4	11.2	10.8	11.2	0.93	0.96
		150	12.1	12.6	12.1	12.6	0.96	0.96
	475-077	50	4.2	4.4	5.7	5.6	0.95	1.02
		100*	6.8	6.6	6.8	6.6	1.03	1.03
		150	6.6	7.0	7.6	7.5	0.94	1.01
	475-057	50*	6.2	6.2	6.2	6.2	1.00	1.00
		100	7.7	7.2	7.4	7.2	1.07	1.03
		150*	8.2	8.1	8.2	8.1	1.01	1.01
		200*	9.5	9.5	9.5	9.5	1.00	1.00
	475-071	50*	6.3	6.3	7.1	6.5	1.00	1.09
		100*	6.4	6.3	7.6	7.3	1.02	1.04
		150*	7.3	7.4	8.8	8.3	0.99	1.06
		200*	8.3	8.3	9.0	8.7	1.00	1.03
1B/25mm	675-027	50	8.5	8.9	11.0	11.7	0.96	0.94
		100	11.9	11.3	13.2	14.9	1.05	0.89
		150	12.2	13.5	14.8	16.1	0.90	0.92
	475-077	50	4.5	4.5	8.0	9	1.00	0.89
		100*	5.6	5	9.5	10	1.12	0.95
		150	6.4	6.6	10.2	10.7	0.97	0.95
	475-057	50*	5.4	5.7	8.2	8	0.95	1.03
		100*	6.3	6.7	9.6	10.2	0.94	0.94
		150*	7.7	7.4	11.2	12	1.04	0.93
		200*	8.6	8.4	12.0	12.5	1.02	0.96
	475-071	50*	6.1	6.5	9.9	10	0.94	0.99
		100*	6.3	6.3	10.7	10	1.00	1.07
		150*	7.2	7.1	11.6	11.6	1.01	1.00
		200*	8.2	7.9	13.0	11.8	1.04	1.10
2B/25mm	675-027	50	9.8	9.5	11.7	11.9	1.03	0.98
		100	11.8	11.6	13.4	14.2	1.02	0.94
		150	13.3	14.1	15.4	17.1	0.94	0.90
	475-077	50	5.1	4.8	8.2	9.1	1.06	0.90
		100*	5.9	5.7	9.8	10.4	1.04	0.94
		150	7.4	7.3	11.0	12	1.01	0.92
	475-057	50*	6.2	6.2	8.3	8.6	1.00	0.97
		100*	7.6	7.1	10.3	10.8	1.07	0.95
		150*	8.1	8.1	11.1	11.9	1.00	0.93
		200*	8.8	8.9	11.6	12.5	0.99	0.93
	475-071	50*	6.6	6.8	10.3	10.5	0.97	0.98
		100*	6.5	6.7	10.6	10.6	0.97	1.00
		150*	7.6	7.5	11.8	12.1	1.01	0.98
		200	8.2	7.8	12.2	12.3	1.05	0.99
Mean							1.00	0.98
COV							0.05	0.05

4.4.2. Load-displacement curves

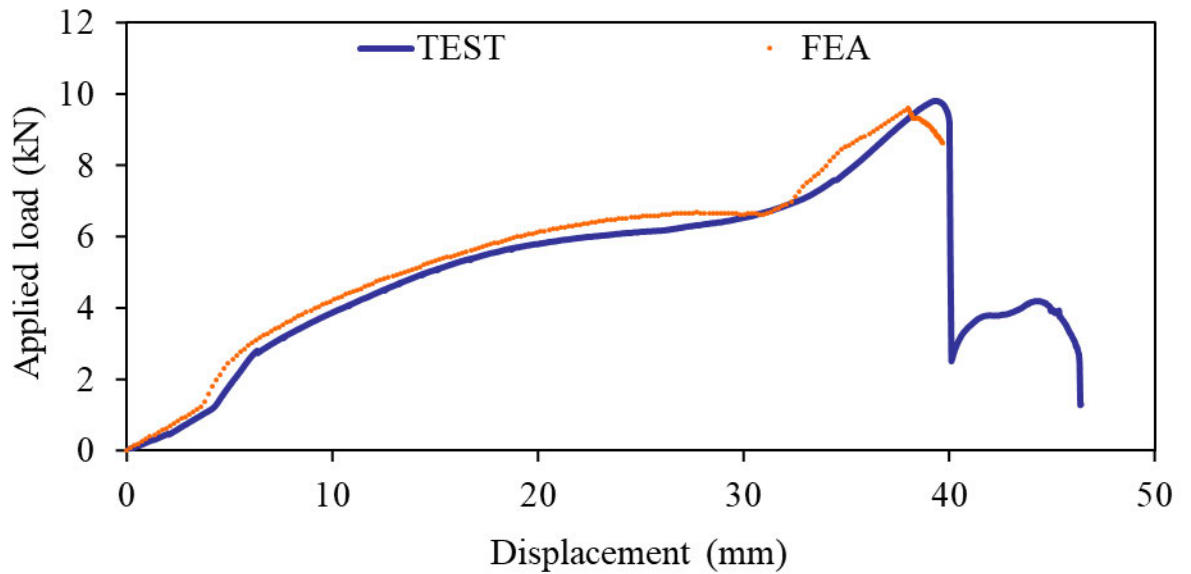
The FEA load-displacement curves of the mid-span of the ASH bottom flange were compared with their corresponding experimental results. Figure 4.12 (a), (b) and (c) show the comparison of the load-displacement curves of the 475-071/15/1B/200, 675-027/25/2B/50 and 475-027/25/1B/50 specimens under the 15 mm and 25 mm load cases. Generally, the FE models were shown to be able to simulate the experimental ultimate capacities, and the load-displacement responses of the ASH sections in both the linear and non-linear stages. Minor discrepancies in the second peak were observed in the failure stage. It is believed that such a difference was due to the complex geometry of the flange grooves and penetration of the bearing plate into the grooves.



15 mm engagement length (475-071/15/1B/200)



(b) 25 mm engagement length (675-027/25/2B/50)



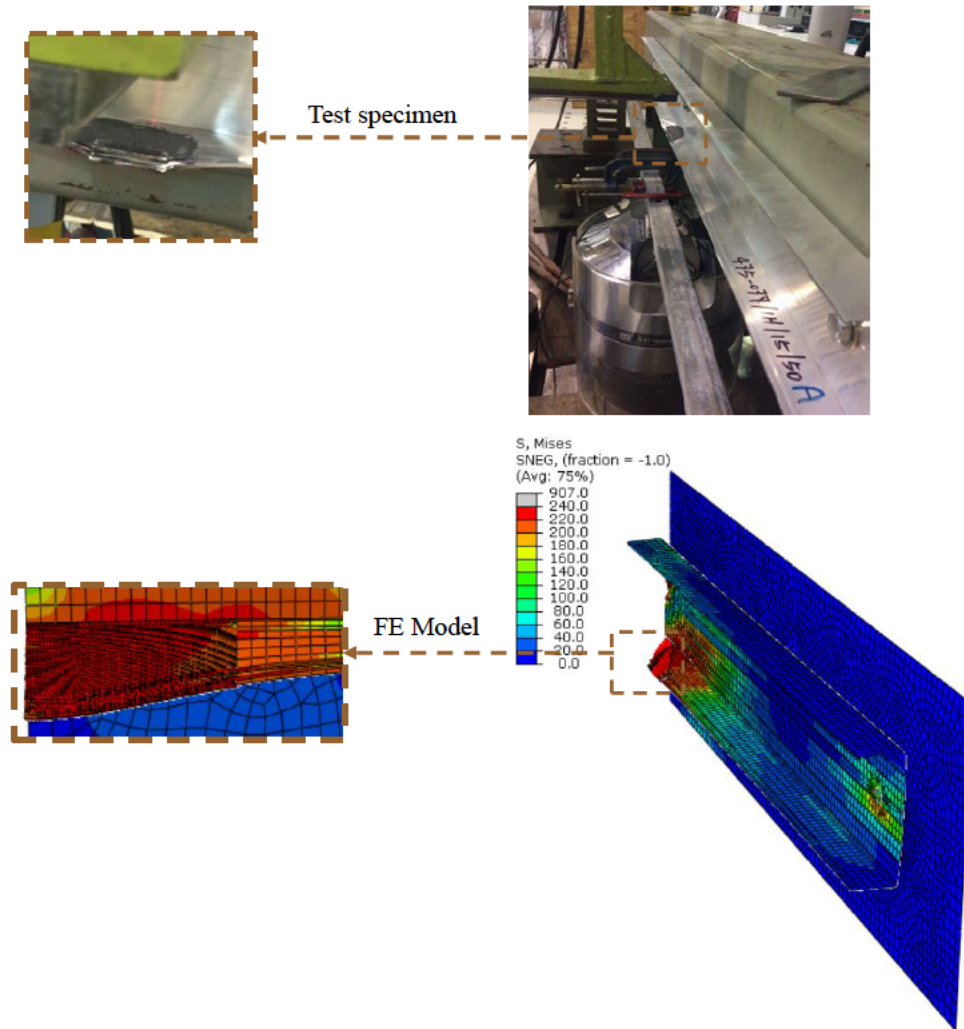
(c) 25 mm engagement length (475-027/25/1B/50)

Figure 4.12 Comparison of experimental and numerical load-displacement curves.

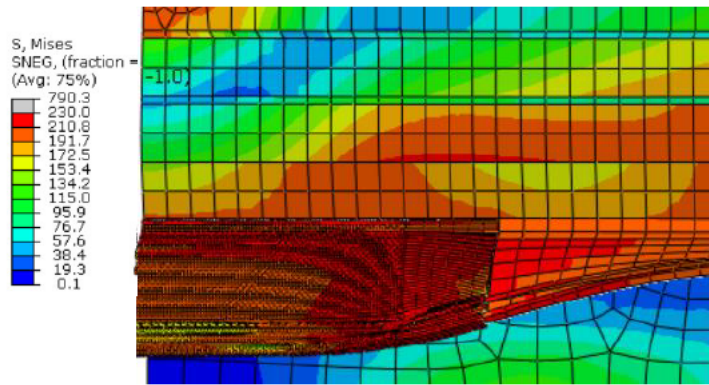
4.4.3. Failure modes

The failure modes of the ASH sections subjected to different bearing loads depend highly on the loading conditions and the cross-sectional shape of the ASH sections. The main failure modes of the ASH sections observed in the test were yielding at the web-flange junction due to flange bending and slipping of the bearing plate after the flange groove was crushed (Akbari et al., 2020a). The comparisons of the failure modes of the ASH sections observed

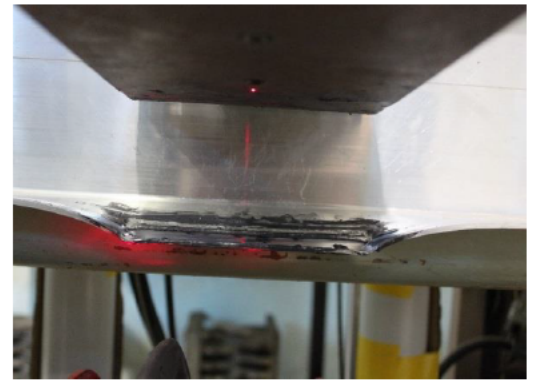
from the experiments and the FE analyses under two engagement lengths of 15 mm and 25 mm are shown in Figure 4.13 and Figure 4.14, respectively. These figures show close agreement between the experimental and the numerical failure modes, hence validated the developed numerical models.



(a) 475-077/1B/15/50A



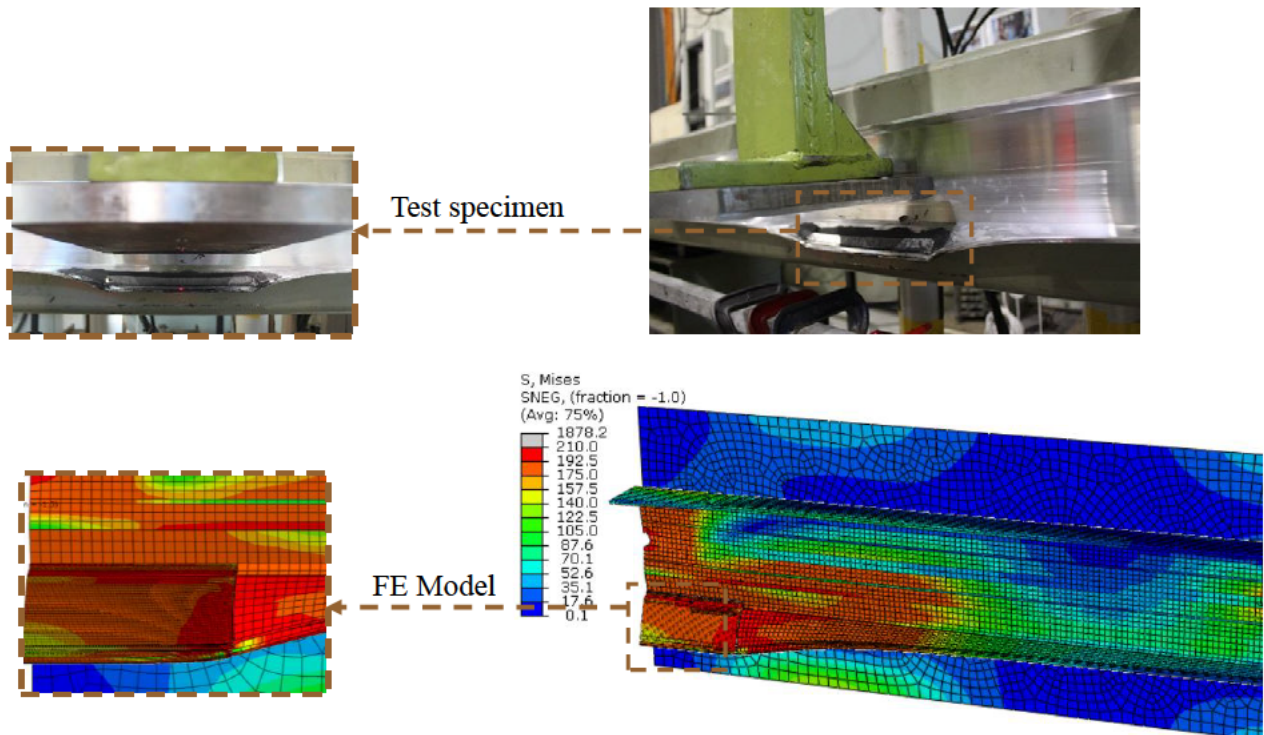
FE Model



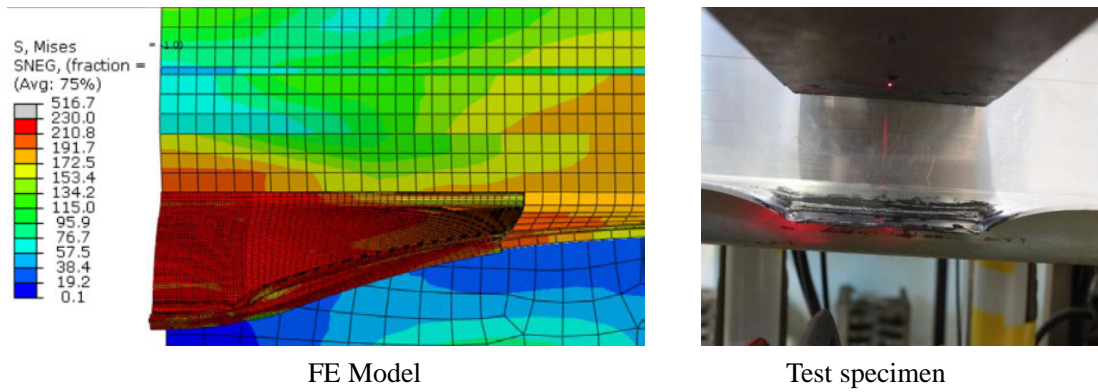
Test specimen

(b) 675-027/1B/15/150

Figure 4.13 Comparison of experimental and numerical failure modes under 15 mm engagement length.



(a) 475-057/1B/25/200



(b) 675-027/1B/25/50

Figure 4.14 Comparison of experimental and numerical failure modes under 25 mm engagement length.

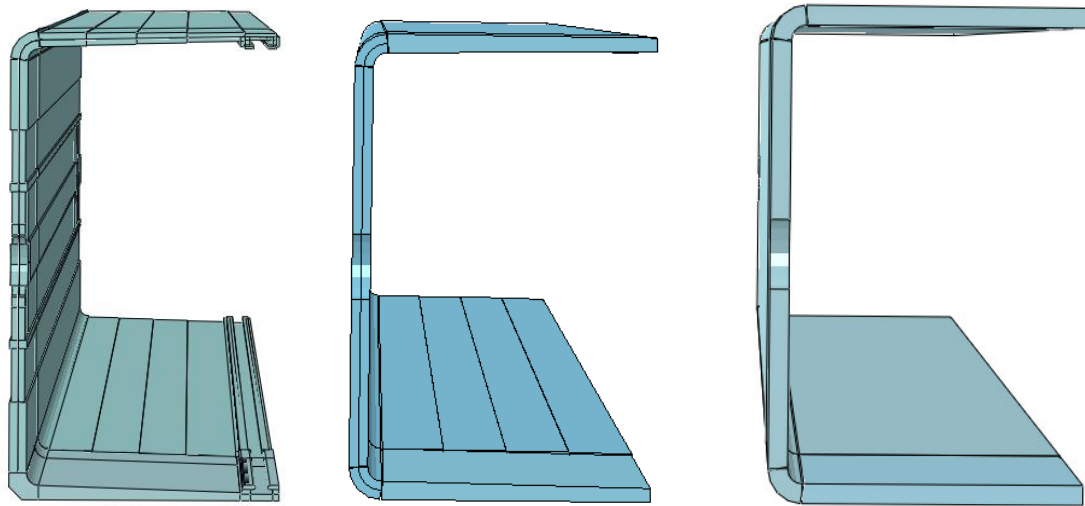
4.5. Parametric study

Based on the validated FE models, a comprehensive parametric study (totaling 288 FE models) was performed to thoroughly investigate the effect of various parameters (bearing width (N), flange width (b_f), thickness (t), and engagement length (D)) on the bearing behaviour of the ASH sections. The results obtained from the parametric studies were then used to investigate the accuracy of the design rules DRSs (Akbari et al., 2020a; AISI S240, 2015; TI 809-07, 1998; SSMA, 2000) and the DRA_I (Akbari et al., 2020a). Details of the parametric study are presented in Table 4.4, in which N was between 50 mm and 150 mm, and D ranged between 5 mm and 30 mm. The specimen length used in the parametric study was 1300 mm. Overall, this parametric study considered 9 ASH sections with their nominal flange widths ranging within the limit of 40 mm to 100 mm, and the nominal thicknesses in the range of 2 mm to 4 mm. Notably, the ASH sections specific to a particular manufacturer were used in our previous experimental study (Akbari et al., 2020a). To comprehensively cover the practical range of the ASH sections utilized in the façade industry, the ASH cross-sections were simplified in the parametric study. The ASH groove shape, in which the bearing plate was wedged, governed the maximum loads acquired from the tests (Akbari et al., 2020a). Since the ASH's groove was responsible for a large deflection and accordingly, unrealistic bearing capacities of the ASH sections, the grooves were removed from the ASH sections in the FE parametric models. Additionally, uniform thickness was assigned to the ASH sections in the parametric study. To determine the optimum cross-section, the effects of

different shapes of the web-flange junction (see Figure 4.15, combination of curved and straight surfaces, curved, and sharpened edge) of the ASH were investigated. As the bearing capacities of the ASH sections were observed not to be considerably affected by this parameter, curved shape was assigned to the web-flange junction, being easily simulated by shell elements. Furthermore, ASH sections with uniform flange thickness (UFT) and non-uniform flange thickness (NUFT) were considered in this parametric study. Figure 4.16 (a) displays the cross-section used in the tests and validated by the FE models, whereas the FE parametric models with UFT and NUFT are shown in Figure 4.16 (b) and (c), respectively. It should be noted that several partitions were created to account for finer mesh under concentrated load and to simulate varying thicknesses. Furthermore, investigation of the effects of the corner radius and the web height showed that the bearing capacities of the ASH sections were not largely influenced by these parameters. Taking this into account, a web height of 100 mm and a corner radius equal to 3 mm were considered in the parametric study.



Figure 4.15 Different shapes of the web-flange junction of the ASH: (a) combination of curved and straight surfaces, (b) curved shape, (c) sharpened edge.



(a) Validated model (b) Parametric model (NUF) (c) Parametric model (UFT)

Figure 4.16 Cross-sections of the FE model used for validation and parametric study.

Table 4.4 Parametric study model details of the ASH sections.

Section	d (mm)	b _f (mm)	t (mm)	Alumini um grade	N (mm)	D (mm)	Flange	No of Models
1	100	40	2	6063-T6	50,100,150	05,10,15,20	UFT, NUFT	24
2	100	40	3	6063-T6	50,100,150	05,10,15,20	UFT, NUFT	24
3	100	40	4	6063-T6	50,100,150	05,10,15,20	UFT, NUFT	24
4	100	65	2	6063-T6	50,100,150	05,10,15,20,25,30	UFT, NUFT	36
5	100	65	3	6063-T6	50,100,150	05,10,15,20,25,30	UFT, NUFT	36
6	100	65	4	6063-T6	50,100,150	05,10,15,20,25,30	UFT, NUFT	36
7	100	100	2	6063-T6	50,100,150	05,10,15,20,25,30	UFT, NUFT	36
8	100	100	3	6063-T6	50,100,150	05,10,15,20,25,30	UFT, NUFT	36
9	100	100	4	6063-T6	50,100,150	05,10,15,20,25,30	UFT, NUFT	36
Total								288

In the façade industry in Australia, window wall systems are typically made of 6063-T6 aluminium alloy. Hence, only this grade was considered in the parametric study. The yield stress and the elastic modulus of 6063-T6 are 172 MPa and 70000 MPa, respectively, based on AS/NZS 1664.1 (1997). To consider the strain hardening effect, a bi-linear model proposed by Su et al. (2014, 2016) for the development of the Continuous Strength Method (CSM) was used in this study. Typically, this model consists of two stages: the initial elastic stage, represented by the elastic modulus of the material (E), and the linear hardening stage with a strain hardening slope (E_{sh}). E_{sh} and the ultimate strain (ε_u) can be determined by Eq. (4.3) and Eq. (4.4), respectively.

$$E_{sh} = \frac{f_u - f_y}{C_2 \varepsilon_u - \varepsilon_y} \quad (4.3)$$

$$\varepsilon_u = C_3 \left(1 - \frac{f_y}{f_u} \right) + C_4 \quad (4.4)$$

where $C_2 = 0.5$, $C_3 = 0.13$, and $C_4 = 0.059$ are constant for 6063-T6 aluminium alloy (Su et al., 2014; Su et al., 2016). f_y is the yield stress (MPa), f_u is the ultimate stress (MPa), and ε_y is

the yield strain. The bi-linear CSM model used in the parametric study is plotted in Figure 4.17.

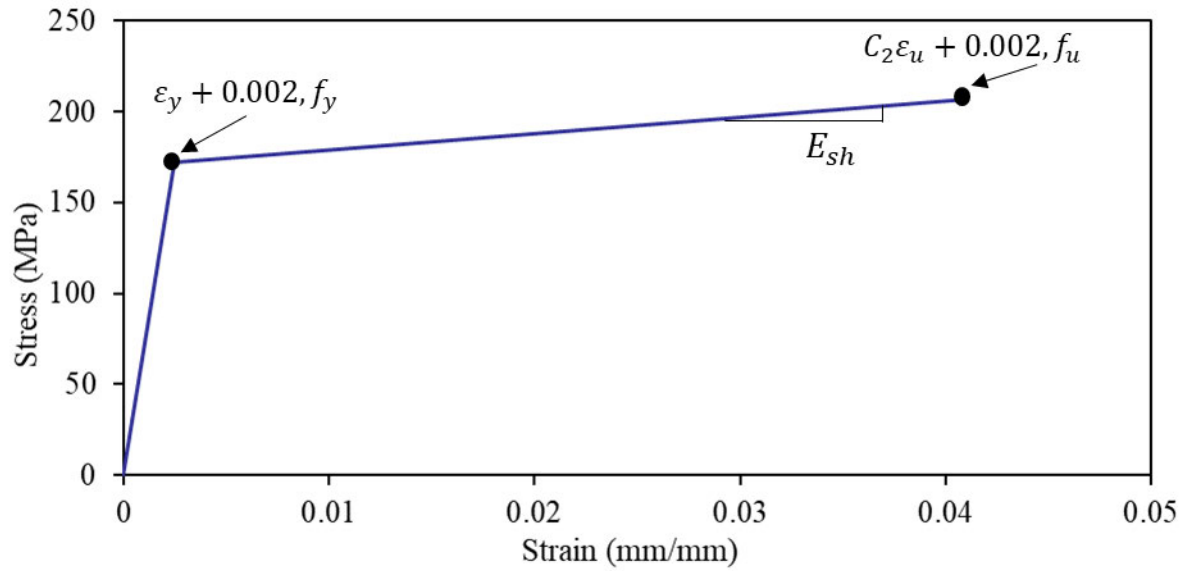


Figure 4.17 Bi-linear CSM model for 6063-T6 aluminium alloy.

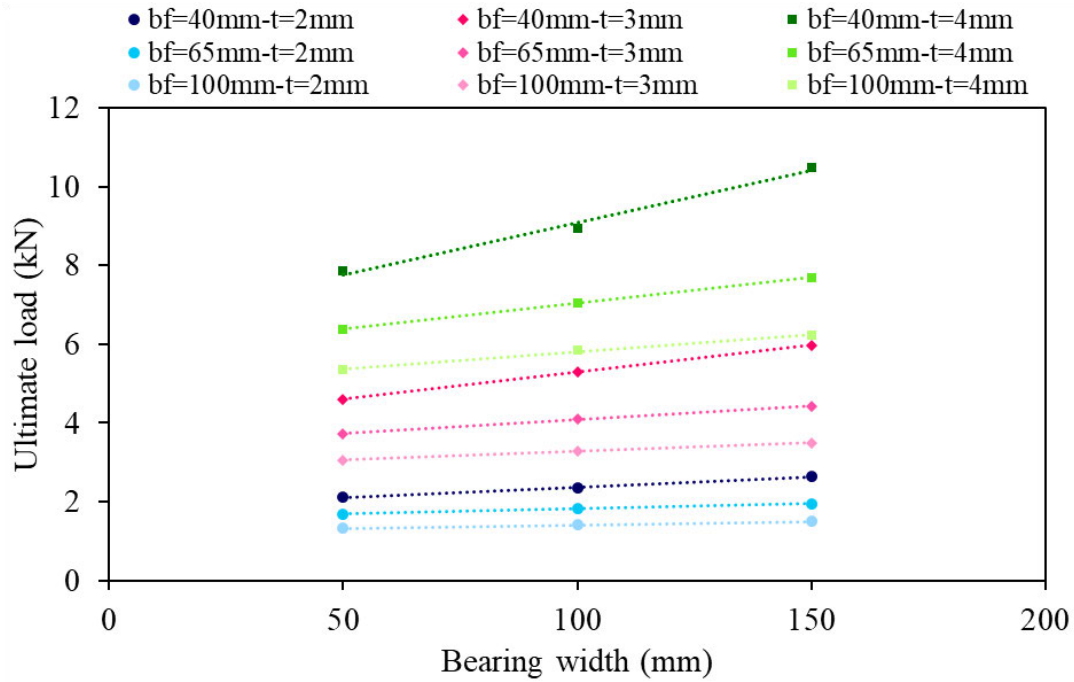
4.5.1. Effects of selected parameters

In this section, the acquired parametric results are analysed to assess the influence of different parameters on the bearing capacities of the ASH sections.

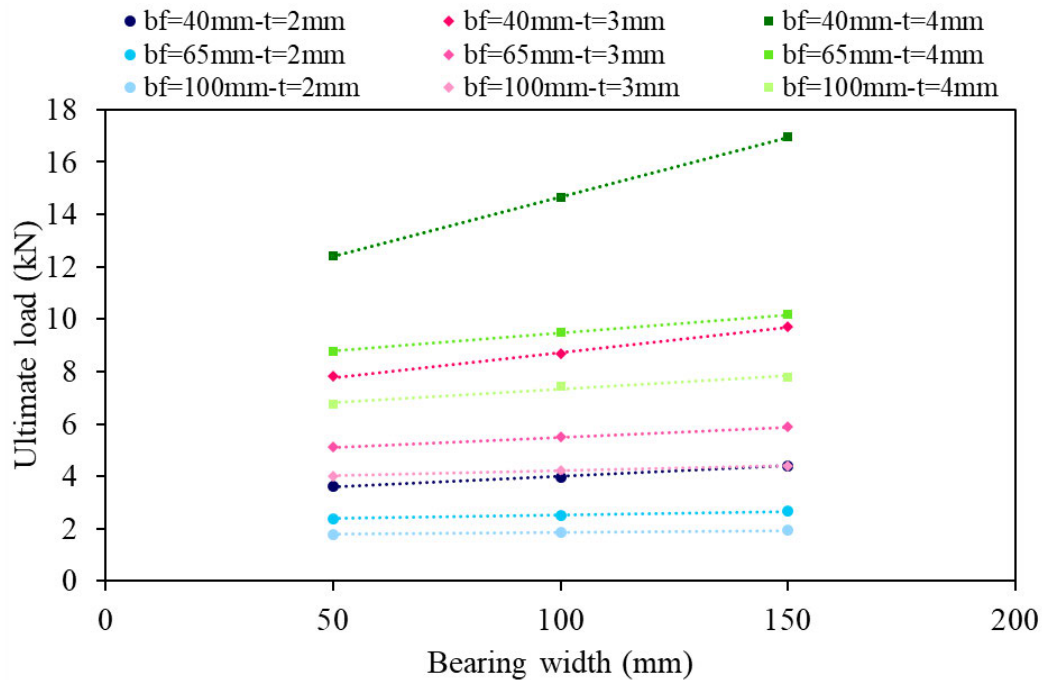
4.5.1.1. Bearing width (N)

Increased bearing widths increase the effective sub-head length, which consequently results in a substantial increase in the overall capacities of the ASH sections. This can be confirmed by Figure 4.18 (a) and (b), in which the ultimate bearing capacities of the ASH sections against varying bearing widths for 9 geometric sections with UFT under the 15 mm and the 25 mm engagement lengths are plotted. These figures show that the bearing capacities of the ASH sections increased linearly with increasing values of bearing width. Bearing capacity variations are more sensitive to shorter flange width ($b_f = 40$ mm). Furthermore, the sections

with a larger bearing width ($N = 150$ mm) are more sensitive to the variations of the sectional geometries compared to a smaller bearing width ($N = 50$ mm).



(a) 15 mm engagement length ($D = 15$ mm)

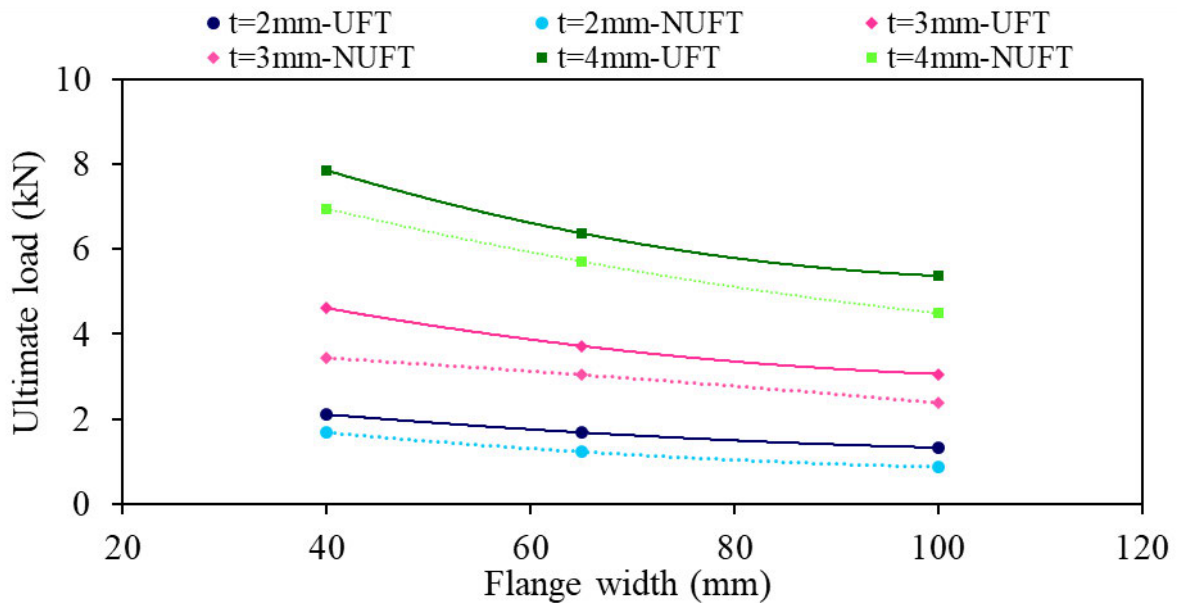


(b) 25 mm engagement length ($D = 25$ mm)

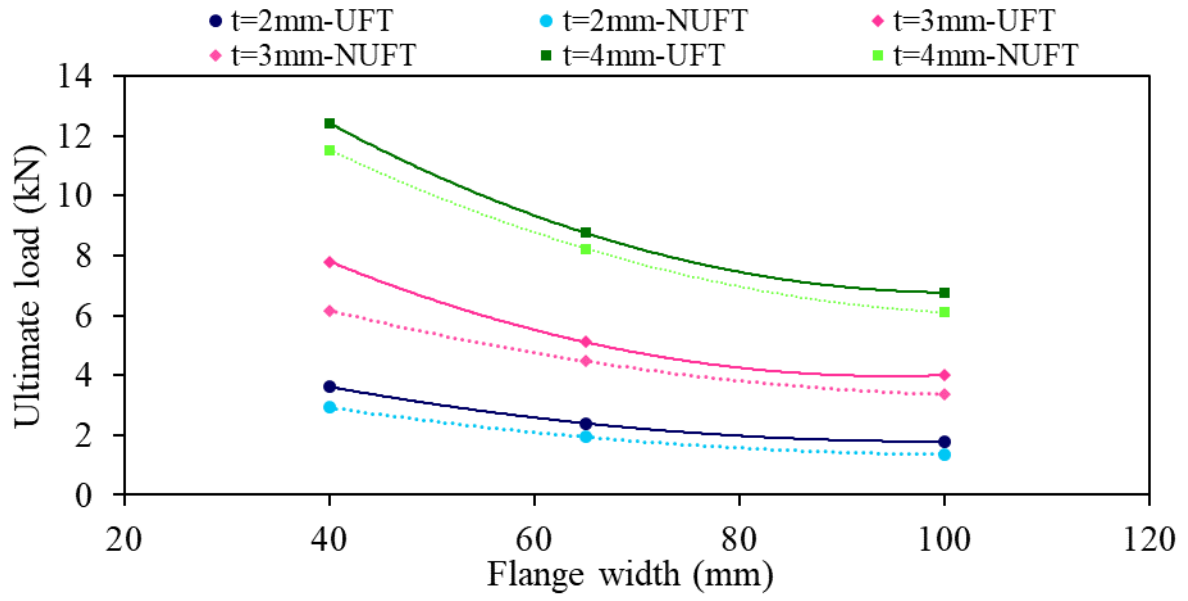
Figure 4.18 Ultimate bearing capacity (P_{FEA}) versus bearing width (N) for different sectional geometries (UFT with different flange widths and thicknesses).

4.5.1.2. Flange width, thickness and flange shape (b_f , t , UFT, NUFT)

The influence of the flange width (b_f), the thickness (t), and the flange shape on the bearing capacities of the ASH sections were examined. Figure 4.19 (a) and (b) illustrate the bearing capacities of the ASH sections (with UFT and NUFT) versus the flange width (b_f) under the 15 mm and the 25 mm engagement lengths, respectively. It can be noticed that increasing the flange width (b_f) leads to a non-linear decrease in the bearing capacity of the ASH sections. However, the bearing capacities of the ASH sections with a shorter flange width ($b_f = 40$ mm) are more affected by the thickness variations than that for a larger flange width ($b_f = 100$ mm). Finally, it was observed from Figure 4.20 (a) and Figure 4.20 (b) that the capacities of the ASH sections (with $b_f = 40$ mm) are considerably increased in a non-linear manner when the thickness (t) increases for three different bearing widths (N), and under the engagement lengths (D) of 15 mm and 25 mm. Furthermore, Figure 4.19 and Figure 4.20 show that the bearing capacities of the ASH sections with NUFT are less than those with UFT.

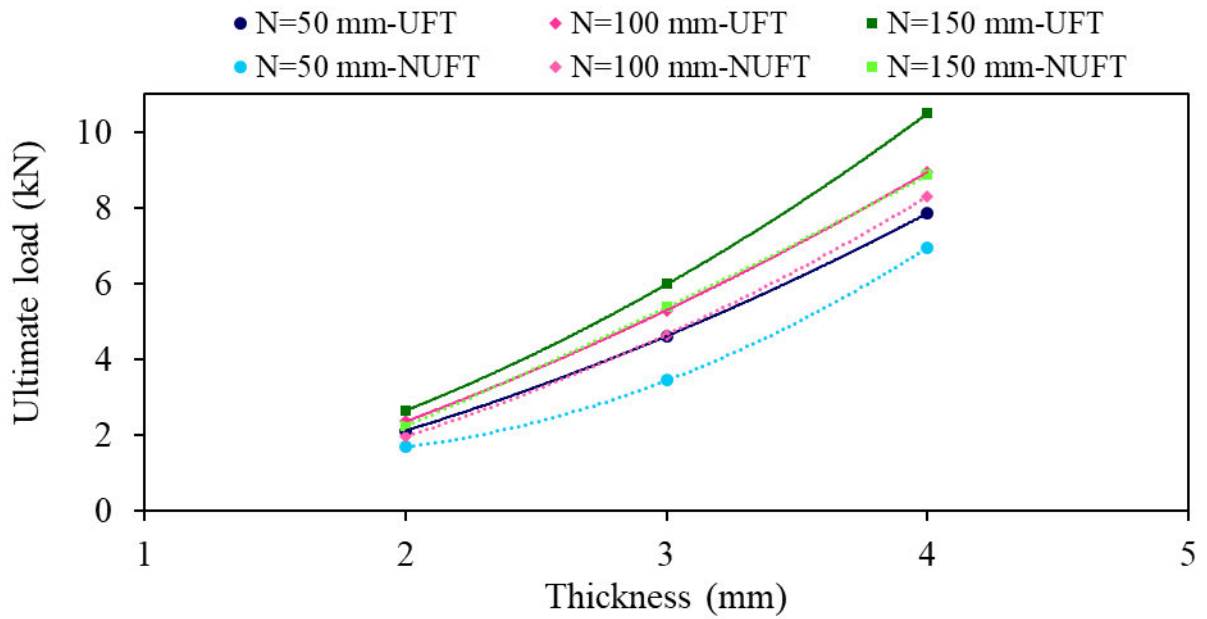


(a) 15 mm engagement length ($D = 15$ mm)

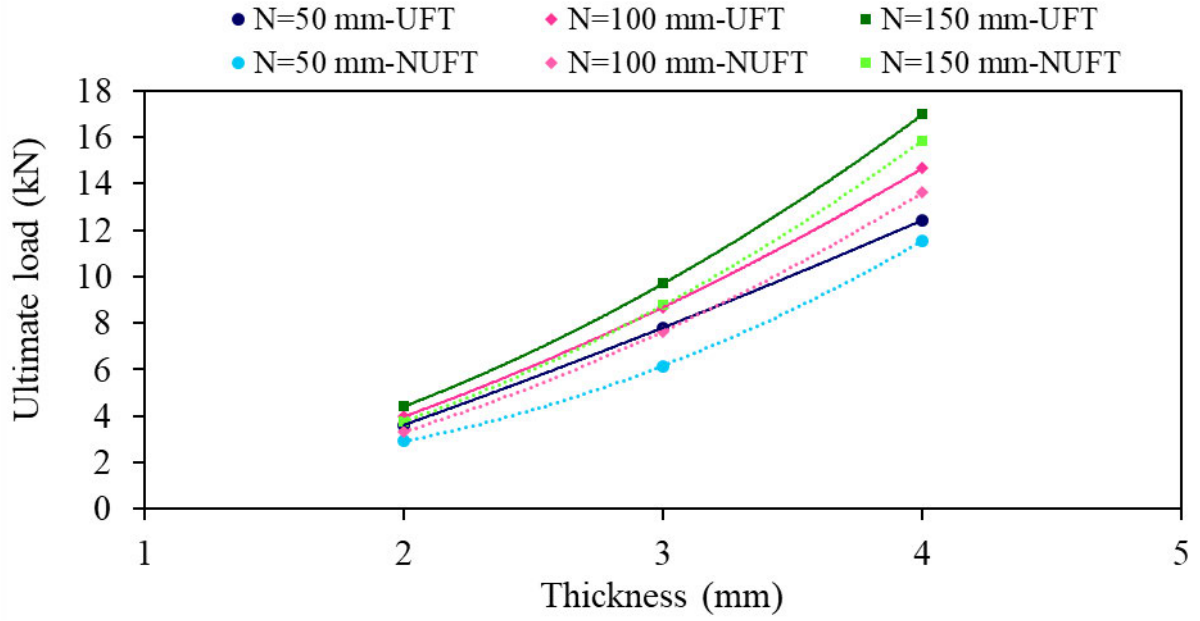


(b) 25 mm engagement length ($D = 25$ mm)

Figure 4.19 Ultimate bearing capacity (P_{FEA}) of ASH sections (with UFT and NUFT) versus flange width (b_f) for different thicknesses (t) (models with $N = 50$ mm).



(a) 15 mm engagement length ($D = 15$ mm)



(b) 25 mm engagement length ($D = 25$ mm)

Figure 4.20 Ultimate bearing capacity (P_{FEA}) versus thickness (t) for different bearing widths (N) (models with $b_f = 40$ mm).

4.5.1.3. Engagement length (D)

Engagement length makes an important contribution to the behaviour and pattern of the load-displacement response. Figure 4.21 compares the load-displacement curves of Section 1 (with $b_f = 40$ mm and $t = 2$ mm) for six engagement lengths ($D = 5, 10, 15, 20, 25$, and 30 mm) under 50 mm bearing width (N). This figure shows that both stiffness and capacity increase significantly, as the engagement length (D) increases. Figure 4.22 demonstrates that as the engagement length (D) increases, the ultimate bearing capacities of the FE models with $b_f = 40$ mm increase non-linearly for all three bearing widths (N) and three thicknesses (t). Notably, the degree of non-linearity is greater for sections with larger thickness (t). Moreover, a relatively minor increase in the ultimate capacities was observed in the section with smaller thickness (t) and shorter engagement length (D) compared to the section with greater thickness (t) and larger engagement length (D).

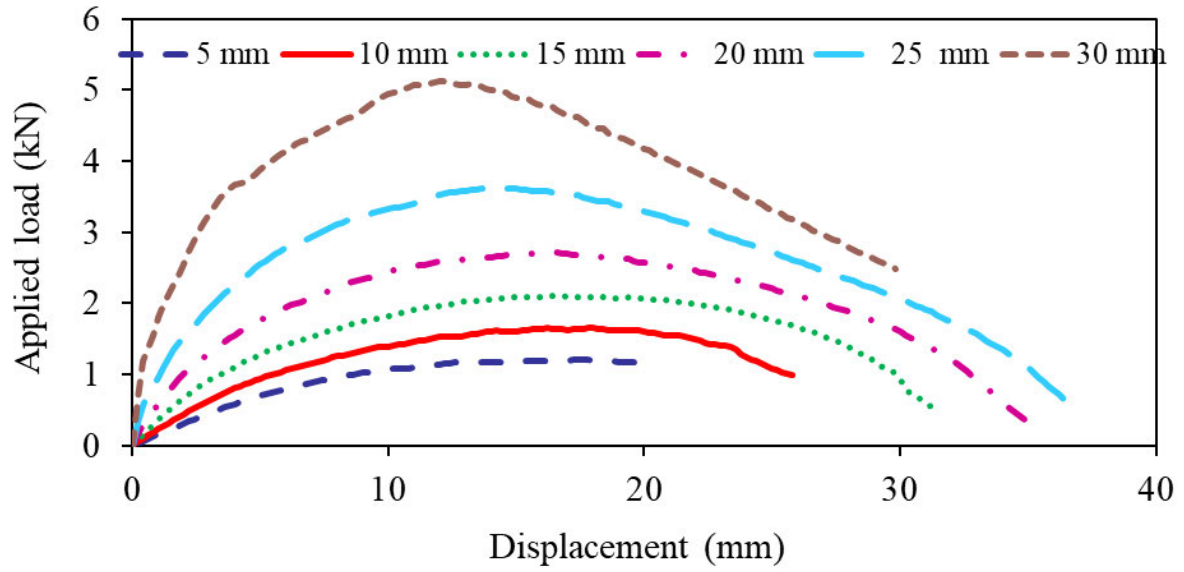
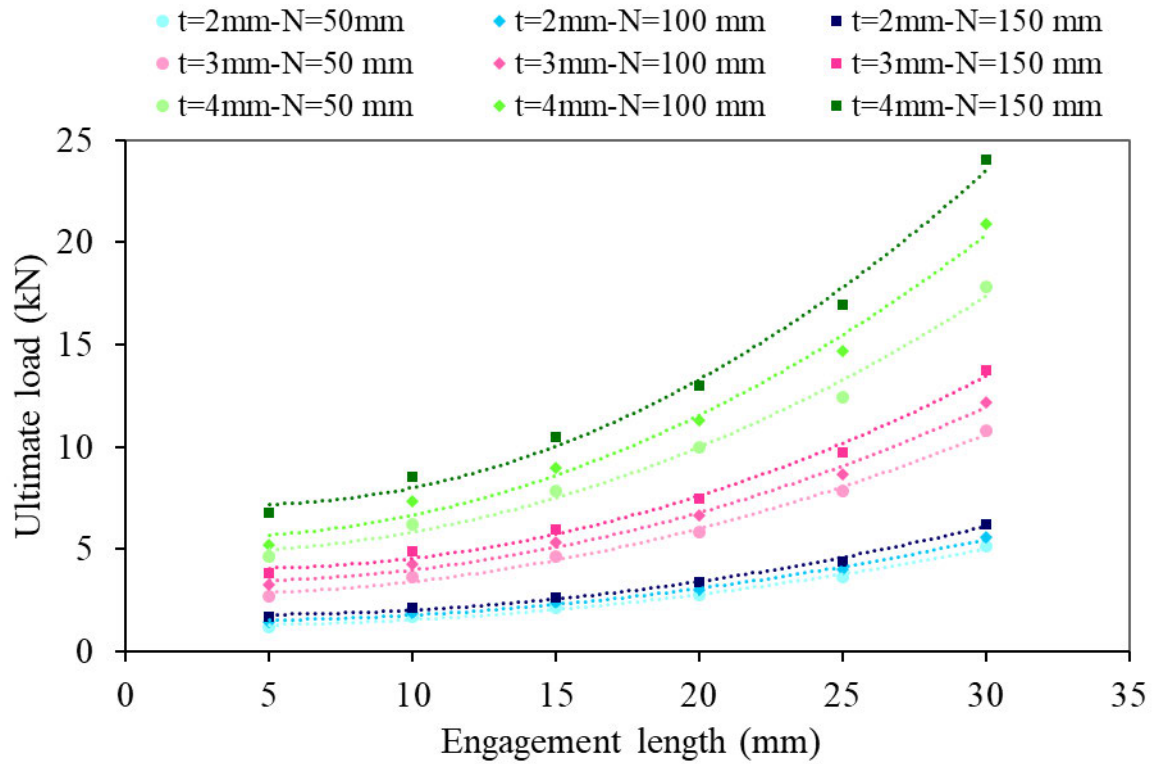
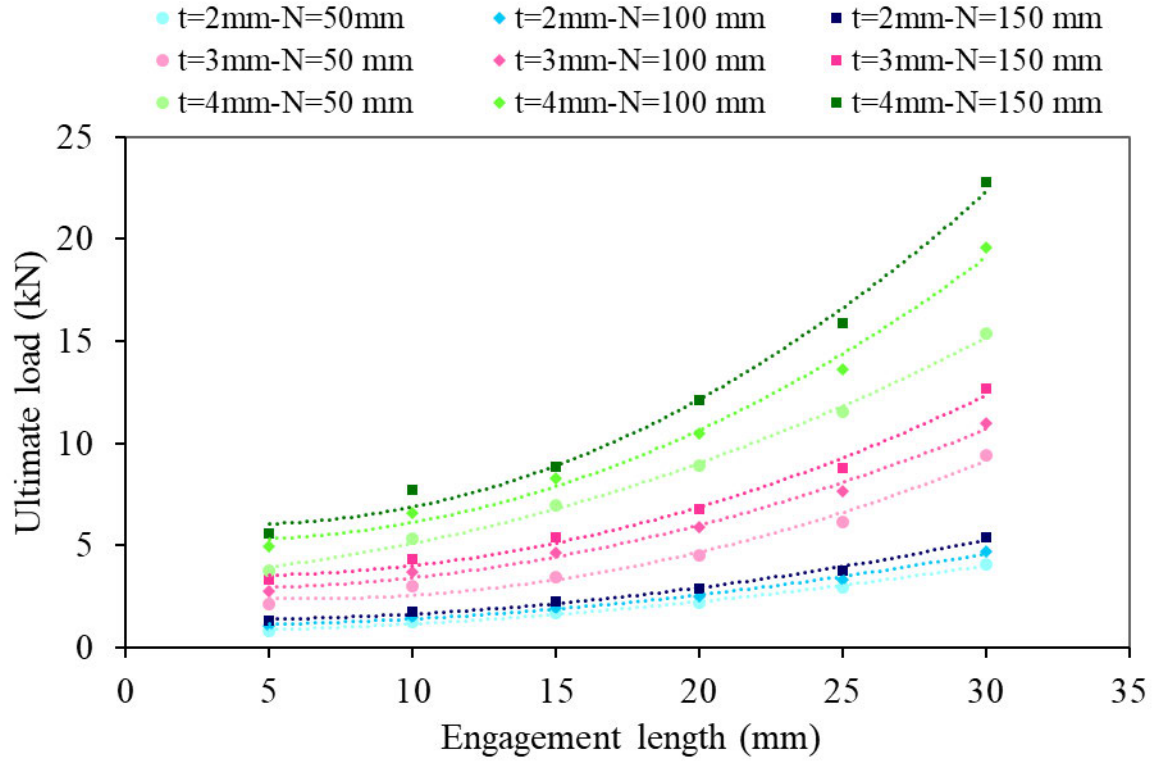


Figure 4.21 Load-displacement curves for different engagement lengths (D) for Section 1 (with $b_f=40$ mm, $t=2$ mm, and $N=50$ mm).



(a) UFT

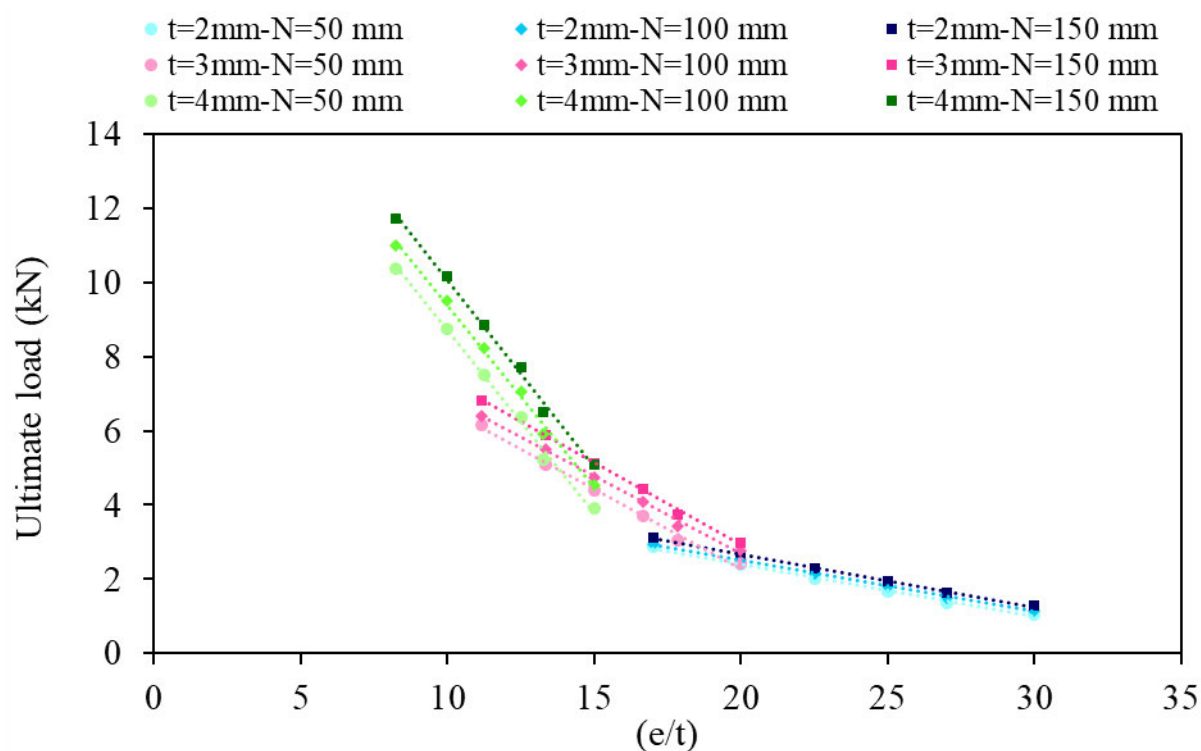


(b) NUFT

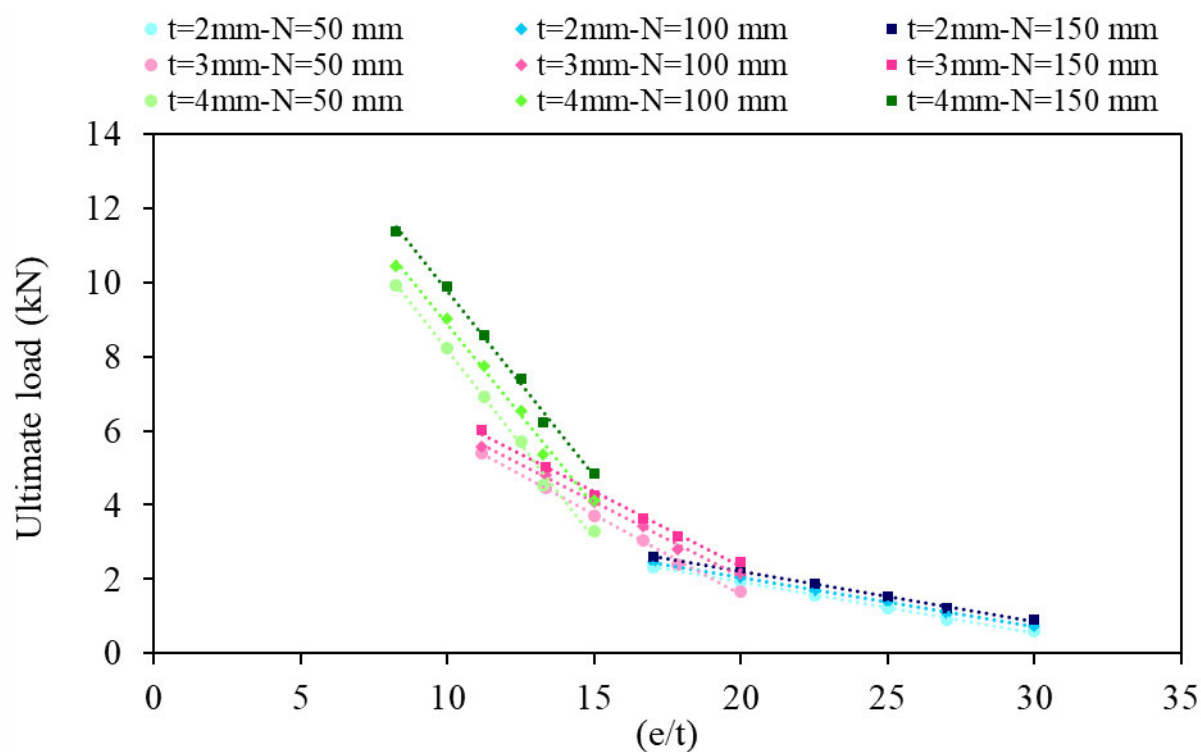
Figure 4.22 Ultimate bearing capacity (P_{FEA}) versus engagement length (D) for different bearing widths (N) and thicknesses (t) (models with $b_f = 40$ mm).

4.5.1.4. Slip gap to thickness ratio (e/t)

The effect of slip gap to thickness ratio (e/t) on the bearing capacities of the ASH sections with UFT and NUFT were investigated, respectively via bearing widths (N) ranging from 50 mm to 150 mm, and the engagement lengths (D) of 5 mm to 30 mm, as shown in Figure 4.23 (a) and (b). It can be deduced from these figures that an increase in e/t leads to a substantial linear reduction in the bearing capacity of the ASH sections. However, as e/t increases, a relatively small decrease in the bearing capacities was observed in the ASH sections with smaller thicknesses (t) compared to the ASH sections with greater thicknesses (t). The relationship between the bearing capacity of the ASH sections (with UFT and NUFT) and the geometrical factor $(e/t)^2$ was also investigated in Figure 4.24 (a) and (b). It is possible to see that increasing the $(e/t)^2$ factor leads to a linear decrease of the bearing capacity.

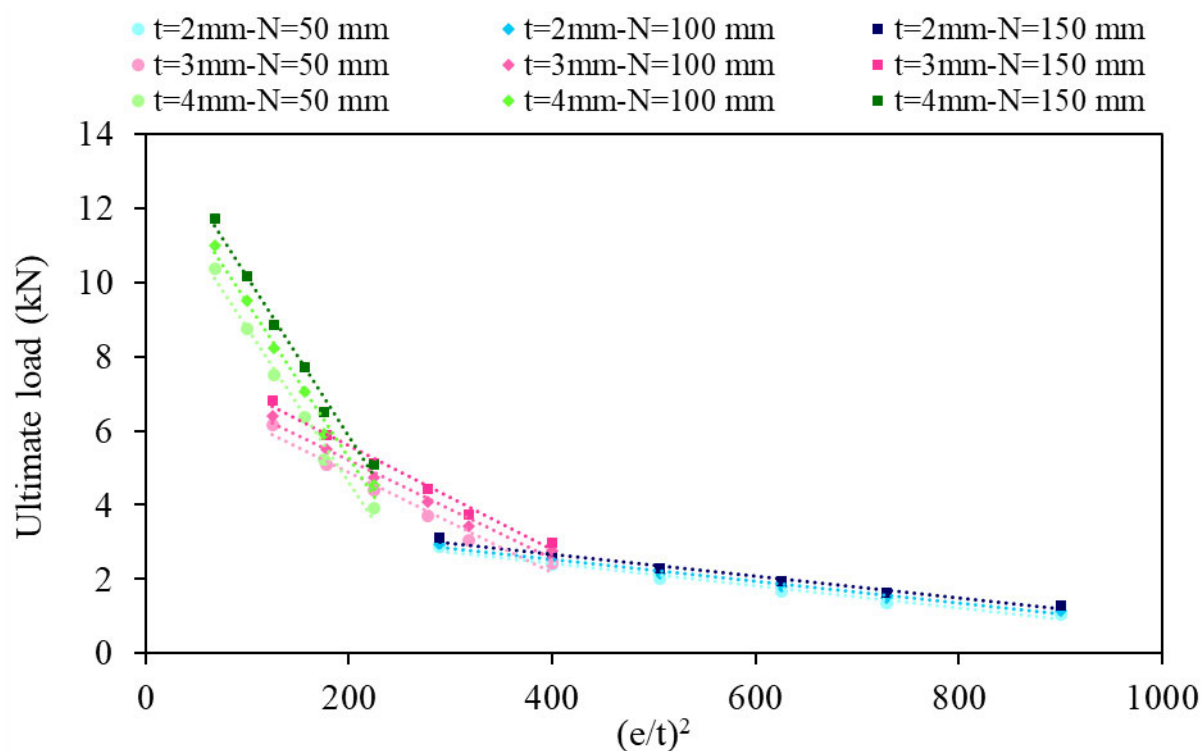


(a) UFT

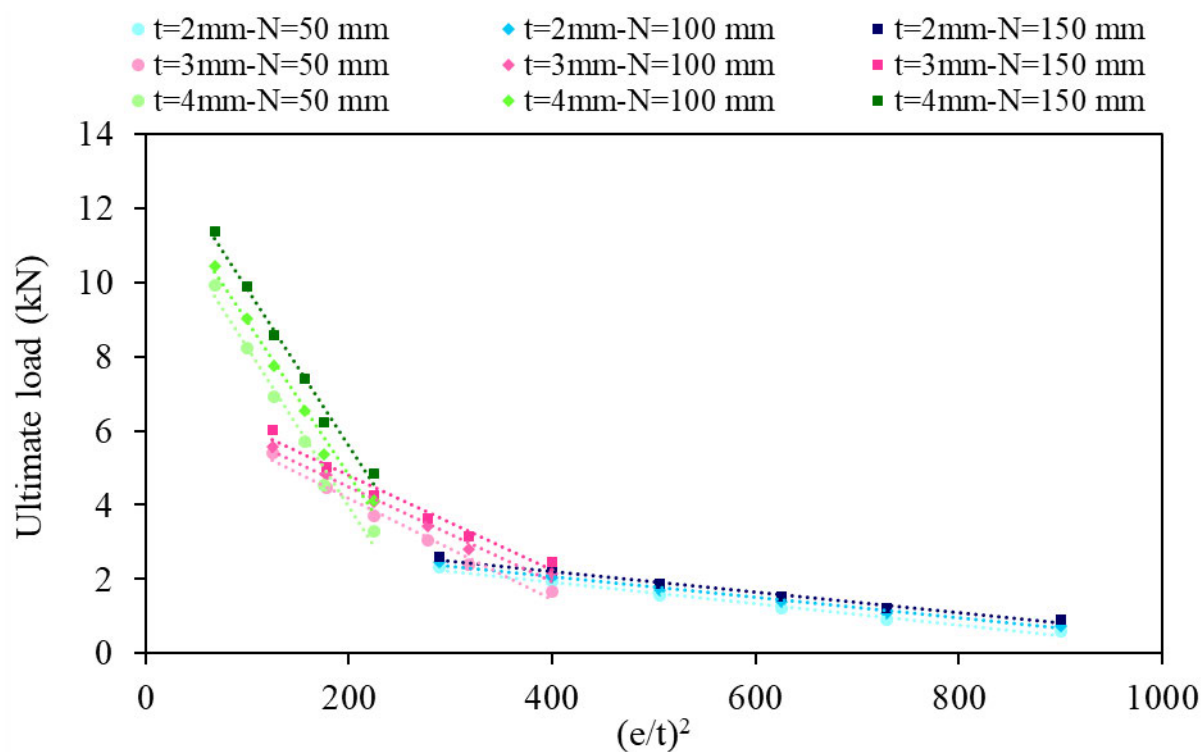


(b) NUFT

Figure 4.23 Ultimate bearing capacity (P_{FEA}) versus (e/t) for different bearing widths (N) and thicknesses (t) (models with $b_f = 65\text{ mm}$).



(a) UFT



(b) NUFT

Figure 4.24 Ultimate bearing capacity (P_{FEA}) versus $(e/t)^2$ for different bearing widths (N) and thicknesses (t) (models with $b_f = 65\text{ mm}$).

4.6. Design rules

4.6.1. Current design rules

As mentioned earlier, no aluminium standards exist to estimate the bearing capacities of the ASH sections in a window wall system subjected to wind load. Thus, to gain a better understanding of the bearing behaviour of the ASH sections, it would be worthwhile to assess relevant standards for the design of similar structural elements. In this regard, three current cold-formed steel specifications provide design rules (DRSs), i.e., Eq. (4.5) (by AISI S240 (2015)) and Eq. (4.6) (by TI 809-07 (1998) and SSMA (2000)), to predict nominal strength of cold-formed steel tracks. It should be mentioned that the theoretical bending equation and the section modulus were used in the derivation of these equations.

$$P_n = \frac{w_{dt} t^2 f_y}{4e} \quad (4.5)$$

where $w_{dt} = 0.11\alpha^2(e^{0.5}/t^{1.5}) + 5.5\alpha \leq S(\text{mm})$, t = track thickness (mm), f_y = yield strength of track (MPa), e = slip gap between end of stud web and track web (mm), (see Figure 4.25), $\alpha = 25.4$ = coefficient for conversion of units, S = stud spacing (mm), and w_{dt} = effective track length (mm).

$$P_n = \frac{w_{dt} t^2 f_y}{6e} \quad (4.6)$$

where $w_{dt} = N + 2 \left[\frac{e+D}{\tan(\varphi)} \right] \leq S$, $\varphi = 30$, N = stud flange width (mm) and D = bearing contact length between end of the stud web and the track flange (mm) (see Figure 4.25), and w_{dt} , t , f_y , and e are outlined as before.

It should be mentioned that the design rules and procedures provided by the Steel Stud Manufacturers Association (SSMA, 2000) for predicting the strength of cold-formed steel

tracks are similar to those of the U.S. Army Corps of Engineers (TI 809-07, 1998) with minor modifications.

Noteworthy is that Eq. (4.5) (AISI S240, 2015) is based on the ultimate strength design and the plastic section modulus; however, Eq. (4.6) (TI 809-07, 1998; SSMA, 2000) is based on the allowable stress design and the elastic section modulus.

Furthermore, Bolte and LaBoube (2004) proposed two equations to estimate the nominal strength of the steel track using the plastic section modulus (Eq. (4.5)) and the effective track length (w_{dt}) (expressed by Eq. (4.7a) and (4.7b)).

$$w_{dt} = 2\Delta + w_{stud} \quad (4.7a)$$

$$2\Delta = \begin{cases} \frac{300(e/t)^2}{100} & \text{for } (e/t)^2 < 100 \\ 300 & \text{for } (e/t)^2 \geq 100 \end{cases} \quad (4.7b)$$

where Δ is the partial track length (mm) in both sides of the bearing width (see Figure 4.25).

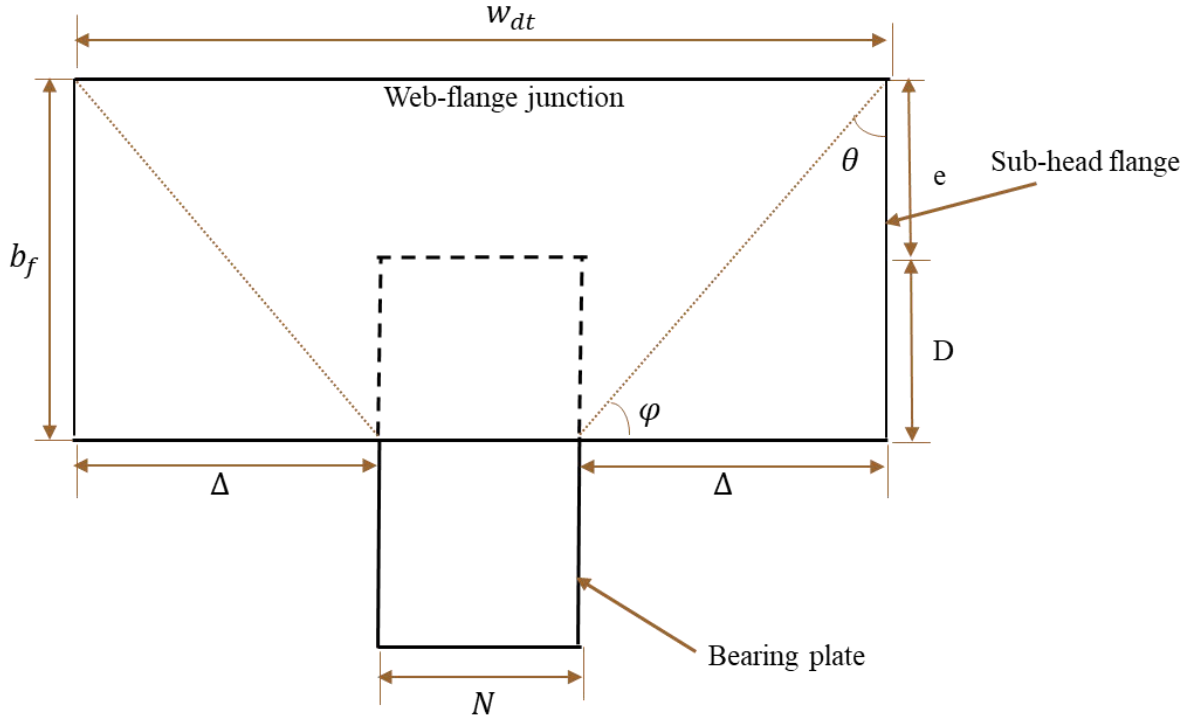


Figure 4.25 Failure pattern for the sub-head flange.

Akbari et al. (2020a) proposed the initial design rules (DRA_I) to estimate the bearing capacity of the ASH sections using the product specific data obtained from the experimental study. The most significant aim of (Akbari et al., 2020a) was to establish an equation which would accurately predict the effective sub-head length (w_{dt}) based on the stress distribution of the bottom flange under concentrated load. Hence, the following equations (Eq. (4.8a) and Eq. (4.8b)) were derived for DRA_I and used in conjunction with Eq. (4.5) to predict the bearing capacities of the ASH sections for two loading conditions (the 15 mm and the 25 mm engagement lengths), as well as two deformation criteria (the maximum load (Max) and the ultimate deformation limit (UDL)) (Akbari et al., 2020a).

$$w_{dt} = N + 2 * b_f * \tan(\theta) \quad (4.8a)$$

$$\theta = a * (e/t)^2 + b \quad (4.8b)$$

The values of the coefficients a and b proposed earlier (Akbari et al., 2020a) are reproduced in Table 4.5.

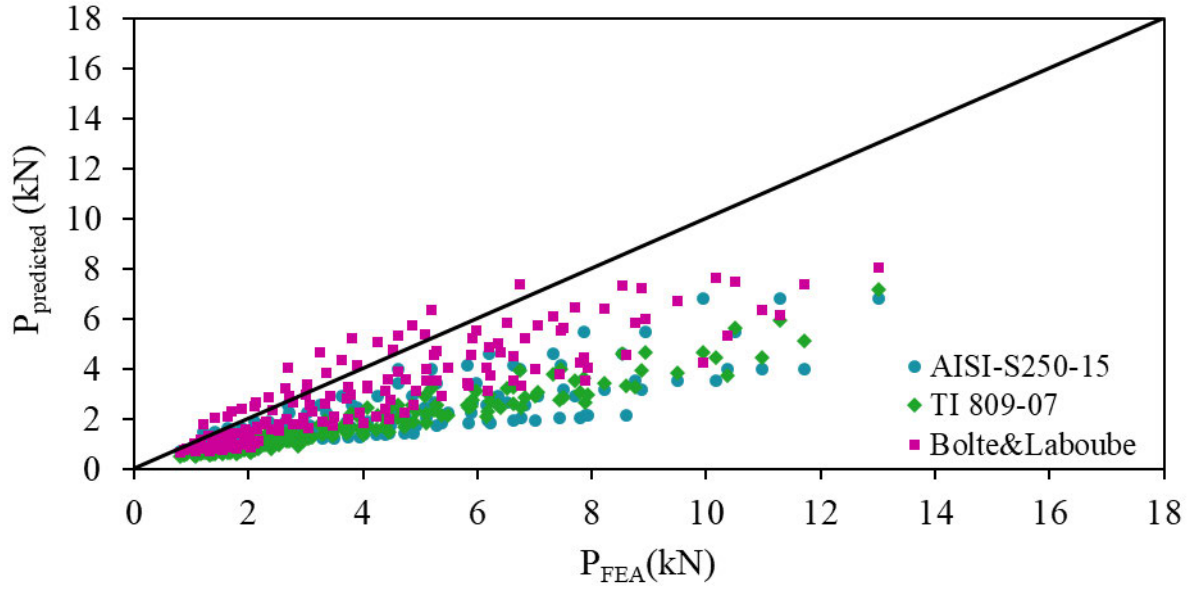
Table 4.5 Proposed coefficients for effective sub-head length (w_{dt}).

Section	Criteria	D (mm)	a	b	c	d
ASH (test)	Maximum load (Max)	15	0	76	-	-
		25	0.1	67	-	-
	Ultimate deformation limit (UDL)	15	-0.02	76.1	-	-
		25	0.1	57.5	-	-
ASH (parametric study)	Maximum load (Max) (UFT)	5, 10, 15, 20, 25 and 30	- 0.006	0.3	0.3	63.0
	Maximum load (Max) (NUFT)	5, 10, 15, 20, 25 and 30	-0.01	0.3	0.56	55.5

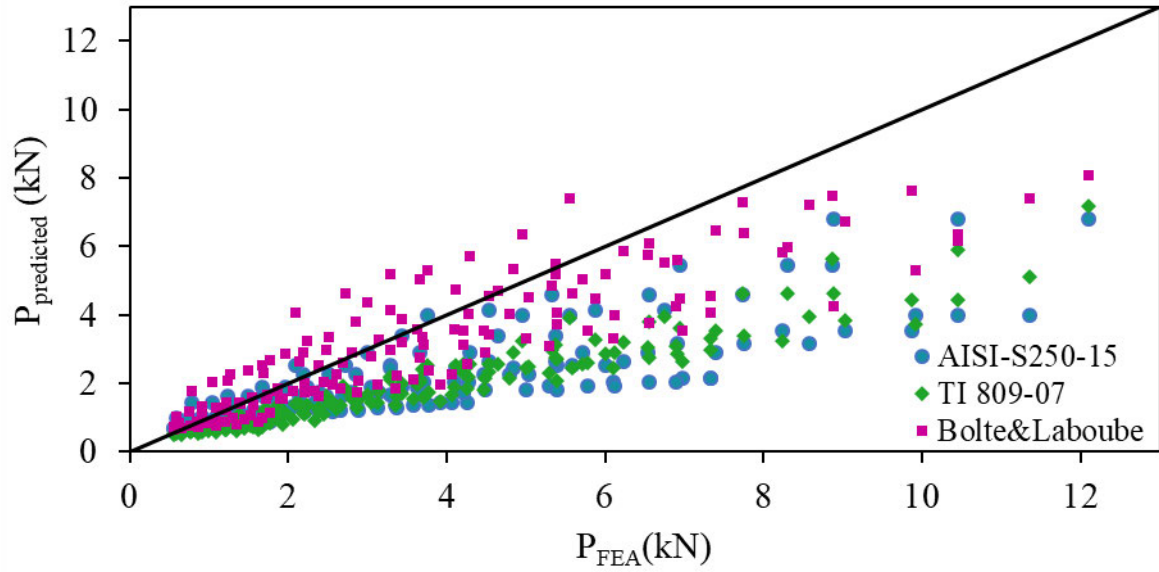
4.6.2. Comparison of the FEA results with current design rules ($P_{FEA}/P_{Predicted}$)

In this section, a comprehensive evaluation of the DRSs (Bolte and LaBoube, 2004; AISI S240, 2015; TI 809-07, 1998; SSMA, 2000) and the DRA_I (Akbari et al., 2020a) was carried out based on the comparison with the parametric study results. The mean and the COV values of the bearing capacity ratios ($P_{FEA}/P_{Predicted}$) yielded by the DRSs (Bolte and LaBoube, 2004; AISI S240, 2015; TI 809-07, 1998; SSMA, 2000) and the DRA_I (Akbari et al., 2020a) are summarised in Table 4.6.

From this table it is evident that the DRSs (Bolte and LaBoube, 2004; AISI S240, 2015; TI 809-07, 1998; SSMA, 2000) are both conservative by an average of 1.29 to 2.08 and unreliable with the COV values between 0.20 and 0.37. Figure 4.26 also shows the comparison between the bearing capacity values ($P_{Predicted}$) yielded by the DRSs (Bolte and LaBoube, 2004; AISI S240, 2015; TI 809-07, 1998; SSMA, 2000), and the ultimate capacities (P_{FEA}) of the ASH sections obtained from the parametric study.



(a) UFT

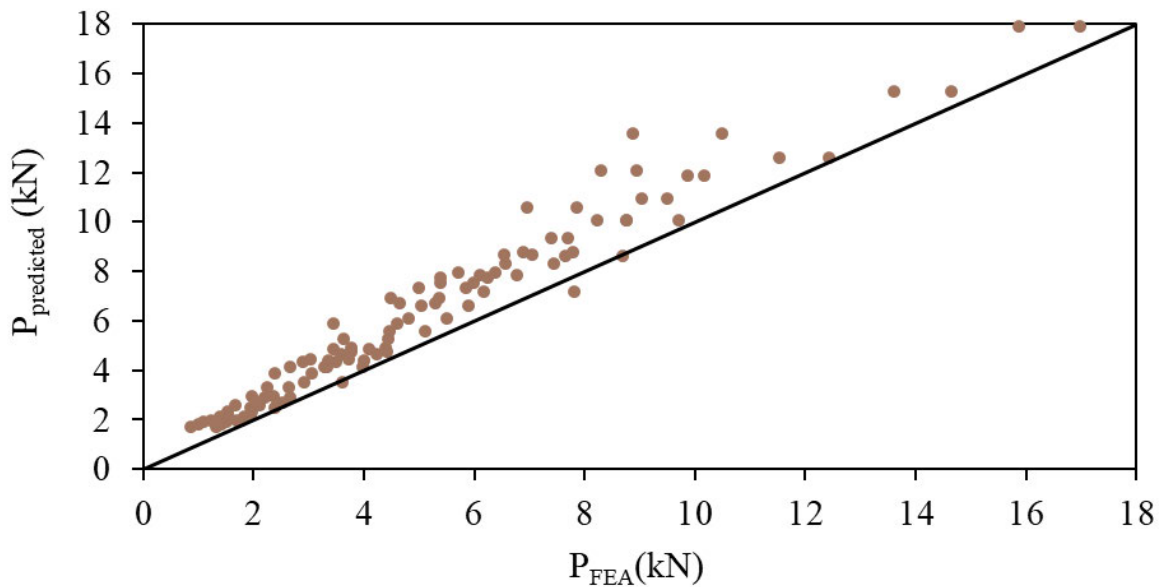


(b) NUFT

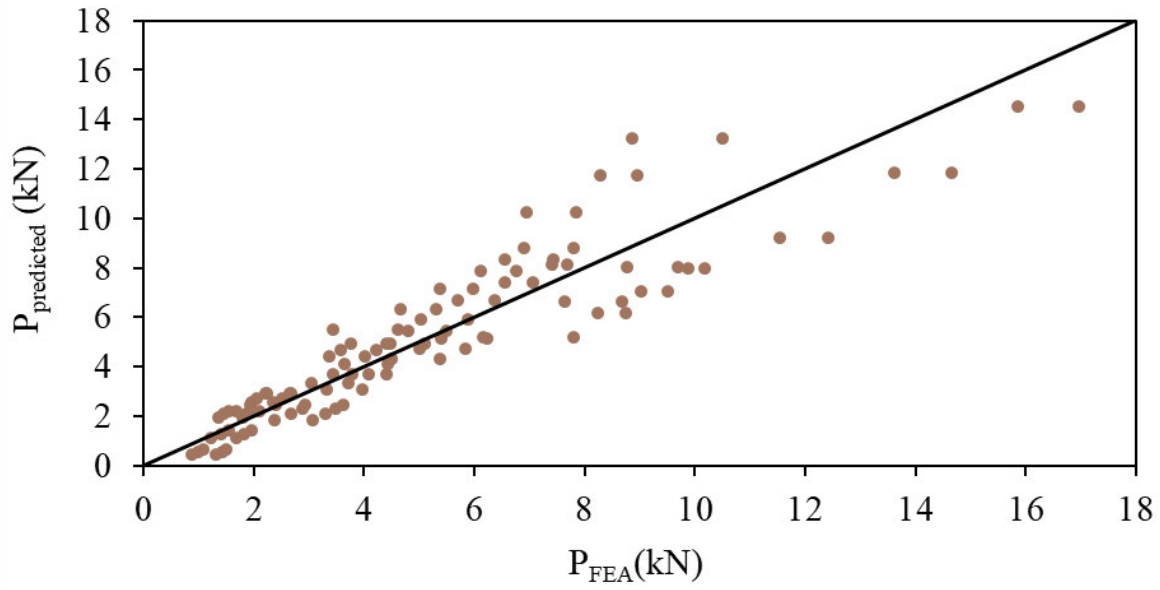
Figure 4.26 Comparison between experimental and numerical bearing capacities, and predictions of the DRSs.

Figure 4.27 (a) and (b) show the comparisons of the FEA bearing capacities of the ASH sections with predictions using Eq. (4.8a) and Eq. (4.8b) (DRA_I) for the maximum load (Max) and the ultimate deformation limit (UDL) criteria, respectively. It should be noted that since the experimental tests were limited to two engagement lengths of 15 mm and 25 mm,

the numerical results not using these two engagement lengths were excluded from the comparison. The main parameter used in the proposed equation for θ is $(e/t)^2$. Substituting e and t (from the parametric study) into Eq. (4.8b) gave rise to large values of $(e/t)^2$ and consequently negative values of $\tan(\theta)$. Thus, in order to avoid inconsistent results, an upper bound of θ was set, not exceeding 76 degrees (based on the coefficients provided in Table 4.5). Generally, Table 4.6 shows that the DRA_I led to non-conservative results based on the Max criterion with a mean value of 0.80 and the corresponding COV value of 0.14; whereas, based on the UDL criterion, the results were conservative but unreliable with the mean value of 1.08 and a large COV value of 0.34. The reason behind such incompatible results is related to the varying patterns of the load-displacement curves in the experiments and the parametric study due to simplifications made in the parametric FE models. Since the groove was removed from the flange in the parametric FE models (with UFT and NUFT), ultimate capacity occurred almost in the middle of the load-displacement curve (see Figure 4.28). By comparing Figure 4.28 and Figure 4.11, it is evident that the load-displacement patterns acquired from the experimental study and FE parametric analyses are different. Therefore, the DRA_I is inappropriate to predict the bearing capacities of the parametric FE models. This finding prompts a need to improve the accuracy of all the current design rules (DRSs and DRA_I). Modified design rules DRA_P are thus proposed to accurately and reliably predict the bearing capacities of the ASH sections through validation against the ultimate capacities acquired from the parametric analyses.



(a) Maximum load (Max)



(b) Ultimate deformation limit (UDL)

Figure 4.27 Comparison between experimental and numerical capacities and predictions of the DRA_I (Akbari et al., 2020a).

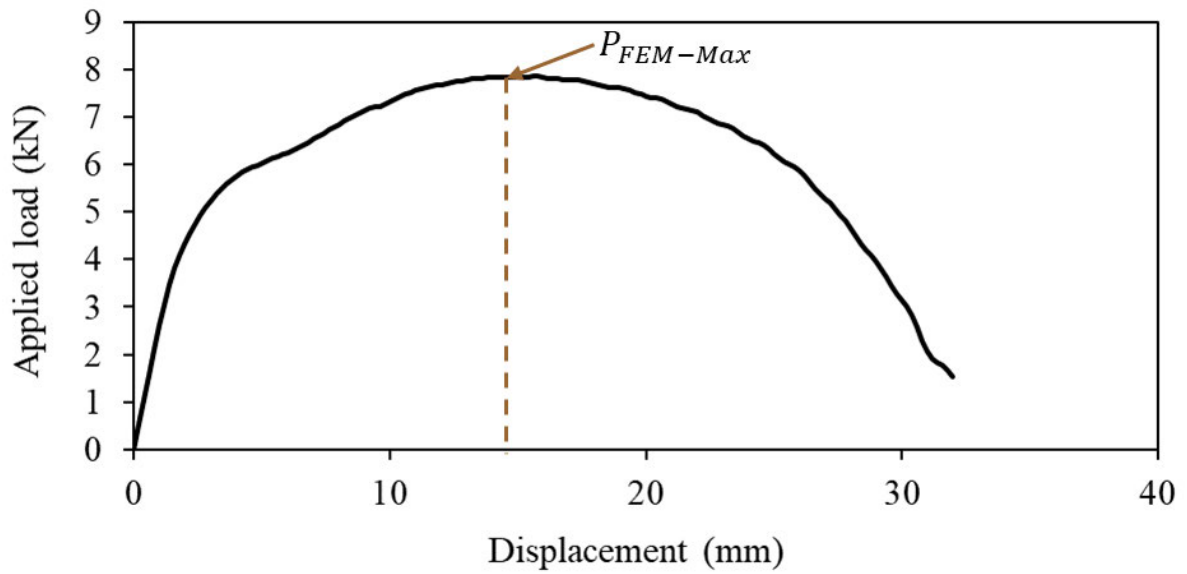


Figure 4.28 Ultimate load obtained from FE parametric models, based on maximum load criterion (Max).

Table 4.6 Comparison of mean and COV values of bearing capacity ratios ($P_{FEA}/P_{Predicted}$).

Rule	Loading criteria and design rules	Equation	Mean	COV	ϕ_w	β_0
Current design rules	DRSs by AISI S240 (2015)	Eq. (4.5)	1.95	0.37	1.10	2.87
	DRSs by TI 809-07 (1998)	Eq. (4.6)	2.08	0.20	1.64	4.40
	DRSs by Bolte and LaBoube (2004)	Eq. (4.7a) and Eq. (4.7b)	1.29	0.31	0.83	2.21
	DRA _I (UDL) (Akbari et al. (2020a))	Eq. (4.8a) and Eq. (4.8b)	0.80	0.14	0.69	1.48
	DRA _I (Max) (Akbari et al. (2020a))	Eq. (4.8a) and Eq. (4.8b)	1.08	0.34	0.65	1.65
Proposed	DRA _P (Max)	Eq. (4.9)	1.02	0.07	0.90	2.71

4.6.3. Proposed design rules

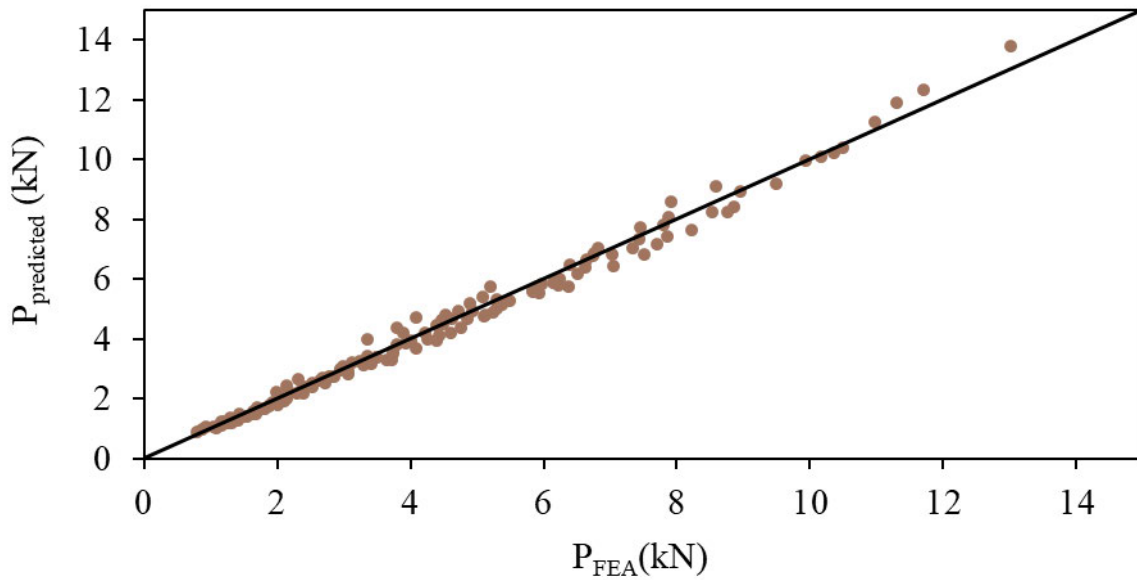
Aiming to improve the bearing capacity prediction of the ASH sections under concentrated load, the width of the bottom flange that effectively resists bending (effective sub-head length (w_{dt})) requires accurate calculation. The coefficients proposed in Eq. (4.8a) and Eq. (4.8b) were developed using a limited number of test results based on manufacturer and product specific specimens covering a small number of key parameters. Hence, improvement was made to these equations according to the parametric study based on generalized test specimens covering a broader range of parameters. Since only one peak load appeared in the load-displacement curve of the FE parametric model, the maximum load criterion (Max) was used to improve the design rules DRA_I.

As discussed in Section 4.6.1, Akbari et al. (2020a) considered the effect of $(e/t)^2$ in Eq. (4.8b) for θ . However, the results of the parametric study did not show a clear trend line between θ and $(e/t)^2$, and θ as a function of $(e/t)^2$ yielded a high COV value with unreliable results. This section therefore investigates the effect of different parameters used in the parametric study on the bearing capacities of the ASH sections. Accordingly, the bearing capacities and the effective sub-head lengths were calibrated with the parametric study database, and the effects of (e/t) and engagement length (D) were also included in the equation of θ . Consequently, suitable coefficients were determined for the ASH sections with

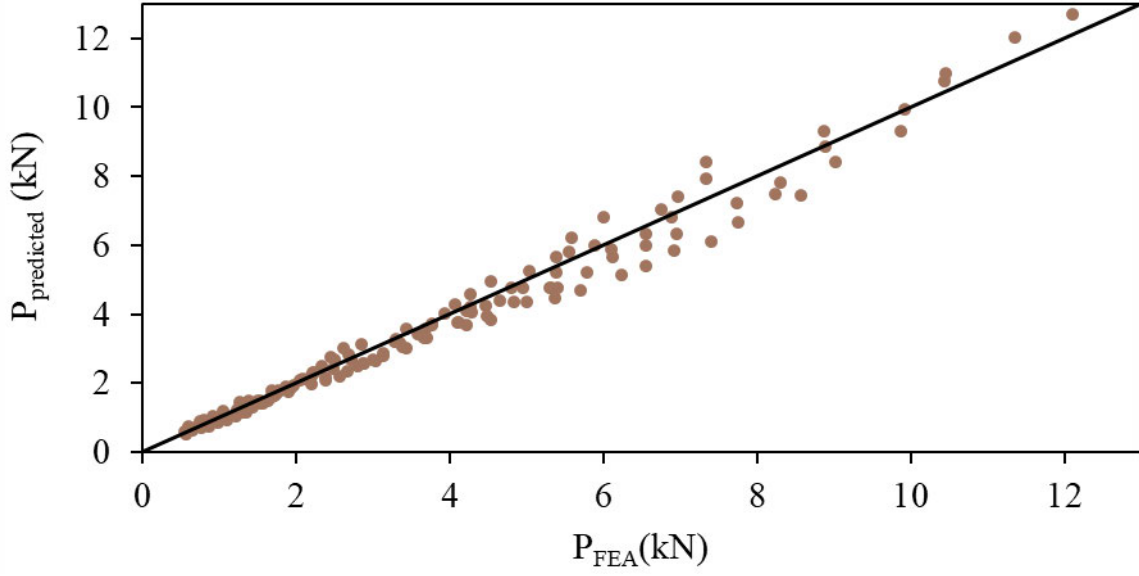
UFT and NUFT by using simple regression analysis, as presented in Table 4.5. These coefficients were included in Eq. (4.9) (DRA_P) to be used in parallel with Eq. (4.8a) and (4.5) to predict the bearing capacities of the ASH sections.

$$\theta = a * (e/t)^2 + b * (e/t) + c * D + d \quad (4.9)$$

Comparisons between the estimations of the DRA_P and the wide-ranged parametric results were conducted. Figure 4.29 (a) and (b) show the comparisons between the predicted capacities ($P_{Predicted}$) obtained from the DRA_P and the FE parametric study (P_{FEA}) of the ASH sections with UFT and NUFT, respectively. The mean and COV values of the bearing capacity ratios ($P_{FEA}/P_{Predicted}$) using the DRA_P are summarised in Table 4.6. It can be inferred that the DRA_P can accurately and reliably estimate the bearing capacities with a mean value of 1.02 and the corresponding COV value of 0.07. However, it needs to be mentioned that the DRA_P cannot be used for comparison with the test results due to the geometrical differences between the FE parametric models and the tested specimens, as well as varied load-displacement behaviour, as described in Section 4.6.2.



(a) UFT



(b) NUFT

Figure 4.29 Comparison between experimental and numerical capacities and predictions of the DRA_P .

4.6.4. Capacity reduction factor

A statistical model provided by the AISI S100 (2012) specification is generally used to calculate the capacity reduction factor (ϕ_w). This model considers the variation in loading, fabrication and material effects. This factor is given by Eq. (4.10a).

$$\phi_w = 1.52 M_m F_m P_m e^{-\beta_0 \sqrt{V_M^2 + V_F^2 + C_n V_P^2 + V_Q^2}} \quad (4.10a)$$

where F_m and $V_F = 1.0, 0.05$ are the mean value and COV of the fabrication factor, respectively, M_m and $V_M = 1.1, 0.06$ are the mean value and COV of the material factor, respectively, $V_Q = 0.21$ is the COV of the load effect, P_m and V_P are, respectively, the mean value and COV of the test-to-predicted load ratios obtained from FEA; $C_n = n^2 - 1/n^2 - 3n$ is the correction factor depending on the number of tests, and $\beta_0 = 2.5$ is the target reliability index for the tested beams. Substituting all the above values into Eq. (4.10a) yields Eq. (4.10b).

$$\phi_w = 1.672P_m e^{-2.5\sqrt{0.0502+C_n V_P^2}} \quad (4.10b)$$

From Eq. (4.10b), the respective capacity reduction factors for the predictions of the DRSs (Bolte and LaBoube, 2004; AISI S240, 2015; TI 809-07, 1998; SSMA, 2000), the DRA_I (Akbari et al., 2020a) and the DRA_P are given in Table 4.6. The resistance factors (ϕ_w) obtained from the DRA_P is 0.90 as shown in Table 4.6. The corresponding reliability index (β_0) based on the recommended ϕ_w is approximately equal to or exceed the target value ($\beta_0 = 2.5$), confirming the reliability of the proposed equations.

4.7. Conclusions

A numerical investigation of the ASH sections in the window wall system through non-linear static analyses with ABAQUS/CAE was presented in this paper. 42 numerical models were first simulated and validated against the previous experimental results conducted using manufacturer and product specific ASH sections. Then a comprehensive parametric study was conducted with generalized ASH sections to further assess the influence of key parameters such as bearing widths, engagement lengths, flange widths and thicknesses. Subsequently, the acquired numerical bearing capacity database was used to evaluate the accuracy and reliability of the DRSs (Bolte and LaBoube, 2004; AISI S240, 2015; TI 809-07, 1998; SSMA, 2000) and the DRA_I (Akbari et al., 2020a). Findings indicated that the DRSs (Bolte and LaBoube, 2004; AISI S240, 2015; TI 809-07, 1998; SSMA, 2000) are both too conservative with a mean value of up to 2.08 and unreliable with a large coefficient of variation of 0.37 in predicting the bearing capacities of the ASH sections. Furthermore, the DRA_I (Akbari et al., 2020a) based on a limited number of tests were also found unreliable to estimate the bearing capacities of the ASH sections. Hence, based on the generalised parametric study results, a new bearing capacity equation (DRA_P) was proposed by including the effect of engagement length (D) and (e/t) in addition to $(e/t)^2$. Comparisons of the bearing capacities from the finite element analyses demonstrated that the DRA_P can accurately and reliably predict the bearing capacities of different ASH sections with varying parameters.

5. BEARING BEHAVIOUR OF ALUMINIUM SUB-HEADS WITH REMOVABLE BEADS IN FAÇADE SYSTEMS

(Under Review)

This chapter includes a co-authored paper. The bibliographic details of the co-authored paper, including all authors, are:

Akbari, M., Gunalan, S., Gilbert, B.P., Guan, H., Baleshan, B.

Bearing Behaviour of Aluminium Sub-Heads with Removable Beads in Façade Systems

Submitted in *Structures*

My contribution to the paper involved:

Literature review, experimental works, result analysis, discussion of the results, writing, editing and response to reviewers.

(Signed) _____ (Date) 14.11.2020

Name of Student: Masoumeh Akbari

(Countersigned) _____ (Date) 14.11.2020

Corresponding author of paper: Shanmuganathan Gunalan

(Countersigned) _____ (Date) 14.11.2020

Supervisor: Shanmuganathan Gunalan

Bearing Behaviour of Aluminium Sub-Heads with Removable Beads in Façade Systems

Abstract

Occupying a substantial proportion of the overall building expense, building envelopes are the subject of ongoing research and improvement in both aesthetic and structural aspects. The aluminium window wall frame, consisting of vertical members (mullions) and horizontal members (head and sill transoms), is placed between sub-heads at the top and sub-sills at the bottom of the wall. These window walls are designed to carry lateral wind loads. Of particular importance to design stability is the bearing behaviour of aluminium sub-heads. The bearing behaviour and capacities of C-shaped sub-heads were recently investigated through a detailed experimental study at Griffith University for the development of strength prediction equations. To allow for easier assembly of façade panels, a kind of sub-head section known as sub-head with removable bead is used in aluminium window wall system. Two parts of this sub-head are connected together without any external mechanisms. The present research places emphasis on assessing the bearing behaviour of aluminium sub-heads with removable beads through comprehensive experimental testing. A total of 36 tests were conducted using six section geometries, two engagement lengths, and three bearing widths. The bearing strengths obtained from tests of aluminium sub-heads with removable beads were compared with the bearing capacities predicted using the design rules developed by the authors for conventional C-shaped aluminium sub-heads and available cold-formed steel design provisions (AISI S240 2015, TI 809-07, and SSMA 2000 specifications). As a result of the investigation, the current design equations were found to be unreliable for estimating the bearing capacity of aluminium sub-head sections with removable beads. Hence, new design expressions have been developed which accurately predict the strengths of aluminium sub-heads with removable beads under out-of-plane loads. Furthermore, the influence of the removable beads on the bearing behaviour and capacity is discussed in detail.

Keywords

Aluminium; Sub-heads; Removable bead; Window wall; Bearing behaviour; Experimental study.

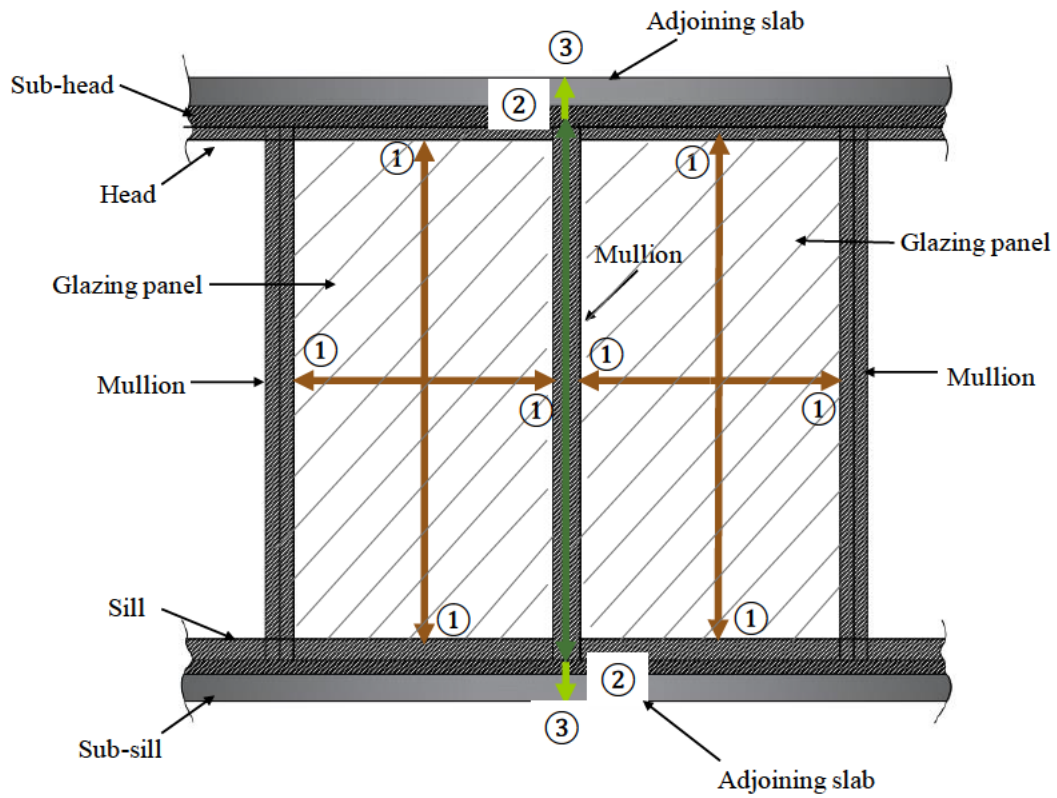
5.1. Introduction

The aluminium industry has evolved steadily over the last century, with the arrival of extrusion technology enabling the initial use of aluminium as façades. These building

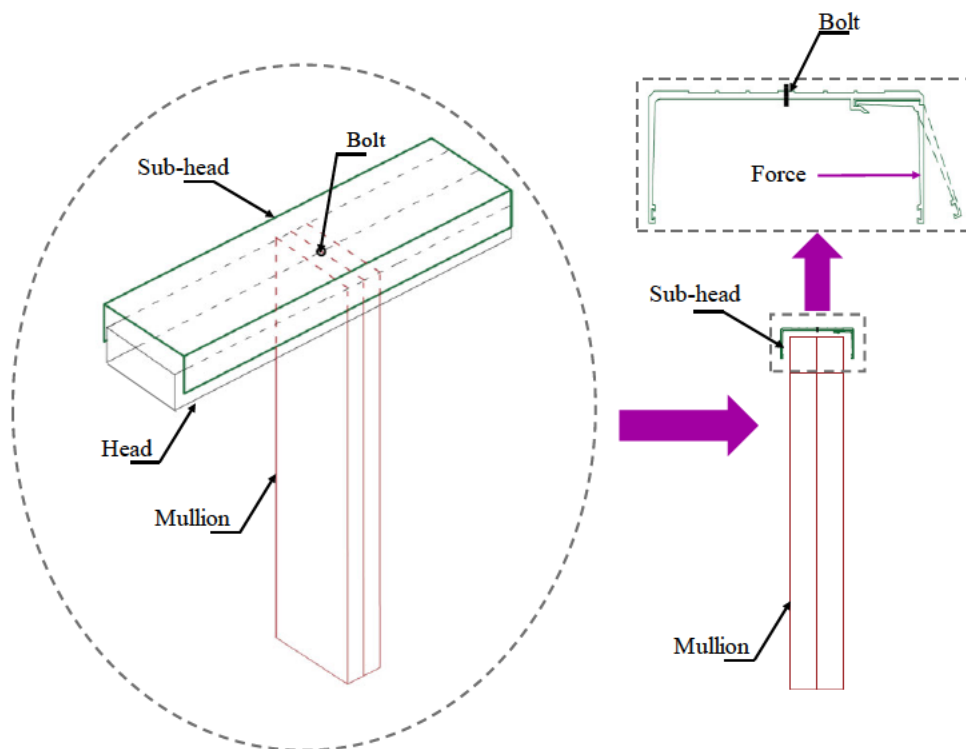
envelopes provide high aesthetic value and a barrier between the outdoor and indoor environments (Figure 5.1). A window wall is a type of building façade, which is installed between a building's slabs, while the slabs act as structural support. Window wall is more suitable for structural projections through facades (e.g. balconies & concrete ledge sunshades) and shorter buildings which are scaffolded during construction. In a window wall, the vertical members known as mullions are screwed to the horizontal members (head and sill transoms) forming frames for fitting the infill elements (typically glass). This aluminium frame is positioned between the sub-head and sub-sill without any connections, as schematically illustrated in Figure 5.2. Cross-sections of these vertical and horizontal elements are most often complex open shapes. The gap between the frame and sub-frame allows vertical movements under wind loads, temperature variations and gravity load changes.



Figure 5.1 Window wall system (Herston quarter- Brisbane).



(a) window wall system



(b) Sub-head to mullion connection

Figure 5.2 Details of window wall frame and sub-head to mullion connection.

Given the diversity and complexity of contemporary façade systems, an assessment of their performance is indispensable to avoid large expense due to damage and ensure safety during the service life of the structures. This assessment is a relatively new field of research, attracting significant attention from academics as well as engineers. Substantial focus has been placed on protecting façades from wind loads which governs the design of façades. In reference to the numbering in Figure 5.2, wind loads are initially imposed on the glazing panels of window walls, then transferred to vertical (mullions) and horizontal (head and sill transoms) members of the aluminium frame (①). The mullions usually act as a simply supported beam under lateral wind load, and do not carry any axial load except for their own weight. The bending behaviour of mullions was recently investigated through a series of experimental tests (Kesawan et al., 2018). As shown in Figure 5.2 (a), mullions transfer the wind load to the horizontal elements of sub-frames (the sub-sill and sub-head) (②). Thereafter, the adjoining slab receives the wind load from the sub-frame (③). Details of two types of typical sub-heads, viz. C-shaped sub-heads and sub-heads with removable beads, are shown in Figure 5.3 (a) and 3 (b), respectively. The main difference between these two sections is that the later one included two parts, which can facilitate installation and achieve desired performance in window walls. The beads act as the critical component in resisting the concentrated load from the mullions. Lateral forces applied to the window wall generate huge force, which can lead to plastic behaviour of the connection between the mullion and the sub-head with removable bead. Under this loading condition, the mullion applies the load on the internal surface of the removable bead flange, which in this study is conservatively assumed to be concentrated at mullion bearing, with some small amount of load redistribution across a short distance of the window head either side of the mullion. As a result, this load induces yielding and fracture at the web-flange junctions of the bead due to the bending and twisting of the removable bead flange. However, this failure mechanism should to be considered in the façade design methodology of window wall.

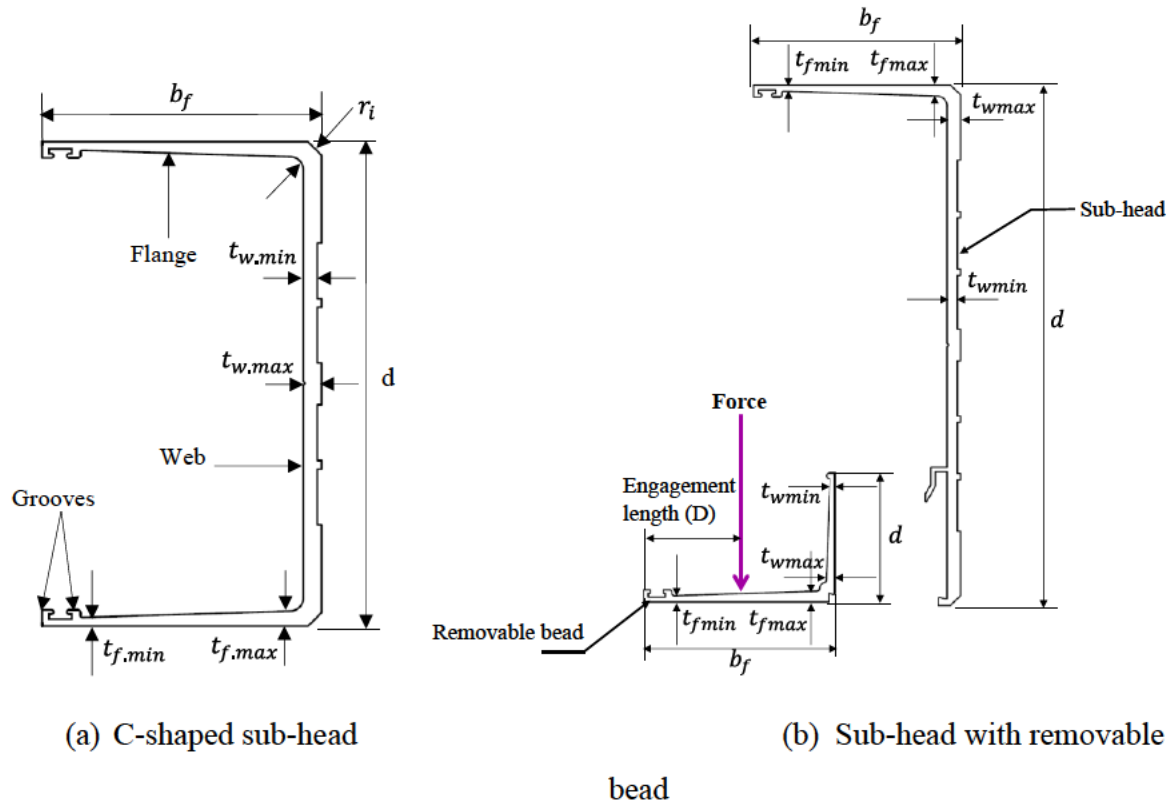


Figure 5.3 Geometric details of sub-head sections.

To improve our understanding in this regard, reviewing the research on the bearing behaviour of other similar structural elements, such as cold-formed steel stud-to-track connections in light gauge steel frame (LSF) walls, are also advantageous. The main test procedure adopted in existing research into LSF walls involved conducting tests on stud-to-track connections. In recent years, extensive research has also been conducted on cold-formed steel stud-to-track connections subjected to earthquake (Wang et al., 2015; Retamales et al., 2013; Rahmanishamsi et al., 2014) and blasts (Bewick et al., 2013; Salim et al., 2005). However, the performance of stud-to-track connections in the out-of-plane direction has only been investigated in exceptional cases (Fox and Schuster, 2000; Lewis, 2008; Espinoza et al., 2018). Recently, a comprehensive experimental study was conducted by Espinoza et al. (2018) to investigate the strength of cold-formed steel slotted track connections subjected to out-of-plane loads. Equations were proposed to predict the design strength and deflection of cold-formed steel slotted tracks. Further, the current cold-formed steel design standards (including the North American Standard for Cold-Formed Steel Structural Framing (AISI S240, 2015), the U.S. Army Corps of Engineers (TI 809-07, 1998), and the Steel Stud

Manufacturers Association (SSMA, 2000)) also provide design provisions and technical information for the design of cold-formed steel stud-to-track connection in LSF walls.

On the other hand, current aluminium standards (AS/NZS1664.1, 1997; AA, 2015; EC9, 2007)) include rules that cover the design of many commonly used aluminium structural elements, but do not have design criteria to predict the bearing strength of aluminium sub-head sections subjected to out-of-plane forces in a non-load bearing window wall. Due to the lack of design provisions in quantifying the bearing behaviour, the bearing capacity of C-shaped sub-head was recently studied at Griffith University through 42 experimental tests (Akbari et al., 2020a). Based on the results of the experimental study, appropriate design rules were proposed which accurately and safely estimate the bearing capacity of aluminium C-shaped sub-heads. Detailed investigation by the authors revealed that similar research on aluminium sub-heads with removable beads was unavailable. Hence, the current study is aimed at addressing the missing information about the bearing behaviour of aluminium sub-heads with removable beads in window walls under wind loading. In this regard, a series of experiments have been performed aiming to characterize the load-displacement responses, ultimate capacities, and failure mechanisms of aluminium sub-heads with removable beads. Then, the bearing capacities obtained from the experimental tests were compared with the predicted bearing capacities, using the design expressions proposed by the authors for conventional C-shaped aluminium sub-heads (Akbari et al., 2020a). Additionally, the current research effort focused on the evaluation of the aforementioned cold-formed steel design standards (AISI S240, 2015; TI 809-07, 1998; SSMA, 2000). As these provisions were found to be unreliable, new design rules were proposed to accurately estimate the bearing capacity of aluminium sub-head sections with removable beads.

5.2. Experimental study

5.2.1. Test specimens

A series of 36 tests (Table 5.1) was conducted in the experimental study to investigate the bearing behaviour of extruded aluminium sub-heads with removable beads and to develop the strength prediction equation for the window wall frame. The test procedure involved conducting a series of single point loading tests on the internal surface (mid-point) of the

removable bead flange. Six different sub-head complex sections, with different geometries made of high strength heat-treated aluminium alloy (6063-T6), were used in this study, including two separate parts (6 types of sub-head and 3 types of removable bead), as shown in Figure 5.3 and Figure 5.4. Of the 36 tests, 10 tests (with 100 mm bearing width) were repeated, as summarised in Table 5.1. All sub-heads with removable beads were obtained from the manufacturer G.James Glass & Aluminium Pty Ltd. Each type of sub-head had the same material properties since these open sections were from the same manufactured batch. The average dimensions of the sub-heads were measured at three points using a vernier calliper, micrometer, and tap meter. The geometric details of the aluminium sub-heads are presented in Table 5.2. The web height ranged from 111 to 215 mm, while the flange widths ranged from 40 to 65 mm. The specimens were cut to a specific length of 1300 mm to simulate the typical mullion spacing of 1200 mm in a window wall frame, and to allow for an overhang of 50 mm on each side. Under wind loading, the mullion and the head transom apply load to the bead flange. In this study, the load is conservatively assumed to be concentrated at the mullion bearing width.

On these grounds, high-grade steel plates of precise lengths with a rounded edge were used as a means of applying the load on the specimens to simulate different bearing widths of 50 mm, 100 mm, and 150 mm. Since the position of mullion to the sub-head flange groove is a variable, two different engagement lengths (distance between flange groove to the bearing plate (D)) of 25 mm and 15 mm were considered to investigate this variation (Figure 5.3 (b)). The engagement length influences how the load is transferred between the mullion and sub-head. Consequently, the slip gap between the end of the bearing plate (loading position) and the web of the sub-head (slip gap in Figure 5.4) ranged from 12 mm to 50 mm.

Table 5.1 Number of tests for all test specimens.

Sub-head		D = 25 mm			D = 15 mm		
Base	bead	N = 50 mm	N = 100 mm	N = 150 mm	N = 50 mm	N = 100 mm	N = 150 mm
675028	475073	1	2	1	1	2	1
475066	165863	1	2	1	1	2	1
475059	520902	1	2	1	1	2	1
875103	475073	1	2	1	1	2	1
675019	520902	1	1	1	1	1	1
475072	475073	1	2	1	1	2	1

Table 5.2 Geometric details of the aluminium sub-head sections with removable beads.

Section	b _f (mm)	d (mm)	r _i (mm)	t _{f,max} (mm)	t _{f,min} (mm)	t _{w,max} (mm)	t _{w,min} (mm)	L (mm)
Base								
675028	64.7	163.1	4.4	3.5	2.0	4.0	3.0	1300
475066	40.0	111.7	4.6	3.5	2.4	4.2	2.5	1300
475059	50.8	111.3	4.1	3.1	1.9	4.0	2.3	1300
875103	64.9	214.1	4.5	4.0	2.9	4.0	3	1300
675019	51.0	162.5	4.4	3.5	2.4	4.1	2.4	1300
475072	64.9	112.5	4.4	3.4	1.9	4	3.0	1300
Bead								
475073	60.1	40.4	-	3.3	2.0	3.1	1.8	1300
520902	46.3	24.1	-	3.1	1.9	3	1.9	1300
165863	33.5	23.9	-	3	2.9	3.0	1.6	1300

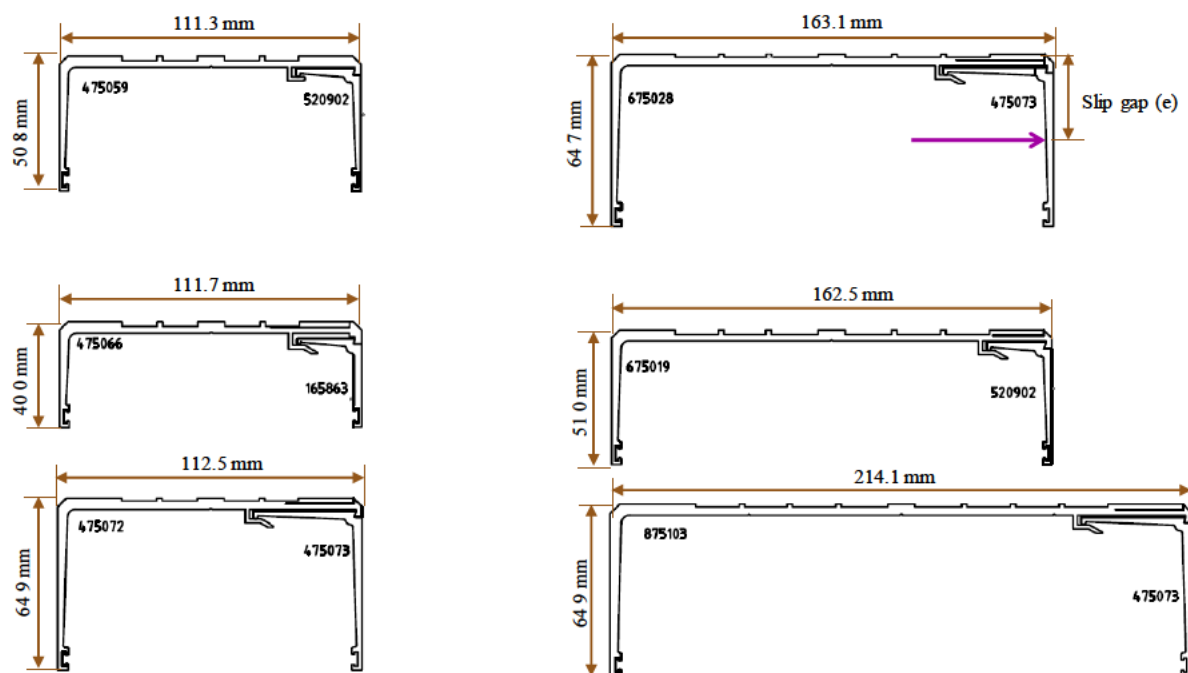


Figure 5.4 Sub-heads with removable beads.

The specimens were labelled in an order that allowed section (base and bead), engagement length and bearing width to be clearly recognized. For example, the label 675028-475073/25/50 denotes the base section being “675028”, the bead section being “475073”, the engagement length being 25 mm, and the bearing width being 50 mm.

5.2.2. Material properties

Two tensile coupon tests per section (base and bead) were conducted according to the Australian Standard AS 1391 (2007) to determine the material properties of the specimens. The tensile coupons were taken from the web of the base and the removable bead in the longitudinal direction for each section. The average measurements of the thickness and width of each specimen were calculated based on the measurements taken at three points, to obtain the cross-sectional area of the coupons. A 30 kN Instron universal testing machine was used to apply the load at a constant strain rate of 0.01 mm/mm/min until failure. Figure 5.5 plots the typical stress-strain curve of structural aluminium alloy 6063-T6 (675028 section). Table 5.3 summarizes the elastic modulus (E_0), the 0.2% tensile proof stress (f_y), and the ultimate tensile strength (f_u). It should be mentioned that the elastic modulus (E_0) is calculated as a

slope of engineering stress strain curve in the elastic range. The material properties reported in this table are the average values taken from two tensile coupon tests.

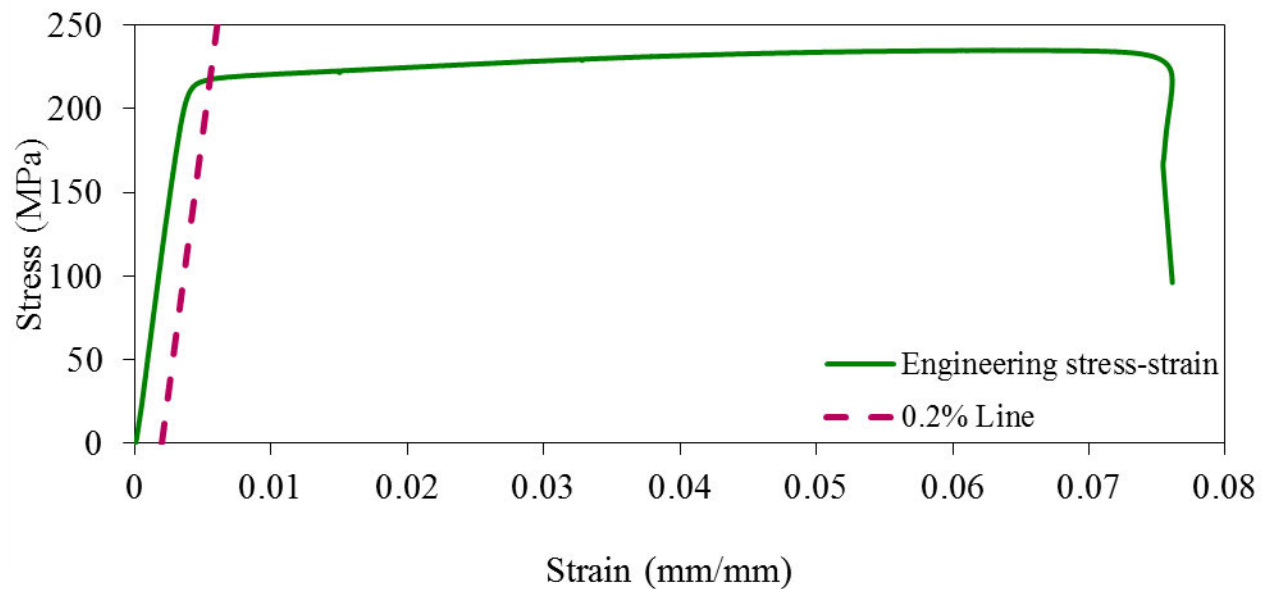


Figure 5.5 Engineering tensile stress-strain plot of Section 675028.

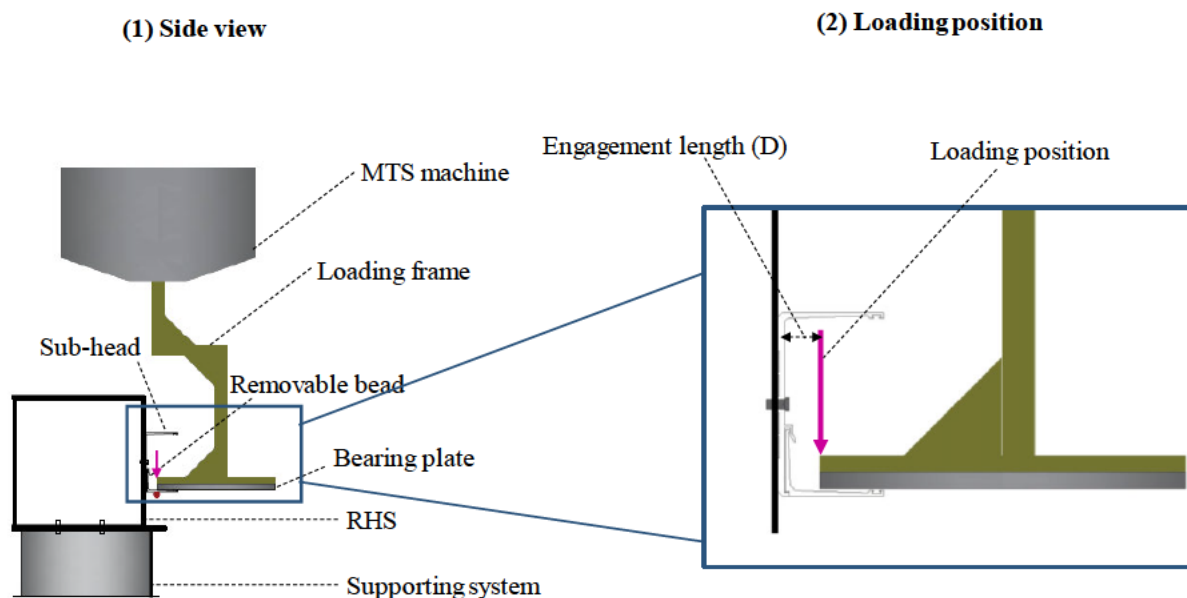
Table 5.3 Mechanical properties of test specimens.

Section	E_0 (MPa)	f_y (MPa)	f_u (MPa)
Sub-head			
675028	61,944	217.6	234.9
475066	61,251	252.0	272.2
475059	66,374	251.9	276.6
875103	62,408	204.7	226.1
675019	62,762	209.6	229.6
475072	68,342	222.6	248.1
Bead			
475073	66,934	249	272.9
520902	63,448	260.5	282.3
165863	69,446	239	260.1

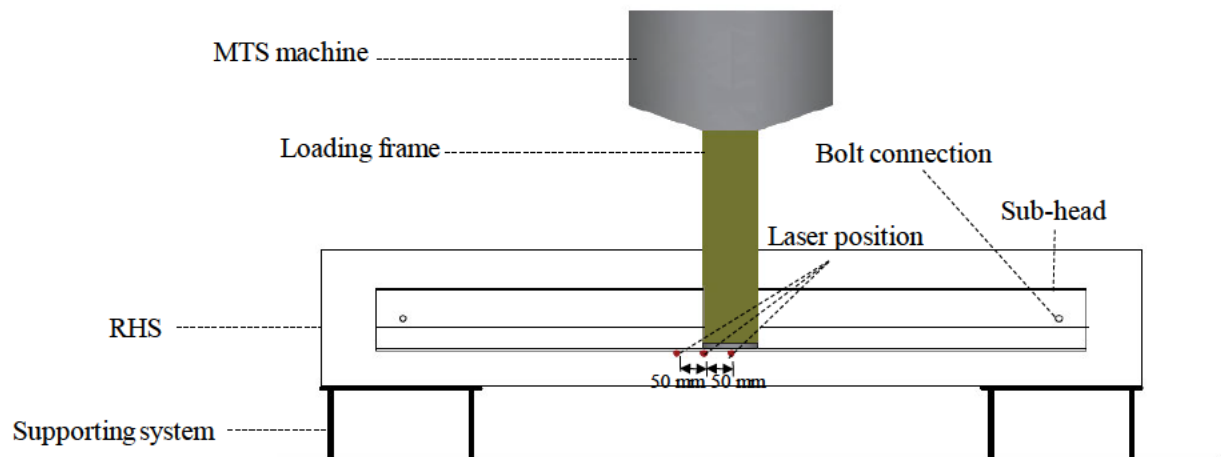
5.2.3. Test set-up and procedure

All test specimens were loaded to failure under concentrated load using a 500 kN MTS universal testing machine at Griffith University in order to investigate the bearing behaviour

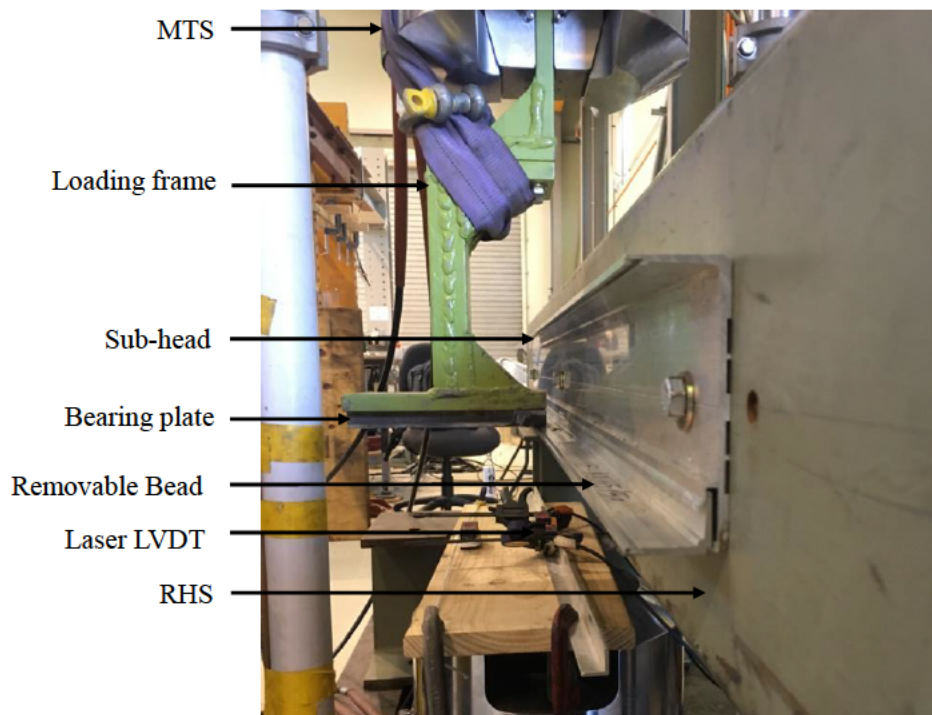
of aluminum sub-head sections. Figure 5.6 (a) and (b) illustrate the test set-up which comprises four elements: the sub-head with removable bead, the supporting structure, the loading frame, and the recording system. The supporting frame consisted of one rectangular hollow section (RHS) to simulate a slab on which the base was fixed using a single bolt at intervals of 600 mm. The loading frame was located at the mid-span of the bead flange to transfer the load from the MTS machine. Grease was smeared on the bearing plates and the bead flanges to minimize friction. Additionally, the bearing plate was rounded at the corners to prevent localised tearing of the flange. A displacement-controlled system was used to move down the cross-head of the MTS machine at a constant rate of 2 mm/min for all test specimens until failure. The recording system included a computer connected to the MTS machine to generate load-displacement curves of the bearing plates. The deflection data was also obtained by placing three low-voltage displacement transducers (LVDTs) at the distance of D from the bead flange groove. Furthermore, these LVDTs were placed at intervals from the mid length as indicated in Table 5.4.



(3) Front view



(a) Schematic views



(b) Actual view

Figure 5.6 Test set up.

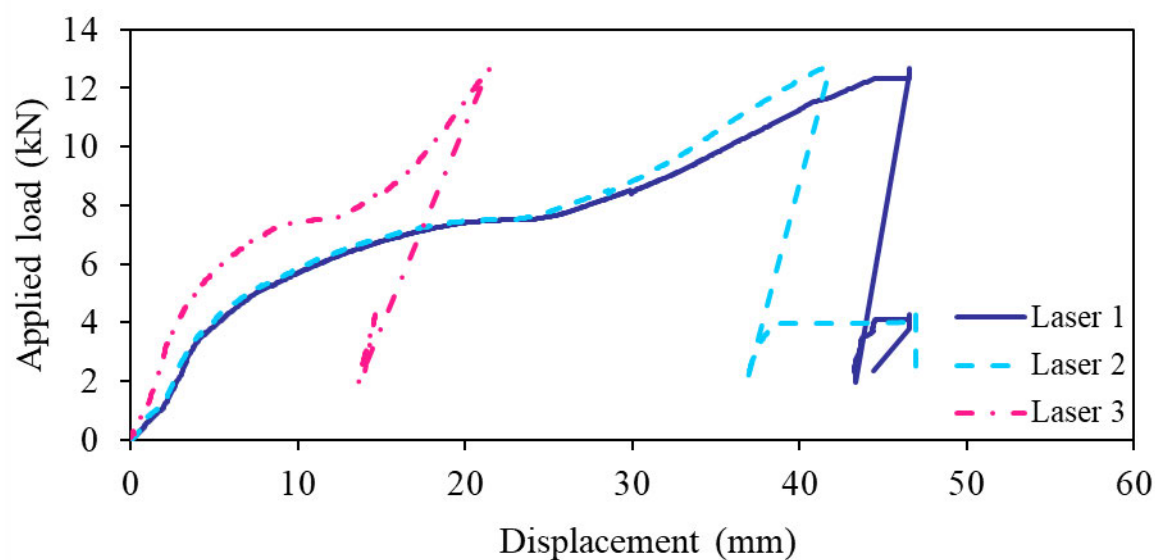
Table 5.4 Laser positions from the mid length in mm.

Bearing width	Laser 1	Laser 2	Laser 3
50 mm	Mid-length	50 mm	100 mm
100 mm	Mid-length	50 mm	100 mm
150 mm	Mid-length	75 mm	125 mm

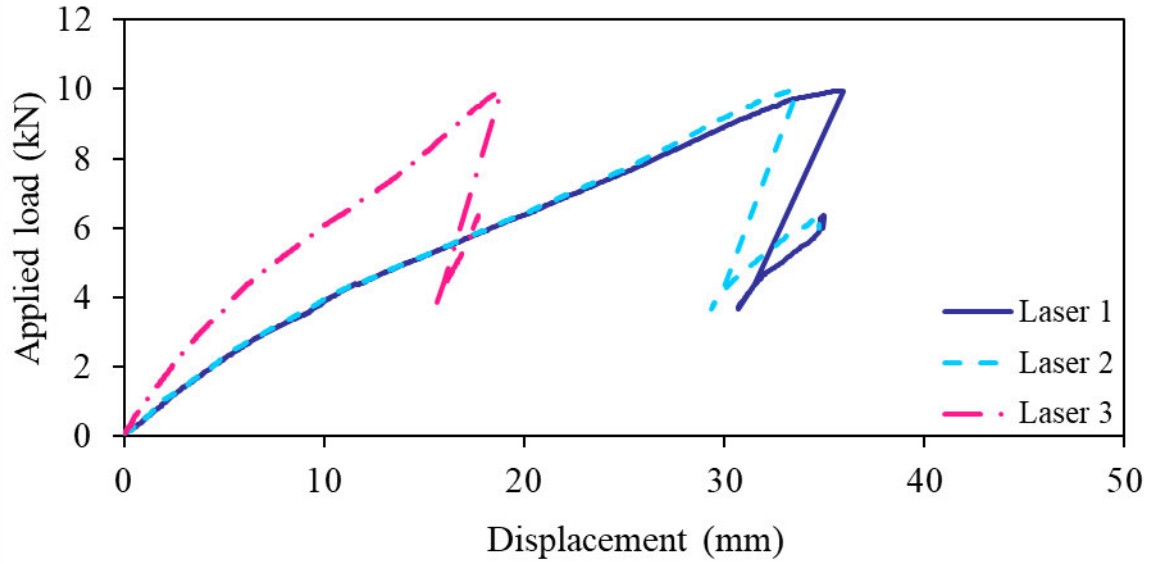
5.3. Test results and discussion

5.3.1. Load-displacement curves

The typical load versus deflection curves obtained from three laser LVDTs for 675028-475073/25/100 and 675028-475073/15/100 specimens are presented in Figure 5.7 (a) and (b), respectively. Test results demonstrate strong correlations between the load-displacement curves and engagement lengths, section geometries and bearing widths which are explained in detail in this section.



(a) 675028-475073/25/100



(b) 675028-475073/15/100

Figure 5.7 Typical load-displacement curves.

5.3.1.1. The effect of engagement length and section geometries

The load-displacement responses of six sub-head sections with removable beads with 50 mm bearing width and 25 mm engagement length are compared in Figure 5.8. As seen in the figure, the load-displacement curve for Section 475066-165863 with the shortest flange length was different from other sections. In this specimen, the load continued to increase until a fracture was noticed at the web-flange junction. Then, the test specimen was not able to carry any further load, despite increased deflection at the flange. It needs to be highlighted that Section 475066-165863 with 25 mm engagement length reached the highest capacity among these geometric sections. This occurred due to the lowest flange slenderness (flange width to thickness ratio) as well as the close proximity of the loading position to the web-flange junction, which consequently led to higher stiffness.

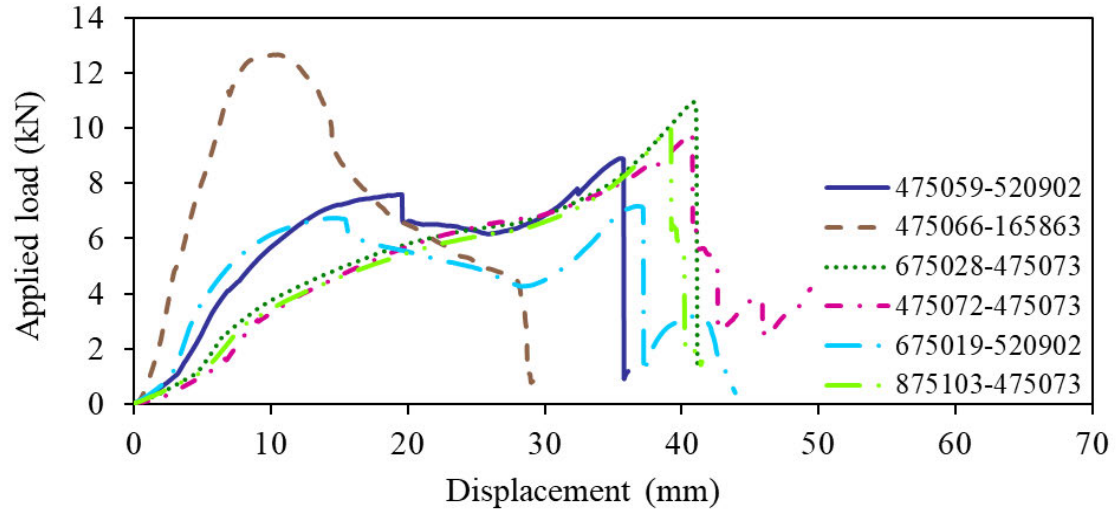
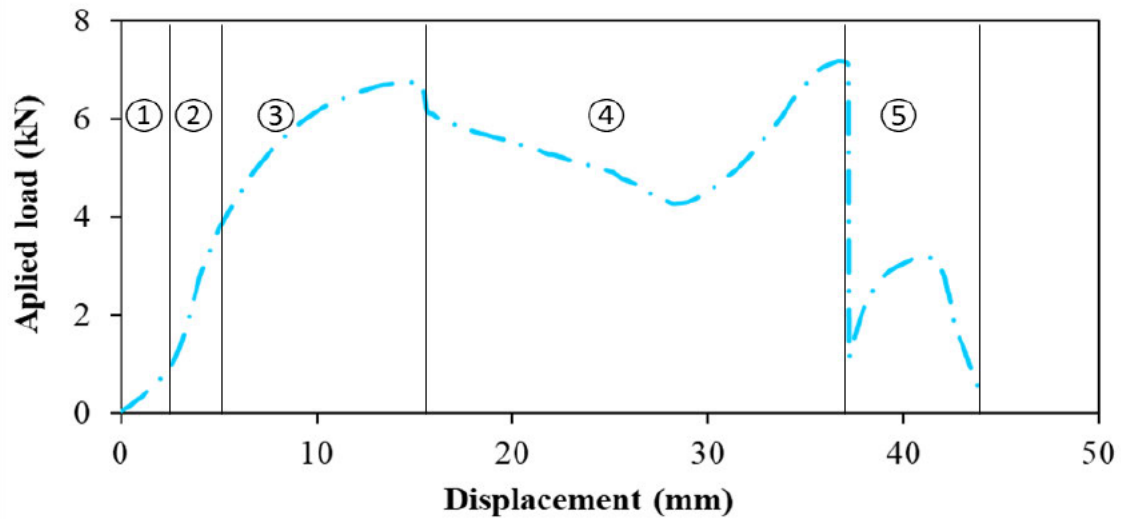
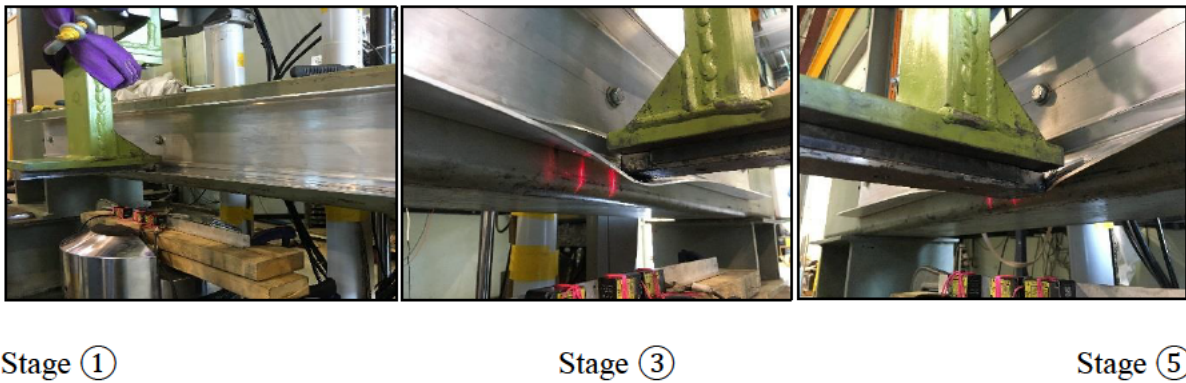


Figure 5.8 Comparison of load-displacement curves for different section geometries with 50 mm bearing width and 25 mm engagement length.

Figure 5.9 (a) and (b) display load-displacement curves and deformed shapes of a sub-head with removable bead for the 675019-520902/25/50 specimen, respectively. As shown in these figures, at the beginning of the test, the bearing plate was in contact with the groove of the flange in Stage ① (see Figure 5.9 (b)). Then in Stage ②, the bearing plate disconnected from the groove and was in contact with the flange, resulting in increased stiffness. At Stage ③, elastic deformation changed to plastic deformation, and the flange started to behave nonlinearly, as shown in Figure 5.9 (b). Consequently, the load continued to increase until it reached a peak value (Stage ③). During this stage, a fracture (visual yielding) was noticed at the web-flange junction at about 6.7 kN for 675019-520902/25/50 specimen, giving rise to a decrease in the loading capacity before the bearing plate was trapped within the groove element. At this stage, the loading capacity of the specimen as well as the stiffness were greatly enhanced. The maximum load was then reached to 7.2 kN at the end of Stage ④, before the bearing plate crushed the first groove element. Then, in Stage ⑤, the failure occurred leading to abrupt drop of the applied load, and the displacement continuously rose until the bearing plate crushed the second element of the groove and was pushed out of the flange (see Figure 5.9 (b)).



(a) Load-displacement curves



(b) Failure modes in different stages during the test

Figure 5.9 Load-displacement curves and stages of the bearing tests corresponding to 25 mm engagement lengths for 675019-520902/25/50.

Figure 5.10 shows the typical load versus displacement curves for six geometric sections with 50 mm bearing width and 15 mm engagement length. Apparent in Figure 5.10 is that the load-displacement curves for all sections follows a similar trend, except for Section 475066-165863. Unlike in Figure 5.8 for 25 mm engagement length, the minimum capacity under 15 mm engagement length is achieved by this section (See Figure 5.10). The displacement corresponding to the ultimate load for this section is almost half of the other sections. Apart from flange slenderness (as discussed in Section 5.3.1.1), other factors such as engagement lengths and flange widths can also be found to contribute to ultimate capacity and load-displacement behaviour. In this case, the shorter engagement length (15 mm) on section 475066-165863 with the shortest flange width led to lower ultimate load.

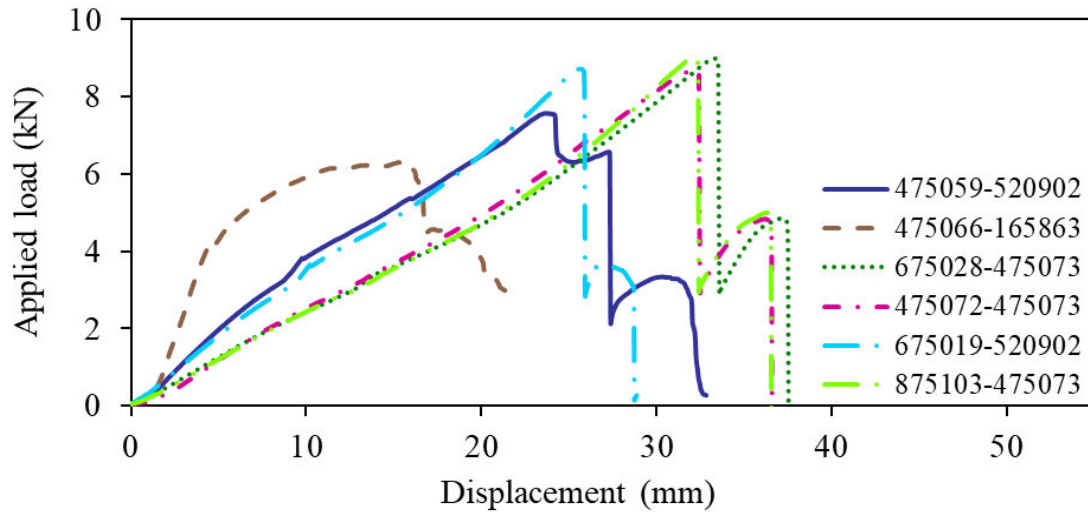
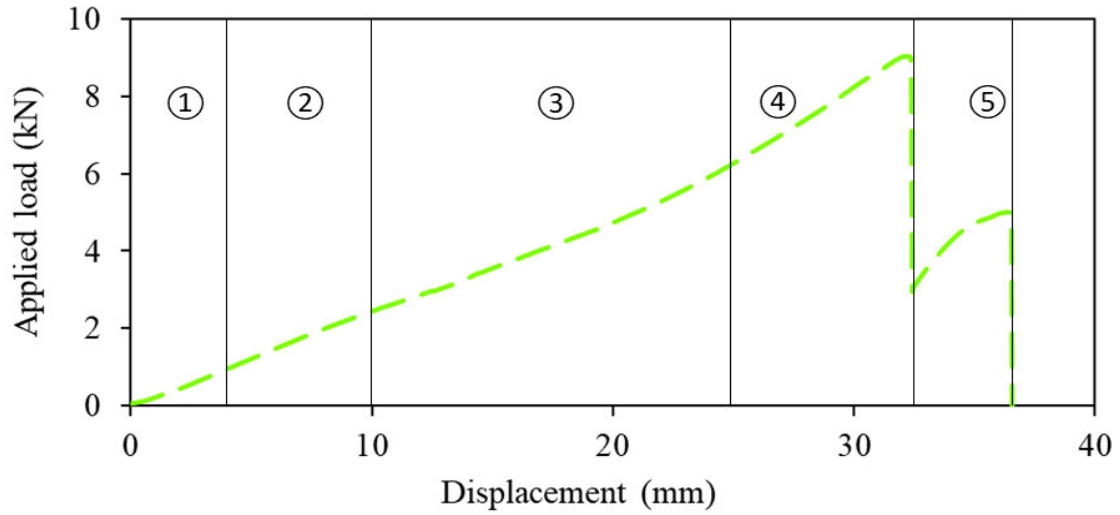
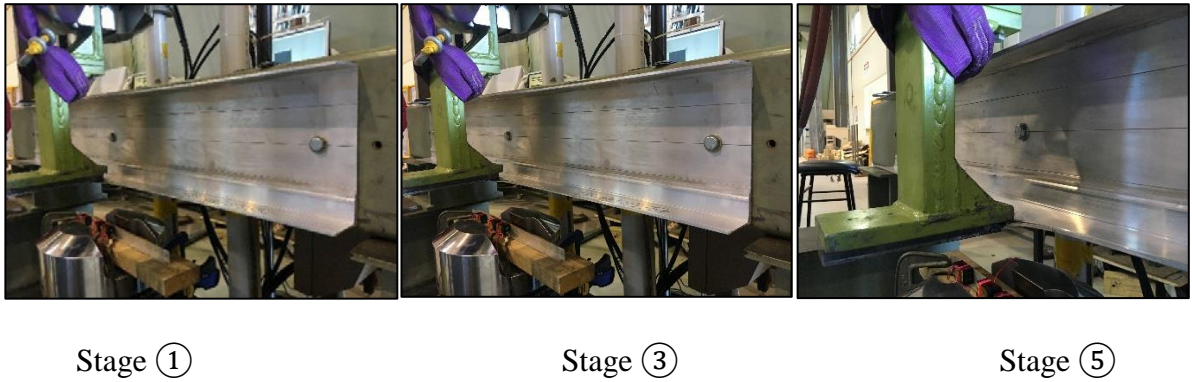


Figure 5.10 Comparison of load-displacement curves for different section geometries with 50 mm bearing width and 15 mm engagement length.

Figure 5.11 (a) and (b) show the load-displacement curve and the deformed shapes of a sub-head with removable bead corresponding to different stages for the 875103-475073/15/50 specimen. As seen in Figure 5.11 (b), this specimen endured approximately 1 kN at Stage ① before the bearing plate was in contact with the flange in Stage 2. During Stage ②, the load continued to increase at the same slope as the first stage, while the bearing plate sliding through the flange. At about 2.3 kN load, elastic deformation changed into plastic deformation (Stage ③) (see Figure 5.11 (b)). The maximum load of 9 kN was reached at the end of Stage ④, due to the sticking of the bearing plate in the inner groove. By Stage ⑤, the bearing plate was wedged in the second groove before the entire failure of the tested specimen happened; meanwhile visual yielding was not obvious, as shown in Figure 5.11 (b).



(a) Load-displacement curves for 875103-475073/15/50



(b) Failure modes in different stages during the test

Figure 5.11 Load-displacement curves and stages of the bearing tests corresponding to 15 mm engagement lengths for 875103-475073/15/50.

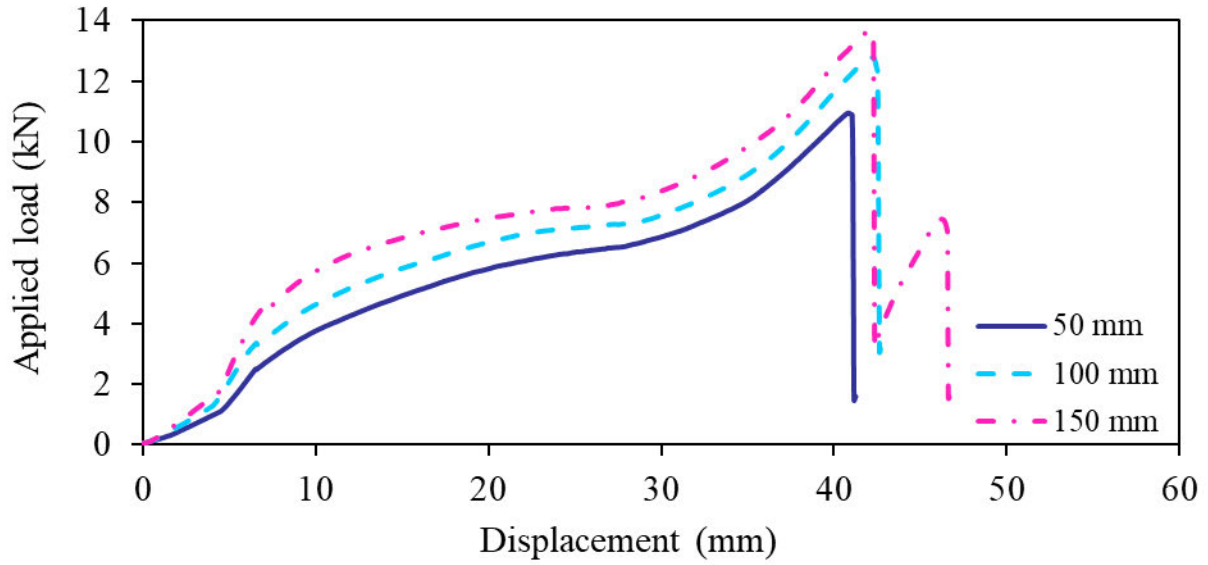
Overall, the complete failure of sub-head with removable bead was generally initiated in smaller displacements during the tests under 15 mm engagement length (see Figure 5.11 (b)) compared to the tests under 25 mm engagement length (see Figure 5.9 (b)). Furthermore, as the loading position was changed from 25 mm to 15 mm from the flange groove, the ultimate capacity and the stiffness were decreased. Also, the load-displacement curves show that the degree of nonlinear behaviour diminished in the 15 mm load case in comparison with the 25 mm load case.

5.3.1.2. The effect of removable beads

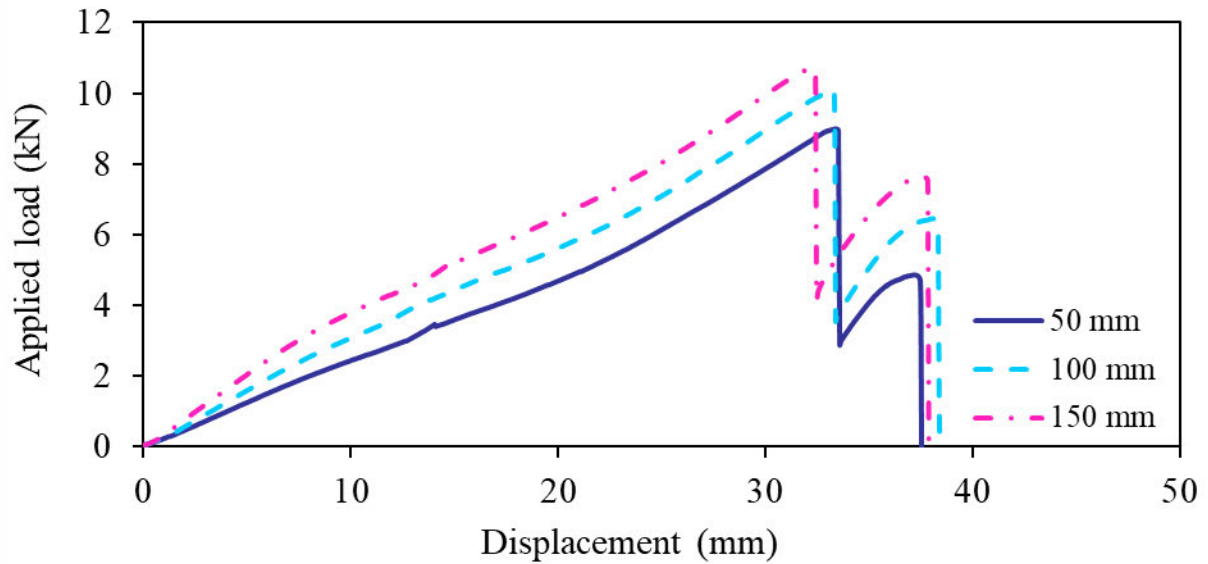
Apparent in Figure 5.8 and Figure 5.10 is that discrepancies between the load-displacement responses are marginal among the specimens with the same beads and different base sections. This means that the base makes little contribution to the bearing capacity and failure mode. Findings of current research studies demonstrate the existence of a close relationship of the load-displacement behaviour of sub-head with flange width and slip gap. Three beads were used in the present experimental study, namely 475073 (with 60.1 mm flange width), 520902 (with 46.3 mm flange width), and 165863 (with 33.5 mm flange width). As expected, in tests with a 15 mm engagement length, the increased flange width, and consequently the slip gap, led to an increase in capacity and displacement. While this trend was observed for tested specimens with bead numbers 475073 and 520902 and of 25 mm engagement length, the tested specimen with 165863 bead did not follow this rule. The main cause of this exception could be related to the fact that the specimen with bead 165863 has a minimum slip gap of 12.6 mm with a 25 mm engagement length. As a result, the concentrated load was in close proximity to the web-flange junction and provided higher stiffness, despite the crack damage being observed at the web-flange junction. However, it should be noted that the stiffness had an inverse relationship in regard to the slip gap (e) and flange width (b_f).

5.3.1.3. The effect of bearing widths

Figure 5.12 (a) and (b) show the comparison of load-displacement curves with respect to bearing widths for specimen 675028-475073 with 25 mm and 15 mm engagement lengths, respectively. It is apparent that in addition to the similar trend in load-displacement curves, the increased bearing widths led to enhancement of the bearing capacity of the aluminium sub-heads with removable beads.



(a) 25 mm engagement length



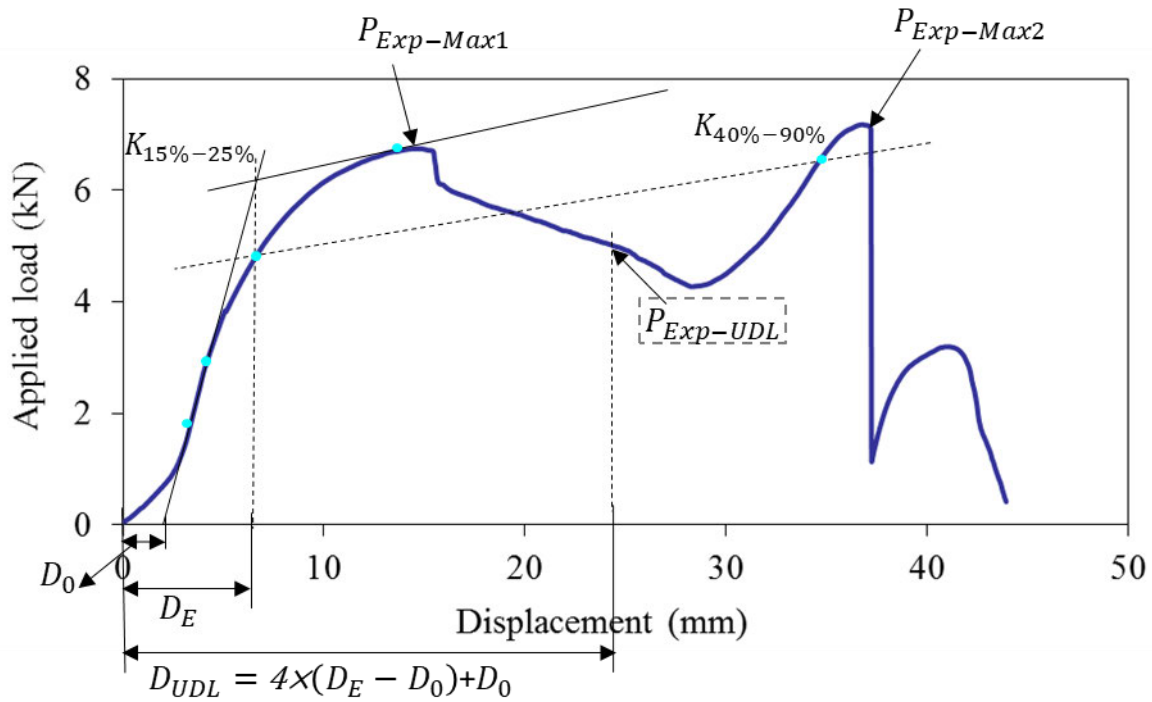
(b) 15 mm engagement length

Figure 5.12 Load-displacement curves with different engagement length for Specimen 675028-475073.

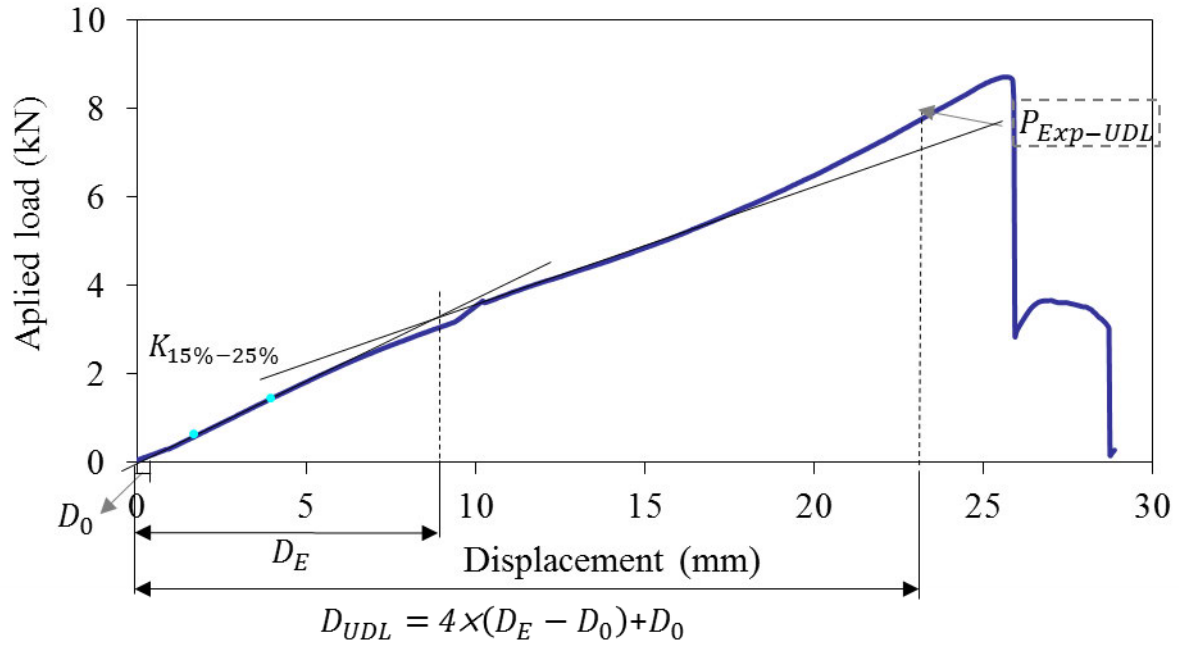
5.3.2 Ultimate loads (based on maximum load and ultimate deformation limit)

The maximum failure load of aluminium sub-head was attained at the second pick of the load-displacement curve ($P_{Exp-Max2}$), when the test specimen was no longer able to sustain an additional load (when the bearing plate was stuck in the first groove of the flange element). As this maximum load was reached at a large deflection, an ultimate deformation limit

(UDL) has been defined by Akbari et al. (2020a) as four times the first yield displacement. The similar procedure was used in this paper to define the ultimate deformation limit (UDL). For the 25 mm engagement length, the yield displacement (D_E) was defined as an intersection point between the initial stiffness, measured between the 15% and 25% of $P_{Exp-Max2}$, and a straight-line tangential to the load–displacement curve with a slope of a secant passing 40% and 90% of $P_{Exp-Max2}$, as set by Akbari et al. (2020a) for C-shaped sub-head (Figure 5.13 (a)). Note that if $P_{Exp-UDL}$ is greater than the first pick of the load-displacement curve ($P_{Exp-Max1}$) then $P_{Exp-UDL}$ is considered as the load corresponding to the ultimate deformation limit; otherwise, $P_{Exp-Max1}$ is taken. For the 15 mm engagement length, the yield displacement (D_E) was calculated as the deformation at the intersection of two lines representing the elastic and inelastic stiffnesses (see Figure 5.13 (b)).



(a) 25 mm engagement length



(b) 15 mm engagement length

Figure 5.13 Ultimate bearing capacity based on ultimate deformation limit (UDL).

Table 5.5 summarizes the experimental bearing capacity of the aluminium sub-head sections with removable beads based on the maximum load ($P_{Exp-Max2.}$) and the ultimate deformation limit (UDL) ($P_{Exp-UDL}$). A minimum difference of less than 5% was observed between the repeated test and the first test, indicating the reliability of test results. Hence, the average values of the repeated tests are reported in this table.

Table 5.5 Experimental ultimate loads for aluminium sub-head with removable bead, based on maximum load and ultimate deformation limit (UDL).

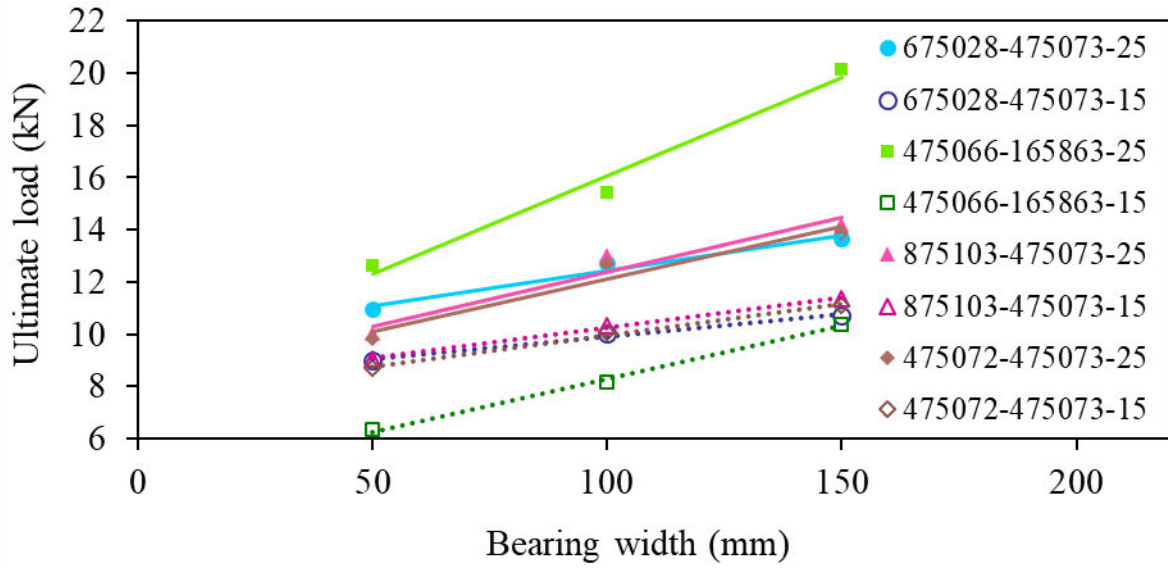
Specimen details			$P_{Exp-Max}$ (kN)	$P_{Exp-UDI}$ (kN)	Specimen details			$P_{Exp-Max}$ (kN)	$P_{Exp-UDI}$ (kN)
D (mm)	Section	N (mm)			D (mm)	Section	N (mm)		
15	675028-475073	50	9	9	25	675028-475073	50	11	6.5
		100*	10	10			100*	12.7	7.1
		150	10.7	10.5			150	13.7	7.4
	475066-165863	50	6.3	6.2		475066-165863	50	12.7	12.7
		100*	8.2	7.9			100*	15.5	15.4
		150	10.4	9.8			150	20.1	20.1
	475059-520902	50	7.6	7.6		475059-520902	50	8.9	7.6
		100*	10.8	10.8			100*	9.4	8.4
		150	12	12			150	10.2	9.8
	875103-475073	50	9	9		875103-475073	50	10	6.1
		100*	10.3	10.3			100*	13	7.3
		150	11.4	11.4			150	14.2	7.6
	675019-520902	50	8.7	8.7		675019-520902	50	7.2	6.7
		100	11	10.9			100	12.1	8.4
		150	11	11			150	12.7	9.9
	475072-475073	50	8.7	8.7		475072-475073	50	9.8	6.6
		100*	10.1	10.1			100*	12.7	7
		150	11.1	11.1			150	13.9	7.2

*Tests were repeated and the average values of two tests are reported.

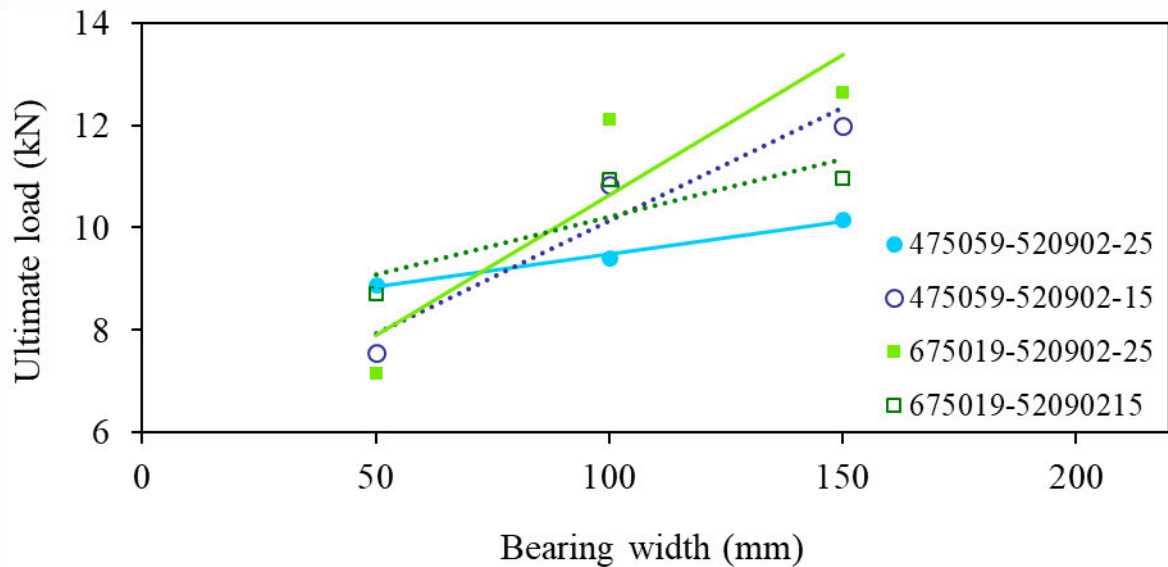
Based on the maximum strengths given in Table 5.5, the average bearing capacity of the sub-heads with removable beads with a 25 mm engagement length was 25% greater than the corresponding values of the 15 mm engagement length. The opposite trend was apparent in terms of the ultimate deformation limit (UDL); this percentage was 8% lower. Secondly, the data displayed in Table 5.5 demonstrates that as the bearing width increased from 50 mm to 100 mm and 150 mm, the overall mean values of the maximum bearing capacity of the six sections increased by 125% and 139%, respectively. These percentages were 119% and 134%, respectively, based on the ultimate deformation limit (UDL).

Figure 5.14 (a) and (b) display a comparison of the maximum bearing capacities as a function of the bearing widths for sub-heads with 475073 and 165863 beads, and 520902 bead, respectively. A linear increase in the ultimate bearing capacity was recognised, as the bearing width increased under each engagement length for sub-heads with 475073 and 165863 beads, while the sub-heads with the 520902 bead did not show a perfect linear trend. Also evident in

Figure 5.14 (a) is that the slopes of both trend lines for the 15 mm and 25 mm engagement lengths are nearly the same, whereas various slopes can be seen for both engagement lengths in Figure 5.14 (b). It was also observed during the experimental study that the sub-heads having 520902 beads under 100 mm and 150 mm bearing widths with 15 mm engagement length reached greater bearing capacity than those with 25 mm engagement length. This outcome stems directly from the fact that these sections produce cracking damage at the web-flange junction under the 25 mm engagement length, hence the damage giving rise to less stiffness and capacity.



(a) Sub-head with removable beads of 475073 and 165863



(b) Sub-head with removable beads of 520902

Figure 5.14 Comparison of ultimate load versus bearing width for different section geometries.

5.3.3. Failure modes

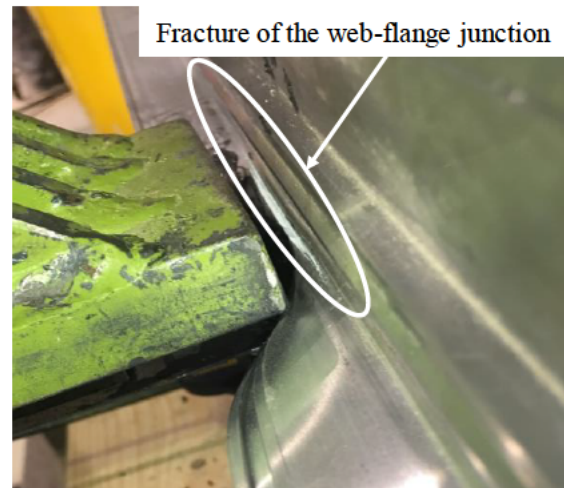
Deformations and failure modes of the test specimens shown in Figure 5.15 illustrate that the governing mode of failure occurred at the web to flange junction of the bead when the bead flange reached the flexural yielding and fractured as a result of the bending of the cantilever

flange. Other failure modes noticed in the tests were excessive deflection of the flange, the rotation of the removable bead, and slipping of the bearing plate caused by the crushing of the flange groove. However, the rotation of the base is considered to be negligible in comparison to excessive rotation of the bead. A slight bead flange deformation was initially observed as the loading frame moved downward. For specimens with larger engagement length, this damage was followed by an excessive deformation of the bead flange that led to permanent displacement. Furthermore, due to non-uniformity in the geometric section of sub-head with removable bead (comprised of two parts), the flange of the removable bead was subjected to twisting, which has resulted in tearing of the flange groove in some tests. Figure 5.16 and Figure 5.17 respectively depict the basic behaviour and damage mechanisms obtained from tests of specimens subjected to an increasing downward displacement, under the 25 mm and 15 mm engagement lengths. Although the same failure modes appeared in both loading cases, the amount of bending, twisting and fracture at the web-flange junction was more notable with the 25 mm engagement length compared to those with the 15 mm engagement length (see Figure 5.16 and Figure 5.17). Furthermore, using a smaller slip gap (e) can change the damage mechanism from yielding of the web-flange junction to fracture at the web-flange junction. Hence, cracking damage in the web-flange intersection was not observed in the specimens with beads of longer flange width (475-073) (see Figure 5.16 (b), Figure 5.16 (c), and Figure 5.17 (c)). Moderate fracture was detected in the specimen with medium size bead flange (520-902) (see Figure 5.17 (a) and Figure 5.17 (b)). In addition, significant fracture in the web-flange junction of Section 475066-165863 with minimum flange width was initiated at a very small displacement, around 10 mm (see Figure 5.16 (a)). The distinction between failure modes of C-shaped sub-head and sub-head with removable bead was that the removable bead was twisted during the bearing tests, which led to a fracture at the web-flange junction and tearing of the flange groove, especially in the specimen with shorter flange length (see Figure 5.18); however, these failures did not occur in C-shaped sub-heads.

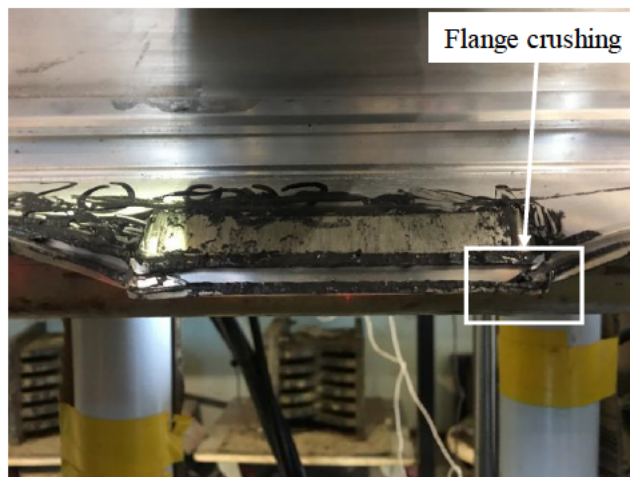
475059-520902/25/100



475066-165863/25/50



675019-520902/25/100



675028-475073/25/100

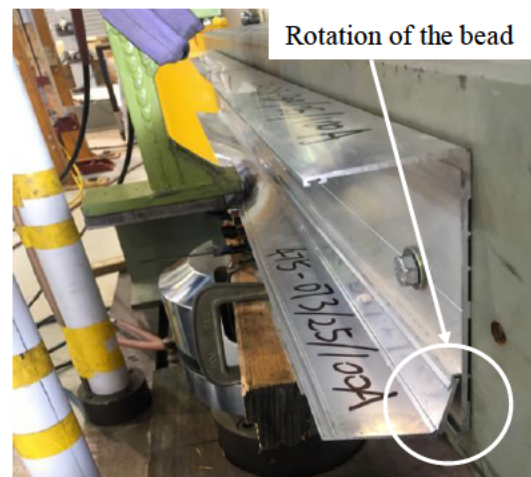


Figure 5.15 Flange deformation and failure modes under concentrated loading.



(a) 475066-165863/25/100



(b) 675028-475073/25/100



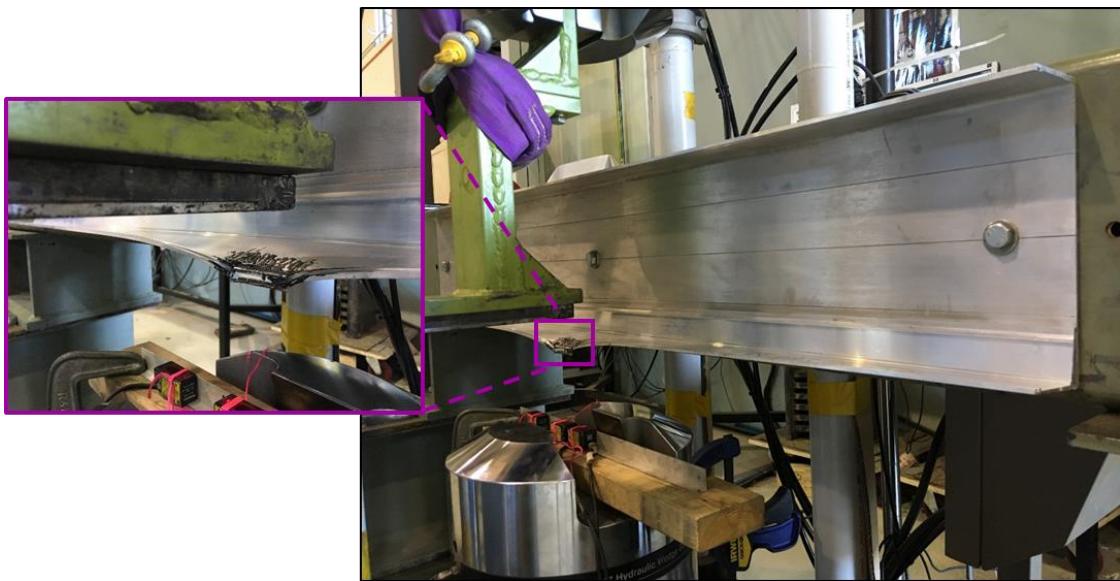
(c) 475072-475073/25/100

Figure 5.16 Bearing failure modes under 25 mm engagement length.



(a) 675019-520902/15/150

(b) 475059-520902/15/100



(c) 875103-475073/15/50

Figure 5.17 Bearing failure modes under 15 mm engagement length.



(a) C-shaped sub-head (475-077)



(b) Sub-head with removable bead (675028-475073)

Figure 5.18 Comparison of experimental failure modes for C-shaped sub-head and sub-head with removable bead.

5.4. Design rule proposal

5.4.1. Current design rules

As mentioned above, despite a broad application of aluminium sub-heads in window walls, no published aluminium standards exist for designing this complex section. Data obtained from physical testing, provided by the manufacturer, is the only source for the design of the aluminium sub-heads. However, design specifications exist to predict the design strength of cold-formed steel deflection tracks under one bearing loaded flange (with similar structural behaviour to the sub-head in the window wall). Thus, to provide a better understanding of the bearing behaviour of an aluminium sub-head with a removable bead subjected to concentrated load, relevant cold-formed steel standards (the North American Standard for Cold-Formed Steel Structural Framing (AISI S240, 2015), the U.S. Army Corps of Engineers (TI 809-07, 1998), and the Steel Stud Manufacturers Association (SSMA, 2000)), as well as Bolte and LaBoube (2004) design equations, are presented and discussed below. Furthermore, a brief summary of the design expressions proposed by the authors (Akbari et al., 2020a) for conventional C-shaped aluminium sub-heads is presented next.

5.4.1.1. Available design rules for cold-formed steel stud-to-track connection strength

The American Iron and Steel Institute (AISI S240, 2015) provides design rules for wall stud design (Eq. (5.1)), based on ultimate strength, to predict the strength of single deflection tracks subjected to a concentrated load.

$$P_n = \frac{w_{dt} t^2 f_y}{4e} \quad (5.1)$$

where:

t = track thickness (mm);

f_y = yield strength of track (MPa);

$e = b_f - D$ = slip gap between end of stud web and track web (mm);

b_f = track flange width (mm); and

D = engagement length (bearing contact length) between stud and track flange (see Figure 5.19).

The effective track length (w_{dt}) was derived through correlation of the test results with Eq. (5.1), and is expressed by:

$$w_{dt} = 0.11\alpha^2(e^{0.5}/t^{1.5}) + 5.5\alpha \leq S(mm) \quad (5.2)$$

where:

$\alpha = 25.4$ = coefficient for conversion of units; and

S = stud spacing (mm).

Notice that some limitations were implemented to Eq. (5.1) and Eq. (5.2) for minimum deflection track thicknesses, section depths, and flange widths (AISI S240, 2015). Additionally, the horizontal distance from the end of the track to the web side of the stud shall not be less than one-half the effective track length (w_{dt}).

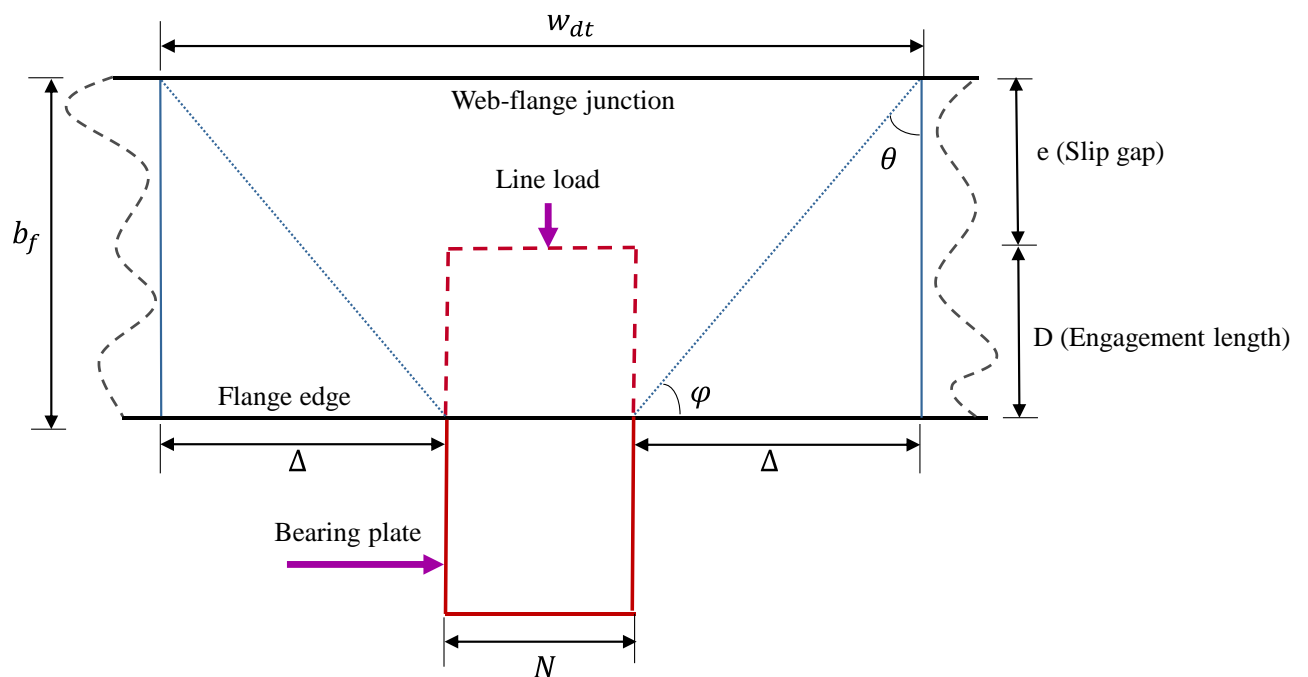


Figure 5.19 Stress distribution in the bead flange.

However, the U.S. Army Corps of Engineers (TI 809-07, 1998) used a different design methodology based on the allowable stress design to estimate the nominal stud-to-track connection strength:

$$P_n = \frac{w_{dt} t^2 f_y}{6e} \quad (5.3)$$

where the effective track length (w_{dt}) was obtained based on an assumption of the stress distribution in the flange of the track, and is given as:

$$w_{dt} = N + 2 \left[\frac{e + D}{\tan(\phi)} \right] \leq S, \phi = 30 \quad (5.4)$$

where N is the stud flange width (mm) (see Figure 5.19); and w_{dt} , t , f_y , e and D are outlined as above.

Notably, the design rule procedures provided by the Steel Stud Manufacturers Association (SSMA, 2000) for estimating the strength of cold-formed steel single deflection tracks are similar to those of the U.S. Army Corps of Engineers (TI 809-07, 1998) practice with minor modifications.

5.4.1.2. Bolte and LaBoube (2004)

Bolte and LaBoube (2004) used plastic section modulus (Eq. (5.1)) to predict the nominal stud-to-track connection capacity of a deflection track. The effective track length (w_{dt}) was defined as a function of the ratio of the slip gap to the track thickness ($(e/t)^2$) as well as the stud flange width (w_{stud}) as expressed by Eq. (5.5) and Eq. (5.6):

$$w_{dt} = 2\Delta + w_{stud} \quad (5.5)$$

$$2\Delta = \begin{cases} \frac{300(e/t)^2}{100} & \text{for } (e/t)^2 < 100 \\ 300 & \text{for } (e/t)^2 \geq 100 \end{cases} \quad (5.6)$$

where Δ is the partial track length (see Figure 5.19).

5.4.1.3. Design rule for C-shaped sub-head

Since the nominal bearing capacities of C-shaped sub-head sections predicted using AISI S240 (2015) and the U.S. Army Corps of Engineers (TI 809-07, 1998) were found to be conservative, Akbari et al. (2020a) improved their recommended equations to suitably predict the bearing capacity of C-shaped aluminum sub-head sections. Due to the nonlinear behaviour of the sub-head flange under a concentrated load, Eq. (5.1) (AISI S240, 2015) (which is based on the plastic limit strength) was used by Akbari et al. (2020a) to predict the bearing capacity of aluminium C-shaped sub-heads. Based on the stress distribution assumption in the sub-head flange (see Figure 5.19), w_{dt} (effective sub-head length) was calibrated using the ultimate loads obtained from the experimental study. Accordingly, Akbari et al. (2020a) proposed a set of design rules for C-shaped aluminium sub-heads to estimate the effective sub-head length, based on the maximum load and ultimate deformation limit (UDL), as well as the two engagement lengths of 15 mm and 25 mm, as expressed by Eq. (5.7a) and Eq. (5.7b).

$$w_{dt} = N + 2 * b_f * \tan(\theta) \quad (5.7a)$$

$$\theta = a * (e/t)^2 + b \quad (5.7b)$$

where, the values of coefficients a and b are given in Table 5.6.

Table 5.6 Proposed coefficients for the effective sub-head length (w_{dt}).

Section	Criteria	D (mm)	a	b
C-shaped sub-head (Akbari et al., 2020a)	Maximum load	15	0	76
		25	0.1	67
	Ultimate deformation limit (UDL)	15	-0.02	76.1
		25	0.1	57.5
Sub-head with removable bead	Maximum load	15	0.02	74
		25	0.06	70
	Ultimate deformation limit (UDL)	15	0.03	72
		25	-0.04	72

5.4.2. Comparison with current design rules

The recorded failure loads of the 36 specimens, based on the maximum load ($P_{Exp-Max2.}$) and the ultimate deformation limit (UDL) ($P_{Exp-UDL.}$), were compared with the predicted failure loads, as calculated by the current design rules in the AISI S240 (2015), the U.S. Army Corps of Engineers (TI 809-07, 1998), and the Bolte and LaBoube's (2004) equations, and summarised in Table 5.7.

Table 5.7 Experimental ultimate loads and comparisons with current design rules.

Specimen details			P _{US ARMY} (kN)	P _{AISI} (kN)	P _{B&L} (kN)	$\frac{P_{Exp-Max2}}{P_{US ARMY}}$	$\frac{P_{Exp-Max2}}{P_{AISI}}$	$\frac{P_{Exp-Max2}}{P_{B\&L}}$	$\frac{P_{Exp-UDL}}{P_{US ARMY}}$	$\frac{P_{Exp-UDL}}{P_{AISI}}$	$\frac{P_{Exp-UDL}}{P_{B\&L}}$
D (mm)	Section	N (mm)									
15	675028- 475073	50	2.5	3.1	4.9	3.59	2.88	1.83	3.59	2.88	1.83
		100*	3	3.1	5.6	3.37	3.21	1.78	3.37	3.21	1.78
		150	3.4	3.1	6.3	3.11	3.43	1.69	3.04	3.35	1.66
	475066- 165863	50	2.9	4.9	5.2	2.21	1.30	1.21	2.16	1.27	1.18
		100*	3.7	4.9	6.4	2.23	1.67	1.27	2.16	1.62	1.23
		150	4.4	4.9	7.6	2.33	2.13	1.36	2.19	2.00	1.28
	475059- 520902	50	2.7	4	6.5	2.77	1.89	1.16	2.77	1.89	1.16
		100*	3.4	4	7.5	3.23	2.70	1.45	3.21	2.68	1.44
		150	4	4	8.4	3.01	2.98	1.42	3.01	2.99	1.43
	875103- 475073	50	2.5	3.1	4.9	3.61	2.90	1.84	3.61	2.90	1.84
		100*	3	3.1	5.6	3.48	3.31	1.84	3.48	3.31	1.84
		150	3.4	3.1	6.3	3.31	3.64	1.80	3.31	3.64	1.80
	675019- 520902	50	2.7	4	6.5	3.19	2.17	1.33	3.19	2.17	1.33
		100	3.4	4	7.5	3.26	2.73	1.46	3.26	2.73	1.46
		150	4	4	8.4	2.75	2.73	1.30	2.75	2.73	1.30
	475072- 475073	50	2.5	3.1	4.9	3.48	2.80	1.77	3.48	2.80	1.77
		100*	3	3.1	5.6	3.39	3.23	1.79	3.39	3.23	1.79
		150	3.4	3.1	6.3	3.24	3.57	1.76	3.24	3.57	1.76
25	675028- 475073	50	3.2	3.8	6.2	3.46	2.89	1.76	2.04	1.71	1.04
		100*	3.8	3.8	7.1	3.39	3.36	1.79	1.88	1.87	0.99
		150	4.4	3.8	8	3.14	3.61	1.71	1.70	1.95	0.92
	475066- 165863	50	5.1	8	4.4	2.47	1.58	2.88	2.47	1.58	2.88
		100*	6.6	8	6.5	2.36	1.92	2.37	2.35	1.92	2.36
		150	8	8	8.7	2.53	2.51	2.33	2.53	2.51	2.33
	475059- 520902	50	3.9	5.4	6	2.29	1.65	1.48	1.96	1.41	1.27
		100*	4.8	5.4	7.3	1.98	1.75	1.29	1.76	1.56	1.15
		150	5.6	5.4	8.6	1.80	1.89	1.17	1.73	1.82	1.13
	875103- 475073	50	3.2	3.8	6.2	3.16	2.65	1.61	1.93	1.61	0.98
		100*	3.8	3.8	7.1	3.46	3.43	1.83	1.95	1.93	1.03
		150	4.4	3.8	8	3.26	3.75	1.78	1.76	2.02	0.96
	675019- 520902	50	3.9	5.4	6	1.85	1.33	1.20	1.73	1.25	1.12
		100	4.8	5.4	7.3	2.54	2.25	1.65	1.76	1.56	1.14
		150	5.6	5.4	8.6	2.24	2.35	1.46	1.75	1.84	1.14
	475072- 475073	50	3.2	3.8	6.2	3.10	2.60	1.58	2.09	1.75	1.07
		100*	3.8	3.8	7.1	3.38	3.35	1.79	1.87	1.86	0.99
		150	4.4	3.8	8	3.18	3.66	1.73	1.64	1.89	0.89
Mean						2.89	2.63	1.64	2.50	2.24	1.43
COV						0.19	0.28	0.22	0.27	0.32	0.32
ϕ_w						2.29	1.75	1.23	1.70	1.37	0.87

*Tests were repeated and the average values of two tests are reported.

As shown in Table 5.7, the nominal strength predicted by the AISI S240 (2015) (Eq. (5.1)) is greater than that suggested by the U.S. Army Corps of Engineers (TI 809-07, 1998) (Eq. (5.3)). These differences are mainly related to the recommended effective track flange width expression and the assumed strength limit moment. The mean values of the tested to the predicted load ratios obtained from the aforementioned specifications are between 2.24 to 2.89 with a large coefficient of variations (COV) of up to 32%. Also, when the Bolte and LaBoube (2004) design equations were applied to this test data, the test-to-predicted ratios had mean values of 1.64 and 1.43 and the corresponding COVs of 0.22 and 0.32, respectively, based on the maximum load and the ultimate deformation limit (UDL), (See Table 5.7).

The strength capacities obtained from the experimental testing were also compared with the predicted values of the bearing capacities calculated by using Eq. (5.1), Eq. (5.7a) and Eq. (5.7b) for C-shaped sub-heads, as given in Table 5.8. The mean values of the test-to-predicted load ratio for the maximum load and the ultimate deformation limit (UDL) are 1.05 (with a COV of 0.20) and 1.19 (with a COV of 0.24), respectively. Considering the ratio of the tested to the predicted loads, it was determined that the current design rules (AISI S240, 2015, TI 809-07, 1998, and Bolte and LaBoube (2004) equations) as well as the proposed equations for conventional C-shaped aluminium sub-heads are unreliable, and fail to predict the bearing capacities of aluminium sub-heads with removable beads. Hence, a simple regression analysis was performed to develop the strength prediction equations for aluminium sub-head sections with removable beads.

Table 5.8 Experimental ultimate loads and comparisons with proposed design rules.

Specimen details			$P_{Prop-C-Max2}$ (kN)	$P_{Exp-Max2}$ (kN)	$P_{Prop-C-UDL}$ (kN)	$P_{Prop-UDL}$ (kN)	$\frac{P_{Exp-Max2}}{P_{Prop-Max-C}}$	$\frac{P_{Exp-Max2}}{P_{Prop-Max2}}$	$\frac{P_{Exp-UDL}}{P_{Prop-UDL-C}}$	$\frac{P_{Exp-UDL}}{P_{Prop-UDL}}$
D (mm)	Section	N (mm)								
15	675028-475073	50	7.7	9.1	6.1	9.2	1.16	0.99	1.48	0.98
		100*	8.4	9.8	6.8	9.9	1.19	1.02	1.48	1.01
		150	9.1	10.5	7.5	10.6	1.17	1.02	1.40	0.99
	475066-165863	50	8.3	7.9	7.8	7.3	0.76	0.80	0.79	0.85
		100*	9.5	9.1	9.0	8.5	0.85	0.90	0.87	0.93
		150	10.7	10.3	10.2	9.7	0.97	1.01	0.96	1.01
	475059-520902	50	8.2	8.5	7.2	8.0	0.92	0.90	1.05	0.95
		100*	9.2	9.4	8.1	8.9	1.18	1.15	1.33	1.20
		150	10.1	10.3	9.1	9.9	1.18	1.16	1.32	1.21
	875103-475073	50	7.7	9.1	6.1	9.2	1.17	0.99	1.49	0.98
		100*	8.4	9.8	6.8	9.9	1.22	1.05	1.53	1.04
		150	9.1	10.5	7.5	10.6	1.24	1.08	1.52	1.07
	675019-520902	50	8.2	8.5	7.2	8.0	1.06	1.03	1.21	1.09
		100	9.2	9.4	8.1	8.9	1.19	1.17	1.35	1.22
		150	10.1	10.3	9.1	9.9	1.08	1.06	1.21	1.11
	475072-475073	50	7.7	9.1	6.1	9.2	1.13	0.96	1.44	0.95
		100*	8.4	9.8	6.8	9.9	1.19	1.03	1.49	1.02
		150	9.1	10.5	7.5	10.6	1.22	1.06	1.49	1.05
25	675028-475073	50	13.7	11.3	7.2	6.1	0.80	0.97	0.89	1.07
		100*	14.6	12.2	8.1	6.9	0.87	1.05	0.87	1.02
		150	15.5	13.0	9.0	7.8	0.88	1.05	0.82	0.94
	475066-165863	50	10.4	11.5	7.5	11.6	1.22	1.10	1.68	1.09
		100*	12.5	13.6	9.7	13.7	1.23	1.14	1.59	1.12
		150	14.6	15.7	11.8	15.9	1.38	1.28	1.71	1.27
	475059-520902	50	9.7	10.1	6.5	8.3	0.91	0.88	1.17	0.91
		100*	11.0	11.4	7.8	9.6	0.85	0.83	1.08	0.87
		150	12.4	12.7	9.1	11.0	0.82	0.80	1.07	0.89
	875103-475073	50	13.7	11.3	7.2	6.1	0.73	0.89	0.84	1.01
		100*	14.6	12.2	8.1	6.9	0.89	1.07	0.90	1.05
		150	15.5	13.0	9.0	7.8	0.91	1.09	0.85	0.97
	675019-520902	50	9.7	10.1	6.5	8.3	0.74	0.71	1.04	0.81
		100	11.0	11.4	7.8	9.6	1.10	1.06	1.07	0.87
		150	12.4	12.7	9.1	11.0	1.02	0.99	1.08	0.90
	475072-475073	50	13.7	11.3	7.2	6.1	0.72	0.87	0.91	1.09
		100*	14.6	12.2	8.1	6.9	0.87	1.04	0.86	1.01
		150	15.5	13.0	9.0	7.8	0.89	1.06	0.79	0.91
Mean							1.02	1.01	1.19	1.02
COV							0.18	0.12	0.24	0.11
ϕ_w							0.82	0.89	0.86	0.91

*Tests were repeated and the average values of two tests are reported.

5.4.3. Derivation of proposed equation for sub-heads with removable beads

The flange of the removable bead in this study is loaded by a bearing plate and the bearing capacity of the sub-head is controlled by the plastic moment capacity at the web-flange junction of the bead. Also, the bearing load is a function of the bead flange and its capability to distribute the mullion load. Analysis of the bearing capacity of the sub-head to mullion connection revealed a complex load path that relies on the estimation of the effective sub-head length w_{dt} (see Figure 5.19). Thus, in order to determine the bearing strength of the sub-heads with removable beads under a concentrated load, the width of the bead flange that can effectively withstand bending must be calculated. Eq. (5.1) can be applied to a sub-head with removable bead to estimate the bearing capacity, provided that t is considered as the maximum thickness of the bead flange at the bead web-flange junction; f_y is recognised as the bead yield strength; e is the slip gap (distance between the point of action of the force and the bead web-flange junction); and w_{dt} is the effective sub-head lengths.

The capacity of a sub-head with removable bead is affected by numerous parameters, such as the bearing width (N), the slip gap (e), and the flange width (b_f). To propose a reliable approach to predict the bearing capacities of aluminium sub-heads with removable beads, the effect of these parameters should be investigated. In this regard, Figure 5.20 to Figure 5.22 show the variation of the effective sub-head lengths (w_{dt}) (derived from Eq. (5.1) and the test results) with respect to the bearing width (N), the flange width (b_f), and the slip gap (e). Figures 20 and 21 illustrate, respectively, that the effective sub-head length increases linearly with the increased bearing width (N) and flange width (b_f). Apparently, the effective sub-head lengths for sub-heads with the same removable bead are very similar. These figures show that 675028-475073, 475072-475073 and 875103-475073 specimens with the maximum flange width of 65 mm have the highest effective sub-head length. In contrast, the minimum amount of the effective sub-head length is attributed to the 475066-165863 specimen with a minimum flange length of 40 mm. Additionally, 475059-520902 and 675019-520902 specimens with the flange width of 51 mm have the second highest effective sub-head length. However, no obvious trend line is notable for w_{dt} in comparison with the slip gap (e) for sub-heads with different bead sections, as shown in Figure 5.22.

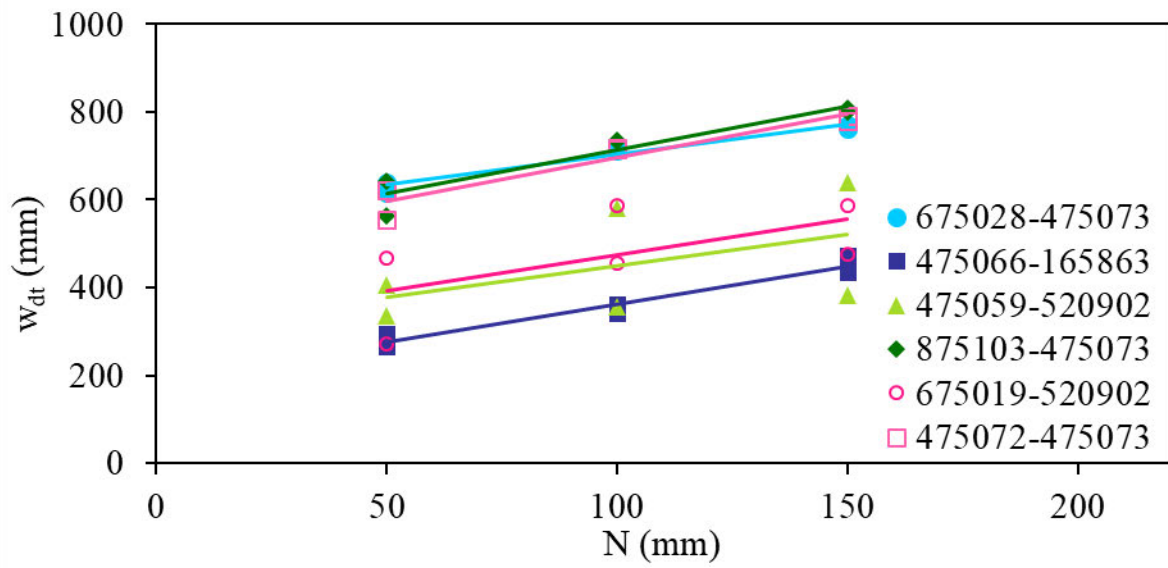


Figure 5.20 Variation of the effective sub-head length (w_{dt}) against bearing width (N).

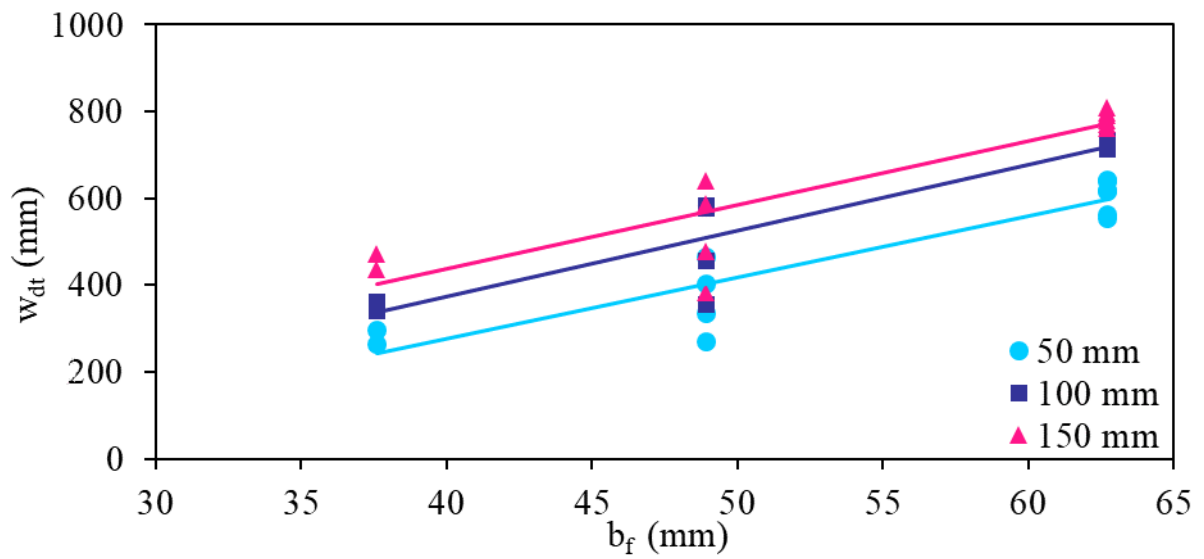


Figure 5.21 Variation of the effective sub-head length (w_{dt}) against flange width (b_f).

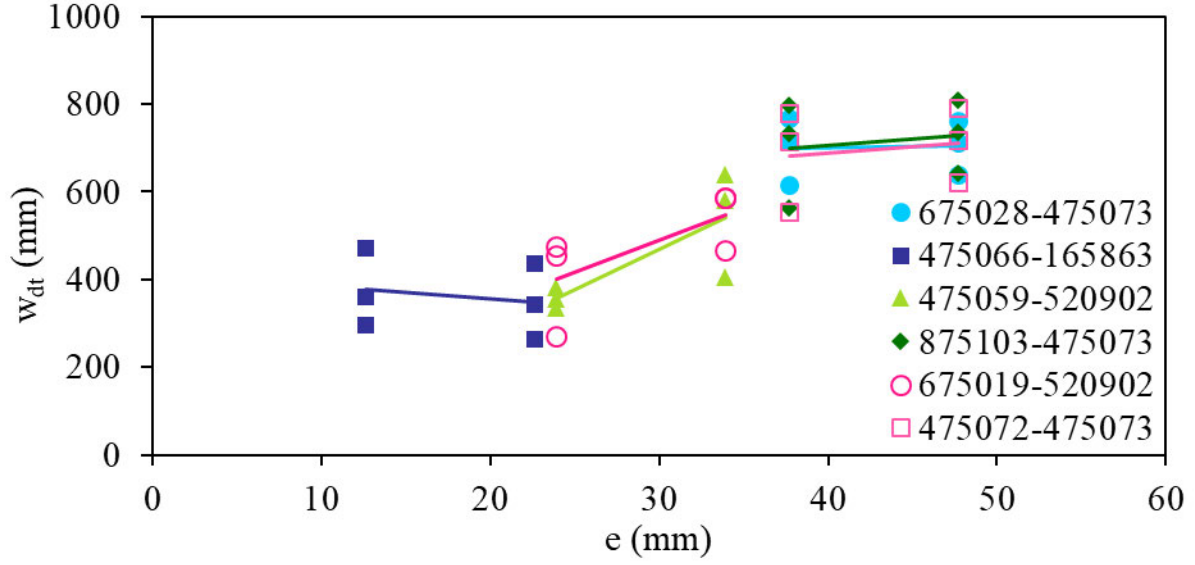
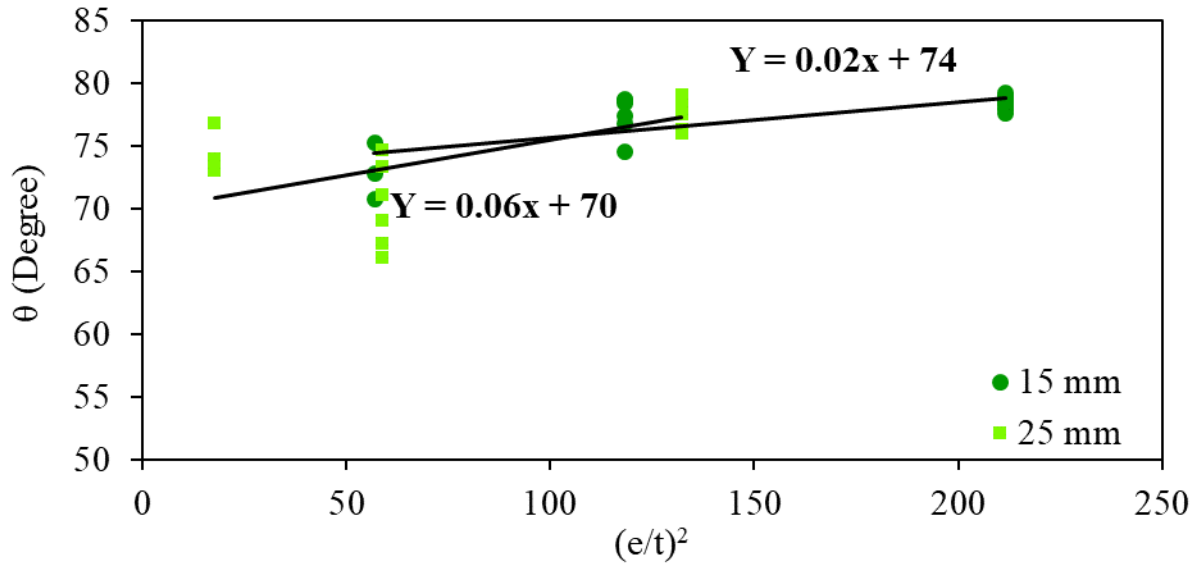
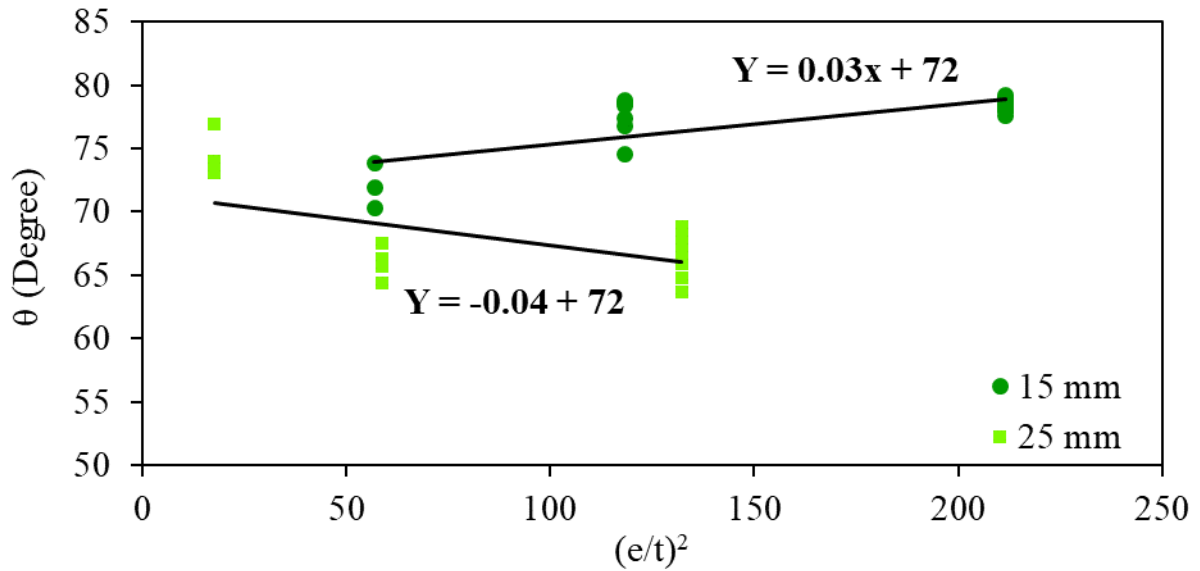


Figure 5.22 Variation of the effective sub-head length (w_{dt}) against slip gap (e).

The sub-heads with a higher engagement length underwent fracture at the bead web to flange junction, whereas in the sub-heads with a shorter engagement length, the dominate failure mode was yielding. Due to these differences in the failure modes, the effective sub-head lengths for the two engagement lengths must be computed by two different equations. It is preferred to follow the same procedure which was adopted by the authors for C-shaped sub-heads (Akbari et al., 2020a) for θ . These design equations are based on the U.S. Army Corps of Engineers (TI 809-07, 1998) procedures for effective track length, with a slight modification implemented to ϕ . In this regard, Figure 5.23 (a) and (b) show the relationship between $(e/t)^2$ and θ , for the maximum load and the ultimate deformation limit (UDL), respectively. Accordingly, Eq. (5.7b) associated with the coefficients given in Table 5.6 is used to calculate the ultimate bearing capacities of aluminium sub-heads with removable beads, alongside Eq. (5.1) and Eq. (5.7a).



(a) Maximum load



(b) Ultimate deformation limit (UDL)

Figure 5.23 Relationship between θ and slip gap-flange thickness.

5.4.4. Comparison of test results with the proposed design equations

The ultimate bearing capacities ($P_{Exp-Max2}$ and $P_{Exp-UDL}$) obtained from the tests were compared with the nominal strengths predicted ($P_{Prop-Max2}$ and $P_{Prop-UDL}$) using the proposed equations, as shown in Table 5.8. In the case of maximum load, the accuracy of the proposed equations as defined by the ratio of $P_{Exp-Max2}/P_{Prop-Max2}$, resulted in a mean ratio of 1.01 and a corresponding COV of 0.12. In terms of ultimate deformation limit (UDL), the mean value of

tested-to-predicted bearing capacity ratios ($P_{Exp-UDL}/P_{Prop-UDL}$) was 1.02, with a corresponding COV of 0.11. This indicates that the bearing capacities predicted based on the proposed new design equations provided the best correlation with the experimental results under both load cases.

Figure 5.24 and Figure 5.25 present the tested-to-predicted bearing capacity ratios from the current cold-formed steel provisions (AISI S240, 2015; TI 809-07, 1998), the Bolte and LaBoube (2004) equations, and the proposed design rules for C-shaped sub-heads and sub-heads with removable beads. Generally, the current design rules fail to predict the bearing capacities of the tested aluminium sub-head sections with removable beads accurately and safely. However, it is evident that the proposed equations have the ability to estimate the bearing capacity of aluminium sub-head sections with removable beads well, as most of the data points lie within the limits of 20%, based on the maximum load and the deformation criterion. Note that ACSH is an acronym used for aluminium C-shaped sub-head and ASHRB is an acronym used for aluminium sub-head with removable bead.

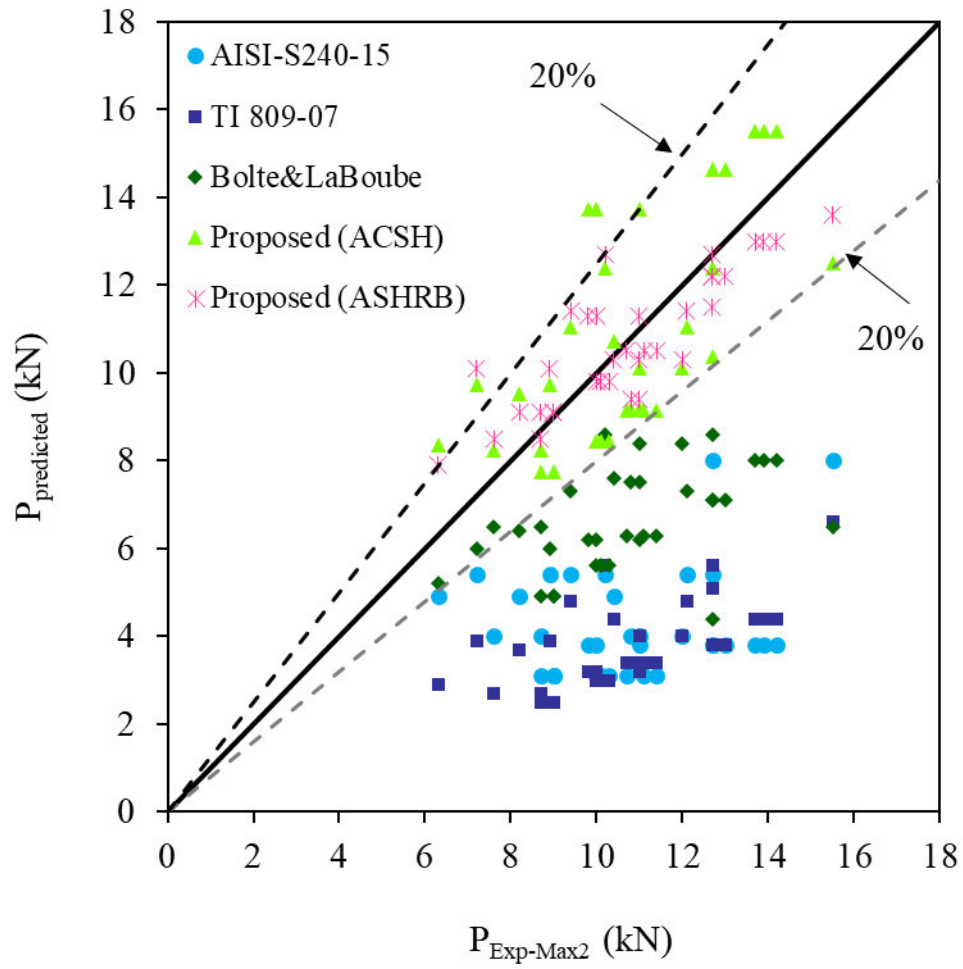


Figure 5.24 Comparison of experimental ultimate strengths ($P_{Exp-Max2}$) with those of current and proposed design rules ($P_{Predicted}$), based on maximum load.

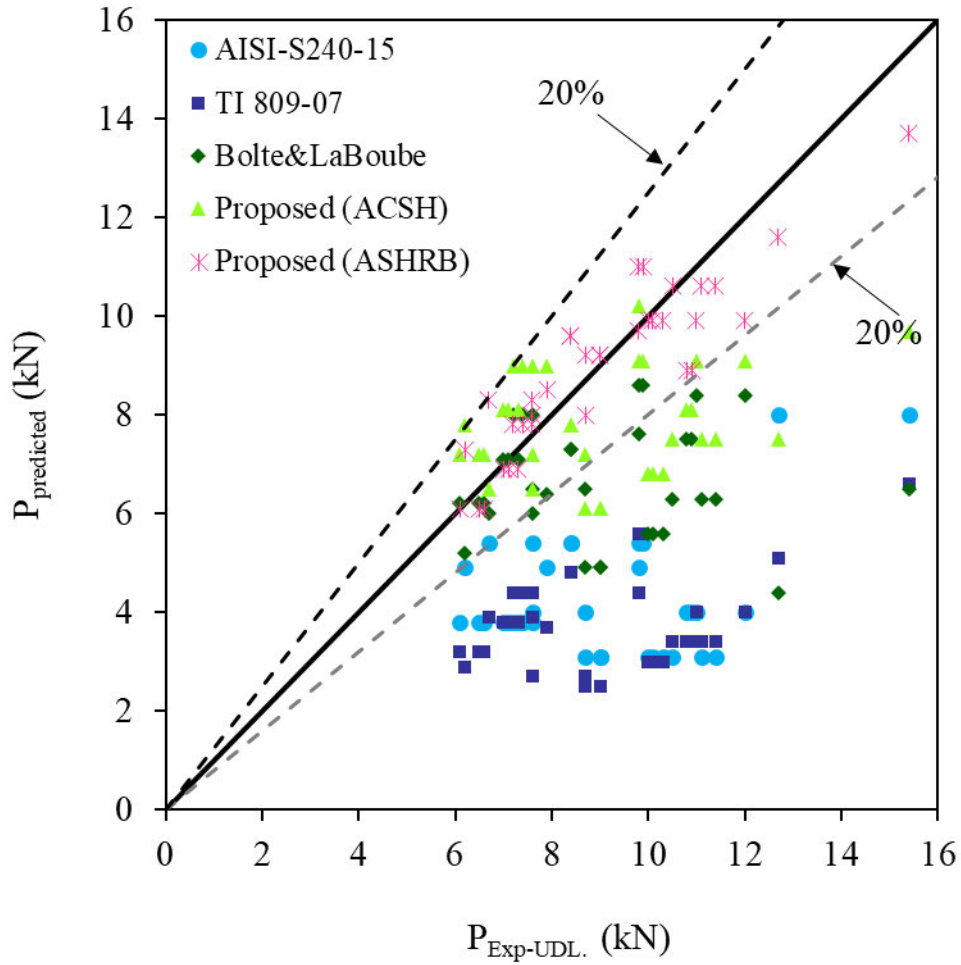


Figure 5.25 Comparison of experimental ultimate strengths ($P_{Exp-UDL.}$) with those of current and proposed design rules ($P_{Predicted}$), based on ultimate deformation limit (UDL).

Although statistically these design expressions yield a favourable prediction to estimate the bearing capacity, the equations are manufacturer specific rather than product specific and should not be used beyond the limits of the material properties and shapes of the tested specimens. Furthermore, assessments of the proposed design rules are required by conducting more numerical and experimental studies for a wide range of sections.

5.5. Capacity reduction factor (ϕ_w)

The North American Specification (AISI, 2016) recommends a statistical model to determine the capacity reduction factor for use with the proposed capacity design equations. This model

accounts for the variations in material, fabrication, and loading effects. The capacity reduction factor can be calculated by Eq. (5.8a):

$$\phi_w = 1.52M_mF_mP_me^{-\beta_0\sqrt{V_M^2+V_F^2+C_nV_P^2+V_Q^2}} \quad (5.8a)$$

where ϕ_w is the resistance factor; M_m , V_m (1.1, 0.06) are the mean and coefficient of variation of the material factor, respectively; F_m and V_F (1.0, 0.05) are the mean and coefficient of variation of the fabrication factor, respectively; V_Q (0.21) is the coefficient of variation of load effect; β_0 is the target reliability index for aluminium structural members which is recommended as a lower limit in the AA Specification (2015); $C_n = \frac{n^2-1}{n^2-3n}$ is the correction factor depending on the number of tests n ; P_m is the mean value of the test-to-predicted load ratios; V_P is the coefficient of variation of the test-to-predicted load ratios.

Eq. (5.8b) can be obtained by substituting all the above values into Eq. (5.8a) as follows:

$$\phi_w = 1.672P_me^{-2.5\sqrt{0.0502+C_nV_P^2}} \quad (5.8b)$$

Eq. (5.8b) was used to determine the capacity reduction factors for the values obtained from the proposed design equations. According to the proposed equations and the mean and COV values in Table 5.8, the capacity reduction factors (ϕ_w) were found to be 0.89 and 0.91. Therefore, it is recommended to use a ϕ_w value of 0.85 for all the proposed equations to estimate the strengths of aluminium sub-heads with removable beads, based on the maximum load and ultimate deformation limit (UDL).

5.6. Conclusion

In this paper, the results of the test program covering 36 tests, along with the proposed design rules to estimate the bearing strength of aluminium sub-head sections with removable beads

in window wall systems, are presented in detail. The specimens were different in terms of geometric sections, engagement length, and bearing width. Yielding and fracture at the web-flange junction, excessive deflection of the flange, rotation of the removable bead, and crushing of the flange groove were the main failure modes observed in the tests. During the tests, the removable bead was twisted, causing greater fracture at the web-flange junction of the bead, which can be referred to as the major distinction between failure modes in C-shaped sub-heads and sub-heads with removable beads, especially in the specimen with shorter flange length. A comparison of ultimate bearing capacities obtained from the tests with predictions from the available cold-formed steel design rules, including the American Iron and Steel Institute (AISI S240, 2015), and the U.S. Army Corps of Engineers (TI 809-07, 1998) showed that the design strengths predicted by the aforementioned specifications are unreliable. The comparison of the ultimate bearing capacities obtained from the tests with the design equations recommended by the authors for conventional C-shaped aluminium sub-heads also showed that those equations are not suitable to accurately predict the bearing capacities of aluminium sub-heads with removable beads. Thus, new design equations have been proposed in this study to accurately estimate the bearing capacity of aluminium sub-head sections with removable beads. The findings of this research signified that the proposed equations are reliable and in precise agreement with the experimental results for both the 15 mm and 25 mm load cases. Furthermore, the bearing capacities were found to be highly dependent on the section geometries of removable beads in comparison with the base section. Additional numerical and experimental studies are suggested to be carried out to expand the applicability of the proposed design equations to aluminium sub-heads with removable beads with a wider range of section geometries. Furthermore, in this study bearing width was conservatively assumed to be concentrated at the mullion reactions, while the head transom distributes the load from the mullion and contact the bead flange. Hence, for accurate prediction of the contact length between the bead flange and window wall frame (mullion and head transom), full-scale test and FEM are required.

6. NUMERICAL STUDY ON BEARING BEHAVIOUR AND DESIGN OF ALUMINIUM SUB-HEAD WITH REMOVABLE BEAD SECTIONS IN FAÇADE SYSTEMS

This chapter includes an unpublished paper. The bibliographic details of the co-authored paper, including all authors, are:

Akbari, M., Gunalan, S., Talebian, N., Gilbert, B.P., Guan, H.

Numerical Study on Bearing Behaviour and Design of Aluminium Sub-Head with Removable Bead Sections in Façade Systems

My contribution to the paper involved:

Literature review, experimental works, result analysis, discussion of the results, writing, editing and response to reviewers.

(Signed) _____ (Date) 14.11.2020

Name of Student: Masoumeh Akbari

(Countersigned) _____ (Date) 14.11.2020

Corresponding author of paper: Shanmuganathan Gunalan

(Countersigned) _____ (Date) 14.11.2020

Supervisor: Shanmuganathan Gunalan

Numerical study on bearing behaviour and design of aluminium sub-head with removable bead sections in façade systems

Abstract:

A window wall is a lightweight external wall composed of glass and aluminium, which does not carry any gravity loads from the building except for its own weight. Wind load is transferred to the main structural system through the connections of sub-frames (consisting of sub-heads and sub-sills) with slabs. An aluminium sub-head with a removable bead (ASHWRB) is a common type of sub-head consisting of two parts: a base and a bead. Under wind load, the bead flange is directly loaded by the mullion and undergoes bearing failure due to its long length. This paper presents a detailed numerical study on the bearing capacities of the ASHWRB sections subject to wind loading. For this purpose, finite element models were simulated using ABAQUS/CAE and validated with our previously conducted experimental work in terms of ultimate loads, load-displacement curves, and failure modes. Validated finite element models of the ASHWRB sections were then used for an extensive parametric study covering a wide range of thicknesses, flange widths, bearing widths, and engagement lengths. Notably, the ultimate loads obtained from the parametric study are not product nor manufacturer specific, whereas, the data obtained from experimental study is specific to the manufacturer products. The acquired bearing database was used for a detailed assessment of the consistency and reliability of the previously proposed design rules by the authors (DRA) based on the experimental tests as well as currently available cold-formed steel design rules (DRSs). It was found that the bearing capacities determined by both DRA and DRSs are unreliable for predicting the bearing capacities of the ASHWRB sections in the window wall. Thus, modifications were made to DRA and DRSs. Consequently, new design rules were proposed in this paper (DRA_P), which accurately predicted the bearing capacities and correlated very well with the numerical results.

Keywords

Aluminium sub-heads; Removable bead; Window wall; Bearing behaviour; Numerical study.

6.1. Introduction

Façade engineering is an area of immense growth, which is attracting significant interest from the building industry in Australia. In modern construction, lightweight materials such as aluminium afford the façade industry an opportunity to design and manufacture high performance elements which are safe, sustainable, environmentally friendly, non-corrosive, and much lighter than traditional designs. A window wall is a kind of non-load bearing building envelope, that provides protection from the exterior environmental actions, as well as an aesthetic appearance to the building. The currently increased demand in the use of aluminium window walls in the building industry has prompted the need for more accurate and up-to-date design standards. Window wall systems are usually installed through unitised panel wall systems. This system is pre-assembled and pre-glazed in the factory or shop as a series of panels in a controlled condition, which are then brought to the site. Unitized window wall systems also minimize on-site labour and erection costs and reduce the installation time (Kawneer, 1999; Allana and Carter, 2012; Kissel and Ferry, 2003). The aluminium window wall frames are comprised of mullions, heads, and sills for fitting the infill elements (generally made of glass). These frames are positioned between sub-heads and sub-sills without any screw connection, as shown in Figure 6.1. In Australia generally, 6063-T6 aluminium alloy is used to fabricate the aluminium framing members. However, aluminium has a distinct disadvantage of being three times more deformable than steel. Therefore, the structural elements made of aluminium are proven to experience excessive deformation and bearing failure. Sub-heads are the horizontal structural members at the top of the aluminium window walls. To accommodate adequate building and thermal movements, as well as fabrication and installation tolerances of an aluminium frame, a gap is left between the top of the mullion and the sub-head. Hence, the sub-head must have a longer flange length compared to the sub-sill. Sub-heads function as connection members that transfer the wind forces from the window wall frames to the main structural system. Under this loading condition, the sub-head undergoes bearing failure, and special attention must be paid to its design. The sub-head cross-sections are complex and vary in dimensions based on the architectural requirements and the connection between the sub-heads and the mullions. A sub-head with a removable bead (ASHWRB) is a kind of sub-head including two parts (a bead and a base), which are connected together without any screw fastener. This enables easy removal of the bead from the system in the event of construction faults. Furthermore, the bead acts as the critical component in resisting the concentrated load. Under wind load the

bead is subjected to bearing failure due to the bending of its long, cantilever flange. Determining the bearing capacity of the ASHWRB sections is challenging due to the complexity of cross sections and the nature of bearing failures. With significant advances in computer technology, advanced numerical analyses have been proven to offer much more detailed results and save a great deal of time and effort compared with the experimental investigations. Hence, in order to obtain reliable bearing capacity data of the ASHWRB sections, numerical analyses are considered an ideal alternative.

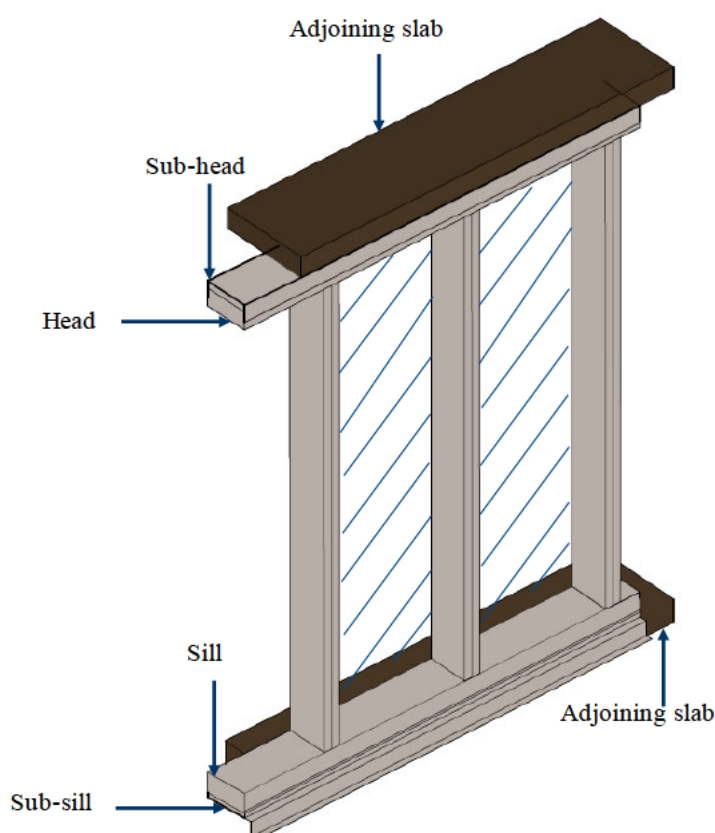


Figure 6.1 Window wall system.

Since aluminium alloys share many similarities with cold-formed steel, the application of the design methods developed for cold-formed steel structures may give insight into the design of similar aluminium structural elements. Several finite element analysis methods were previously utilised to simulate the cold-formed steel stud-to-track connections (with similar structural behaviour as aluminium sub-heads to mullion connections) subjected to different loads such as blast and earthquake (Bondok et al., 2015; Bondok and Salim, 2014; Bewick,

and Williamson, 2014; Shakeel et al., 2019; Rahmanishamsi et al., 2016; Fiorino et al., 2015; Fiorino et al., 2017). Experimental tests were carried out to investigate the bearing capacities of aluminium C-shaped sub-head (ACSH) sections and the ASHWRB sections at Griffith University by Akbari et al. (2020a, 2020b) using the products supplied by a particular Australian's manufacturer. Although, bearing capacities of the ACSH sections were recently investigated through FEA by Akbari et al. (2020c), no numerical analysis has been implemented to further evaluate the bearing failure mechanisms of the ASHWRB sections subjected to wind loads in window wall systems. Hence, further research and design guidelines are required to improve the accuracy of the previously proposed design rules (DRA) in (Akbari et al., 2020b, 2020c) to predict the bearing strengths of the ASHWRB sections based on a large number of numerical results.

Owing to the lack of numerical studies on the ASHWRB sections, this study was conducted to numerically investigate the bearing behaviour of the ASHWRB sections under the wind load and further investigate the influence of a wider range of design parameters. Accurate and reliable numerical models, using nonlinear static analysis with implicit integration scheme in ABAQUS/CAE, were firstly simulated and then validated against the experimental results Akbari et al. (2020b). The outcomes of this study show that the numerical results agreed well with the experiments in terms of the ultimate bearing loads, the load-displacement curves, and the failure modes. Subsequently, the validated finite element models based on the bearing capacity test results were extended to investigate the bearing capacities of the ASHWRB sections with various thicknesses, flange widths, bearing widths, and engagement lengths. Currently available aluminium provisions (AA, 2015, AS, 1997; EC9, 2007) do not cover the design of aluminium sub-head sections under bearing loads. Therefore, the applicability the DRSs (AISI S240, 2015; TI 809-07, 1998; SSMA, 2000; Bolte and LaBoube, 2004) and the previously proposed design rules by the authors based on the experimental tests (DRA) (Akbari et al., 2020b, 2020c) for the ASHWRB sections were evaluated based on the results of the parametric study presented in this paper. Specifically, the DRSs refer to the cold-formed steel design rules (including the guidelines given by the North American Standard for Cold-Formed Steel Structural Framing (AISI S240, 2015), the U.S. Army Corps of Engineers (TI 809-07, 1998), the Steel Stud Manufacturers Association (SSMA, 2000), and Bolte and LaBoube (2004)) for predicting the nominal strength of the stud-to-track connections. As the design guidelines given in both DRSs (AISI S240, 2015; TI 809-07, 1998; SSMA, 2000;

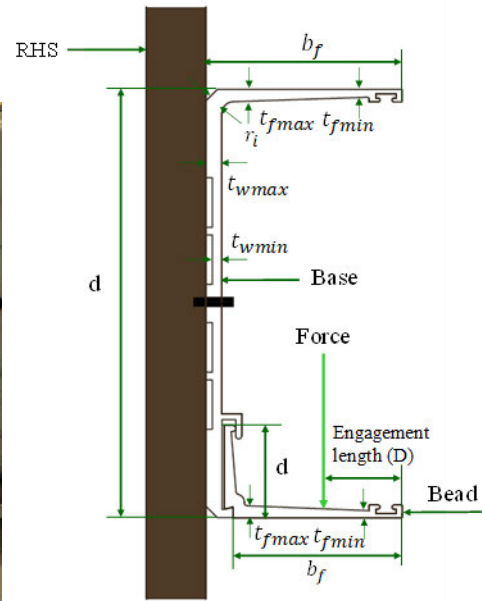
Bolte and LaBoube, 2004) and the DRA (Akbari et al., 2020b, 2020c) were found to be unreliable to predict the bearing capacities of a broad range of ASHWRB sections through the parametric study, suitable modifications were implemented to the available design equations (DRSs and DRA) and new design rules (DRA_P) were therefore proposed to accurately predict the bearing capacities of the ASHWRB sections.

6.2. Brief overview of experimental investigation

Akbari et al. (2020b) previously conducted an experimental study comprising 46 tests (including 10 repeated tests) on the ASHWRB sections. Figure 6.2 (a) and Figure 6.2 (b) show the detailed test set-up and the cross-section of an ASHWRB section, respectively. The experiments covered six different ASHWRB sections including two parts (i.e., 6 bases and 3 beads). The measured dimensions of the ASHWRB sections are given in Table 6.1. The web height ranged from 111 mm to 215 mm, while the flange widths ranged from 40 mm to 65 mm, and the specimen length was 1300 mm. The bearing tests were performed using a 500 kN MTS universal testing machine through displacement control at a constant speed of 2 mm/min. A specially designed loading frame was used to apply the force at the mid span of the bead flange. High-grade steel plates of precise lengths of 50 mm, 100 mm and 150 mm were bolted to the bottom of the loading frame for different tests. The centerline of the base's web was bolted to a stiff rectangular hollow section (rigid support) made of steel using three M12 bolts (See Figure 6.2 (a)). Two engagement lengths (D) (distance between the loading position and the outer edge of the flange grooves) of 15 mm and 25 mm were considered in the experimental study, as shown in Figure 6.2 (b). Note that a representative label “475059-520902/15/100” indicates that the base section is 475059, the bead section is 520902, the engagement length (D) is 15 mm, and the bearing width (N) is 100 mm.



(a) Test set-up



(b) Cross-section profile

Figure 6.2 Bearing test set-up and ASHWRB section profile Akbari et al., 2020b).

Table 6.1 Geometric details of the ASHWRB sections (Akbari et al., 2020b).

Section	b_f (mm)	d (mm)	r_i (mm)	$t_{f,max}$ (mm)	$t_{f,min}$ (mm)	$t_{w,max}$ (mm)	$t_{w,min}$ (mm)	L (mm)
Sub-head								
675028	64.74	163.05	4.38	3.46	1.97	4.02	2.96	1300
475066	39.99	111.68	4.6	3.47	2.40	4.24	2.54	1300
475059	50.81	111.33	4.14	3.12	1.91	3.99	2.27	1300
875103	64.88	214.1	4.48	4.03	2.92	3.98	3	1300
675019	51.01	162.5	4.39	3.53	2.39	4.1	2.37	1300
475072	64.94	112.46	4.415	3.41	1.94	4	2.99	1300
Bead								
476073	60.1	40.4	-	3.28	2.04	3.12	1.79	1300
520902	46.26	24.06	-	3.12	1.9	3	1.85	1300
165863	33.46	23.94	-	3	2.92	2.96	1.64	1300

6.3. Finite Element modelling

In this paper, the general-purpose analysis program ABAQUS version 6.14 was used to simulate the ASHWRB sections subjected to bearing failure due to the wind load. Nonlinear geometric and material quasi-static implicit dynamic analyses were performed on the models (ABAQUS, 2014).

The FE model in this study is comprised of four main components, namely: the base section, the bead, the bearing plates, and the rigid support, as shown in Figure 6.3. It should be noted that the influence of initial geometrical imperfections on the bearing capacities of the ASHWRB sections is barely perceptible. As a result, this was not considered in this study.

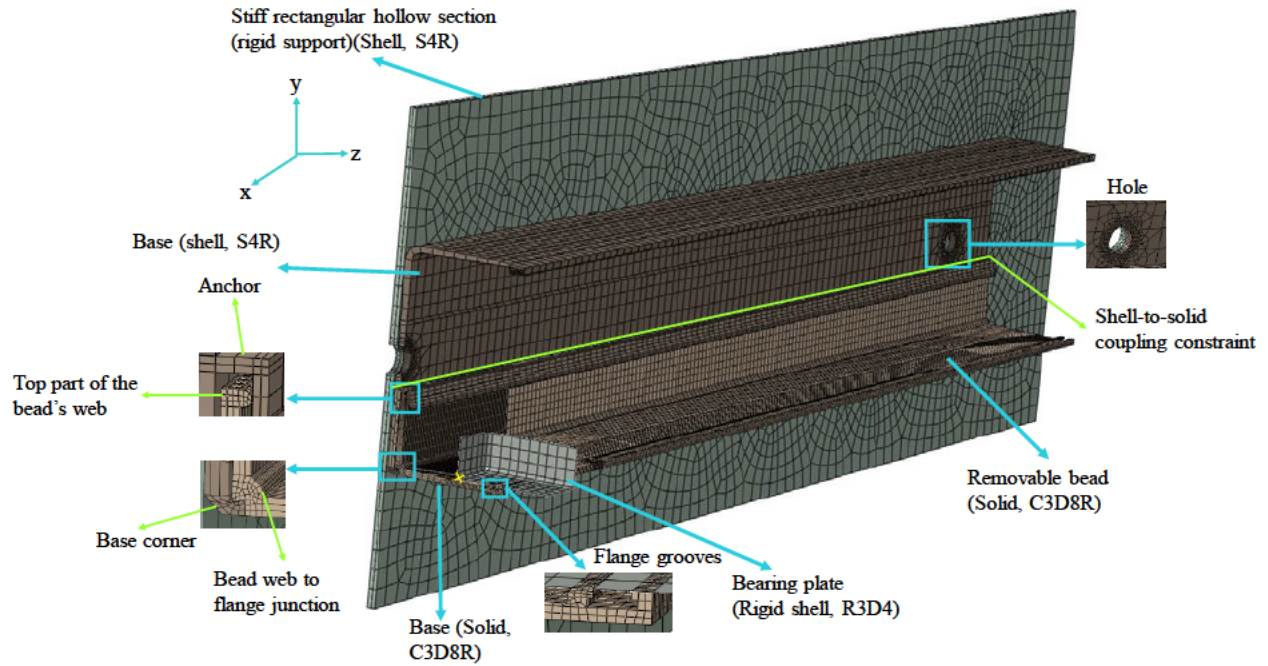


Figure 6.3 Simplified FE models (Test set-up).

6.3.1. Geometry, element types and mesh

The base and the rigid support were simulated using linear, 4-node deformable shell elements with reduced integration (S4R), due to their simple geometry as well as their broad usage in thin-walled structural analyses (recommended by (Natario et al., 2014)) (see Figure 6.3). However, an ASHWRB section has complicated geometric details and it is impossible to model these features by shell elements in ABAQUS, especially in areas when the bead is connected to the base, as shown in Figure 6.3. Hence, the bead and a part of the base in contact with the bead were modelled using 8-node, linear brick, solid elements (C3D8R) (see Figure 6.3). The cross sections of the solid elements were imported from Auto CAD, which enabled the accurate simulation of these areas. The rest of the base's cross-section modelled

using shell elements was partitioned to assign different measured thicknesses to different parts of the model. Thickness assignment and coordinates were explained by Akbari et al. (2020c) in detail. The respective solid and shell parts of the base were tied together using a shell-to-solid coupling connection, as shown by the green line in Figure 6.3. The bearing plate was modelled using 4-node rigid shell elements (R3D4) (see Figure 6.3).

For the FE model to accurately predict the bearing capacities of the ASHWRB section, suitable sizes of mesh for different parts of the FE model should be selected depending on the desired accuracy and time of analysis. Similar convergence studies reported by Akbari et al. (2020c) is adopted in this study for the ASHWRB sections. The global mesh size of 8 mm × 8 mm was adopted for the base with the shell elements. The C3D8R elements were modelled with the element size of 6 mm (for the base) and 4 mm (for the bead), whereas finer mesh of 1 mm was assigned to the bead flange (under the bearing plate). Also, finer meshes (between 0.5 mm to 1 mm) were used in the bead flange grooves, the web to flange junction of the bead, the top part of the bead's web (in contact with the anchor), the anchor, the base corner, and around the holes to capture the bearing behaviour accurately (Talebian et al., 2019). Additionally, a mesh size of 3 mm × 3 mm and 15 mm × 15 mm were used for the bearing plate and the rigid support, respectively (see Figure 6.3).

6.3.2. Material properties

Material properties of the ASHWRB sections were modelled using the von Mises yield criterion and isotropic hardening. Tensile coupons were taken from the web of the base and the bead in the longitudinal direction for each section in (Akbari et al., 2020b) based on AS 1391 (1997). The results of coupon tests in terms of the elastic modulus (E), as well as the yield and ultimate strengths (f_y and f_u) are reported in Table 6.2. Since excessive deflection occurred in the bearing tests, the engineering stress-strain curves obtained from coupon tests were converted to true stress–plastic strain curves using Eq. (6.1), Eq. (6.2a) and Eq. (6.2b).

$$\sigma_{true} = \sigma_{eng}(1 + \varepsilon_{eng}) \quad (6.1)$$

$$\varepsilon_{true} = \ln(1 + \varepsilon_{eng}) \quad (6.2a)$$

$$\varepsilon_{true(pl)} = \varepsilon_{true} - \frac{\sigma_{true}}{E} \quad (6.2b)$$

where σ_{true} is the true stress (MPa), ε_{true} is the true strain, $\varepsilon_{true(pl)}$ is the true plastic strain, σ_{eng} is the engineering stress (MPa), and ε_{eng} is the engineering strain. Figure 6.4 shows the typical true stress-strain curve for the aluminium alloy 6063-T6 (675028 section).

Table 6.2 Mechanical properties of the ASHWRB sections (Akbari et al., 2020b).

Section	E (MPa)	f _y (MPa)	f _u (MPa)
Sub-head			
675028	61944	217.6	234.9
475066	61251.5	252.0	272.2
475059	66374.5	251.9	276.6
875103	62408	204.7	226.1
675019	62762	209.6	229.6
475072	68342	222.6	248.1
Bead			
475073	66934.2	249	272.9
520902	63448.3	260.5	282.3
165863	69446	239	260.1

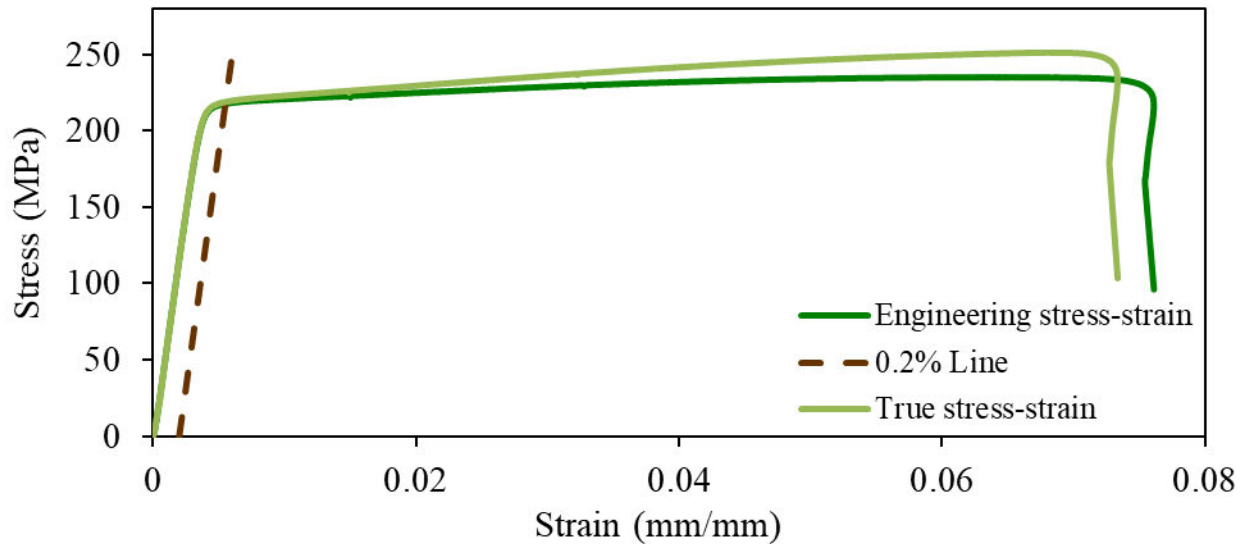


Figure 6.4 Stress-strain curve (675028 section).

6.3.3. Load and boundary conditions

To simulate the actual experimental scenario, precise boundary conditions were assigned to the models. Due to symmetry in the loading and boundary conditions as well as in the geometry, half FE model (half of the test set-up) by considering the vertical symmetric plane was developed in this study, as shown in Figure 6.5. To simulate the symmetrical conditions, rotations about the X and Y axes (R_x and R_y) and displacement along the Z axis (U_z) were restrained at the mid-span. The wind load transferred from the mullion to the sub-head is simulated by applying vertical displacement on top of the bearing plate at the midspan of the bead flange. As illustrated in the Figure 6.5, the boundary conditions were assigned to the bearing plates using reference points, in which all the translational displacements (U_x , U_y , U_z) and the rotations (R_x , R_y) except for the displacement in the Y direction (R_y) were fixed. Since the steel rectangular hollow section (RHS) was unable to move or rotate in the bearing test, six degrees of freedom were all fixed to zero, as shown in Figure 6.5. In the bearing test, the base was fixed on the RHS using three bolts (M12) along the centre line of the web. Hence, in the half FE model, the 12 mm holes were created at the corresponding bolt locations at the base's web and the rigid support, and the perimeter of the holes in the base were connected to the rigid support using MPC tie connections (ABAQUS, 2014), as shown in Figure 6.5.

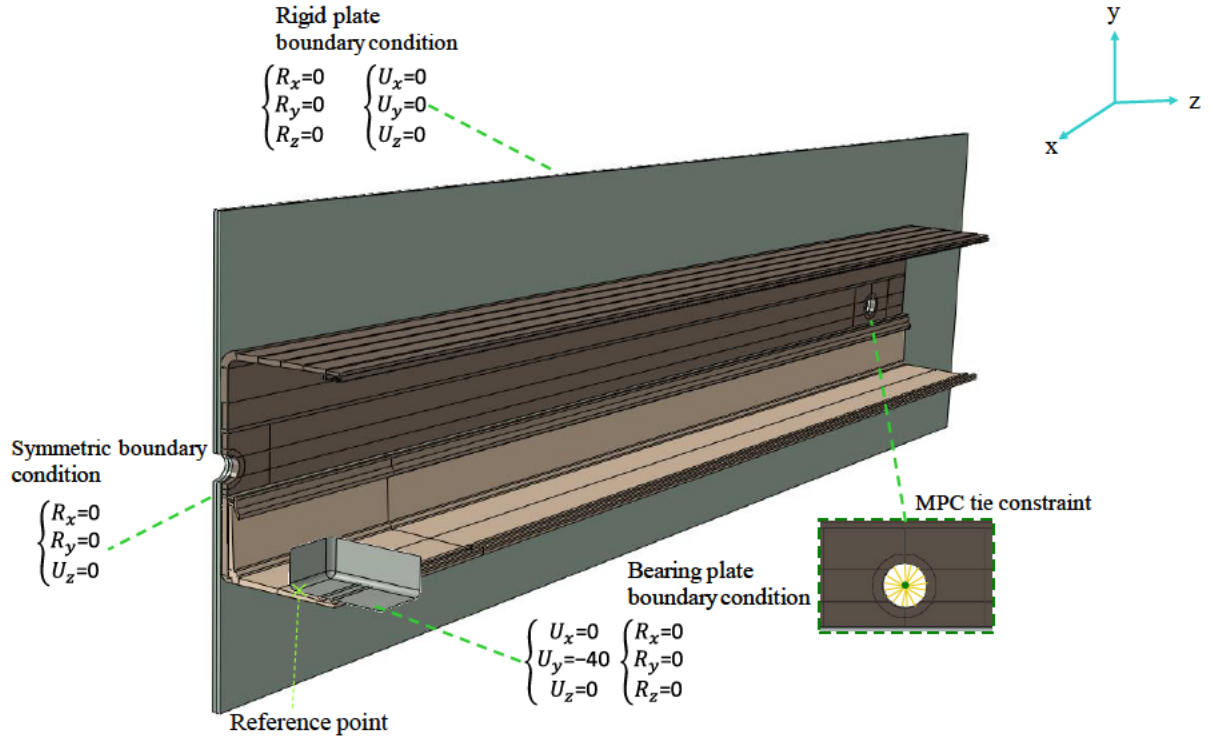


Figure 6.5 FE boundary conditions and bolted connection.

6.3.4. Contact definition

In this study, the contact pair algorithm with finite sliding was employed to simulate the contact between the deformable bodies (the base and bead) and the rigid elements (bearing plate and steel plate). Consequently, suitable contacts were defined between the bead's bottom flange and the bearing plate, between the base and the bead, as well as between the base's web and the steel plate, as illustrated in Figure 6.6 (a), Figure 6.6 (b), and Figure 6.6 (c), respectively. The normal behaviour of contacts was defined in the contact formulation by the hard contact algorithm, which ensures no penetration of the slave surface into the master surface. The classical isotropic Coulomb model with penalty friction formulation methods was also used in this study to define the tangential contact and the friction between the bead's flange and the bearing plate. In the bearing tests, grease was smeared on the bead's flange and the bearing plate. Hence, zero friction coefficient was assigned in this study in the contact between the bearing plate (master) and the bead's flange (slave) to replicate the real situation of the test.

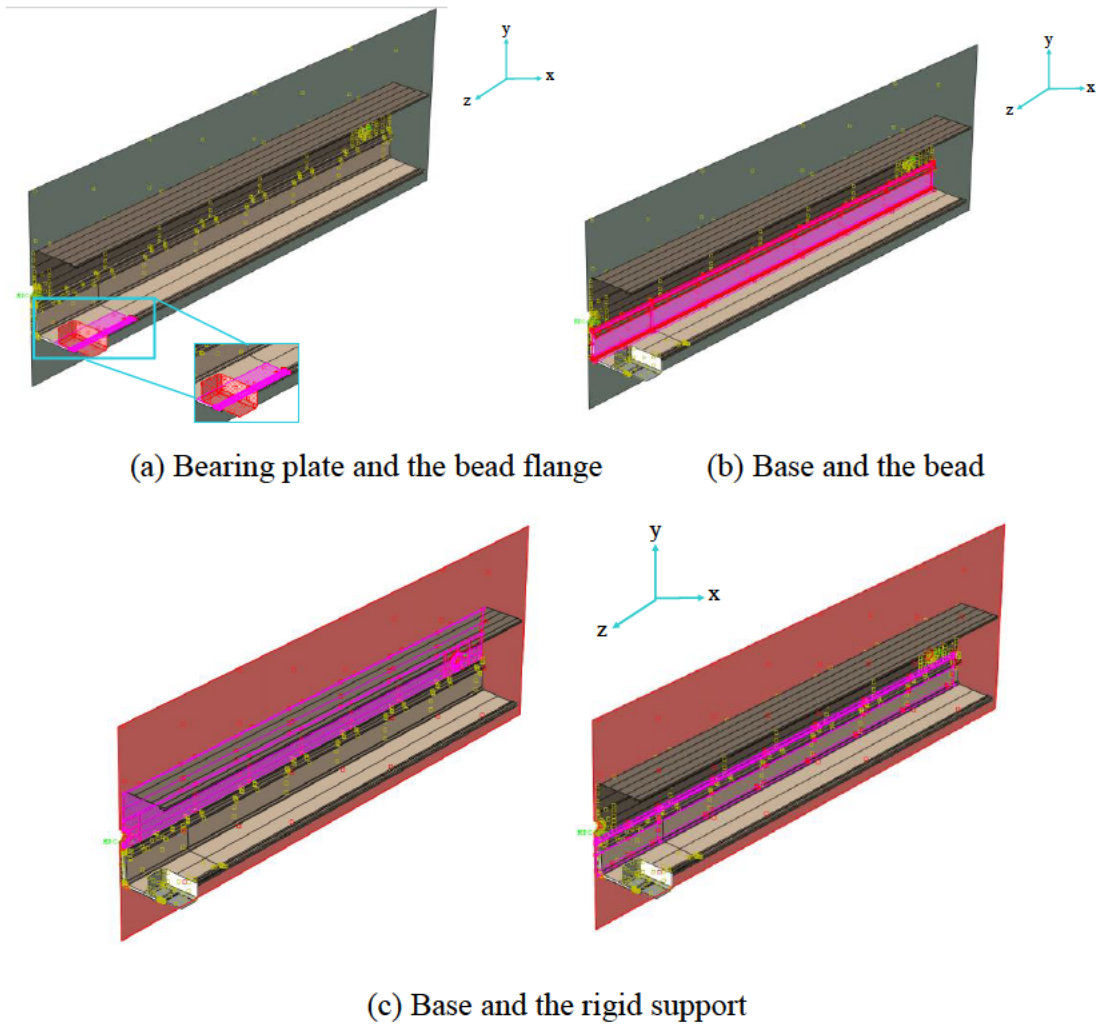


Figure 6.6 Interactions between elements (master surface shown in red and slave surface shown in purple).

6.4. Analysis results and validation

The developed FE model was analysed using non-linear static analysis solver, and was validated against Akbari et al.'s (2020b) bearing test results (36 tests) for the ASHWRB sections in terms of the ultimate failure loads, the load-displacement curves, and the failure modes.

In the bearing test, a maximum load (second peak) ($P_{Exp-Max2}$) occurred at a very large deformation, when the bearing plate was wedged in the groove element of the bead. In order to put a limitation on the deflection of the bead flange, an ultimate deformation limit (UDL) (Gilbert and Rasmussen, 2011; Yura et al., 1981; AS 4084, 2012; Brühl et al., 2011;

Yasumura and Kawai, 1998) was set by Akbari et al. (2020b) to define the ultimate capacities, as shown in Figure 6.7. If $P_{Exp-UDL}$ was greater than $P_{Exp-Max1}$ (first peak in the load-displacement curve) then $P_{Exp-UDL}$ was taken as the load corresponding to the ultimate deformation limit; otherwise, $P_{Exp-Max1}$ was considered. Table 6.3 shows a strong agreement between the experimental bearing capacities ($P_{Exp-UDL}$ and $P_{Exp-Max2}$) and the FEA results ($P_{FEA-UDL}$ and $P_{FEA-Max2}$) satisfying the maximum load (Max) and the ultimate deformation limit (UDL) criteria. The mean (both being 1.00) and COV (both being 0.07) values of the P_{Exp}/P_{FEA} ratios suggest that the numerical models can accurately predict the bearing capacities of the ASHWRB sections for both criteria (Max and UDL).

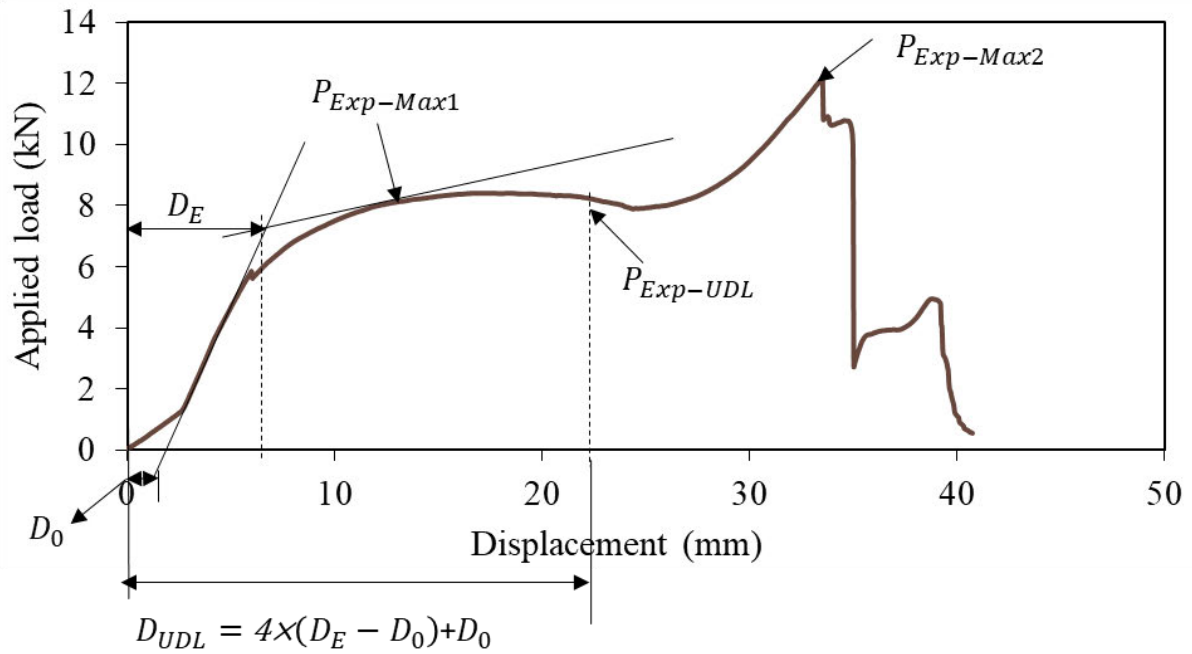


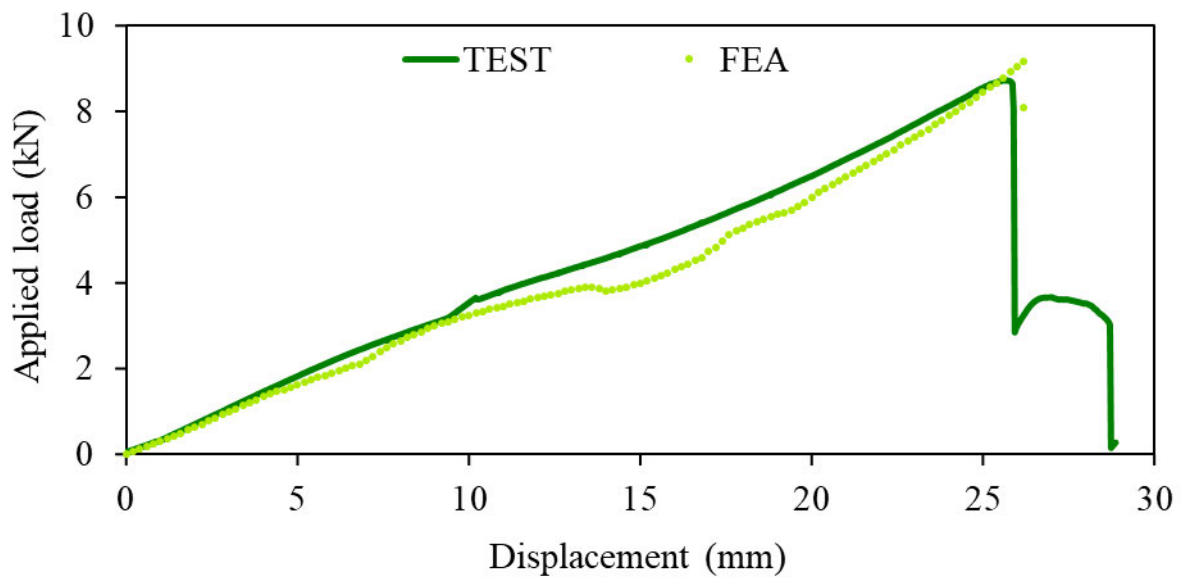
Figure 6.7 Typical experimental load-displacement curve showing the maximum load (Max) and ultimate deformation limit (UDL) Akbari et al. (2020b).

Table 6.3 Comparison of test and FEA results for maximum load and ultimate deformation limit.

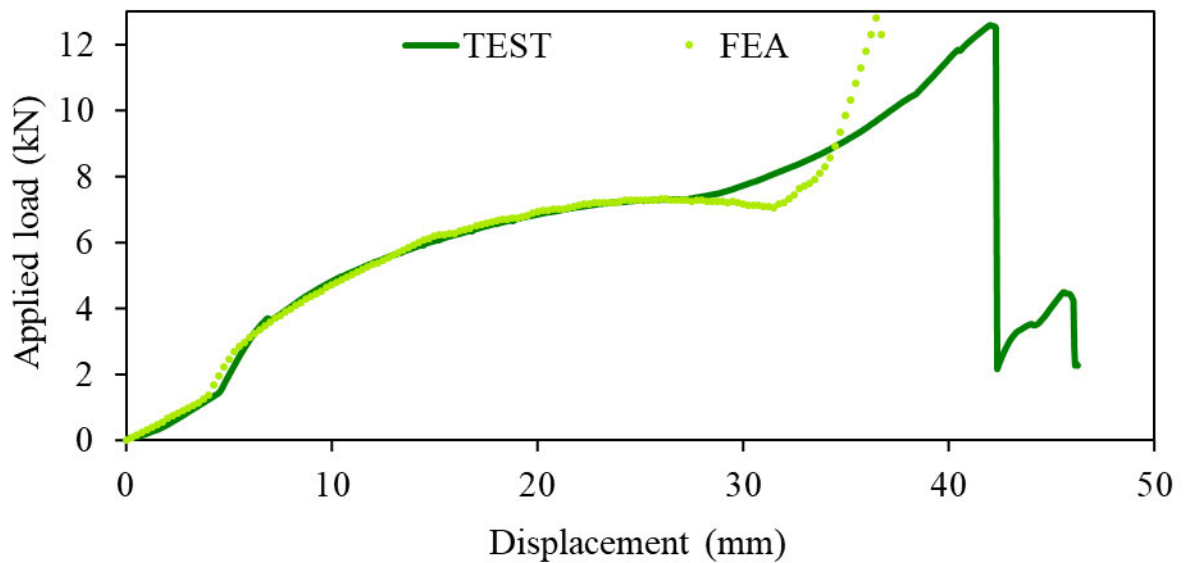
Specimen details			$P_{Exp-Max2.}$ (kN)	$P_{FEM-Max2.}$ (kN)	$P_{Exp-UDL.}$ (kN)	$P_{FEM-UDL.}$ (kN)	$\frac{P_{Exp-UDL.}}{P_{FEA-UDL.}}$	$\frac{P_{Exp-Max2.}}{P_{FEA-Max2.}}$
D (mm)	Section	N (mm)						
15	675028-475073	50	9	9.4	9	8.6	0.96	1.05
		100*	10	9.8	10	9.8	1.02	1.02
		150	10.7	10.8	10.5	10.8	0.99	0.98
	475066-165863	50	6.3	6.7	6.2	6.3	0.94	0.98
		100*	8.2	8.2	7.9	8.0	1.00	0.98
		150	10.4	9.4	9.8	9.7	1.11	1.01
	475059-520902	50	7.6	8.7	7.6	8.7	0.88	0.88
		100*	10.8	10.9	10.8	10.9	0.99	0.99
		150	12	12.2	12	12.2	0.99	0.99
	875103-475073	50	9	8.2	9	8.2	1.09	1.09
		100*	10.3	9.8	10.3	9.8	1.05	1.05
		150	11.4	11.9	11.4	11.9	0.96	0.96
	675019-520902	50	8.7	9.2	8.7	9.2	0.95	0.95
		100	11	10.1	10.9	10.1	1.09	1.08
		150	11	11.1	11	11.1	0.99	0.99
	475072-475073	50	8.7	7.9	8.7	7.9	1.10	1.10
		100*	10.1	9.0	10.1	9.0	1.12	1.12
		150	11.1	10.1	11.1	10.1	1.09	1.09
25	675028-475073	50	11	10.7	6.5	6.8	1.03	0.95
		100*	12.7	12.0	7.1	7.5	1.06	0.94
		150	13.7	12.9	7.4	8.0	1.06	0.92
	475066-165863	50	12.7	12.7	12.7	12.7	1.00	1.00
		100*	15.5	17.3	15.4	17.3	0.90	0.89
		150	20.1	19.7	20.1	19.7	1.02	1.02
	475059-520902	50	8.9	8.9	7.6	6.3	1.00	1.21
		100*	9.4	10.2	8.4	8.5	0.93	0.99
		150	10.2	11.3	9.8	9.6	0.90	1.03
	875103-475073	50	10	9.9	6.1	7.3	1.01	0.84
		100*	13	12.9	7.3	7.5	1.01	0.98
		150	14.2	13.2	7.6	8.0	1.08	0.95
	675019-520902	50	7.2	8.1	6.7	7.0	0.89	0.96
		100	12.1	12.5	8.4	8.5	0.96	0.98
		150	12.7	13.4	9.9	9.4	0.95	1.05
	475072-475073	50	9.8	9.7	6.6	6.8	1.01	0.97
		100*	12.7	12.8	7	7.0	0.99	1.00
		150	13.9	14.8	7.2	7.5	0.94	0.96
Mean							1.00	1.00
COV							0.07	0.07

The load-vertical displacement curves of the mid-span of the bead's flange obtained from the numerical analyses were also compared with the experimental results for the engagement

lengths of 15 mm and 25 mm, as shown in Figure 6.8 (a) and Figure 6.8 (b), respectively. Both comparisons show a strong agreement in terms of the ultimate loads and the load-displacement behaviours of the ASHWRB sections in the linear and non-linear stages. Minor discrepancies in the second peak were observed in the failure stage. It is believed that such a difference was due to the complex geometry of the flange grooves and penetration of the bearing plate into the grooves, as observed in the experiments Akbari et al. (2020b).



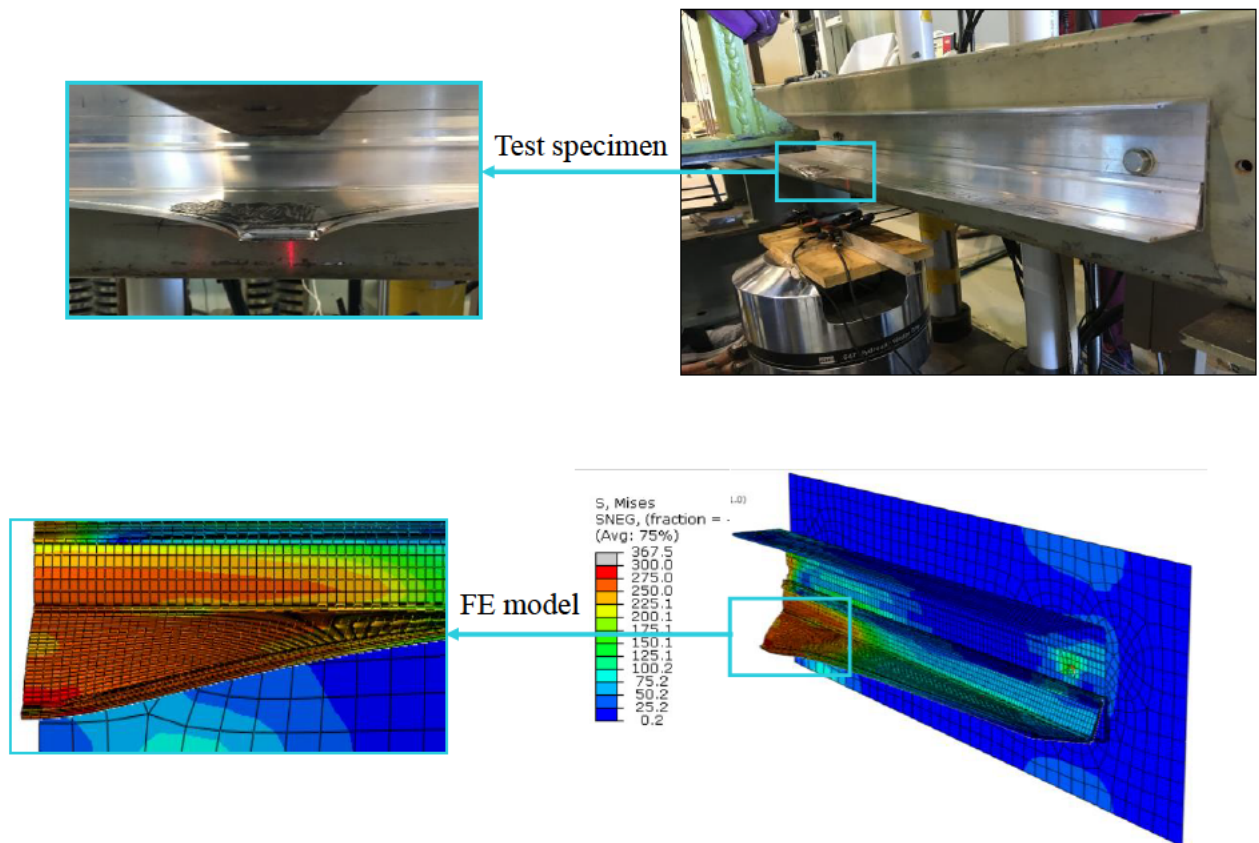
(a) 15 mm engagement length (675019-520902/15/50)



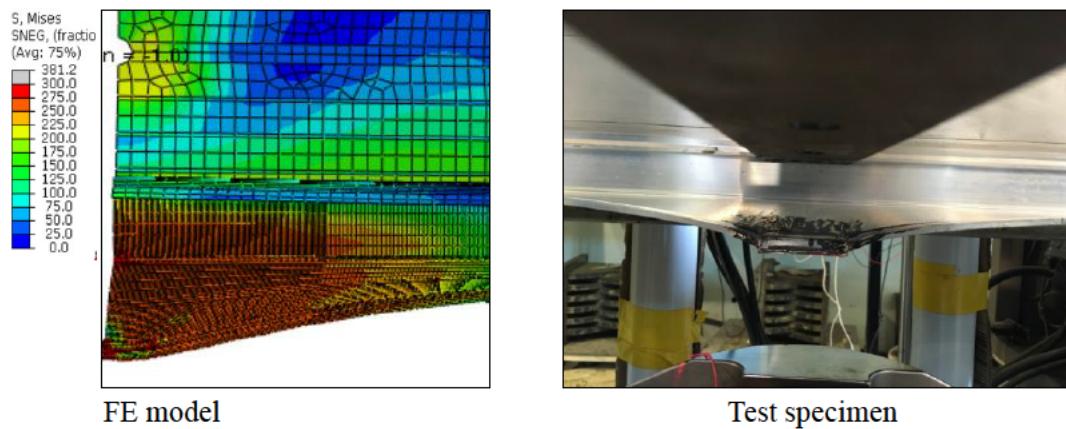
(b) 25 mm engagement length (475072-475073/25/100)

Figure 6.8 Comparison of experimental and numerical load versus vertical displacement curves.

The governing modes of failure observed in the bearing tests of the ASHWRB sections were yielding and fracture at the web-flange junction of the bead, excessive deflection of the bead's flange, the rotation of the bead, as well as slipping of the bearing plate caused by the crushing of the flange Akbari et al. (2020b). The loading conditions and the section geometries of the bead were found to be critical factors affecting the failure mode of the ASHWRB sections. The developed FE models were validated based on the failure modes observed in the bearing tests. The failure modes of the ASHWRB sections under two engagement lengths of 15 mm and 25 mm as observed in the experiments and predicted from the numerical analyses are compared in Figure 6.9 and Figure 6.10, respectively. It is evident that similar failure modes were exhibited both experimentally and numerically.

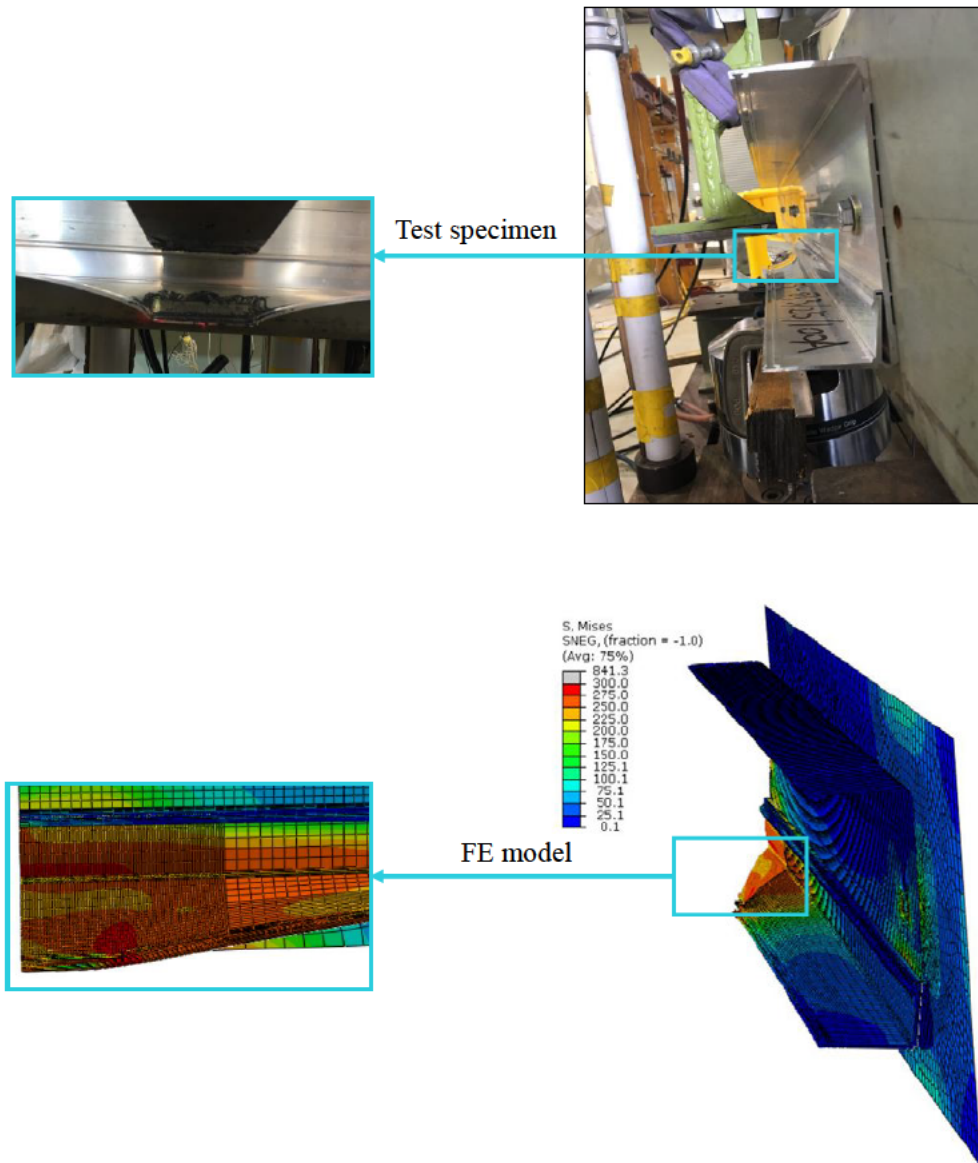


(a) 475072-475073/15/50

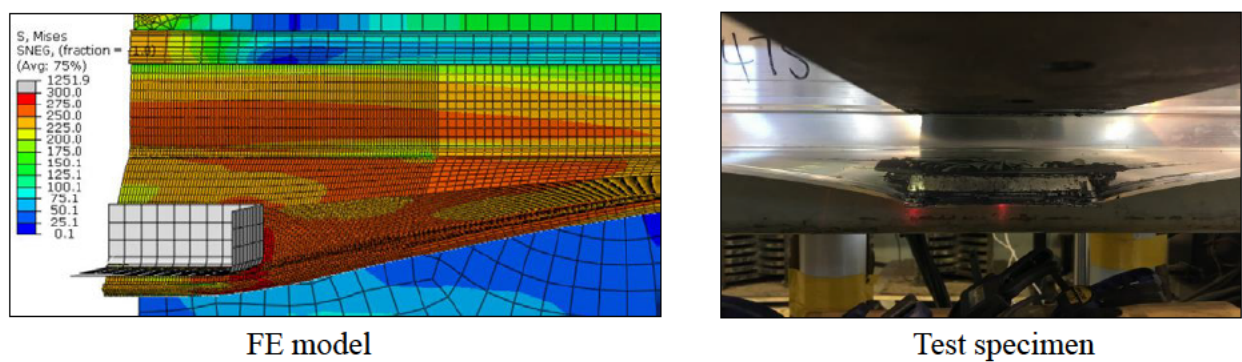


(b) 875103-475073/15/50

Figure 6.9 Comparison of experimental and numerical failure modes under 15 mm engagement length.



(a) 675028-475073/25/100



(b) 475072-475073/25/100

Figure 6.10 Comparison of experimental and numerical failure modes under 25 mm engagement length.

6.5. Parametric study

The validated FE model, discussed in the previous section, was utilised as a basis for the parametric study to create an extensive bearing capacity database. In the parametric study, the impacts of four key parameters (bearing width (N), flange width (b_f), thickness (t), and engagement length (D)) on the bearing behaviour of the ASHWRB sections were investigated using 144 FE models. Table 6.4 presents the detailed parameters. These parameters were chosen based on the design equations derived from the experimental results Akbari et al. (2020b). This parametric study covered 8 ASHWRB sections with their flange widths (b_f) in the range of 50 mm to 100 mm, and the nominal thickness (t) in the range of 2 mm to 4 mm. Also, three bearing widths (N) of 50 mm, 100 mm and 150 mm and six engagement lengths (D) of 5 mm, 10 mm, 15 mm, 20 mm, 25 mm and 30 mm were considered. The same specimen length of 1300 mm was also used herein. The results acquired from the parametric study are used to assess the suitability of the relevant design rules given in DRSs (AISI S240, 2015; TI 809-07, 1998; SSMA, 2000; Bolte and LaBoube, 2004) and DRA (Akbari et al., 2020b, 2020c).

Table 6.4 Parametric study model details of the ASHWRB sections.

Section	d (base) (mm)	d (bead) (mm)	b_f (mm)	t (mm)	Aluminium grade	N (mm)	D (mm)	No of Models
1	100	25	50	2	6063-T6	50,100,150	05,10,15,20,25,30	18
2	100	25	50	3	6063-T6	50,100,150	05,10,15,20,25,30	18
3	100	25	65	2	6063-T6	50,100,150	05,10,15,20,25,30	18
4	100	25	65	3	6063-T6	50,100,150	05,10,15,20,25,30	18
5	100	25	65	4	6063-T6	50,100,150	05,10,15,20,25,30	18
6	100	25	100	2	6063-T6	50,100,150	05,10,15,20,25,30	18
7	100	25	100	3	6063-T6	50,100,150	05,10,15,20,25,30	18
8	100	25	100	4	6063-T6	50,100,150	05,10,15,20,25,30	18
	Total							144

The ASHWRB sections considered in the previous experimental study by Akbari et al. (2020b) have complex cross sections and are manufactured by a specific company. Hence, some simplifications to the cross section of ASHWRB were made in this numerical study, to

cover a wide range of the ASHWRB sections utilized in the façade industry. In the FE parametric model, the bead and the parts of the base with more details (including the bottom corner and the anchor in the middle of the base) were modeled with the solid elements, whereas the rest of the base were modeled with the shell elements. Cross-sections of the FE parametric model and the FE model validated by the tests are shown in Figure 6.11 (a) and Figure 6.11 (b), respectively. As can be seen, the inner part of the web to flange junction of the bead, comprised of three curves, was converted to an inclined line (①). Furthermore, the outer part of this area, consisting of curves and inclined lines (②), was simulated by straight horizontal and vertical lines, as shown in Figure 6.11. Another simplification was related to the bottom corner of the base (③). In this area, all the inclined and curved lines were also replaced by the horizontal and vertical lines to provide proper interlocking with the beads. Additionally, the anchor and the top part of the bead's web were simplified to rectangular shapes (④). In the experimental study (Akbari et al., 2020b) the maximum load occurred when the bearing plate was trapped within the groove element of the bead. In this situation, the bead's flange undergoes excessive deformation, and the ultimate load was influenced by the shape of the bead's flange grooves. To overcome this issue, the flange grooves were omitted from the parametric FE model. It should be noted that uniform thickness was assigned to the base and the bead in the parametric study. Furthermore, the effects of the web height of the base and the bead on the bearing capacities of the ASHWRB sections were investigated, and these parameters were shown not to influence the bearing capacities considerably (see Figure 6.12). Consequently, the web heights of $d = 120$ mm and 25 mm, respectively, were assigned to the base and the bead in the FE parametric models.

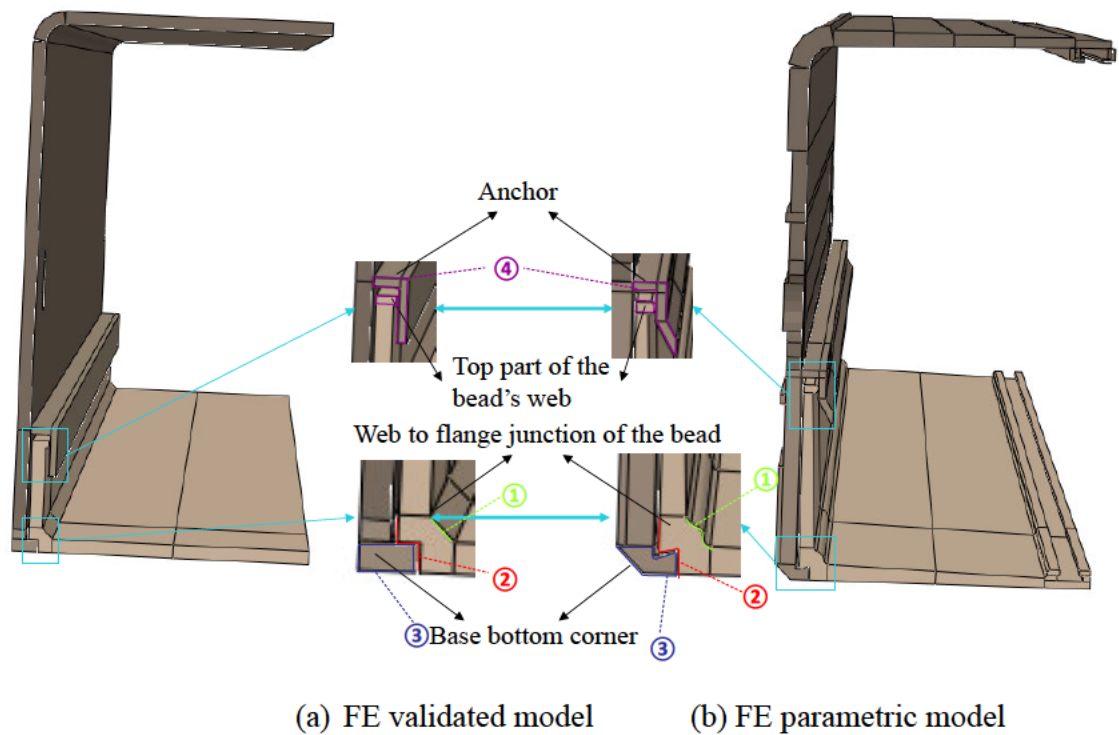


Figure 6.11 Cross sections of the FE model used for parametric study and validation.

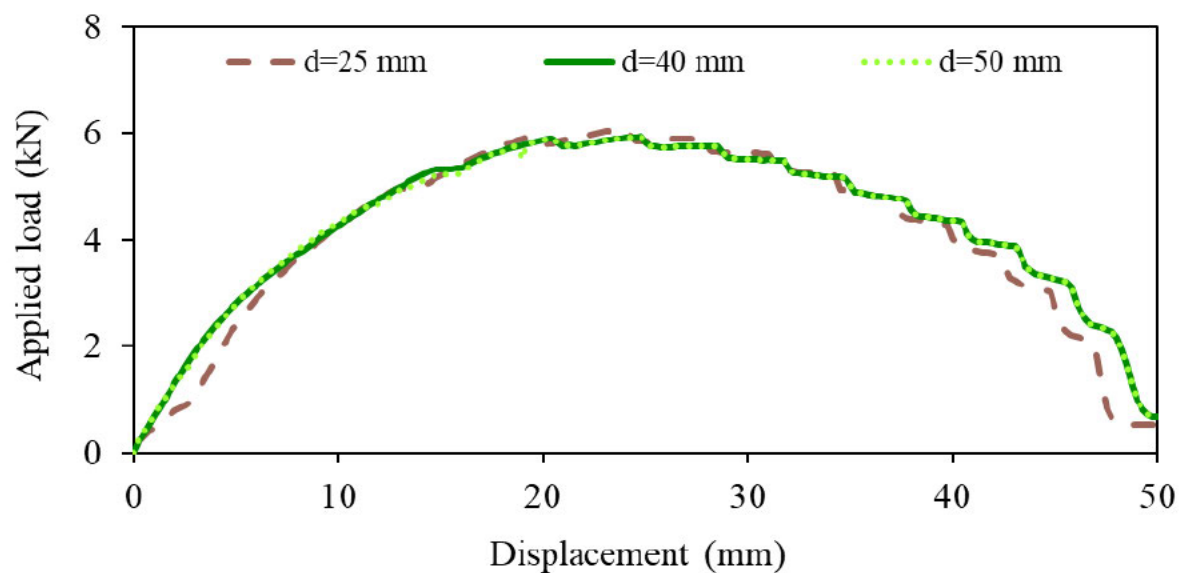


Figure 6.12 Load-displacement curves for different web height (d) of the bead ($b_f=65$ mm and $t=3$ mm, $N=50$ mm).

Since 6063-T6 aluminium alloy is generally used in the window wall systems in Australia, only this grade was used in the parametric study. This aluminium alloy has the nominal yield strength, the ultimate tensile strength, and Young's modulus of 172, 207 and 70,000 MPa, respectively (AS/NZS 1664.1, 1997). To define the material properties in the FE parametric analyses, a bi-linear material model implemented by Su et al. (2014, 2016) for the design of aluminium alloy structures was used in this study. This model considers the strain hardening and is composed of two stages: the initial elastic stage by the elastic modulus of the material (E), and the linear hardening stage with a strain hardening slope (E_{sh}). E_{sh} and the ultimate strain (ε_u) are expressed by Equations (3) and (4), respectively.

$$E_{sh} = \frac{f_u - f_y}{C_2 \varepsilon_u - \varepsilon_y} \quad (6.3)$$

$$\varepsilon_u = C_3 \left(1 - \frac{f_y}{f_u} \right) + C_4 \quad (6.4)$$

where f_y is the yield stress (MPa), f_u is the material ultimate stress (MPa), and ε_y is the yield strain. $C_2 = 0.5$, $C_3 = 0.13$, and $C_4 = 0.059$ are constants for 6063-T6 aluminium alloy (Su et al., 2014, 2016). Figure 6.13 shows the CSM material bilinear model used in the parametric study.

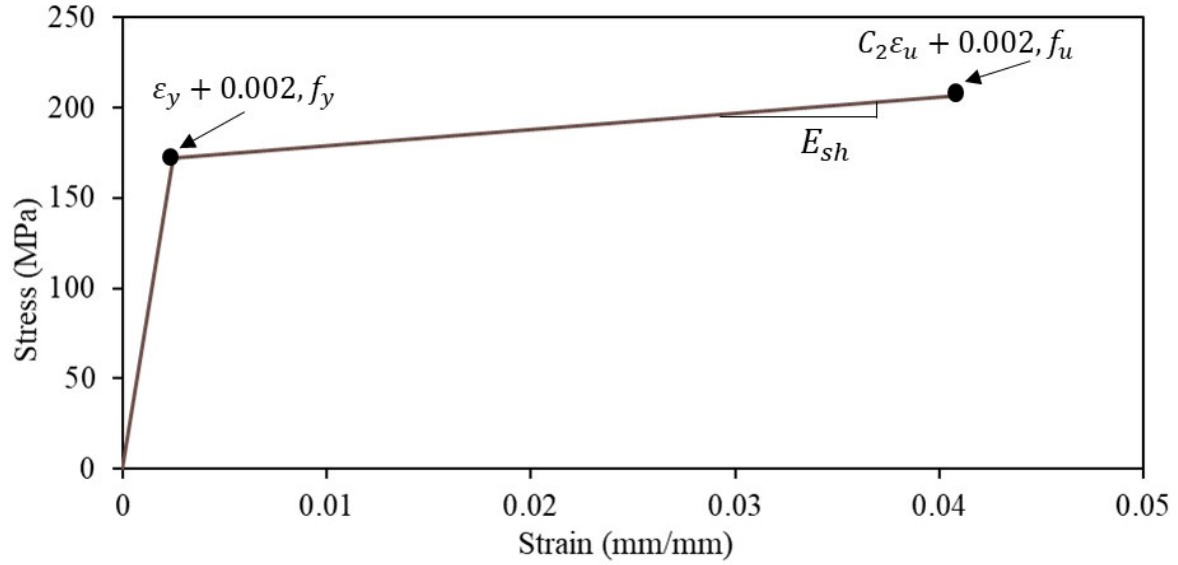


Figure 6.13 Bi-linear CSM model for 6063-T6 aluminium alloy.

6.5.1. Effects of different parameters on the bearing capacities

The influences of the main parameters on the overall bearing capacities of the ASHWRB sections are investigated in this section. Figure 6.14 shows the comparisons of the load-displacement curves under three bearing widths for Section 6 (Table 6.4). The figure reveals that increased bearing widths (N) enhance the bearing capacities of the ASHWRB sections. Figure 6.15 (a) and (b) also show the ultimate bearing capacities of the ASHWRB sections with the 15 mm and the 25 mm engagement lengths (D) versus different bearing widths (N). It is evident that increased bearing widths (N) from 50 mm to 150 mm give rise to a linear increase in the bearing capacities of the ASHWRB sections. These figures also show that the bearing capacities of the ASHWRB sections are more sensitive to section geometries with a greater bearing width ($N = 150$ mm) compared to a smaller bearing width ($N = 50$ mm).

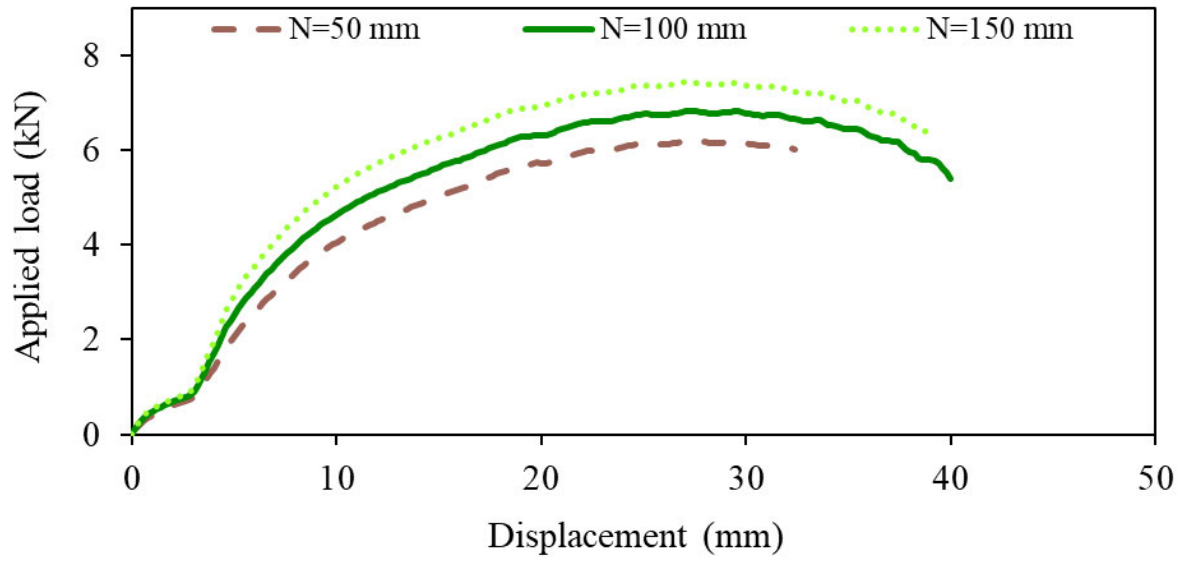
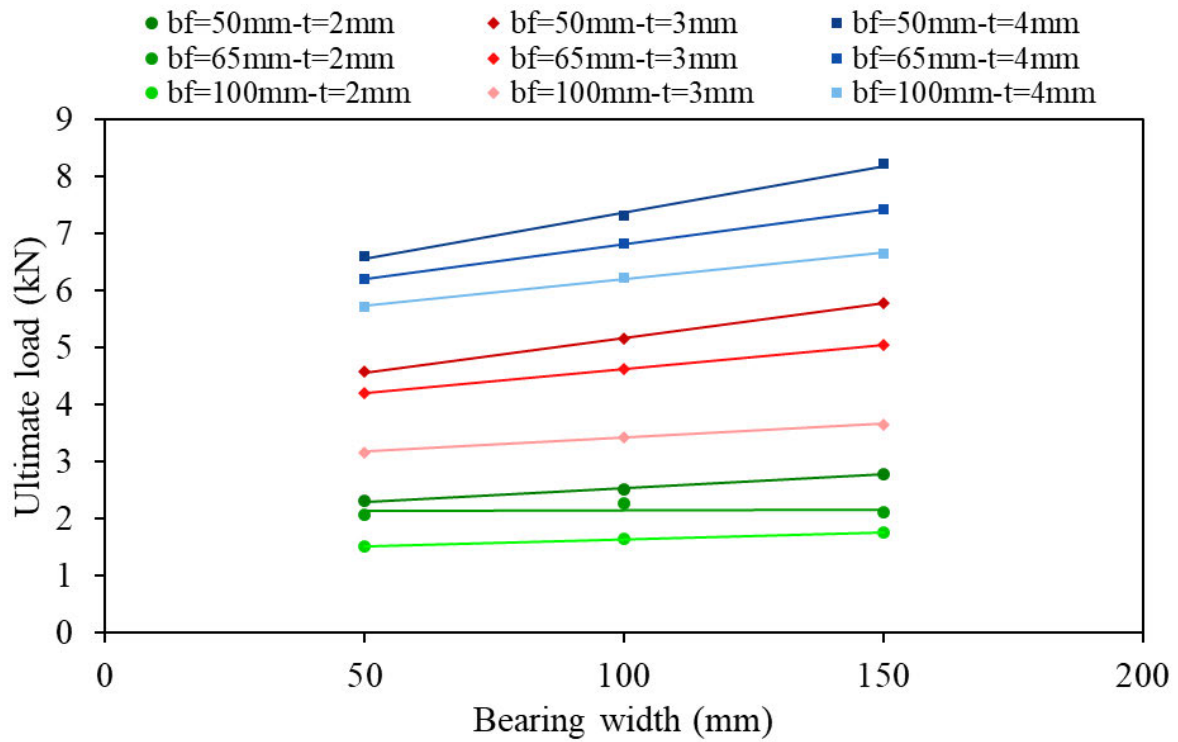
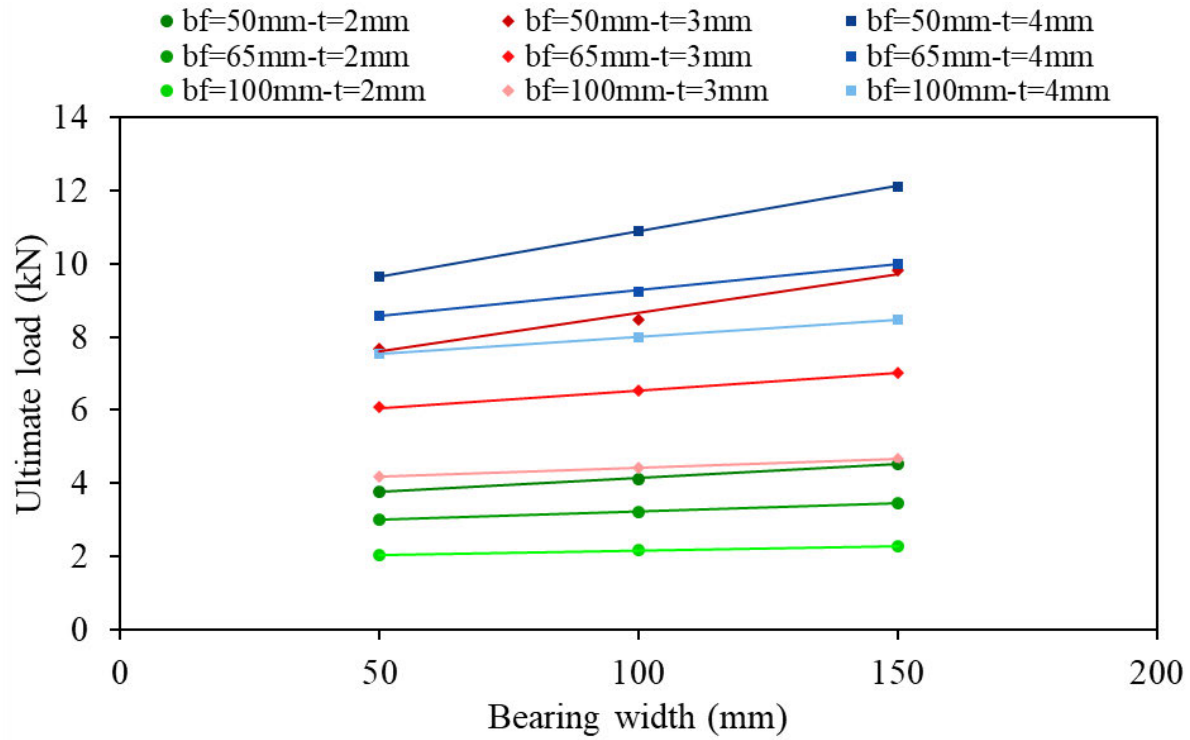


Figure 6.14 Load-displacement curves for different bearing widths (N) with 15 mm engagement length (D) for Section 6 ($b_f = 65$ mm and $t = 4$ mm).



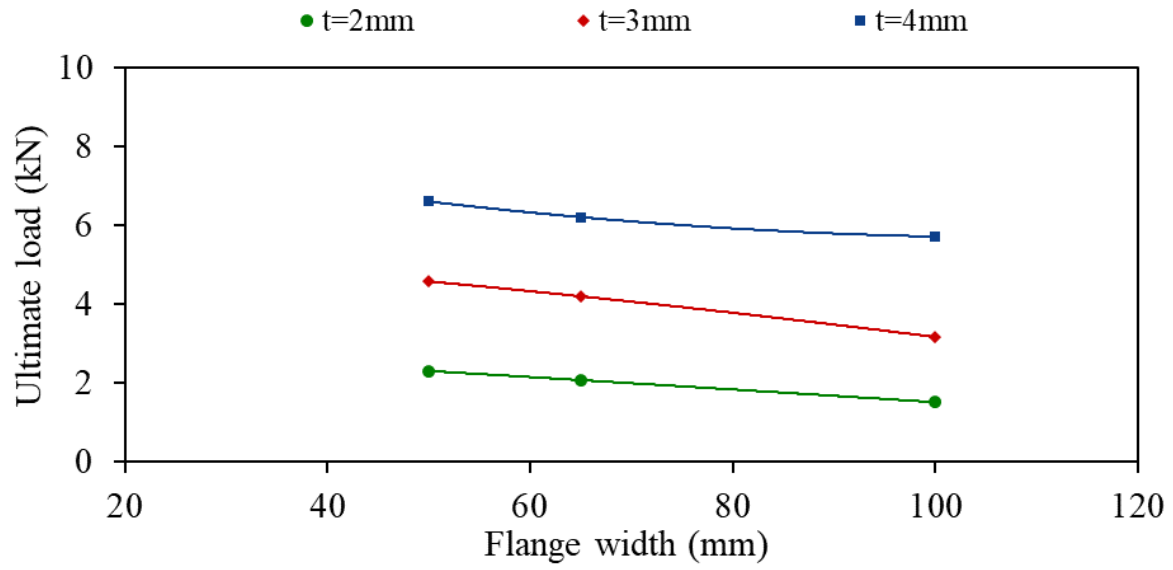
(a) 15 mm engagement length ($D = 15$ mm)



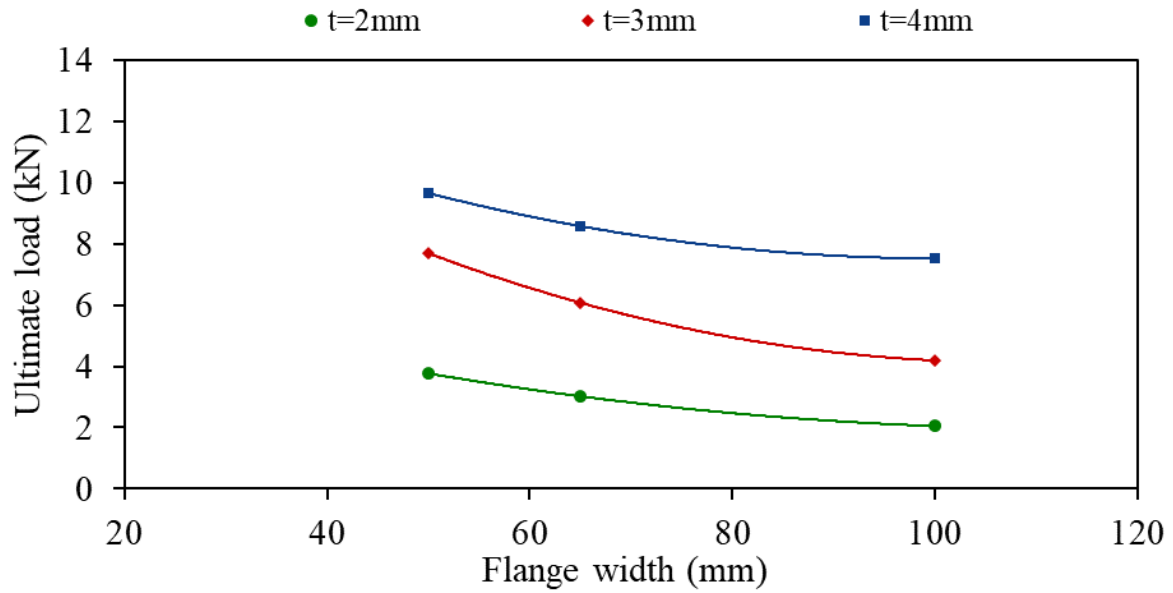
(b) 25 mm engagement length ($D = 25$ mm)

Figure 6.15 Ultimate bearing capacity (P_{FEA}) versus bearing width (N) for different sectional geometries (with different flange widths (b_f) and thicknesses (t)).

Figure 6.16 (a) and (b) illustrate the bearing capacities of the ASHWRB sections versus the flange width (b_f). It is observed from these figures that increasing the flange width (b_f) decreases the capacities of the ASHWRB sections in a moderate non-linear manner. The comparisons of the load-displacement curves (See Figure 6.17) for different flange widths (b_f) show that increased flange widths (b_f) lead to a reduction of the stiffness and an increase of the displacement.



(a) 15 mm engagement length ($D = 15\text{ mm}$)



(b) 25 mm engagement length ($D = 25\text{ mm}$)

Figure 6.16 Ultimate bearing capacity (P_{FEA}) of the ASHWRB sections versus flange width (b_f) for different thicknesses (t) (models with $N=50\text{ mm}$).

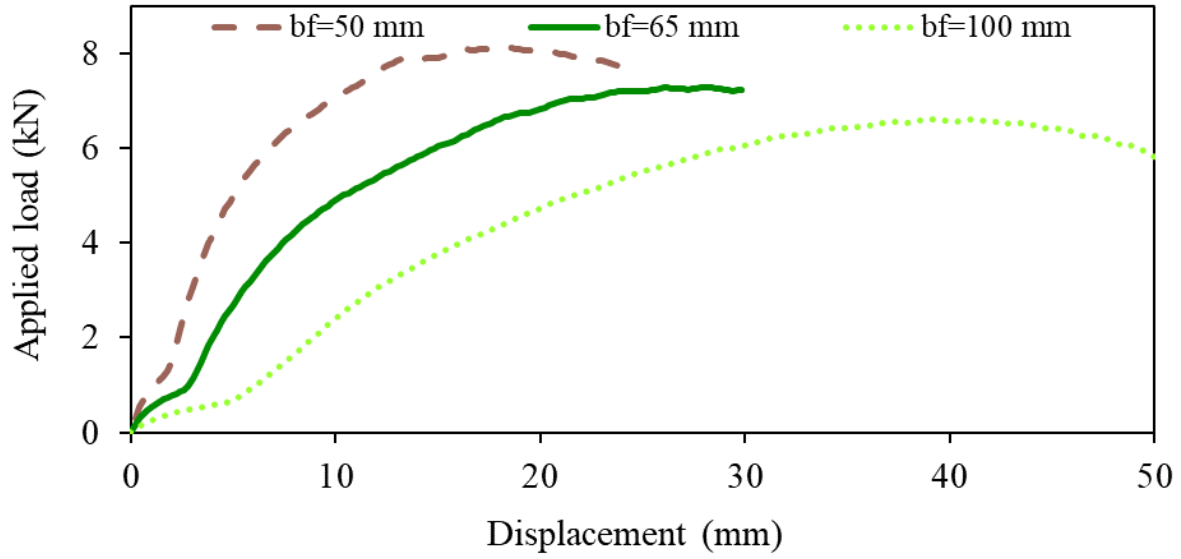


Figure 6.17 Load-displacement curves for different flange widths (b_f) (models with $D=20$ mm, $N = 50$ mm, and $t = 4$ mm).

Figure 6.18 displays the comparisons of the load-displacement curves against three different thicknesses (t) for sections with 30 mm engagement length, 150 mm bearing width (N), and 65 mm flange width (b_f). Figure 6.19 (a) and (b) demonstrate the effects of the thickness (t) on the bearing capacities of the ASHWRB sections with various bearing widths (N), and under the 15 mm and the 25 mm engagement lengths (D), respectively. Generally, it can be inferred that the bearing capacities are considerably increased in a nonlinear manner when the thickness (t) increases from 2 mm to 4 mm. Furthermore, it is evident that the bearing capacities of the ASHWRB sections with greater thicknesses (t) are much more affected by the increased bearing widths (N).

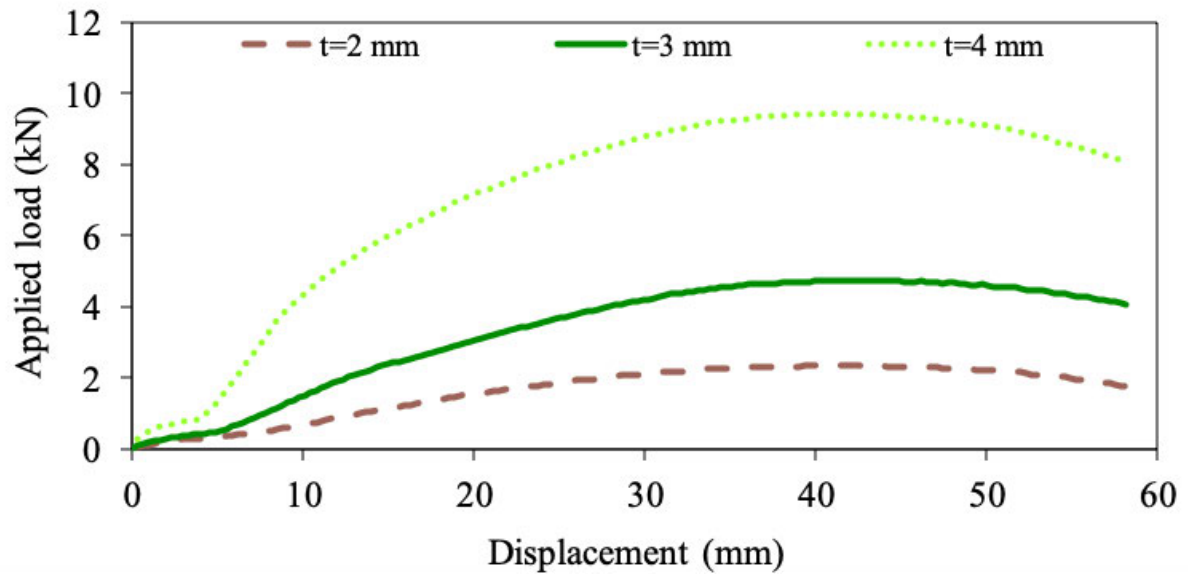
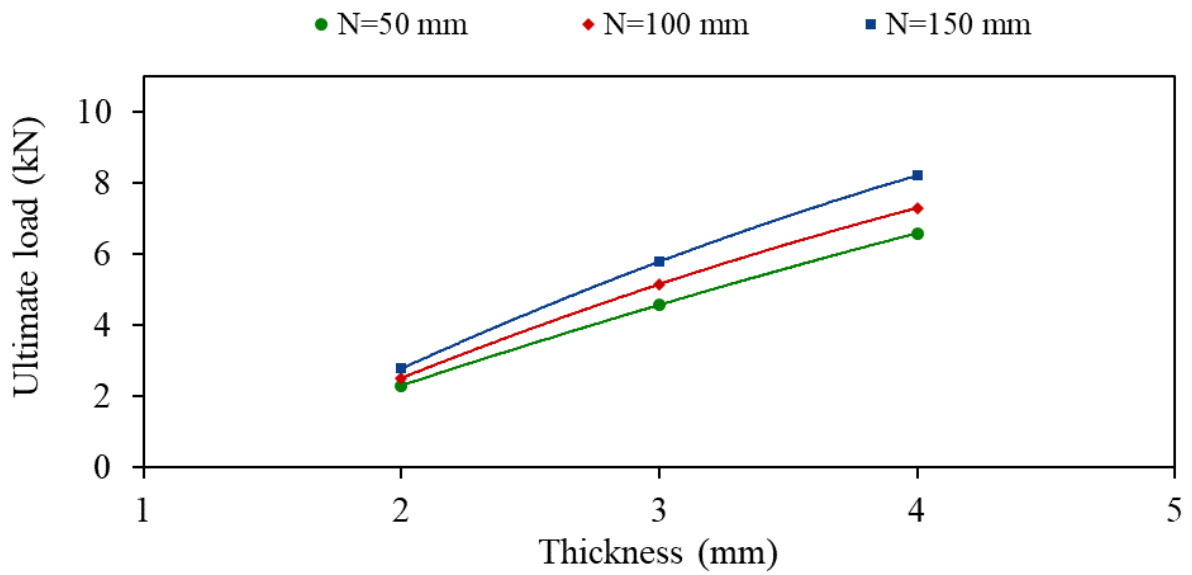
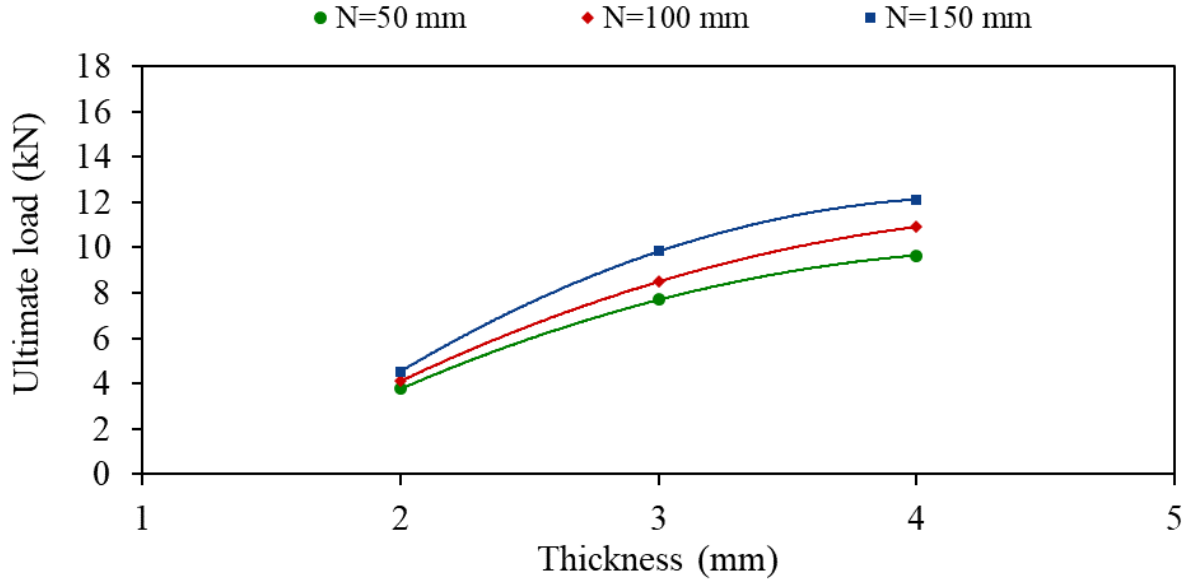


Figure 6.18 Load-displacement curves for different thicknesses (t) (models with $D = 30$ mm, $N = 150$ mm, and $b_f = 65$ mm).



(a) 15 mm engagement length ($D = 15$ mm)



(b) 25 mm engagement length ($D = 25$ mm)

Figure 6.19 Ultimate bearing capacity (P_{FEA}) versus thickness (t) for different bearing width (N) (models with $b_f = 50$ mm).

The load-displacement curves of Section 6 (Table 6.4) with a 150 mm bearing width (N) for different engagement lengths (D) are illustrated in Figure 6.20. As can be seen, both the stiffness and the ultimate capacity are increased with increased engagement lengths (D). Figure 6.21 shows the bearing capacities versus the engagement lengths (D) for three different bearing widths (N) and three thicknesses (t) of the models with a flange width (b_f) of 50 mm. It can be seen that increased engagement lengths (D) result in a non-linear increase of the bearing capacity of the ASHWRB sections. The bearing capacities with greater thicknesses (t) are more sensitive to such an influence than those for the specimens with smaller thicknesses (t). Furthermore, the bearing capacity of the sub-heads with a greater engagement length ($D = 30$ mm) is much more affected by the thickness (t) and the bearing width (N) variations than that for the ASHWRB sections with a smaller engagement length ($D = 5$ mm).

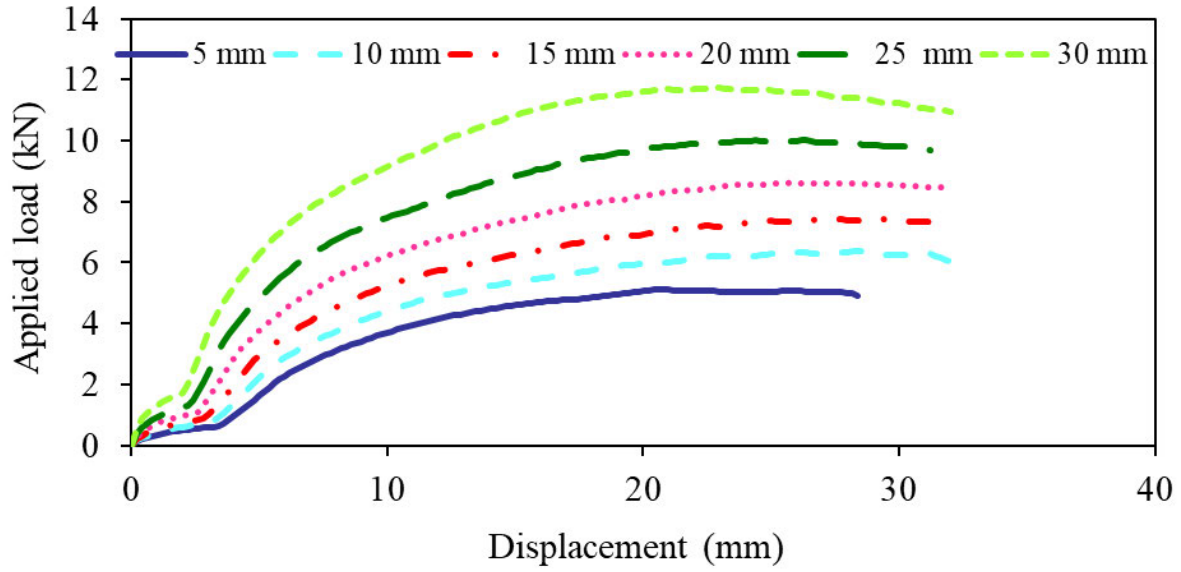


Figure 6.20 Load-displacement curves for different engagement lengths (D) for Section 6 (with $b_f=65$ mm and $t = 4$ mm, $N = 150$ mm).

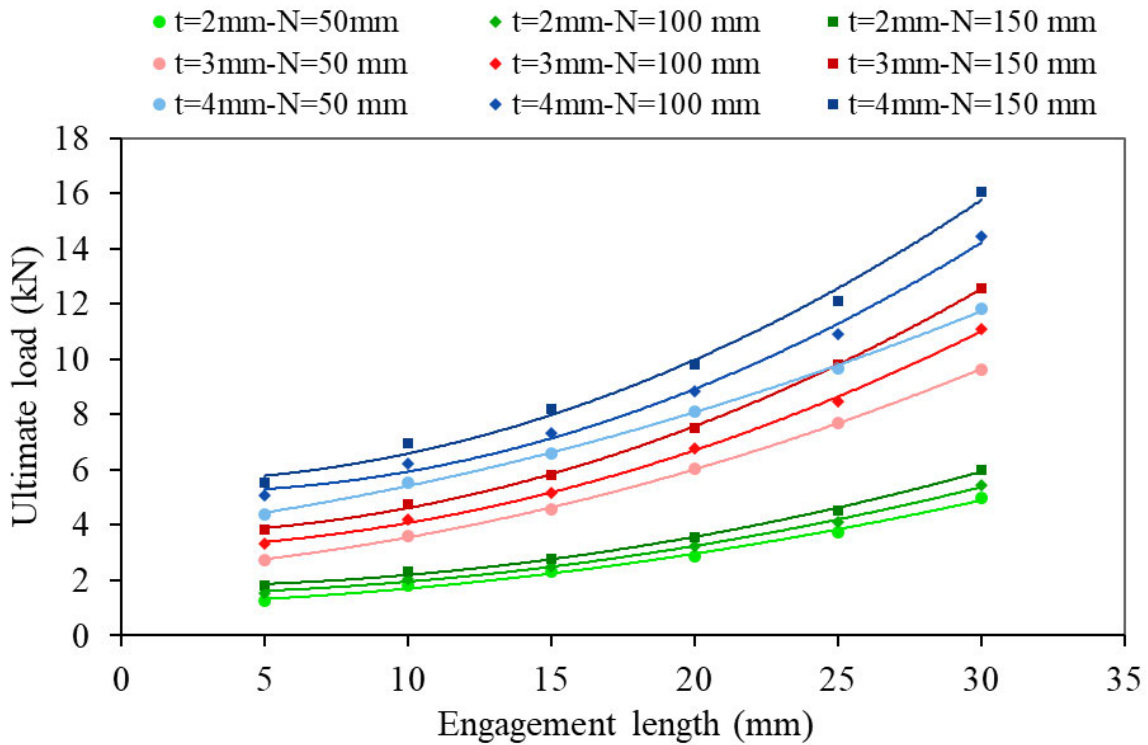


Figure 6.21 Ultimate bearing capacity (P_{FEA}) versus engagement length (D) for different bearing widths (N) and thicknesses (t) (models with $b_f = 50$ mm).

Figure 6.22 and Figure 6.23 illustrate the influences of the geometrical parameters (e/t) and $(e/t)^2$, respectively, on the bearing capacities of the ASHWRB sections, considering different

bearing widths (N) and various thicknesses (t). It is shown that these parameters have a considerable influence on the bearing capacities of the ASHWRB sections. The bearing capacities decrease nonlinearly with an increase of e/t and $(e/t)^2$. However, the impact of e/t and $(e/t)^2$ on the ultimate bearing capacities is more profound in the ASHWRB sections with a larger thickness ($t = 4$ mm) compared to the specimens with a smaller thickness ($t = 2$ mm).

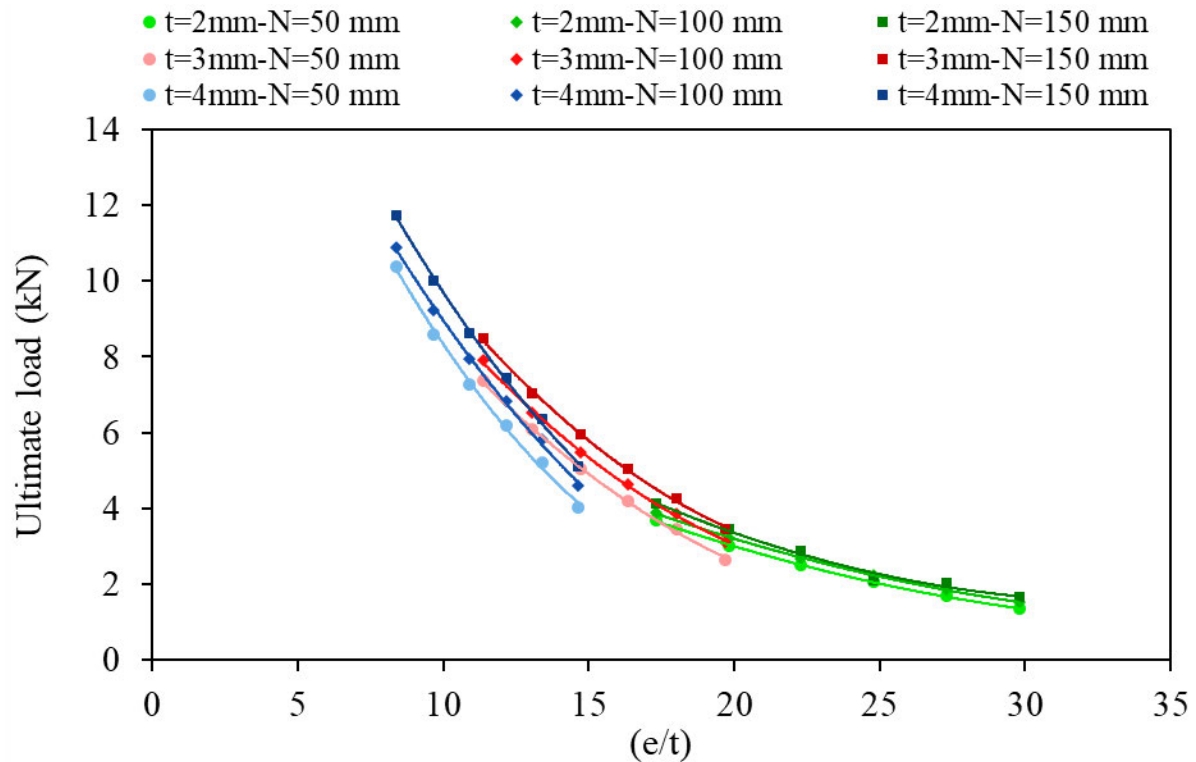


Figure 6.22 Ultimate bearing capacity (P_{FEA}) versus (e/t) for different bearing width (N) and thicknesses (t) (models with $b_f = 65$ mm).

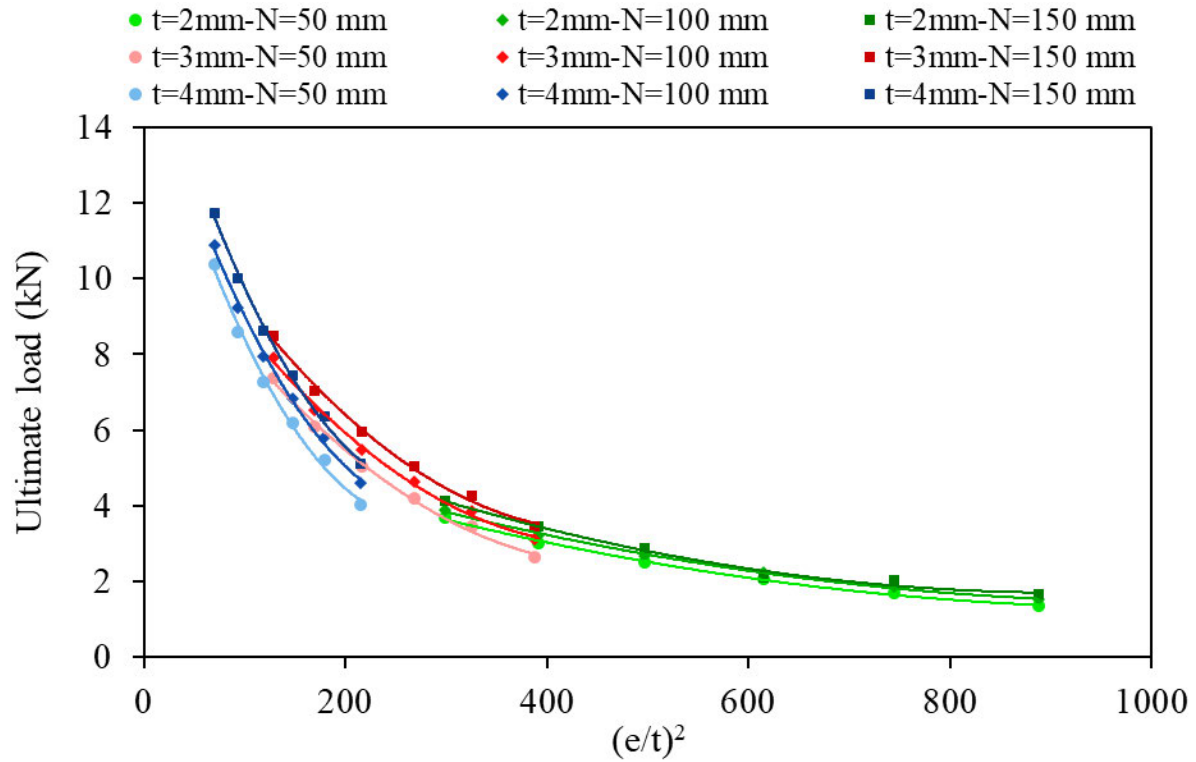


Figure 6.23 Ultimate bearing capacity (P_{FEA}) versus $(e/t)^2$ for different bearing widths (N) and thicknesses (t) (models with $b_f = 65$ mm).

6.5.2. Comparison between the ACSH sections and the ASHWRB sections

Table 6.5 shows comparisons of the average bearing capacity ratios obtained from parametric studies on the ACSH sections and the ASHWRB sections considering the effects of different parameters. In general, bearing capacities of the ASHWRB sections are greater than those of the ACSH sections. As can be seen, the average values of the ASHWRB to the ACSH bearing capacity ratios for different bearing widths (N), engagement lengths (D), and flange widths (b_f) are somewhat similar, being in the vicinity of 1.1. However, with respect to various flange thicknesses (t), the ratios are different. Increasing the flange thicknesses (t) from 2 mm to 4 mm, the total mean values of the bearing capacity ratios decreased from 1.23 to 1.03.

Table 6.5 Comparison of the average values of the ACSH to the ASHWRB bearing capacity ratios considering different parameters.

Parameters	ASHWRB (P_{RB}) (kN)	ACSH (P_C) (kN)	P_{RB}/P_C
$N = 50 \text{ mm}$	4.2	3.9	1.08
$N = 100 \text{ mm}$	4.6	4.2	1.08
$N = 150 \text{ mm}$	4.9	4.5	1.09
$D = 5 \text{ mm}$	2.8	2.5	1.09
$D = 10 \text{ mm}$	3.5	3.3	1.07
$D = 15 \text{ mm}$	4.2	3.9	1.06
$D = 20 \text{ mm}$	4.8	4.5	1.07
$D = 25 \text{ mm}$	5.6	5.2	1.09
$D = 30 \text{ mm}$	6.5	5.9	1.11
$b_f = 65 \text{ mm}$	5.1	4.7	1.08
$b_f = 100 \text{ mm}$	4	3.7	1.08
$t = 2 \text{ mm}$	2.2	1.8	1.23
$t = 3 \text{ mm}$	4.4	4	1.12
$t = 4 \text{ mm}$	7.1	6.9	1.03

Table 6.6 Comparison of average bearing capacity ratios between different parameters for the ACSH sections and the ASHWRB sections.

Average bearing capacity ratios	ASHWRB	ACSH
$P(N = 150 \text{ mm})/P(N = 100 \text{ mm})$	1.08	1.07
$P(N = 100 \text{ mm})/P(N = 50 \text{ mm})$	1.08	1.08
$P(D = 30 \text{ mm})/P(D = 25 \text{ mm})$	1.17	1.15
$P(D = 25 \text{ mm})/P(D = 20 \text{ mm})$	1.16	1.14
$P(D = 20 \text{ mm})/P(D = 15 \text{ mm})$	1.16	1.15
$P(D = 15 \text{ mm})/P(D = 10 \text{ mm})$	1.19	1.19
$P(D = 10 \text{ mm})/P(D = 5 \text{ mm})$	1.27	1.29
$P(b_f = 100 \text{ mm})/P(b_f = 65 \text{ mm})$	0.78	0.78
$P(t = 4 \text{ mm})/P(t = 3 \text{ mm})$	1.59	1.73
$P(t = 3 \text{ mm})/P(t = 2 \text{ mm})$	2.05	2.25

Comparisons of the average bearing capacity ratios resulted from different parameters for both ACSH sections and ASHWRB sections are shown in Table 6.6. As can be seen, the impact of all parameters on the bearing capacity ratios is more or less similar for the ACSH sections and the ASHWRB sections, except for the ratios due to thickness (t) variations. This comparison also confirms that the effect of increasing thickness (t) is more substantial on the ACSH sections compared to the ASHWRB sections, with a difference of up to 20%.

Figure 6.24 compares the load-deflection curves for the ACSH sections (dashed-dotted line) and the ASHWRB sections (solid line) for three bearing widths ($N = 50, 100, 150$ mm) and with a 25 mm engagement length (D). The overall behaviour of the load-displacement curves in Figure 6.24 shows that the ultimate loads of the ACSH sections was less than those of the corresponding ASHWRB sections.

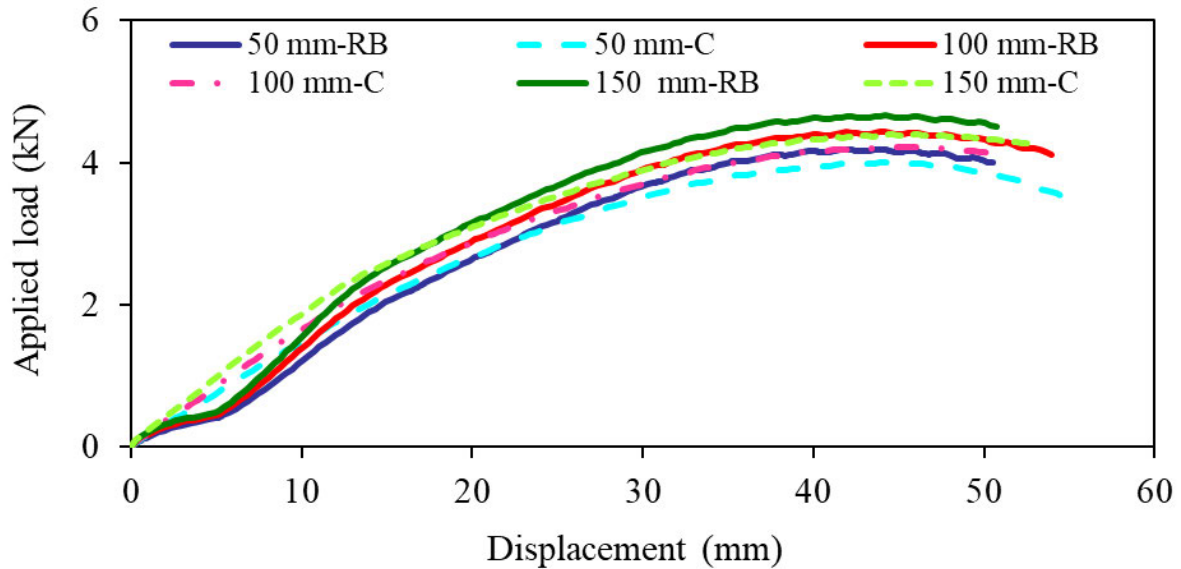


Figure 6.24 Comparison of load-displacement curves for the ACSH sections (C) and ASHWRB (RB) for 25 mm engagement length (models with $b_f = 100$ mm and $t = 3$ mm).

6.6. Design rules

6.6.1. Current design rules

6.6.1.1. International specifications (DRSs)

Façade industry intends to use a unique design approach to estimate the bearing capacities of the ASHWRB sections, which is not only practical but can also be implemented to increase productivity and efficiency. Consequently, this research has aimed to meet manufacturing concerns through the development of a reliable standard for the economic design of the ASHWRB sections. To gain a deeper insight of the bearing behaviour of the ASHWRB sections, a detailed assessment of the accuracy of the DRSs (AISI S240, 2015; TI 809-07, 1998; SSMA, 2000; Bolte and LaBoube, 2004) (for cold-formed steel stud-to-track

connections) was conducted in this study, by comparing them with the parametric study results. The design rules provided by the DRSs (AISI S240, 2015; TI 809-07, 1998; SSMA, 2000; Bolte and LaBoube, 2004) are presented in the following sections in brief.

TI 809-07 (1998) and SSMA (2000) recommend Equation (5) for estimating the bearing capacities P_n of cold-formed steel stud-to-track connections,

$$P_n = \frac{w_{dt} t^2 f_y}{6e} \quad (6.5)$$

where $w_{dt} = N + 2 \left[\frac{e+D}{\tan(\varphi)} \right] \leq S$, $\varphi = 30^\circ$, S = stud spacing (mm), N = stud flange width (mm), t = track thickness (mm), f_y = yield strength of the track (MPa), e = slip gap between the end of the stud web and the track web (mm), D = engagement length (bearing contact length) between stud and track flange, and w_{dt} = effective track length (mm) (see Figure 6.25).

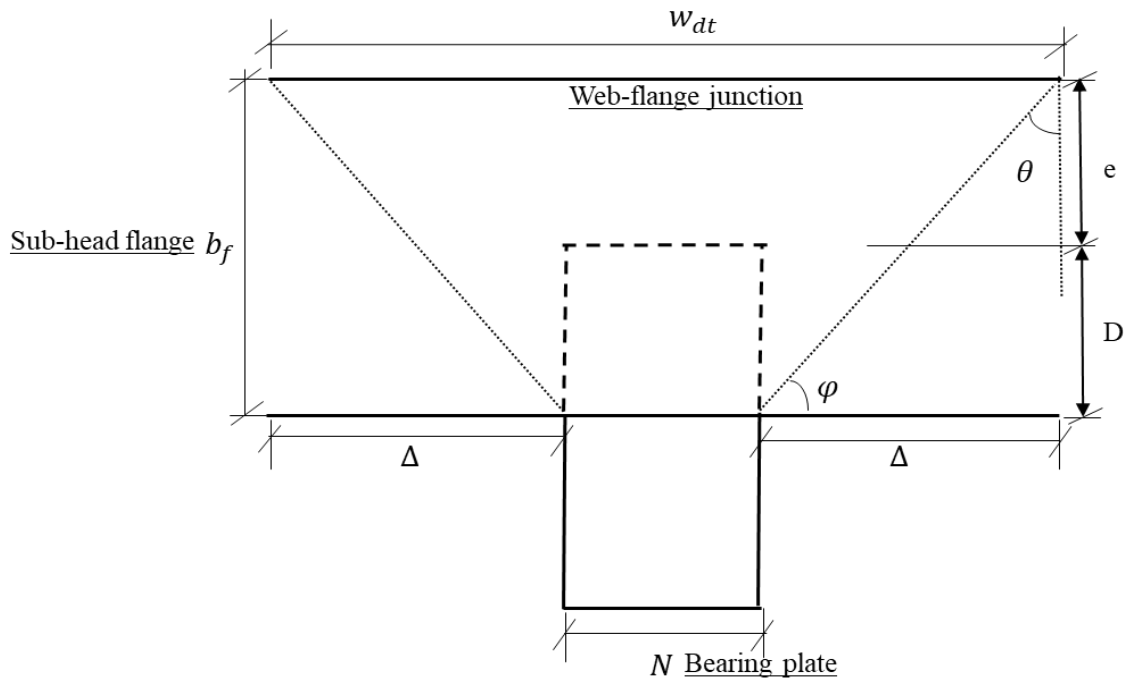


Figure 6.25 Simplified stress distribution on the bead flange.

AISI S240 (2015) suggests Equation (6) for calculating P_n ,

$$P_n = \frac{w_{dt} t^2 f_y}{4e} \quad (6.6)$$

where $w_{dt} = 0.11\alpha^2(e^{0.5}/t^{1.5}) + 5.5\alpha \leq S(\text{mm})$, $\alpha = 25.4 =$ coefficient for conversion of units, $S =$ stud spacing (mm), and w_{dt} , t , f_y , and e are outlined as above.

Bolte and LaBoube's (2004) used Equation (6) to predict the nominal strength of the deflection track alongside Equation (7).

$$w_{dt} = 2\Delta + w_{stud}, 2\Delta = \begin{cases} \frac{300(e/t)^2}{100} \text{ for } (e/t)^2 < 100 \\ 300 \text{ for } (e/t)^2 \geq 100 \end{cases} \quad (6.7)$$

where Δ is the partial track length (mm) on both sides of the bearing width (see Figure 6.25).

6.6.1.2. Modified design rules (DRA (Akbari et al., 2020b, 2020c))

Akbari et al. (2020b) have improved the accuracy of the DRSs (AISI S240, 2015; TI 809-07, 1998; SSMA, 2000; Bolte and LaBoube, 2004) for predicting the bearing capacities of the ASHWRB sections (DRA) by calibrating them with their experimental results (Akbari et al., 2020b).

In this respect, design equations for the effective sub-head length (w_{dt}) were proposed for two loading conditions (the 15 mm and the 25 mm engagement lengths), and two deformation criteria (the maximum load (Max) and the ultimate deformation limit (UDL)), as expressed

by Equations (8a) and (8b). These equations were used in parallel with Equation (6) to predict the bearing capacities of the ASHWRB sections.

$$w_{dt} = N + 2 * b_f * \tan(\theta) \quad (6.8a)$$

$$\theta = a * (e/t)^2 + b \quad (6.8b)$$

Table 7 presents the values of the proposed coefficients a and b (Akbari et al., 2020b).

Akbari et al. (2020c) also proposed design equations (DRA, Equation 9) to predict the bearing capacities of the ACSH sections using the results of a previous parametric study (Akbari et al., 2020c). Accordingly, the effective sub-head length (w_{dt}) was calibrated using the ultimate loads obtained from the parametric study in (Akbari et al., 2020c), and θ was expressed as follows for the ACSH sections with uniform flange thickness (UFT) and non-uniform flange thickness (NUFT).

$$\theta = a * (e/t)^2 + b * (e/t) + c * D + d \quad (6.9)$$

The coefficients included in Equation (9) are also presented in Table 6.7. Notably, Equation (9) was used in conjunction with Equations (8a) and (6) to predict the bearing capacities of the ACSH sections.

Table 6.7 Proposed coefficients for the effective sub-head length (w_{dt}).

Section	Criteria	D (mm)	a	b	c	d
ASHWRB (test) (Akbari et al., 2020b)	Max	15	0.02	74	-	-
		25	0.06	70	-	-
	UDL	15	0.03	72	-	-
		25	-0.04	72	-	-
ACSH (parametric study) (Akbari et al., 2020c)	Max (NUF)	5, 10, 15, 20, 25 and 30	-0.006	0.3	0.3	63.0
ACSH (parametric study) (Akbari et al., 2020c)	Max (NUFT)	5, 10, 15, 20, 25 and 30	-0.01	0.3	0.56	55.5
ASHWRB (parametric study)	Max	5, 10, 15, 20, 25 and 30	-0.002	-2.5	0.25	78

6.6.2. Comparison of the FEA results with current design rules ($P_{FEA}/P_{Predicted}$)

Table 6.8 summarises the mean and the COV values of the bearing capacity ratios ($P_{FEA}/P_{predicted}$), where P_{FEA} is the ultimate bearing capacities obtained from numerical analyses, and $P_{predicted}$ is the bearing capacities predicted by the DRSs (AISI S240, 2015; TI 809-07, 1998; SSMA, 2000; Bolte and LaBoube, 2004). It was found that these design rules underestimate the bearing capacities of the ASHWRB sections, with the mean values of $P_{FEA}/P_{predicted}$ ranging from 1.60 to 2.70. These DRSs are also unreliable to predict the bearing capacities of the ASHWRB sections with the COV values between 0.18 and 0.29.

Table 6.8 Comparison of mean and COV values of bearing capacity ratios ($P_{FEA}/P_{Predicted}$).

Rule	Sub-head type	Loading criteria and design rules	Equation	Mean	COV	ϕ_w	β_0
Current design rules	ASHWRB	DRSs by AISI S240 (2015)	Eq. (6.6)	2.48	0.27	1.67	4.33
		DRSs by TI 809-07 (1998)	Eq. (6.5)	2.70	0.18	2.10	5.58
		DRSs by Bolte and LaBoube (2004)	Eq. (6.6) and Eq. (6.7)	1.60	0.29	1.00	2.95
		DRA (UDL) (Akbari et al., 2020b)	Eq. (6.8a) and Eq. (6.8b)	1.70	0.82	0.23	1.07
		DRA (Max) (Akbari et al., 2020b)	Eq. (6.8a) and Eq. (6.8b)	0.99	0.13	0.72	1.74
	ACSH	DRA (Max) (Akbari et al., 2020c)	Eq. (6.9)	1.18	0.11	1.03	3.14
Proposed	ASHWRB	DRA _p (Max)	Eq. (6.10)	1.01	0.07	0.90	2.68

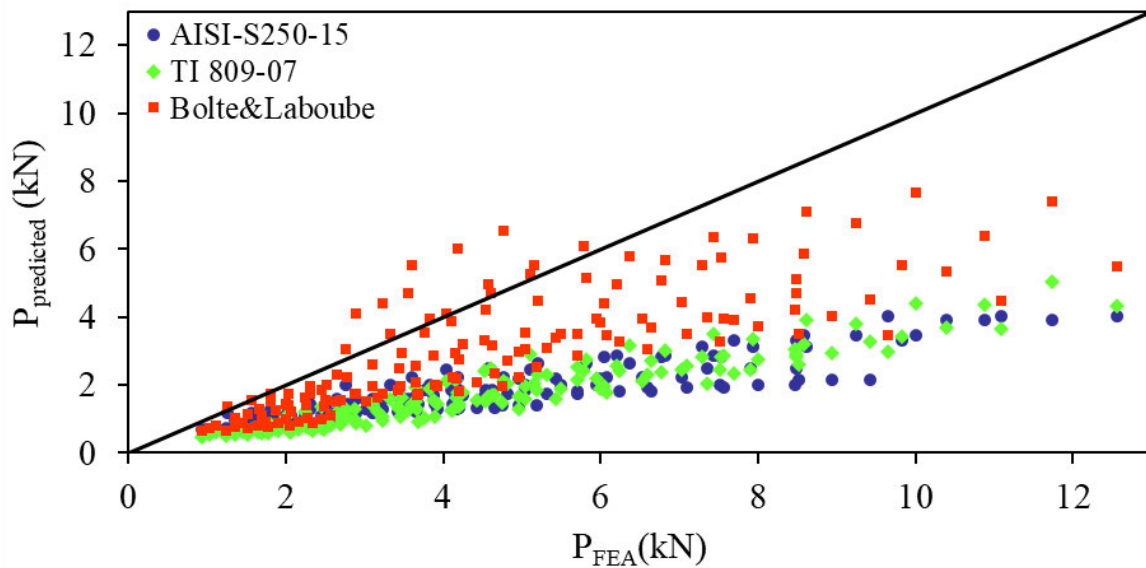
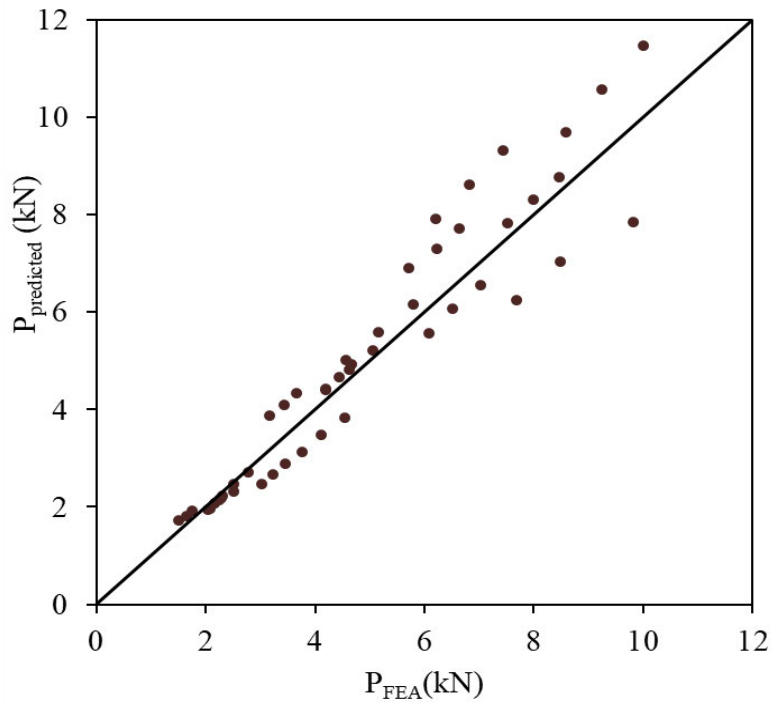


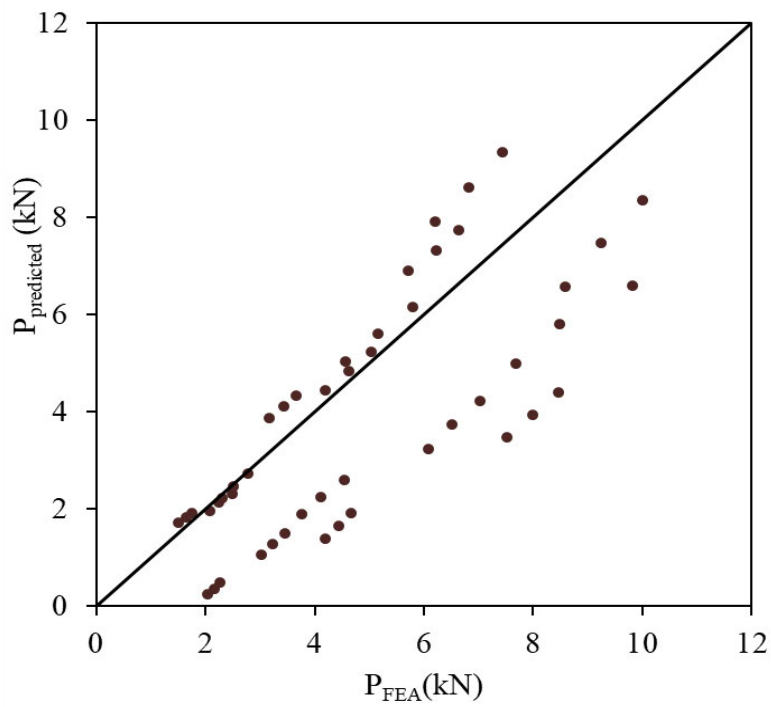
Figure 6.26 Comparison between numerical bearing capacities, and predictions based on DRSs (AISI S240, 2015; TI 809-07, 1998; SSMA, 2000; Bolte and LaBoube, 2004).

Figure 6.26 displays the comparisons between the bearing capacities ($P_{predicted}$) predicted by the DRSs (AISI S240, 2015; TI 809-07, 1998; SSMA, 2000; Bolte and LaBoube, 2004) and the ultimate bearing capacities (P_{FEA}) of the ASHWRB sections acquired from the parametric studies.

The bearing capacities yielded by the numerical parametric analyses were also compared with those predicted by Equations (8a) and (8b) (DRA (Akbari et al., 2020b)), considering two engagement lengths of 15 mm and 25 mm, as well as two loading criteria (Max and UDL). It should be noted that θ is comprised of the term $(e/t)^2$, and the larger value of $(e/t)^2$ leads to a negative value of $\tan(\theta)$. Hence, to avoid this issue, an upper bound of 76 degrees set on the term θ by Akbari et al. (2020c) is applied in this study. The ultimate bearing loads obtained from the parametric study (Akbari et al., 2020b)) were compared with the predictions of the DRA (Akbari et al., 2020b)) based on the maximum load (M) and the ultimate deformation criterion (UDL) in Figure 6.27 (a) and (b), respectively. The mean values of $P_{FEA}/P_{Predicted}$ using the DRA are 0.99 for the Max criterion and 1.70 for the UDL criterion, as shown in Table 6.8. Furthermore, the UDL criterion led to unreliable results with a large COV of up to 0.82. This means that the DRA based on the UDL criterion (Akbari et al., 2020b)) is unreliable to predict the bearing capacities of the ASHWRB sections in this parametric study. It needs to be mentioned that the flange groove of the bead plays a key role in the load-displacement patterns. In this parametric study, the groove elements were omitted from the models. As a result, only one peak appeared in the load-displacement curves of the parametric models (see Figure 6.28). It can be concluded that the difference in the cross-sectional geometries of the tested specimens and the FE parametric models is the main source of unreliable and incompatible predictions acquired from the DRA (Akbari et al., 2020b)) (See Figure 6.11), which leads to different load-displacement patterns.



(a) Maximum load (Max)



(b) Ultimate deformation limit (UDL)

Figure 6.27 Comparison between numerical capacities and predictions based on DRA (Akbari et al., 2020b).

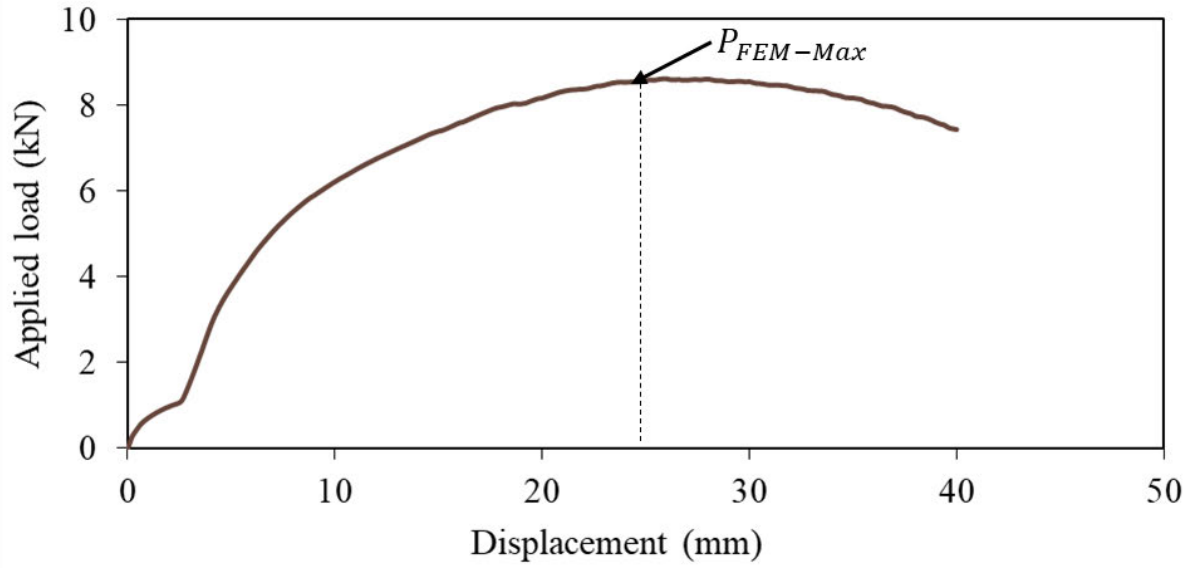


Figure 6.28 Ultimate load obtained from the FE parametric models.

The ultimate bearing capacities of the ASHWRB sections obtained from the present parametric study were also compared with the DRA (Akbari et al., 2020c)) for ACSH sections with a uniform flange thickness (Equation (9)), as given in Table 6.7. Figure 6.29 shows the comparisons of the FEA bearing capacities of the ASHWRB sections P_{FEA} with predictions using Equation (9) $P_{Predicted}$. This implies that the DRA (Akbari et al., 2020c)) for the ACSH sections is too conservative with a mean value of the $P_{FEA}/P_{Predicted}$ ratios of 1.18 (Table 6.8).

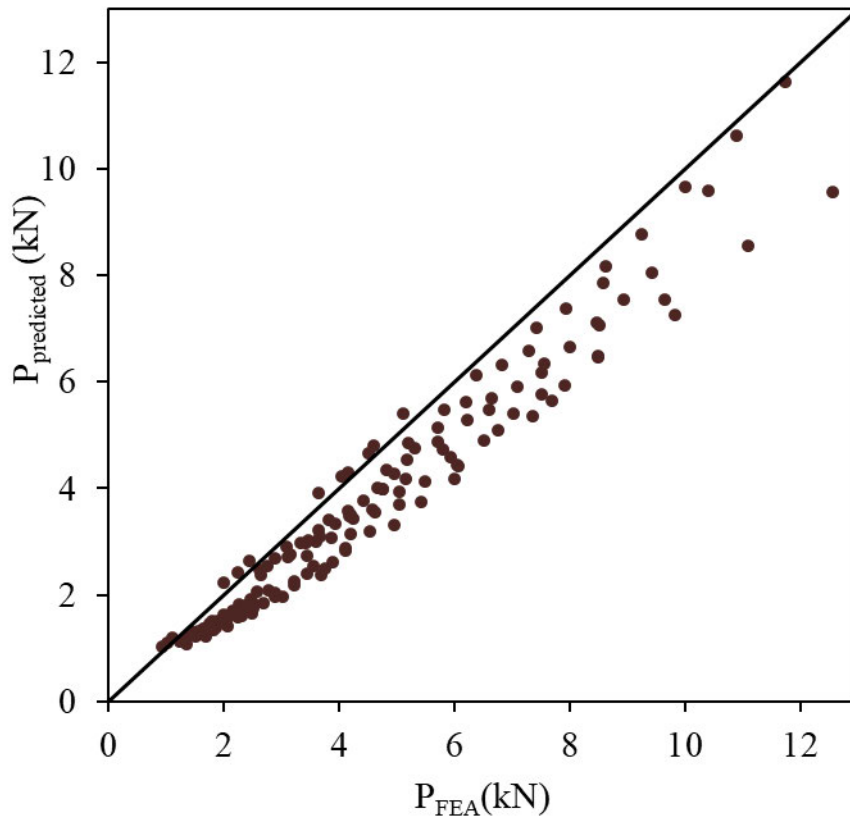


Figure 6.29 Comparison between numerical capacities and predictions based on DRA (Akbari et al., 2020b).

Therefore, referring to the above argument, the DRA (Akbari et al., 2020b, 2020c) and DRSs (AISI S240, 2015; TI 809-07, 1998; SSMA, 2000; Bolte and LaBoube, 2004) must be suitably modified to accurately predict the bearing capacities of the ASHWRB sections obtained from the present parametric study.

6.6.3. Proposed design rules

As mentioned above, the DRA (Akbari et al., 2020b) for the ASHWRB sections based on the experimental study (Equations (8a) and (8b)) (Akbari et al., 2020b) was developed using a limited number of manufacturer and product specific test specimens covering a small number of key parameters. Furthermore, the DRA (Akbari et al., 2020c) (w_{dt}) for the ACSH sections based on the parametric study (Equation (9)) (Akbari et al., 2020c) was inappropriate to predict the bearing capacities of the ASHWRB sections. Therefore, this section puts forward

more accurate prediction equations for estimating the effective sub-head lengths (w_{dt}) and the bearing capacities of the ASHWRB sections based on the present parametric study. As only one peak was reached in the load-displacement curves of the FE parametric models, the maximum load criterion (Max) was used herein to propose the new design rules (DRA_P).

Akbari et al. (Akbari et al., 2020b) considered the effect of $(e/t)^2$ in Equation (8b) for the ASHWRB sections based on their experimental study. However, the effects of $(e/t)^2$, (e/t) and the engagement length (D) were all included in Equation (9) for the ACSH sections based on the parametric study in (Akbari et al., 2020c). In the present study the effects of different parameters were investigated, and the effective sub-head lengths were calibrated with the parametric study database. Consequently, e , t and D were incorporated in the prediction equation for θ (Equation (10)). Suitable coefficients were determined for the ASHWRB sections by using regression analysis method according to the present parametric study results, as presented in Table 6.7. Equation (10) (DRA_P) must be substituted in Equations (6) and (8a) to predict the bearing capacities of the ASHWRB sections.

$$\theta = a * (e/t)^2 + b * t + c * D + d \quad (6.10)$$

Table 8 shows the mean and COV values of the ratios between the finite element bearing capacities (P_{FEA}) and the predicted ones ($P_{predicted}$) obtained from the proposed DRA_P. Figure 6.30 also illustrates the comparisons between $P_{predicted}$ obtained from the DRA_P and P_{FEA} for the ASHWRB sections. The mean value of $P_{FEA}/P_{predicted}$ is 1.01 with the corresponding COV value is 0.07, as presented in Table 6.8. It can be concluded that the DRA_P is able to accurately estimate the bearing capacities of the ASHWRB sections.

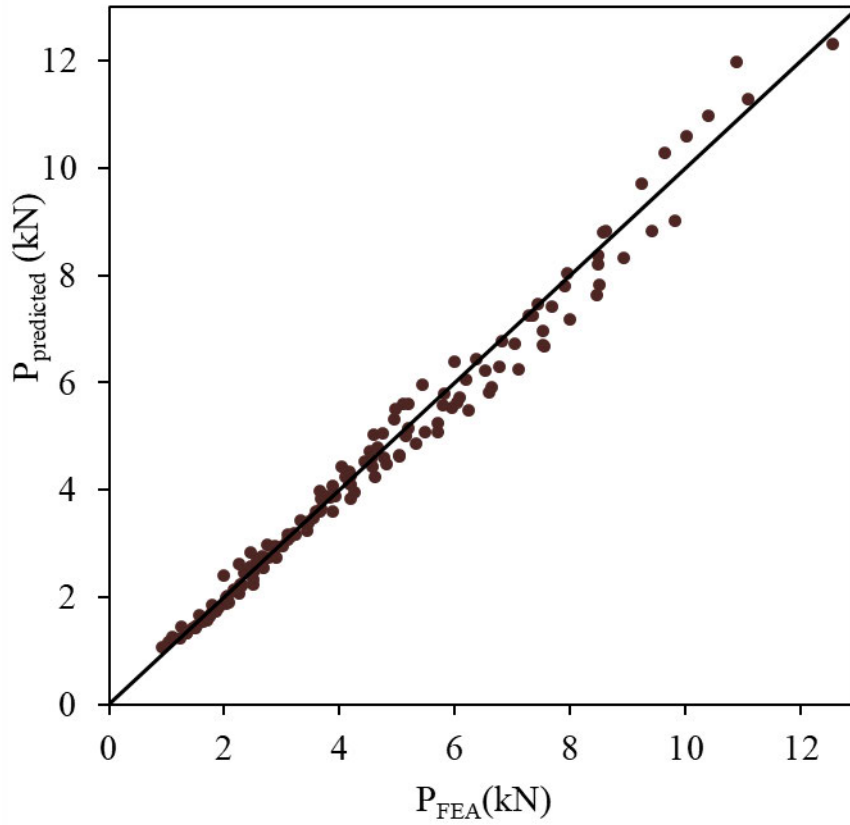


Figure 6.30 Comparison between numerical capacities and predictions based on DRAP.

6.6.4. Capacity reduction factor

The North American Specification AISI S100 (2012) presents a statistical model to calculate the capacity reduction factor (ϕ_w). The variation of material, fabrication and loading effects is included in this model, as expressed by Equation (11a).

$$\phi_w = 1.52M_mF_mP_me^{-\beta_0\sqrt{V_M^2+V_F^2+C_nV_P^2+V_Q^2}} \quad (6.11a)$$

where $M_m = 1.1$, $V_M = 0.06$, $F_m = 1.0$, $V_F = 0.05$ were taken from AISI S100 (2012). M_m and V_M are the mean values and the COVs of the material factor, respectively. F_m and V_F are the mean values and the COVs of the fabrication factor, respectively. $V_Q = 0.21$ is the COV of the load effect. The parameters P_m and V_P are the mean values and the COVs of the test-to-

predicted load ratios obtained from FEA. C_n is a correction factor to cater for the limited number of tests ($C_n = n^2 - 1/n^2 - 3n$), and $\beta_0 = 2.5$ is the target reliability index for beams. All the above values can be substituted into Equation (11a) to lead to Equation (11b).

$$\phi_w = 1.672P_m e^{-2.5\sqrt{0.0502+C_nV_P^2}} \quad (6.11b)$$

The capacity reduction factors (ϕ_w) and reliability indexes (β_0) acquired from the DRSs (AISI S240, 2015; TI 809-07, 1998; SSMA, 2000; Bolte and LaBoube, 2004) and the DRA (Akbari et al., 2020b, 2020c) are also summarised in Table 6.8. This table shows that the value of ϕ_w obtained from the proposed equation (11b) is 0.94. Therefore, it is suggested to use a ϕ_w factor of 0.90 for the proposed equation to predict the bearing capacities of the ASHWRB sections. The results showed that the corresponding reliability index (β_0) based on the recommended capacity reduction factor (ϕ_w) is equal to or exceeds the target value ($\beta_0 = 2.5$), which indicates the reliability of the proposed equation.

6.7. Conclusions

This paper presented a nonlinear finite element analysis and practical design equations for predicting the bearing capacities of the ASHWRB sections in window wall systems using ABAQUS/CAE. For this purpose, 36 symmetrical half finite element models considering material nonlinearity were developed and verified against previous test results using manufacturer and product specific test specimens, by comparing the ultimate loads, the failure modes, and the load-displacement responses. Parametric study was subsequently performed with generalized ASHWRB sections to further study the effect of different parameters including, engagement lengths, bearing widths, flange widths, and thicknesses. The bearing capacities predicted by the finite element analysis were then compared with the DRSs AISI S240, 2015; TI 809-07, 1998; SSMA, 2000; Bolte and LaBoube, 2004). Results showed that the bearing capacities predicted by these design codes are unreliable for the ASHWRB sections. Furthermore, the comparison of the bearing capacities calculated by the DRA (Akbari et al., 2020b, 2020c) with those obtained from this parametric study signifies the uncertainty and unreliability of the equations in the DRA. Hence, the coefficients and

parameters in previously proposed design formulae were updated based on the parametric study results, and a new bearing capacity equation (DRA_p) was proposed for the ASHWRB sections. This study yields accurate predictions of the bearing capacities of the ASHWRB sections, which ensures safety and economical design of the sections under wind load using a wide range of bearing capacity data obtained from a series of numerical parametric studies.

7. Conclusions and Recommendations

7.1. Thesis findings

Window wall systems typically comprise extruded aluminium framing with infill glazing. The window wall resists all the loads and displacements it is exposed to and transmits them to the main supporting structures. Window wall assemblies are located between the slabs and supported by horizontal structural members at the top of the window wall system, known as ‘sub-heads’ with open cross-sections. One of the most common damage type and problem in window wall is the bearing failure and yielding of the sub-head flange under lateral wind load. Hence, the manufacturer intends to use an appropriate design approach for aluminium sub-heads, which is practical and can be implemented to increase productivity and efficiency. Consequently, this research has aimed to meet engineering concerns through the development of a reliable guidelines for the economical design of aluminium sub-heads.

Since no research was found which investigates the bearing behaviour of the aluminium sub-heads in the window wall systems subjected to wind load, Chapter 2 of this thesis was mainly focused on a literature review of the histories of windows, as well as experimental and numerical studies on the bearing strength of cold-formed steel stud-to-track connections in light gauge steel framing walls (with similar structural behaviour to the aluminium sub-heads in the window walls) under different loads. The empirical design rules in the international design standards for the determination of bearing capacities of cold-formed steel stud-to-track connections were also presented in this chapter.

Numerical and experimental studies were conducted on the bearing behaviour of two types of typical sub-heads (C-shaped sub-heads and sub-heads with removable beads) manufactured by G.James Glass and Aluminium Pty Ltd in this research. Hence, chapters 3 and 4 were devoted to experimental and numerical investigations of aluminium C-shaped sub-heads and chapters 5 and 6 were devoted to experimental and numerical investigations of aluminium sub-heads with removable beads. Brief overview of these chapters is provided below:

Chapters 3 and 4 presented the details of the experimental study and numerical analysis conducted on the bearing behaviour of aluminium C-shaped sub-head sections in window walls under wind load. Details of the test set-up, testing process and test results including the load-deflection responses, the failure modes, and the bearing capacities were presented. The main failure modes in the experimental testing were yielding of the sub-head web to flange junction due to the flange bending and slipping of the bearing plate due to crushing of the flange groove. Furthermore, it was found that the ultimate bearing capacity increased linearly with the increased bearing width, and the larger engagement length (loading position) gave rise to an increase of the ultimate capacity, as well as nonlinear behaviour of load-displacement response. Furthermore, finite elements were developed and validated with test results to capture the experimental results. Based on the validated FE models, a detailed parametric study was carried out covering wide-ranging aluminium sub-head dimensions, loading conditions, and bearing lengths. The bearing capacities acquired from experimental and parametric results were compared with the predictions of the current cold-formed steel specifications (AISI S240-15, 2015; TI 809-07, 1998; and SSMA, 2000). The code-predicted design strengths were found to be overly conservative for aluminium sub-head sections in window walls under wind load. Thus, the design rules in the current cold-formed steel design equations were improved. Consequently, new design rules were proposed, based on experimental results and the parametric database, which accurately predict the bearing capacities of aluminium C-shaped sub-heads.

Chapter 5 presented the details of the experimental studies carried out on aluminium sub-head sections with removable beads in window walls under wind load. Details of the test set-up, testing process, and tests results were presented through the load-deflection responses, the failure modes, and the bearing capacities. It was found that the bearing capacities were highly dependent on the section geometries of the removable beads. Furthermore, the governing modes of failure were yielding and fracture at the web to flange junction of the bead as a result of the bending of the cantilever flange. Chapter 6 presented a validated FE model against the experimental bearing behaviour of aluminium sub-head sections with removable beads, reported in Chapter 5. Based on the validated FE models, extensive parametric studies with varying bearing widths, sectional geometries, and loading conditions were also performed. The acquired results obtained from the experimental results and parametric studies were then used to assess the accuracy of current cold-formed steel design rules. Thus,

new design equations have been proposed to accurately estimate the bearing capacity of aluminium sub-head sections with removable beads.

7.2. Significant outcomes of this research

The main contributions and outcomes in this thesis are summarised as below.

- This research has significantly improved the understanding and filled the research gap of the bearing behaviour of aluminium sub-head sections in window wall systems under wind load.
- A comprehensive experimental study was conducted. Reliable bearing capacity data for aluminium sub-head sections have been produced with different loading and boundary conditions, various geometric parameters, and different bearing widths. It is expected that the designers and researchers can use the data obtained from experiments for accurate design of aluminium sub-heads.
- Reliable FE models were developed to simulate the bearing behaviours of two types of aluminium sub-heads. Several parameters were carefully investigated, such as element types, mesh size, boundary conditions, aluminium material model, and contact. The developed FE models were found to accurately capture the bearing behaviour aluminium sub-heads when compared to the experimental tests, with differences of less than 10%. The validated FE models can appropriately be used as a basis for future numerical investigation in the relevant field of research.
- Two series of parametric studies based on the validated FE models were performed on two types of aluminium sub-heads. The parametric studies covered wide ranges of parameters and provided a better understanding of bearing behaviour of aluminium sub-heads.
- This research was the first attempt to propose design formulae for aluminium sub-head sections in window wall systems under wind load. The bearing design formulae have the ability to accurately estimate the bearing capacity of aluminium sub-head sections.

7.3. Recommendations for future research

Based on the work presented in this thesis, the following research gaps need to be addressed in future studies to further extend the knowledge base of aluminium sub-heads in window wall systems.

- Even though the bearing behaviour and capacity of the aluminium C-shaped sub-heads and sub-heads with removable beads were investigated in detail in this research, the proposed design rules still represent a firsthand approach in the design of aluminium sub-head profiles. Hence, further verification using experimental and numerical studies with a wide range of sub-head sections is needed for improvements of the proposed design rules.
- Accurate estimation of the contact length between the aluminium sub-heads and window wall frame (mullion and head) is crucial. This issue could be investigated through experimental and numerical studies using full scale tests on window wall systems.
- Further research can be carried out on the bearing behaviour of other sub-head sections commonly used in the industry, such as sub-heads with removable beads having internal supports.
- Further research is recommended for the geometric optimisation of different aluminium sub-head sections to increase their bearing capacities.
- The fracture in the web to flange junction of sub-heads was not thoroughly investigated in this thesis as it is beyond the scope of this research. Further research into the combined effects of fracture and flange bending should be conducted in the future to develop comprehensive design guidelines for aluminium sub-head sections.

REFERENCE LIST

- Allana, P.K., Carter, D. (2012). Curtain walls issues, problems and solutions, Proc. Of the Building Envelope Technology Symposium, RCIInc., 97–111. <https://iibec.org/wp-content/uploads/2012-bes-allana-carter.pdf>.
- Akbari, M., Gunalan, S., Gilbert, B.P., Guan, H., Baleshan, B. (2020a). Experimental investigation on the bearing behaviour of aluminium sub-heads in façade systems, Thin-walled structures, 42, 1431–1443.
- Akbari, M., Gunalan, S., Gilbert, B.P., Guan, H., Baleshan, B. Bearing behaviour of aluminium sub-heads with removable beads in façade systems. Structures, Under review, 2020b.
- Akbari, M., Gunalan, S., Gilbert, B.P., Talebian, N., Guan, H., Numerical study on bearing behaviour and design of aluminium sub-heads in façade systems. Thin-Walled Structures, Under review, 2020c.
- Aluminium Association. (2015). Aluminium Design Manual (AA). Washington D.C., USA.
- American Iron and Steel Institute. (2007). North American Specification for the Design of Cold-Formed Steel Structural Members (AISI S100-07). Washington D.C., USA.
- American Iron and Steel Institute. (2007). North American Standard for Cold-Formed Steel Framing – Wall Stud Design (AISI 211-07). Washington D.C., USA.
- American Iron and Steel Institute. (2016). Specifications for the cold-formed steel structural members (AISI S100-16). Washington D.C., USA.
- American Iron and Steel Institute. (2015). North American Standard for Cold-Formed Steel Framing – Wall Stud Design (AISI S240-15). Washington D.C., USA.
- Bewick, B., & Williamson, E. (2014). Computational modelling of steel stud wall systems for applications to blast-resistant. Journal of Structural Engineering, 140 (8). <https://ascelibrary.org/doi/abs/10.1061/%28ASCE%29ST.1943-541X.0000942>
- Bewick, B., Casey O.L., & Williamson, E. (2013). Evaluation of conventional construction techniques for enhancing the blast resistance of steel stud walls. Journal of Structural

Bewick, B., O’Laughlin, C., & Williamson, E. (2013). Evaluation of conventional construction techniques for enhancing the blast resistance of steel stud walls. *Journal of Structural Engineering*, 139 (11).
<https://ascelibrary.org/doi/abs/10.1061/%28ASCE%29ST.1943-541X.0000760>

Bewick, B., Hoemann, J., & Williamson, E. (2010). Performance of steel stud walls subjected to blast loads. *Structures Congress*.
<https://ascelibrary.org/doi/10.1061/41130%28369%29185>

Bolte, W.G., & LaBoube R.A. (2004). Behaviour of curtain wall stud to track connections. *Thin-walled structures*, 42, 1431–1443.
<https://www.sciencedirect.com/science/article/abs/pii/S0263823104000928>

Bolte, W.G. (2003). Behaviour of cold-formed steel stud-to-track Connections, (M.S. Thesis, University of Missouri-Rolla, Rolla, MO, USA)
https://scholarsmine.mst.edu/masters_theses/2319/

Bondok, D.H., Salim, H.A., & Agee, B.M. (2015). Improved static resistance and failure mechanisms of conventional cold-formed steel stud walls. *Journal of Performance of Constructed Facilities*, 29 (3).
<https://ascelibrary.org/doi/10.1061/%28ASCE%29CF.1943-5509.0000525>

Bondok, D., Salima, H., Sauciera, A., & Dinan, R. (2015). Static resistance function of cold-formed steel stud walls. *Thin-Walled Structures*, 94, 177–187.
<https://www.sciencedirect.com/science/article/abs/pii/S0263823115001275>

Bondok, D., Salima, H. (2014). Numerical Modeling of Conventional Steel Stud Walls, Static Resistance for Blast Response Predictions, *Journal of Structural Engineering*, 140 (7).
<https://ascelibrary.org/doi/abs/10.1061/%28ASCE%29ST.1943-541X.0000968>

Brühl, F., Kuhlmann, U., & Jorissen, A. (2011). Consideration of plasticity within the design of timber structures due to connection ductility. *Engineering Structures*, 33, 3007–3017. <https://www.sciencedirect.com/science/article/pii/S0141029611003270>

Drysdale, R.G., & Breton, N. (1991). Strength and stiffness characteristics of steel stud backup walls designed to support brick veneer. Part 1 of the McMaster University

Laboratory Test Program on Brick Veneer/Steel Stud Wall Systems, McMaster University, Ontario, Canada.

- Espinoza, J., Hall, G., & Serrette, R. (2018). Strength of cold-formed steel slotted track connections for out-of-plane wall loads. *Journal of Constructional Steel Research*, 151, 253–262. <https://www.sciencedirect.com/science/article/pii/S0143974X18303729>
- European Committee for Standardization. (2007). Design of aluminum structures—part 1.1: general rules—general rules and rules for buildings, EC9, (DD ENV 1999-1-1:2007).
- Fiorino, L. Iuorio, O., Macillo, V., Terracciano, M.T., Pali, Landolfo, T.R. (2015). Seismic design method for CFS diagonal strap-braced stud walls: experimental validation, *Journal of Structural Engineering*, 142. <https://ascelibrary.org/doi/10.1061/%28ASCE%29ST.1943-541X.0001408>.
- Fiorino, L., Shakeel, S., Macillo, V., Landolfo, R. (2017). Behaviour factor (q) evaluation the CFS braced structures according to FEMA P695, *Journal of Constructional Steel Research*, 138, 324–339. <https://www.sciencedirect.com/science/article/pii/S0143974X17301128>
- Fox, S.R., & Schuster, R.M. (2000). Lateral strength of wind loadbearing wall stud-to-track connections. *Proceedings of the Fifteenth International Specialty Conference on Cold-Formed Steel Structures*, University of Missouri-Rolla, Rolla, MO, USA.
- Gerloff, J.R., Hutte1maier, P., & Ford, P.W. (2004). Cold-formed steel slip-track connection. *17th International Specialty Conference on Cold-Formed Steel Structures*, University of Missouri-Rolla, Rolla, MO, USA.
- Gilbert, B.P., & Rasmussen, K.J.R. (2011). Determination of the base plate stiffness and strength of steel storage racks. *Journal of Constructional Steel Research*, 67, 1031–1041. <https://www.sciencedirect.com/science/article/pii/S0143974X11000150>
- Hui, C., Zhu, Y., Wang, B., Wang, Y., & Tao, W. (2015). Experimental and theoretical investigation on mechanical performance of aluminum alloy beams in unit curtain walls. *Advances in Structural Engineering*, 18 (12), 2103–2115. <https://journals.sagepub.com/doi/abs/10.1260/1369-4332.18.12.2103>

- Iuorio, O., Macillo, V., Terracciano, M.T., Pali, T., Fiorino, L., Landolfo, R. (2014). Seismic response of Cfs strap-braced stud walls: Experimental investigation, *Thin-Walled Structures*, 85, 466–480.
<https://www.sciencedirect.com/science/article/abs/pii/S0263823114002742>
- Jenkins, C., Soroushian, S., Rahmanishamsi, E., & Maragakis, E.M. (2016). Experimental fragility analysis of cold-formed steel-framed partition wall systems. *Thin-Walled Structures*, 103, 115–127.
<https://www.sciencedirect.com/science/article/abs/pii/S0263823116300453>
- Kawneer White Paper. (1999). Principle of Curtain Walling.
http://beta.lecture.ub.ac.id/files/2014/02/Principles_of_Curtain_Walling.pdf
- Kesawan, S., & Mahendran, M. (2019). Member moment capacity of complex-shaped aluminium mullions under wind suction loading. *Thin-Walled Structures*, 144, 106258.
<https://www.sciencedirect.com/science/article/abs/pii/S0263823118308826>
- Kesawan, S., Mahendran, M., & Baleshan, B. (2018). Section moment capacity tests of complex-shaped aluminium mullions. *Thin-Walled Structures*, 131, 855–868,
<https://www.sciencedirect.com/science/article/abs/pii/S0263823118304257>
- Kesawan, S., & Mahendran, M. (2018). Buckling behaviour and design of complex-shaped aluminium mullion sections. *Advances in Structural Engineering*, 22 (2), 547–564.
<https://journals.sagepub.com/doi/abs/10.1177/1369433218795118>
- Kissell, J. R., & Ferry, R.L. (2002). Aluminium structures: A guide to their specifications and design. Second edition. New York, USA. <https://www.wiley.com/en-us/Aluminum+Structures%3A+A+Guide+to+Their+Specifications+and+Design%2C+2nd+Edition-p-9780471275541>
- LaBoube, R.A., & Findlay, P.F. (2007). Wall stud-to-track gap: experimental investigation. *Journal of Architectural Engineering*, 13.
<https://ascelibrary.org/doi/full/10.1061/%28ASCE%2910760431%282007%2913%3A2%28105%29>
- Lewis, A.V. (2008). Strength of cold-formed steel jamb stud-to-track connections. Research Report, University of Waterloo, Waterloo, Ontario, Canada.

- Lewis, V., Fox, S.R., & Schuster, R.M. (1999). A further study into the web crippling behaviour at the stud to track connection. Canadian Cold Formed Steel Research Group report, University of Waterloo, Waterloo, Ontario, Canada.
- Marinovic, I. (1994). Thin-walled metal structural members (M.S. Thesis, Cornell University, Ithaca, New York, USA).
- Mazzolani, FM. (1978), Design bases and strength of aluminium alloy structures, Jornadas Tecnicas sobre Estructuras en Aluminio, Bilbao.
- Mazzolani, FM. (2004), Structural use of aluminium alloys in civil engineering, Proceedings of the 2nd International Conference on Structural Engineering, Mechanics and Computation (SEMC 2004), Cape Town.
- Mijović, D.Đ., Milanović, D., & Savić, J. (2018). Curtain walls: history and a continuing challenge. Xviii anniversary international scientific conference by construction and architecture, Sofia, Bulgaria.
- Moghimi, H., Ronagh, H.R. (2009). Performance of light-gauge cold-formed steel strap-braced stud walls subjected to cyclic loading. *Engineering Structures*, Vol. 31, pp. 69-83.
- Naqash, M.T., Formisano, A., & Gianfranco, D.M. (2016). Aluminium Framing Members in Facades. *Key Engineering Materials*, 710, 327-332.
<https://www.scientific.net/KEM.710.327>
- Natario, P., Silvestre, N. Camotim, D. (2014). Web crippling failure using quasi-static FE models. *Thin Walled Struct*, 84:34–49.
- Pekoz, T. (1990). Design of cold-formed steel screw connections. Tenth International Specialty Conference on Cold-formed Steel Structures, Missouri, USA.
- Rahman, N.A. (2005). Design of single deep leg track to accommodate vertical deflection (Technical note). TSN, Durham, NC.
- Rahmanishamsi, E., Soroushian, S., & Maragakis. M. (2014). System-Level Experiments on Ceiling/Piping/Partition Systems at UNR-NEES Site. Tenth U.S.. National Conference on Earthquake Engineering, Anchorage, AK.
<https://scinapse.io/papers/2182329288>

- Rahmanishamsi, E., Soroushian, S., & Maragakis, E.M. (2016). Analytical model for the in-plane seismic performance of cold formed steel-framed gypsum partition walls. *Earthquake engineering & structural dynamics*, 45, 619–634. <https://ascelibrary.org/doi/10.1061/9780784479117.147>
- Ramberg, W., & Osgood W. R., (1943). Description of stress-strain curves by three parameters. National advisory Committee for Aeronautics (Technical Note, No. 902).
- Retamales, R., Davies, R., Mosqueda, G., & Filiatrault, A. (2013). Experimental seismic fragility of cold-formed steel framed gypsum partition walls. *Journal of Structural Engineering*, 139, 1285–1293. <https://ascelibrary.org/doi/10.1061/%28ASCE%29ST.1943-541X.0000657>
- Salim, H.A., Muller, P., & Dinan, R. (2005). Response of conventional steel stud wall systems under static and dynamic pressure. *Journal of Performance of Constructed Facilities*, 19 (4). <https://trid.trb.org/view/766924>
- Salim, H.A., & Townsend, P.T. (2004). Explosion-resistant steel stud wall system, Structures Congress 2004. <https://ascelibrary.org/doi/abs/10.1061/40700%282004%2920>
- Schumacher, C., Fox, S.R., & Schuster, R.M. (1998). Web crippling behaviour of laterally loaded cold formed steel studs at the stud/track connection. Canadian Cold Formed Steel Research Group report, University of Waterloo, Waterloo, Ontario, Canada.
- Skejic, D., Lukic, M., Buljan, N., & Vido, H. (2016). Lateral torsional buckling of split aluminium mullion. *Key Engineering Materials*, 710, 445–450. <https://www.scientific.net/KEM.710.445>
- Shakeel, S., Landolfo, R., Fiorino, L. (2019). Behaviour factor evaluation of CFS shear walls with gypsum board sheathing according to FEMA P695 for Eurocodes, *Thin-Walled Structures* 141, 194–207. <https://www.sciencedirect.com/science/article/abs/pii/S0263823118313600>.
- Standards Australia. (2012). Steel storage racking (AS 4084-2012). Sydney, Australia.
- Standards Australia. (1997). Aluminium structures - Part 1: Limit state design Aluminium structures (AS/NZS1664.1:1997). Sydney, Australia.
- Standards Australia. (2014). Windows and external glazed doors in buildings (AS 2047-2014), Sydney, Australia,

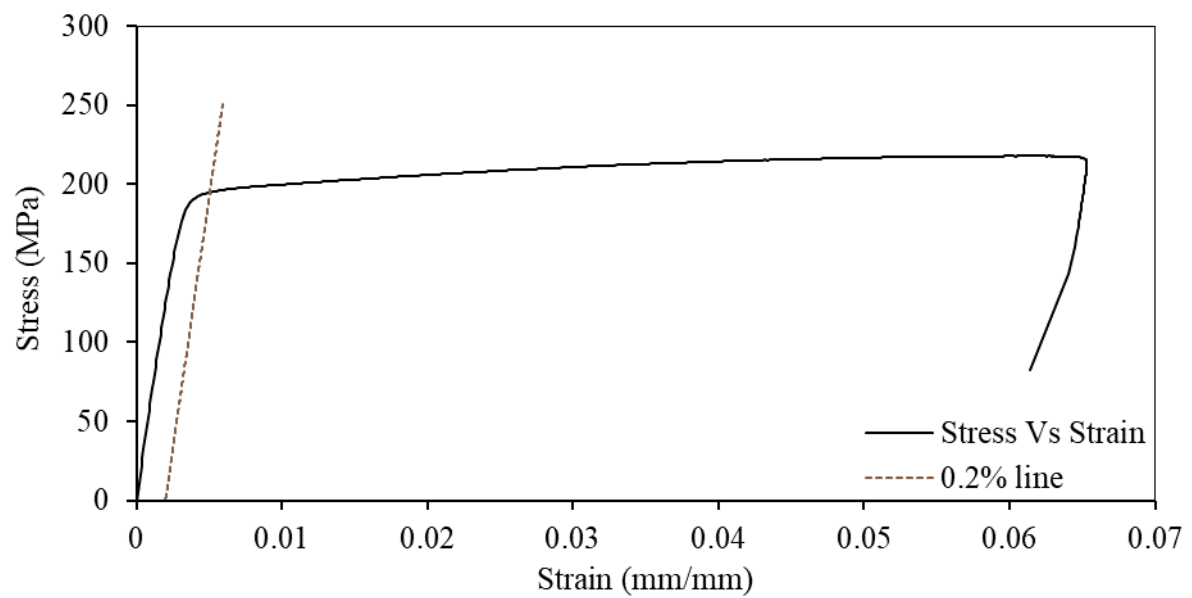
- Standards Australia. (2012). Wind loads for housing (AS 4055-2012). Sydney, Australia.
- Standards Australia. (2006). Glass in buildings-Selection and installation (AS 1288-2006). Sydney, Australia.
- Standards Australia (2018), Cold-formed Steel Structures (AS/NZS 4600), Sydney, Australia.
- Australian/New Zealand Standard (2011), Structural design actions, Part 2: Wind actions (AS/NZS 1170.2:2011). Sydney, Australia.
- Steel Stud Manufacturers Association. (2000). Single deflection track selection, industry double note cold formed steel construction (SSMA). Chicago, IL. USA.
- Su, M.N., Young, B., Gardner, L. (2014). Testing and design of aluminium alloy cross-sections in compression. *Journal of structural engineering*, 140 (9).
- Su M.N., Young B., Gardner L. (2016), The continuous strength method for the design of aluminium alloy structural elements, *Engineering structures*, 122 (1), 338 – 348.
- Talebian, N., Gilbert, B.P., Baldassino, N. (2019). Factors contributing to the transverse shear stiffness of bolted cold-formed steel storage rack upright frames with channel bracing members, *Thin-Walled Structures*, 136. <https://www.sciencedirect.com/science/article/abs/pii/S0263823118308346>
- Talebian, N., Gilbert, B.P., Pham, C.H., Chariere, R. (2020). Parametric Studies and Design Rules for Local and Distortional Biaxial-Bending Capacity of Cold-Formed Steel Storage-Rack Uprights, *Journal of Structural Engineering*, 146. <https://ascelibrary.org/doi/10.1061/%28ASCE%29ST.1943-541X.0002548>
- United States Army Corps of Engineers. (1998). Design of cold-formed load-bearing steel systems and masonry veneer/steel stud wall, Technical Instructions (TI 809-07). Washington, DC, USA.
- Wang, Y. (2006). Structural behaviour and design of two custom aluminum extruded shapes in custom unitized curtain wall systems (MSc thesis, School of Civil Engineering, University of Cincinnati, Ohio, USA).
- Wang, X., Pantoli, E., Hutchinson, T., Restrepo, J., Wood, R., Hoehler, M., Grzesik, P., & Sesma, F. (2015). Seismic performance of cold-formed steel wall systems in a full-

- scale building. *Journal of Structural Engineering*, 141.
<https://ascelibrary.org/doi/10.1061/%28ASCE%29ST.1943-541X.0001245>
- Whelan, M.J., Ralston, A.D., & Weggel, D.C. (2016). Blast testing of cold-formed steel-stud wall panels. *Journal of Performance of Constructed Facilities*, 30 (2).
<https://ascelibrary.org/doi/abs/10.1061/%28ASCE%29CF.1943-5509.0000734>
- Yang, Y., Huang, J., & Li, X. (2017). The effect of the bolt spacing on the performance of the steel-aluminium composite mullions of curtain wall. *Thin-Walled Structures*, 117, 239–246. <https://www.sciencedirect.com/science/article/abs/pii/S0263823116307455>
- Yura, J.A., Edwards, I. F., & Zettlemoyer, N. (1981). Ultimate capacity of circular tubular joints. *Journal of the Structural Division*, 107, 1965– 1985.
<https://cedb.asce.org/CEDBsearch/record.jsp?dockkey=0010508>
- Yasumura, M., & Kawai, N. (1998). Estimating seismic performance of wood-framed structures. *Proceedings of 1998 I.W.E.C. Switzerland*, 2, 564-571.

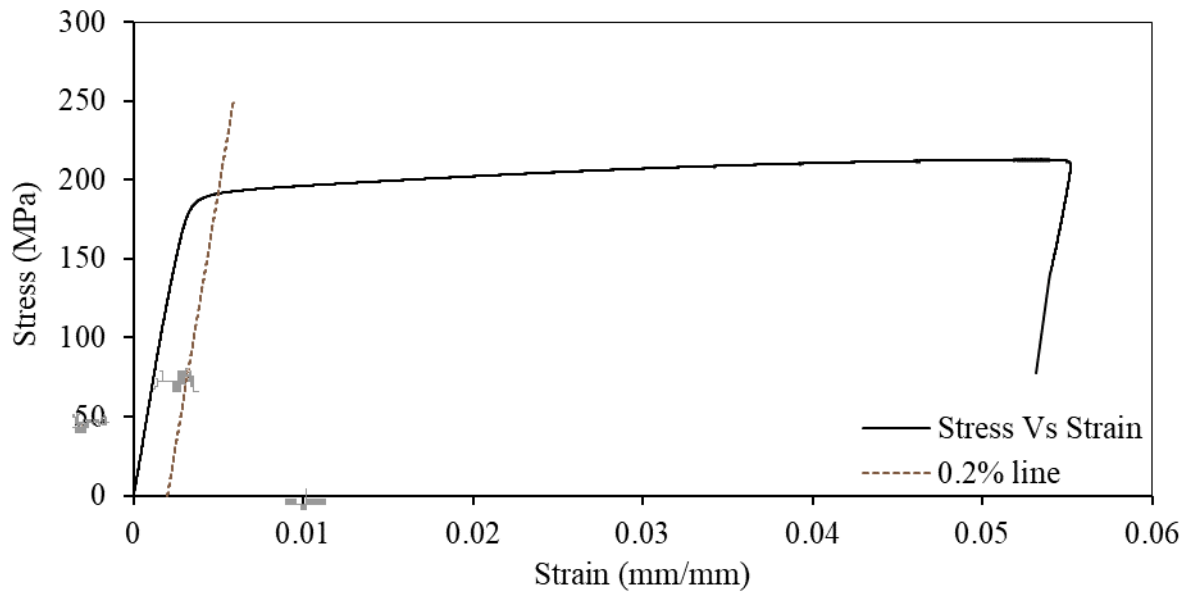
APPENDIX A. ALUMINIUM TENSILE COUPON TEST RESULTS

A.1. Section 675-027

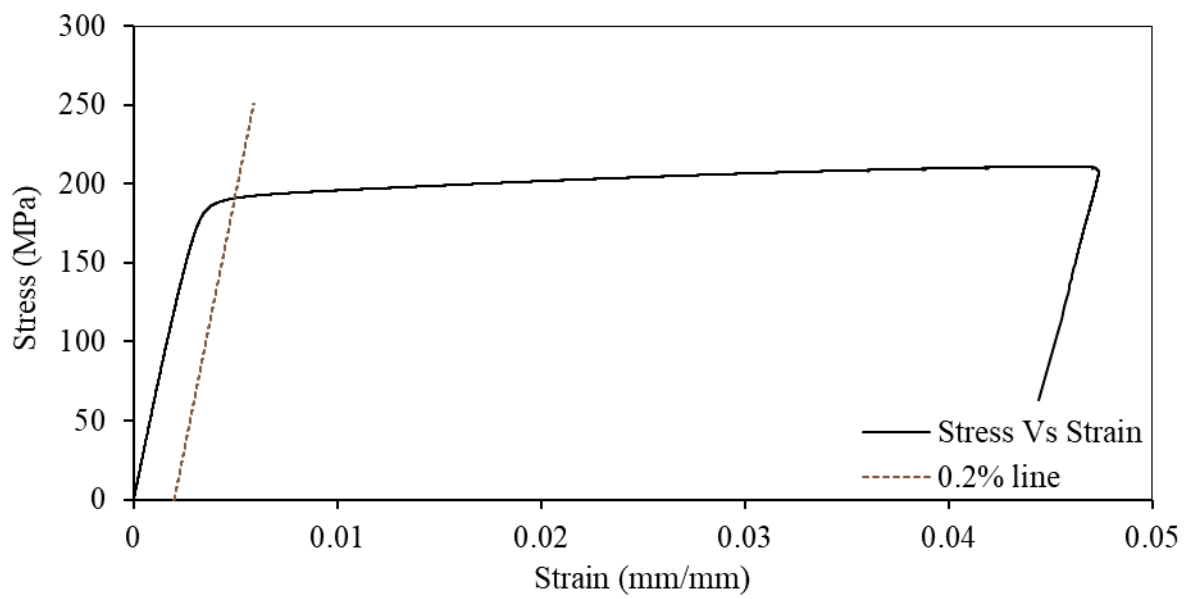
A.1.1. 675-027-1



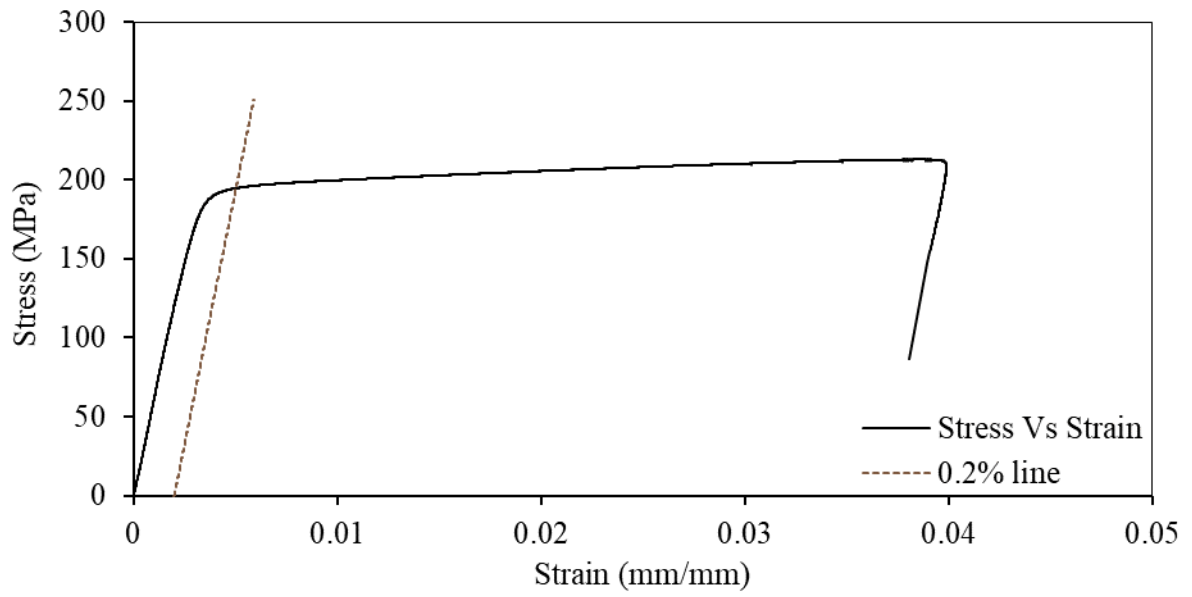
A.1.2. 675-027-2



A.1.3. 675-027-3

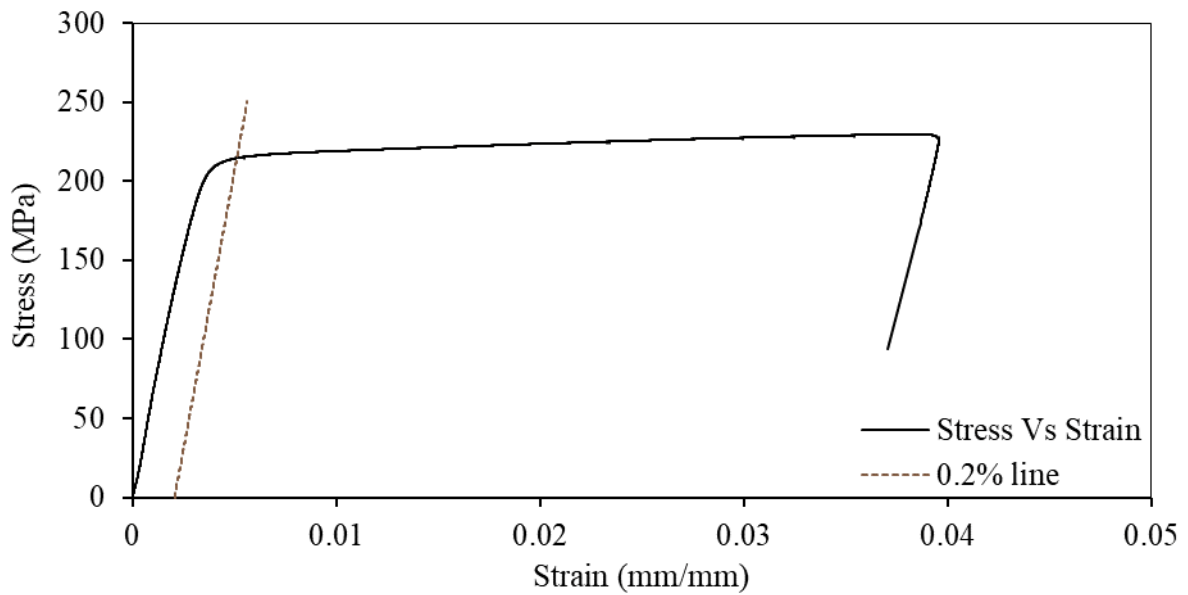


A.1.4. 675-027-4

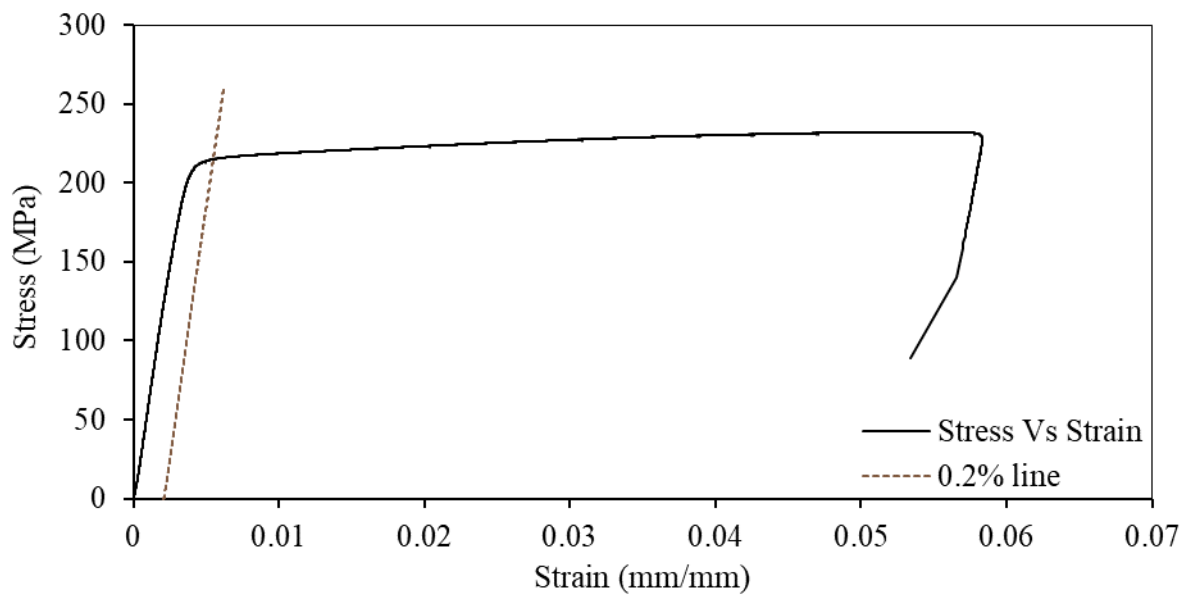


A.2. Section 475-077

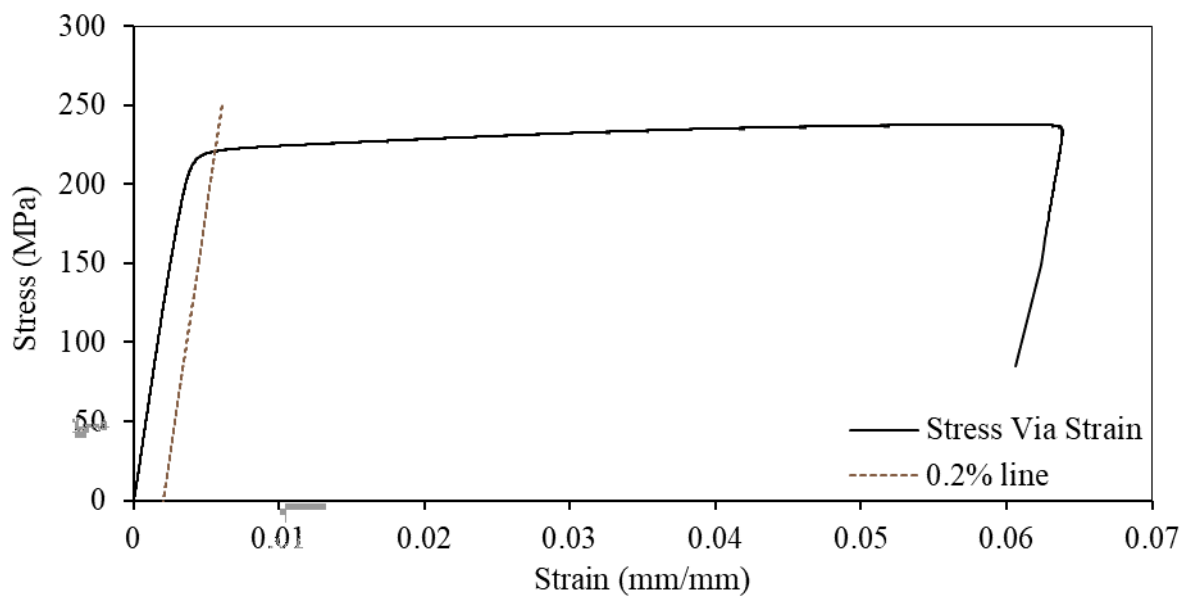
A.2.1. 475-077-1



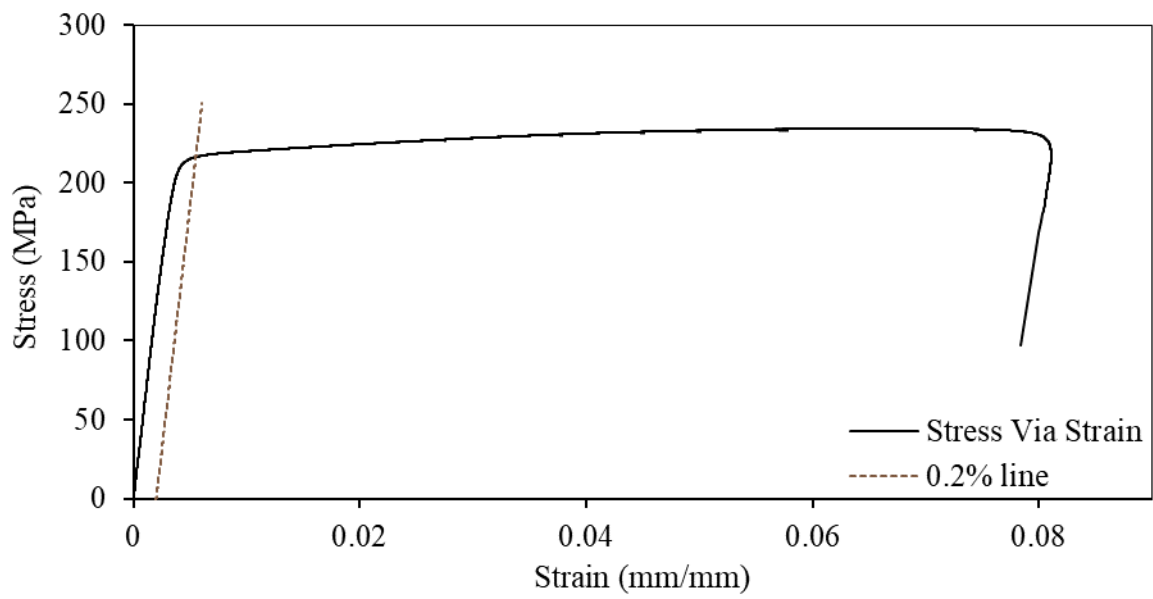
A.2.2. 475-077-2



A.2.3. 475-077-3

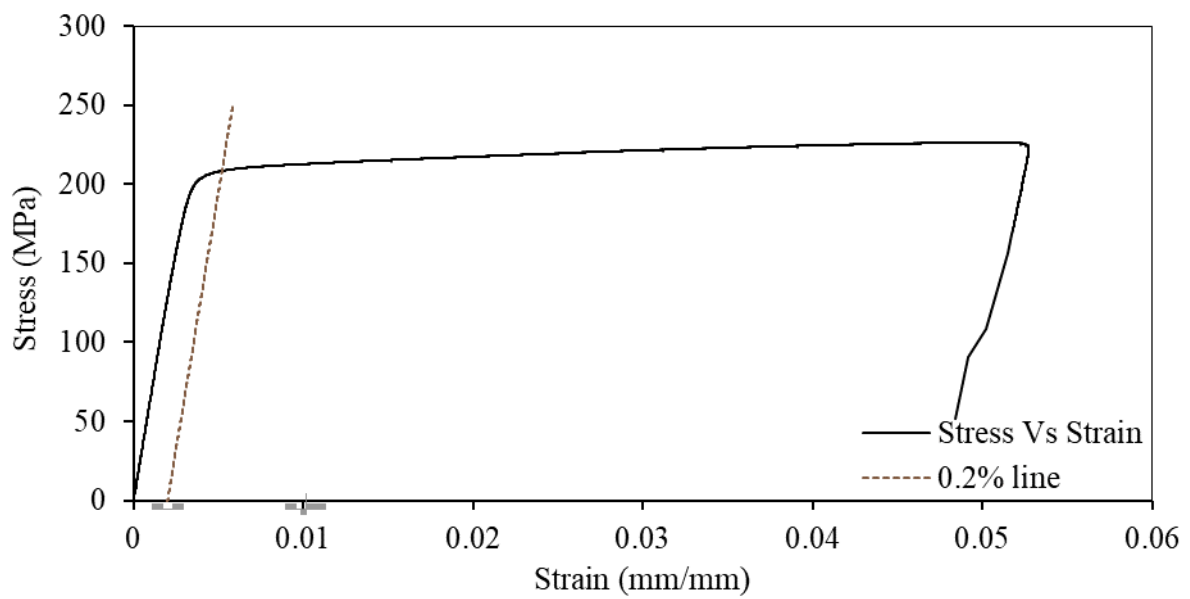


A.2.4. 475-077-4

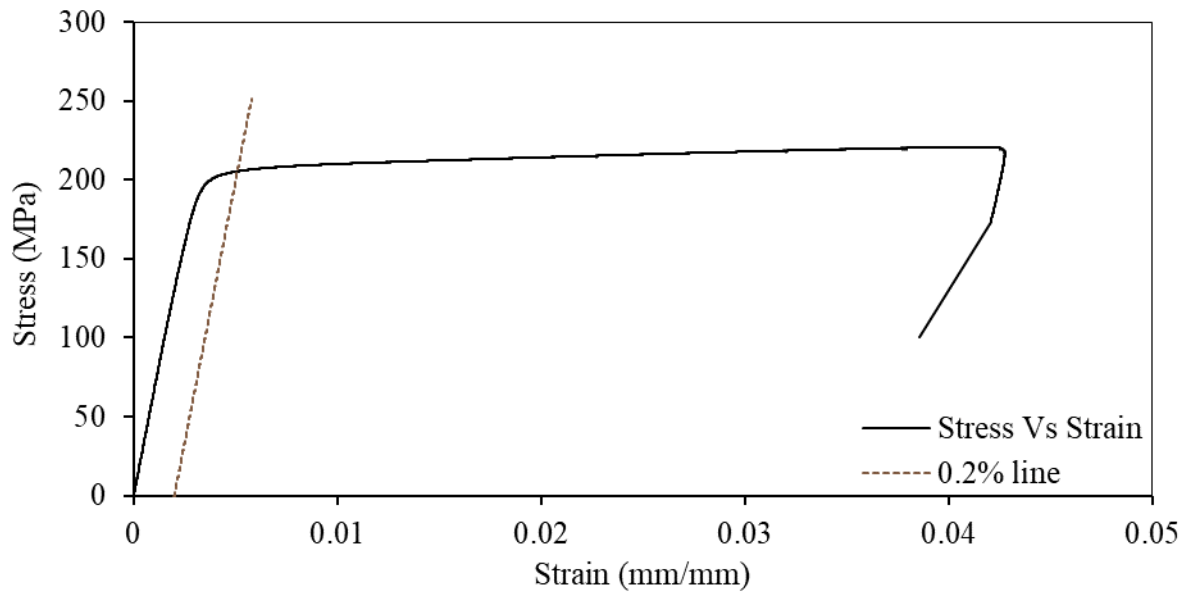


A.3. Section 475-057

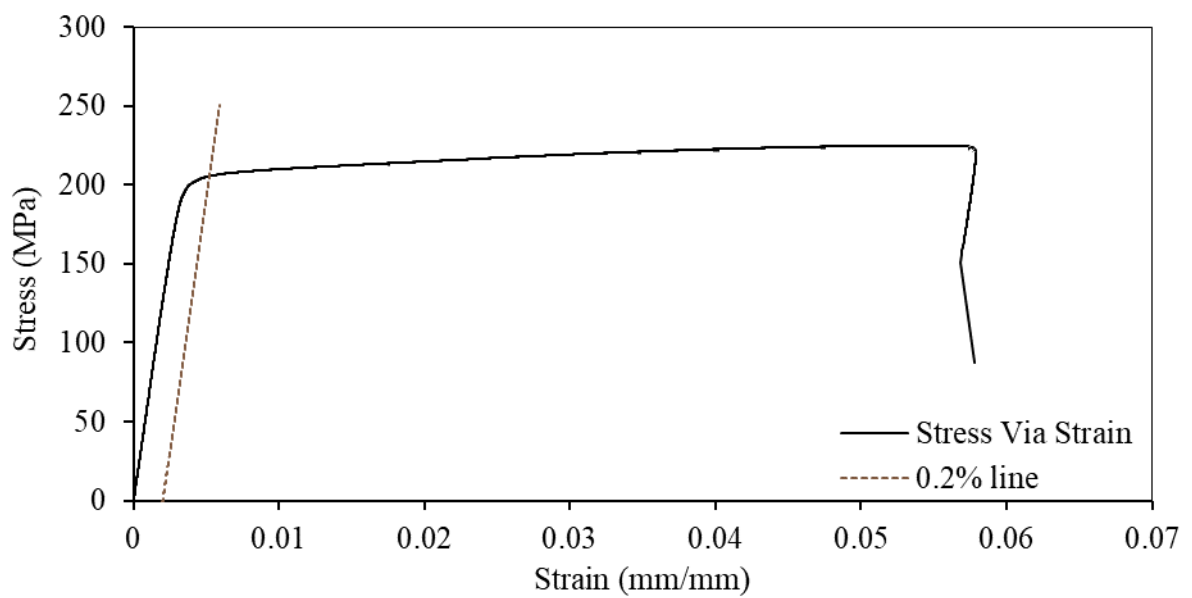
A.3.1. 475-057-1



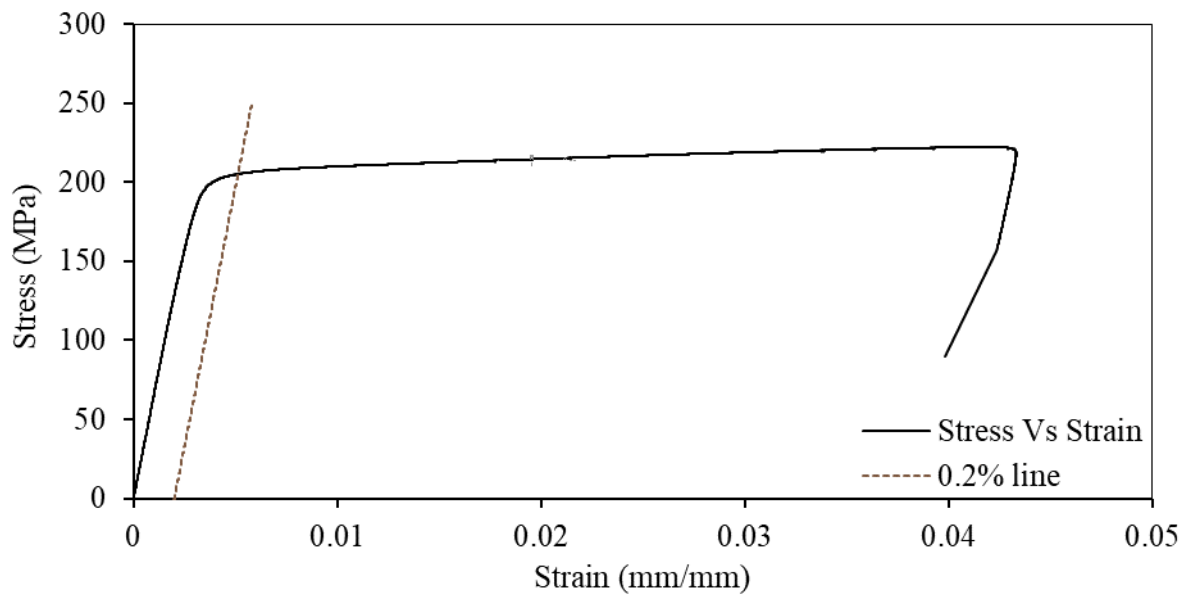
A.3.2. 475-057-2



A.3.3. 475-057-3

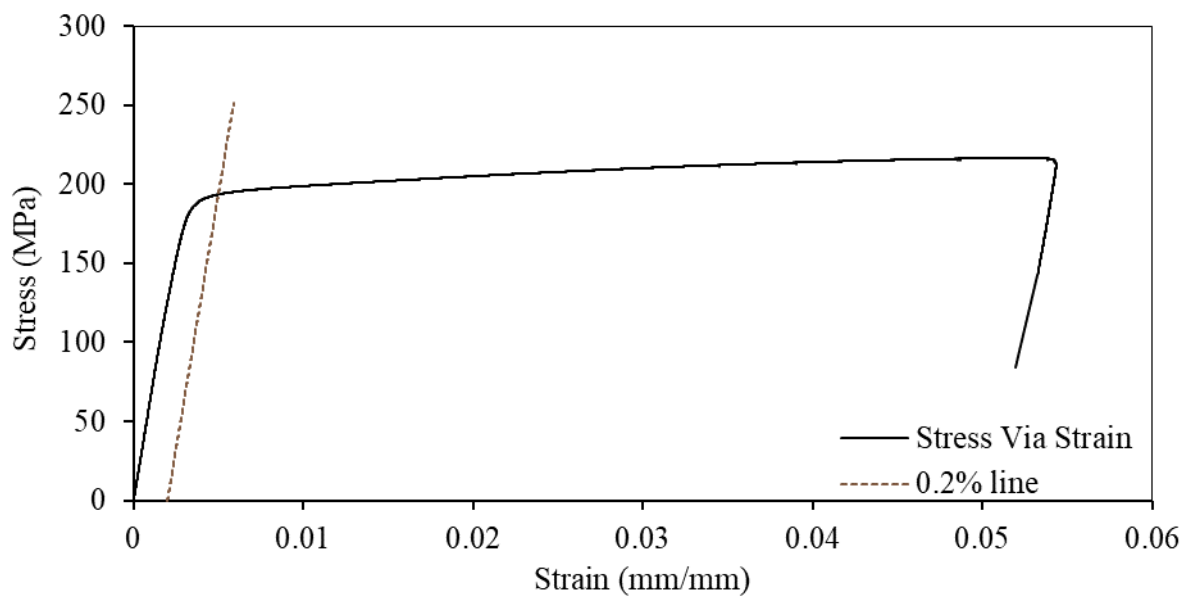


A.3.4. 475-057-4

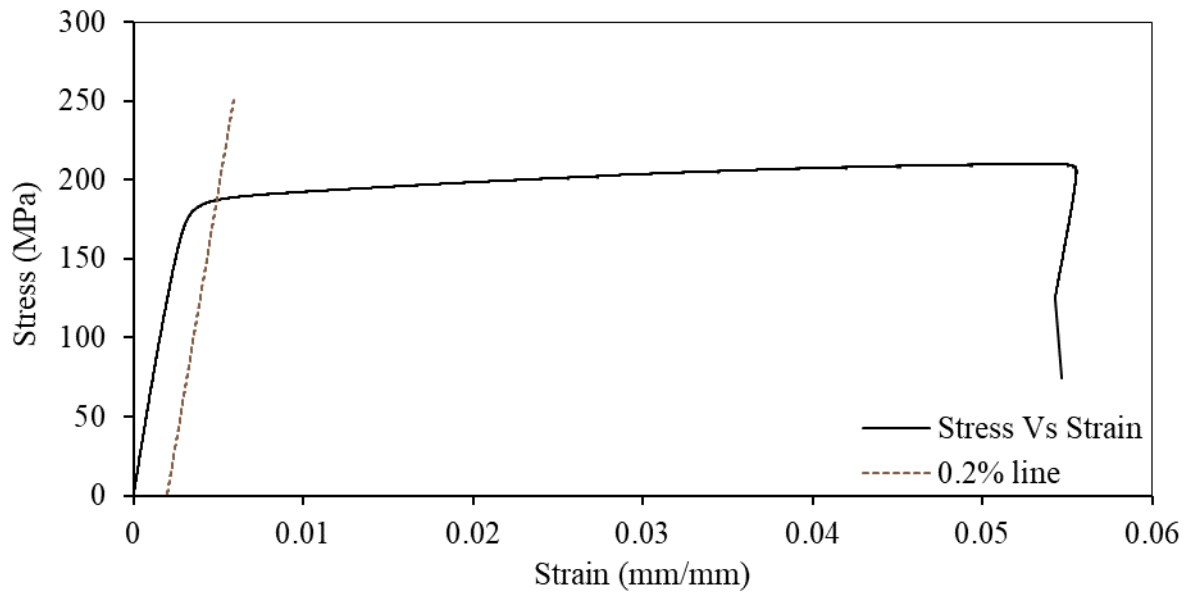


A.4. Section 475-071

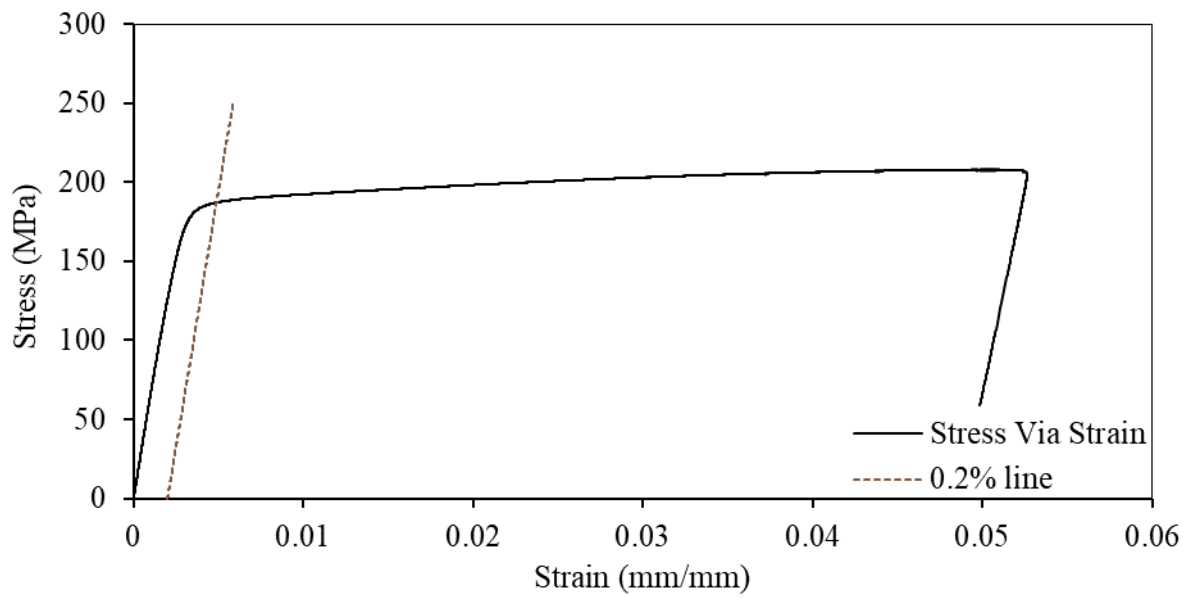
A.4.1. 475-071-1



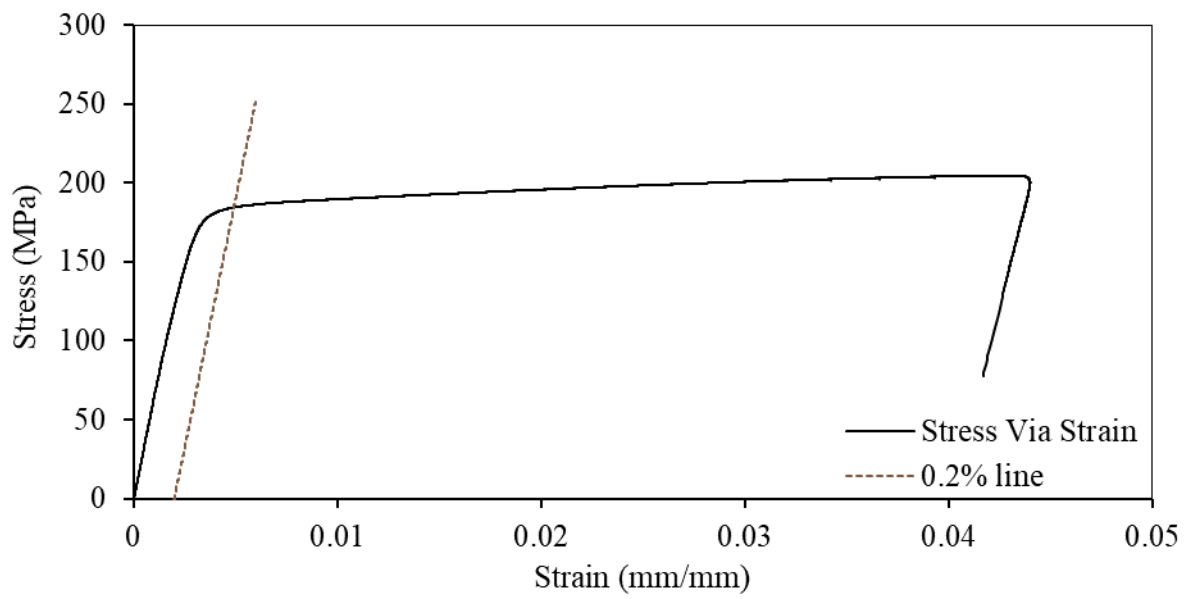
A.4.2. 475-071-2



A.4.3. 475-071-3

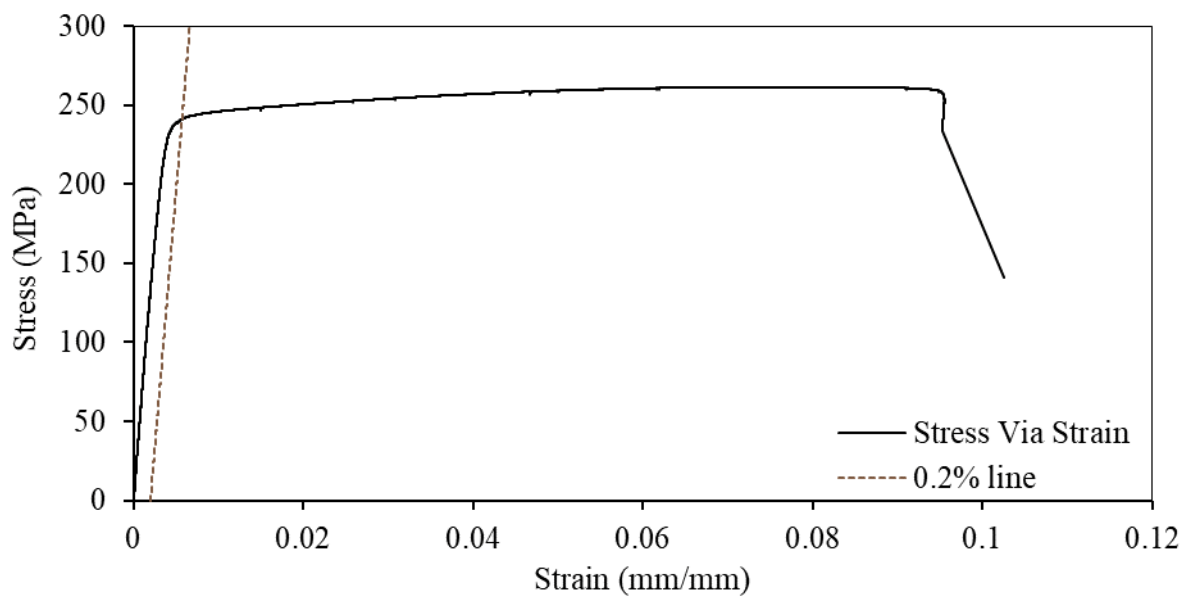


A.4.4. 475-071-4

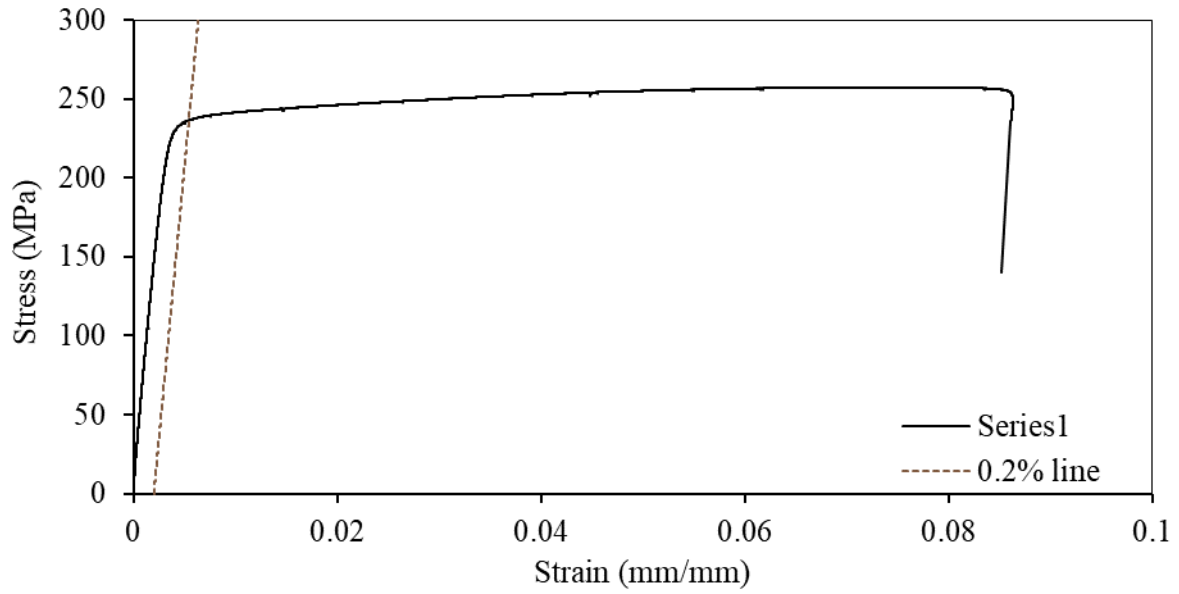


A.5. Section 165863

A.5.1. 165863-1

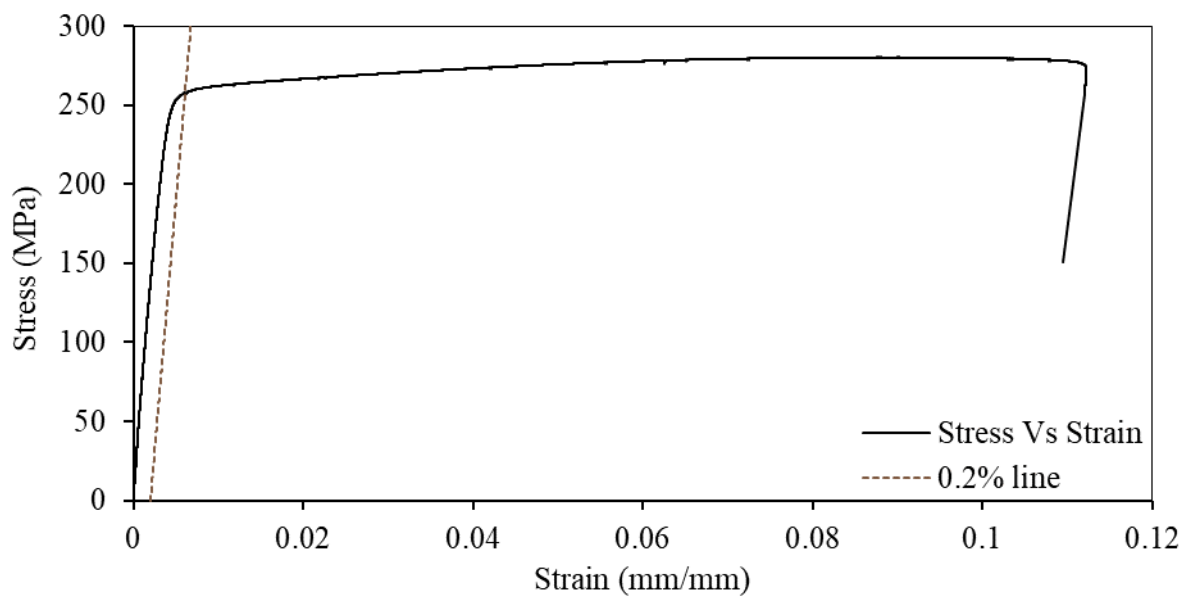


A.5.2. 165863-2

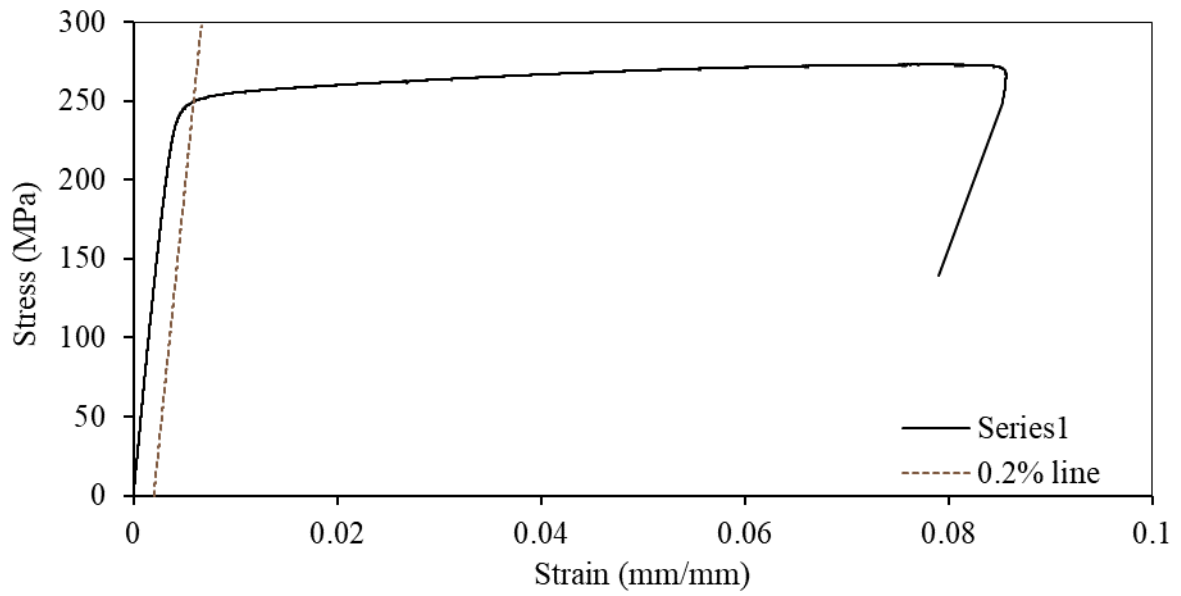


A.6. Section 475059

A.6.1. 475059-1

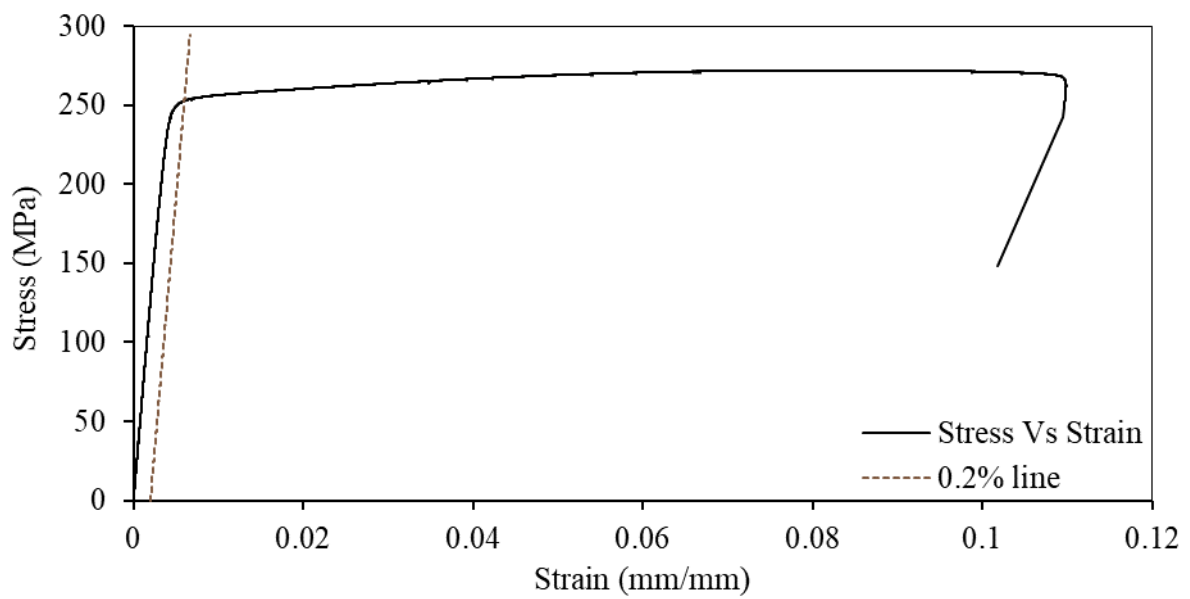


A.6.2. 475059-2

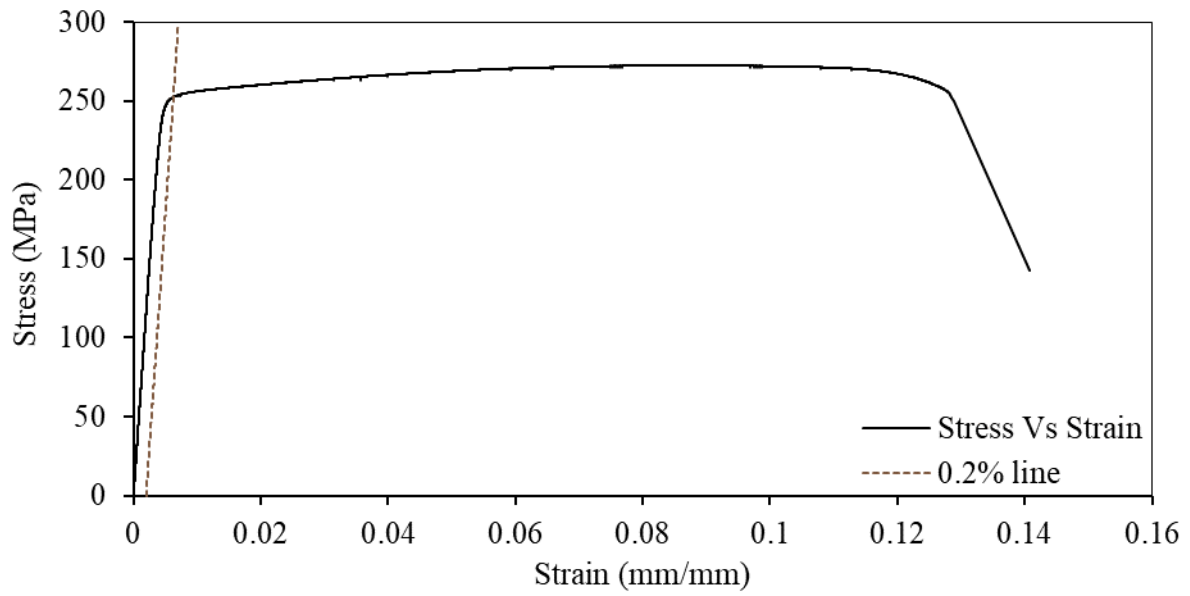


A.7. Section 475066

A.7.1. 475066-1

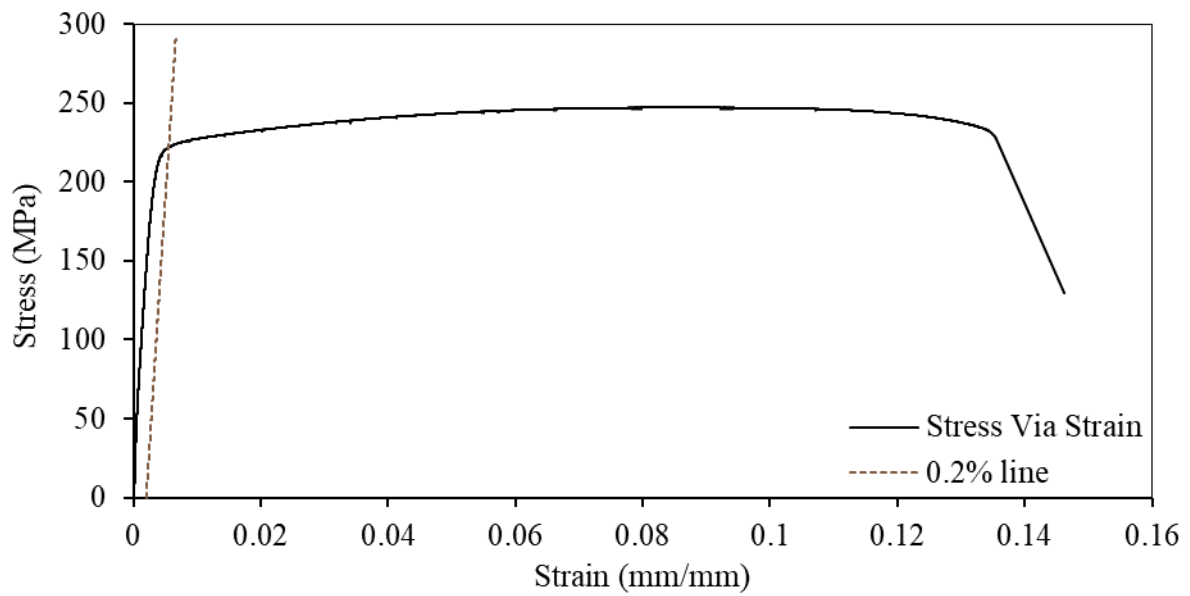


A.7.2. 475066-2

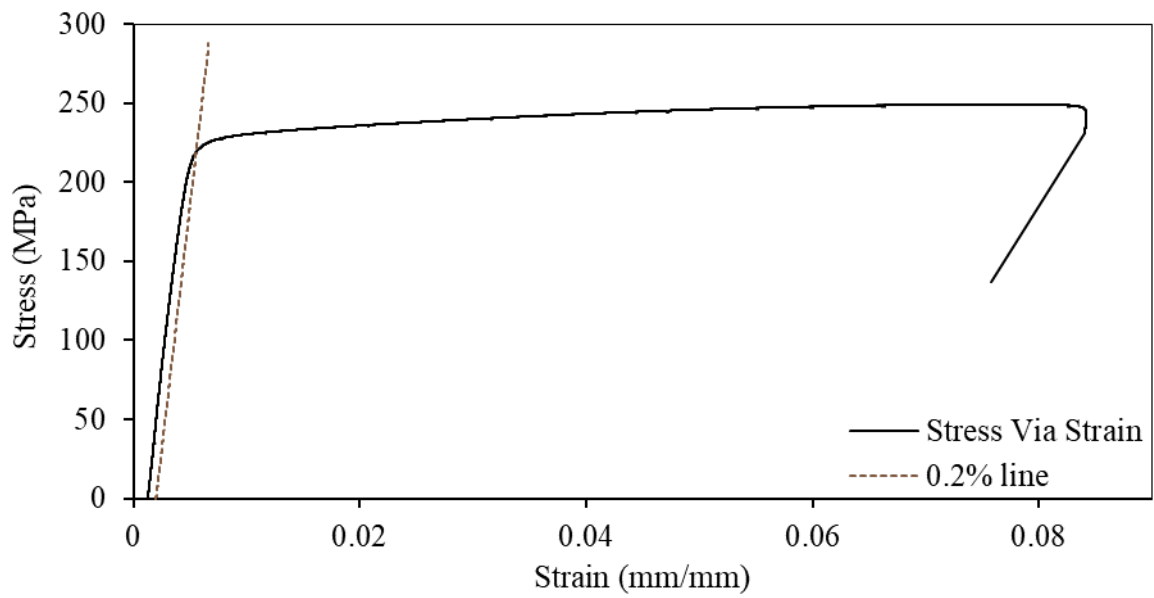


A.8. Section 475072

A.8.1. 475072-1

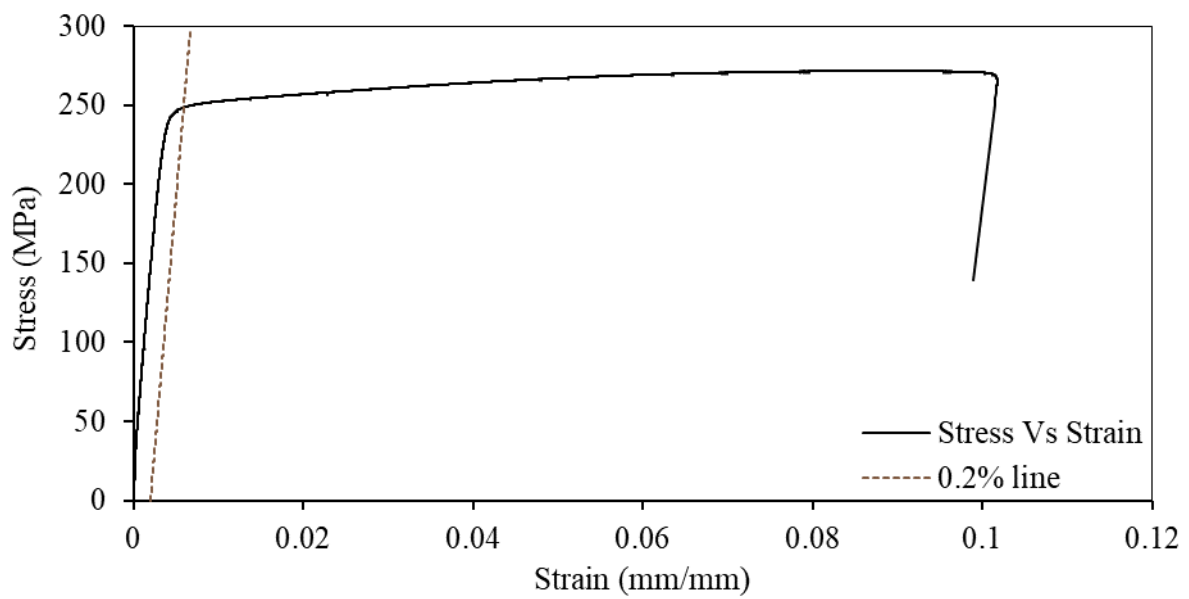


A.8.2. 475072-2

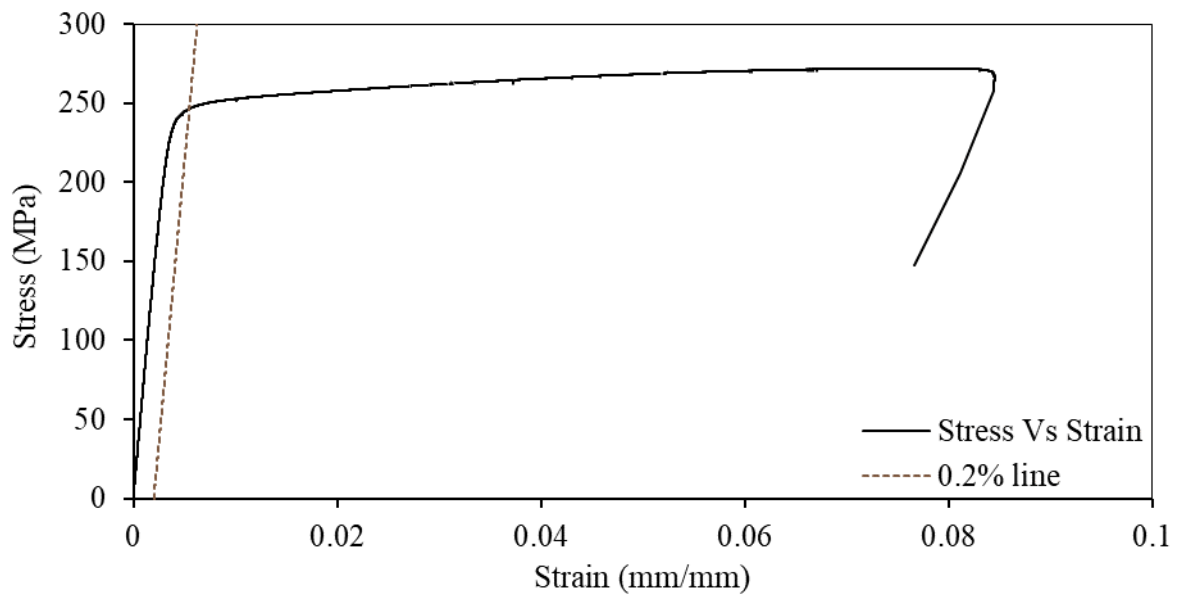


A.9. Section 475073

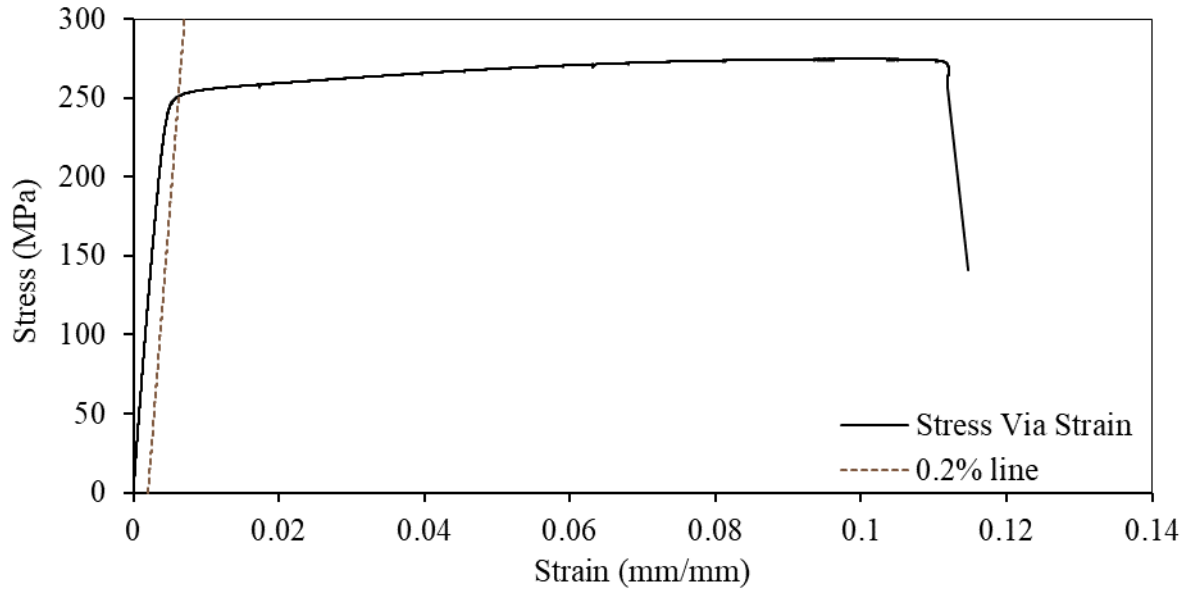
A.9.1. 475073-1



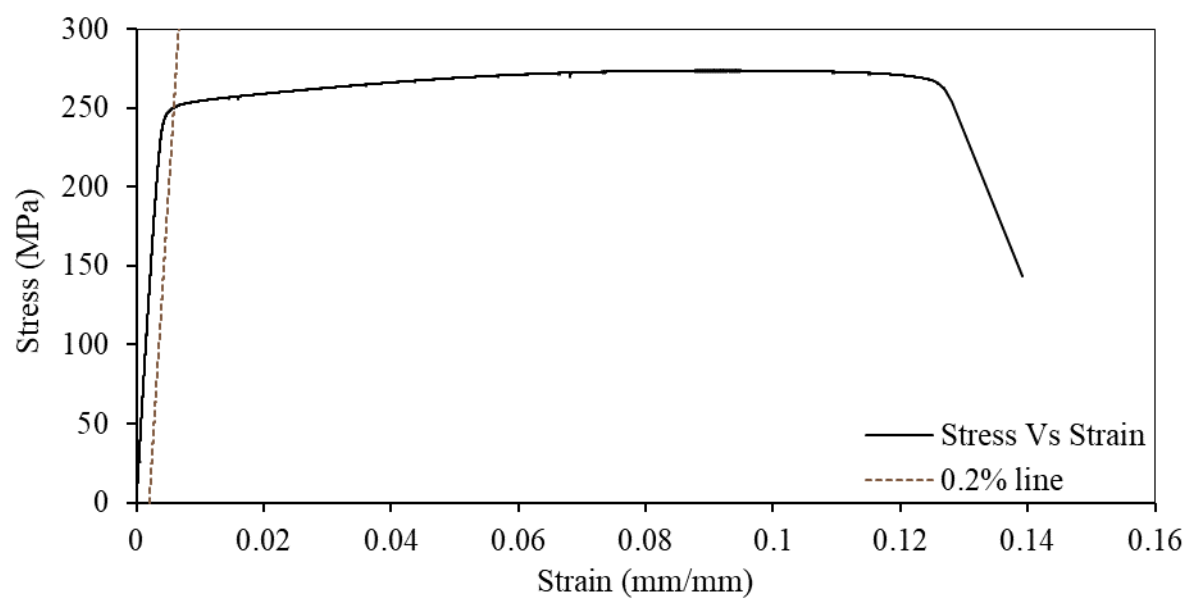
A.9.2. 475073-2



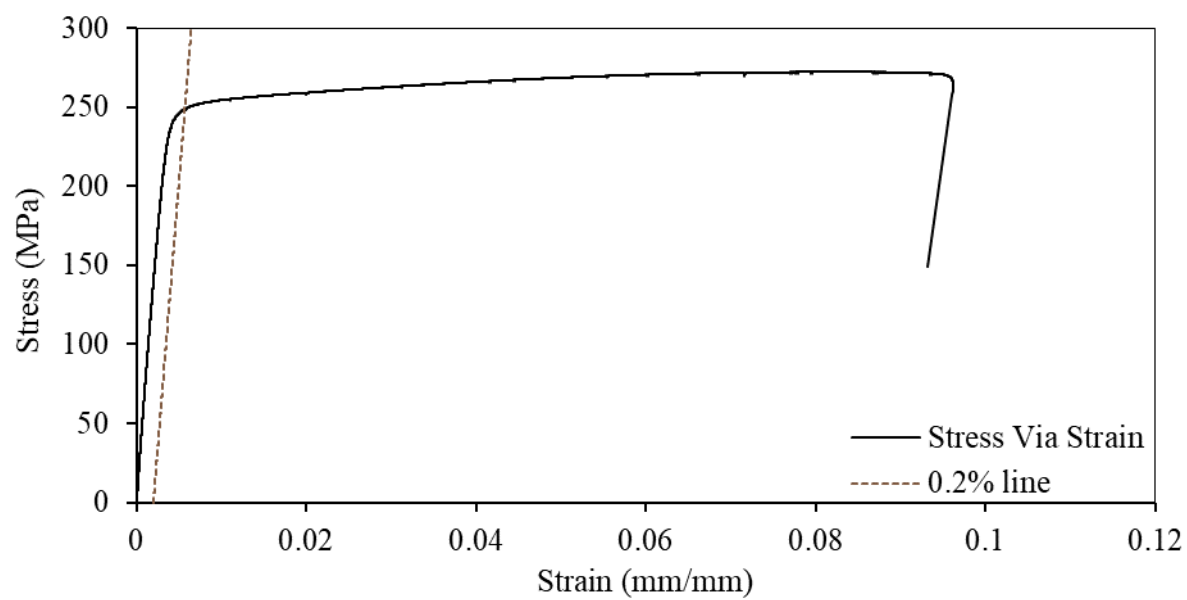
A.9.3. 475073-3



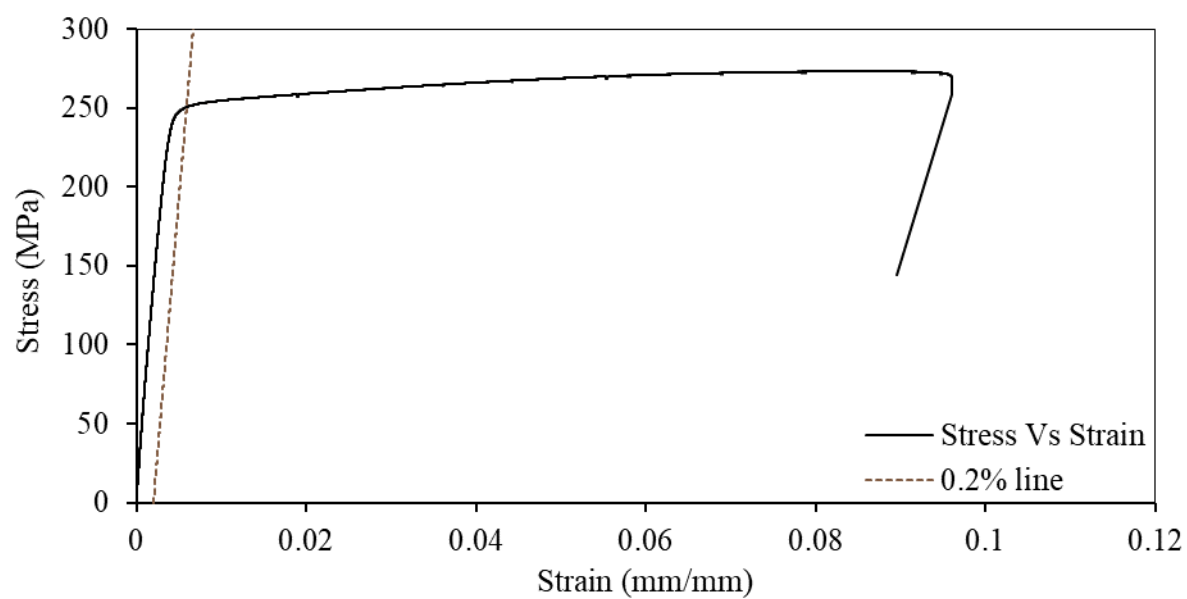
A.9.4. 475073-4



A.9.5. 475073-5

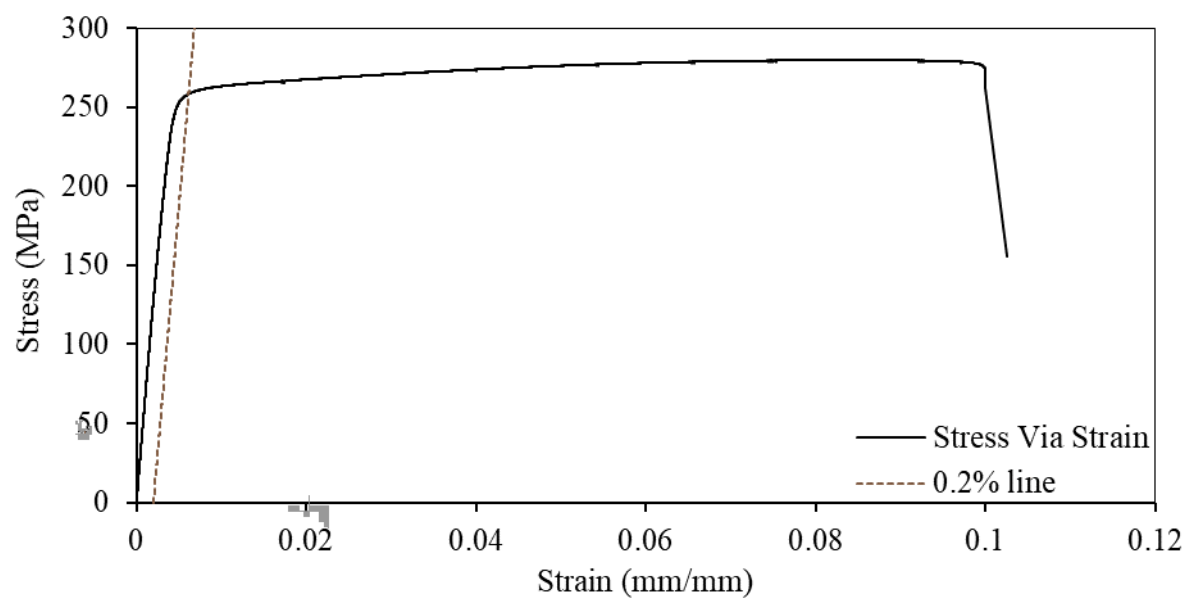


A.9.6. 475073-6

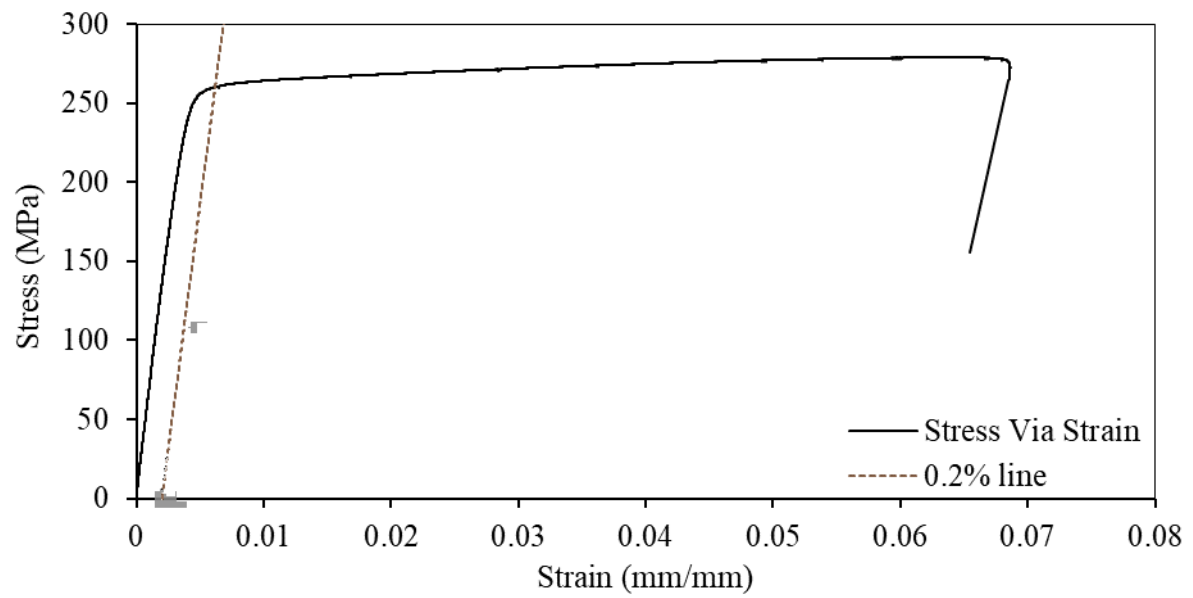


A.10. Section 520902

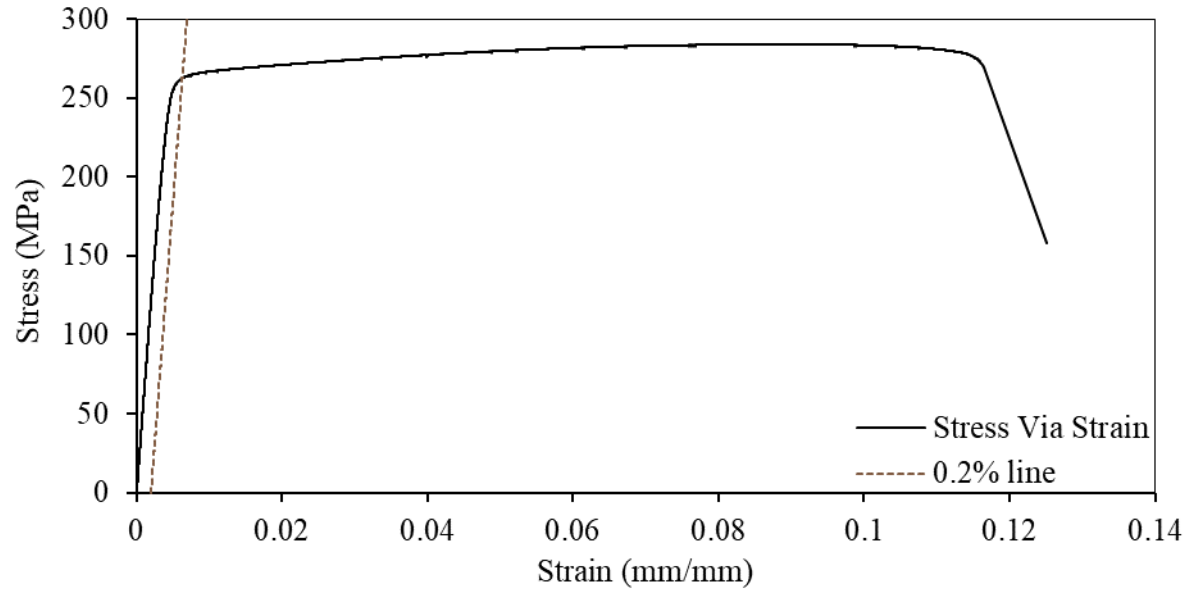
A.10.1. 520902-1



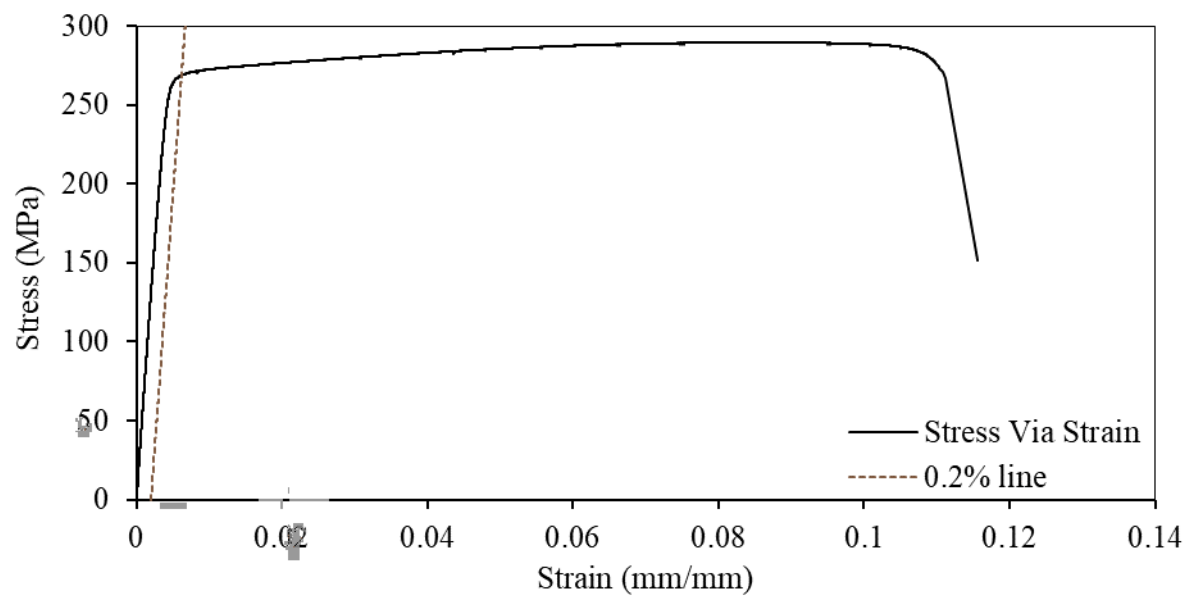
A.10.2. 520902-2



A.10.3. 520902-3

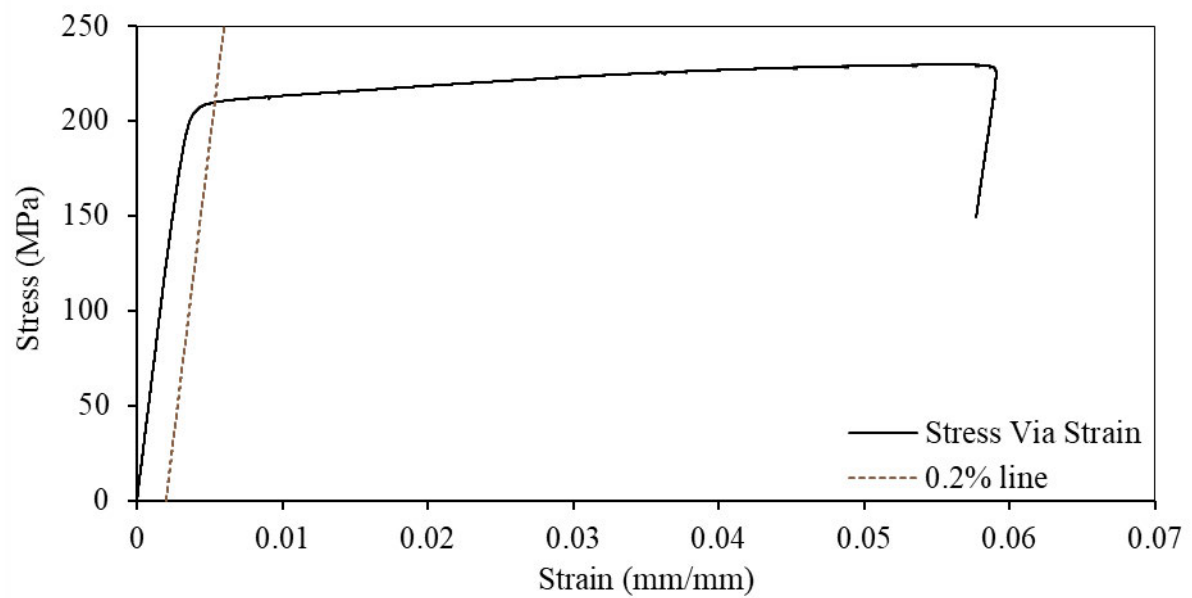


A.10.4. 520902-4



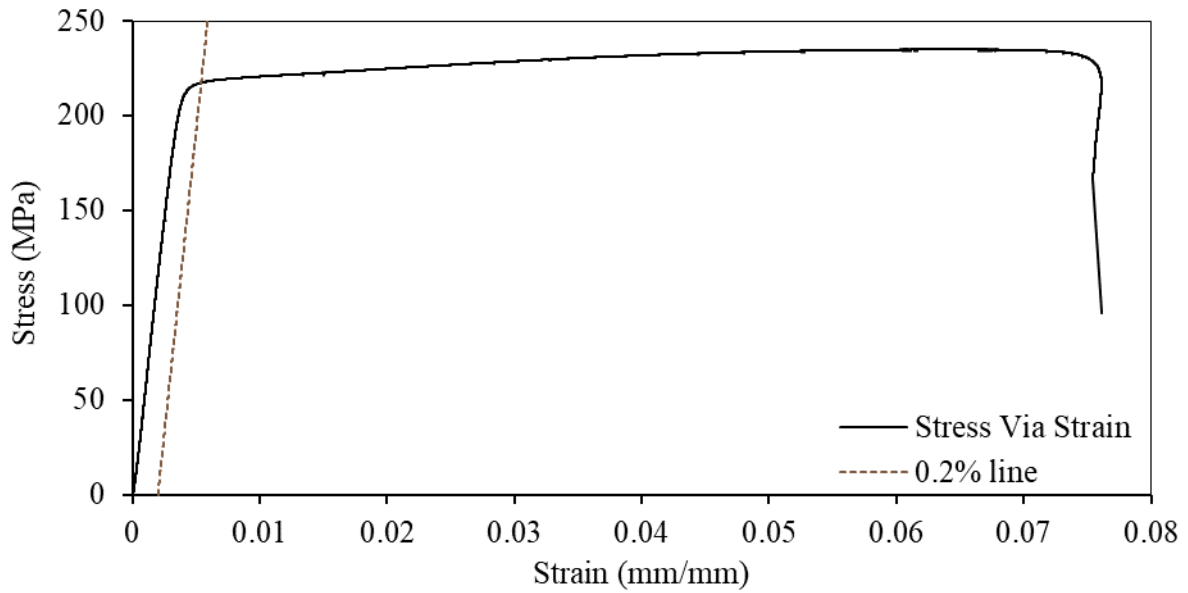
A.11. Section 675019

A.11.1. 675019-1



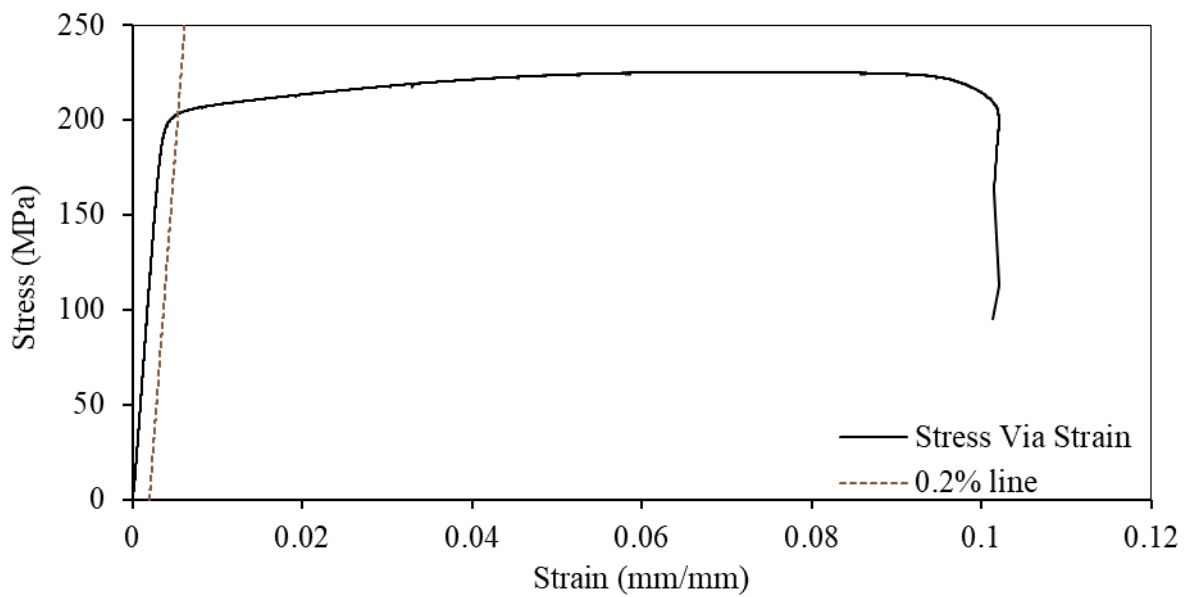
A.12. Section 675028

A.11.2. 675028-1

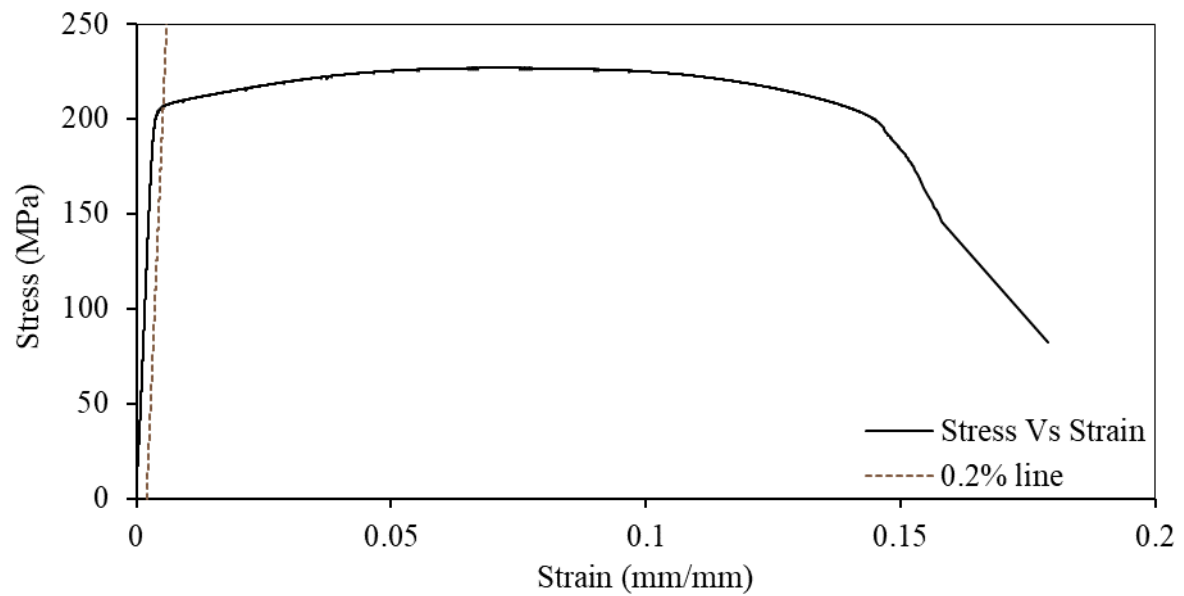


A.13 Section 875103

A.13.1. 875103-1



A.13.2. 875103-2

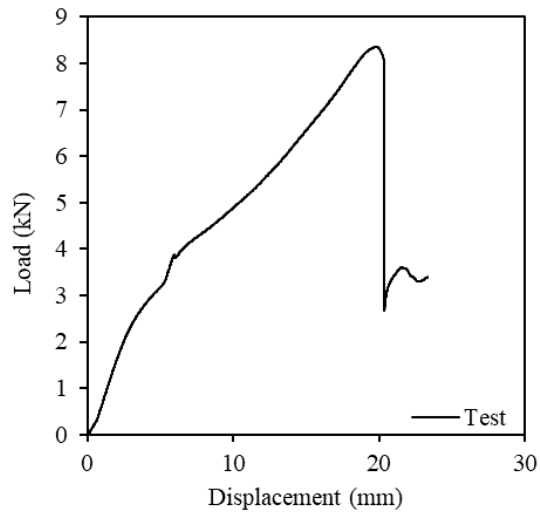


APPENDIX B. EXPERIMENTAL LOAD-DEFLECTION CURVES AND FAILURE MODES

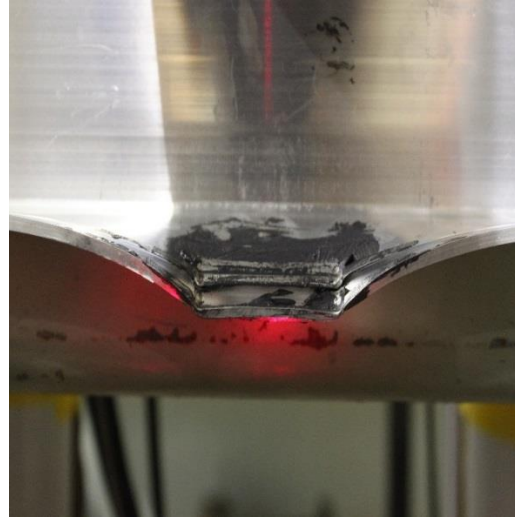
B.1 C-shaped sub-heads

B.1.1. 675-027

B.1.1.1. 675-027/1B/15/50

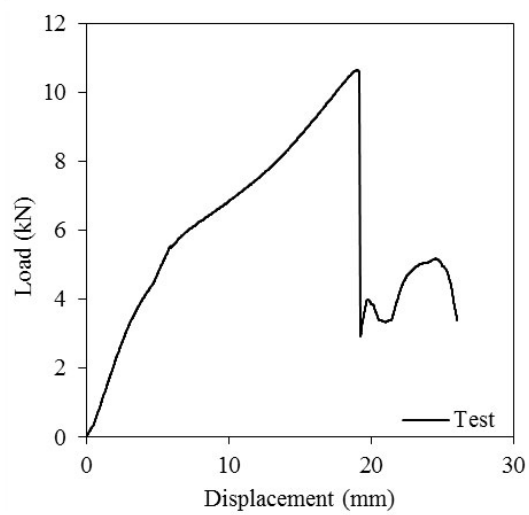


(a) Load-deflection curve

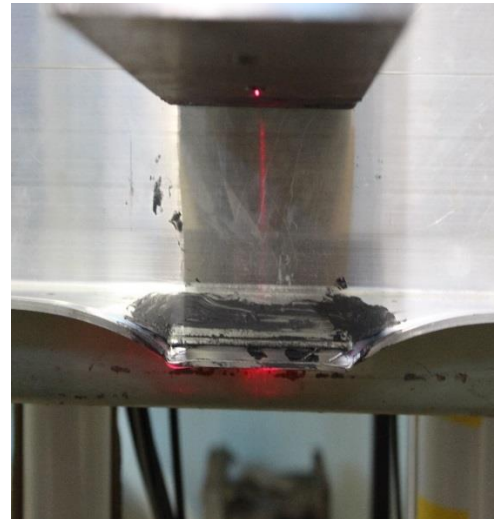


(b) Failure mode

B.1.1.2. 675-027/1B/15/100

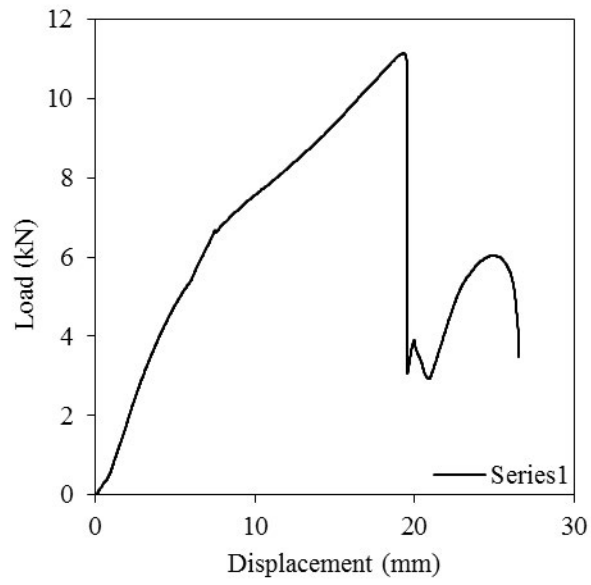


(a) Load-deflection curve

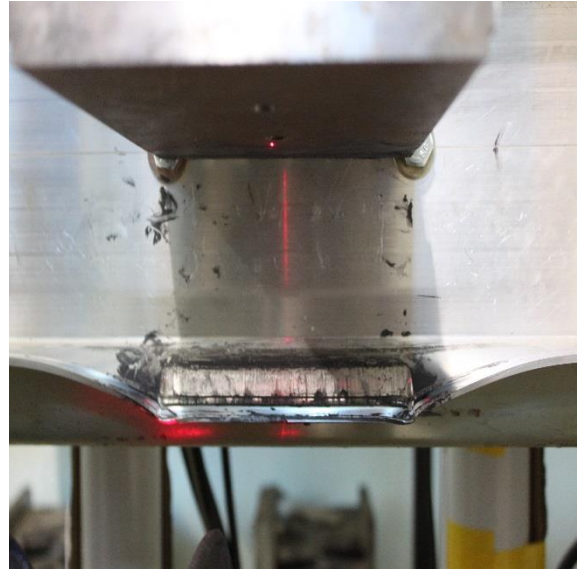


(b) Failure mode

B.1.1.3. 675-027/1B/15/150

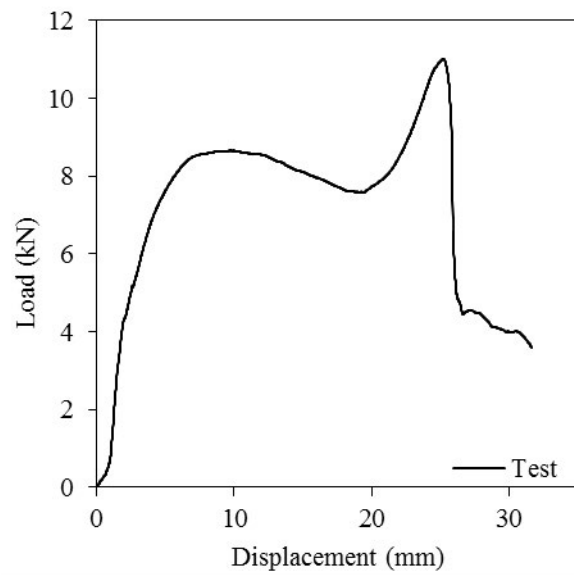


(a) Load-deflection curve

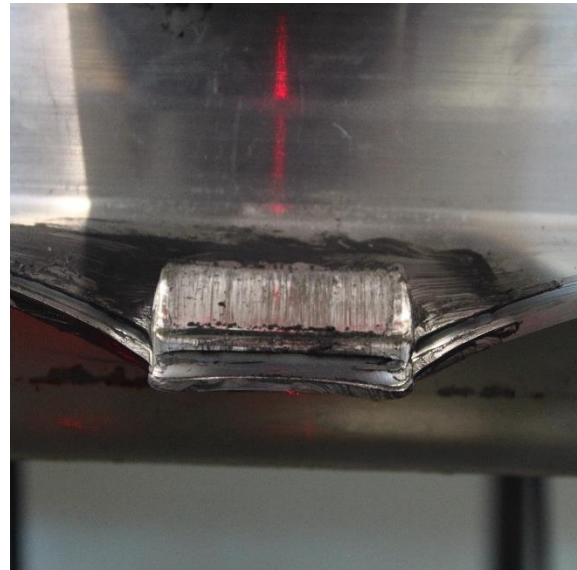


(b) Failure mode

B.1.1.4. 675-027/1B/25/50

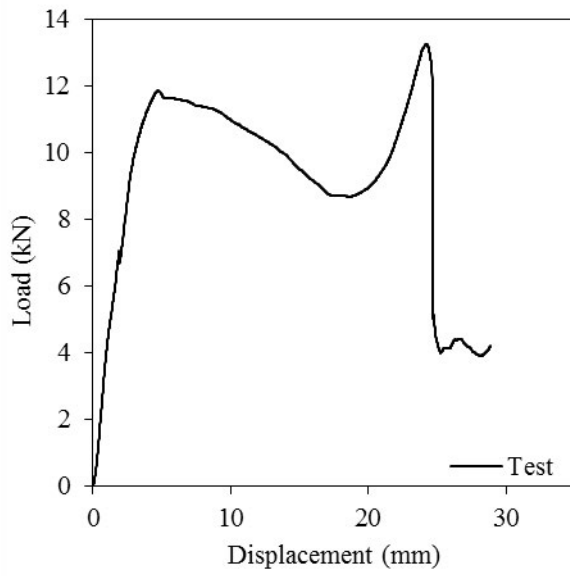


(a) Load-deflection curve

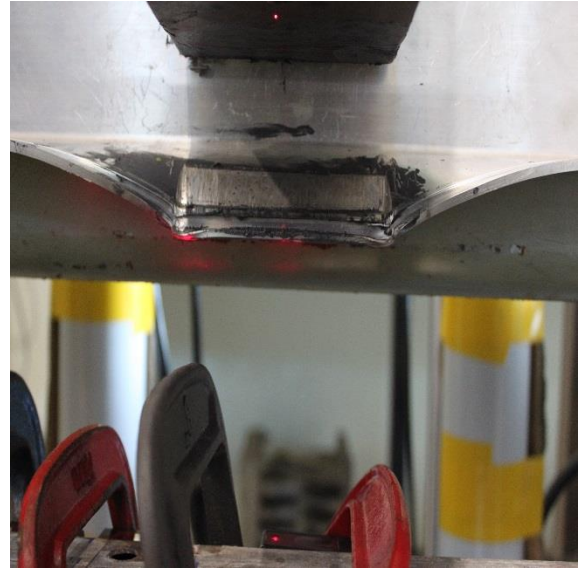


(b) Failure mode

B.1.1.5. 675-027/1B/25/100

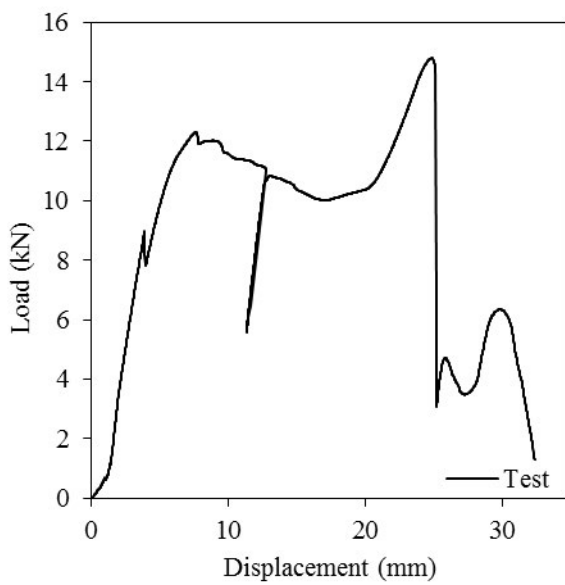


(a) Load-deflection curve

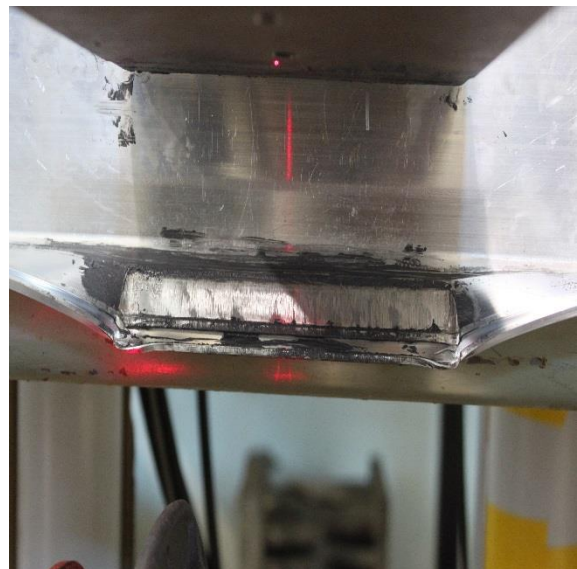


(b) Failure mode

B.1.1.6. 675-027/1B/25/150

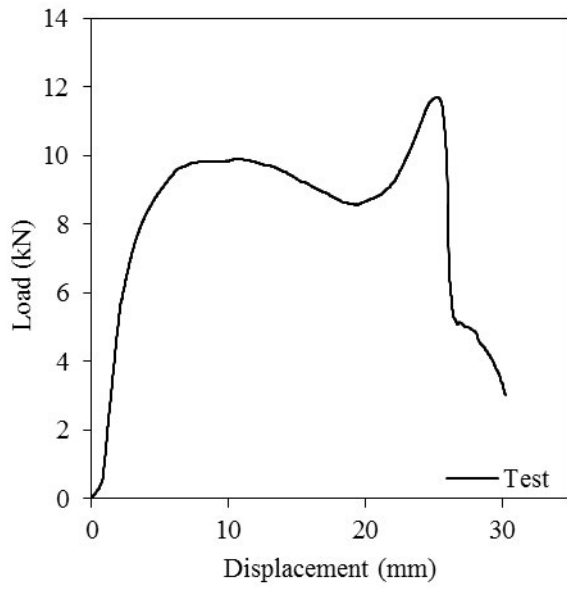


(a) Load-deflection curve

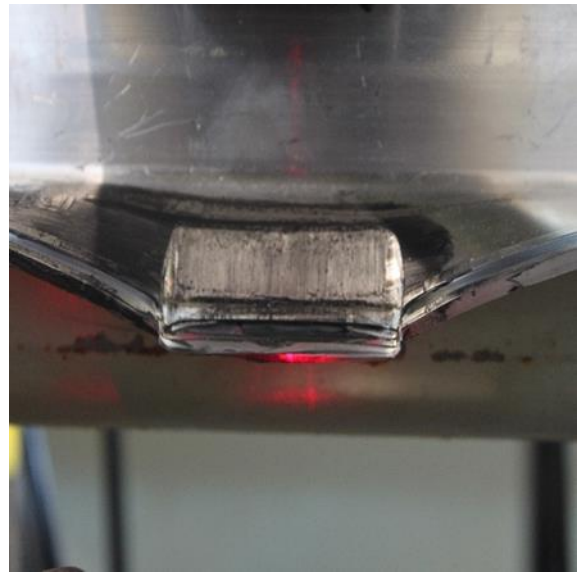


(b) Failure mode

B.1.1.7. 675-027/2B/25/50

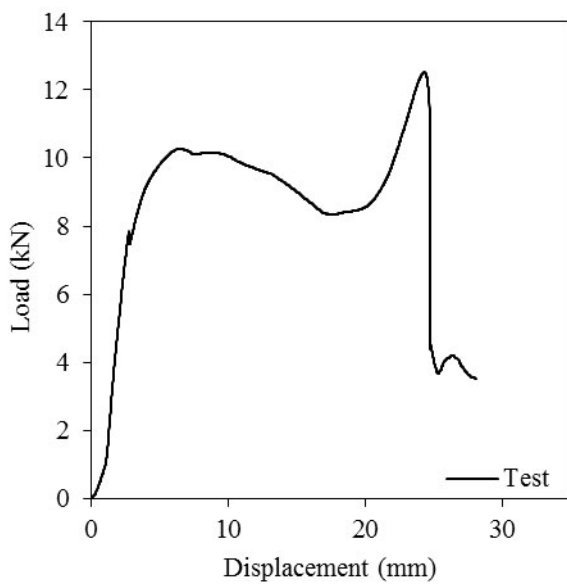


(a) Load-deflection curve

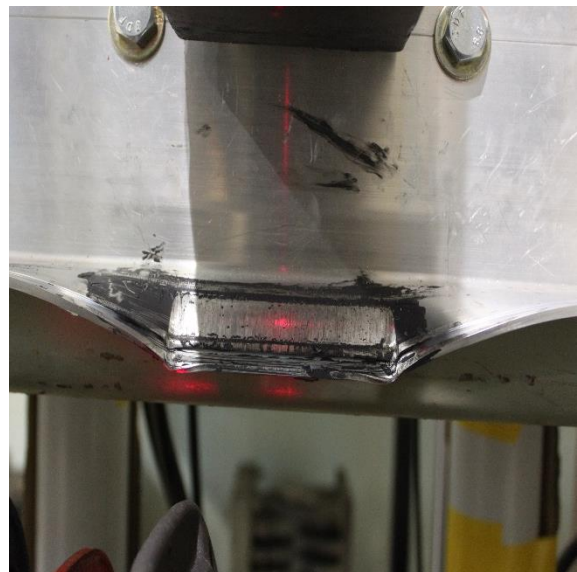


(b) Failure mode

B.1.1.8. 675-027/2B/25/100

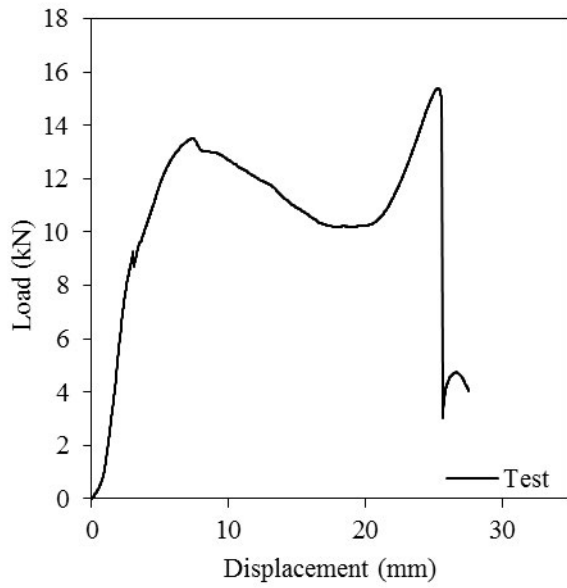


(a) Load-deflection curve

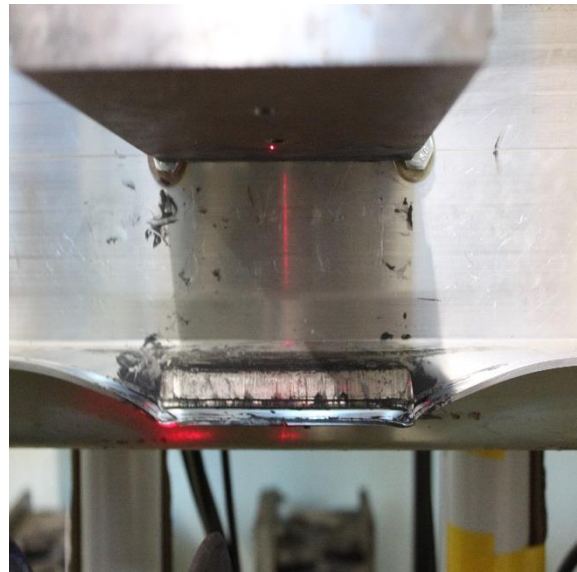


(b) Failure mode

B.1.1.9. 675-027/2B/25/150



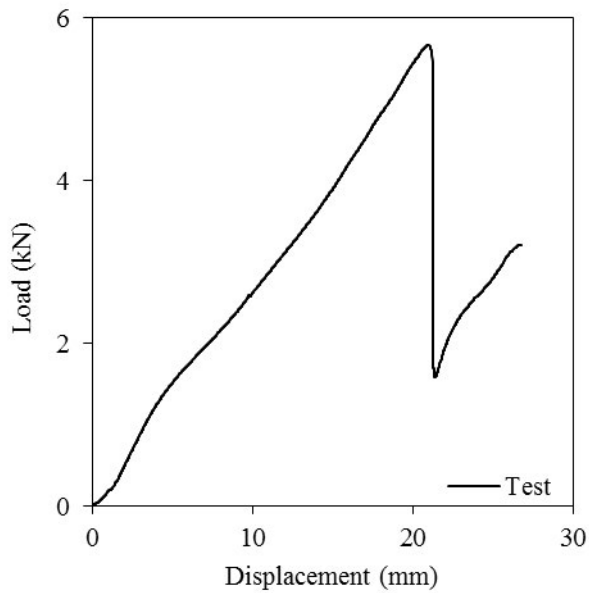
(a) Load-deflection curve



(b) Failure mode

B.1.2. 475-077

B.1.2.1. 475-077/1B/15/50

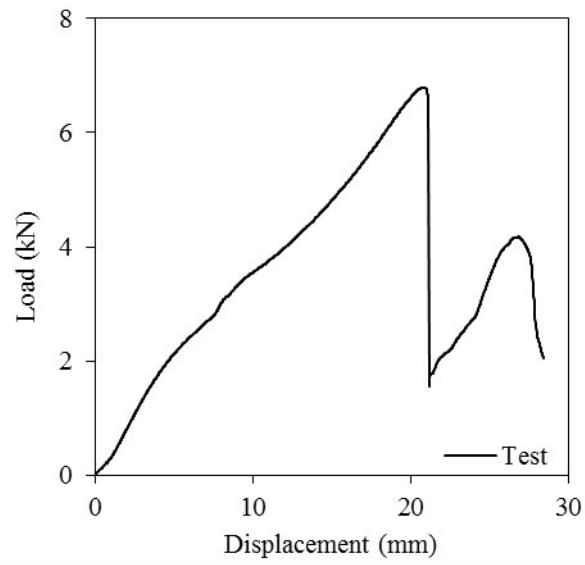


(a) Load-deflection curve



(b) Failure mode

B.1.2.2. 475-077/1B/15/100a

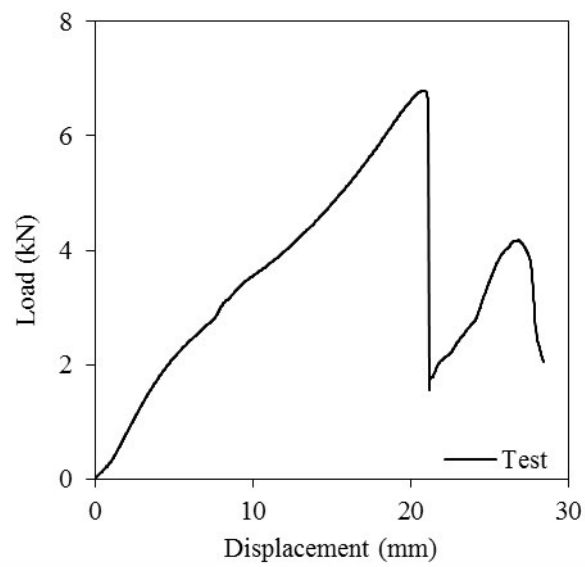


(b) Load-deflection curve

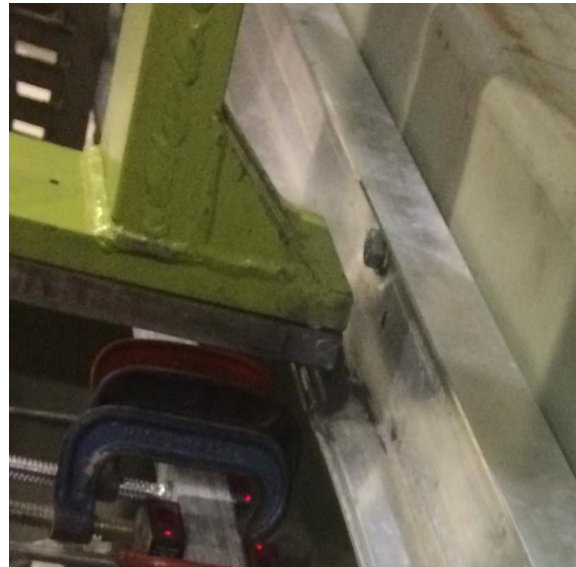


(b) Failure mode

B.1.2.3. 475-077/1B/15/100b

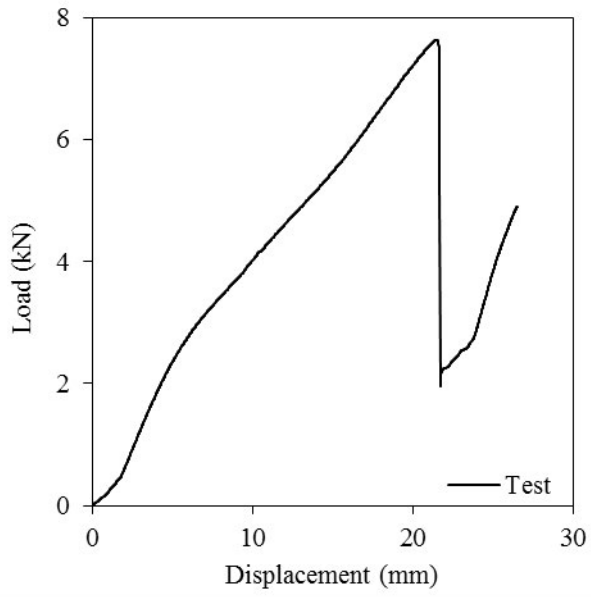


(a) Load-deflection curve



(b) Failure mode

B.1.2.4. 475-077/1B/15/150

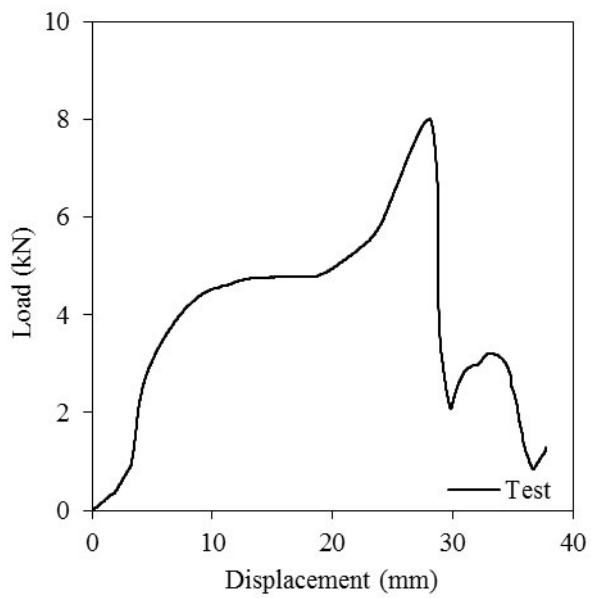


(b) Load-deflection curve



(b) Failure mod

B.1.2.5. 475-077/1B/25/50

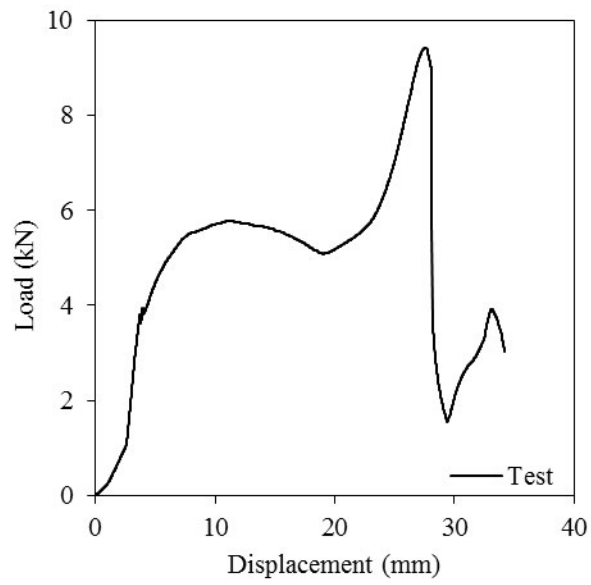


(b) Load-deflection curve

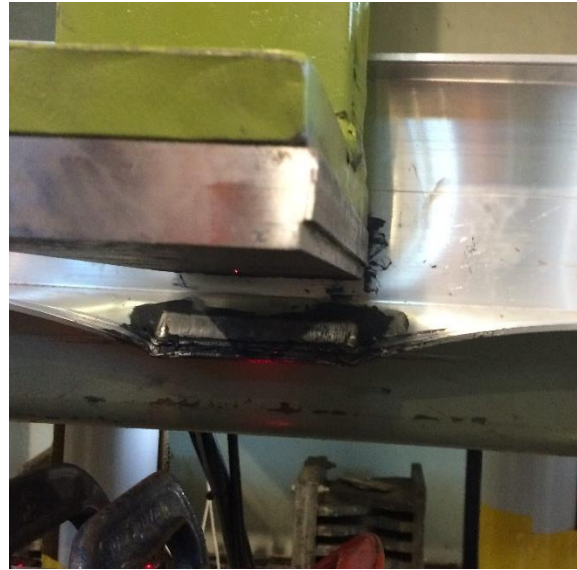


(b) Failure mode

B.1.2.6. 475-077/1B/25/100a

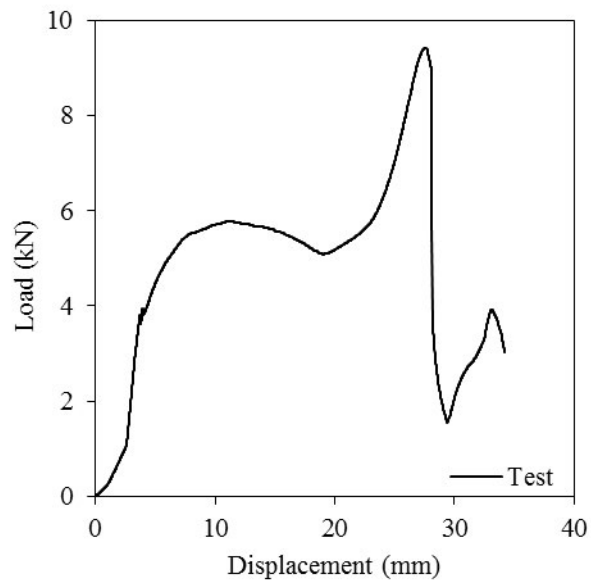


(b) Load-deflection curve



(b) Failure mode

B.1.2.7. 475-077/1B/25/100b

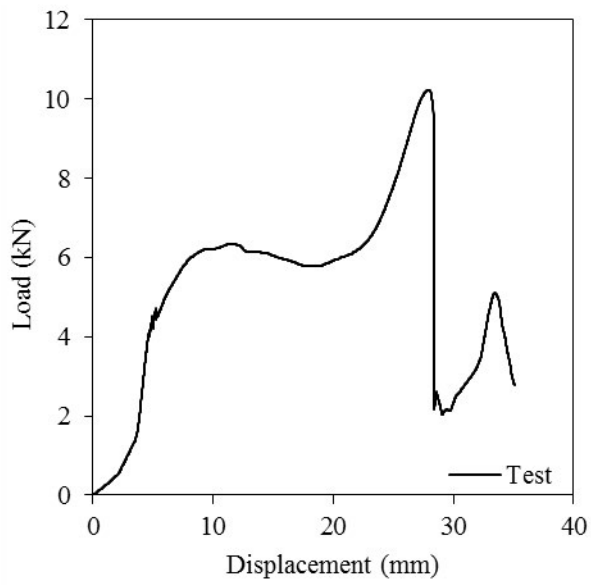


(a) Load-deflection curve



(b) Failure mode

B.1.2.8. 475-077/1B/25/150

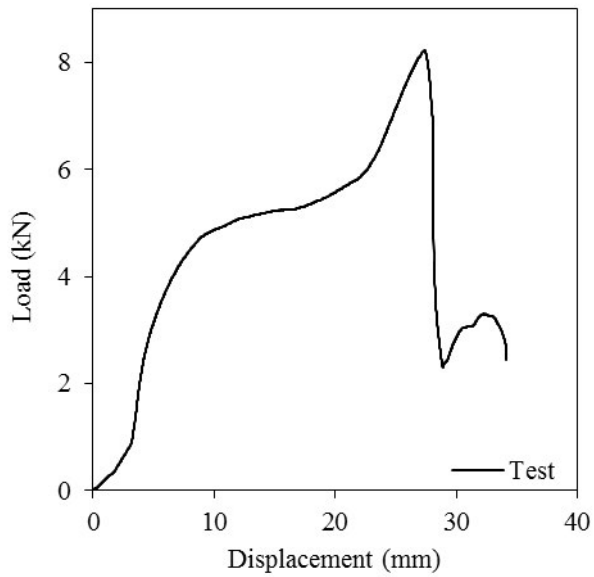


(b) Load-deflection curve

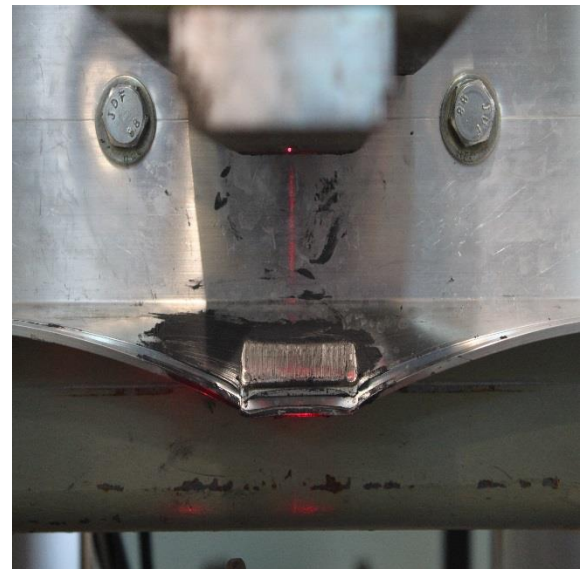


(b) Failure mode

B.1.2.9. 475-077/2B/25/50

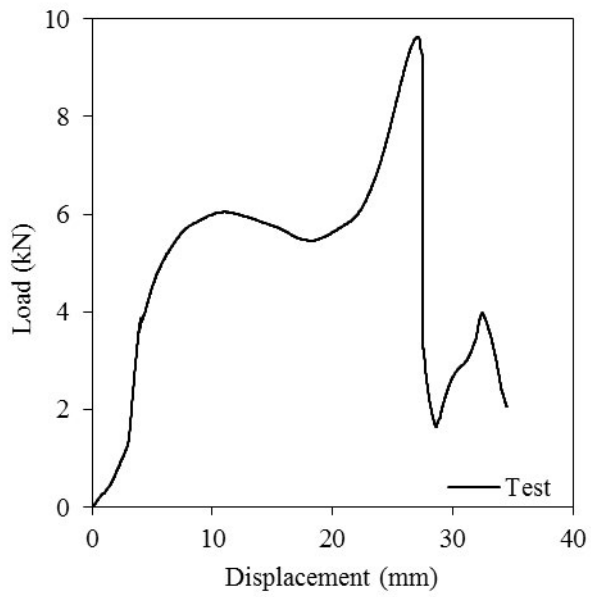


(a) Load-deflection curve

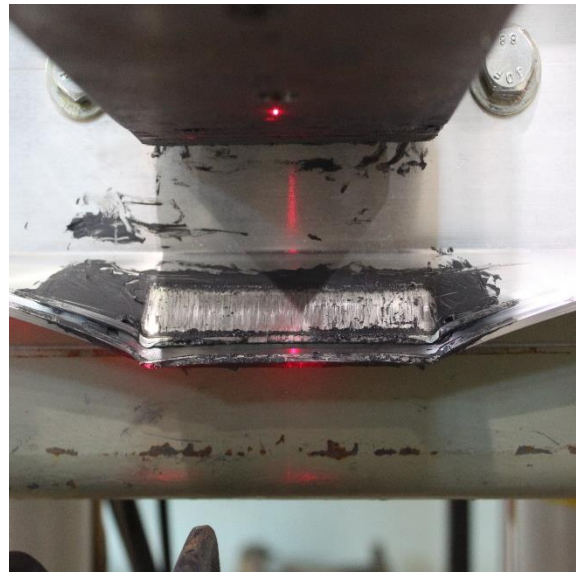


(b) Failure mode

B.1.2.10. 475-077/2B/25/100a

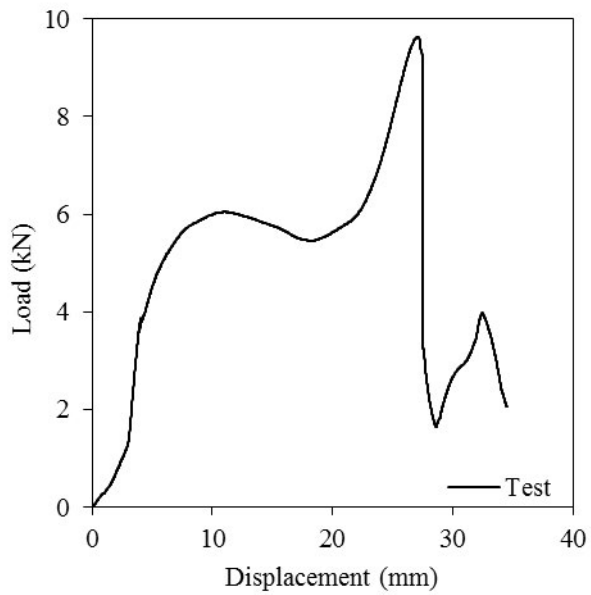


(b) Load-deflection curve



(b) Failure mode

B.1.2.11. 475-077/2B/25/100b

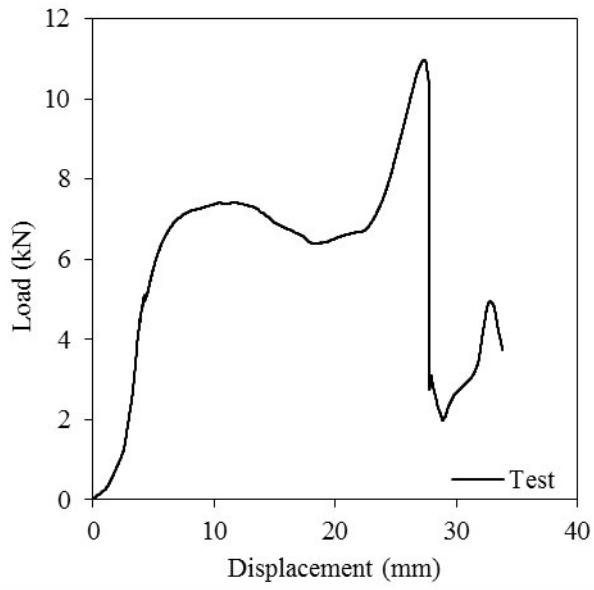


(a) Load-deflection curve



(b) Failure mode

B.1.2.12. 475-077/2B/25/150



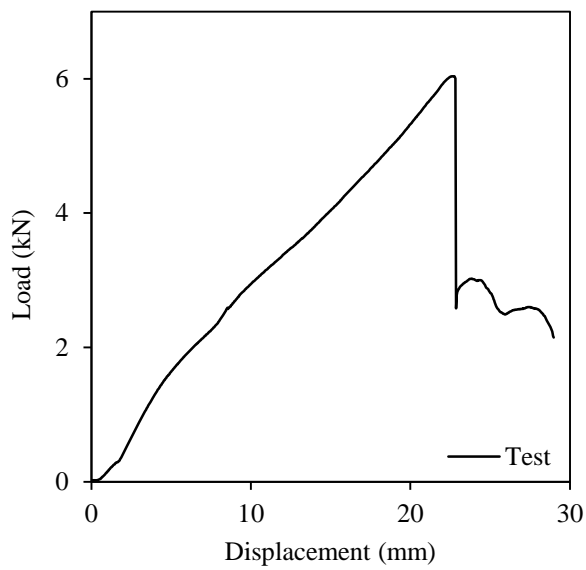
(a) Load-deflection curve



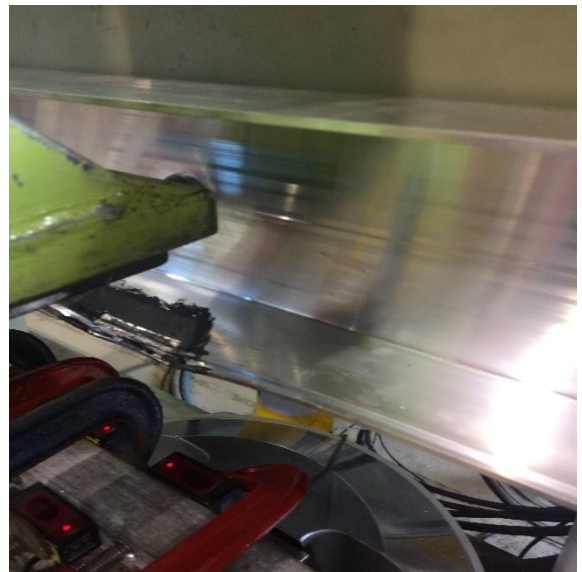
(b) Failure mode

B.1.3. 475-057

B.1.3.1. 475-057/1B/15/50a

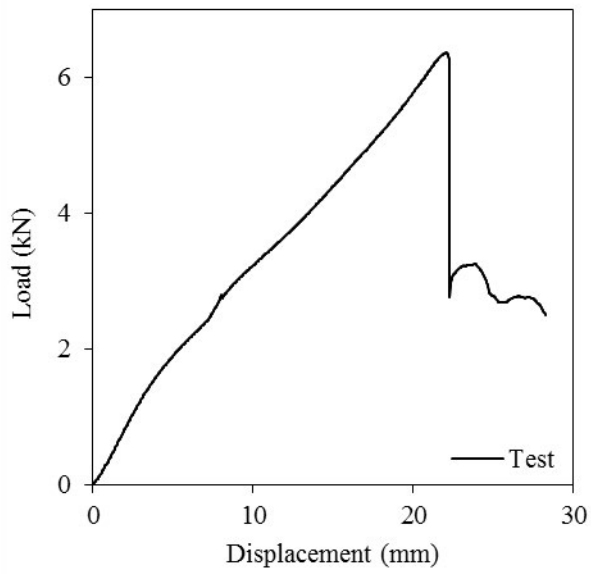


(a) Load-deflection curve



(b) Failure mode

B.1.3.2. 475-057/1B/15/50b

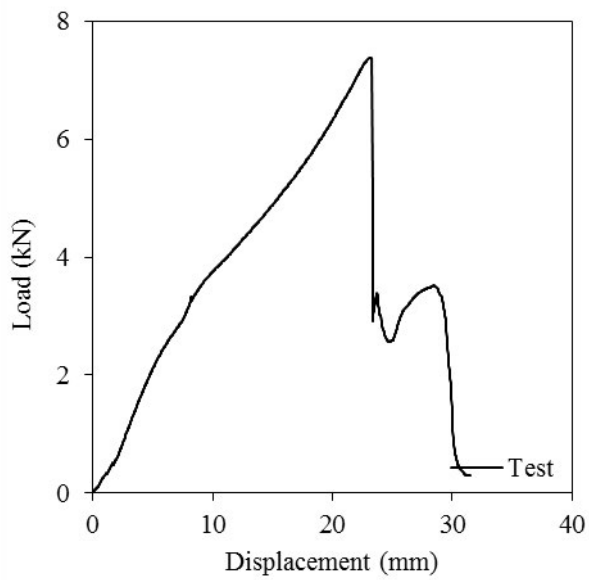


(a) Load-deflection curve

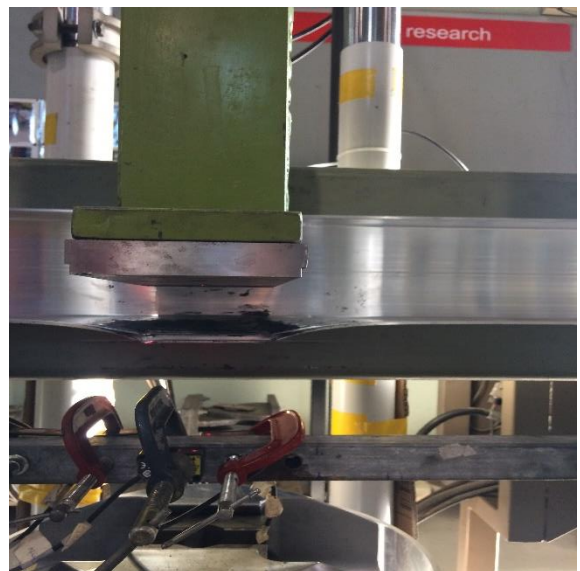


(b) Failure mode

B.1.3.3. 475-057/1B/15/100

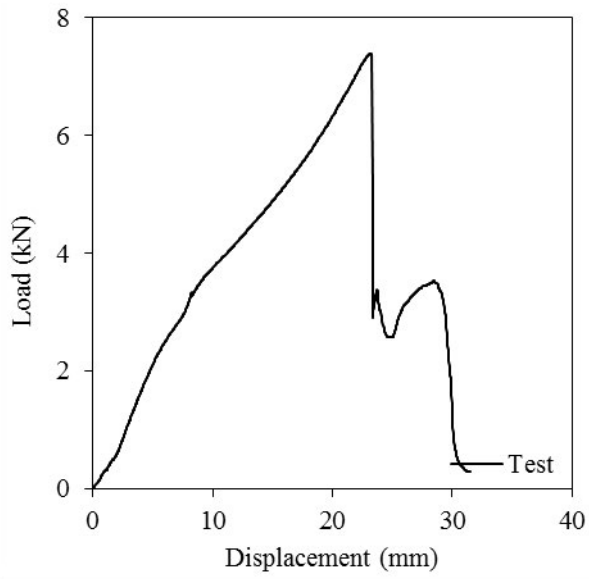


(a) Load-deflection curve



(b) Failure mode

B.1.3.4. 475-057/1B/15/150a

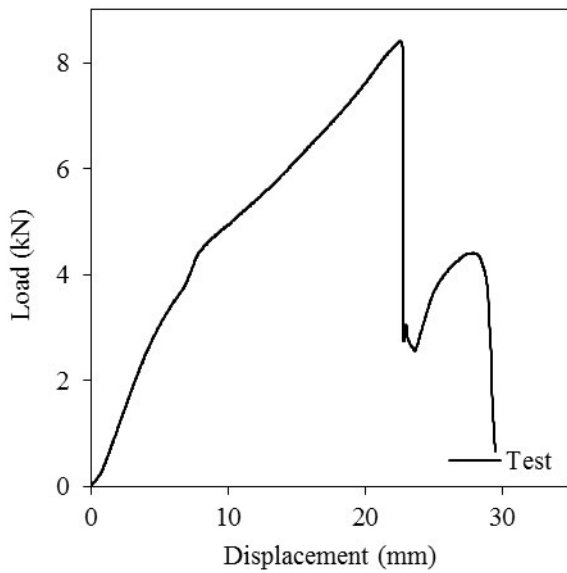


(a) Load-deflection curve



(b) Failure mode

B.1.3.5. 475-057/1B/15/150b

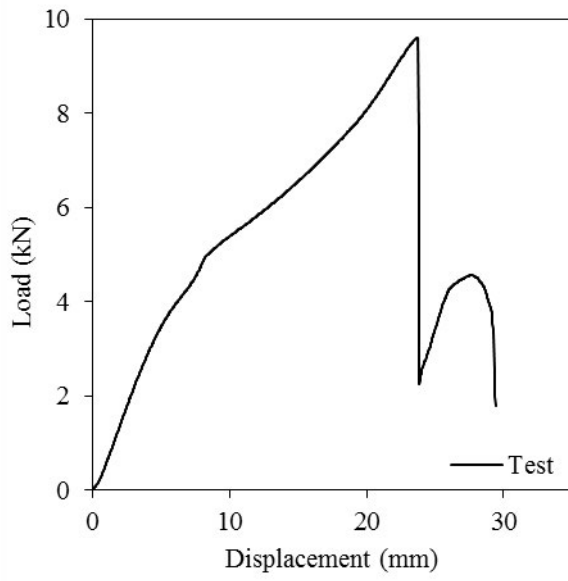


(a) Load-deflection curve



(b) Failure mode

B.1.3.6. 475-057/1B/15/200a

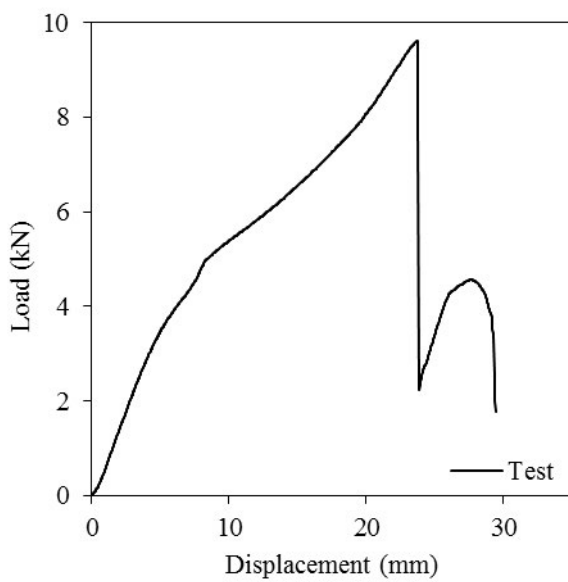


(a) Load-deflection curve



(b) Failure mode

B.1.3.7. 475-057/1B/15/200b

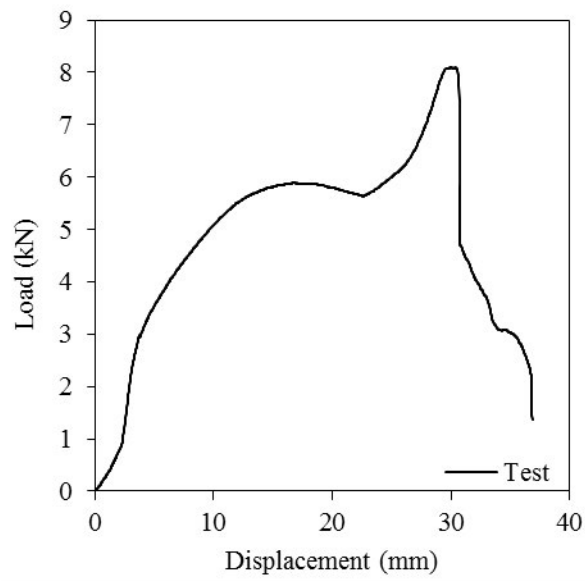


(a) Load-deflection curve

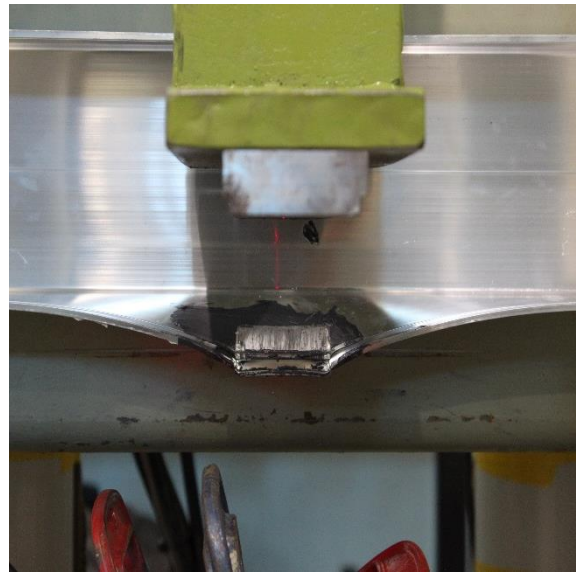


(b) Failure mode

B.1.3.8. 475-057/1B/25/50a

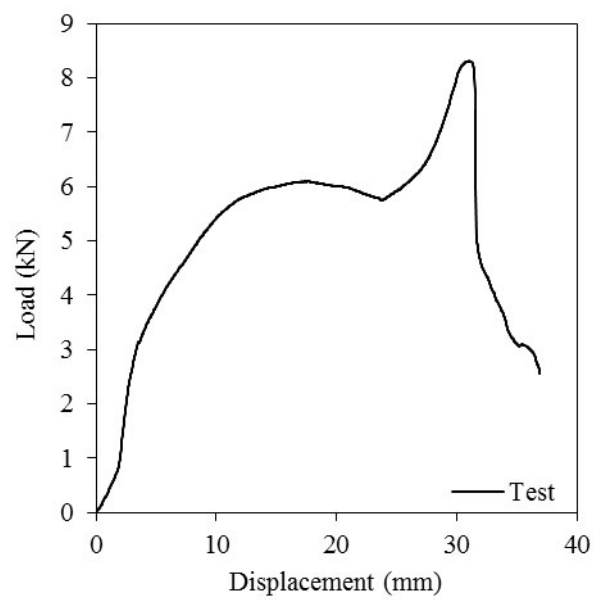


(a) Load-deflection curve

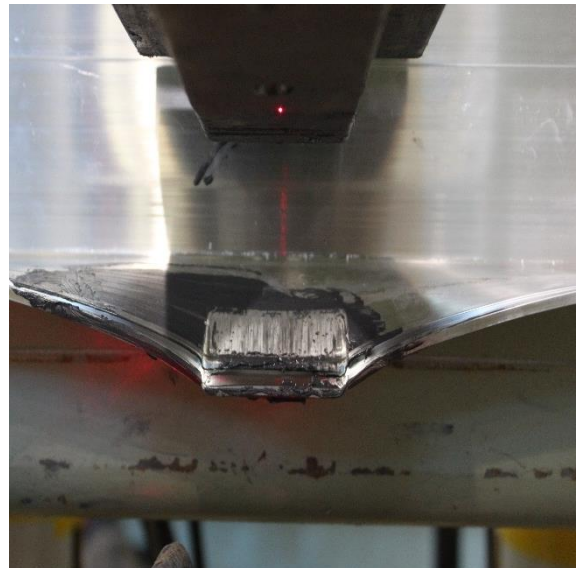


(b) Failure mode

B.1.3.9. 475-057/1B/25/50b

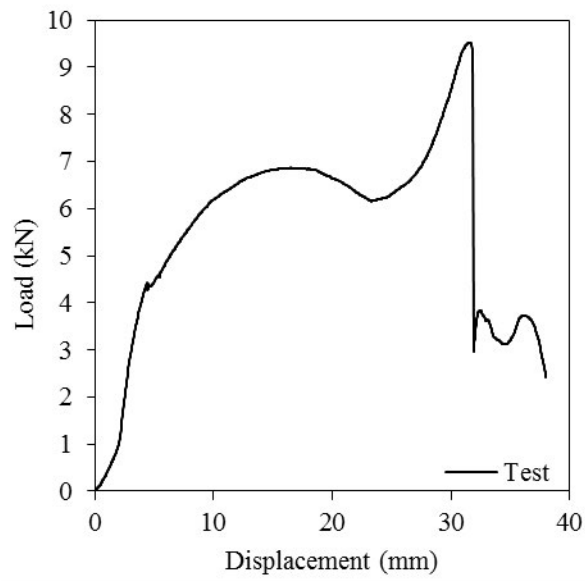


(a) Load-deflection curve

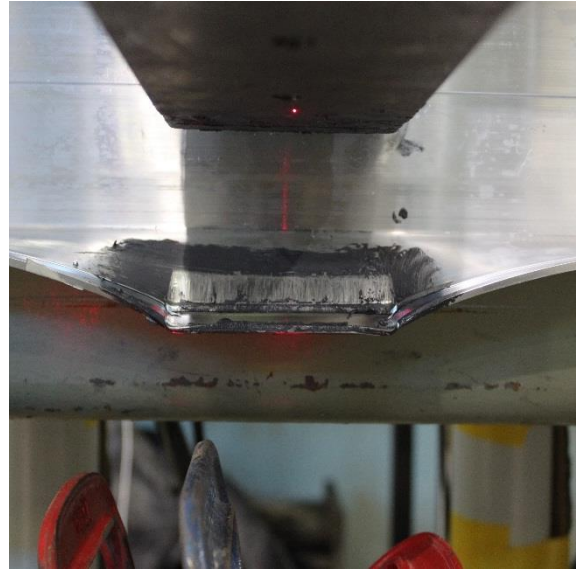


(b) Failure mode

B.1.3.10. 475-057/1B/25/100a

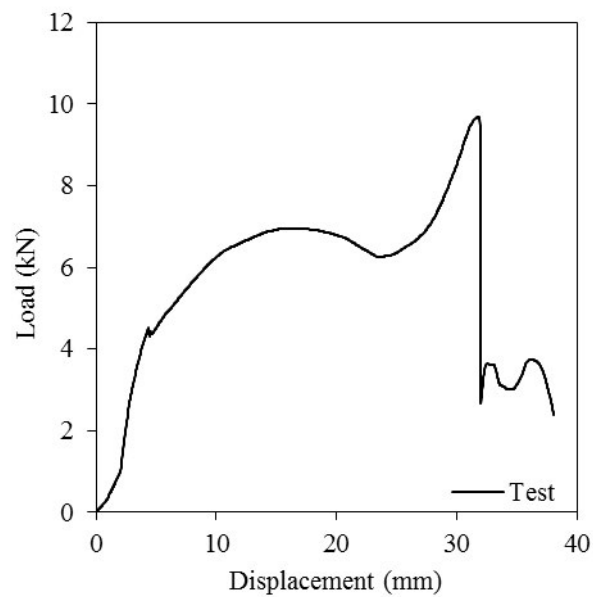


(a) Load-deflection curve

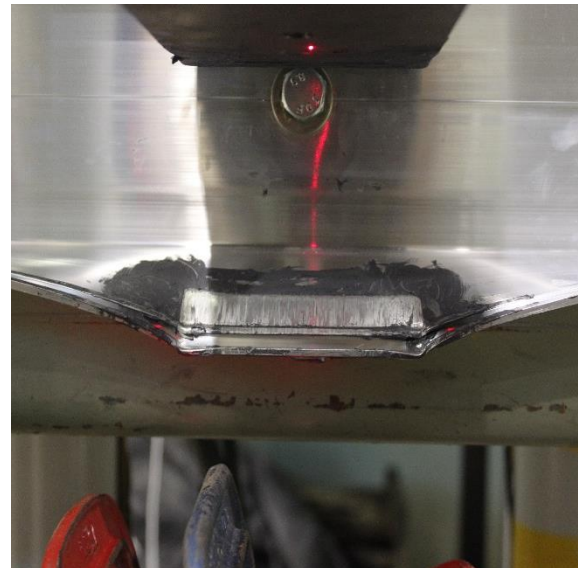


(b) Failure mode

B.1.3.11. 475-057/1B/25/100b

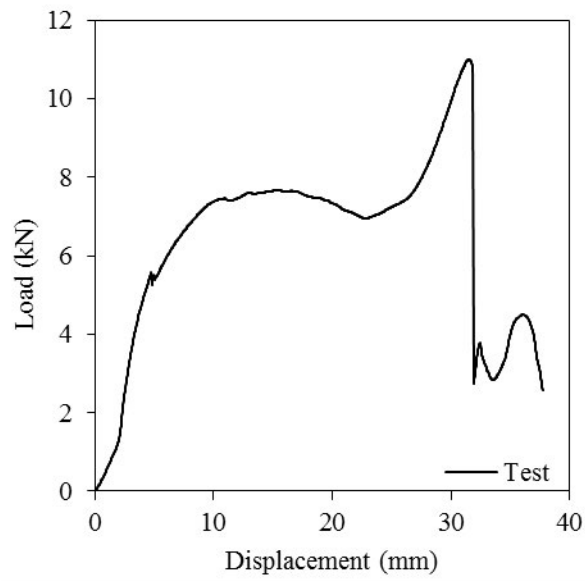


(a) Load-deflection curve

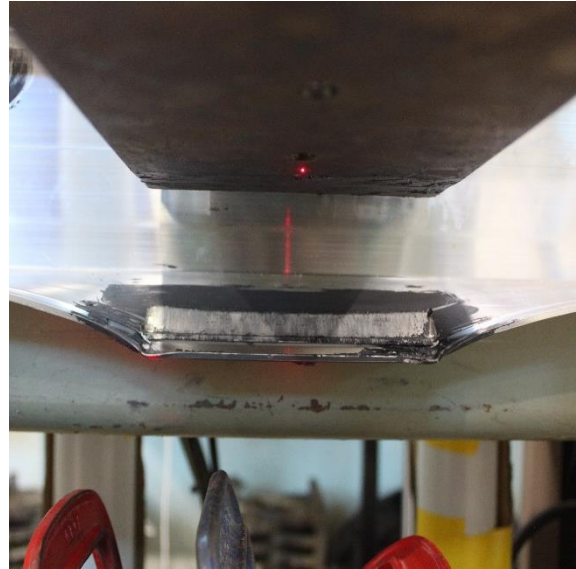


(b) Failure mode

B.1.3.12. 475-057/1B/25/150a

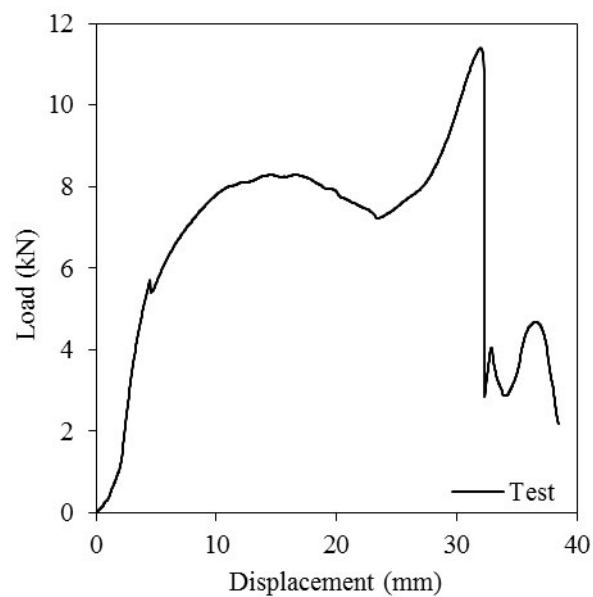


(a) Load-deflection curve

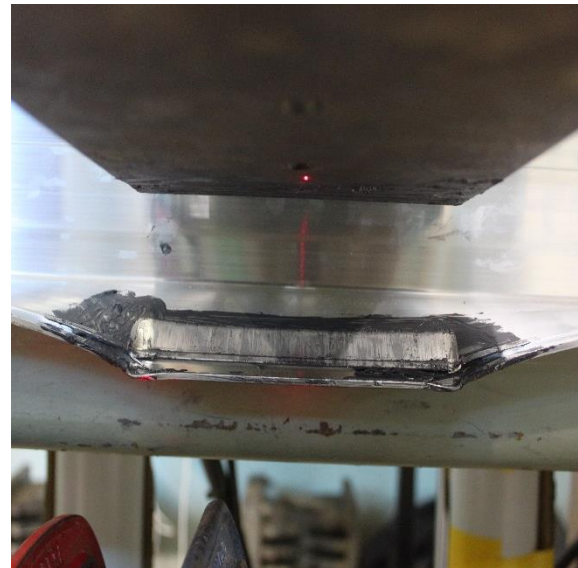


(b) Failure mode

B.1.3.13. 475-057/1B/25/150b

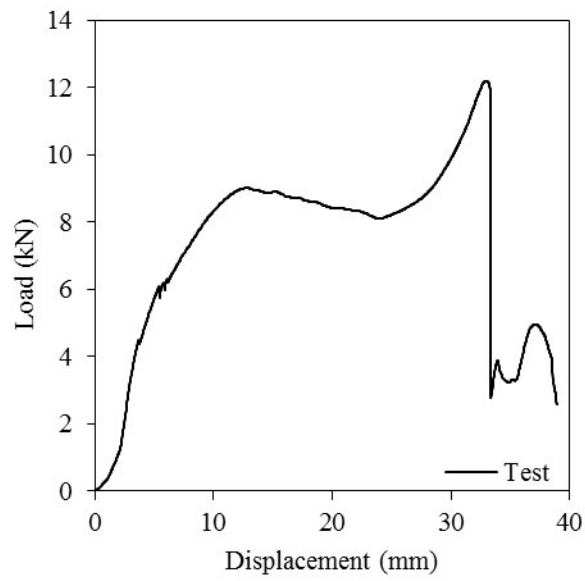


(a) Load-deflection curve

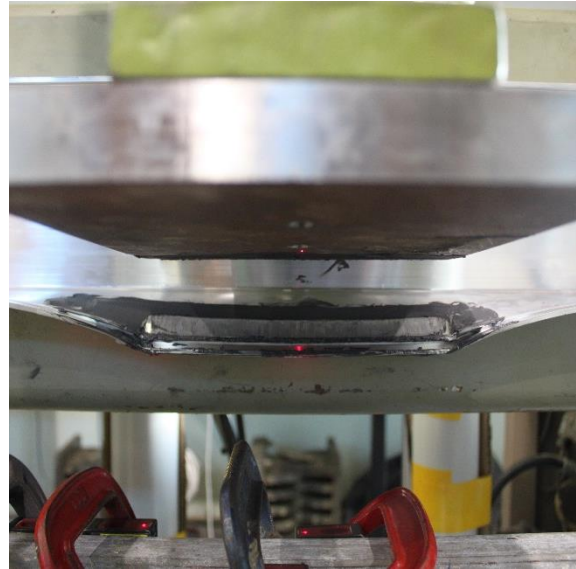


(b) Failure mode

B.1.3.14. 475-057/1B/25/200a

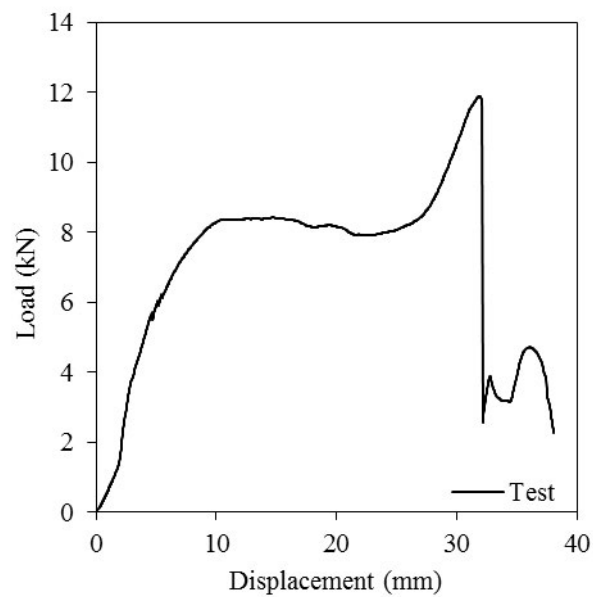


(b) Load-deflection curve

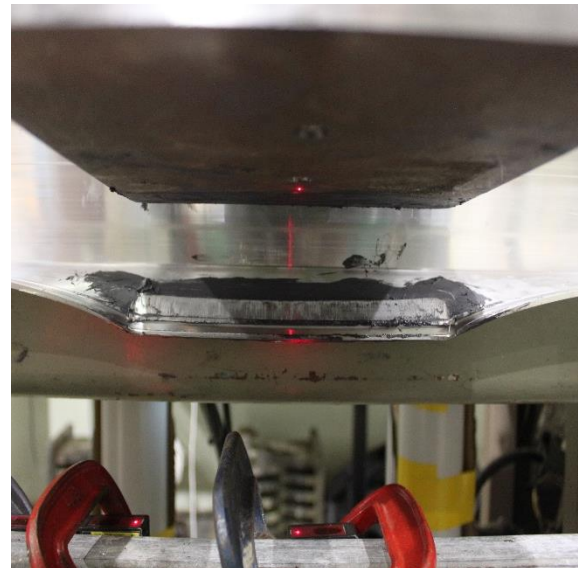


(b) Failure mode

B.1.3.15. 475-057/1B/25/200b

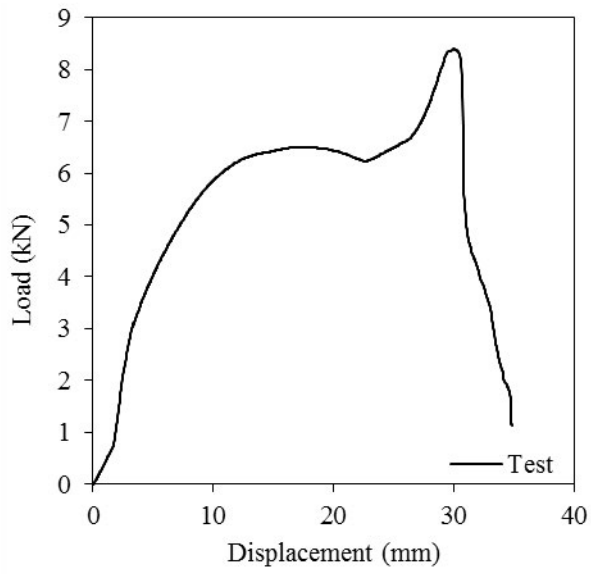


(a) Load-deflection curve

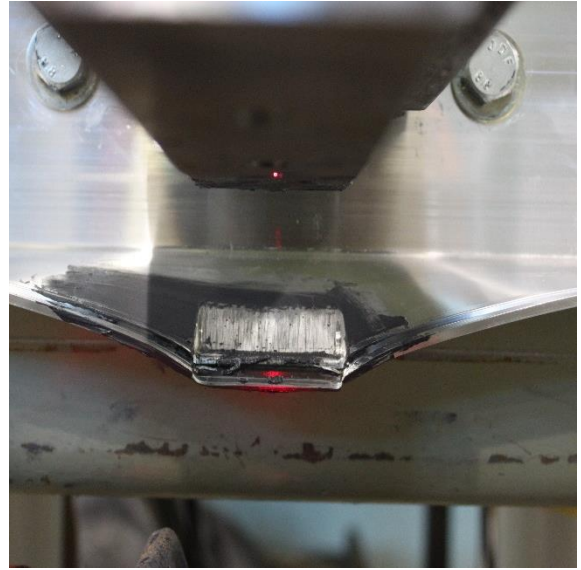


(b) Failure mode

B.1.3.16. 475-057/2B/25/50a

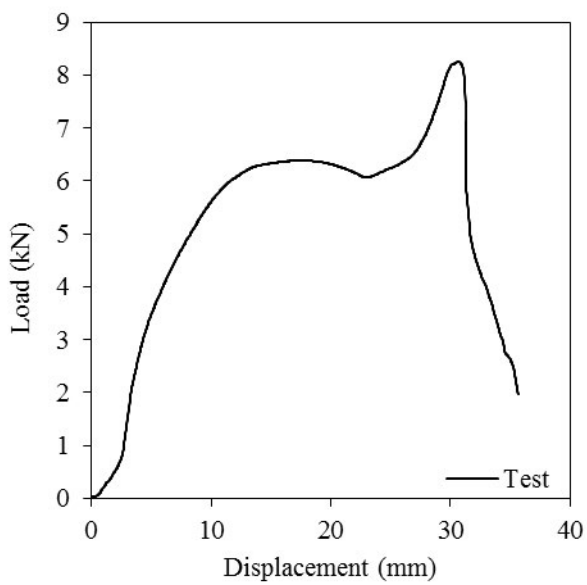


(a) Load-deflection curve

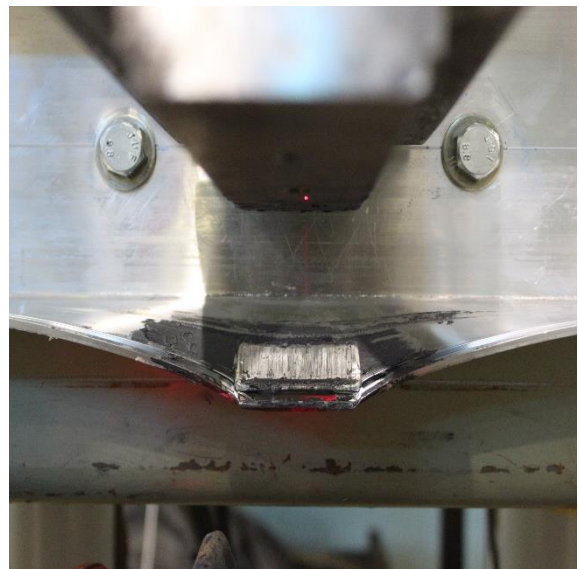


(b) Failure mode

B.1.3.17. 475-057/2B/25/50b

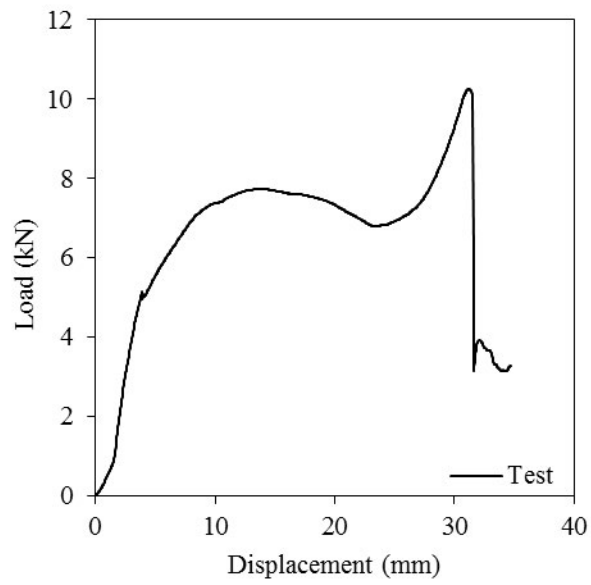


(a) Load-deflection curve

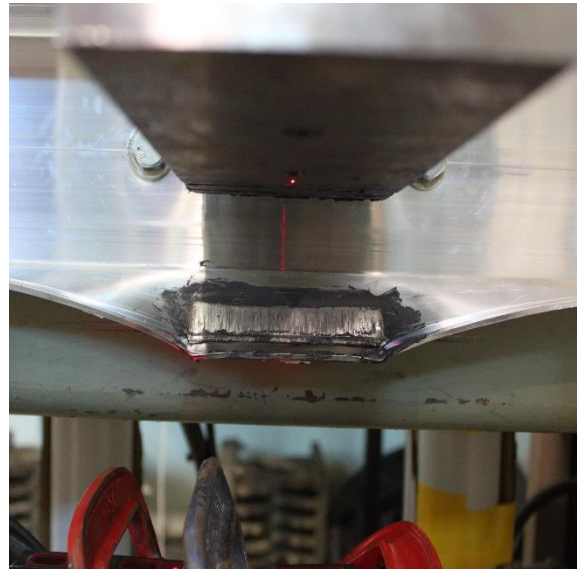


(b) Failure mode

B.1.3.18. 475-057/2B/25/100a

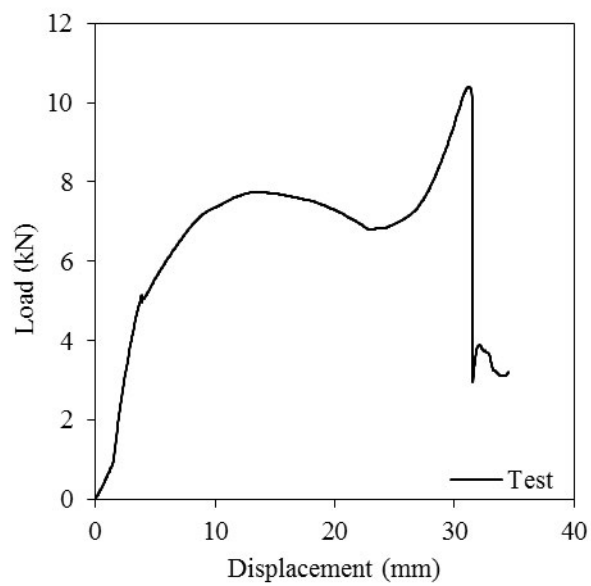


(a) Load-deflection curve



(b) Failure mode

B.1.3.19. 475-057/2B/25/100b

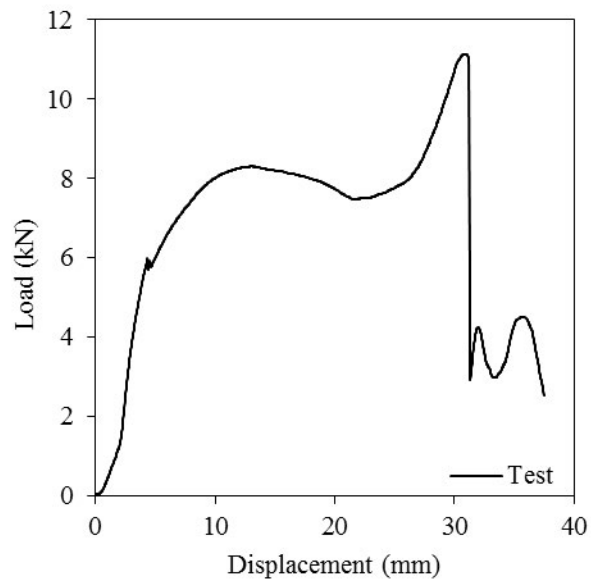


(a) Load-deflection curve

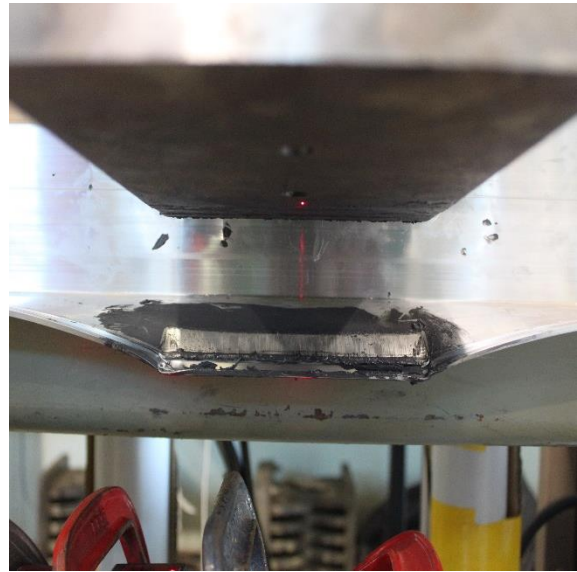


(b) Failure mode

B.1.3.20. 475-057/2B/25/150a

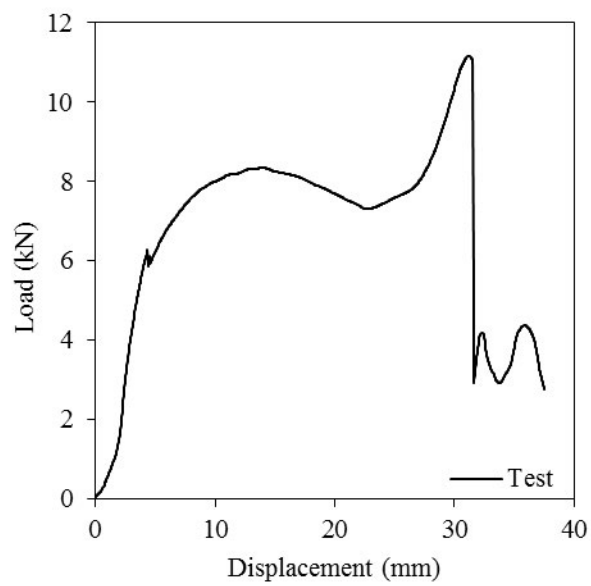


(c) Load-deflection curve



(b) Failure mode

B.1.3.21. 475-057/2B/25/150b

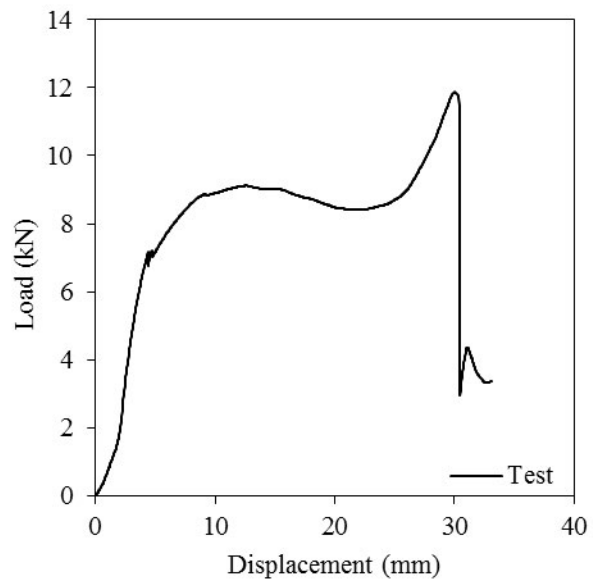


(a) Load-deflection curve

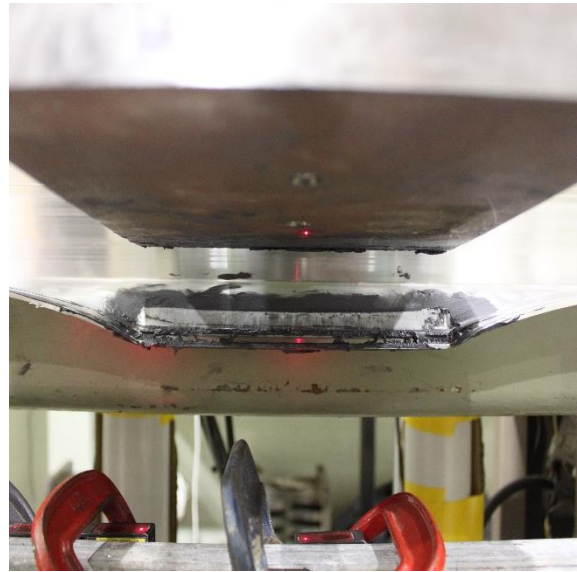


(b) Failure mode

B.1.3.22. 475-057/2B/25/200a

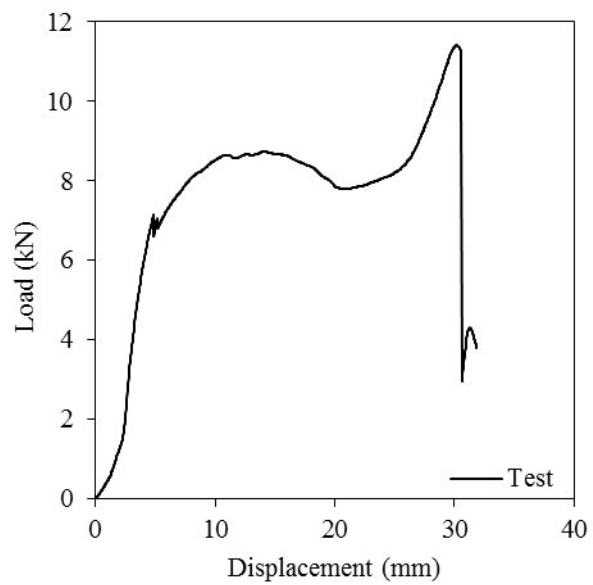


(a) Load-deflection curve

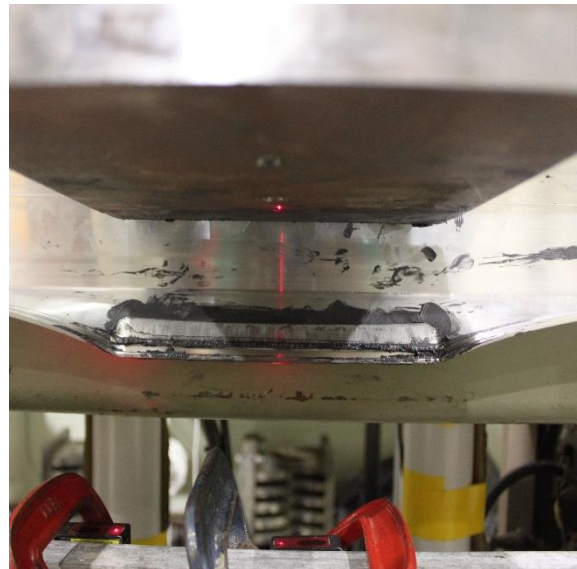


(b) Failure mode

B.1.3.23. 475-057/2B/25/200b



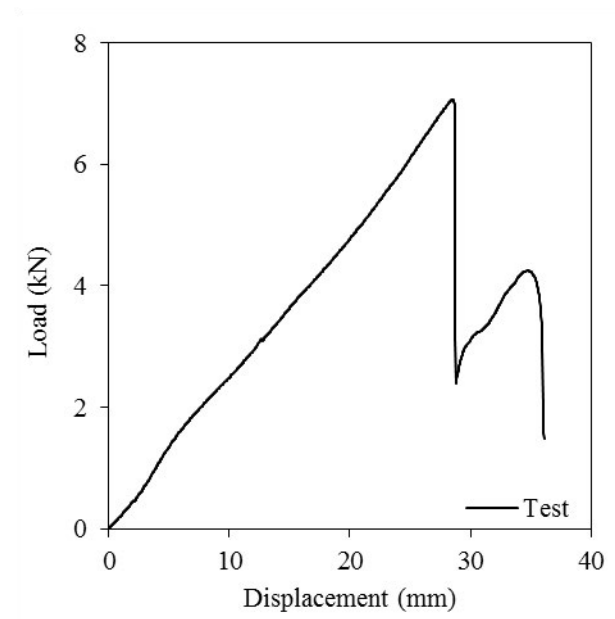
(a) Load-deflection curve



(b) Failure mode

B.1.4. 475-071

B.1.4.1. 475-071/1B/15/50a

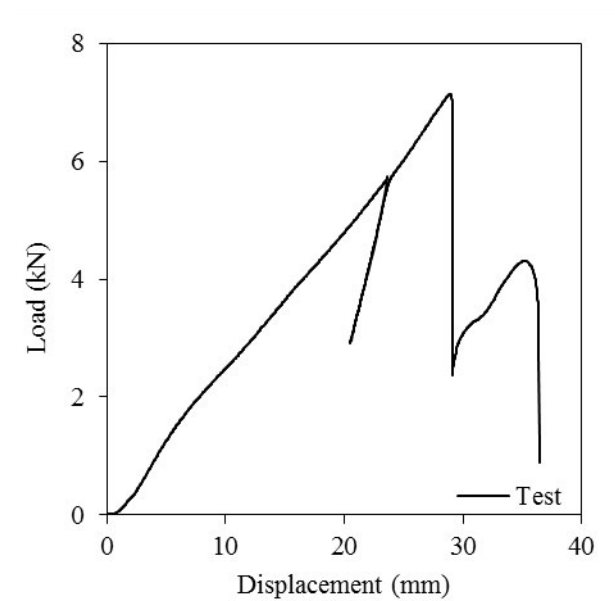


(a) Load-deflection curve

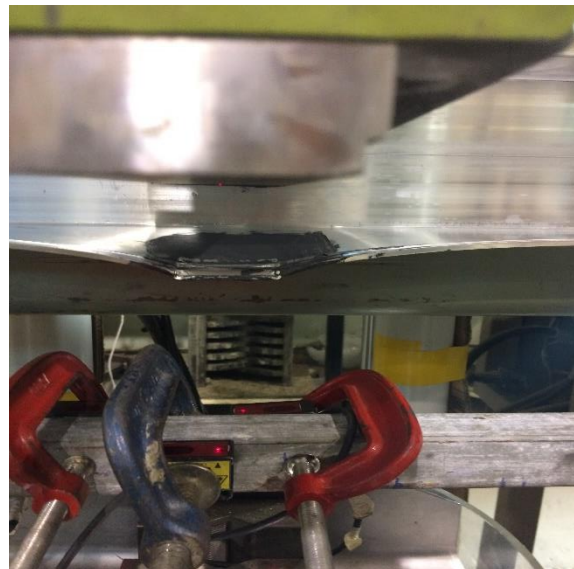


(b) Failure mode

B.1.4.2. 475-071/1B/15/50b

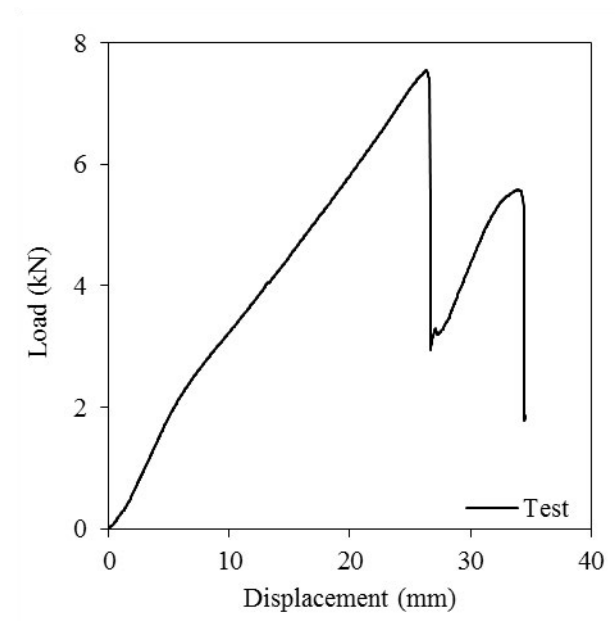


(a) Load-deflection curve



(b) Failure mode

B.1.4.3. 475-071/1B/15/100a

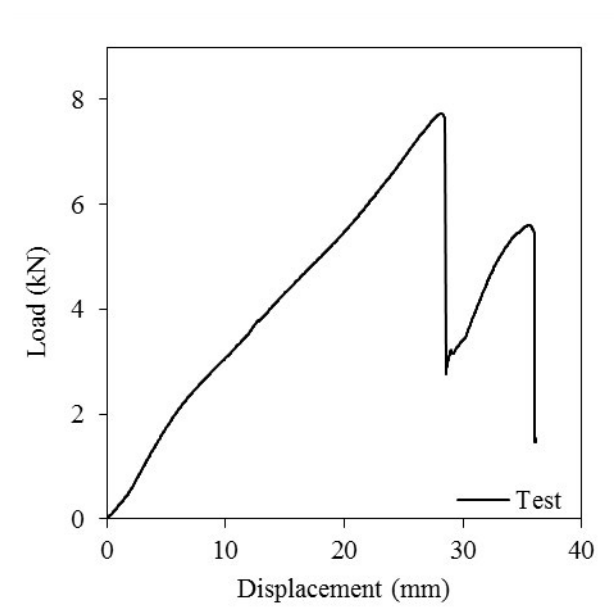


(a) Load-deflection curve

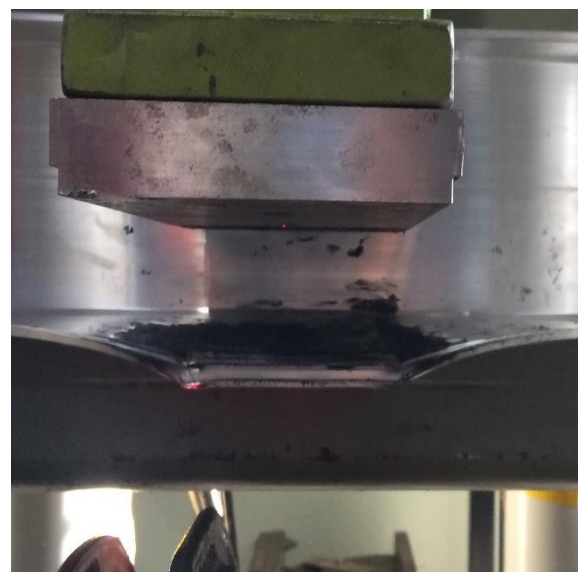


(b) Failure mode

B.1.4.4. 475-071/1B/15/100b

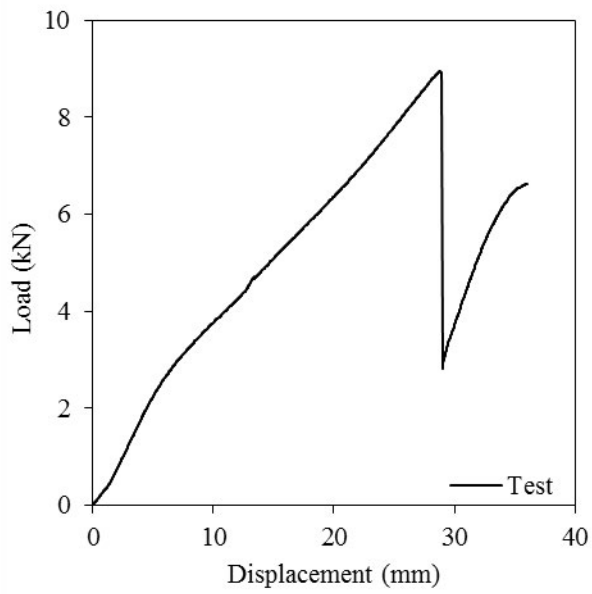


(a) Load-deflection curve

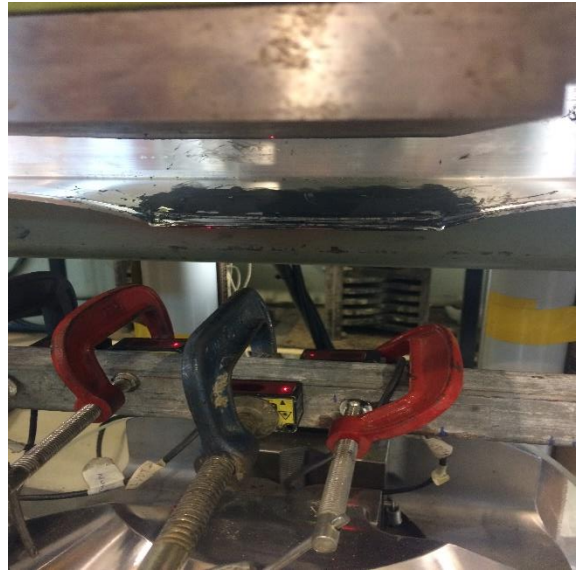


(b) Failure mode

B.1.4.5. 475-071/1B/15/150a

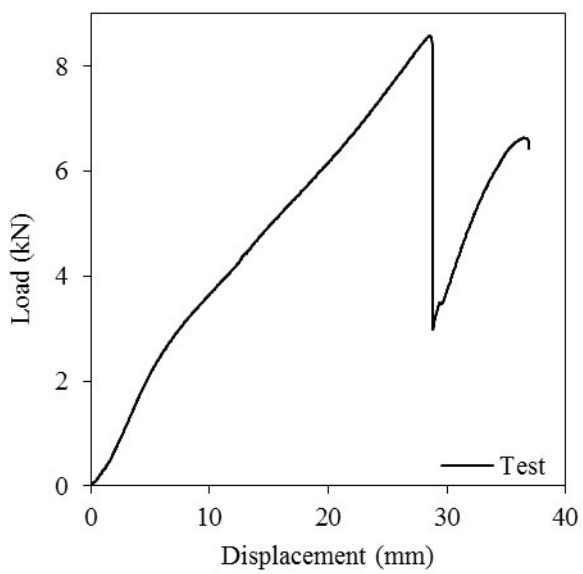


(a) Load-deflection curve



(b) Failure mode

B.1.4.6. 475-071/1B/15/150b

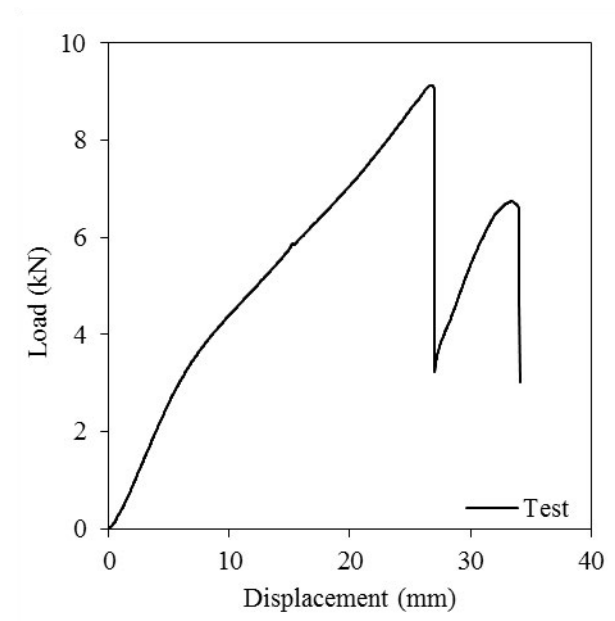


(a) Load-deflection curve

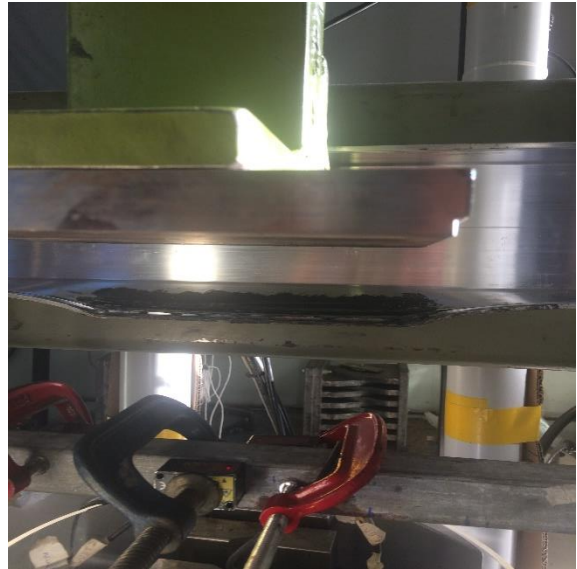


(b) Failure mode

B.1.4.7. 475-071/1B/15/200a

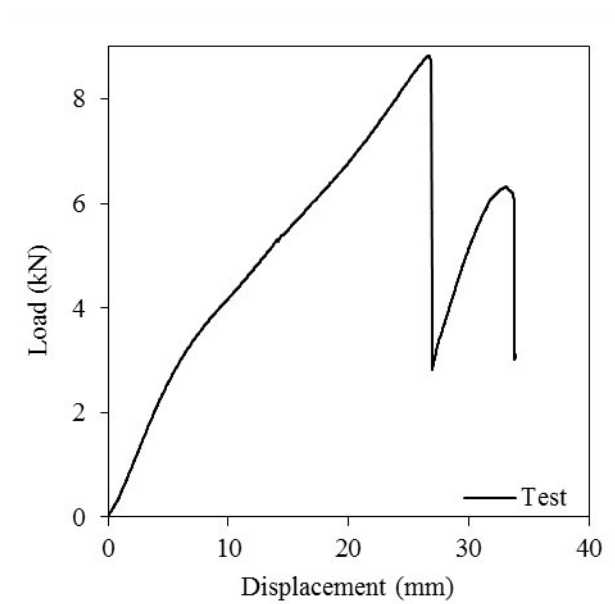


(c) Load-deflection curve

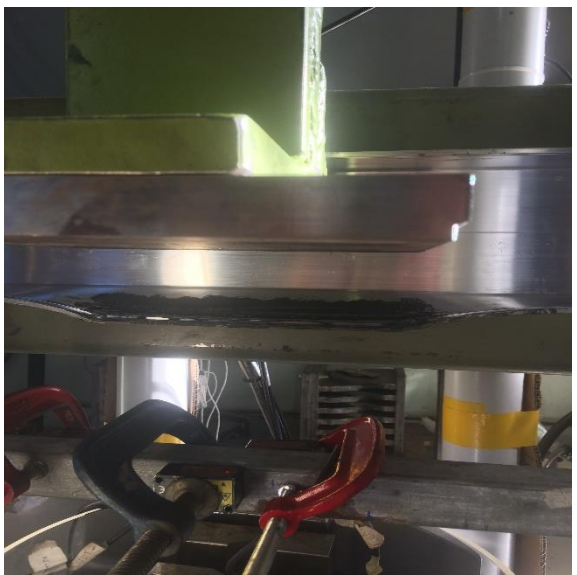


(b) Failure mode

B.1.4.8. 475-071/1B/15/200b

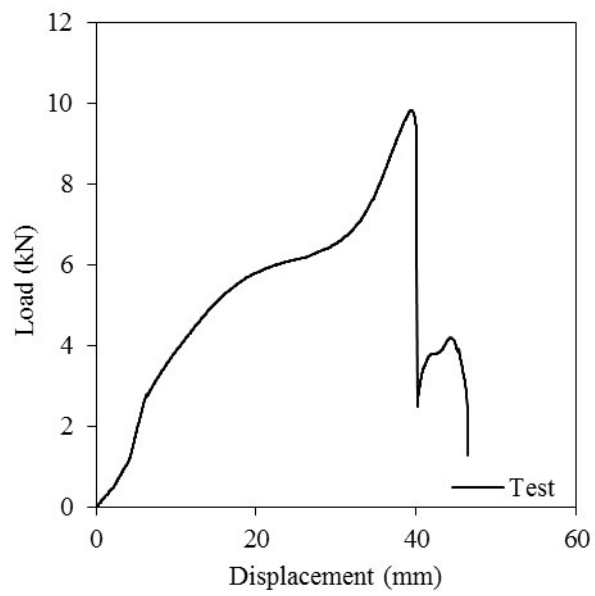


(a) Load-deflection curve



(b) Failure mode

B.1.4.9. 475-071/1B/25/50a

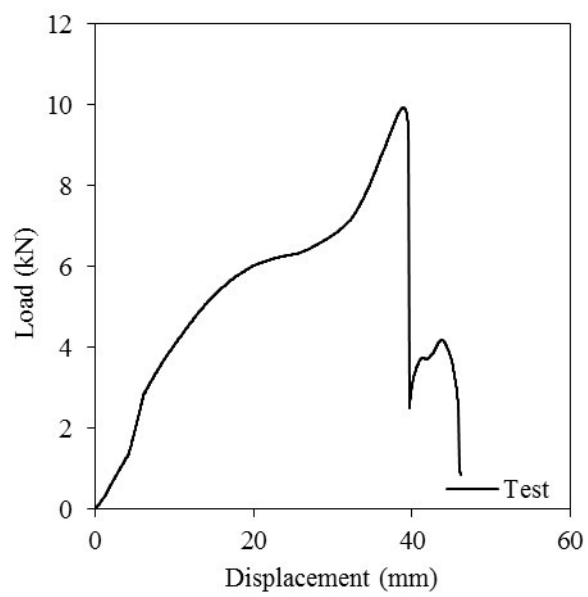


(a) Load-deflection curve

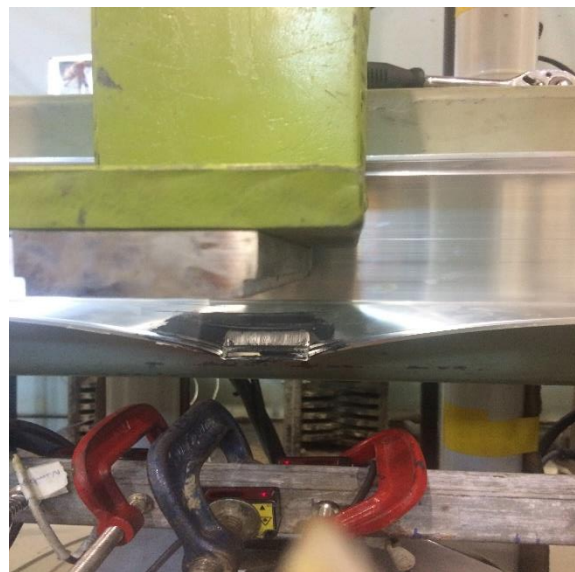


(b) Failure mode

B.1.4.10. 475-071/1B/25/50b

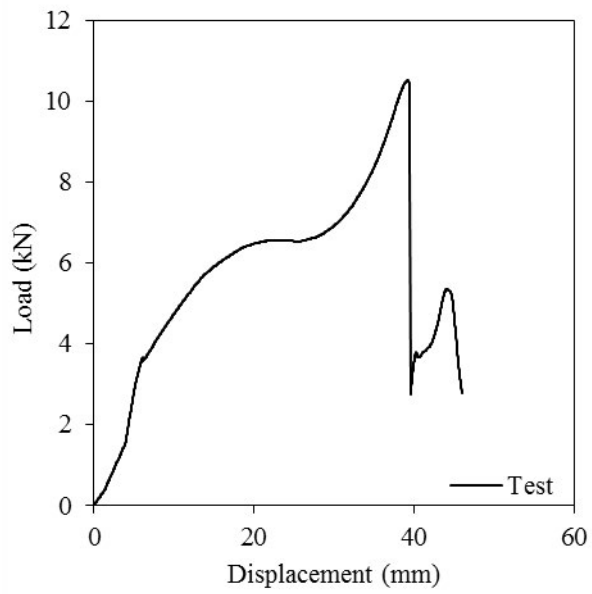


(a) Load-deflection curve



(b) Failure mode

B.1.4.11. 475-071/1B/25/100a

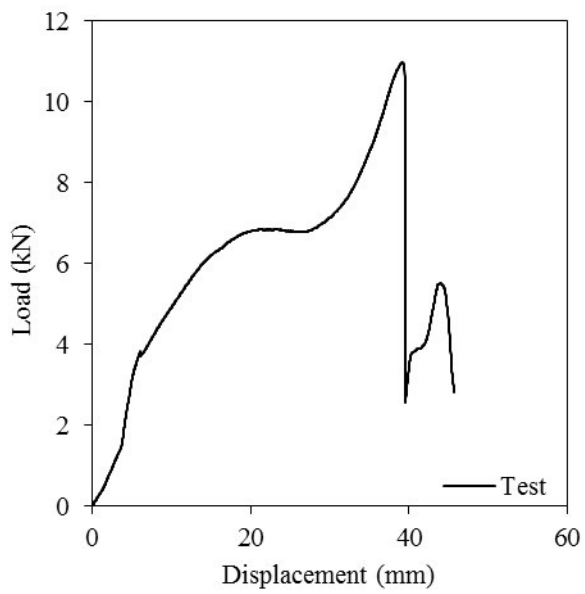


(a) Load-deflection curve



(b) Failure mode

B.1.4.12. 475-071/1B/25/100b

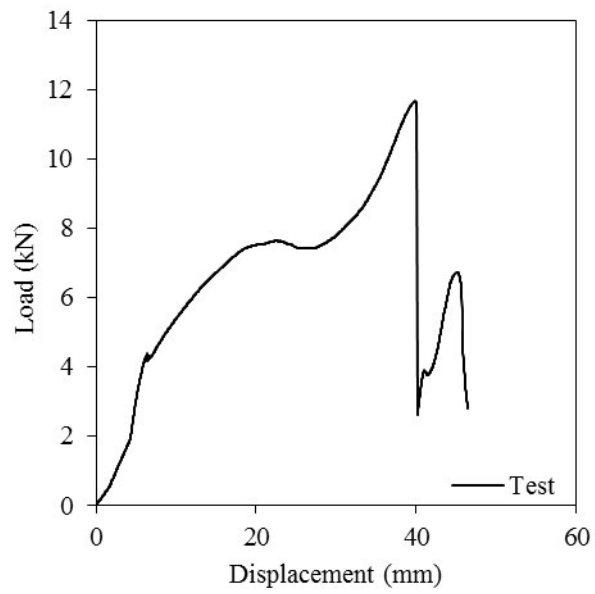


(a) Load-deflection curve

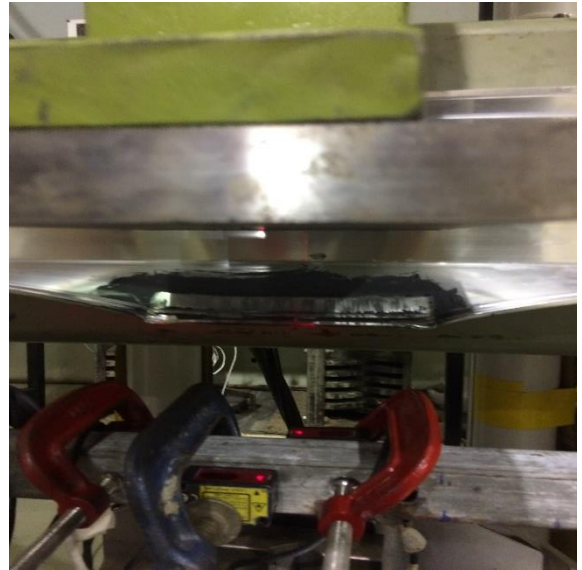


(b) Failure mode

B.1.4.13. 475-071/1B/25/150a

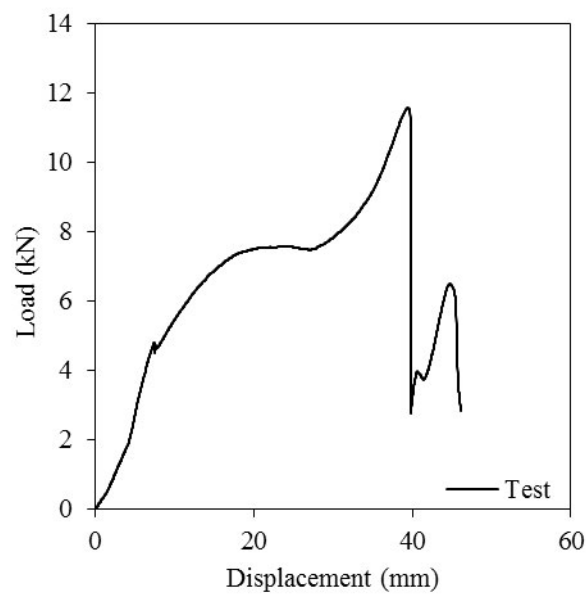


(a) Load-deflection curve



(b) Failure mode

B.1.4.14. 475-071/1B/25/150b

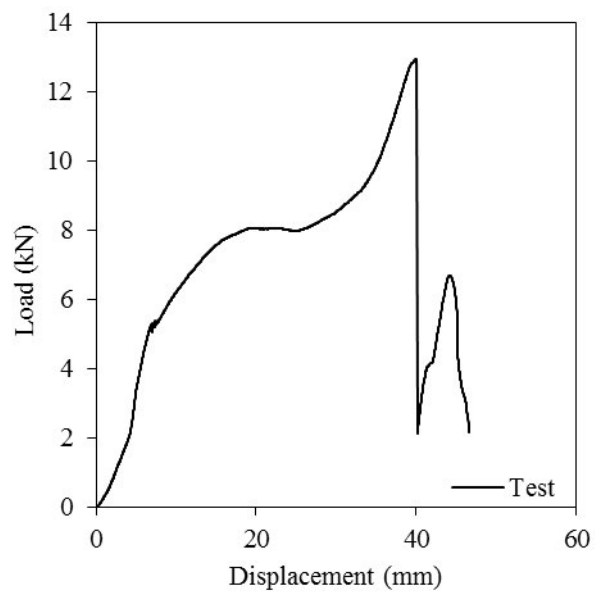


(a) Load-deflection curve



(b) Failure mode

B.1.4.15. 475-071/1B/25/200a

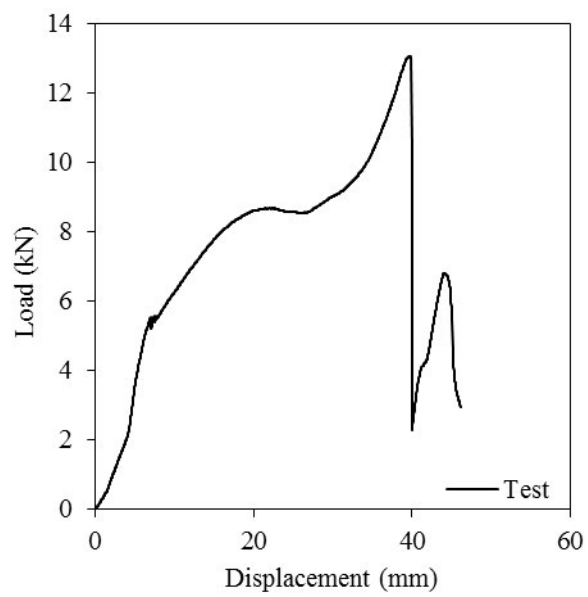


(a) Load-deflection curve



(b) Failure mode

B.1.4.16. 475-071/1B/25/200b

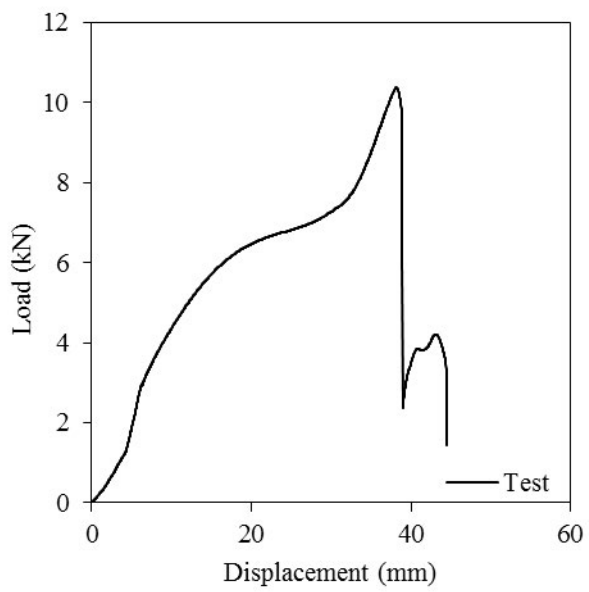


(a) Load-deflection curve



(b) Failure mode

B.1.4.17. 475-071/2B/25/50a

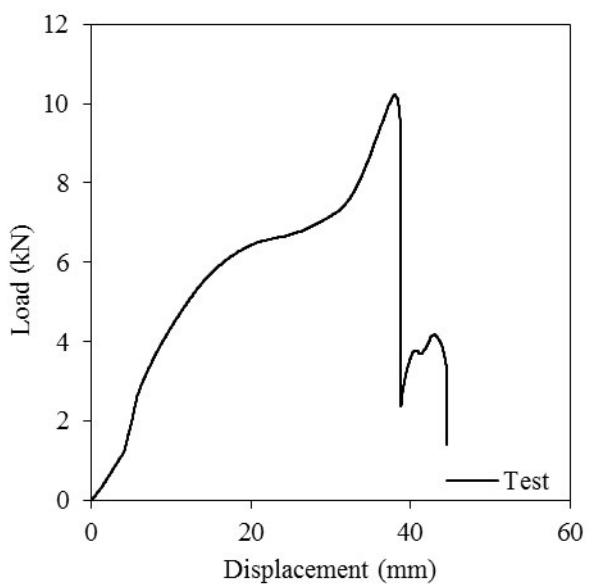


(a) Load-deflection curve



(b) Failure mode

B.1.4.18. 475-071/2B/25/50b

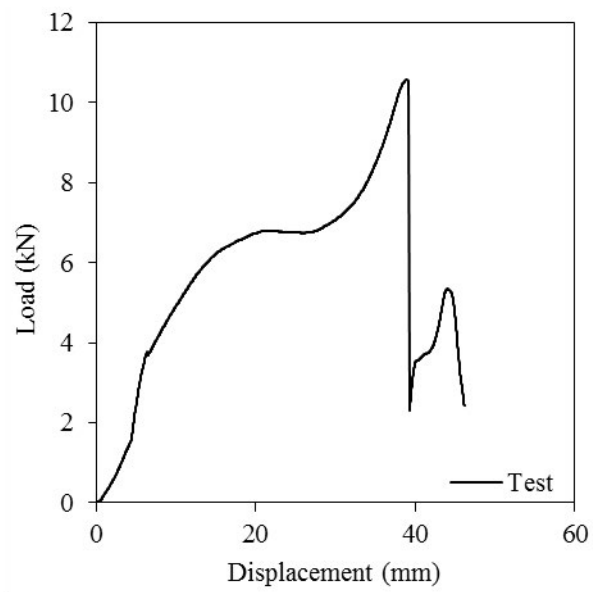


(a) Load-deflection curve

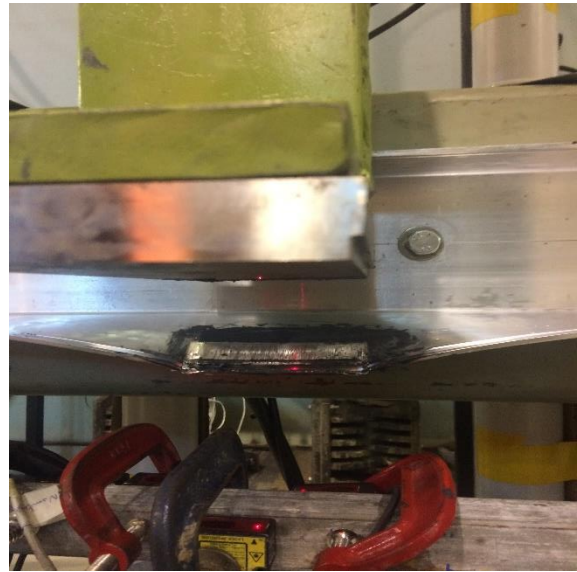


(b) Failure mode

B.1.4.19. 475-071/2B/25/100a

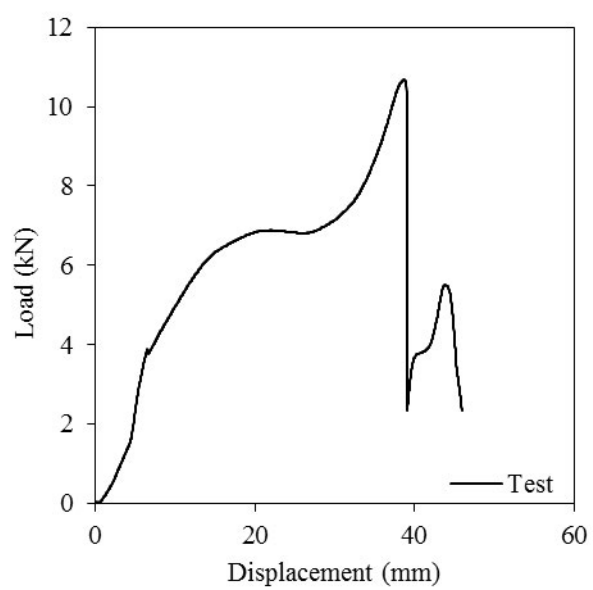


(b) Load-deflection curve



(b) Failure mode

B.1.4.20. 475-071/2B/25/100b

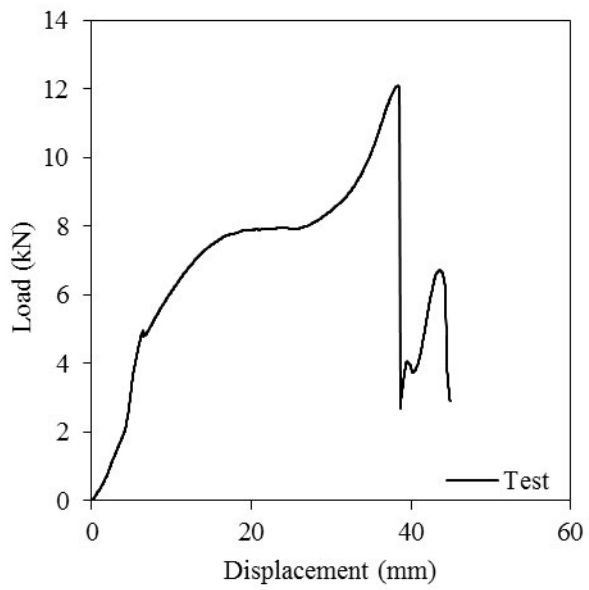


(a) Load-deflection curve



(b) Failure mode

B.1.4.21. 475-071/2B/25/150a

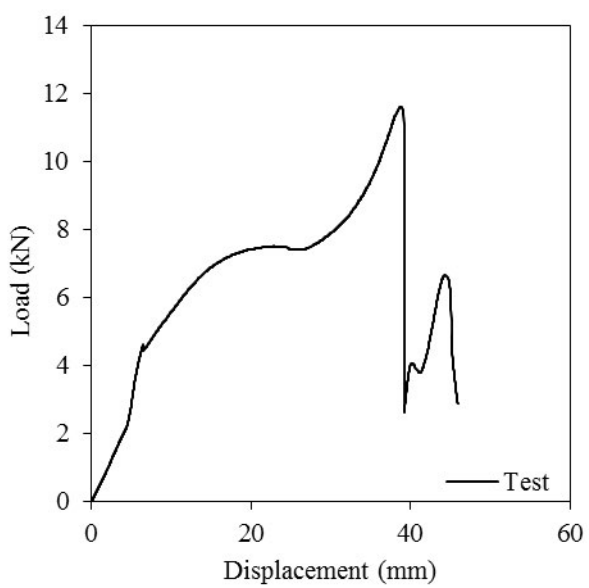


(a) Load-deflection curve



(b) Failure mode

B.1.4.22. 475-071/2B/25/150b

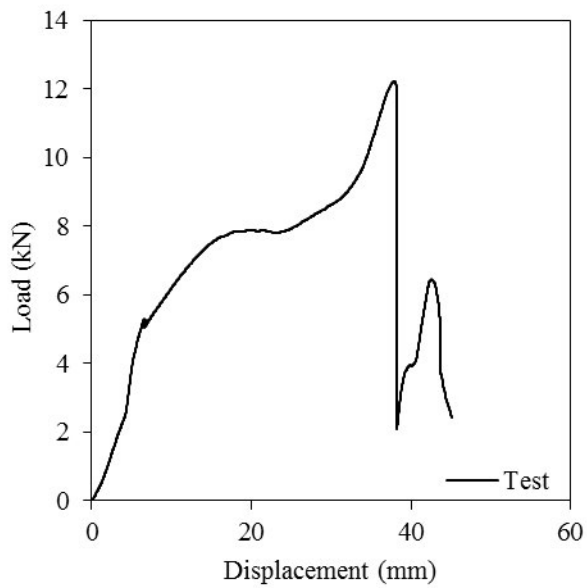


(a) Load-deflection curve



(b) Failure mode

B.1.4.23. 475-071/2B/25/200



(a) Load-deflection curve

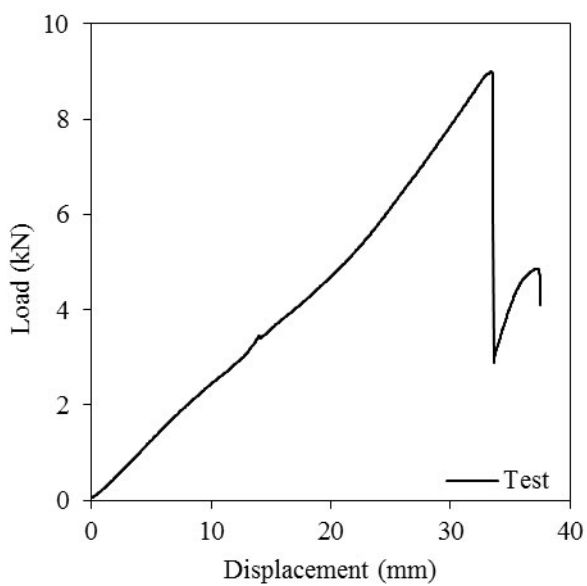


(b) Failure mode

B.2. Sub-heads with removable beads

B.2.1. 675028-475073

B.2.1.1. 675028-475073/1B/15/50

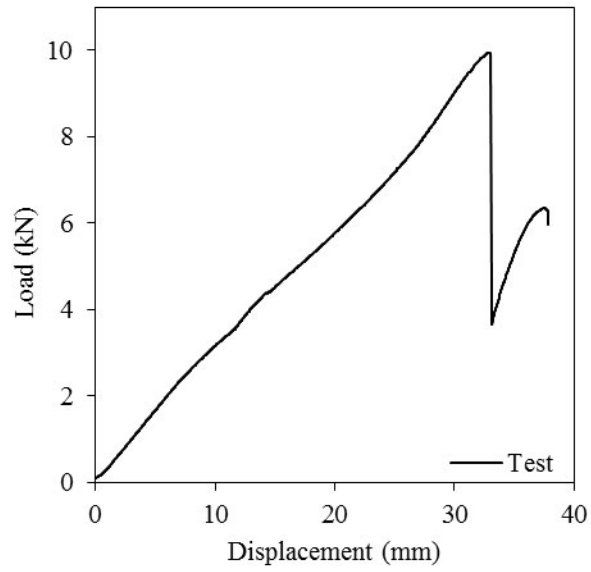


(a) Load-deflection curve



(b) Failure mode

B.2.1.2. 675028-475073/1B/15/100a

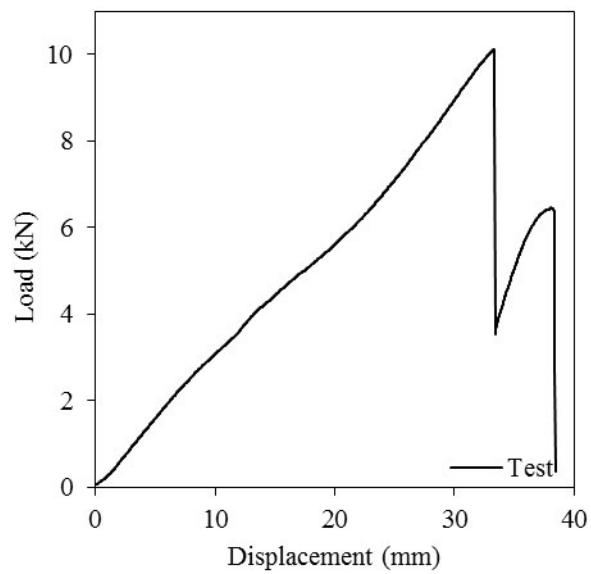


(a) Load-deflection curve



(b) Failure mode

B.2.1.3. 675028-475073/1B/15/100b

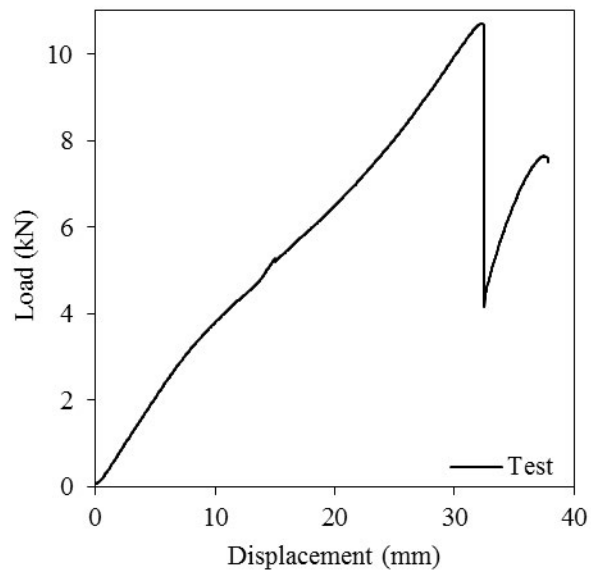


(a) Load-deflection curve



(b) Failure mode

B.2.1.4. 675028-475073/1B/15/150

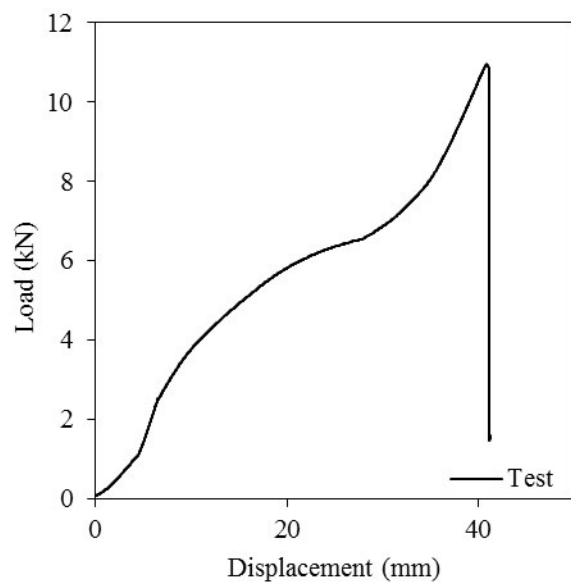


(a) Load-deflection curve

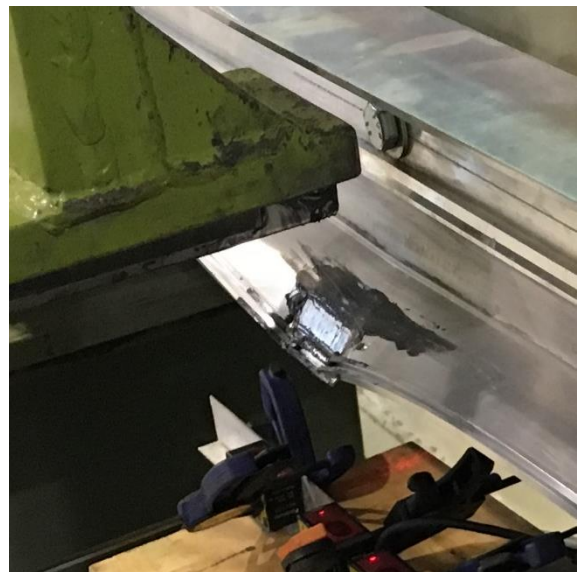


(b) Failure mode

B.2.1.5. 675028-475073/1B/25/50

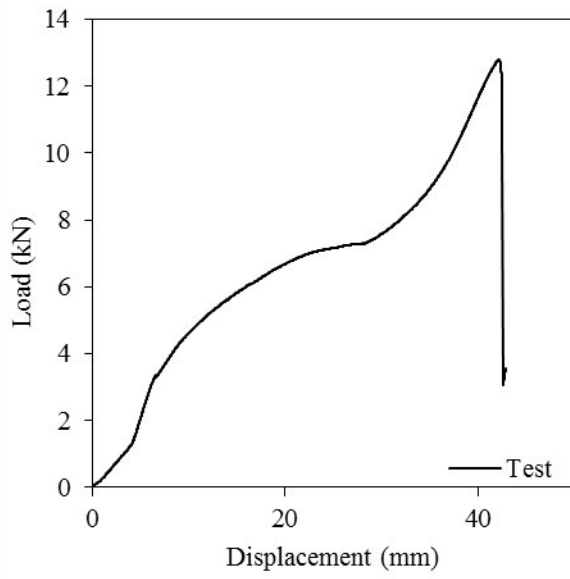


(a) Load-deflection curve



(b) Failure mode

B.2.1.6. 675028-475073/1B/25/100a

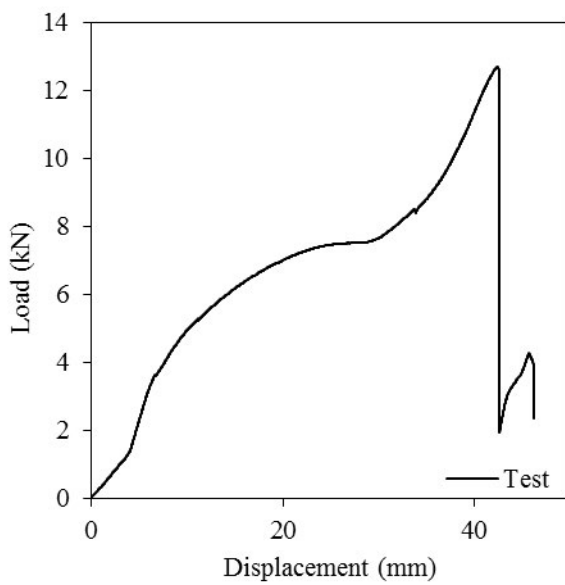


(a) Load-deflection curve



(b) Failure mode

B.2.1.7. 675028-475073/1B/25/100b

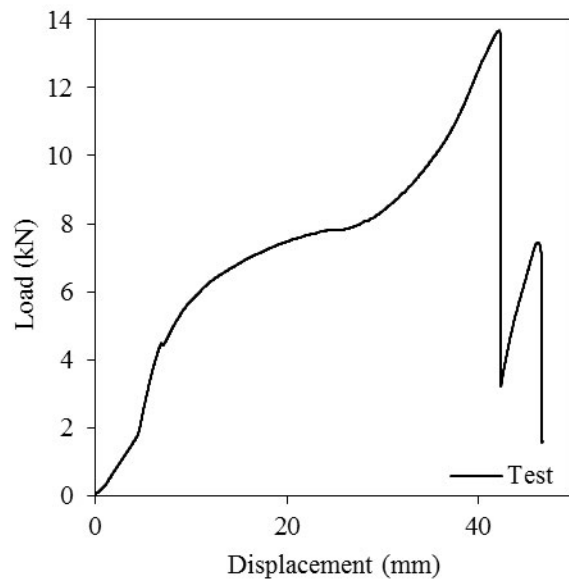


(a) Load-deflection curve



(b) Failure mode

B.2.1.8. 675028-475073/1B/25/150



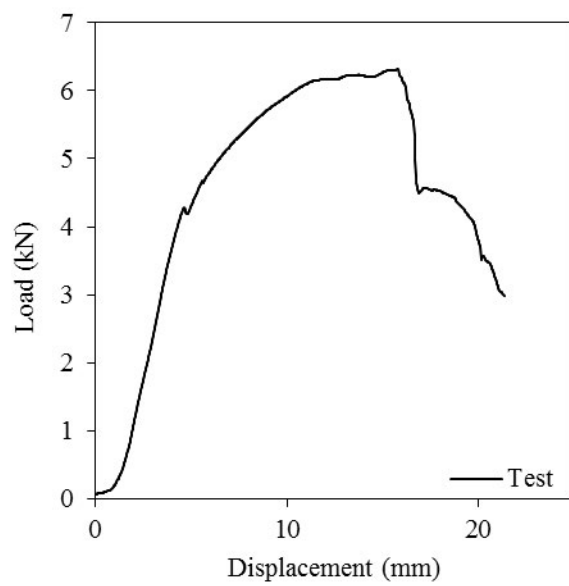
(a) Load-deflection curve



(b) Failure mode

B.2.2. 475066-165863

B.2.2.1. 475066-165863/1B/15/50

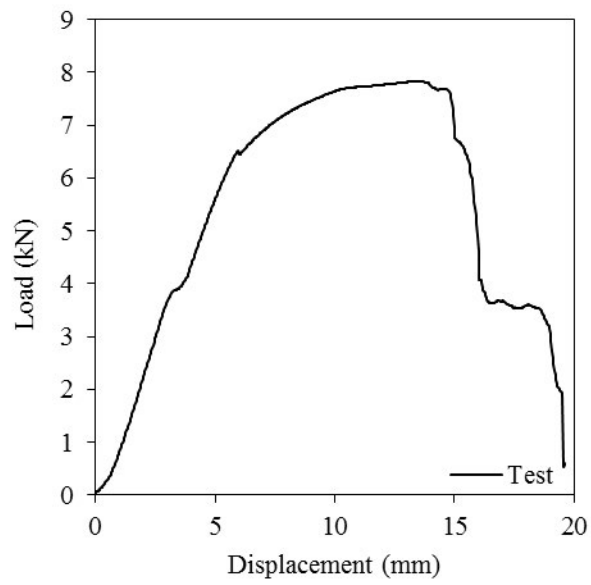


(a) Load-deflection curve



(b) Failure mode

B.2.2.2. 475066-165863/1B/15/100a

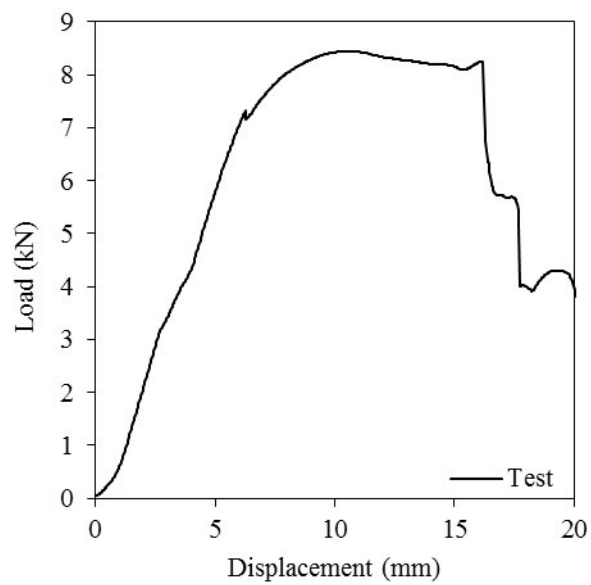


(a) Load-deflection curve



(b) Failure mode

B.2.2.3. 475066-165863/1B/15/100b

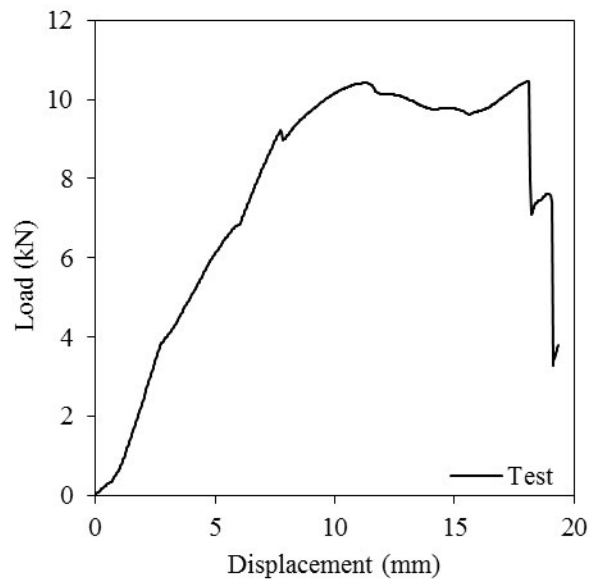


(a) Load-deflection curve



(b) Failure mode

B.2.2.4. 475066-165863/1B/15/150

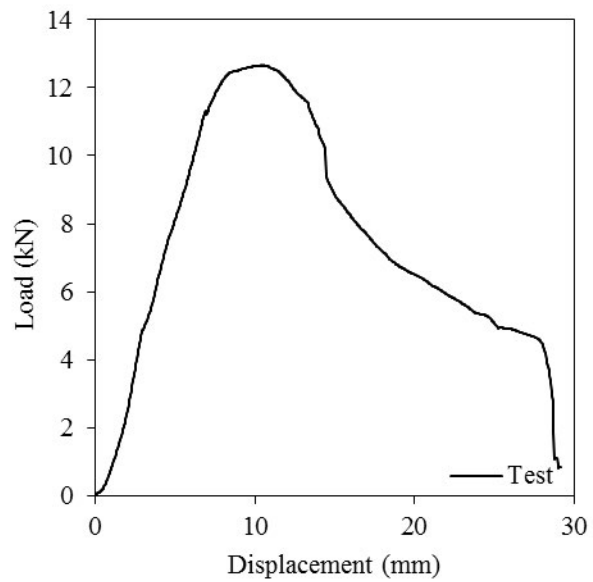


(a) Load-deflection curve

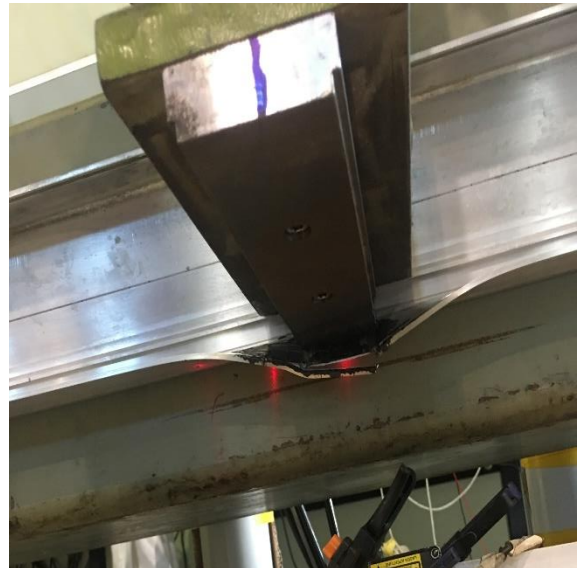


(b) Failure mode

B.2.2.5. 475066-165863/1B/25/50

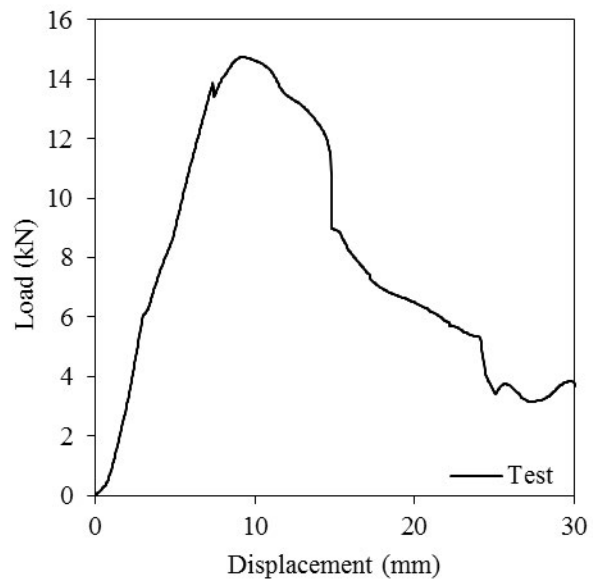


(a) Load-deflection curve



(b) Failure mode

B.2.2.6. 475066-165863/1B/25/100a

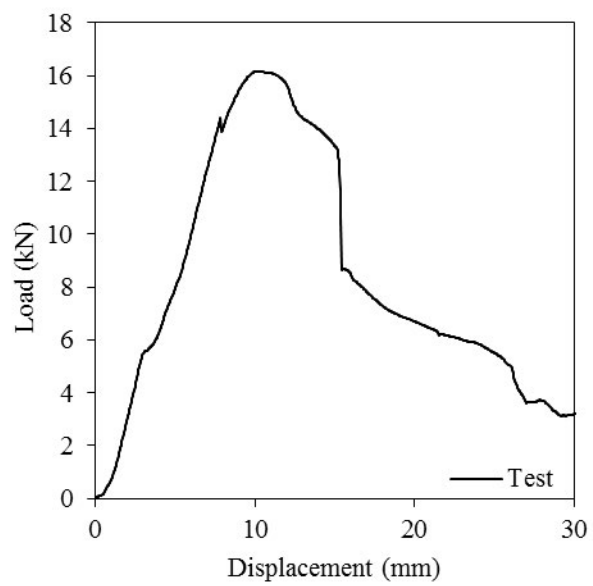


(a) Load-deflection curve



(b) Failure mode

B.2.2.7. 475066-165863/1B/25/100b

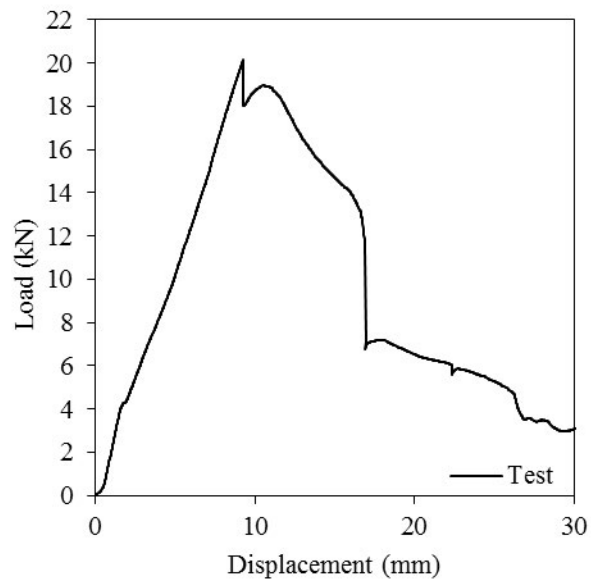


(a) Load-deflection curve



(b) Failure mode

B.2.2.8. 475066-165863/1B/25/150



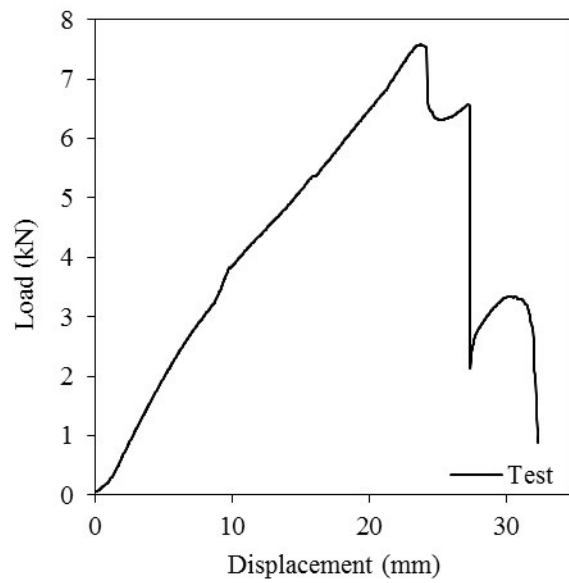
(a) Load-deflection curve



(b) Failure mode

B.2.3. 475059-520902

B.2.3.1. 475059-520902/1B/15/50

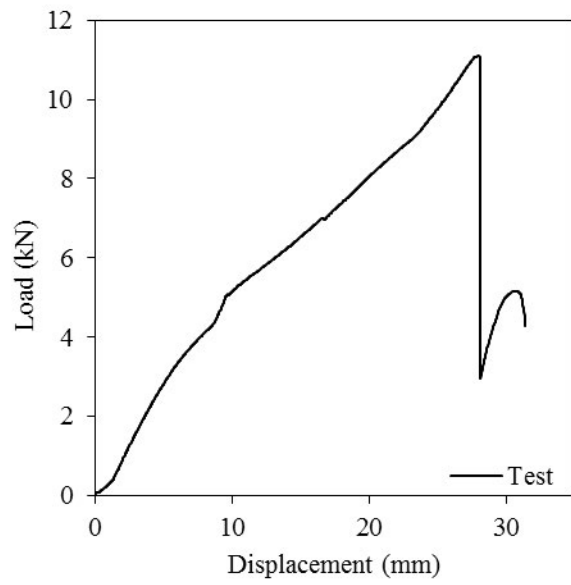


(a) Load-deflection curve



(b) Failure mode

B.2.3.2. 475059-520902/1B/15/100a

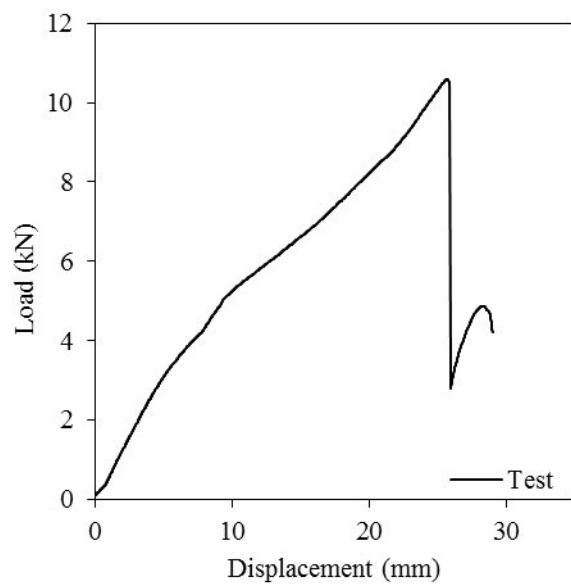


(a) Load-deflection curve



(b) Failure mode

B.2.3.3. 475059-520902/1B/15/100b

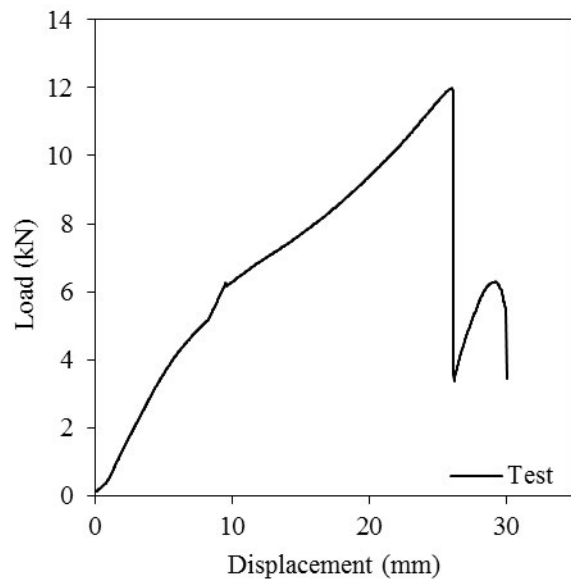


(a) Load-deflection curve



(b) Failure mode

B.2.3.4. 475059-520902/1B/15/150

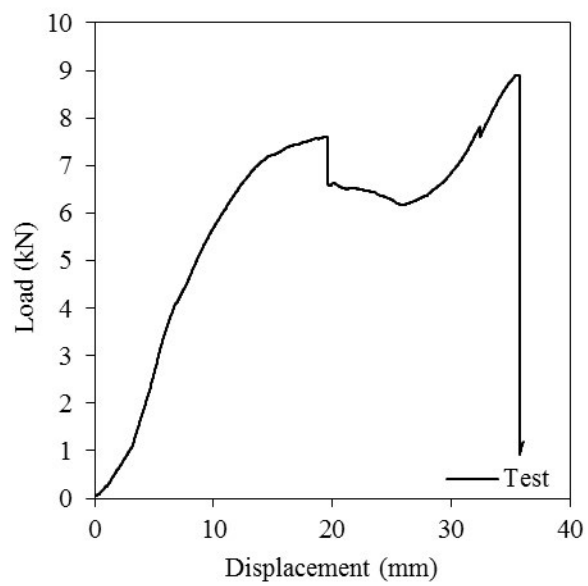


(a) Load-deflection curve



(b) Failure mode

B.2.3.5. 475059-520902/1B/25/50

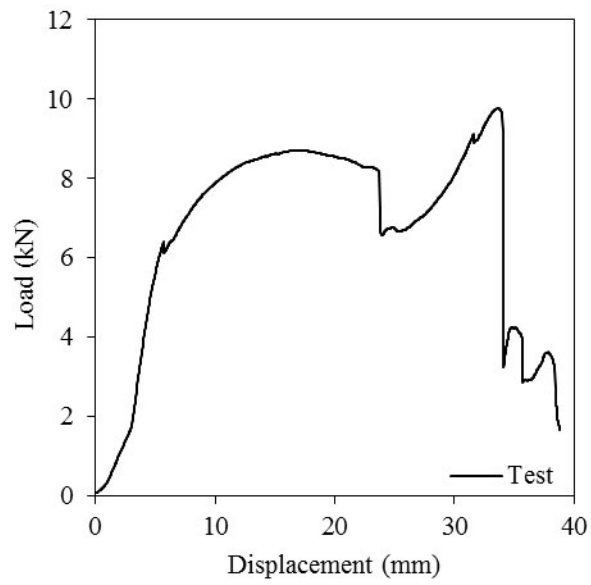


(a) Load-deflection curve



(b) Failure mode

B.2.3.6. 475059-520902/1B/25/100a

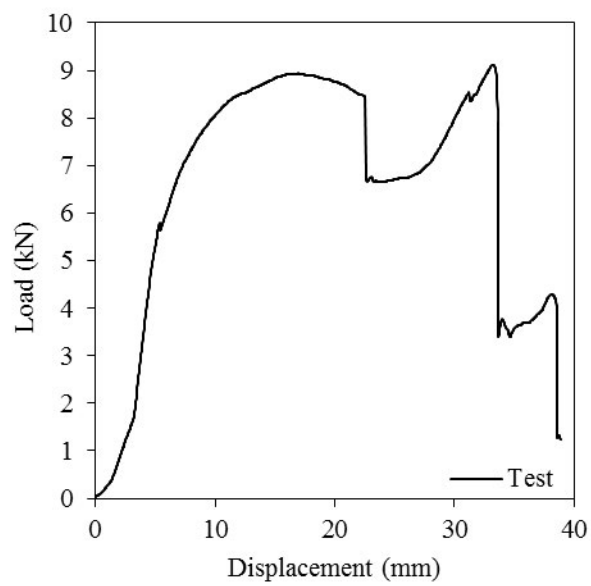


(a) Load-deflection curve



(b) Failure mode

B.2.3.7. 475059-520902/1B/25/100b

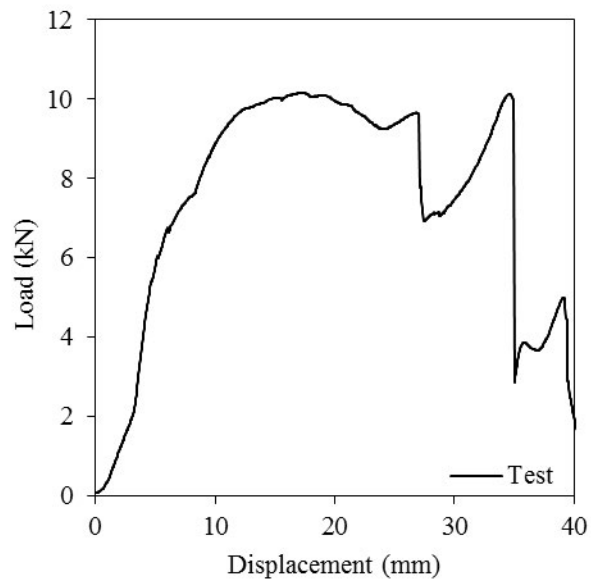


(a) Load-deflection curve



(b) Failure mode

B.2.3.8. 475059-520902/1B/25/150



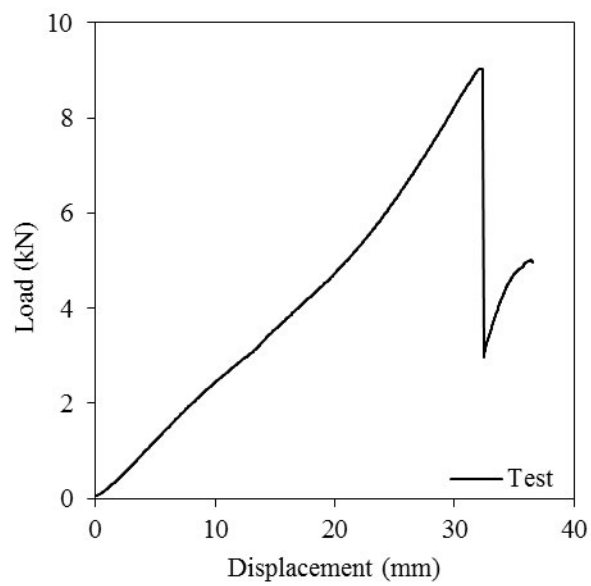
(a) Load-deflection curve



(b) Failure mode

B.2.4. 875103-475073

B.2.4.1. 875103-475073/1B/15/50

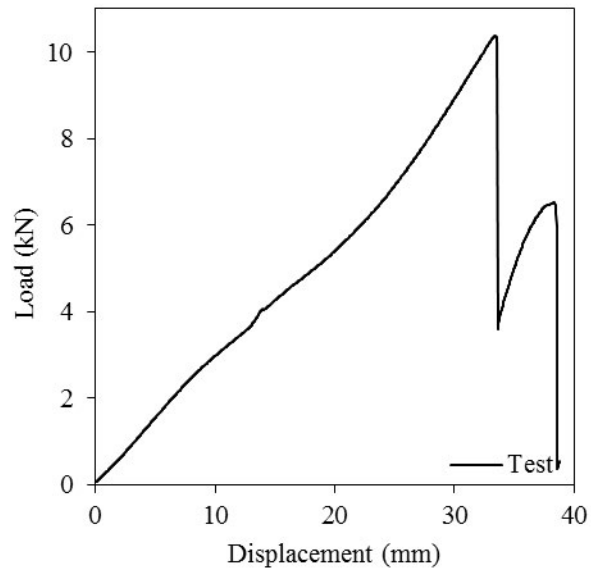


(a) Load-deflection curve



(b) Failure mode

B.2.4.2. 875103-475073/1B/15/100a

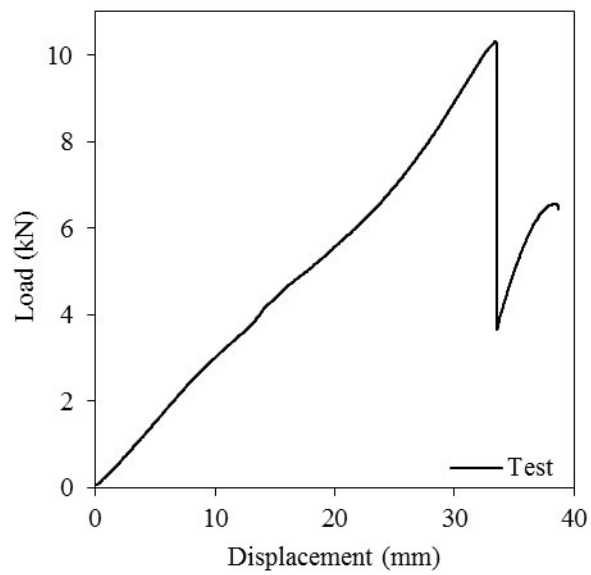


(a) Load-deflection curve



(b) Failure mode

B.2.4.3. 875103-475073/1B/15/100b

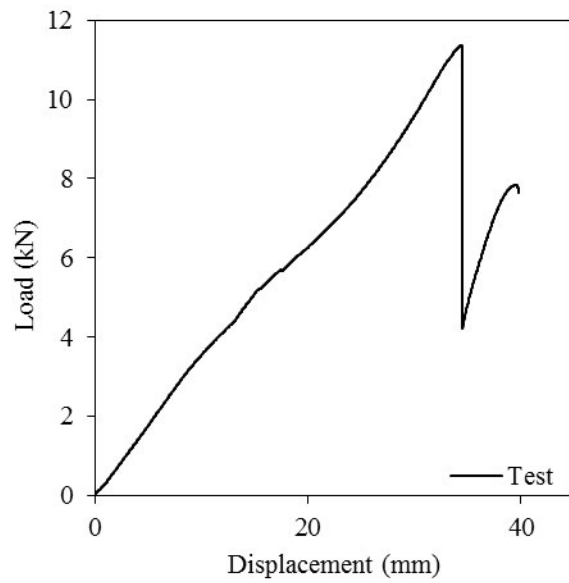


(a) Load-deflection curve

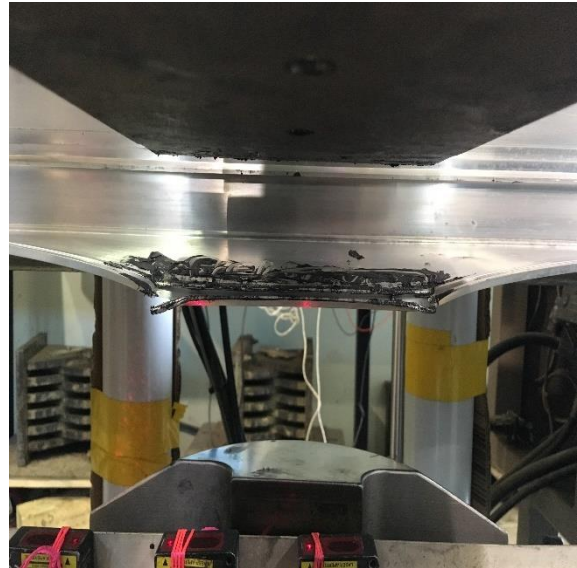


(b) Failure mode

B.2.4.4. 875103-475073/1B/15/150

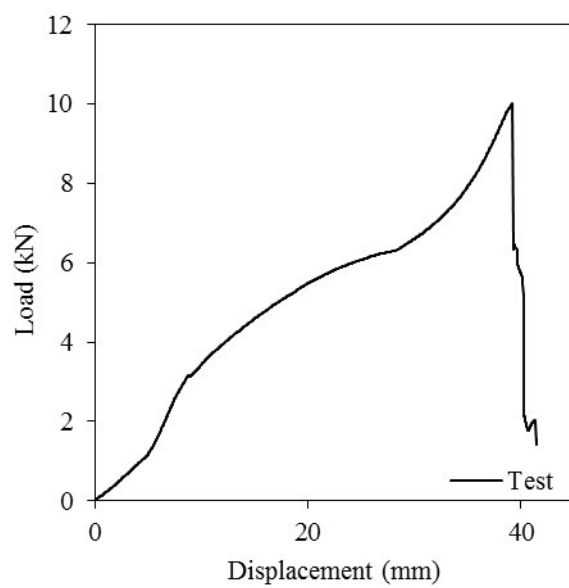


(a) Load-deflection curve



(b) Failure mode

B.2.4.5. 875103-475073/1B/25/50

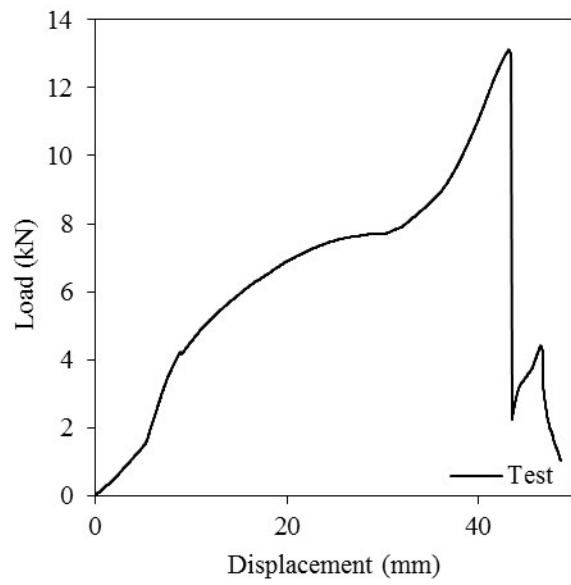


(a) Load-deflection curve



(b) Failure mode

B.2.4.6. 875103-475073/1B/25/100a

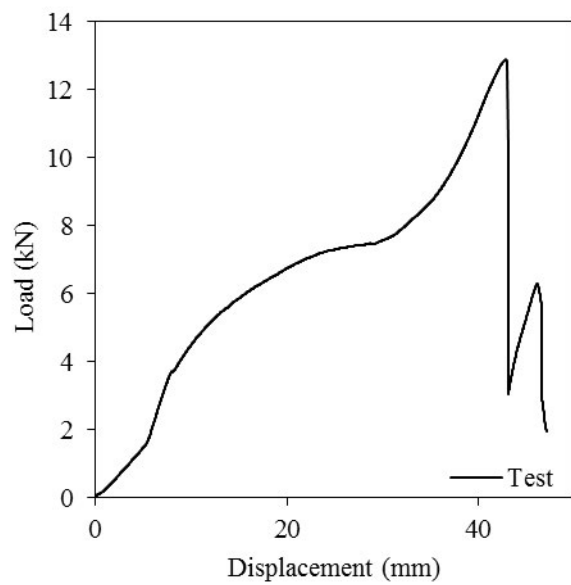


(a) Load-deflection curve



(b) Failure mode

B.2.4.7. 875103-475073/1B/25/100b

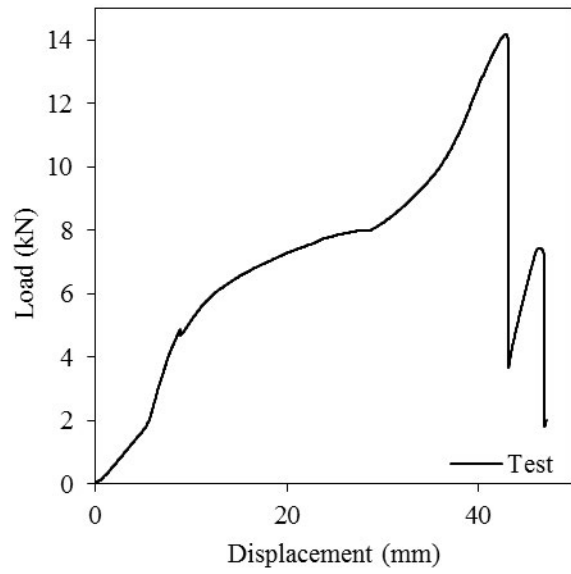


(a) Load-deflection curve



(b) Failure mode

B.2.4.8. 875103-475073/1B/25/150



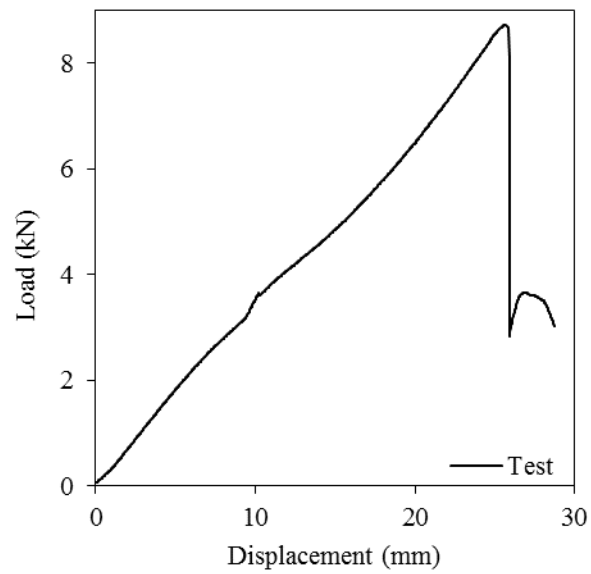
(a) Load-deflection curve



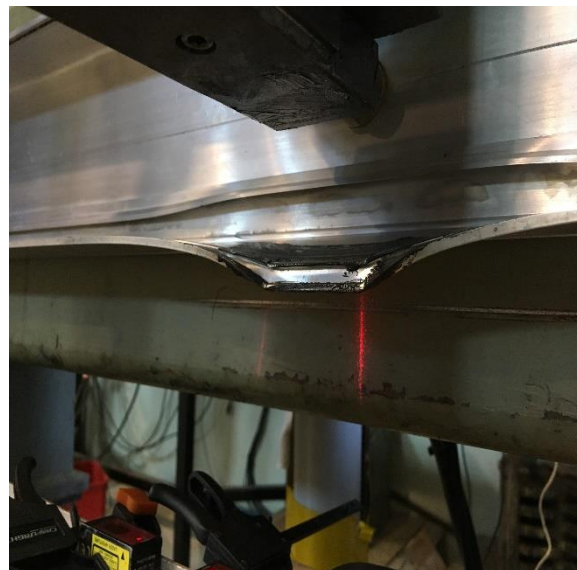
(b) Failure mode

B.2.5. 675019-520902

B.2.5.1 675019-520902/1B/15/50

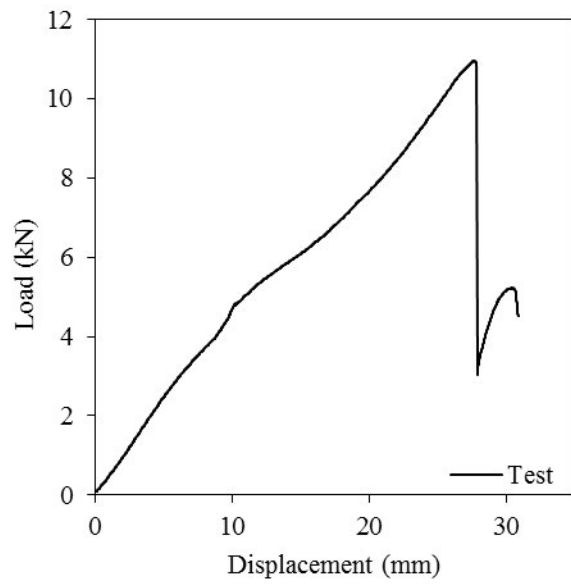


(a) Load-deflection curve

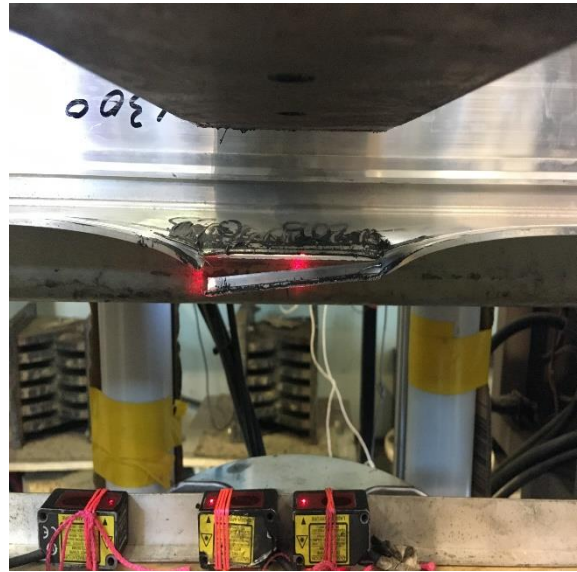


(b) Failure mode

B.2.5.2. 675019-520902/1B/15/100

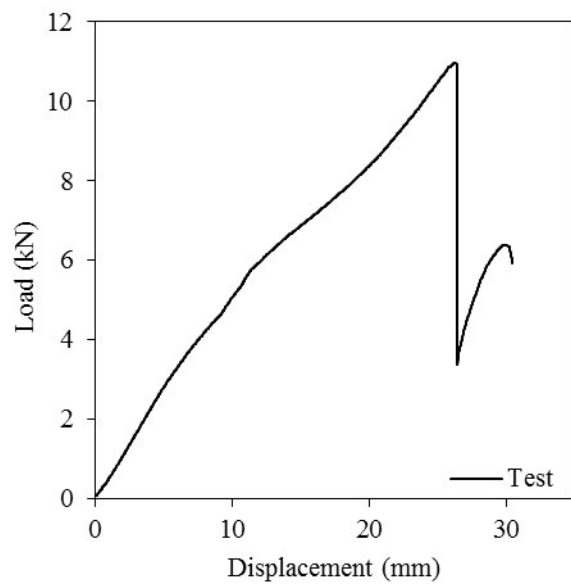


(a) Load-deflection curve

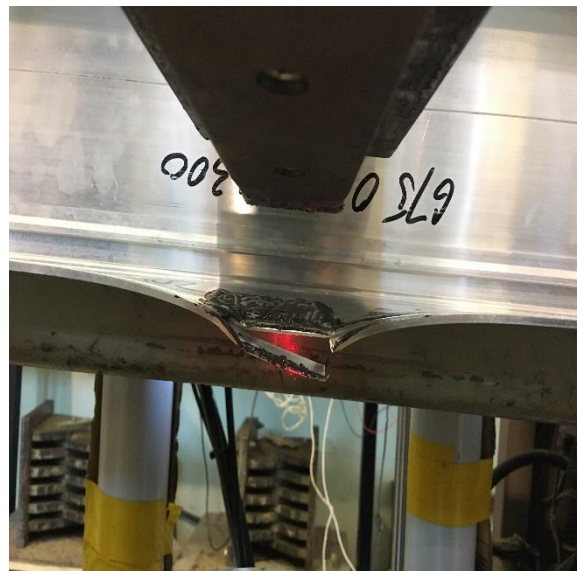


(b) Failure mode

B.2.5.3. 675019-520902/1B/15/150

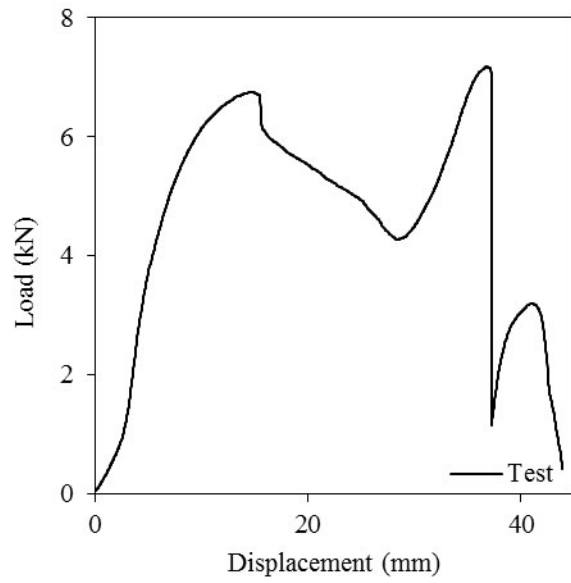


(a) Load-deflection curve



(b) Failure mode

B.2.5.4. 675019-520902/1B/25/50

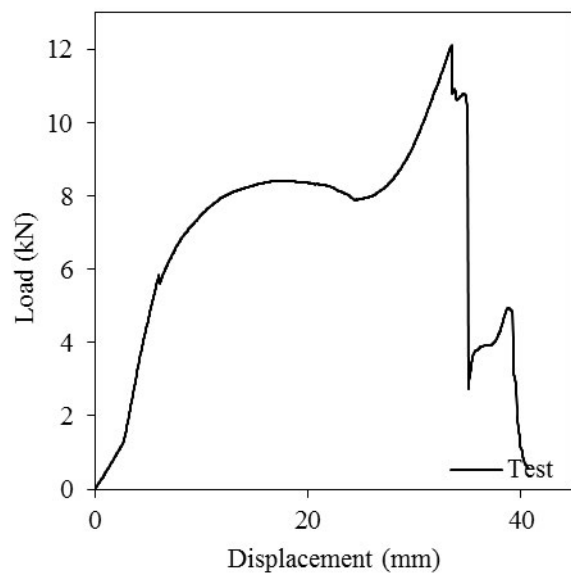


(a) Load-deflection curve



(b) Failure mode

B.2.5.5. 675019-520902/1B/25/100

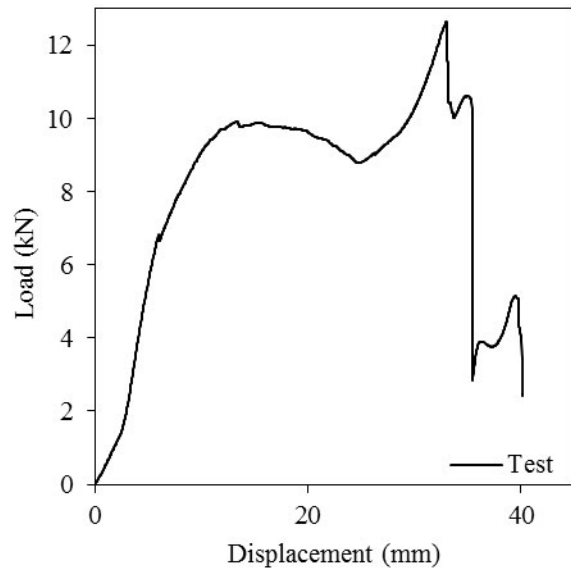


(a) Load-deflection curve



(b) Failure mode

B.2.5.6. 675019-520902/1B/25/150



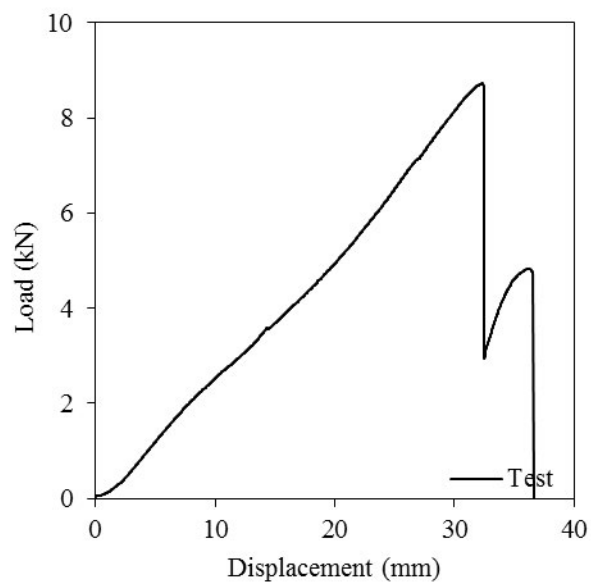
(a) Load-deflection curve



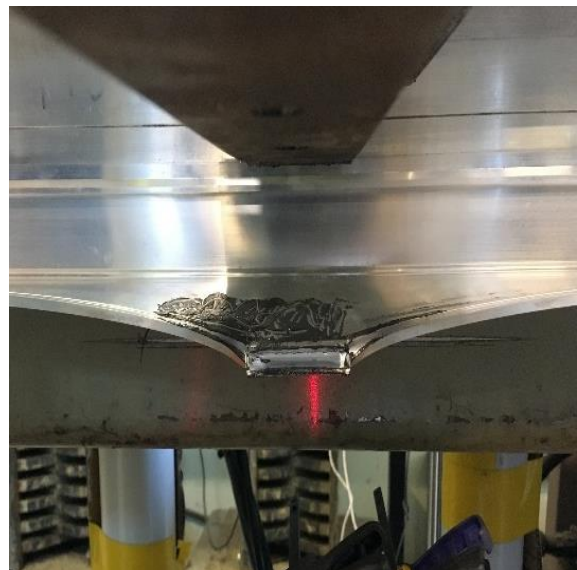
(b) Failure mode

B.2.6. 475072-475073

B.2.6.1. 475072-475073/1B/15/50

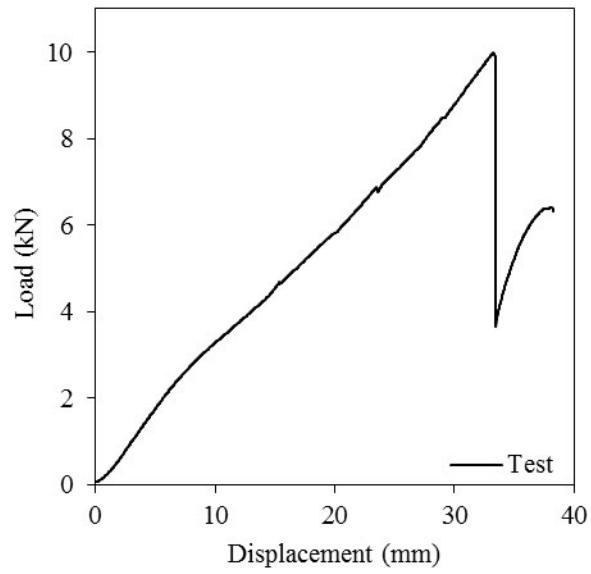


(a) Load-deflection curve

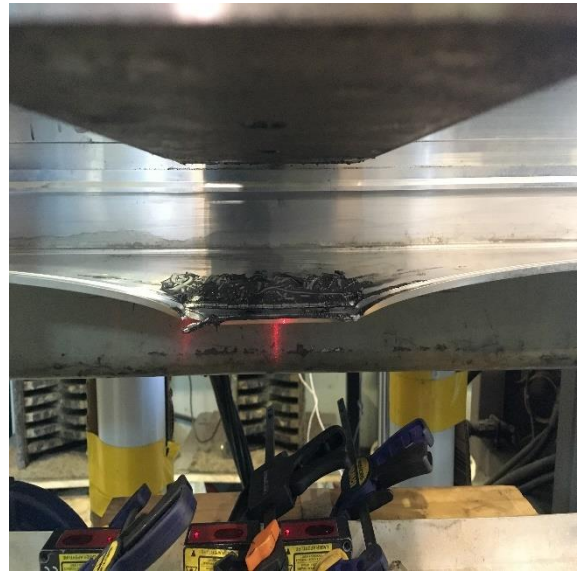


(b) Failure mode

B.2.6.2. 475072-475073/1B/15/100a

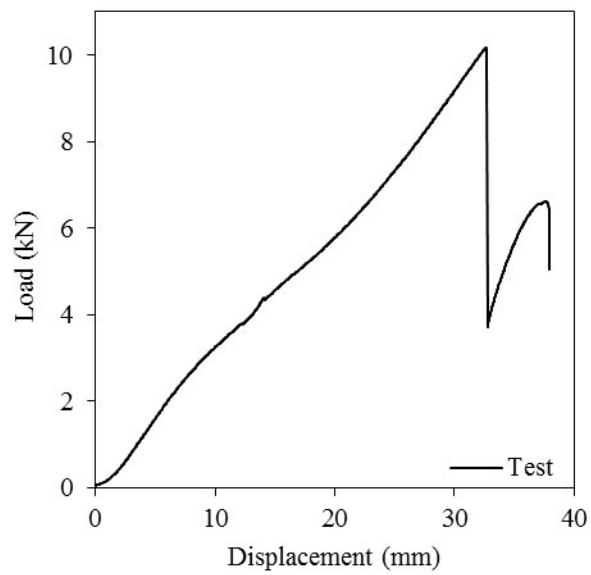


(a) Load-deflection curve

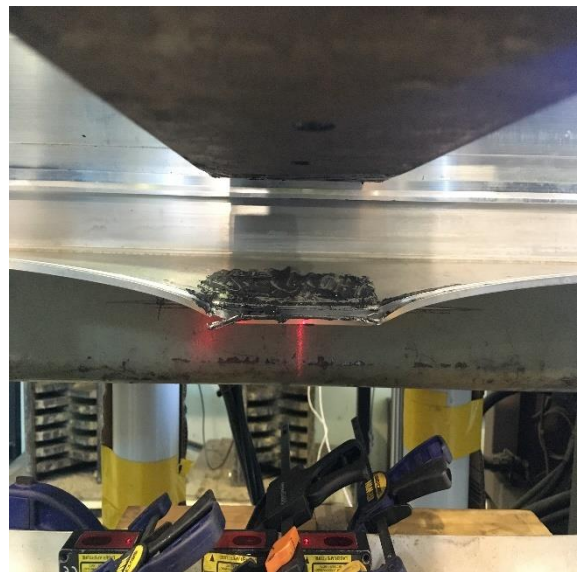


(b) Failure mode

B.2.6.3. 475072-475073/1B/15/100b

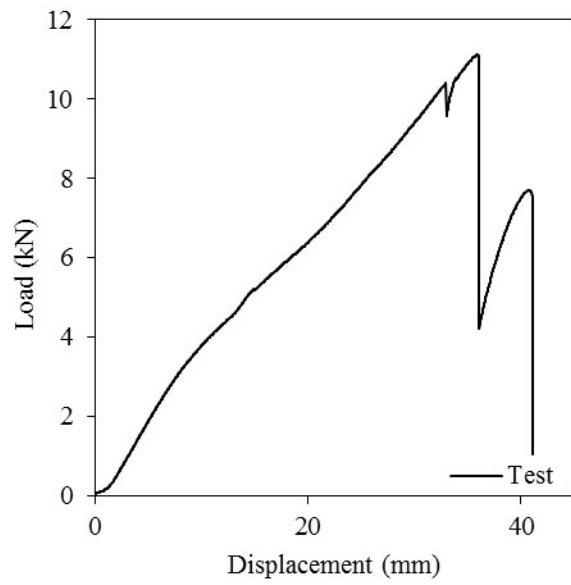


(a) Load-deflection curve



(b) Failure mode

B.2.6.4. 475072-475073/1B/15/150

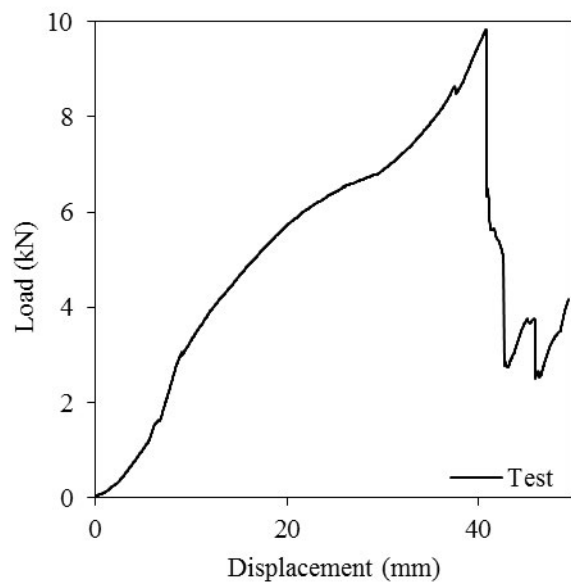


(a) Load-deflection curve



(b) Failure mode

B.2.6.5. 475072-475073/1B/25/50

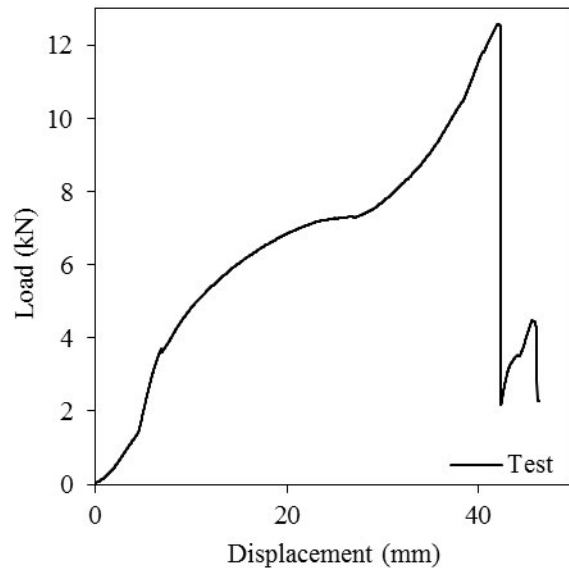


(a) Load-deflection curve

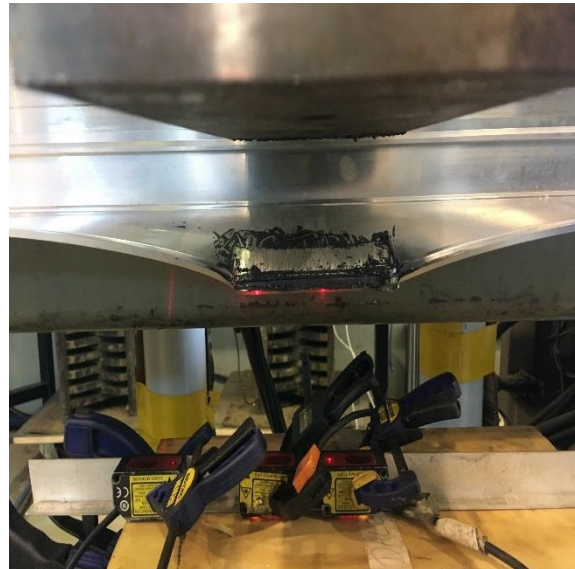


(b) Failure mode

B.2.6.6. 475072-475073/1B/25/100a

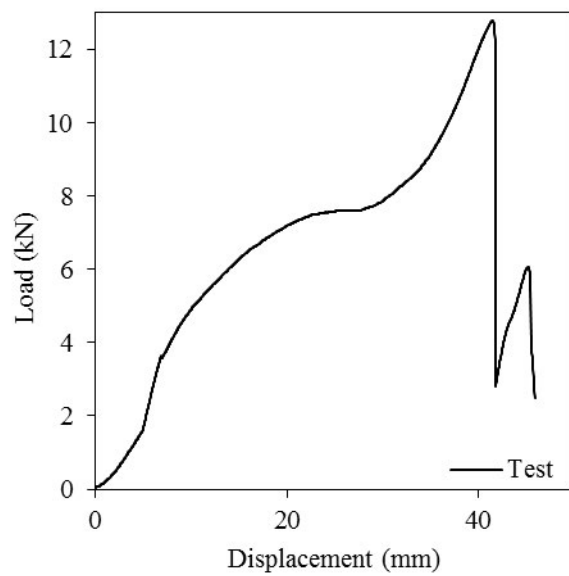


(a) Load-deflection curve



(b) Failure mode

B.2.6.7. 475072-475073/1B/25/100b

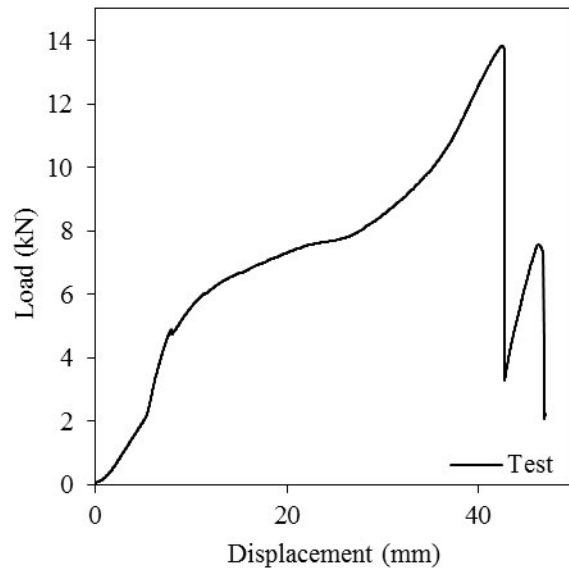


(a) Load-deflection curve

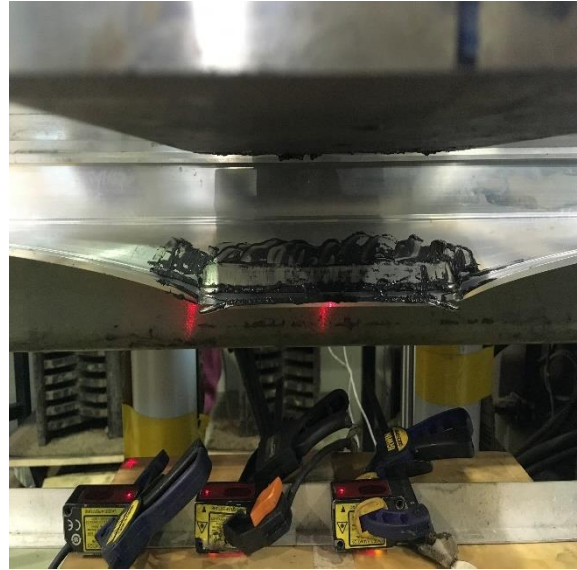


(b) Failure mode

B.2.6.8. 475072-475073/1B/25/150



(a) Load-deflection curve



(b) Failure mode